eli

EUROPEAN UNION

Project co-financed by the European Regional Development Fund through the Competitiveness Operational Programme "Investing in Sustainable Development"

Extreme Light Infrastructure-Nuclear Physics (ELI-NP) - Phase II

LASER POWER ELI NP

Annual Report 2020 2021

EXTREME LIGHT INFRASTRUCTURE

WWW.ELI-NP.RO

Editor-in-Chief: Klaus Michael Spohr
Coordinating Editors for all Groups: Ioan Dancus (LSD), Guanling Chen (GSD), Klaus Michael Spohr (LDED), Violeta Iancu (GDED), Stefan Ataman (LGED), Adrian Mihai Vodă (BBA), and Victor Leca (TL)

This work is supported by Extreme Light Infrastructure - Nuclear Physics (ELI-NP) Phase II, a project co-financed by the Romanian Government and by the European Regional Development Fund the Competitiveness Operational Programme (1/07.07.2016, COP, ID 261 1334). Additional funding sources are mentioned if relevant.

Final Release, 6th of June 2022

Contents

Introduction

THE EXTREME LIGHT INFRASTRUCTURE - NUCLEAR PHYSICS (ELI-NP) is part of a pan-European project with the same name. The ELI-NP project is implemented in Măgurele, Romania, by the "Horia Hulubei" National Institute of Physics and Nuclear Engineering and it is co-funded by the European Commission through the European Regional Development Fund (ERDF) and the Romanian Government.

ELI-NP aims to become one of the major research facilities worldwide in the field of high-power laser-driven nuclear physics by implementing two extreme systems with hitherto unprecedented characteristics: the high-power laser system (two beams of 10 PW at 825 nm central laser wavelength with around 225 J of maximum energy and a pulse width of ≤ 23 fs *and* the Variable Energy Gamma System (VEGA) providing a tunable gamma beam with energies between 1 MeV and 19.5 MeV with a bandwidth of $\leq 0.5\%$ at an expected intensity of $\approx 5 \times 10^3$ photons/eV/s.

In 2020 ELI-NP became the host of the most powerful laser system in the world. After the completion of the 2×10 PW laser system in 2019, the laser beam transport system at 10 PW power was commissioned in 2020. This achievement was made public on November 17$^{\text{th}}$, 2020, with a live demonstration of the 10 PW laser pulse generation and transport to the interaction chamber during the 'Inaugural 10 PW Laser and Users Symposium': *Moving into Unchartered Territories* that had more than 230 participants as live audience from all over the world. Among the distinguished scientists who witnessed the event were also the 2018 Nobel Prize Laureates Professor Gerard Mourou (IZEST, France) and Professor Donna Strickland (University of Waterloo, Canada). Their groundbreaking invention from 1985, the Chirped Pulse Amplification, is the core enabling technology that allowed to reach the unprecedented levels of laser power, thus paving the way for the ELI-NP project.
Following the commissioning of the 10 PW high-power laser system, we aim that all three laser power level installations (100 TW, 1 PW, and 10 PW) will be operating at maximum repetition frequencies for user access. The two 100 TW arms will be operating at a repetition frequency of $f = 10$ Hz those of the 1 PW installation at $f = 1$ Hz, and finally, the two 10 PW arms are aimed to run at 1 pulse/minute.

Recently, ELI-NP entered into a new phase, transitioning from implementation to operation, a core benchmark on the pathway to becoming a user facility. The very first milestone experiment at 100 TW power level was performed in March 2020. Since then, the commissioning of the experimental setups at 100 TW and 1 PW power levels was successfully performed to demonstrate laser-driven electron and proton acceleration. Moreover, preliminary work regarding dark matter research was conducted at the 100 PW beamline. Expert users from Japan, the USA, the UK, and Italy have participated in all commissioning campaigns. The ELI-NP International Scientific Advisory Board recommended and endorsed all these programs. Commissioning of the experimental setups at the 10 PW laser power will start in 2022 and will

extend up to the end of 2023.
As the commissioning experiments are concluded, the experimental setups will become gradually available for scientists worldwide, as ELI-NP will fulfill its core mission of becoming a 'User Facility'. Future user access will be granted based on scientific merit evaluated by our International Program Advisory Committee (ISAB), consisting of distinguished scientists in nuclear physics. The ISAB members will also continue to monitor and evaluate the entire width of activities at ELI-NP on an ongoing base. In the period covered by this report, the ISAB has met twice in September 2020 and October 2021. We feel grateful to their guidance that emerged from their work.

Within the H2020 INFRADEV-04-2019 IMPULSE project, ELI-NP collaborates with the two ELI pillars in the Czech Republic and Hungary and 11 other institutions from six European countries. The aim is to establish the framework for the transition of the three ELI infrastructures into a single organization, called ELI-ERIC. The overarching organization structure will guaranteeing stable and harmonized user-focused operation. A first initiative within this framework was to define and plan 'Flagship Experiments' to highlight the unique character and scientific versatility of the three pillars of ELI. Currently under preparation the related experiments will commence in 2023.

It is with pride that we present our first full ELI-NP Annual Report on this occasion to the worldwide audience of scientist and other interested stakeholders in the new technology of high-power, laser-driven research. The report contains results of the multitude of successful research and engineering activities performed at ELI-NP during the 2020-2021 period, giving evidence of the specialist work undertaken aimed at establishing a world-class research facility in Romania.

Sincerely,

Dr. Călin Alexandru Ur

Dr. Călin Alexandru Ur
Director ELI-NP

Prof. Dr. Sidney Benjamin Gales
Scientific Director ELI-NP

Prof. Dr. Kazuo Tanaka
Scientific Director ELI-NP (2016-21)

1. Laser System Department (LSD)

Introduction

THE MISSION OF THE LASER SYSTEM DEPARTMENT (LSD) IS: ***to deliver the best laser pulses for the experiments!*** The Laser System Department was in charge of the successful implementation of the High-Power Laser Systems (HPLS) at ELI-NP. Naturally, this duty now extends to the operation and maintenance of the HPLS, aiming to deliver the highest-quality laser beams to the entry points of the experimental areas. Our HPLS achieved the highest human-made power of 10 PW for the first time in the world during a dedicated endurance test on the 19th of August 2020, facilitating the 10 PW Laser Beam Transport System (LBTS). Furthermore, a second demonstration of the 10 PW peak power in front of a distinguished international live audience, including the Nobel Laureates Gerard Mourou and Donna Strickland, was performed on the 17th of November 2020 during and ELI-NP organized online colloquium entitled, "Moving into Uncharted Territories".

Team

To achieve its mission, the department structure is oriented toward operations and maintenance activities, with engineers forming the majority of personnel. A major role in the department development focuses on training laser engineers and scientists. Thales, the company that produced the HPLS and LBTS, supports the operations, maintenance, and knowledge transfer of our local ELI-NP team.

The department is organized into three main groups: Operation and Maintenance, Technical Support, and Science. To ensure a total of 12-hour laser operations per day, the Operation and Maintenance group consists of two teams. A third team will be formed soon to support these activities to ensure an even higher beam availability for international users in the years to follow. The Technical support group is in charge of the activities related to the auxiliary support systems, with responsibilities reaching from the water cooling to IT. Finally, the Science group is the 'talent incubator' of the department through scientific and technical development activities dedicated to the laser field.

We are proud of our former members that continue their careers in highly technical or scientific domains: Tiberiu Georgescu, Amelie Lachapelle, Radu Secareanu, Veselin Aleksandrov, Vlad Luta, Bogdan Ispas,

Gabriel Emil Urian, Loredana Caratas, Georgios Kolliopoulos, Vinod Mohanan, Aurelian Costea, Masruri Masruri, George Prodan, Stefan Babatie, Bertrand de Boisdeffre, and Miklos Kiss.

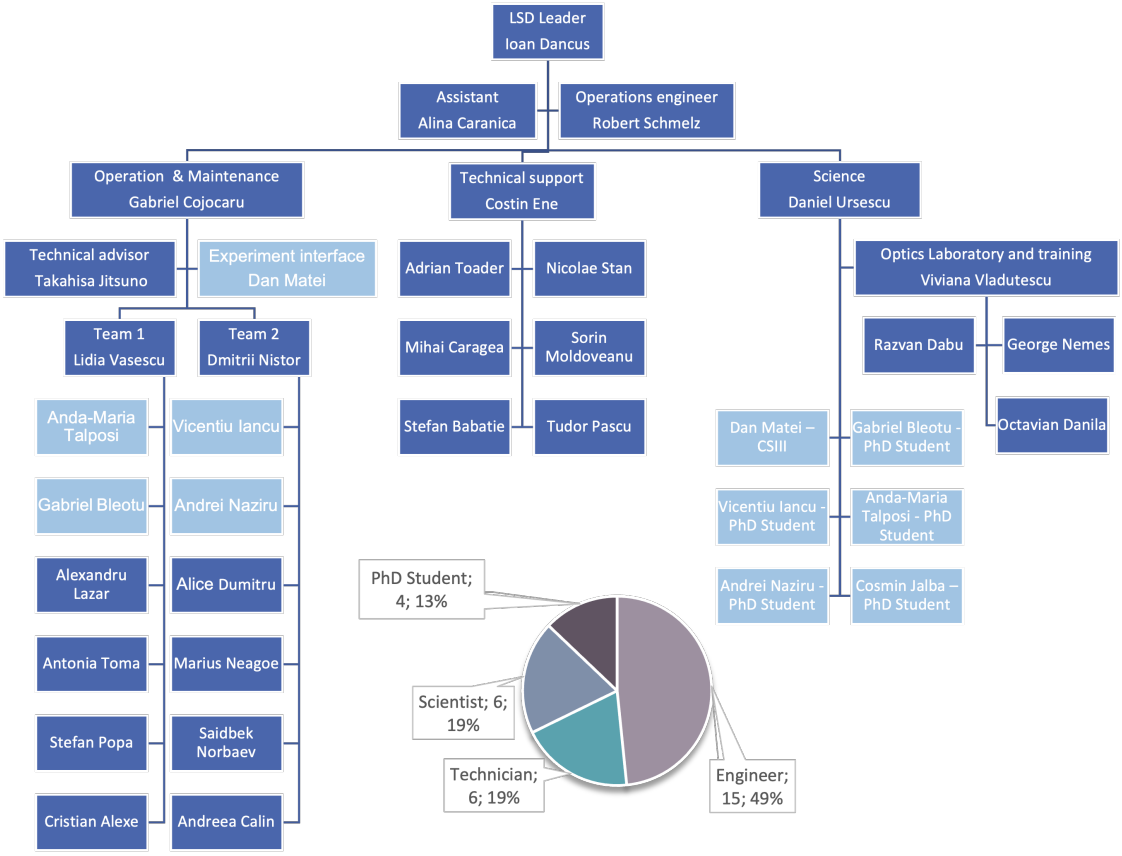

Figure 1.0.1: *The structure of the Laser System Department at the end of 2021*

The LSD capability and skill set cover various competencies encompassing different domains such as optics, physics, IT, electronics, vacuum, and others. Our staff consists of engineers, researchers, and technicians is completed by non-scientific support staff.

Main infrastructure

The High Power Laser System (HPLS) and the Laser Beam Transport System (LBTS) are critical components of the ELI-NP facility. These systems together allow the creation and delivery of the required laser pulses to the experimental areas where the experiments take place.
The ELI-NP HPLS is a hybrid OPCPA - CPA dual arm laser system with six outputs: 2×100 TW at 10 Hz repetition rate, 2×1 PW at 1 Hz repetition rate and 2×10 PW at 1 shot/minute repetition rate. A complete description of the HPLS and the commissioning results are presented in [Lur+20].
The LBTS is made of meter-large aperture adjustable mirrors installed in a vacuum system of pipes and enclosures that can direct the laser pulses to the required experimental setups with micrometric accuracy. The systems are operated and monitored using specialized hardware and software interfaces. The operation of HPLS and LBTS demands controlled environmental conditions in terms of air quality and mechanical vibrations that have to meet specified quality parameters.

A virtual tour [Ecl22] of the HPLS and LBTS is available on the Laser System Department section of the ELI-NP web page at https://www.eli-np.ro/thales_eli-np.php.

The other complementary infrastructure whose operation lies within the responsibility of the Laser System Department is the Optics Laboratory, with its main mission in providing support for the users of ELI-NP. The Optics Laboratory has a full spectrum of optical materials and equipment. This includes *e.g.*, laser sources, lenses, and mounts. One of the main current activities of the Optics Laboratory is providing training for laser engineers. In addition, the Optics Laboratory is an open-access infrastructure for scientific

teams to perform research and development projects. A complete list of equipment and procedures for access is available on the Optics Laboratory web page at https://www.eli-np.ro/optics_lab.php.

Highlights

The main achievements of the Laser System Department are the successful ***implementation of the HPLS and LBTS***, the first worldwide demonstration of the ***production and propagation of pulses with a peak power of*** 10 PW, and the ***starting of operations*** and delivery of pulses to experiments at the 100 TW and 1 PW outputs with the nominal power. The timeline of the most important milestones for the Laser System Department at the ELI-NP is given as follows:

- 2013 June 11 - HPLS contract sign
- 2018 December 21 - LBTS contract sign
- 2019 March 13 - HPLS demonstration of the 10 PW capability
- ***2020 March 18 - First HPLS beam on target*** in a spectral broadening experiments in collaboration with Prof. Gerard Mourou, 2018 Physics Nobel Prize Laureate
- ***2020 August 19 - First*** 10 PW ***propagated pulses***, during the LBTS endurance test
- ***2020 November 17 -*** 10 PW ***public demonstration***, during the 'Moving into Uncharted Territories' - Users workshop

Figure 1.0.2: *The HPLS was on the cover of the Photonics Spectra journal on the anniversary of 60 years of lasers in May 2020; The first beam on target was the subject of the News and Views article of the Nuclear Physics News Vol 30, No 2, 2020; Laser Focused World published the article "Visiting the most powerful laser in the world" by Andreas Thoss in September 2020*

In December 2020, a milestone article was published on the design of the HPLS and the results obtained during the commissioning of the laser system. The article [Lur+20] was on the cover of the High Power Laser Science and Engineering journal of the Cambridge University Press (Figure 1.1.10).

During 2020-2021 period we started to ramp-up the operations and deliver beam time for experiments:

- 2020 - Beam time delivery: 100 TW – ***23 weeks;*** 1 PW – ***1 week;*** 10 PW – ***2 weeks***
- 2021 - Beam time delivery: 100 TW – ***16 weeks;*** 1 PW – ***20 week***
- 2021 - Successful ***parallel beam time demonstrated*** during the first 2021 beam time period
- 2021 - Successful ramp-up of the laser system to a power level of $\sim sI0.9PW$ during the beam time

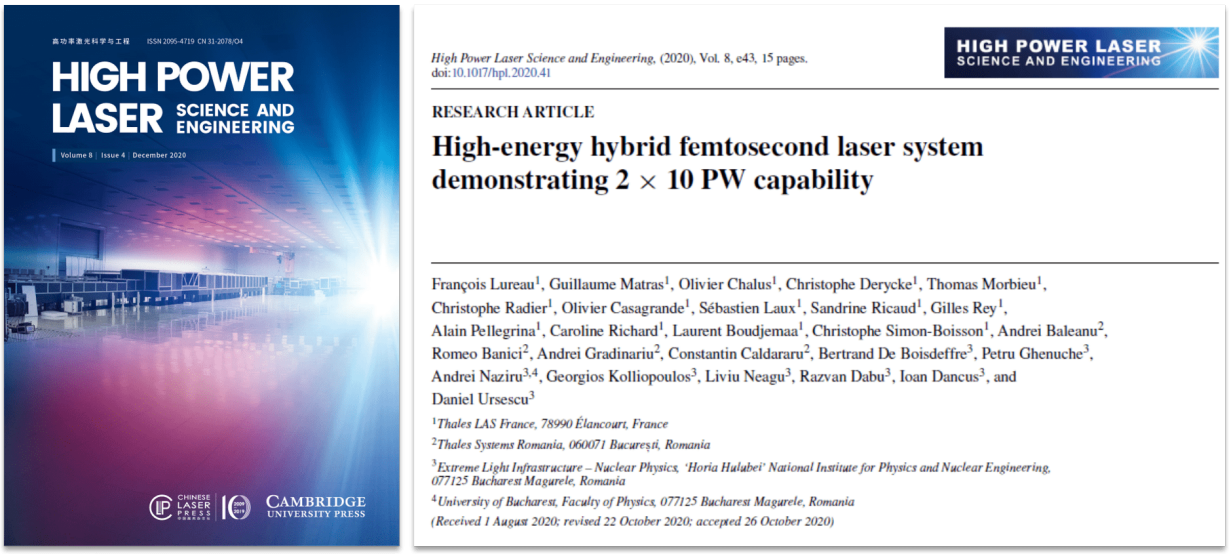

Figure 1.0.3: *Milestone article on the HPLS design and commissioning results on the cover of the HPL journal of Cambridge University Press.*

Funding

Our Extreme Light Infrastructure Nuclear Physics (ELI-NP) installation is a project co-financed by the Romanian Government and the European Union through the European Regional Development Fund and the Competitiveness Operational Program (1/07.07.2016, COP, ID 1334). The Laser system department's research and development program is supported by the Romanian Ministry of Research and Innovation through the Nucleu program PN 19 06 01 05, the PMIHLB project (PN-III-P4-ID-PCCF-2016), and a diversity of ELI-Ro projects. Our research activity was also supported by CERN through HPLM project in the ATTRACT program and the EU-founded IMPULSE project. Furthermore, the operations and maintenance of the laser systems (HPLS and LBTS) and Optics laboratory are supported through the National Interest Facility program of the Romanian Government through the IOSIN contract.

References

[Ecl22] Ecliptique. *ELI-NP HPLS virtual tour*. en. 2022. URL: http://ecliptique.com/ (cited on page 4).

[Lur+20] F. Lureau *et al.* "High-energy hybrid femtosecond laser system demonstrating 2 × 10 PW capability". en. In: *High Power Laser Science and Engineering* 8 (2020). Publisher: Cambridge University Press. ISSN: 2095-4719, 2052-3289. DOI: 10.1017/hpl.2020.41. URL: https://www.cambridge.org/core/journals/high-power-laser-science-and-engineering/article/highenergy-hybrid-femtosecond-laser-system-demonstrating-2-10-pw-capability/C10005F3B8BA78E4FA3EF9EAF06C3BFB (visited on 03/30/2022) (cited on pages 4, 5).

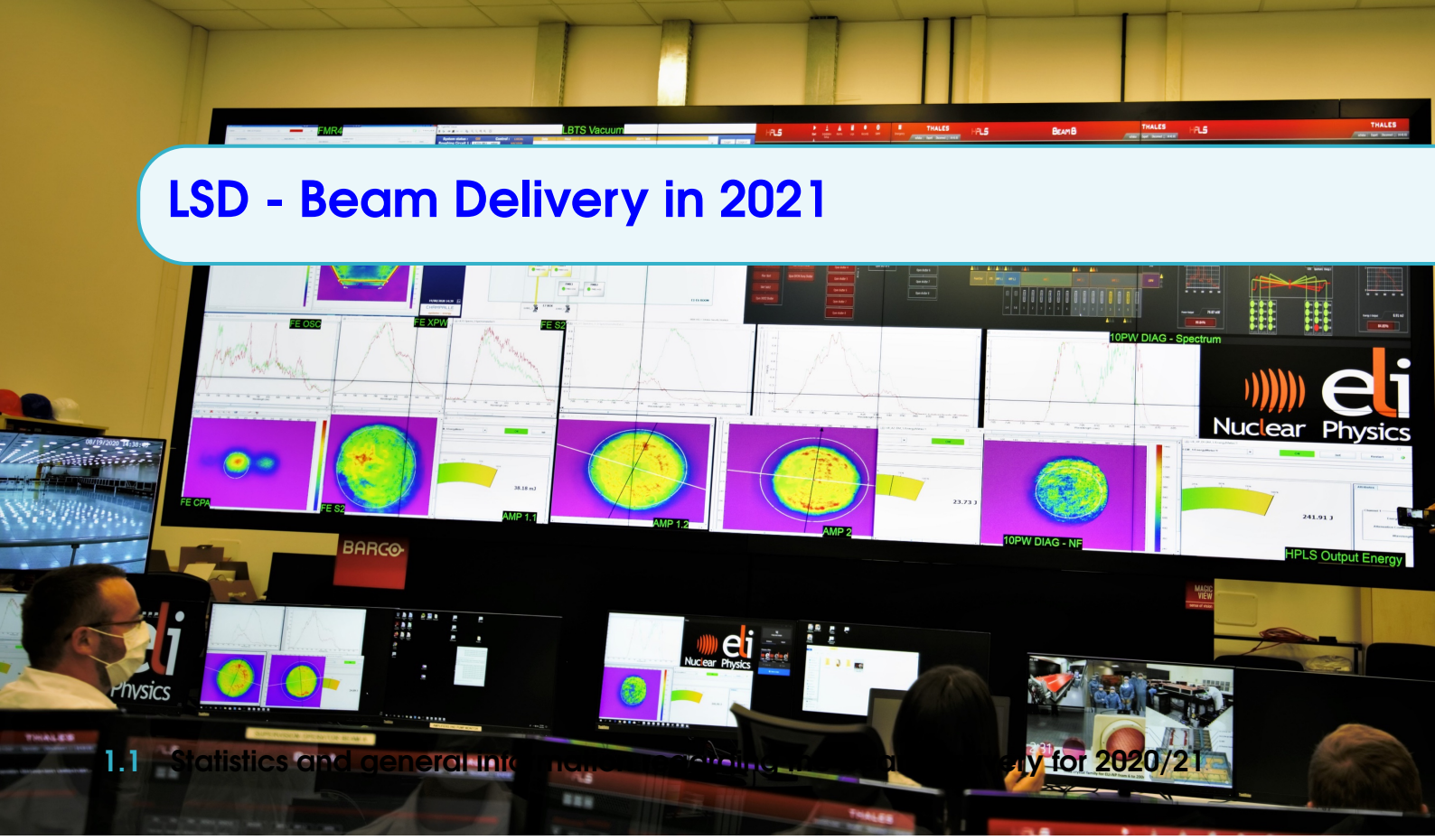

LSD - Beam Delivery in 2021

1.1 Statistics and general information [illegible] for 2020/21

The HPLS beam delivery in 2021 started in 28th July 2021 and ended on the 10th December that year. We have delivered beams to seven experimental campaigns during this time during 111 calendar days. In addition, we operated the two arms of the HPLS, delivering beams in parallel to the two experimental areas for a cumulative period of 177 days. The operation team was formed by ELI-NP Laser Systems Department (LSD) members and Thales engineers under the umbrella of operations, maintenance, and support contracts.

1.1.1 Beam delivery timeline

In 2021 a total number of seven experimental campaigns (two dedicated to the same '4 Wave Mixing' experiment) were planned according to the timeline from Figure 1.1.1. A significant milestone in this period was the parallel operation of the two HPLS arms towards either two different experiments or supporting the same experiment. In Figure 1.1.1 one can observe the parallel operation of the HPLS Arm A and Arm B, including a 100 TW - jitter characterization beam time, that requires both arms operating on the same experiment.

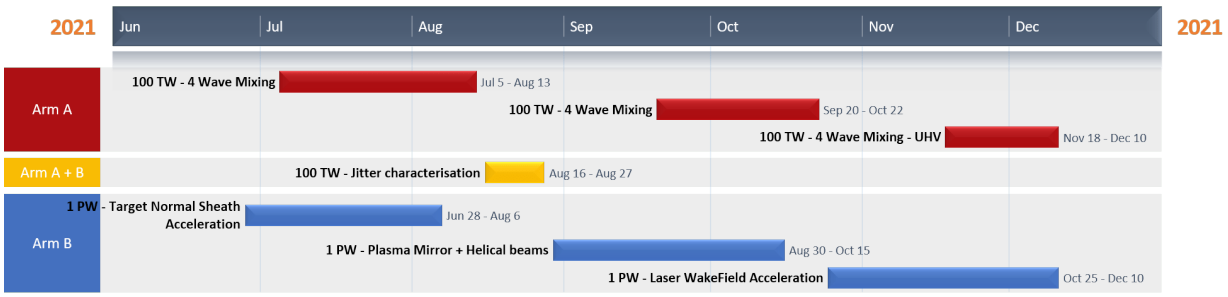

Figure 1.1.1: *Beam delivery timeline for second half of 2021. One can observe the parallel operation of the HPLS Arm A and Arm B, including a* 100 TW *- jitter characterization beam time, that requires both arms to be operated supporting the same experiment.*

During the second half of 2021, in general, the beam was available for experiments between 9:30 in the morning to 18:30 in the evening, as shown in Figure 1.1.2.

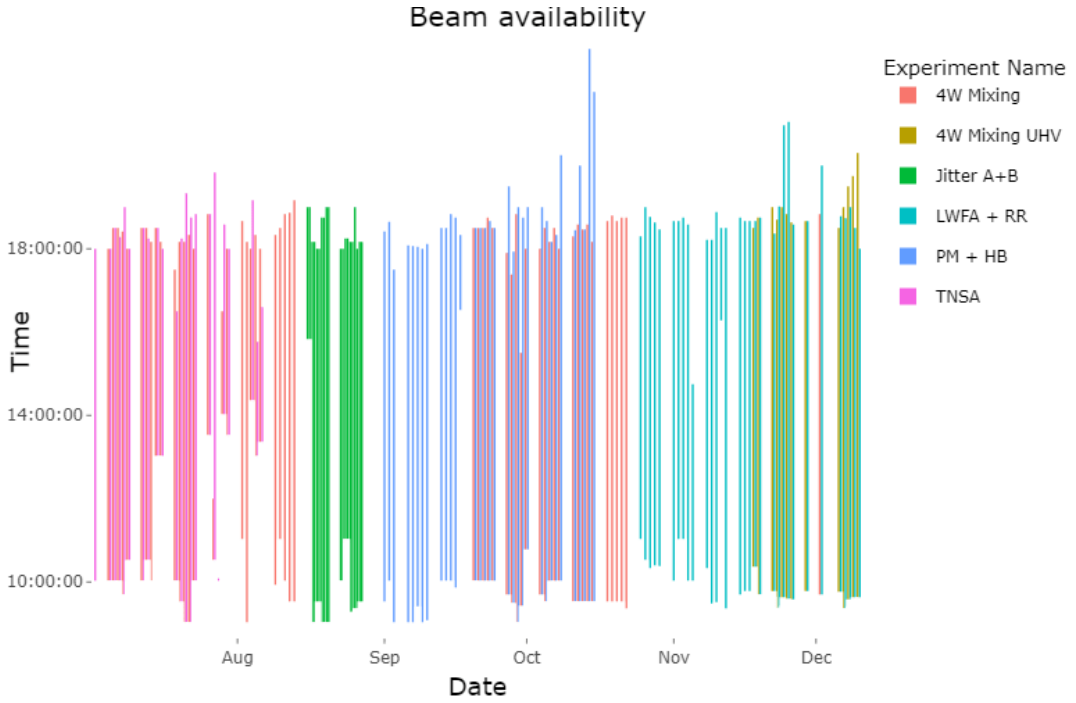

Figure 1.1.2: *Beam availability for the second half of 2021. For most of the times, the beam was available for experiments between 9:30 to 18:30.*

1.1.2 Beam delivery in numbers

During the second half of 2021, we delivered laser beams for a total 466 number of hours from the HPLS 100 TW output to E4 experimental area and a total 730 number of hours from the HPLS 1 PW output to E5 experimental area. A total number of 1192 pulses on the 1 PW output were delivered on target during this time.

The following figures show some statistical data about the 1 PW shots delivered on target. Figure 1.1.3 shows that the majority of 1 PW pulses, more than 700, were delivered at energies greater than 20 J. The number of shots per day delivered on the gas target installation was greater than the number of shots per day on solid target, as it is evident from Figure 1.1.4. The figure depicts the arrangement of the experiments in time. The first two campaigns were dedicated to solid targets and the last two to gas targets experiments.

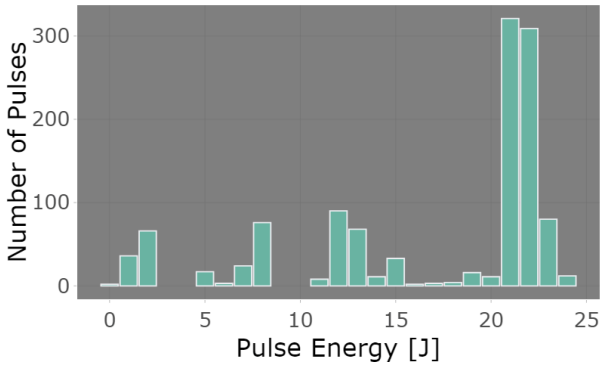

Figure 1.1.3: *Histogram of the energy of the shots delivered on target at the* 1 PW *output showing that the majority of the pulses were delivered at more than* 20 J *of energy.*

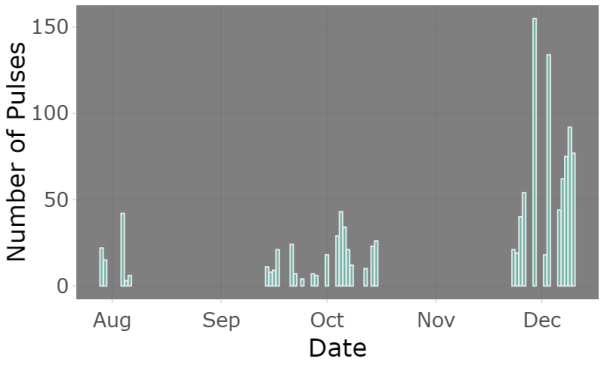

Figure 1.1.4: *Number of shots per day delivered on target at the* 1 PW *output showing that the number of shots per day are greater during the last experimental campaign.*

Figures 1.1.5 and 1.1.6, show the energy per shot for two days of the experimental campaigns: Figure 1.1.5 displays the maximum energy of shots delivered on a solid target, during 15th of October and Figure 1.1.6 illustrates the maximum number of shots per day, delivered on gas target, on 29th of November. The figures demonstrate the stability of laser pulse delivery giving evidence of the robustness of our laser system.

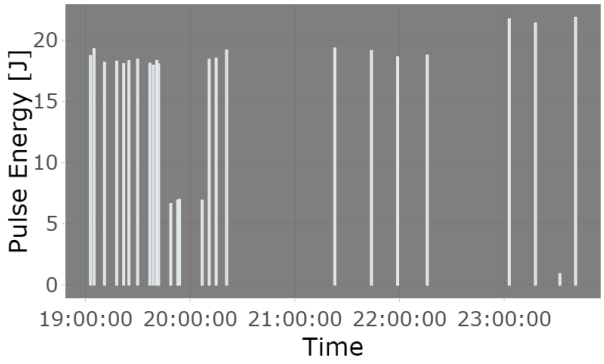

Figure 1.1.5: *Shot energy versus time during 15th of October 2021, the last day of beam time of the solid target campaign in 2021.*

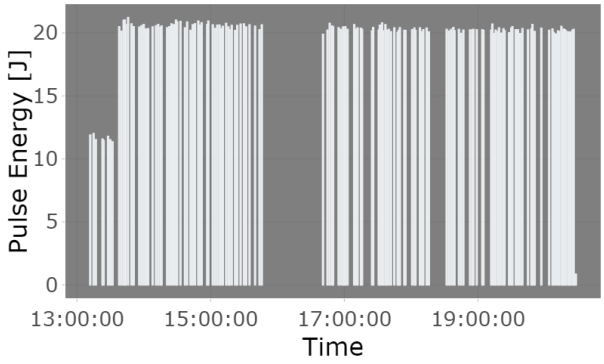

Figure 1.1.6: *Shot energy versus time during 29th of November 2021, the day during which the maximum number of shots on the gas target were delivered in 2021.*

1.1.3 Laser challenges and solutions

A major challenge during the second half of 2021 was the presence of a strong back reflection into the HPLS from the 1 PW experimental area. Members of the Laser Driven Experiments Department (LDED) undertook a series of complex investigations and analytics to identify the origin of this back reflection, supported by members of our LSD group. The conclusions led to identifying a pre-pulse induced by a plasma mirror on the target that reflected a good part of the main pulse back into the laser system. As a result, two further actions were undertaken, identification and suppression of the pre-pulses responsible for this effect and the isolation of parts susceptible to damage by using a temporary optical isolator. A permanent solution for the optical isolator was established and is currently implemented (Figure 1.1.7).

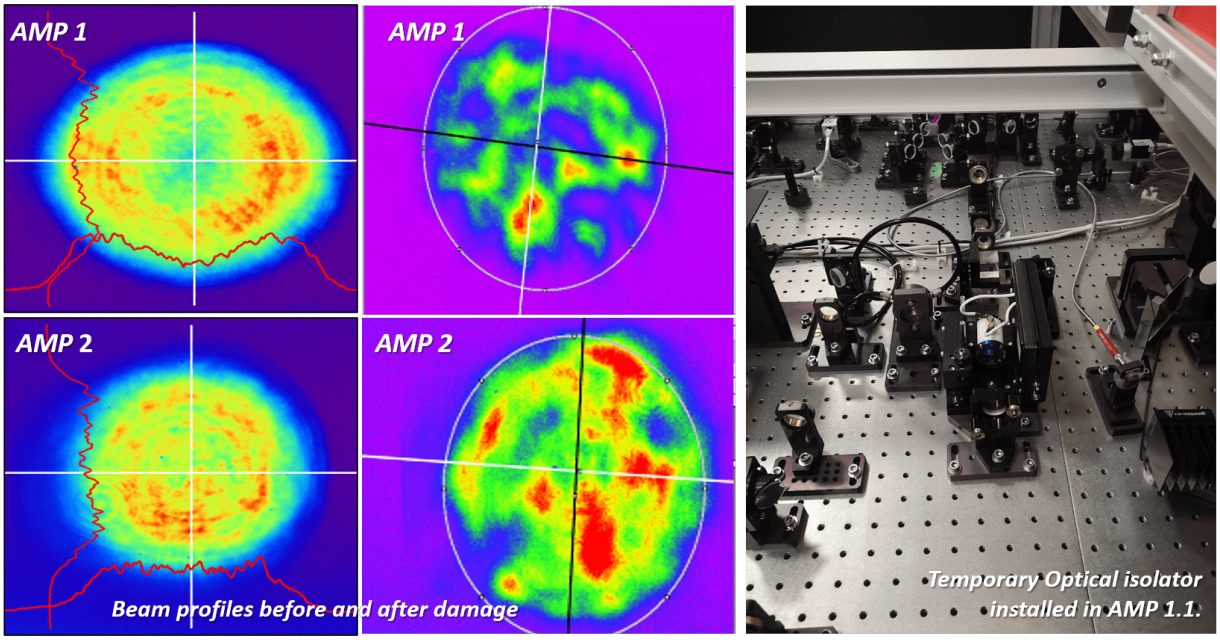

Figure 1.1.7: *AMP 1 and AMP 2 beam profiles before and after the damage, left and central images; Temporary Optical isolator installed in AMP 1.1., right image.*

Another important challenge was the stabilization of the laser room conditions in terms of temperature and humidity with the system running under nominal parameters for experiments. To gain control, we developed a mesh of sensors to monitor the conditions in the laser room and tuned the HVAC system to get a stable temperature value. We succeeded to stabilize the temperature to less the 0.5 °C daily and in day-to-day variation. See Figure 1.1.8

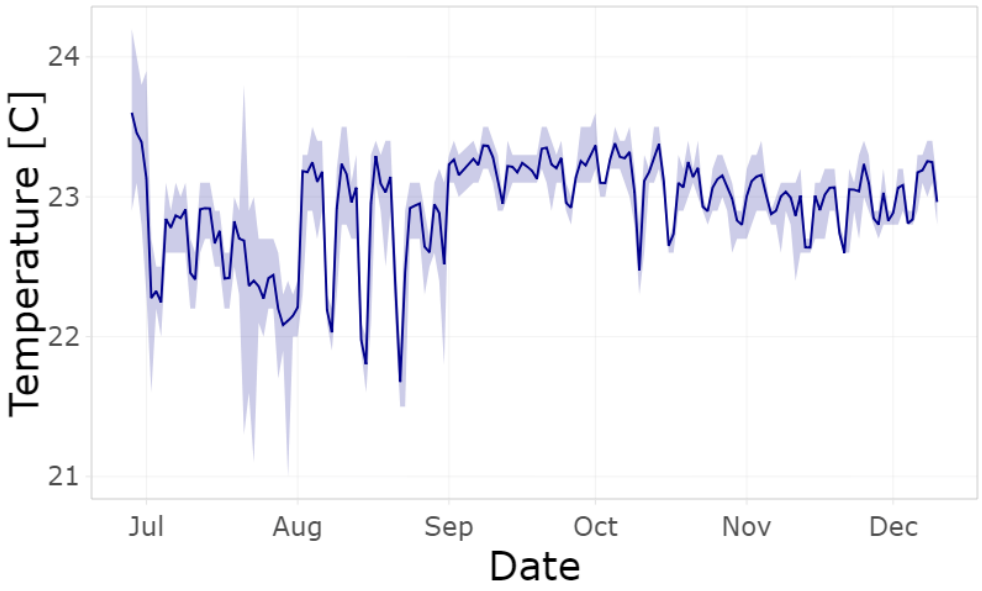

Figure 1.1.8: *Temperature in the Front End area of the laser system. One can observe the improvement of the temperature stability starting with September 2021.*

After these updates and further measures improving the beam delivery, the pulse compressors suffered no damaged. Figure 1.1.9 presents pictures of the last-stage compressor grating on the left and the extraction mirror on the right. Both show no visible damage to the optical surfaces. However, visible damage was observed on the 1 PW transport mirrors, which are classified as 'consumables' at this level of power. Figure 1.1.10 presents pictures of these three transport mirrors. New mirrors were installed for the start of the 2022 beam time campaigns.

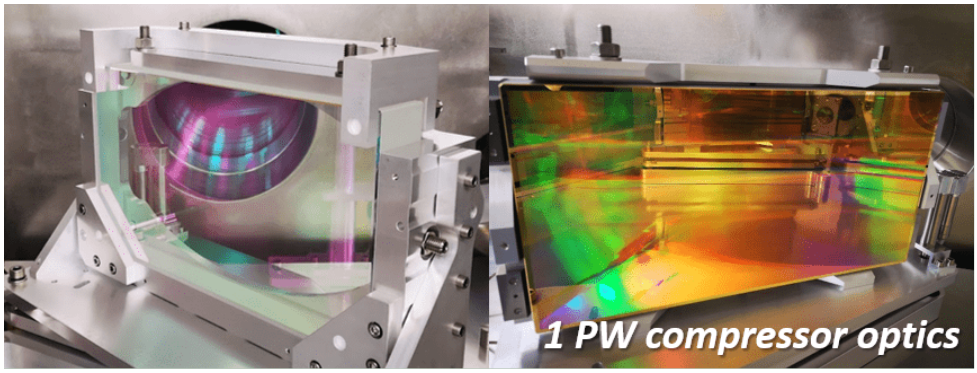

Figure 1.1.9: 1 PW

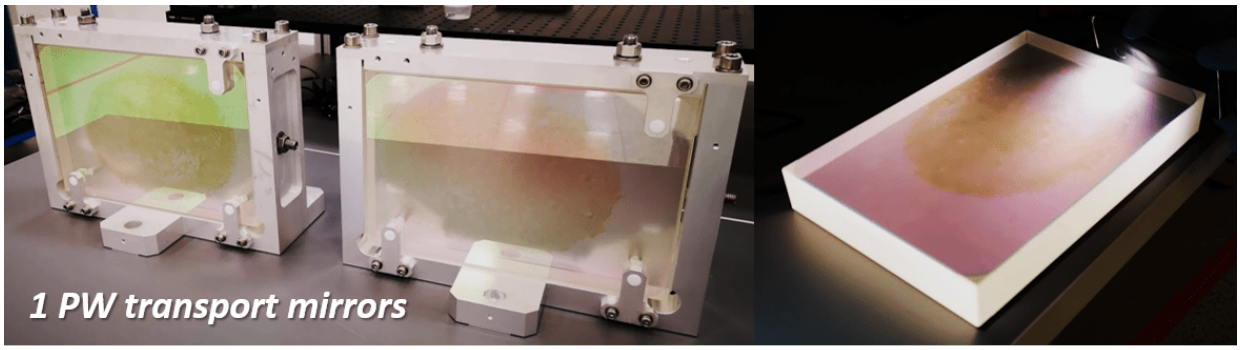

Figure 1.1.10: 1 PW *transport mirrors at the end of 2021.*

1.1.4 Funding

The operations and maintenance of the laser systems (HPLS and LBTS) are supported through the National Interest Facility program of the Romanian Government through the IOSIN contract.

1.1.5 Acknowledgment

We gratefully acknowledge the contribution of the entire Thales, Alsyom/Seiv, and ELI-NP teams and collaborators.

Applied & Technical Work at LSD

1.2 HPLS damage protection against back-reflected laser radiation

Cojocaru G.[1] , Naziru A.[1] , Dancus I.[1] , and Dabu R.[1,*]

[1] Extreme Light Infrastructure (ELI-NP) & Horia Hulubei National Institute for R & D in Physics and Nuclear Engineering (IFIN-HH), Str. Reactorului No. 30, 077125 Bucharest– Măgurele, Romania

[*] **razvan.dabu@eli-np.ro**

Abstract

In PW laser experiments, a small part of the laser radiation is back-reflected towards the laser system in experiments with solid targets. Due to the spatial beam compression and residual laser amplification in Ti:Sapphire crystals, the fluence of the back-reflected radiation significantly increases after propagation through the laser system. To avoid damage to the HPLS optical components, we designed an Optical Isolator, which will be installed next to the A1.2 amplifier.

1.2.1 Back-reflected laser radiation amplification in HPLS

In multi-PW-class femtosecond laser systems, laser pulses are amplified in several chirped pulse amplification (CPA) stages to reach an output pulse energy in the range of hundred-J. After temporal compression, the high-energy femtosecond laser pulses propagate through the beam transport system and interact with targets in the experimental chambers. A small part of the laser radiation, more significant in the case of solid-state targets, is back-reflected towards the laser system. After passing through the compressor, the back-reflected laser pulse, with a pulse duration similar to the amplified chirped pulse duration, propagates through the laser system amplifiers. Depending on the saturation regime of each amplifier, the laser energy accumulated by optical pumping in the Ti:Sapphire crystal is partially extracted by the forward CPA process. The round-trip time from amplifiers to experimental chambers is usually much shorter than the fluorescence time of the Ti:Sapphire upper laser level. The depletion of the Ti:Sapphire crystal upper laser level by fluorescence is not significant until the passing of the back-reflected laser pulse. As a result, the back-reflected laser radiation can be amplified due to the residual laser energy accumulated on the upper laser level of the Ti:Sapphire crystals. In a CPA laser system, the laser beam diameter is expanded step-by-step for keeping a laser fluence under the damage threshold of optical components. Moreover, in the case of backward laser radiation propagation, the beam expanders of the laser system will work as laser beam spatial compressors, thus significantly contributing to the increase in fluence of the back-reflected radiation. A detailed description of the HPLS has been presented in the Reference [Lur+20]. The high energy amplification of 1 PW arm of HPLS consists of three multi-pass Ti:Sapphire chirped-pulse amplifiers: A1.1 and A1.2 five-pass amplifiers, and A2 three-pass amplifier. The amplified chirped laser pulse is expanded by BE1, BE2, and BE3 beam expanders, starting from ~ 2 mm diameter after A1.1 to ~ 180 mm before the compressor. The increase of the fluence during the propagation of the amplified back-reflected laser radiation through the HPLS 1 PW arm is described in Figure 1.2.1. The beam diameter of the back reflected radiation will be spatially compressed by the propagation from the compressor to the A1.1 amplifier with a factor of about 90. Without any amplification in the Ti:Sapphire amplifiers, considering the compressor efficiency of $\sim 64\%$ and the spectral shaping mirror (SSM) transmission of $\sim 57\%$, the fluence FBR of the back-reflected radiation increases up to $F0 \approx 3300 \times FBR$ due to the beam compression in the backward propagation through the laser system.

The residual laser energy/fluence available for amplification in the Ti:Sapphire amplifier crystals and the single-pass small-signal gain are calculated in Table 1.2.1. The laser pulses energy gain, G, has been calculated using the Frantz-Nodvik equation [FN63; Koe06]. Calculations of the back-reflected fluence radiation (Table,1.2.2) were performed considering available laser energy for amplification in Ti:Sapphire crystals of about 50% from the pump energy, 600 ns round-trip propagation time to the target for all amplifiers, 3.2 µm lifetime on the Ti:Sapphire upper laser level, uniform laser radiation fluence on the reflected beam area, and negligible losses in optical components.

	Pump energy (J)	Amplified pulse energy (J)	Energy extraction efficiency	Residual laser energy (J)	Beam diameter (mm)	Residual laser fluence (J/cm^2)	G_0
A1.1	0.11	0.025	22%	0.0248	2	0.789	2.403
A1.2	11	3.5	31%	1.683	22	0.442	1.634
A2	85	35	39%	7.8	55	0.33	1.44

Table 1.2.1: *Residual laser energy/fluence in Ti:sapphire crystals of 1-PW HPLS arm and single-pass small-signal gain G_0 for the back-reflected radiation. Energy extraction efficiency has been calculated versus pump energy.*

δ	10^{-5}	10^{-4}	10^{-3}	10^{-2}	10^{-1}	1
F_7(J/cm^2)	0.0588×10^{-5}	0.0588×10^{-4}	0.0588×10^{-3}	0.0588×10^{-2}	0.0588×10^{-1}	0.0588
F_6(J/cm^2)	0.0588×10^{-4}	0.0588×10^{-3}	0.0588×10^{-2}	0.0588×10^{-1}	0.0588	0.588
F_5(J/cm^2)	1.76×10^{-5}	1.76×10^{-4}	1.76×10^{-3}	1.76×10^{-2}	0.153	0.9
F_4(J/cm^2)	10^{-5}	10^{-4}	10^{-3}	10^{-2}	0.087	0.51
F_3(J/cm^2)	6.25×10^{-5}	6.25×10^{-4}	6.25×10^{-3}	6.25×10^{-2}	0.54	3.2
F_2(J/cm^2)	7.2×10^{-4}	7.2×10^{-3}	6.5×10^{-2}	0.35	0.98	3.64
F_1(J/cm^2)	0.088	0.88	7.86	42	118	440
F_0(J/cm^2)	0.8	1.66	8.65			

Table 1.2.2: *Fluence of the amplified back-reflected radiation in the HPLS* 1 PW *arm for different values of the back-reflection coefficient δ. Potentially dangerous laser fluence values are marked in red color.*

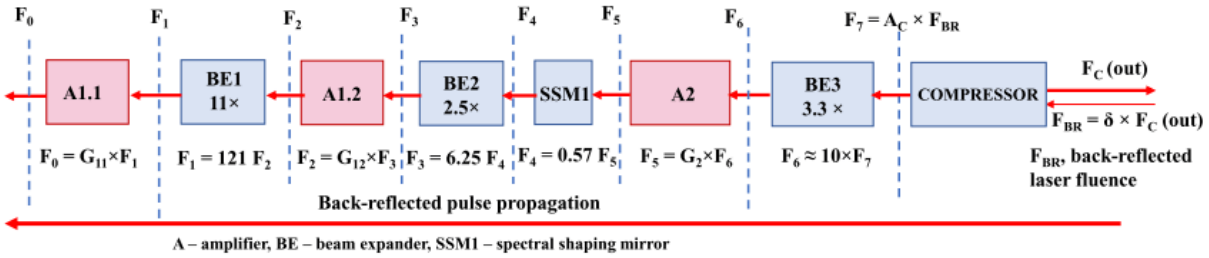

Figure 1.2.1: *Amplification of the back reflected laser radiation fluence in the HPLS* 1 PW *arm; G11, G12, and G2 are the energy gain of the back-reflected radiation in A1.1, A1.2, and A2 amplifiers respectively; δ is the back-reflection coefficient.*

The last high-energy amplifiers are working in the near-saturation regime in the forward amplification. Most of the stored laser energy in their Ti:Sapphire crystals is extracted during amplification. In the case of the back-reflected radiation amplification, the final amplifiers are working in a quasi-exponential regime due to the small input fluence of the back-reflected radiation. The lower energy amplifiers are working in the near-saturation regime due to the amplification of the back-reflected radiation in the high energy amplifiers. For $\delta \approx 1\times10^{-3}$, the coatings of the BE1 convex mirror and A1.1 amplifier optical components can be damaged. This convex mirror can act as a "fuse" for the frontal part of the amplification system, hampering, due to its own surface coating damage, the propagation of the amplified back-reflected laser pulses towards the A1.1 optical components. For $\delta > 1\times10^{-3}$, the convex mirror of the BE1 expander will be significantly damaged, not only on its coating. Some cracks in its substrate can be produced too. Optical components of the A1.1 amplifier are also in danger because of the very high radiation fluence that will be reached after the beam compression in BE1. All other optical

components of the amplification system, including the concave mirror of the BE1, are not in danger to be damaged, even in case of high back-reflection coefficients, close to the mirror-like reflection from the targets. For HPLS optical components protection, we propose to insert an optical isolator (OI) between the BE1 beam expander and A1.2 amplifier. In the case of the 1 PW running, if we consider an OI extinction factor of 1:1000, the back-reflected amplified radiation fluence will be lower than $0.45\,\mathrm{J\,cm^{-2}}$ on BE1 convex mirror for all values of the back-reflection coefficient, including the very unlikely mirror-like back reflection from the experimental chamber. After amplification at saturation in A1.1 the back-reflected laser fluence could reach at most $1.2\,\mathrm{J\,cm^{-2}}$, which is lower than the damage threshold of all optical components. In the actual case of $\delta < 0.1$, an extinction factor of two orders of magnitude could be good enough for protection. In the case of 10 PW HPLS configuration, the OI installed just before A1.2 can ensure the protection of the optical components for $\delta < 0.05$, which could be considered an upper limit value for the solid targets currently used. However, in the case of higher back-reflection coefficients of solid targets, $\delta > 0.05$, for the protection of all-optical components of the 10 PW laser system, notably the BE2 convex mirror and A1.2 optical components, it would be necessary to install an additional optical isolator between the BE2 expander and A2 amplifier.

1.2.2 Optical Isolator Design

Optical Isolator will be installed between the output of the BE1 beam expander and the input in the A1.2 amplifier.

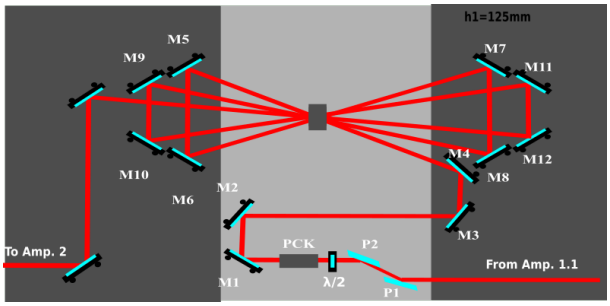

Figure 1.2.2: *Optical Isolator layout of the optical table at the HPLS.A1.2 amplifier.*

In the forward amplification process, stretched laser pulses with $\sim 25\,\mathrm{mJ}$ energy, expanded up to $\sim 22\,\mathrm{mm}$ beam diameter in BE1, s-polarization, are reflected by the P1, P2 pair of one face coated high-power broad-band thin-film polarizers, AOI 72 °. The polarizer coating reflectance for s-polarized beams is about 90%, resulting in the polarizer pair's $\sim 80\%$ energetic efficiency. At the same time, the transmission of each polarizer coating for p-polarized beams is more than 90%, giving rise to less than 1% reflectance of the polarizer pair.

The achromatic $\lambda/2$ waveplate, with 35 mm of clear aperture, transforms the incoming s-polarized beam into a p-polarized beam. The PCK Pockels cell has a clear aperture of about 50 mm. High power M1, M2 mirrors have a 3-inch diameter HR in the 750 nm to 850 nm spectral range. When the PCK is not activated, a p-polarized beam, reflected by the steering mirrors M1, M2, will be transmitted to the A1.2 amplifier. The PCK will be activated by applying a nanosecond $V_{\lambda/2}$ voltage pulse, with fast-rising and falling time, just before the passing of the stretched laser pulse that must be amplified. The activated PCK rotates the beam p-polarization in the s-plane. As a result, the s-polarized laser pulse will be normally amplified in the Ti:Sapphire crystals of the HPLS high-energy amplifiers.

A couple of nanoseconds after laser pulse passing, the PCK is disabled. The later back-reflected s-polarized laser radiation will be transmitted through the PCK with unchanged polarization to the $\lambda/2$ waveplate, which rotates the beam polarization in the p-plane. The p-polarized radiation will be transmitted through the coatings of the polarizer pair. Less than 1% energy of the backward propagating laser radiation will be reflected by the polarizer pair to the HPLS optical components located before A1.2 amplifier, ensuring their protection against damages produced by the amplified back-reflected laser radiation.

On the other hand, the OI helps to improve the nanosecond intensity contrast of HPLS femtosecond pulses. The Ti:Sapphire crystal emission cross-section for the p-polarized radiation, orthogonally oriented versus the optical axis of the crystal, is about two times lower compared to the emission cross-section for the s-polarization. For p-polarized laser radiation, the gain in multi-pass Ti:Sapphire amplifiers is much lower than that of the s-polarized laser radiation. This way, after pulse amplification in high-energy HPLS amplifiers, we can obtain a significant increase of the intensity contrast of the s-polarized main laser pulse versus p-polarized pre-pulses in the nanosecond range.

References

[FN63] L. M. Frantz and J. S. Nodvik. "Theory of Pulse Propagation in a Laser Amplifier". In: *Journal of Applied Physics* 34.8 (Aug. 1963), pages 2346–2349. DOI: 10.1063/1.1702744. URL: https://doi.org/10.1063/1.1702744 (cited on page 15).

[Koe06] W. Koechner. *Solid-State Laser Engineering*. Springer New York, 2006. DOI: 10.1007/0-387-29338-8. URL: https://doi.org/10.1007/0-387-29338-8 (cited on page 15).

[Lur+20] F. Lureau *et al.* "High-energy hybrid femtosecond laser system demonstrating 2 × 10 PW capability". In: *High Power Laser Science and Engineering* 8 (2020), e43. URL: https://doi.org/10.1017/hpl.2020.41 (cited on page 15).

1.3 Laser room air-conditioning: Monitoring and temperature stabilization

Ene C.*, Babatie S., Dancus I., Jitsuno T., and Stefan R.

Extreme Light Infrastructure Nuclear Physiscs (ELI-NP) & Horia Hulubei National Institute for R & D in Physics and Nuclear Engineering (IFIN-HH), Str. Reactorului No. 30, 077125 Bucharest–Măgurele, Romania

* costin.ene@eli-np.ro

Abstract

High power laser system equipment at ELI-NP are hosted in a 6.000 sqm ISO7 clean room. The safety of the equipment as well as the stability of the laser beam delivered to the experimental areas are key to the performance of laser system and to the outcome of the experiments. Air condition parameters influence such outcome.
For an improved control in terms of stability of the air quality in the Laser room, this project enhances the capability of monitoring the air temperature and relative humidity. For this purpose, a set of mobile sensors - placed inside or close to the laser equipment casings - forms a wireless network that, connected via a dedicated application, measures, collects, stores, and displays relevant information. This information is made available to the laser operators in the control room or remotely. We can observe a clear improvement in the control of the air quality provided by the Technical Building Facilities, based on the newly implemented continuous monitoring project.

1.3.1 Introduction

Ambient strict conditions are essential to the ELI-NP facility. That is why the High Power Laser System (HPLS) equipment is mainly hosted inside an ISO7 cleanroom. Optical equipment is sensitive to dust particles, humidity, and temperature variations; these can induce electrical discharge, deformation and tension, and, ultimately, damage. In addition, focal drifting of the laser beam can be induced by, among other factors, the spatial and temporal variations of the ambient conditions: air temperature and relative humidity.

Temperature variation is the most critical element to control. Due to the physical correlation, humidity will be the trade-off entity. However, it must be kept within high and low boundaries for equipment safety.

The air quality in terms of cleanliness is controlled *via* a set of HEPA filters and monitored via mobile particle counters and differential pressure indicators. The air temperature and relative humidity inside the laser room are controlled via a set of six individual automated heaters (CTA) and de/humidifiers as part of the Heating, Ventilation, and Air-Conditioning (HVAC) system. The measurements for the feedback control are provided by six sensors placed inside the CTAs' ducts.

However, the operation of the HPLS is interested in more accurate measurements and, ultimately, tighter control of temperature and humidity inside and around the various laser equipment components.

For this purpose, a network of wireless mobile sensors has been developed by the Technical Support Group of the Laser system Department. The sensors can measure and send data about the temperature and relative humidity of the ambient air. Due to the small size and mobility, the sensors can be easily positioned in any desirable place. A dedicated application communicates with the sensors and stores and displays historical data in a user-friendly manner.

The continuous data provided by this network is used, on the one hand, by the HPLS Operation team to monitor the ambient parameters and, on the other hand, by the Technical Building Facilities to help improve the automatic control of the temperature and relative humidity in the laser room.

1.3.2 Sensor Network Design

The ambient requirements inside the cleanroom at ELI-NP define the air temperature stability around the value of 22°C and relative humidity within a range of 30-75%.

The mobile wireless sensor box has been designed and built to fulfill:

- precision: the SHTC3 element ensures temperature precision of 0.2°C and relative humidity precision of 2%;

- connectivity: the XBee PCB micro-controller and radio antenna use the ZigBee 3.0 protocol;
- low-power-consumption: the SHTC3 and ZigBee protocol ensures ultra-low power usage.

Figure 1.3.1: *Air conditions Monitoring Application Dashboard*

1.3.3 Monitoring Application

The data collected from the mobile wireless sensors are displayed via a custom-built web-based application. The landing page is the dashboard, which maps the physical layout of the laser room, highlighting the Front-End, Amplification Stages, and Compressor Stages of HPLS, see Figure 1.3.1.

The monitoring application can display various information from individual or multiple sensors on the same chart. The user can choose the time range. The data is also available in .csv downloadable format. An example of one week of trends is in Figure 1.3.2.

The spatial distribution of the heat in the Laser Room can be seen via the instant "heat map" for temperature or humidity, space-wise distribution, as shown in Figure 1.3.3.

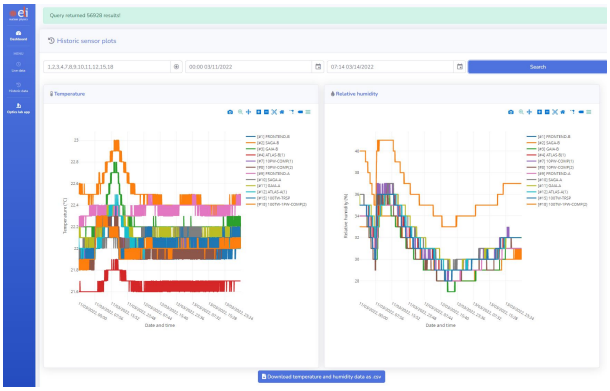

Figure 1.3.2: *Temperature and Humidity from multiple sensor on a given time range*

Starting from the safety objectives of operating the laser equipment in the cleanroom, a series of alarms have been defined, list as follows:

- if the temperature value from any sensor varies by more than 1°C over 24 hours, an alarm is triggered: visual and sound message;
- if the relative humidity recorded by any sensor lays outside the pre-defined range of 30-75%, an alarm is triggered.

The audio alarm is played for 5 minutes when the event occurs or when the operator accesses the application. The alarm sign will be displayed on the dashboard for 24 hours after the last event. Warning messages will also be displayed if the sensor's accumulators need recharging.

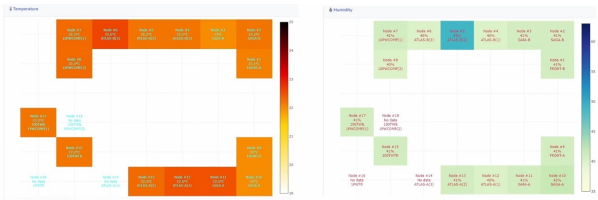

Figure 1.3.3: *Heat map for temperature and humidity across the Laser Room*

Improvement: Since the application has been available to the laser operators and to the Building Facilities team responsible for the ambient air quality, one can observe an improvement which translates into a smoother control of the air conditions inside the laser room.

1.3.4 Conclusions

Achievement: The most important achievement is temperature stabilization. One can notice an improvement in the final CTA control, *i.e.*, a smaller variation of the air temperature - down to 0,5°C/24hours - and humidity around their mean values. This is also due to better monitoring of the parameters throughout the laser room space and the capability to straightforward visualize the data trends. Any upsets or rapid deterioration of the ambient conditions trigger alarms and thus can be spotted by the operators. The Building Facility Team can be notified and can take action for remedy in due time.

Availability: The application is continuously accessible remotely for parameter monitoring Maintenance can be done remotely, too, if required.

Scalability: The monitoring application can be easily extended with additional sensors or new features. It can also be reproduced on other premises (experimental rooms, technical chambers, laboratories, etc.).

Development: A supervision layer of optimized predictive control of the CTA's can be envisaged, should the HVAC allow remote setpoints. The new control could be based on a mathematical model identified with the help of the data provided by the network of sensors.

1.4 Technical report on the high energy attenuation system

Naziru A.[1,*] , Nistor D.[1] , Talposi M.[1] , and Udup E.[1] ,

[1] Extreme Light Infrastructure (ELI-NP) & Horia Hulubei National Institute for R & D in Physics and Nuclear Engineering (IFIN-HH), Str. Reactorului No. 30, 077125 Bucharest– Măgurele, Romania

[*] **andrei.naziru@eli-np.ro**

Abstract

Laser-driven experiments are being prepared at ELI-NP. The current experimental plan involves the usage of the 100 TW and 1 PW beamlines of the High Power Laser System (HPLS). The laser experimental activity involves numerous preparation phases which are defined by the experimentalists based on the nature of the experiment, but in a general sense, such activities could be placed in three distinct categories: alignment activities, laser diagnostics activities, and experimental activities. A diverse regime of usage coupled with a wide variety of experiments requires high "tunability" of the HPLS parameters including the energy level. In this work, an in-house designed and built tunable attenuation system is presented.

1.4.1 Introduction

The energy of the laser pulses is one of the most common laser parameters that need adjustment based on the experimental activity. In the current state of the HPLS configuration, the adjustment of the delivered beam energy is done by manually replacing the three transport mirrors (M1, M2, and M3) with wedge prisms (W1, W2, and W3), as indicated in Figure 1.4.1. During an experiment, the energy of the delivered pulses needs to be shifted from one level to another several times per day. Carrying this task out manually is time-consuming and comes with a high risk of damaging the optics and laser safety implications.

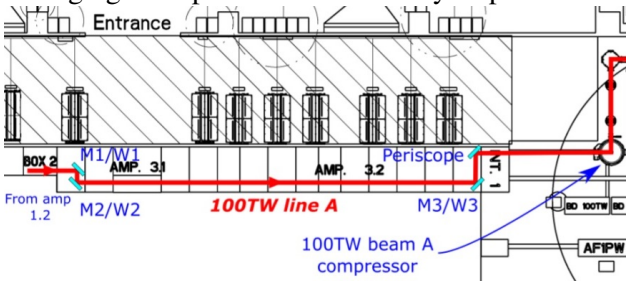

Figure 1.4.1: *100 TW line A beam propagation path before compressor*

1.4.2 Attenuation system target characteristics

The main requirements that the variable beam attenuation system should meet are:

- At least two levels of attenuation,
- Preserve the beam pointing stability of the system to the nominal values,
- Preserve the pulse duration,
- Preserve the wave-front quality,
- Remote-controlled,
- Allow for manual control,

1.4.3 Technical proposal

The current conceptual design is based on an optical setup consisting of a series of wedge prisms and mirrors with predefined positions. The optical elements are installed in pairs on translation stages that will facilitate the transitioning from one attenuation configuration to another.

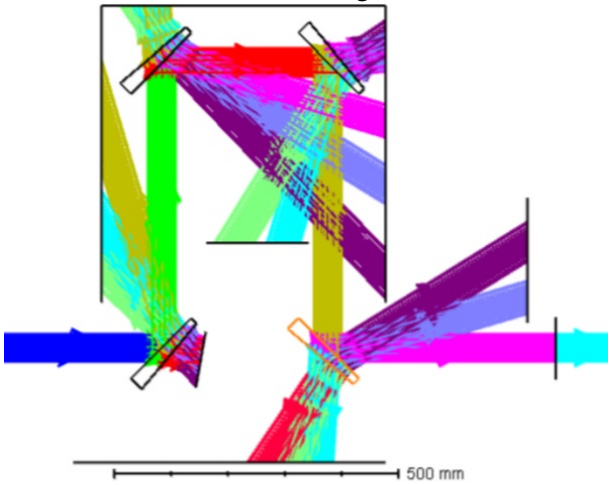

Figure 1.4.2: *Light propagation simulation using a fan of rays*

The unwanted transmitted and reflected light is

trapped in beam dumps that will be installed in appropriate positions, according to the ray-tracing simulations performed in Zemax (Figure 1.4.2). Two different types of wedge prisms are used, anti-reflection coated and uncoated. This corresponds 1.5 % reflectance for the coated wedges and 8 % reflectance for the uncoated wedges at a 45° angle of incidence for S polarized light for a spectral bandwidth of 730 nm to 880 nm. Depending on the configuration, the system can perform from two up to six orders of magnitude attenuation.

The optical simulation also yields crucial information regarding the spatial overlap of the parasitic reflections inside the attenuation system. The positions of the optical elements was carefully chosen in such a manner that no spatial overlap is present in the propagation. The results are depicted in Figure 1.4.3.

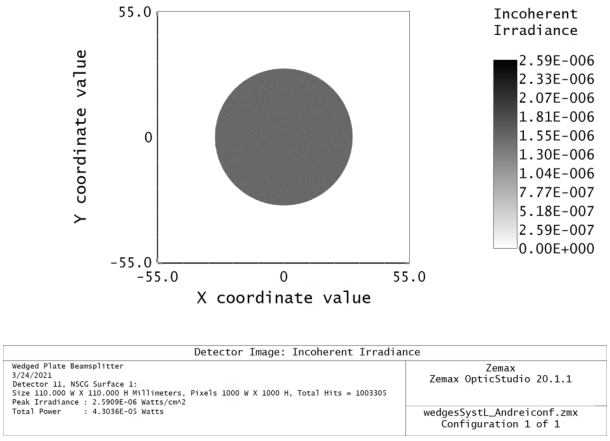

Figure 1.4.3: *Parasitic beam spatial overlap*

1.4.4 Mechanical design

Optomechanical mounts were designed to accommodate the optical elements based on the available space constraints. To increase the mechanical stability, only the first and last optical components are installed on an adjustable mount with the possibility to control the tip and tilt for fine-tune laser alignment.

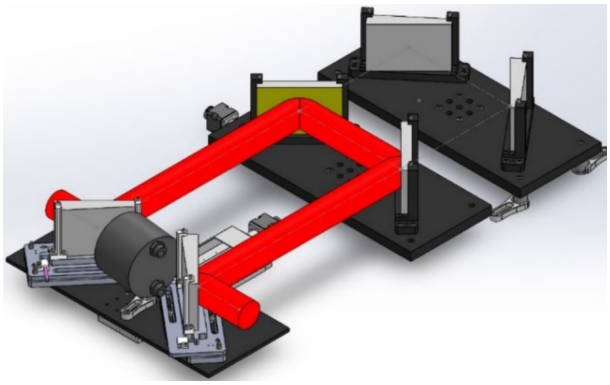

Figure 1.4.4: *Isometric view of the attenuation system*

Depending on the desired energy level, the attenuation system can be placed automatically in three different configurations, as follows:

- Configuration 1: no attenuation - full energy is propagated
- Configuration 2: three orders of magnitude attenuation
- Configuration 3: six orders of magnitude attenuation

In Figure 1.4.5, schematics of the previously described configurations are shown.

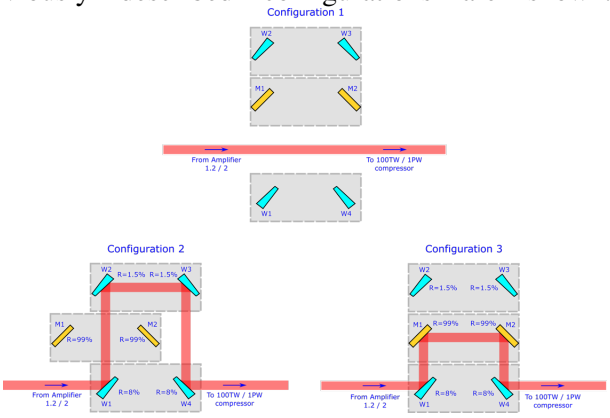

Figure 1.4.5: *Attenuation configurations*

1.4.5 Conclusion

The results obtained through the optical ray-tracing simulation give a preliminary insight into the future performance of the system, which is satisfactory. The output beam intensity pattern indicates no undesired beams overlapping with the main output beam. The optical configuration does not facilitate the apparition of retroreflected parasitic beams which could damage the laser system. The long-term stability of the system was determined through extensive use during the 1 PW experimental campaign in 2021 (in experiments such as TNSA, LWFA+RR) and was deemed sufficient. Further upgrade of the attenuation system is in progress and consists of a redesign of the kinematic mounts to further increase the stability, allow for front-face reference of the optics, and remote-controlled motorization. This would almost completely cut manual intervention and further decrease the alignment time.

1.4.6 Acknowledgements

The success of this project was achieved thanks to the numerous and fruitful technical discussions and advice received from George Nemes, Takahisa Jitsuno, Miklos Kiss, Ioan Dancus, Daniel Ursescu, Razvan Dabu, and Olivier Chalus.

1.5 Spatial properties of the 100 TW HPLS output – preliminary diagnosis

Matei D. G.[1,*]

[1] Extreme Light Infrastructure (ELI-NP) & Horia Hulubei National Institute for R & D in Physics and Nuclear Engineering (IFIN-HH), Str. Reactorului No. 30, 077125 Bucharest– Măgurele, Romania

[*] **dan.matei@eli-np.ro**

Abstract

Design considerations for a diagnosis bench for characterizing the spatial properties of the laser beam in the experimental area E4 are presented. Results obtained after a preliminary implementation are shown and discussed.

1.5.1 Introduction

Experiments that use ultra-short, high-power laser pulses often require the focusing of the laser to a focal spot of tens of micrometers in diameter [Tan+20]. Reproducible conditions require therefore position and pointing stability of the incoming beam. The propagation distance of the 100 TW HPLS beam from the compressor chamber to the entrance of the experimental area E4 exceeds 35 m [Gal+18]. Even a small shift of the beam due to realignment of the laser system or thermally-induced displacements of the steering optics would result in a large shift of the position of the focal spot on the target.

A diagnosis bench would therefore sample a part of the beam for each incoming pulse and derive its transversal position and pointing angle. This should happen for all pulse energies used during alignment or actual shots on target.

1.5.2 Design of the diagnosis bench

The first optical element encountered by the beam in E4 is a 45° angle of incidence dielectric mirror (M_0 henceforth). The diagnosis bench analyzes the transmitted beam leaking through M_0. The parameters relevant for the design of the bench are:

- pulse energies: 5×10^{-5} J to 2.5 J,
- laser wavelength: 820 nm,
- beam diameter: 55 mm,
- estimated M^2: 1.7,
- beam Rayleigh range: 2.0 km,
- transmittance of M_0: $\approx 1\%$.

Spatial characterization of the beam would be done through the following sets of numbers:

- coordinates of the beam on M_0;
- horizontal and vertical pointing angles;
- the M^2 factor of the beam.

Additionally, the irradiance profile of the beam on M_0 provides a qualitative information about its uniformity, and the shape of the focal spot, if focused, indicates the quality of the incoming wavefront.

The first set of parameters is obtained by optical imaging of M_0 on a CMOS camera and extracting the position of the image on the camera sensor. Camera pixel size and magnification of the optical system used for imaging are required for conversion to coordinates of the beam. These parameters, along with the transverse irradiance pattern, are commonly said to be related to the near-field (NF) of the beam if they describe the part which is situated in the middle region of the Rayleigh length (beam waist) [Sie86].

The second set of parameters is obtained by using the property of a focusing optical system to focus an incoming collimated beam to a spot contained in its back-focal plane [Nem18]. The position of this spot in the plane is determined by the angle between the propagation direction of the beam and the optical axis of the focusing system. Placing a camera in the back focal plane and measuring the horizontal and vertical shift, in pixels, from a reference position allows an immediate calculation of the corresponding angular shift. For a paraxial beam, the angle is given (in radians) by:

$$\theta = \frac{N \cdot p}{f}, \tag{1.5.1}$$

with N the number of pixels, p pixel size, and f the effective focal length (EFL) of the system, using simple geometric considerations. In this case, these parameters describe what happens with the beam when propagating far beyond the Rayleigh range, in the so-called far-field (FF).

Consequently, the diagnosis bench has to provide two functions: image the plane of M_0 on a camera

for the NF characterization, and focus the beam on another camera for FF parameters. The former is achieved with a demagnifying telescope and the latter with a convergent, or focusing, system.

The bench must also be able to supply these parameters for pulse energies spanning almost five orders of magnitude. A common method for energy attenuation is to employ stacks of absorptive glass filters. To avoid artifacts induced by the propagation through the filters, especially in the FF parameters, the filters should be placed where the beam is collimated. Since filters with sizes above 50 mm are less common, the diagnosis bench should first provide an intermediate, collimated, and demagnified beam suitable for the absorptive filters, before reducing it further for imaging or focusing.

Under these considerations and the available space constraints, the system was designed according to the schematic presented in Figure 1.5.1 [Nem21].

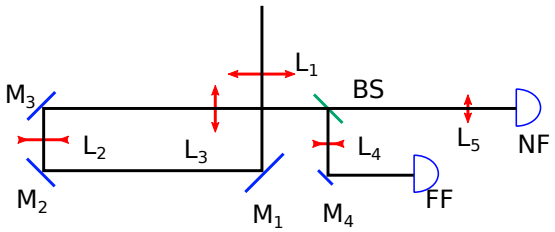

Figure 1.5.1: *Optical layout of the diagnosis bench. The beam enters from the top.*

Lenses L_1 and L_2 form together a telescope that reduces the beam to a diameter suitable for the absorptive filters, which can be placed between the mirror M_3 and lens L_3. After the lense L_3, the beam is divided by a beam-splitter. The transmitted beam goes through lens L_5 which, together with L_3, forms a second telescope which reduces the beam to less than the sensor size of the NF camera (Basler acA2440-20gm). The focal distances of L_1, L_2, L_3 and L_5 are, respectively, 600 mm, −150 mm, 250 mm, and 75 mm. The total demagnification of the series of two telescopes is 13.3. The position of the camera along the beam is calculated to image a plane situated in front of L_1, corresponding to the position of M_0.

The beam reflected by the beam-splitter passes through L_4 and is focused on the sensor of the FF camera (Basler acA2440-20gm). L_3 and L_4 form what is called a telephoto lens: a converging compound optical system with a very long focal distance. An EFL of 2500 mm would ensure a sensitivity of the FF detection of 1.38 μrad, according to Equation 1.5.1 for $N = 1$ and $p = 3.45\,\mu$m. This can be attained for the $L_3 - L_4$ system together with the telescope $L_1 - L_2$ if the focal distance of L_4 is −100 mm and the distance $L_3 - L_4$ is 190 mm. The distance between L_1 and the FF camera is about 1 m. Thus, the use of a 2500 mm focal length lens, usually manufactured upon request, and the requirement to have a distance of 2500 mm to the FF camera are avoided.

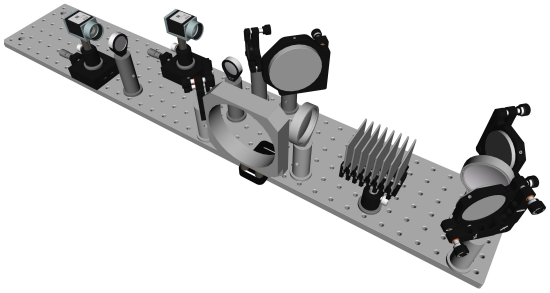

Figure 1.5.2: *Three-dimensional rendering of the optical bench for spatial diagnostics of the beam*

The focal lengths of the lenses, the distances between them, and the beam diameter at each position along the optical setup have been calculated using the *ABCD* matrix formalism [Nem18; Sie86]. The resulting system requires an optical table with a length of 73 cm and a width of 20 cm. A rendering of this system is presented in Figure 1.5.2.

1.5.3 Instability analysis of the HPLS beam

The diagnosis bench was used for alignment and spatial diagnosis of the 100 TW HPLS beam during the fall 2021 campaign of the four-wave mixing experiment conducted in E4. It was installed just outside of the vacuum chamber that contains the M_0 mirror. Images of the full-aperture 100 TW HPLS output are shown in Figure 1.5.3.

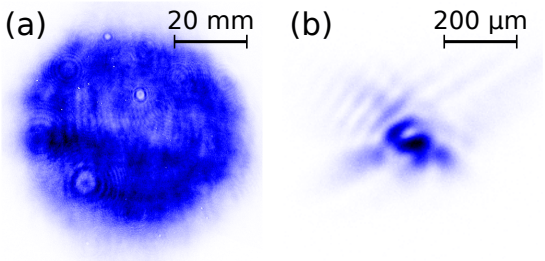

Figure 1.5.3: *Images of the* 100 TW *HPLS output in E4: (a) Near-field image. (b) Far-field image of the beam in (a). The scale bar in (a) corresponds to the object plane. The scale bar in (b) is on the camera sensor.*

The near-field image shows a non-clipped, circular beam with a diameter of about 54 mm. The far-field shows a bright central spot with a diameter estimated around 80 μm. The focal spot in the interaction chamber was optimized with a deformable

mirror to exhibit as little aberrations as possible. The additional optical elements encountered by the same beam before reaching the diagnosis bench are the substrate of M_0 and the vacuum viewport (Pfeiffer PF 412 013-T). The viewport is not specified for optical setups therefore it is reasonable to assume that it distorts the wavefront resulting in the image seen in Figure 1.5.3 (b), instead of a circular spot.

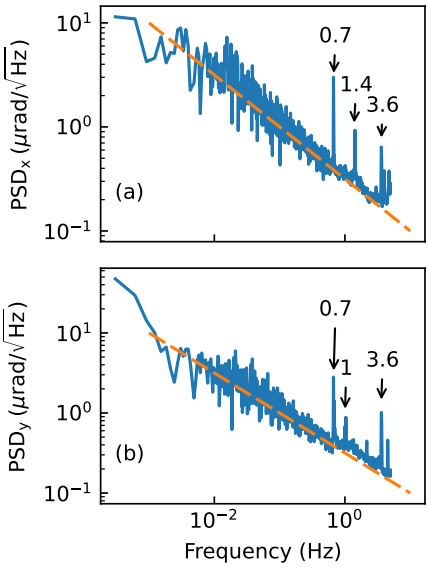

Figure 1.5.4: *Power spectral density (PSD) plots of the pointing instability along (a) x (horizontal) direction, and (b) y (vertical) direction. The dashed lines indicate a curve with the equation* $0.32\,\mu rad \cdot f^{-1/2}$.

The pointing instability in the laser beam arriving in E4 was analyzed by monitoring the movement of the centroid of the far-field image and translating the lateral movement on the camera sensor into angle variations along with two orthogonal directions, perpendicular to the propagation direction (Equation 1.5.1).

The graphs in Figure 1.5.4 show the power-spectral density (PSD) of pointing fluctuations recorded over an interval of 93 minutes.

Since the sampling frequency for this data is the repetition frequency of the laser, 10 Hz, the measurement bandwidth is half of this frequency. The most prominent feature of these graphs is a background similar to a $1/f$ noise, with a level of about $1\,\mu\text{rad}/\sqrt{\text{Hz}}$ at 0.1 Hz, marked with dashed lines in Figure 1.5.4. Moreover, some peaks appear at Fourier frequencies of 0.7 Hz, 1.4 Hz, and 3.6 Hz for the horizontal direction, and 0.7 Hz, 3.6 Hz, 1 Hz for the vertical, in decreasing order of amplitude. These peaks could be attributed to seismic perturbations in the ground plate that supports the laser room and the experimental area. Since their frequency is close to the maximum frequency of the PSD spectra, it is highly possible that they are aliased signals with real Fourier frequencies close to the sampling frequency of 10 Hz. Further measurements of the seismic background are required to validate these assumptions.

1.5.4 Acknowledgments

The initial concept of the diagnosis system was developed by Dr. George Nemeș. Support and valuable advice during the development and operation of the setup from Dr. Ioan Dăncuș and Dr. Daniel Ursescu are gratefully acknowledged. Reliable operation of HPLS was ensured by the joint effort of Thales and ELI-NP laser operation teams.

References

[Gal+18] S. Gales *et al.* "The extreme light infrastructure—nuclear physics (ELI-NP) facility: new horizons in physics with 10 PW ultra-intense lasers and 20 MeV brilliant gamma beams". In: *Reports on Progress in Physics* 81.9 (2018), page 094301. DOI: 10.1088/1361-6633/aacfe8 (cited on page 23).

[Nem18] G. Nemeș. *Lecture notes: Optics Fundamentals and Elements of Quantum Electronics*. 2018 (cited on pages 23, 24).

[Nem21] G. Nemeș. *Near-field – far-field (NF-FF) conceptual design*. Technical report. ELI-NP, 2021 (cited on page 24).

[Sie86] A. Siegman. *Lasers*. University Science Books, 1986. ISBN: 9780935702118. URL: https://opg.optica.org/books/bookshelf/lasers.cfm (cited on pages 23, 24).

[Tan+20] K. A. Tanaka *et al.* "Current status and highlights of the ELI-NP research program". In: *Matter and Radiation at Extremes* 5.2 (Mar. 2020), page 024402. DOI: 10.1063/1.5093535. URL: https://doi.org/10.1063/1.5093535 (cited on page 23).

1.6 Temporary laser interlock system for delivering the HPLS pulses to the experimental areas

Toader A.[1,*] de Boisdeffre B.[1,*] , and Stan N.[1,*]

[1] Extreme Light Infrastructure (ELI-NP) & Horia Hulubei National Institute for R & D in Physics and Nuclear Engineering (IFIN-HH), Str. Reactorului No. 30, 077125 Bucharest– Măgurele, Romania

[*] **adrian.toader@eli-np.ro**

Abstract

The interlock of a laser system is a mechanism that can contribute to laser safety by automatically turning off the laser or by blocking a laser beam via a beam blocker. The system described in this article intends to protect people working in the E4 experimental area when experimenting with the High Laser Power System (HPLS) at ELI-NP.

1.6.1 Introduction

The HPLS consists of two independent laser beams pumping arms, having a common laser source known as Front-End. Each laser beam arm (A or B) has three configurations corresponding to three levels of power 100 TW at 10 Hz, 1 PW at 1 Hz, and 10 PW at one shot per minute. To ensure the protection of the personnel during the experiments and while preparing these experiments, laser and radiation-related risks must be considered. In real life, interlocks can be seen as annoying by workers. Therefore, they are often manipulated, particularly in research laboratories, by the people they are trying to protect. An interlock system for the E4 experimental area was developed in this context.

1.6.2 Interlock System Report

The E4 interlock system is composed of a few electronic modules, each of them with its role, modules which will be presented and detailed further.
The first electronic module is the Configurator box hardware check (See Figure1.6.1: This electronic module checks the logic states from the output of the HPLS configurator box (on laser state connector) and, according to these signals, provides the corresponding laser configuration from the hardware point of view (100 TW, 1 PW, 10 PW) at the output. This verification through this electronic module is essential because one can compare the configuration set in the HPLS supervision software (Panorama) with the hardware configuration from the field (the position of the motors).

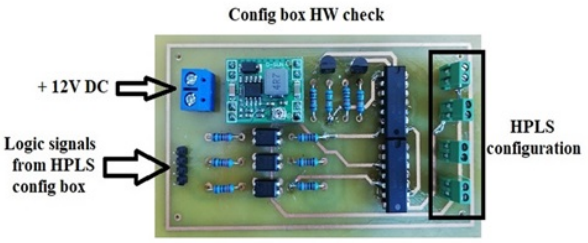

Figure 1.6.1: *Configurator box hardware check electronic module.*

Another module of the system is the SAGA interlock depicted in Figure 1.6.2. This electronic module will be connected to the SAGA pump lasers' power supplies to interlock them for sending a low-power laser beam in the experimental area.

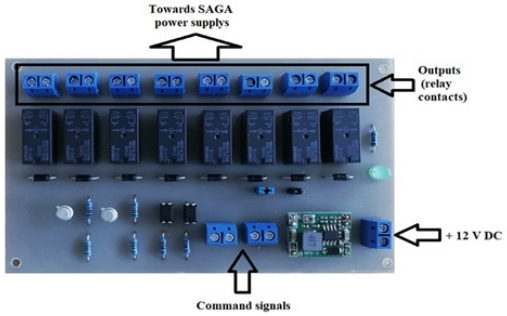

Figure 1.6.2: *SAGA interlock module.*

The core of the entire interlock system is the Control module. It will retrieve all the logical signals from the field equipment, and based on them, depending on the selected operating mode, it will send the corresponding control signals to the output (for instance: actuate the SAGA relay module, turn on/off the E4 warning light, close/open HPLS loop and so on). This electronic module is depicted in Figure 1.6.3

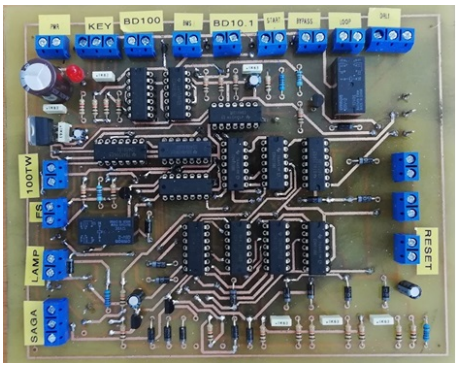

Figure 1.6.3: *The Control module.*

1.6.3 Functional and logic description of the entire interlock system

As presented previously, the Control module is the core of the system. It will manage all the electronic signals from the rest of the modules and field sensors. In the function of operation mode selected, the Control module will act on the system's outputs accordingly. Figure 1.6.4 depicts the block diagram with all electrical connections between the modules, sensors, keys, and buttons.

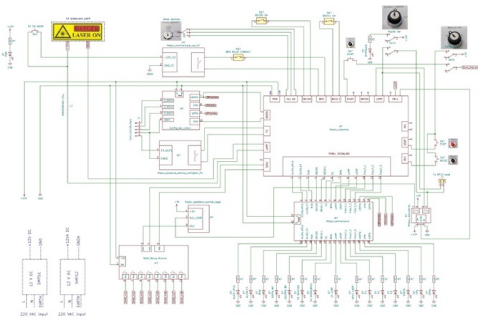

Figure 1.6.4: *Block diagram of the interlock system.*

To start the system, certain conditions must be fulfilled: Mechanical key of operation modes must be on ALIGN HPLS, Master key must be in ON position, Beam shutters of the 100 TW, 1 PW, and 10 PW lines must be in position. After pressing the START button, the interlock system will be ON if these conditions are fulfilled. At this moment, the system is in ALIGN HPLS mode, and the LOOP will be closed. Therefore the class IV lasers can be enabled.

In ALIGN E4 operation mode, the HPLS loop is closed. Therefore class IV lasers can be enabled except for some SAGA lasers. So, the system will ensure a low energy beam towards the E4 experimental area. Also, the warning lamp placed around the E4 area will light up to announce the peoples that can be performed alignment procedures inside E4. If the lamp is broken or not correctly functioning, the system will stop the lasers by closing the HPLS loop. In RUN operation mod,e the HPLS loop is closed. Therefore class IV lasers can be enabled. So, the system will ensure a full energy beam towards the E4 experimental area.

All the signals are transferred on the system's front panel and shown in the form of LED ' s (See Figure 1.6.5). Thus, the operator from the control room will know the position/state of all the sensors/signals from the field.

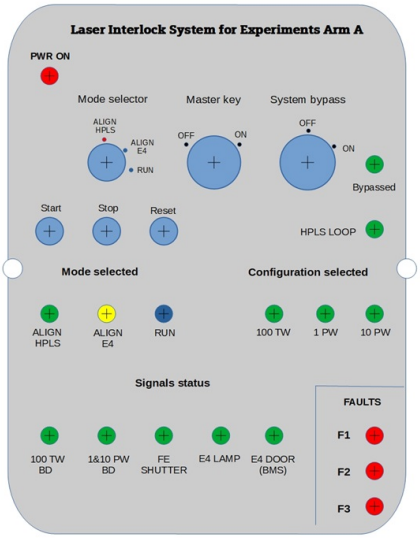

Figure 1.6.5: *Front panel of the interlock system.*

The front panel of the LISE box is provided with three LED s (F1, F2, F3), which indicates the fault states of the system. When something wrong occurs in the system's functionality, the fault LED s will light accordingly. F1- corresponds to ALIGN HPLS mode of operation, F2- corresponds to ALIGN E4 mode of operation, and F3- corresponds to RUN mode of operation.

1.6.4 Conclusion

The interlock should be of a fail-safe design such that it maintains its protective function in the event of component failure. It also should require the resetting of the system (*e.g.*, reset button) to control the restart of the laser rather than permitting continued operation as soon as the door or other trigger point is closed. The interlock system presented in this article has those features implemented.

1.7 Raspberry Pi based IR-Viewer for laser alignment

Lazar A.[1,*]

[1] Extreme Light Infrastructure (ELI-NP) & Horia Hulubei National Institute for R & D in Physics and Nuclear Engineering (IFIN-HH), Str. Reactorului No. 30, 077125 Bucharest– Măgurele, Romania

[*] **alexandru.lazar@eli-np.ro**

Abstract

The HPLS operates with high-intensity laser beams that generate electromagnetic radiation in the spectral ranges of 527 nm to 532 nm, 750 nm to 850 nm, and 1064 nm. As a result, one must avoid direct exposure of the eyes to this radiation. This requires the wearing of goggles that attenuate all these wavelengths generated by the laser beams of the HPLS. The disadvantage of goggles is that one cannot use them all the time in work regarding the beam's orientation. To this end, a laser beam display system has been developed that allows the beam to be adjusted wearing goggles.

1.7.1 Introduction

The system based on the Raspberry Pi Mini-PC that allows the visualization of the laser beam was developed for use both in the laser room for beam alignment in various HPLS modules and for beam orientation in experimental areas such as E4 and E5. The Raspberry Pi Mini-PC, a CCD camera, a 7-inch display, and an external battery as a power source have been integrated into a 3D printed structure. The connection between these integrated modules was made using dedicated connectors. The operating system used to test the device is Debian with Raspberry Pi Desktop. Communication between the CCD camera and the Raspberry Pi Mini-PC is done mainly using code syntax from the OpenCV [Adr08] library.

1.7.2 Design Report

The system's structure was designed in SolidWorks and contained the dimensions of the system's electronic components. This structure consists of the front and the back parts from Figure 1.7.1 a) and b). The component a) shows certain cutouts that allow the integration of the display of the mini-pc and the external battery. Certain design details make connecting the Raspberry Pi Mini-PC system effortless to various external components. Some dimensions have tolerances for easier integration of components into the mechanical structure. The structure has been designed to have small dimensions that make handling more accessible and easier.

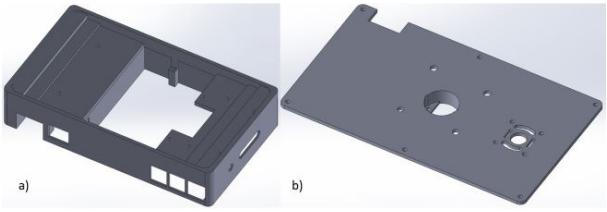

Figure 1.7.1: *The components of the mechanical structure a) the front part and b) the back part.*

The final assembly is shown in Figure 1.7.2, and shows the main components and their position in the mechanical structure. The display (1) was mounted on the front of the structure (a) and the Raspberry Pi Mini-PC (2) was fixed on the backside of the structure (a). An external battery (4) was used as the system power source. On the second component of Figure 1.7.2 b) the system cooling fan and the CCD camera (3) were mounted. Finally, Figure 1.7.3 shows the overall dimensions of the system.

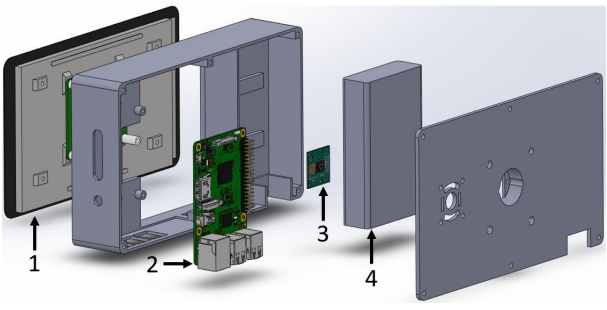

Figure 1.7.2: *General system components.*

Figure 1.7.3: *Overall dimensions of the IR Viewer based on Raspberry Pi Mini-PC. It is* 203 mm *long,* 118 mm *wide and* 43 mm *thick.*

1.7.3 3D Printing and Assembly

After the design stage, the 3D virtual models were obtained by the additive manufacturing method. The material used to manufacture the two components is onyx, which allows for precise structures. The physically obtained 3D models are shown in Figure 1.7.4. In the area marked in red (a) is the dedicated Raspberry Pi display, which has a diagonal of 7 inches (1). In zone (b), the Raspberry Pi module (2) is inserted, and zone (c) is for the power supply. In addition, the CCD camera (3) and the cooling system fan (4) have been inserted into the back of the housing. The positioning and orientation of the components are shown in Figure 1.7.5.

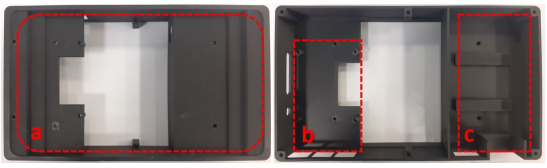

Figure 1.7.4: *Top and rear view of the front part of the mechanical structure obtained by 3D printing.*

Figure 1.7.5: *Integration of electronic components in the 3D printed mechanical structure.*

1.7.4 Electrical Connection and Software

The center screen connects to the mini-pc via a dedicated connector. The camera is connected *via* a special 15-pin band to the Raspberry Pi Mini-PC. An external battery that supplies all electronic components was used as a power source. The software development was undertaken in Python. That required the import of libraries referred to by different syntaxes in the described algorithm sequences. In addition, the OpenCV real-time library for computer-camera functions was used. Figure 1.7.6 shows the image frame processed by Mini PC using algorithms and Python libraries.

Figure 1.7.6: *Example of using the Raspberry Pi IR-viewer in E4. Following the laser at wavelength of* 1064 nm.

1.7.5 Acknowledgments

The idea of making such a device came from Dr. Ioan Dancus, whom I want to thank for the support given in carrying out this project. Also, I want to express my thanks to colleagues at several departments of ELI-NP who gave suggestions for improving this device.

References

[Adr08] B. G. ; K. Adrian. “Learning OpenCV: Computer Vision with the OpenCV Library”. In: (2008) (cited on page 29).

Scientific developments at LSD

1.8 First HPLS experiments at ELI-NP: Spectral broadening in Thin Films

Ursescu D.[1,2,*] , Matei D.[1] , Talposi M.[1,2] , Iancu V.[1,2] , Aleksandrov V.[1] , Bleotu G.[1,2,3] , Naziru A.[1,2] , Tesileanu O.[1] , Rosu M.[1] , Nakamiya Y.[1] , Cernaianu M. O.[1] , de Boisdeffre B.[1] , Ene C.[1] , Caragea M.[1] , Lazar A.[1] , Kiss M.[1] , Masruri M.[1] , Caratas L.[1] , Toader A.[1] , Nistor D.[1] , Luta V.[1] , Tatulea, B.[1] , Popa, D.[1] , Stan N.[1] , Jitsuno T.[1] , Banici R.[4] , Baleanu A.[4] , Gradinariu A.[4] , Wheeler J.[5] , Mourou G.[5] , and Dancus I.[1]

[1] Extreme Light Infrastructure (ELI-NP) & Horia Hulubei National Institute for R & D in Physics and Nuclear Engineering (IFIN-HH), Str. Reactorului No. 30, 077125 Bucharest– Măgurele, Romania
[2] Physics Doctoral School, Bucharest University, Măgurele, Ilfov, 077125, Romania
[3] Laboratoire pour l'Utilisation des Lasers Intenses - CNRS, CEA, UPMC Univ Paris 06: Sorbonne Université , Ecole Polytechnique, Institut Polytechnique de Paris, F-91128 Palaiseau cedex, France
[4] Thales Systems Romania, Șoseaua Orhideelor 15a, 060071 București, Romania
[5] International Center for Zetta-Exawatt Science and Technology (IZEST), Ecole Polytechnique, Route de Saclay, F-91128 Palaiseau cedex, France

[*] **daniel.ursescu@eli-np.ro**

Abstract

Following the completion of the installation and testing of the 2×10 PW High Power Laser System (HPLS) laser at ELI-NP, prospective experiments related to spectral broadening in thin films for post-compression were performed at the HPLS 100 TW output.

1.8.1 Introduction

The high-power laser system (HPLS) that came online at the end of 2019 at ELI-NP is the world's first 10 PW laser. The HPLS has dual chirped pulse amplification arms that operate at a central wavelength of 810 nm, delivering 23 fs pulses for two 100 TW outputs at 10 Hz repetition rate, two 1 PW arms at 1 Hz and two 10 PW arms providing 1 shot/minute. In parallel with the in-house nuclear physics setups implementation [Gal+18], users are welcomed to perform experiments at all these power levels with their own equipment.

Despite the system only recently coming online, studies are already underway on extending the future peak power capabilities for users. One path reaching even above the current 10 PW peak power is to reduce the pulse duration without sacrificing the energy of the pulses. This is possible through non-linear optical processes such as self-phase modulation (SPM) [Mou+14]. Historically gas, liquid, optical fiber, and solid transparent materials have been used to achieve spectral broadening and re-compression to a shorter pulse duration. Characterizing SPM non-linear processes during the earliest stages of laser operation aids in the qualification of the stability of the pulses delivered by the HPLS.

Several features are critical for performing such post-compression experiments at a laser facility. First, the initial spectral composition is highly sensitive to non-linear processes within the amplification chain and beam transport. Thus the laser itself can be unstable. It is shown that the HPLS meets the requirements for the experiments on spectral broadening in transparent thin film materials by providing stable spectral composition at the Front End level, in spite of the high complexity of the double stage, 25 ps pump and optical parametric chirped-pulse amplifier.

Moreover, dispersion control for the laser pulses is also a challenge, particularly when the pulses exceed a few mJ levels and with beams over 5 cm in diameter. HPLS provides excellent control of the dispersion through two mechanisms: the intergrating distance control and the acousto-optic programmable dispersive filter (AOPDF - Dazzler produced by Fastlite) [Tou97], implemented on each amplification arm.

1.8.2 Experiments

The reported experiments took advantage of the stable spectral composition of the HPLS pulses at the 100 TW output to investigate spectral broadening in 1 mm thick borosilicate glass BK7 and in a novel

OKP material from Osaka Gas Chemicals Co., Ltd. (0.1 mm thick), a special polyester for optical applications, possessing a high refractive index of 1.6 or more and extremely low birefringence.

The experiments were performed at the 100 TW laser-induced damage threshold station in the E4 experimental area, in high vacuum, at 1×10^{-6} mbar residual pressure, where pulses up to 2.3 J were available. A focusing mirror with 48" (1219 mm) focal distance reduced the initial 60 mm beam diameter to about 11 mm on target. The targets were placed at 45° incidence angle on a 10 mm long translation stage, making it possible to vary the beam area by a factor of 2.8.

Variation of the irradiance on the targets was obtained through the change in position of the target placed more than 10 cm before the focal point and by tuning the pulses' dispersion with the AOPDF, up to 3000 fs^2 positive or negative linear chirp. The energy stability of the laser pulses was 2.8% rms, hence a negligible impact in terms of spectral fluctuations.

1.8.3 Results

Results are presented in Figure 1.8.1. The two data sets were taken on separate days with different nonlinear materials of distinct thickness to compensate for the expected difference in their non-linear responses. The significant difference in the thickness of the samples indicates much stronger Kerr nonlinearity in OKP compared to BK7. The results indicate that OKP is a promising material for future spectral broadening experiments. Their similarity also highlights the control and high reproducibility of the input ELI-NP HPLS spectral amplitude and phase.

1.8.4 Acknowledgment

We gratefully acknowledge the contribution of the entire Thales and ELI-NP teams and collaborators. This work was realized through "Nucleu" program, funded by the Romanian Ministry for Education and Research, project number 19 06 01 05 2020. Extreme Light Infrastructure Nuclear Physics (ELI-NP) Phase II, is a project co-financed by the Romanian Government and the European Union through the European Regional Development Fund and the Competitiveness Operational Programme (1/07.07.2016, COP, ID 1334).

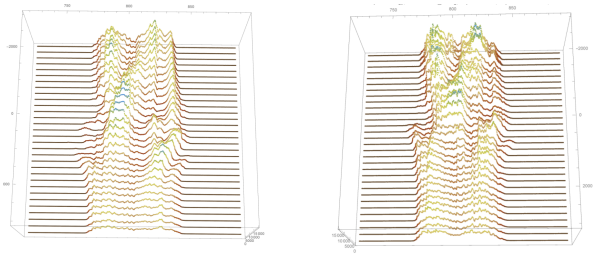

Figure 1.8.1: *Spectral broadening in* 1 mm *BK7 (left) and* 0.1 mm *OKP (right) when the group delay dispersion of* 24 fs *pulses with* 45 mJ *was varied from* $-3000\,fs^2$ *to* $3000\,fs^2$. *The reference* $0\,fs^2$*0 corresponds to the best pulse compression.*

References

[Gal+18] S. Gales *et al.* "The extreme light infrastructure—nuclear physics (ELI-NP) facility: new horizons in physics with 10 PW ultra-intense lasers and 20 MeV brilliant gamma beams". In: *Reports on Progress in Physics* 81.9 (2018), page 094301. DOI: 10.1088/1361-6633/aacfe8 (cited on page 33).

[Mou+14] G. Mourou *et al.* "Single cycle thin film compressor opening the door to Zeptosecond-Exawatt physics". en. In: *The European Physical Journal Special Topics* 223.6 (May 2014), pages 1181–1188. ISSN: 1951-6401. DOI: 10.1140/epjst/e2014-02171-5. URL: https://doi.org/10.1140/epjst/e2014-02171-5 (visited on 02/09/2022) (cited on page 33).

[Tou97] P. Tournois. "Acousto-optic programmable dispersive filter for adaptive compensation of group delay time dispersion in laser systems". en. In: *Optics Communications* 140.4 (Aug. 1997), pages 245–249. ISSN: 0030-4018. DOI: 10.1016/S0030-4018(97)00153-3. URL: https://www.sciencedirect.com/science/article/pii/S0030401897001533 (visited on 02/09/2022) (cited on page 33).

1.9 Spectral phase characterization for ultrashort pulses far from the Fourier Limit duration

Naziru A.[1,2,*] , Popa S.[1,2] , Bleotu G.[1,2] , Iancu V.[1,2] , Matei D. G.[1] , Talposi M.[1,2] , Dancus I.[1] , Dumitru A.[1] , Alexe C.[1] , Lupu A. M.[1] , Vasescu L.[1] , and Ursescu D.[1,2]

[1] Extreme Light Infrastructure (ELI-NP) & Horia Hulubei National Institute for R & D in Physics and Nuclear Engineering (IFIN-HH), Str. Reactorului No. 30, 077125 Bucharest– Măgurele, Romania
[2] Doctoral School of Physics, University of Bucharest, Măgurele, Ilfov, 077125, Romania

[*] **andrei.naziru@eli-np.ro**

Abstract

The HPLS dual-arm configuration unlocks the possibility for high complexity laser-driven experiments. The usage of ultrashort laser pulses requires a good theoretical and practical grasp of the pulse duration and spectral phase measurement techniques. Issues arise when stretched laser pulses with picosecond (ps) scale durations are used in the experimental activities because the spectral phase and temporal measurement techniques are bound to work based on pulses with a temporal profile close to Fourier Limit. A plasma-mirror-based FROG technique measurement of the spectral phase for laser pulses far from the Fourier limited duration, in the few ps range, is presented.

Experiments for high energy density physics require pulses with duration in the ps to ns range, with energies exceeding 1 J. Such pulses can be obtained starting from fs range, Fourier-limit (FL) duration by significant optical stretching, *i.e.* spectral phase modification. In the case of the Extreme Light Infrastructure – Nuclear Physics (ELI-NP) [Gal+18],[Lur+20] facility, the stretching to the picosecond range would increase the pulse duration to at least 40 times the FL. Hence, metrology for the spectral phase for pulses away from the FL is necessary.
Another reason for the implementation of a technique for the characterization of strongly chirped pulses is related to the diagnosis needs associated with the full aperture beam sampling after compression in PW-class laser systems. In such cases, the pulse is extracted from a vacuum through leaky mirrors and relatively thick windows, that introduce significant spectral phase distortion (*e.g.* > 20 FL) at the high power laser system from ELI-NP). However, most of the existing methods to characterize the spectral phase of ultrashort pulses have limited capabilities and cannot measure pulses larger than 20 FL in the time domain.

One previously reported approach [Ung+14] used a cross-correlation frequency-resolved optical gating (X-FROG) technique to measure the spectral phase for pulses with a duration of 300 ps. In such a device, the plasma mirror induced with one reference pulse is used as an ultrafast optical switch to gate the strongly stretched pulse to be measured, as shown in Figure 1.9.1. Spectral phase reconstruction resolution demonstrated in the article [Ung+14] was in the range of 3 ps, limited by the resolution of the spectrometer and the stretching factor of the pulse. We demonstrate here that the FROG method in [Ung+14] can also cover pulses with a duration of a few ps.

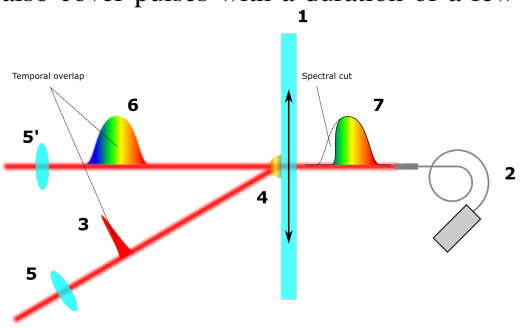

Figure 1.9.1: *The principle of the experiment: the reference pulse at best compression generates a plasma mirror/ultrafast optical switch on a moving piece of glass. The passing part of the measured stretched pulse is measured with a spectrometer.*

An amplified ultrashort optimized pulse is focused on the translating microscope slab, generating a plasma mirror. A focused, ps-scale stretched pulse is directed towards the microscope slab as well. If a temporal delay is present between the two pulses, the stretched pulse will pass through the microscope slab and its spectrum will be registered by the spectrometer. If the spatial and temporal overlap is achieved between

the two pulses, a part of the stretched pulse spectrum will be reflected by the plasma mirror. The result is a spectral cut in the measured spectrum.

A temporal scan is conducted by modifying the optical path difference between the two pulses and registering the wavelength at which the spectral cut is manifested for each pair of pulses. This leads to a spectrogram (collected spectra as a function of the delay), from which the spectral phase of the pulse can be reconstructed. In Figure 1.9.2, an example of such a spectrogram is shown.

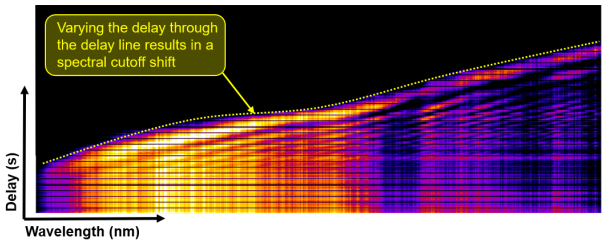

Figure 1.9.2: *Calibration spectrogram.*

By knowing the speed of the delay stage, the length of the optical path difference and the position of the cutoff between the spectra, a calibration curve was determined, which is shown in Figure 1.9.3.

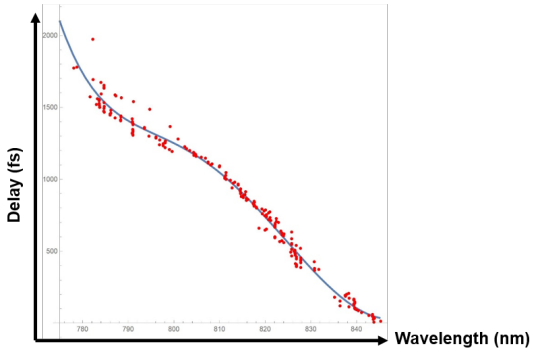

Figure 1.9.3: *Calibration curve extracted from the spectrogram.*

The temporal reconstruction of a pulse can be done by using the calibration curve from Figure 1.9.3 and the spectral intensity profile of the pulse.

We have converted the spectral information for few-picosecond scale pulses, using the calibration curve, as shown in Figure 1.9.4.

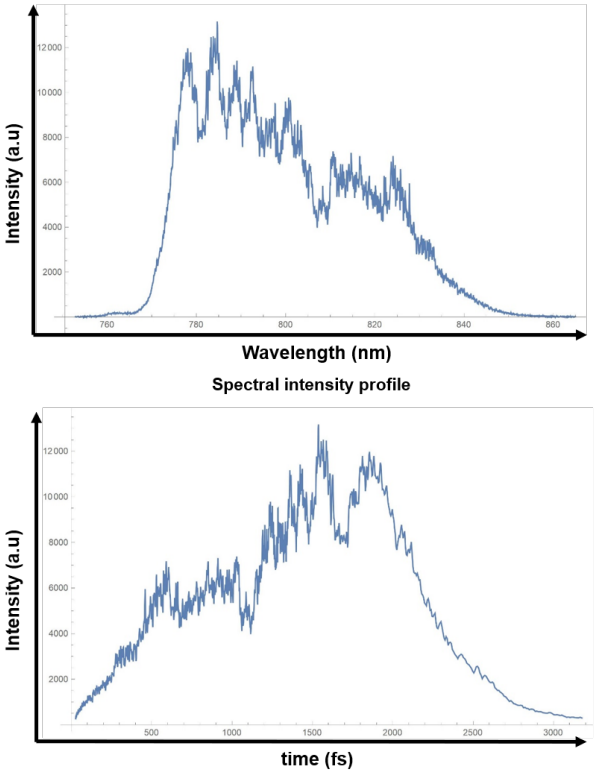

Figure 1.9.4: *Spectral intensity profile conversion to temporal intensity profile.*

Therefore, we have a frequency-resolved optical gating device with a very large dynamic range, 10 times larger than existing devices at ELI-NP. Compared to the previously mentioned literature reference [Ung+14], we demonstrated that the method works also in the few ps range, with sufficient resolution that allows reconstructing complex pulses far from the FT limit.

References

[Gal+18] S. Gales *et al.* "The extreme light infrastructure—nuclear physics (ELI-NP) facility: new horizons in physics with 10 PW ultra-intense lasers and 20 MeV brilliant gamma beams". In: *Reports on Progress in Physics* 81.9 (2018), page 094301. DOI: 10.1088/1361-6633/aacfe8 (cited on page 35).

[Lur+20] F. Lureau *et al.* "High-energy hybrid femtosecond laser system demonstrating 2 × 10 PW capability". In: *High Power Laser Science and Engineering* 8 (2020), e43. URL: https://doi.org/10.1017/hpl.2020.41 (cited on page 35).

[Ung+14] R. G. Ungureanu *et al.* "Phase measurement in long chirped pulses with spectral phase jumps". In: *Optics Express* 22.13 (2014), pages 15918–15923 (cited on pages 35, 36).

1.10 Qualification and optimization of helical phase pulses in PW-class laser systems at ELI-NP

Iancu V.[1,2 *] , Talposi M.[1,2] , Popa S.[1,2] , Ghenuche P. V.[1], Cernaianu M. O.[1], Doria D.[1] , Cojocaru G.[1,3] , Dancus I.[1] , Ungureanu R.[3] , Chalus O.[4] , Matei D. G.[1] , and Ursescu D.[1,2]

[1] Extreme Light Infrastructure (ELI-NP) & Horia Hulubei National Institute for R & D in Physics and Nuclear Engineering (IFIN-HH), Str. Reactorului No.30, 077125, Măgurele, Romania
[2] Faculty of Physics, University of Bucharest, Șoseaua Panduri, Nr. 90, Sector 5, 050663, Bucharest, Romania
[3] Center for Advanced Laser Technologies (CETAL), National Institute for Laser, Plasma and Radiation Physics (INFLPR), Str. Atomistilor No.409, 077125, Măgurele, Romania
[4] THALES Optronique, 2 Ave Gay Lussac CS90502, Elancourt,78995, France

[*] **vicentiu.iancu@eli-np.ro**

Abstract

Optical vortices, generated by a spiral phase plate, were propagated over long distances and focused in the PW experimental area. A deformable mirror was used to correct the low-order distortions, obtaining a doughnut focus.

1.10.1 Introduction

For the last thirty years, high-intensity large-scale laser facilities have provided a wide range of applications, ranging from fundamental laser-matter interaction to nuclear and astrophysics research. The High-Power Laser System (HPLS) within the Extreme Light Infrastructure – Nuclear Project (ELI-NP) project [Lur+20], is to be used to study particle acceleration, nuclear and high energy physics, and also industrial applications such as medical science or materials processing, etc. [Gal+18; Tan+20]. The HPLS is a two-arm hybrid laser system, based on an optical parametric chirped-pulse amplification (OPCPA) – used mainly in the front end - combined with Ti:Sapphire (Ti:Sa) high energy amplifiers, which is able to deliver femtosecond (fs) pulses with power of $2 \times 10\,\mathrm{PW}$ and peak irradiances over $1 \times 10^{20}\,\mathrm{Wcm}^{-2}$ to $1 \times 10^{23}\,\mathrm{Wcm}^{-2}$ [Lur+20].

Optical vortices (OVs), also known as Laguerre-Gaussian (LG) modes, are helical modes of light that are defined by a spiral moving wavefront. These LG modes are characterized by a property called a topological charge l, where the wavefront (WF) moves around the propagation axis with an azimuthal phase change of $2\pi l$. OVs have some unique features, such as an annular spatial form with a central null region (dark core) denoted as a phase singularity and an orbital angular momentum (OAM) of $l\hbar$ per photon (where $\hbar$ is the reduced Planck constant) [She+19]. Their particular topological characteristics have enabled OVs to find potential applications in various fields including laser-matter interaction, for charged particle acceleration [Bra+15; MS21].

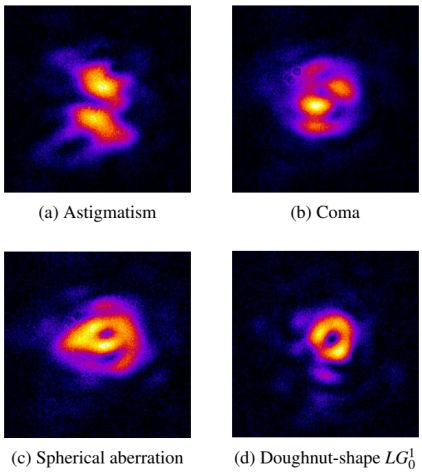

(a) Astigmatism (b) Coma

(c) Spherical aberration (d) Doughnut-shape LG_0^1

Figure 1.10.1: *The measured FF ring intensity distributions of the beam with OAM, showing the influence of (a) astigmatism, (b) coma, (c) spherical aberrations, and (d) corrected "doughnut-like".*

1.10.2 Experiment

We investigated the visibility and effects of WF aberrations on focused OAM laser beams after a propagation distance of over 30 m without relay imaging.

The experimental study took place in two phases, on the 1 PW amplification stage and diagnostics

bench and in the experimental area E5 of the ELI-NP facility. A spiral phase plate (SPP) generated the LG_0^1 doughnut-shaped laser pulses. The retractable SPP was implemented at the end of the 1 PW high energy amplification stage, in the proximity of the Deformable Mirror (DM) placed in front of the optical compressor [Lur+20].

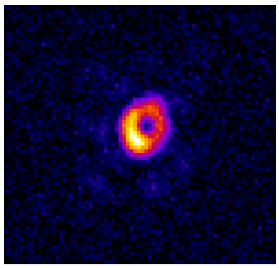

Figure 1.10.2: *Measured FF intensity distribution after* 30 m *free-space propagation, at the focal plane in the* 1 PW *interaction chamber.*

The preliminary optimization of the far-field (FF) was performed using the diagnostics bench placed at the exit of the 1 PW output of HPLS. The near field (NF) spatial profile was monitored to observe the intensity modulations using a CMOS Basler camera, and the WF with a HASO wavefront sensor (WFS) developed by Imagine Optic^{TM}. An energy of around 25 µJ was used for the full aperture (55 mm diameter), optically stretched pulses. The FF measurements on the diagnostics bench showed that the doughnut-like OV is extremely sensitive to low-order optical distortions, as pointed out also in [Ohl+19]. The correction of the low-order optical distortions was carried out with the DM. A sequence of various FF profiles obtained during the optimization is presented in Figure 1.10.1, resulting in a doughnut shape being obtained on the diagnostics bench.

The second optimization step took place after propagating the OV to the experimental area E5. This involved monitoring the intensity modulation of the NF and the shape of the FF in the experimental chamber at the target position. After readjusting the low-order distortions using the same DM in front of the 1 PW compressor, the doughnut shape FF was obtained, as shown in Figure 1.10.2.

1.10.3 Conclusion

In conclusion, the influence and correction of low-order aberrations on ultrashort pulses carrying OAM were studied experimentally in the specific conditions of ultra-intense laser systems. The doughnut-like tailored focus of LG laser pulses has shown high sensitivity to WF deformations, with astigmatism as the most critical aberration. Furthermore, the two-step approach presented here has made it possible to obtain the characteristic OV doughnut shape in the focal plane of an off-axis parabolic mirror even after more than 30 m of free space propagation. This opens the possibility of implementing laser-driven acceleration experiments with helical pulses at the 1 PW output at ELI-NP.

References

[Bra+15] C. Brabetz *et al.* "Laser-driven ion acceleration with hollow laser beams". In: *Physics of Plasmas* 22.1 (Jan. 2015), page 013105. DOI: 10.1063/1.4905638 (cited on page 37).

[Gal+18] S. Gales *et al.* "The extreme light infrastructure—nuclear physics (ELI-NP) facility: new horizons in physics with 10 PW ultra-intense lasers and 20 MeV brilliant gamma beams". In: *Reports on Progress in Physics* 81.9 (2018), page 094301. DOI: 10.1088/1361-6633/aacfe8 (cited on page 37).

[Lur+20] F. Lureau *et al.* "High-energy hybrid femtosecond laser system demonstrating 2 × 10 PW capability". In: *High Power Laser Science and Engineering* 8 (2020), e43. URL: https://doi.org/10.1017/hpl.2020.41 (cited on pages 37, 38).

[MS21] E. Molnár and D. Stutman. "Direct Laser-Driven Electron Acceleration and Energy Gain in Helical Beams". In: *Laser and Particle Beams* 2021 (May 2021), pages 1–13. DOI: 10.1155/2021/6645668 (cited on page 37).

[Ohl+19] J. B. Ohland *et al.* "A study on the effects and visibility of low-order aberrations on laser beams with orbital angular momentum". In: *Applied Physics B* 125.11 (Oct. 2019). DOI: 10.1007/s00340-019-7317-6 (cited on page 38).

[She+19] Y. Shen *et al.* "Optical vortices 30 years on: OAM manipulation from topological charge to multiple singularities". In: *Light: Science & Applications* 8.1 (Oct. 2019). DOI: 10.1038/s41377-019-0194-2 (cited on page 37).

[Tan+20] K. A. Tanaka *et al.* “Current status and highlights of the ELI-NP research program”. In: *Matter and Radiation at Extremes* 5.2 (Mar. 2020), page 024402. DOI: 10.1063/1.5093535. URL: https://doi.org/10.1063/1.5093535 (cited on page 37).

1.11 Development of a variable optical attenuator

Matei D. G.[1,*] , Naziru A.[1,2] , Sobetskii A.[3] , and Ursescu D.[1]

[1] Extreme Light Infrastructure (ELI-NP) & Horia Hulubei National Institute for R & D in Physics and Nuclear Engineering (IFIN-HH), Str. Reactorului No. 30, 077125 Bucharest– Măgurele, Romania
[2] University of Bucharest, Doctoral School of Physics, 077125 Bucharest-Măgurele, Romania
[3] SC MGM Star Construct SRL, Str. Pancota, Nr.7, Bl.13, Sc.1, Ap.19 Bucuresti, Sector 2, Romania

[*] **dan.matei@eli-np.ro**

Abstract

Two glass prisms are brought in close proximity. The evanescent field from the total internal reflection in one prism is used to obtain a beam with an irradiance tunable over 110 dB, with potential applications from medicine to materials processing.

1.11.1 Introduction

Complex high-power laser systems such as the one which is being commissioned at the Extreme Light Infrastructure - Nuclear Physics facility (ELI-NP) [Gal+18; Tan+20] comprise a large number of pump lasers with energies per pulse of several Joule of energy and above as well as a pulse duration in the nanosecond range. Owing to the high power involved, changes in beam properties like spatial profile or pointing could propagate and be amplified further in the chain, leading to possible damage to optical components. For this reason, permanent monitoring of the beam properties helps to achieve a long operating life-cycle of the system mainly consiting of expensive components.
In order to be monitored with CCD cameras or energy meters, the beam needs first to be attenuated several orders of magnitude using optical components that reflect or absorb a part of the incoming beam with high quality benchmarks. To achieve the required attenuation factor, several such components with fixed attenuation are placed in series.

The phenomenon of frustrated total internal reflection (FTIR) has been known for long [Zhu+86]. The use of the evanescent field that appears in the reflection surface for building attenuators up to 105 dB for the far-infrared has been reported earlier [AFM66; Lee76; OS71]. Its use for the visible range was hampered at that time by limitations in the precision of the machining of optical surfaces and positioning of the components. Recently, an attenuator for the visible range with a tunable range of 70 dB has been reported [GDU18].

1.11.2 Operating principle

Whenever a beam traveling in a medium is totally reflected at the interface with a lower refractive index medium, an evanescent field appears behind the reflecting surface. This field is known to decay exponentially with a characteristic length which is comparable with the wavelength of the beam.

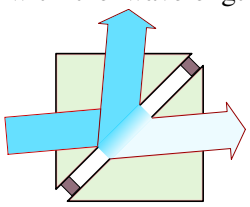

Figure 1.11.1: *Two prisms brought in close proximity and separated by spacers. The evanescent field from the total internal reflection of a beam at a prism-air interface is transmitted through the second prism.*

This fast decay can be exploited to sample a small and adjustable part of the incident beam by bringing a second medium within the range of the evanescent field. In practice, this can be achieved by using prisms as the propagation media for the beam, with an air gap between them. This is illustrated in Figure 1.11.1.

For a beam that is linearly polarized in the plane of incidence, the power transmitted through the prism-air-prism interfaces is [CW64; Orf03]:

$$T_p = |T|^2 = 1 - \left| \frac{r_a^{\parallel}(1 - e^{-2\alpha d})}{1 - (r_a^{\parallel})^2 e^{-2\alpha d}} \right|^2 \tag{1.11.1}$$

where d is the separation between prisms and α is the attenuation coefficient:

$$\alpha = \frac{2\pi}{\lambda}(n_a^2 sin^2\theta - n_b^2)^{1/2} \tag{1.11.2}$$

and $r_a^{\parallel}$ is Fresnel's electric field amplitude coefficient for reflection at the first interface [Orf03]:

$$r_a^{\parallel} = \frac{-in_a(n_a^2 sin^2\theta - n_b^2)^{1/2} - n_b^2 cos\theta}{-in_a(n_a^2 sin^2\theta - n_b^2)^{1/2} + n_b^2 cos\theta}. \quad (1.11.3)$$

In Equation 1.11.2 and Equation 1.11.3, n_a and n_b denote the refractive indices of the prism material and air, respectively, and θ is the incidence angle on the first prism-air interface.

1.11.3 Results and Outlook

Since the transmission coefficient from Equation 1.11.1 depends on both incidence angle and prism separation, a complete characterization in this two-dimensional space was performed by fixing the distance between prisms with spacers and changing the incidence angle through rotation of the prisms assembly relative to the incoming beam. The measurement was then repeated for different gap widths. The results are shown in Figure 1.11.2. The present measurements were limited by the optical noise in the setup. The preliminary analysis shows an excellent agreement between the measurement and the theory.

The high dynamic range of this FTIR-based attenuator for free-space optics industrial applications will generate technological advances. The development of versatile metrology for high power lasers would allow transforming pump lasers used in PW-class lasers from research-grade to industrial-grade, hence the production of industrial-grade PW laser systems. Complementary, such attenuators would enhance the capabilities of lasers in medical applications, materials processing with high power lasers and in laser-based additive manufacturing.

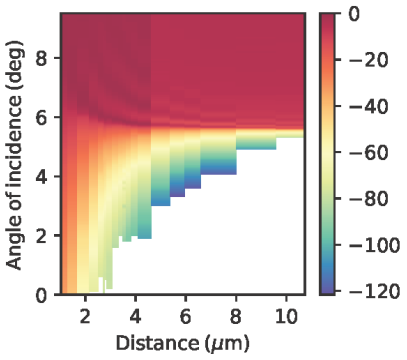

Figure 1.11.2: *The transmission coefficient in dB for the transmitted beam (right handside in Figure 1.11.1), measured as a function of (i) incidence angle at the entrance of the first prism, and (ii) prism separation.*

1.11.4 Acknowledgments

This project has received funding from the ATTRACT project funded by the EC under Grant Agreement 777222, part of the European Union's Horizon 2020 Research and Innovation Programme.

References

[AFM66] R. W. Astheimer, G. Falbel, and S. Minkowitz. "Infrared Modulation by Means of Frustrated Total Internal Reflection". In: *Appl. Opt.* 5.1 (Jan. 1966), pages 87–91. DOI: 10.1364/AO.5.000087. URL: http://ao.osa.org/abstract.cfm?URI=ao-5-1-87 (cited on page 41).

[CW64] I. N. Court and F. K. von Willisen. "Frustrated Total Internal Reflection and Application of Its Principle to Laser Cavity Design". In: *Appl. Opt.* 3.6 (June 1964), pages 719–726. DOI: 10.1364/AO.3.000719. URL: http://ao.osa.org/abstract.cfm?URI=ao-3-6-719 (cited on page 41).

[Gal+18] S. Gales *et al.* "The extreme light infrastructure—nuclear physics (ELI-NP) facility: new horizons in physics with 10 PW ultra-intense lasers and 20 MeV brilliant gamma beams". In: *Reports on Progress in Physics* 81.9 (2018), page 094301. DOI: 10.1088/1361-6633/aacfe8 (cited on page 41).

[GDU18] T. S. Georgescu, I. Dancus, and D. Ursescu. "Free space variable optical attenuator using frustrated total internal reflection with 70 dB dynamic range". In: *Applied Optics* 57.34 (Dec. 2018), pages 10051–10055. DOI: 10.1364/AO.57.010051. URL: http://ao.osa.org/abstract.cfm?URI=ao-57-34-10051 (cited on page 41).

[Lee76] W. R. Leeb. "Variable beam attenuator for 10.6 μm". In: *Review of Scientific Instruments* 47.5 (1976), pages 553–555. DOI: 10.1063/1.1134689. eprint: https://doi.org/10.1063/1.1134689. URL: https://doi.org/10.1063/1.1134689 (cited on page 41).

[Orf03] S. J. Orfanidis. *Electromagnetic Waves and Antennas*. Prentice-Hall, 2003 (cited on pages 41, 42).

[OS71] T. Oseki and S. Saito. “A Precision Variable, Double Prism Attenuator for CO2 Lasers”. In: *Appl. Opt.* 10.1 (Jan. 1971), pages 144–149. DOI: 10.1364/AO.10.000144. URL: http://ao.osa.org/abstract.cfm?URI=ao-10-1-144 (cited on page 41).

[Tan+20] K. A. Tanaka *et al.* “Current status and highlights of the ELI-NP research program”. In: *Matter and Radiation at Extremes* 5.2 (Mar. 2020), page 024402. DOI: 10.1063/1.5093535. URL: https://doi.org/10.1063/1.5093535 (cited on page 41).

[Zhu+86] S. Zhu *et al.* “Frustrated total internal reflection: A demonstration and review”. In: *American Journal of Physics* 54.7 (1986), pages 601–607. DOI: 10.1119/1.14514. eprint: https://doi.org/10.1119/1.14514. URL: https://doi.org/10.1119/1.14514 (cited on page 41).

1.12 Development of liquid optics and targets for laser-driven experiments

Aleksandrov V.[1] , Andrei V. C.[1,3] , Lupu A. M.[1] , Matei D. G.[1] , Popa S.[1,2,*] , Stan C. A.[4] , Ursescu D.[1] , and Vamesu M.[1]

[1] Extreme Light Infrastructure (ELI-NP) & Horia Hulubei National Institute for R & D in Physics and Nuclear Engineering (IFIN-HH), Str. Reactorului No. 30, 077125 Bucharest– Măgurele, Romania
[2] Doctoral School of Physics, University of Bucharest, Măgurele, Ilfov, 077125, Romania
[3] Technische Universität München, München, Germany
[4] Department of Physics, Rutgers University Newark, Newark, New Jersey 07102, US

[*] **stefan.popa@eli-np.ro**

Abstract

This report presents a series of developments aimed at the generation and characterization of liquid targets consisting of water microjets, droplets, and thin films with possible applications in laser-plasma interaction studies such as particle acceleration and plasma mirror optical switching.:

- A liquid microjet source was tested at ELI-NP. Stable water microjets, 40 µm diameter were produced and characterized using optical microscopy. Micro-droplets of various sizes, from 20 µm to 80 µm were generated using a piezoelectric actuator.
- Computer vision methods were implemented to make measurements of the geometrical properties of microdroplets by devising a two-stage detection and characterization algorithm. This enabled the extraction of geometrical features of each droplet separately and thus studying these features' time-evolution by incorporating a tracking stage.
- A setup capable of generating targets by colliding two liquid microjets is being developed in the Optics Laboratory at ELI-NP. Preliminary tests have shown the ability to produce liquid sheet targets in the air using water driven by nitrogen gas. Further developments will focus on vacuum integration and automation of the liquid target deployment system.

1.12.1 Introduction

As developments in high-power laser systems are reaching repetition rates higher than ever, targets have become one of the limitations in performing laser-plasma interaction experiments at such rates. Liquid targets offer an alternative to conventional solid targets, providing a regenerable substrate for plasma generation at high repetition rates. Liquid targets in the form of jets, sheets, and droplets have shown excellent performance at kHz repetition rates in laser-plasma interaction applications such as electron [Fei+17] and proton [Mor+18] acceleration or are used as reflective optical components in plasma mirror optical switches [Geo+19].

As outlined by Prencipe *et al.* [Pre+17], liquid targets and gas jets can overcome issues that affect their solid counterparts, such as: long replacement time, debris generation from ablation, and target fabrication lead time. In addition, the density of plasma produced in gases is typically 2-4 orders of magnitude lower than the critical density of lasers in the visible domain. Therefore, liquids are the most promising alternative, readily enabling over-critical density plasma formation.

1.12.2 Water microjets and droplets

Besides their potential as a general class of targets for ELI-NP, liquid jets and droplets are useful in the short term for setting up other experiments, including those with solid targets. A liquid jet, for example, can be used to locate with 1 µm accuracy the full-intensity focal region in the plane perpendicular to the beam. Also, liquid ablation experiments at X-ray lasers suggest that it will also be possible to locate the focal spot along the beam, leading to 3D micrometer-precision determination of the maximum-intensity position. Last, future investigations may lead to a method to measure and calibrate the maximum optical intensity.

Here a setup is tested that produces a water microjet with 40 µm diameter and length in excess of 2 mm. In addition, micro-droplets are also produced using a piezoelectric actuator.

The experimental setup used, depicted in Figure 1.12.1, consists of a pressurized nitrogen bot-

tle with a pressure regulator (PR1) that is providing 3 bar over-pressure at the input of a second pressure regulator (PR2). The second regulator is model 700-BE from ControlAir Inc. (Amherst, New Hampshire, USA) and allows excellent control of the overpressure of the gas in the liquid tank reservoir (LR). The reservoir, made from type 316 stainless steel, has a capacity of 300 mL and is filled with deionized water. The water is pushed through a tapered-hole borosilicate glass nozzle (MicroFab Technologies Inc., Plano, Texas, USA) with an outer diameter of 700 µm and an orifice diameter of 40 µm. The nozzle is also equipped with a piezoelectric actuator that can induce vibrations on the nozzle when connected to a signal generator. A Tektronix oscilloscope model MDO3104 with a waveform generator was used.

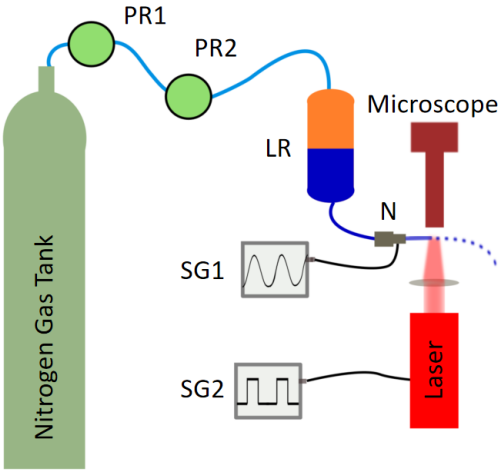

Figure 1.12.1: *Experimental setup: PR1 and PR2 rough pressure regulators, LR liquid reservoir, SG1 and SG2 signal generators, N Nozzle*

The microjet produced at the exit of the nozzle was visualized with a Leica Microscope model DM2700M, using an objective magnification of 5x. Two types of light sources were used for the illumination of the microjet under investigation. The built-in microscope light source (inline bright-field illumination) was used for liquid jets, while a low-power diode operated in a pulsed mode was used as a light strobe (inline bright-field illumination) to visualize the droplets produced. A typical image of the nozzle and microjet is presented in Figure 1.12.2.

Figure 1.12.2: *Image of the conical nozzle and the microjet recorded with the Leica microscope.*

When a sinusoidal electrical signal is added to the piezoactuator of the nozzle with 25 kHz, 1 V_{pp} measured in 50 Ω output impedance, the jet breaks at few hundreds of micrometer from the nozzle in droplets whose dynamics is synchronized with the piezo driving signal. The stroboscopic technique of synchronous illumination was used for the visualization of such droplets. The diode laser light source was driven by a square signal with less than 3.5 V, having 1 µs duration at 25 kHz repetition rate, generated from an AlphaNOV Tombak delay generator, 50 Ω output impedance.

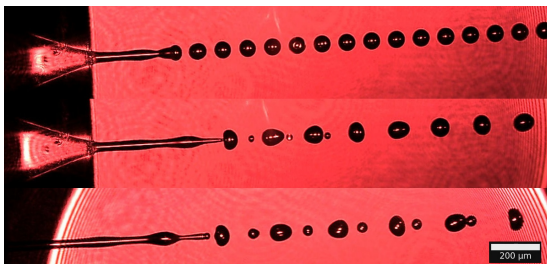

Figure 1.12.3: *Three images obtained using the strobe technique illustrating different types of droplets produced when varying the back pressure from* 180 mbar *to* 400 mbar.

The images of the droplets in Figure 1.12.3 were obtained using the strobing technique at different nitrogen backing pressure conditions. At overpressures as low as 180 mbar, similar round droplets are obtained as in the upper inset.

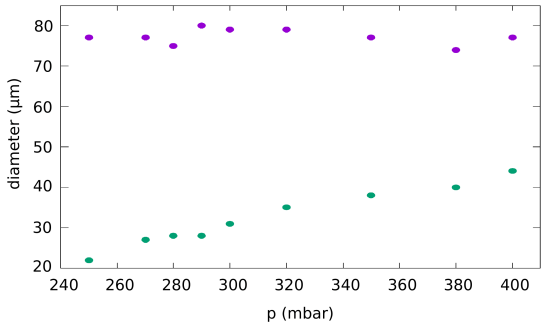

Figure 1.12.4: *Plot of the droplet size versus water pressure.*

Through the increase of the backpressure, two types of droplets are produced [DCM06; Le98]. The larger ones have a diameter two times bigger than the nozzle. They tend to have stronger initial deformation with the pressure increase, then they oscillate and tend to damp towards a circular shape. The smaller ones have a varying diameter, smaller than the nozzle diameter, as depicted in Figure 1.12.4. As they are slower, they are caught up by the big droplets.

To conclude, water microjets with lengths in excess of 2 mm were produced in air and visualized in the Optics Laboratory of the ELI-NP facility. In addition, droplets of various sizes were generated in a controlled manner with the help of a built-in piezoelectric actuator.

The setup shall also be implemented in vacuum [Sel+14; Sta+16] and then used in conjunction with ultrashort laser pulses at 100 TW 10 Hz or 1 PW 1 Hz outputs of ELI-NP.

1.12.3 Water droplets meet computer vision

Interest in microdroplets has increased substantially in the past years [See+11]. This is due to the convenient handling of miniature volumes, better mixing properties, and suitability to high-throughput experiments [See+11; Teh+08]. Acquiring certain physical or geometrical parameters of the droplets is a challenge, as the small size hinders one from making direct measurements. Computer Vision methods can be employed to solve this problem by estimating such characteristics from still microscope images or time-series of images (video data).

In this report, a two-stage detection and characterization algorithm was used to gather position, orientation, ellipticity, area, and perimeter measurements from three video files that were generated with the experimental setup presented in 1.12.2. In addition, we were able to track single droplets and associate single time series with them.

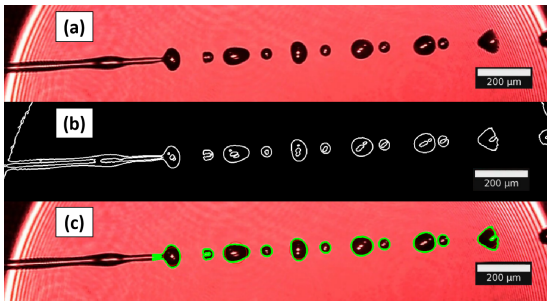

Figure 1.12.5: *(a) Example frame (adapted from 1.12.2); (b) Same frame after the pre-processing step; (c) Detected droplets.*

The method employed consists of two stages. First, the image is pre-processed in order to eliminate unwanted effects, such as speckle and diffraction patterns, and to emphasize the elliptical structure of the droplets. Then, the resulting grayscale image with smoothened images is fed to a blob detection algorithm [HU16]. The output of this stage is a list of key points consisting of center coordinates and spatial extent. Next, a binary mask is constructed out of the key points and applied to the grayscale image of smoothened edges. Finally, the contours are found using the algorithm presented in [SA06] from the masked image, which now only contains the edges corresponding to the droplets. For droplet tracking, the detection stage is run only once at the beginning of the video, then the image is masked, and the droplets are tracked using the Kernelized Correlation Filter [Hen+15] algorithm.

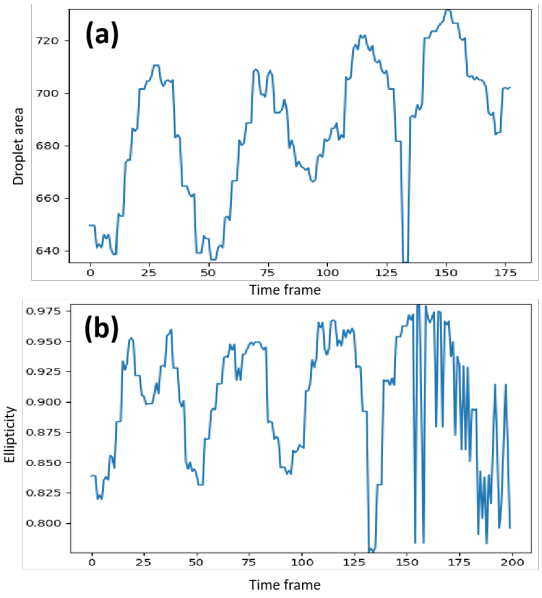

Figure 1.12.6: *(a) Area plot for one droplet; b) Ellipticity plot for one droplet.*

Figure 1.12.5 (a) shows a frame captured on video by the setup in 1.12.2. Figure 1.12.5 (b) showcases the pre-processing step. It can be seen that the background is eliminated almost completely, and the only details that are not filtered out are the shape of the nozzle and the droplets themselves. Figure 1.12.5 (c) shows the detected droplets with the shape of the contour drawn. It can be seen that droplets can be detected even if they have an irregular shape and even if they still did not get out of the nozzle.

Finally, by tracking droplets, we were able to plot the area and the ellipticity versus the time it could be observed on the screen. Figures 1.12.6 (a) and 1.12.6 (b) showcase this. Here we defined the ellipticity $\eta = m_a/M_a$ where m_a and M_a are the minor and the major axis of the ellipse fitted to the droplet.

We have demonstrated the ability of computer vision methods to make robust measurements of the geometrical properties of microdroplets by devising a two-stage detection and characterization algorithm. Furthermore, we were able to extract the geometrical features of each droplet individually and study the time evolution of these features.

Future work will use the acquired data in conjunction with a model of the physical phenomenon

behind droplet generation to find a method to extract droplets with desired features. Such a method should be implemented in hardware and integrated into the setup presented in 1.12.2.

1.12.4 Design of colliding microjet target

In laser-plasma acceleration experiments, target characteristics such as curvature [Bur+11], [Sen+04] and thickness [Gre+14] impact the proton yield and beam quality. Liquid targets generated from the collision of two jets or droplets offer a flexible geometry that can be modified *in situ* during experiments to tune the desired particle beam properties.

The setup being developed at ELI-NP, shown in Figure 1.12.7, is able to control the interaction of liquid jets and droplet trains created from piezoelectrically controlled nozzles. Similar to the design presented in 1.12.2, pressurized nitrogen gas is used to pump deionized water from a liquid reservoir through capillary tubing into two nozzles. The nozzles available can produce liquid jets with diameters in the range of 20 µm to 70 µm. A series of pressure regulators are used for precise control of the over-pressure.

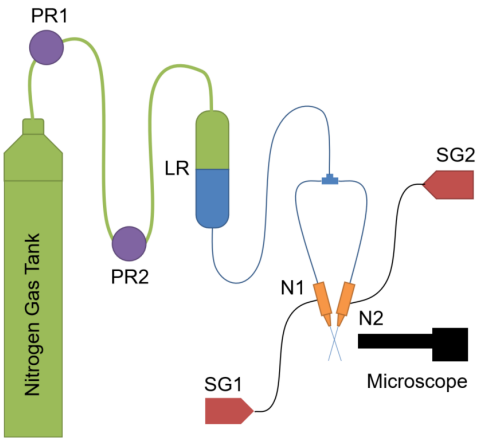

Figure 1.12.7: *Experimental setup for creating and imaging targets from two colliding microjets. PR1, PR2 - pressure regulator, LR - liquid reservoir, SG1, SG2 - signal generators, N1, N2 - nozzles.*

One of the two nozzles is fixed in position while the other can be moved relative to the first one. This is achieved by securing the second nozzle with a clamp attached to a tip-tilt mount which is connected to two translation stages and one rotation stage, allowing fine-tuning of the intersection plane and incidence angle of the two jets. The two nozzles can be connected to a signal generator to modulate the liquid jets into droplet trains with controllable frequency. One type of target demonstrated using the setup described is a liquid sheet obtained from the collision of two laminar microjets with diameters 30 µm and 40 µm, respectively. The two laminar flowing jets have been intersected 1.4 mm away from the nozzle exit, at an angle of 30° to the vertical direction, with an overpressure of 1.80 bar. The interaction produced the laminar sheet of liquid having a fusiform shape, as shown in Figure 1.12.8 (a). The image obtained, Figure 1.12.8 (b), reveals a length of 0.72 mm

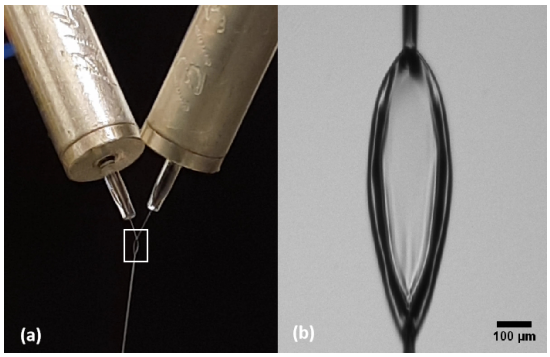

Figure 1.12.8: *(a) Image of two colliding microjets forming a laminar liquid film. (b) Microscope image of a laminar liquid film. The imaging direction is in the plane of the two jets (appearing overlapped at the top of the liquid film), perpendicular to the liquid sheet.*

and a maximum width of 0.20 mm, measured from the inner edge of the rim. The water sheet was imaged using a CCD camera fitted with an infinity-corrected 4× microscope objective. The imaging setup was calibrated using a standard resolution target.

Current efforts are aimed at characterizing the thickness profile of the obtained liquid films. Morrison *et al.* [Mor+18] have shown that the collision of two 30 µm jets can result in films as thin as 500 nm thick. Therefore, it is expected that the liquid targets developed at ELI-NP will have similar sub-micron thickness minima.

The development of liquid targets is a very active research field complementary to the development of high repetition ultra-intense lasers with applications beyond particle acceleration such as shock dynamics studies, high harmonic generation, and X-ray generation. In addition, further advances in target geometry control will enable the use of laser-plasma accelerated particles in nuclear physics and medical applications. The setup presented in this report provides a framework for future developments to produce a vacuum-compatible liquid target deployment system with real-time control of the target geometry.

1.12.5 Author contribution

CAS, DGM, VA, MV, and DU carried out the work on water microjet and droplet generation; VCA and DU developed and tested the droplet characterization software; SP, DGM, AML, DU and CAS carried out the work on colliding jet target development; SP compiled this manuscript with input from CAS, VCA and DU; DU and CAS conceived the study and coordinated this research.

References

[Bur+11] M. Burza *et al.* "Hollow microspheres as targets for staged laser-driven proton acceleration". In: *New Journal of Physics* 13.1 (2011), page 013030 (cited on page 48).

[DCM06] H. Dong, W. W. Carr, and J. F. Morris. "An experimental study of drop-on-demand drop formation". In: *Physics of Fluids* 18.7 (2006), page 072102. DOI: 10.1063/1.2217929. eprint: https://doi.org/10.1063/1.2217929. URL: https://doi.org/10.1063/1.2217929 (cited on page 46).

[Fei+17] S. Feister *et al.* "Relativistic electron acceleration by mJ-class kHz lasers normally incident on liquid targets". In: *Optics express* 25.16 (2017), pages 18736–18750 (cited on page 45).

[Geo+19] K. George *et al.* "High-repetition-rate ($\geq$ kHz) targets and optics from liquid microjets for high-intensity laser–plasma interactions". In: *High Power Laser Science and Engineering* 7 (2019) (cited on page 45).

[Gre+14] J. Green *et al.* "High efficiency proton beam generation through target thickness control in femtosecond laser-plasma interactions". In: *Applied Physics Letters* 104.21 (2014), page 214101 (cited on page 48).

[HU16] K. T. M. Han and B. Uyyanonvara. "A Survey of Blob Detection Algorithms for Biomedical Images". In: *2016 7th International Conference of Information and Communication Technology for Embedded Systems (IC-ICTES)*. Mar. 2016, pages 57–60. DOI: 10.1109/ICTEmSys.2016.7467122 (cited on page 47).

[Hen+15] J. F. Henriques *et al.* "High-Speed Tracking with Kernelized Correlation Filters". In: *IEEE Transactions on Pattern Analysis and Machine Intelligence* 37.3 (Mar. 2015), pages 583–596. ISSN: 2160-9292. DOI: 10.1109/tpami.2014.2345390. URL: http://dx.doi.org/10.1109/TPAMI.2014.2345390 (cited on page 47).

[Le98] H. P. Le. "Progress and Trends in Ink-jet Printing Technology". In: *Journal of Imaging Science and Technology* 42.1 (1998), pages 49–62. ISSN: 1062-3701. URL: https://www.imaging.org/Site/IST/Resources/Tutorials/Inkjet.aspx?WebsiteKey=6d978a6f-475d-46cc-bcf2-7a9e3d5f8f82&hkey=4af47800-9584-4480-be8d-45fc3ee53e86&TemplateType=P (cited on page 46).

[Mor+18] J. T. Morrison *et al.* "MeV proton acceleration at kHz repetition rate from ultra-intense laser liquid interaction". In: *New Journal of Physics* 20.2 (2018), page 022001 (cited on pages 45, 48).

[Pre+17] I. Prencipe *et al.* "Targets for high repetition rate laser facilities: needs, challenges and perspectives". In: *High Power Laser Science and Engineering* 5 (2017) (cited on page 45).

[See+11] R. Seemann *et al.* "Droplet based microfluidics". In: *Reports on Progress in Physics* 75.1 (Dec. 2011), page 016601. DOI: 10.1088/0034-4885/75/1/016601. URL: https://doi.org/10.1088/0034-4885/75/1/016601 (cited on page 47).

[Sel+14] J. A. Sellberg *et al.* "Ultrafast X-ray probing of water structure below the homogeneous ice nucleation temperature". In: *Nature* 510 (June 2014), page 381. URL: https://doi.org/10.1038/nature13266 (cited on page 47).

[Sen+04] Y. Sentoku *et al.* "Laser light and hot electron micro focusing using a conical target". In: *Physics of Plasmas* 11.6 (2004), pages 3083–3087 (cited on page 48).

[Sta+16] C. A. Stan *et al.* "Liquid explosions induced by X-ray laser pulses". In: *Nature Physics* 12 (May 2016), page 966. URL: https://doi.org/10.1038/nphys3779 (cited on page 47).

[SA06] S. Suzuki and K. Abe. "Topological structural analysis of digitized binary images by border following." In: *Computer Vision, Graphics, and Image Processing* 30.1 (Sept. 4, 2006), pages 32–46. URL: http://dblp.uni-trier.de/db/journals/cvgip/cvgip30.html#SuzukiA85 (cited on page 47).

[Teh+08] S.-Y. Teh *et al.* “Droplet Microfluidics”. In: *Lab on a chip* 8 (Mar. 2008), pages 198–220. DOI: 10.1039/b715524g (cited on page 47).

1.13 Laser induced damage threshold station developed at ELI-NP

Bleotu G.-P.[1,2,3*], Matei D. G.[1], Cojocaru G.[1], Naziru A.[1,2] , Dancus I.[1] , and Ursescu D.[1]

[1] Extreme Light Infrastructure (ELI-NP) & Horia Hulubei National Institute for R & D in Physics and Nuclear Engineering (IFIN-HH), Str. Reactorului No. 30, 077125 Bucharest– Măgurele, Romania
[2] LULI-CNRS, CEA, Universite Sorbonne, Ecole Polytechnique, Institut Polytechnique de Paris, F-91128 Palaiseau Cedex, France
[3] University of Bucharest, Doctoral School of Physics, 077125 Bucharest-Măgurele, Romania

[*] **gabriel.bleotu@eli-np.ro**

Abstract

HPLS performance of 10 PW was made possible by the latest advances in the field of optical components developments. The optical components should be designed to withstand high values of fluence and irradiance, and thus they require a high laser-induced damage threshold (LIDT). A complete automatized experimental setup, using similar pulse duration and wavelength as the HPLS of ELI-NP (femtosecond regime, 800 nm) was designed to estimate, *in situ*, the LIDT, in both reflection and transmission.

1.13.1 Introduction

The Laser Induced Damage Threshold (LIDT) is an important qualification criterion for high power laser system components, providing information about the irradiance limits which can be used without affecting the component. Following the ISO 21254-1-4:2011 standards, multiple groups were developing dedicated setups and laboratories (i.e. Spica Technologies, Laser Zentrum Hannover, LIDARIS, ISOTEST) to measure the LIDT [Str+12] or methods to qualify the LIDT [Hu+11; Zha+21]. The value of the LIDT is dependent on the wavelength, beam diameter, and, most importantly, the pulse duration [DSK02; GNA02; GN03].

Different testing methods, such as 1-on-1 (one shot and one spot), R-on-1 (fixed number of R shots on the same spot ramping the energy), S-on-1 (several measurements using S shots on multiple spots), and pass-fail are used to qualify the damage. The increase in light scattering at the test site is interpreted as altering the bulk or surface properties by the contributing damage mechanism. The chosen LIDT detection methods for this work were based on ex-situ microscopy and *in situ* beam profile monitoring. These combined methods provide multiple advantages: high sensitivity and clear correlation to functional damage, direct image generation, high reliability, and suitability for both surface and bulk damages.

1.13.2 Method

A long working distance imaging system (LWDIS) (see Figure 1.13.1) was designed and manufactured to efficiently monitor and diagnose, in real-time, the intensity pattern in the interaction area of a laser beam with the sample. This imaging system was also proposed to qualify the focal spot of the high power laser systems [Dro+09]. The LWDIS is realized using an 8-inch aperture spherical mirror to gather the light and a microscope objective to magnify the image further and transfer it to the CMOS detector plane. A 6-inch diameter beamsplitter with a transmitted wavefront of $\lambda/20$ is used to redirect the light reflected from the spherical mirror to the microscope objective and to attenuate the incoming light amplitude. A series of LWDIS object plane images were recorded with the CMOS camera to monitor the appearance of damage at each energy step. After laser irradiation, a novel LIDT method based on the spatial frequencies analysis (SFA) in the recorded beam profile was used to estimate the damage threshold.

Complementary, the samples were analyzed at the Leica microscope (model Leica-dm2700-m) to establish at which energy level the damage starts and also to validate the SFA method.

The SFA method is based on image processing and Fourier analysis. The image processing includes: background subtraction and image cropping around the center of the beam. The Fourier analysis is used to compute the 2-dimensional discrete Fourier Trans-

form of the images and to sample the frequencies for x and y axis. The process is followed by a weighted radius histogram on the Fourier transformed data that provides a power spectrum curve.

In situ monitoring of the LWDIS data was the quickest method to estimate when the damage occurred in real-time. It also provides an alternative method to qualify the image analysis's optical nonlinearities.

1.13.3 Experimental Setup

The experimental setup used is depicted in Figure 1.13.1. The main sub-assembly is LWDIS that measures the laser focus and through image processing, can qualify the LIDT.

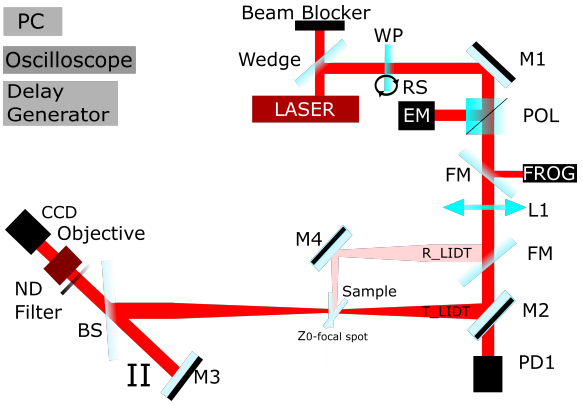

Figure 1.13.1: *Experimental Setup: Long Working Distance Imaging System (LWDIS) for LIDT measurements (in transmission T_{LIDT} in reflection R_{LIDT}). Optical elements: BS - beam splitter, EM - energy meter, FM - flip mirror, LASER - Ti:Sapphire, L1 - focusing lens, M1, M4 - high-reflectance mirrors, M2- 99% reflectivity mirror, M3 - spherical mirror, ND - neutral density filter, POL - polarizer, PD1 - photodiode, TS - translation stage, RT - rotation stage, WP - half-wave birefringent plate*

A Ti:sapphire laser system provides close to Fourier transform limit laser pulses (40 fs, 800 nm, 10 Hz, 1 mJ) to the experimental setup. The pulse energy was reduced down to 0.1 µm 0.1 by using the combination of a half-waveplate (WP) and polarizer cube (POL). The energy on the sample is monitored using 1% of the transmitted energy through the mirror M2 on PD1 calibrated using Malus' law.

The pulse duration (60 ± 3) fs was measured using an SHG FROG [Tre+97] and can be tuned using the optical compressor of the laser system up to hundreds of fs. The beam area was measured using the LWDIS calibrated with 1951 USAF slit targets.

1.13.4 Discussion

The SFA method was used to estimate the LIDT through two methods. The first method takes into account the extracted power spectrum of each image. A clear jump in the curves is observed when the damage occurs (see Figure 1.13.2). A cross-check with the microscope validated the LIDT on both axes. Different measurements at different input energies show the difference between the image without damage (blue) and the damaged ones.

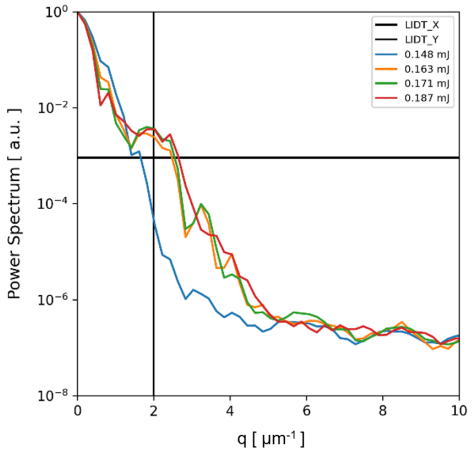

Figure 1.13.2: *Power spectrum as a function of beam's spatial frequencies*

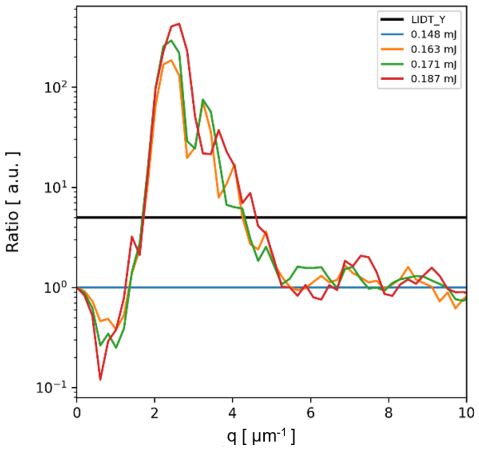

Figure 1.13.3: *The ratio between the power spectra and a reference power spectrum (no damage)*

The second method is based on the ratio magnitude where each power spectra is divided by the reference one, recorded at low energy where no damage is observed *ex situ*.

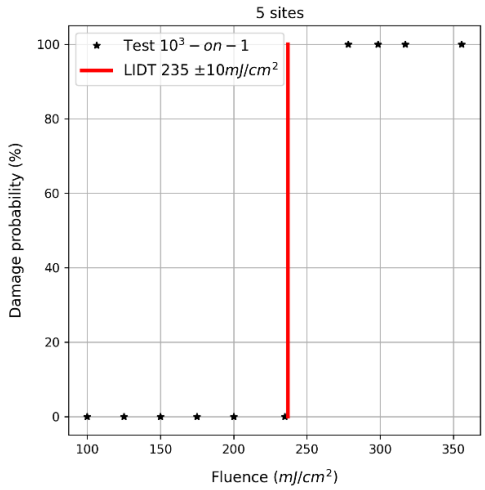

Figure 1.13.4: *Damage probability (5 sites /energy value were used for statistics)*

The results were summarized in the Figure 1.13.4 where the damage probability is shown.

1.13.5 Conclusion

We demonstrated the capabilities of an in-house built LIDT station at the existing laser system in the Optics Lab, based on Ti:Sapphire amplification (800 nm) similar to HPLS and having femtosecond pulse duration. The station can determine the LIDT of optical components in transmission. In reflection (dedicated to coated surfaces), 10 Hz or single shot, 1-on-1 or R-on-1 using the corresponding *in situ* and *ex situ* LIDT monitoring methods. The LIDT station is entirely automated.

References

[DSK02] S. G. Demos, M. Staggs, and M. R. Kozlowski. "Investigation of processes leading to damage growth in optical materials for large-aperture lasers". en. In: *Applied Optics* 41.18 (June 2002), page 3628. ISSN: 0003-6935, 1539-4522. DOI: 10.1364/AO.41.003628. URL: https://www.osapublishing.org/abstract.cfm?URI=ao-41-18-3628 (visited on 09/28/2020) (cited on page 51).

[Dro+09] B. Dromey *et al.* "Third harmonic order imaging as a focal spot diagnostic for high intensity laser-solid interactions". en. In: *Laser and Particle Beams* 27.2 (June 2009). Num Pages: 5 Number: 2, pages 243–248. ISSN: 0263-0346. DOI: 10.1017/S0263034609000329. URL: http://dx.doi.org/10.1017/S0263034609000329 (visited on 07/26/2021) (cited on page 51).

[GNA02] L. Gallais, J. Natoli, and C. Amra. "Statistical study of single and multiple pulse laser-induced damage in glasses". en. In: *Optics Express* 10.25 (Dec. 2002), page 1465. ISSN: 1094-4087. DOI: 10.1364/OE.10.001465. URL: https://www.osapublishing.org/oe/abstract.cfm?uri=oe-10-25-1465 (visited on 09/04/2020) (cited on page 51).

[GN03] L. Gallais and J.-Y. Natoli. "Optimized metrology for laser-damage measurement: application to multiparameter study". en. In: *Applied Optics* 42.6 (Feb. 2003), page 960. ISSN: 0003-6935, 1539-4522. DOI: 10.1364/AO.42.000960. URL: https://www.osapublishing.org/abstract.cfm?URI=ao-42-6-960 (visited on 09/09/2020) (cited on page 51).

[Hu+11] J. Hu *et al.* "Image processing method for laser damage probability measurement by single-shot of laser pulse". In: *Opt. Express* 19.11 (May 2011). Publisher: OSA, pages 10625–10631. DOI: 10.1364/OE.19.010625. URL: http://opg.optica.org/oe/abstract.cfm?URI=oe-19-11-10625 (cited on page 51).

[Str+12] A. Stratan *et al.* "Automated test station for laser-induced damage threshold measurements according to ISO 21254-1,2,3,4 standards". In: *Proc SPIE* (Nov. 2012). DOI: 10.1117/12.976845 (cited on page 51).

[Tre+97] R. Trebino *et al.* "Measuring ultrashort laser pulses in the time-frequency domain using frequency-resolved optical gating". en. In: *Review of Scientific Instruments* 68.9 (Sept. 1997), pages 3277–3295. ISSN: 0034-6748, 1089-7623. DOI: 10.1063/1.1148286. URL: http://aip.scitation.org/doi/10.1063/1.1148286 (visited on 11/12/2020) (cited on page 52).

[Zha+21] Y. Zhang *et al.* "Effect of interface on femtosecond laser damage of metal-dielectric low dispersion mirror". In: *Optics Express* 29 (Feb. 2021). DOI: 10.1364/OE.416141 (cited on page 51).

1.14 Peer-reviewed publications, talks, PhD/MSc, & Grants for LSD in 2020-2021

Peer-reviewed publications by LSD staff: 01.01.2020 to 31.12.2021

[Ale+20] V. Aleksandrov *et al.* "Upgrading design of a multi-TW femtosecond laser". In: *Romanian Reports in Physics* 72 (2020), page 413.

[Dab21] R. Dabu. "Optical parametric amplification at critical wavelength degeneracy-a proposed approach for 100-PW class femtosecond laser development". In: *OSA CONTINUUM* 4.5 (May 2021), pages 1658–1668. ISSN: 2578-7519. DOI: 10.1364/OSAC.416451.

[Kol+20] G. Kolliopoulos *et al.* "Cleansing Data from the High-Power Laser System in ELI-NP: a Holistic System Approach". In: *Romanian Reports in Physics* 72.3 (2020). ISSN: 1221-1451.

[Kum+21] Y. Kumagai *et al.* "Suppression of thermal nanoplasma emission in clusters strongly ionized by hard x-rays". In: *Journal of Physics B - Atomic Molecular and Optical Physics* 54.4 (Feb. 2021). ISSN: 0953-4075. DOI: 10.1088/1361-6455/abd878.

[Las+21] A. Laso Garcia *et al.* "ReLaX: the Helmholtz International Beamline for Extreme Fields high-intensity short-pulse laser driver for relativistic laser-matter interaction and strong-field science using the high energy density instrument at the European X-ray free electron laser facility". In: *High Power Laser Science and Engineering* 9 (Oct. 2021). ISSN: 2095-4719. DOI: 10.1017/hpl.2021.47.

[Lur+20a] F. Lureau *et al.* "10 petawatt lasers for extreme light applications". In: *Solid State Lasers XXIX: Technology and Devices*. Volume 11259. International Society for Optics and Photonics. 2020, 112591J.

[Lur+20b] F. Lureau *et al.* "High-energy hybrid femtosecond laser system demonstrating 2× 10 PW capability". In: *High Power Laser Science and Engineering* 8 (2020).

[Tan+20] K. Tanaka *et al.* "Current status and highlights of the ELI-NP research program". In: *Matter and Radiation at Extremes* 5.2 (2020), page 024402.

[Urs+20b] D. Ursescu *et al.* "Generation of shock trains in free liquid jets with a nanosecond green laser". In: *Physical Review Fluids* 5.12 (2020), page 123402.

Invited talks delivered by LSD staff: 01.01.2020 to 31.12.2021

[Ble+21] G. P. Bleotu *et al.* "Experimental setup for optical films Laser Induced Damage Threshold measurements". In: *13th International Conference on Physics of Advanced Materials (ICPAM-13) (24-30 September 2021) - Spain*. 2021.

[Dab20a] R. Dabu. "Optical Parametric Amplification at Critical Wavelength Degeneracy – a Way towards 100-PW Femtosecond Lasers". In: *Laser Congress 2020 (13–16 October 2020) Washington, D.C. United States*. 2020.

[Dab20b] R. Dabu. "Optical Parametric Chirped Pulse Amplification at Critical Wavelength Degeneracy - a proposed solution for 100-PW Femtosecond Lasers Development". In: *OSA Frontiers in Optics + Laser Science APS/DLS (14-17 September 2020) - Washington, DC, United States*. 2020.

[Dab20c] R. Dabu. "Proposed Approach Based on Optical Parametric Amplification at Critical Wavelength Degeneracy for the Development of 100-PW Class Femtosecond Lasers". In: *The 22nd International Conference on Ultrafast Phenomena (16–19 November 2020) Washington, D.C. United States*. 2020.

[Dan20a] I. Dancus. "High power laser systems at ELI-NP - status and perspectives". In: *LOEWE Nuclear Photonics Workshop (24-25 September 2020) - TU-Darmstadt, Online*. 2020.

[Dan20b] I. Dancus. “Prospects for Ultra High lrradiance at Extreme Light Infrastructure - Nuclear Physics”. In: *OSA Frontiers in Optics + Laser Science APS/DLS (14-17 September 2020) - Washington, DC, United States*. 2020.

[Dan20c] I. Dancus. “The ELI-NP High Power Laser System and the High Irradiance Perspectives”. In: *LPA Online Seminars, hosted by GSI and LMU Munich (3 November 2020) - Online*. 2020.

[Dan21a] I. Dancus. “High Power Laser System at ELI-NP”. In: *Carpathian Summer School (18-27 August 2021) - Sinaia, Romania*. 2021.

[Dan21b] I. Dancus. “High Power Laser System at ELI-NP”. In: *ELI Summer School 2021 (24-27 August 2021) - Online*. 2021.

[TU21] A.-M. Talposi and D. Ursescu. “Propagation of ultra-short laser fields”. In: *Advances in 3OM: Opto-Mechatronics, Opto-Mechanics and Optical Metrology (13-16 December 2021) - Timisoara, Romania - Best Doctoral Student Paper Award*. 2021.

[Urs20c] D. Ursescu. “First HPLS Experiments at ELI-NP: Spectral Broadening in Thin Films”. In: *OSA Frontiers in Optics + Laser Science APS/DLS (14-17 September 2020) - Washington, DC, United States*. 2020.

[Urs21a] D. Ursescu. “At the core of the Extreme Light Infrastructure: Laser pulses metrology”. In: *CLEO2021 - Super Topical Review on High Power Laser Technology symposium (9-14 May 2021) San Jose, California, United States*. 2021.

[Urs21b] D. Ursescu. “Ultra-intense laser pulses and the High Power Laser System at Extreme Light Infrastructure - Nuclear Physics”. In: *Femto-UP 2020-21: Ultrafast lasers technologies and applications (8-29 Mar 2021) Online, France*. 2021.

Grants with LSD staff as coordinator: 01.01.2020 to 31.12.2021

[Urs20a] D. Ursescu. “High power laser beam profile and pointing measurement - HPLM”. In: *ATTRACT - CERN* (2020).

[Urs20b] D. Ursescu. “Spectral broadening for ultrashort focused pulses - SBUF”. In: *ELI-RO* (2020).

2. Gamma System Department (GSD)

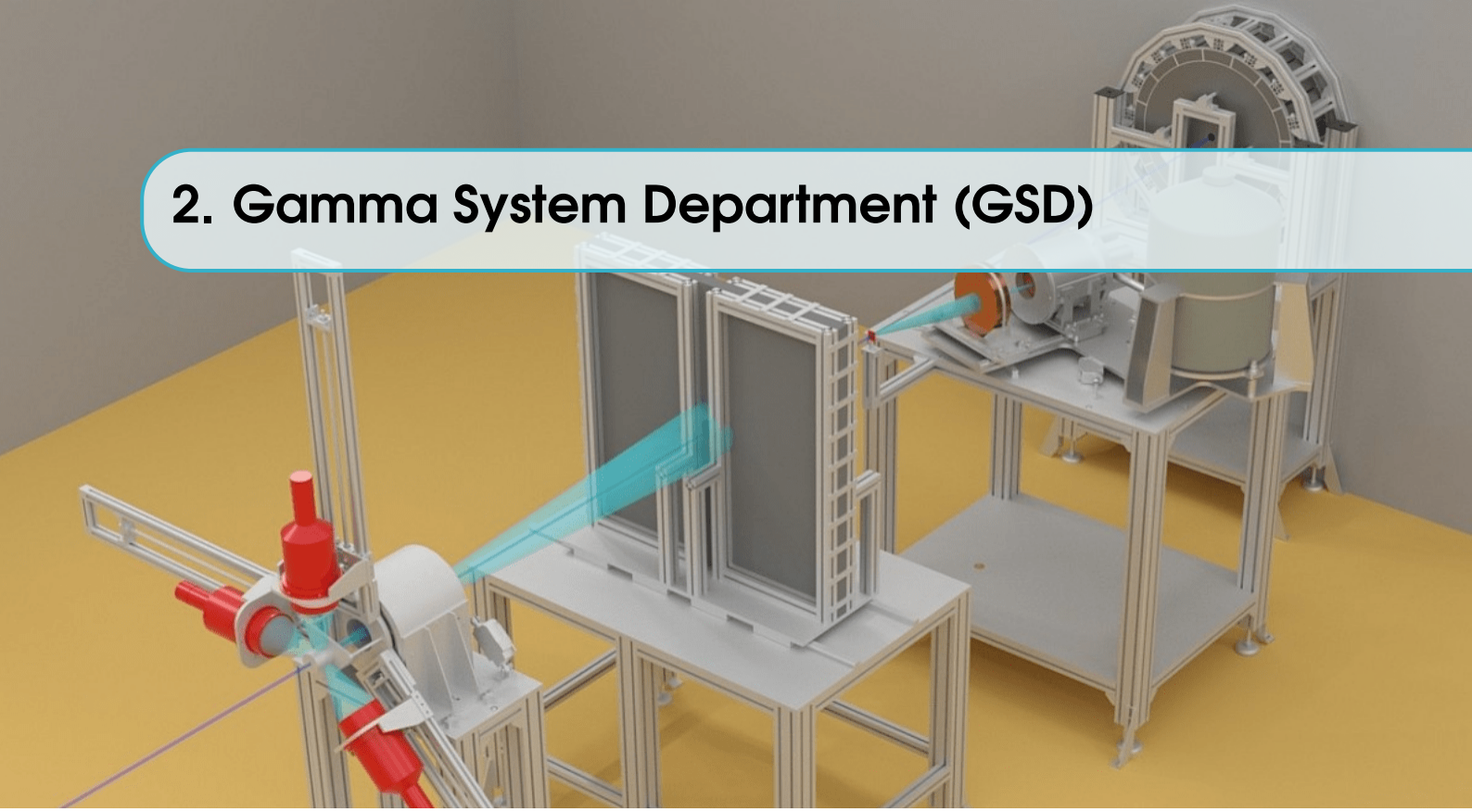

Introduction

THE VARIABLE ENERGY GAMMA SYSTEM (VEGA) [ELI22] is a dedicated system for delivering gamma-ray beams to users. The construction of the VEGA System was awarded to Lyncean Technologies Inc., and its delivery, installation, and acceptance are scheduled to be completed in early 2023.
The system will deliver gamma-rays with energy continuously variable from 1 MeV up to 19.5 MeV covering the energy range relevant for low-energy nuclear physics and astrophysics studies and applied research in materials science, management of nuclear materials, and life sciences. In addition, the beams will be quasi-monochromatic by having a relative energy bandwidth better than 0.5%, high intensity with a spectral density higher than 5×10^3 photons/eV/s and a high degree of linear polarization at more than 95%. With these parameters, the VEGA System will be the most advanced gamma-ray source globally, having about one order of magnitude higher gamma-ray flux and at least a factor of two smaller relative bandwidths than the current state-of-the-art installations.
The VEGA System is based on the use of a storage ring and a high-finesse Fabry-Perot cavity. The electron beam and the interaction laser parameters are optimized at the interaction point to provide gamma-rays with the features discussed above. The electron beam system will operate in the range of 234 MeV to 742 MeV. For a given interaction laser wavelength, this electron energy range allows at least a factor of 10 in gamma-ray energy continuous tunability. Two separate optical cavity laser systems, one at $\sim 1\,\mu$m ('IR') and one at $\sim 0.5\,\mu$m ('Green') wavelengths, will be provided to cover the gamma-ray energy range from 1 MeV to 19.5 MeV. The laser systems use a passive, high-finesse Optical Cavity to build up pulsed laser power resonantly. The Optical Cavity provides gains of 5,000-10,000 in laser power, which reduces the complexity of the interaction laser drive system.

References

[ELI22] ELI-NP. *Variable Energy Gamma (VEGA) System at ELI-NP*. 2022. URL: http://www.eli-np.ro/rd2_second.php (visited on 01/10/2022) (cited on page 57).

2.1 Implementation of an analogue data acquisition system for optimizing the anti-Compton shield for the HPGe detector in the Gamma Energy Station

Baruta S.[1] , Pappalardo A.[1,*] , and Matei C.[1]

[1] Extreme Light Infrastructure (ELI-NP) & Horia Hulubei National Institute for R & D in Physics and Nuclear Engineering (IFIN-HH), Str. Reactorului No. 30, 077125 Bucharest– Măgurele, Romania

[*] **alfio.pappalardo@eli-np.ro**

Abstract

We present a method to reduce the Compton background from the spectra acquired with the HPGe and NaI(Tl) detectors, which form the Beam Energy Station, used to measure the energy of the gamma beams implemented at ELI-NP. Gamma-ray beams generated at ELI-NP , characterized by relatively high energies, produce a significant Compton background in the acquired spectra. The reduction of this background will allow to determine the energy of the gamma beams with improved precision.

2.1.1 Introduction

In gamma-ray spectrometry performed with High-Purity Germanium (HPGe) detectors, the detection of low-intensity gamma-ray lines is complicated by the presence of Compton scattered gamma rays from higher energy interactions. At energies above a few hundred keV, the main interaction in the relatively low-Z High-purity Germanium crystal is *via* Compton interaction. The Compton scattered gamma rays give rise to a continuous background in the gamma-ray spectrum, which consequently raises the detection limit for lines at low energies.
A way to suppress these Compton scattered gamma rays is to surround the HPGe crystal with a scintillation material. When Compton scattered gamma rays escape from the HPGe detector and are absorbed and detected in this so-called Compton Suppression shield, they are coincident in time with the gamma photon detected in the HPGe crystal. When one observes coincident signals in the HPGe detector and Compton suppression shield, a signal can be set to block the recording of the Compton interaction event.
This technique is called Compton suppression spectrometry [KMH66]. The detector with which this is done is called an "Anti-Compton Shield" (ACS).

2.1.2 Experimental apparatus.

As mentioned in the introduction, the detectors involved in the energy measurements of the gamma beam are the HPGE detector manufactured by Canberra and the ACS manufactured by Scionix Holland. The HPGe detector geometry is a coaxial one open-end, closed end-facing window. The relativity efficiency is 150% with an energy resolution of 2.4 keV at 1.33 MeV. The detector is powered by a Caen power supply DT5521EMH with a positive high voltage of 4000 V.

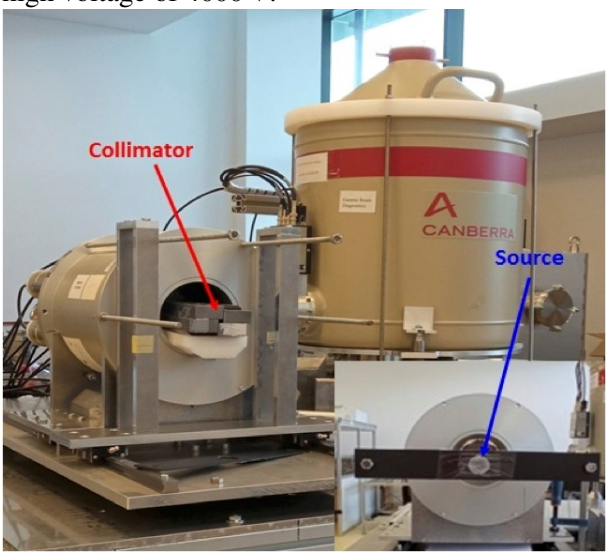

Figure 2.1.1: *Experimental apparatus (HPGe+ACS).*

The ACS is constituted by an annular NaI(Tl). The total length of the crystal is 305 mm and the outer diameter 280 mm, the diameter of the central hole being 110 mm. The crystal is viewed by six ETL 9266 photomultiplier tubes coupled to one end of the annulus. The high voltage for the photomultiplier tubes is supplied by a common CAEN DT5533 high-voltage supply. Each voltage divider of the PMT is provided with a trimmer in order to equalize the

gains of the tubes. The signals of the photomultipliers are summed by simply feeding them into the same preamplifier input. This arrangement was found electronically satisfactory. Both detectors are equipped with a charge preamplifier that delivers a signal proportional to the energy deposited inside the detectors. The HPGe is equipped with a Canberra preamplifier, model 2002C, with a sensitivity of 100 mV/MeV, the ACS instead, is connected with a CAEN preamplifier, model A1424 (Figure 2.1.1).

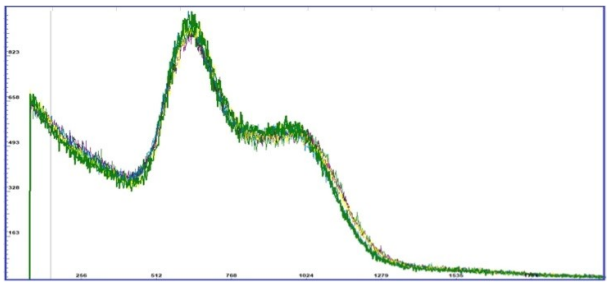

Figure 2.1.2: *Balancing of the six ACS photomultiplier.*

In general, Compton suppression systems do not require fast timing and fast coincidence electronics in order to provide good suppression [Bik+12]. Coincidence resolving times with values of 0.5 µs to 1.0 µs are suitable for the desired purpose. In order to perform the electronic setup to evaluate the performance of the experimental configuration consisting of the HPGe detector and the anti-Compton shield, two different electronic approaches were considered: one using "Fast timing" and the other using "Easy timing".
The "Fast timing" system uses filter amplifiers and constant fraction discriminators, which are necessary for the ultimate timing resolution. Setting up and adjusting electronics using this approach requires a lot of skill and experience.
Instead, the "Easy timing" system uses the spectroscopic amplifier (Ortec 671) with its CRM (Counter Rate Meter) fast discriminator circuit for coincidence, resulting in a simple system, without special adjustment procedures.
The CRM circuit is easily adjusted using the discriminator pile-up rejector, there are no delays between the HPGe detector and the guard detectors, and the resolving time is in the same optimal range of 0.5 µs to 1.0 µs.

2.1.3 System performance

In this work, the “easy timing” electronic approach was implemented, a user-friendly system able to be handled by the machine operators. For all the measurements performed with this electronic setup, as a figure of merit, the area suppression factor was used (P/T without suppression divided by P/T with suppression). The quantitative measure of overall system performance is given by peak area to total ratios in which we compare the net area counts, both ^{60}Co peaks, to the total number of counts in the entire spectrum.

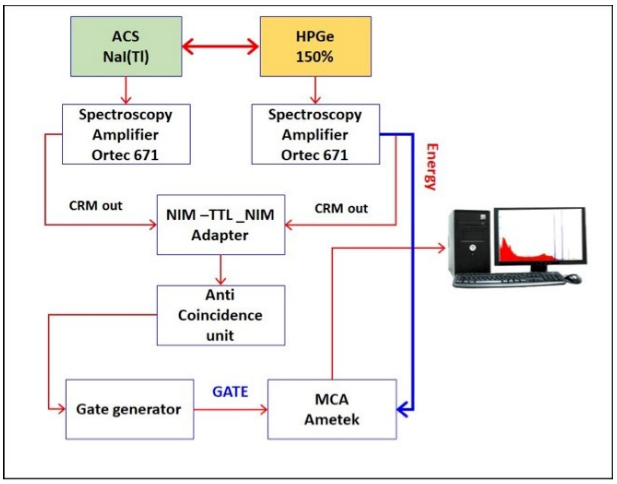

Figure 2.1.3: *Electronic setup implemented for the anti-Compton suppression.*

As said, the experimental apparatus consists of HPGe placed inside the ACS detector at approximately 150 mm. In front of the detector a long collimator, 20 cm is placed, which is made out of four lead bricks. At the end of this collimator, outside the ACS, a ^{60}Co radioactive source was positioned. The collimator configuration prevents direct interaction with the ACS. In this configuration, data were acquired by changing the anti-coincidence window for the MCA gate in order to find the most appropriate value for the anti-coincidence window. The following Table shows the results for three different values using a certificated radioactive source of ^{60}Co.

	Anular Na(Tl)		
	Coinc window [ns]		
	300 ns	750 ns	1000 ns
With suppression	0.04	0.05	0.06
Without suppression	0.03	0.03	0.03
Area suppression ratio	1.47	1.87	1.97

Figure 2.1.4: *Results obtained with different values of the coincidence window.*

An example of obtained spectra with the coincidence window of 1 µs is shown in Figure 2.1.5.

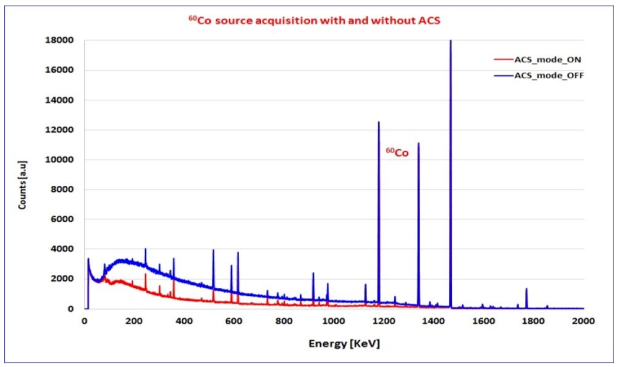

Figure 2.1.5: *Acquired spectra with and without anti-Compton shield.*

2.1.4 Conclusion

The results are in line with the proposed objective, namely the study of an easy method to reduce the Compton background from the acquired spectra using HPGe, NaI(Tl) detectors, and associated electronics. This configuration is used to determine the gamma-ray beam energy at ELI-NP.

References

[Bik+12] I. Bikit *et al.* "Coincidence Techniques in Gamma-ray Spectroscopy". In: *Physics Procedia* 31 (2012), pages 84–92. DOI: 10.1016/j.phpro.2012.04.012. URL: https://doi.org/10.1016/j.phpro.2012.04.012 (cited on page 60).

[KMH66] J. Kantele, O. Marttila, and J. Hattula. "Gamma spectrometer systems employing an anti-compton annulus". In: *Nuclear Instruments and Methods* 39.2 (Jan. 1966), pages 194–216. DOI: 10.1016/0029-554x(66)90225-4. URL: https://doi.org/10.1016/0029-554x(66)90225-4 (cited on page 59).

2.2 ELIADE LN2 Automatic filling control system: the software architecture

Ramirez F.[1,*]

[1] Extreme Light Infrastructure (ELI-NP) & Horia Hulubei National Institute for R & D in Physics and Nuclear Engineering (IFIN-HH), Str. Reactorului No. 30, 077125 Bucharest– Măgurele, Romania

[*] **frangil.ramirez@eli-np.ro**

Abstract

The ELIADE LN2 control system is a stand-alone LabView application running in a controller, periodically filling germanium detectors with liquid nitrogen as the main task. Those kind of detectors must remain cooled to avoid leakage current-induced noise a decline in the energy resolution of the detectors. The control system takes care of the cooling by filling the detectors with liquid nitrogen using temperature as feedback signals and can issue alert notifications by monitoring the inner temperature of the detectors. Hence, users and operators are aware of the system status at any time. The system also interfaces with other systems, receiving orders, and sharing all data from detectors and filling procedures.

2.2.1 Introduction

The ELIADE [Ur+16] [Söd+19] LN2 (Liquid Nitrogen) automatic filling system is a stand-alone LabView [Ins05] [Ins22e] [Ins22b] application in charge of keeping high-purity germanium detectors (HPGe) permanently cooled by running a supervized filling cyclic control procedure twice a day during experiments. At our system at ELI-NP, a NI-cRio-9024 [Ins22a] is used as a controller, which hosts the control application.

Besides controlling the filling procedure, the system monitors the detector's temperatures in between filling so trends in these temperatures can be detected, and programmed actions and email notifications can be sent.

The filling system has the following tasks:

- Control the LN2 filling
- Monitor the temperatures of the detectors
- Run the scheduled filling cycle
- Notify filling status (start/end and filling results)
- Integration with other systems (*via* a custom communication protocol and based on EPICS).
- Using an interface to interact with the system (command-line and graphical GUI)
- Logging data (*e.g.* temperature) and also executed commands by the user of the control system.

In the next sections, a detailed description of the system's software architecture is shown, as well as a short explanation of the filling procedure.

2.2.2 LN2 System Configuration

The LN2 control system general configuration comprises a NI-cRio that host the LabView control application, analog input temperature modules for (PT-100), a digital output module that drives the solenoid valves (24 VDC), cryogenic valves to control the LN2 flow, temperature sensors (PT-100) located at each valve for feedback control and the detectors, each one containing a PT-100 sensor used to monitor the temperature inside the detectors. Figure 2.2.1 shows a schematic diagram of the full system:

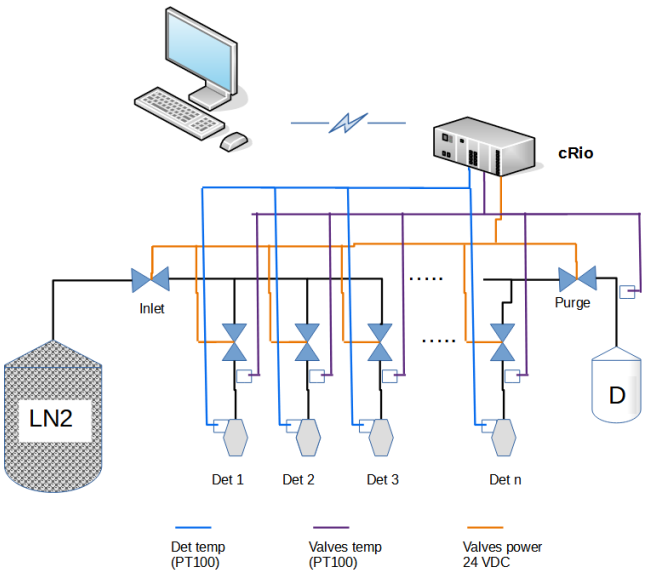

Figure 2.2.1: *LN2 System Setup*

The filling control procedure can be described as follows: every x hours (in units of seconds), the

controller runs what is called “Purge”, this is, opens two valves simultaneously (inlet and purge, see Figure 2.2.1) intending to extract all air/vapor in the pipelines and control the closing using the “Purge” valve temperature as feedback. Then, when the “Purge” is finished, the pipelines are filled with liquid nitrogen, and the proper filling procedure for the detectors can be started. The controller starts to open the respective valves corresponding to each detector, and the filling procedure is also stopped using the corresponding “valve temperature” as a feedback signal. It is worth mentioning that the control system can fill detectors one by one or N by N simultaneously ($2 \leq N \leq 4$), reducing the overall filling time considerably (with respect to the available flow capacity of the piping system).
There are two modes to run the system: ’Auto’ and ’Manual’. When in ’Auto’ Mode, the system only accepts the commands of the regular filling, while in ’Manual’ Mode, the system can accept direct commands from the user.

2.2.3 Software Design

The software design for the LN2 control application follows an independent process design. The whole program has been divided into smaller programs called processes that work independently from each other but interfacing to achieve a common goal. Figure 2.2.2 shows the core processes of the system:

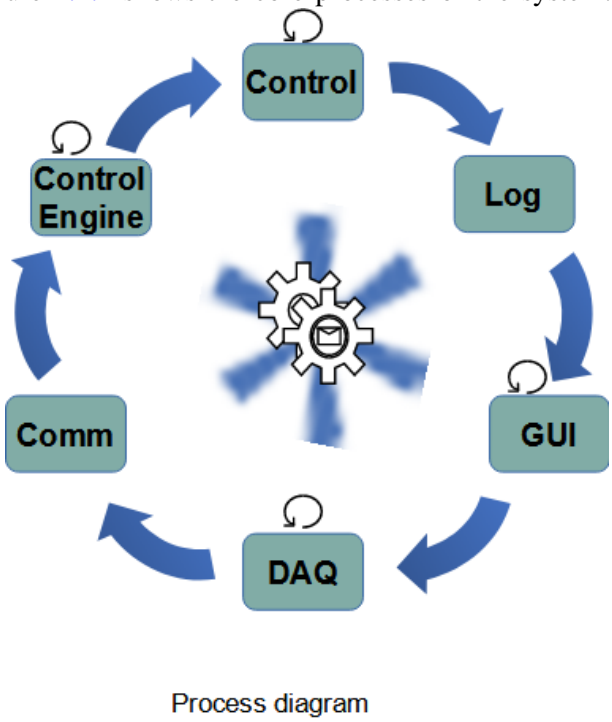

Figure 2.2.2: *LN2 filling, LabView processes and IPC*

When having independent processes working together, it is necessary to implement a way to synchronize the work, so the inter-process communication (IPC) known as “queues” was implemented. The synchronization comes by interchanging messages between processes. The main process is called ’Control Engine’ and is in charge of controlling the synchronization of control orders (*i.e.*, purge, fill, settings) coming from the users using the CLI (command-line interface) and the GUI (graphical user interface).
The DAQ module is in charge of accessing the system’s AD-IO (analog and digital inputs-outputs). The IO is scanned every 0.1 s, and the one-second average is then used as the actual reading for the analog inputs (temperatures from valves and detectors). The programming pattern in this module is a typical producer-consumer, so data can be later shared in a safe way.
The communication module is in charge of interfacing with the user through the (CLI. A custom interface protocol has been implemented to receive and respond to commands received over a fixed port using a connection-less UDP protocol. Here, all commands received from users are validated and then processed if the validation succeeds.
The control module processes orders like purge and fills, which may be generated automatically (by the cycling time) or by users. Priorities have been implemented to handle orders from the user. In case the system is in ’Auto’ Mode, the filling order includes all detectors enable for filling. On the other hand, if the system is in ’Manual’ Mode the queue can hold several fill orders for different detectors. This is useful when the user wants to manually fill detector on occasion. The ’purge’ order has priority over a fill order for obvious reasons. The “stop” order is self-explaining and empties the normal priority order.
The Log module just wait for a message and then log it to a file and if required, send it by email.
The GUI is a module that shows the system state in real-time. It was not considered in the initial design since the CLI requirement. However, it has shown its usefulness to the user because all relevant data is shown on a simple screen. A new version of this GUI (web-based) is under construction.
As an example, let us examine the event when a message is received from a user:
Figure 2.2.3 shows life-time of a message received by the “Comm” module using a UML [UML22] sequence model. UML is used to do the system modeling.

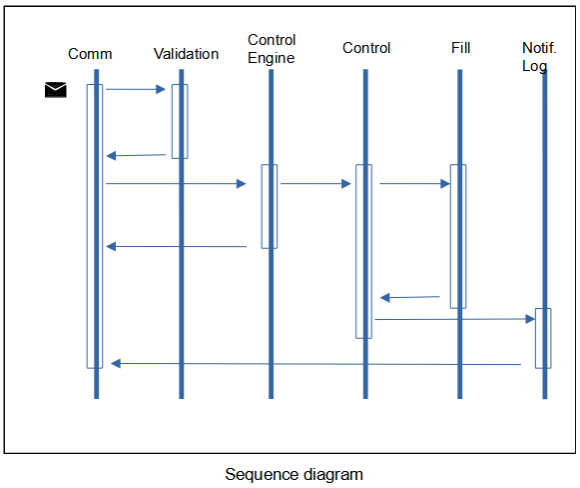

Figure 2.2.3: *Sequence Diagram for a msg received by a Comm module*

This sequence demonstrates how the system processes a message. The 'Comm' module receives an MSG on a monitored port and immediately fires a user event to process it, starting by validating its format and existence, then sending the MSG to the 'Control Engine' to verify a preset of acceptance conditions to execute the command. If everything is fine, the MSG is sent to the 'Control' module to be queued and processed. Finally, a logfile is updated with the request its result and possibly sends feedback to the user.

The filing control is finally carried out using 'Valves temperatures' as feedback signals. As mentioned before, these are PT-100 compensated signals coming from LN2 return pipelines, so the detector's filling can be assured if certain conditions are met. Figure 2.2.4 shows how the control of the filling works:

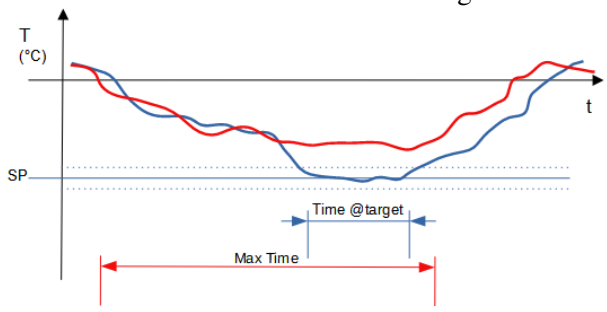

Figure 2.2.4: *Temperature control of the Filling*

Figure 2.2.4 shows how the 'Control' module executes the control of the filling procedure by using the 'Valves temperature' as feedback signals. The blue line in this graph represents a normal temperature behavior during a regular filling. As the PT-100 sensor is located in the return pipeline of each detector, the read-out at the beginning is around room temperature, then after valves are opened, and the LN2 start flowing through the signal drops following the LN2 temperature; the filling end when the temperature reaches a preset setpoint and remains there for some time. The red line represents the temperature behavior when, for some reason, the temperature does not reach the setpoint; the filling ends by a MAX TIME filling condition. The result is written into a logfile and reported *via* email in both cases. The system can disable a detector that had not had a successful filling. All conditions mentioned above are set by the CLI, validated and verified to ensure they are within reasonable system benchmarks.

2.2.4 Results

The modular design as shown in Figure 2.2.5.

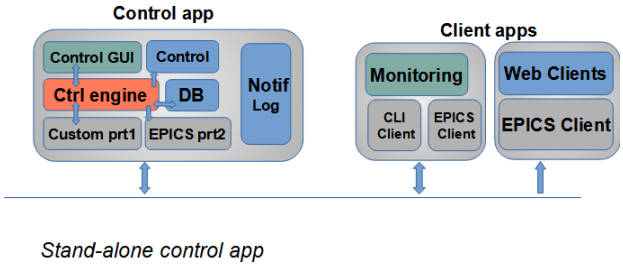

Figure 2.2.5: *Modular design of the LN2 automatic filling control*

The model facilitates maintenance, changes, debugging, and new functionalities when required. It also has a bonus module that implements an EPICS [EPI21] server to share all data, so integration to other systems can be accomplished effortlessly. LabView 2013 was used and deployed to a NI-cRio-9024. The back-plane is a compatible CompactRIO Chassis that allows the combination of C-Series Input/Output modules. The temperature modules are NI-9217 [Ins22c] and the digital output module is a 24 V NI-9476 [Ins22d].

The dominant programming pattern follows a so-called 'Producer-Consumer' relation. FGV variables are implemented, and queues as inter-process communications make connect the modules. This implementation allows the integration of a fully detached new web-based GUI and a temperature signal analysis at run-time to improve fault detection. All related work is still under construction. Currently a GUI environment is implemented.

Also, a text-based user interface written in Python and using CLI and EPICS environments for small devices like smartphones is implemented. It will serve monitoring and a command interface requests (see Figure 2.2.6).

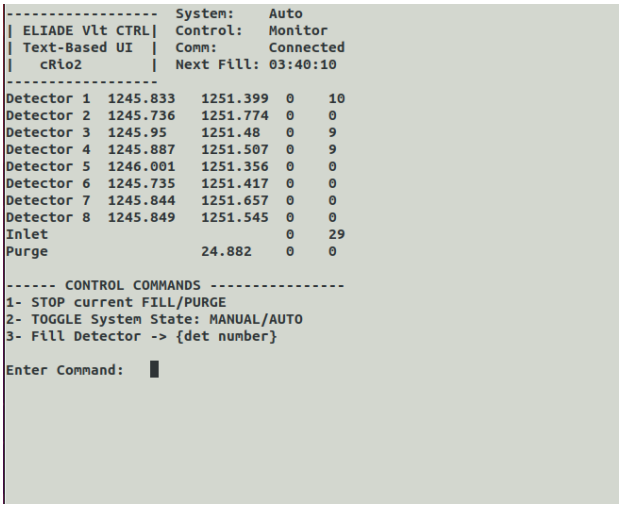

Figure 2.2.6: *LN2 automatic filling control text user interface - TUI*

2.2.5 Conclusion

A reliable control system was developed. The system can effectively communicate using a protocol for a custom CLI implementation and refer to EPICS to raise alarms.
The data is shared safely within the system modules through queues and FGV variables. All requirements were implemented, including additional functionality like an EPICS server and a GUI.

References

[EPI21] EPICS. *The Experimental Physics and Industrial Control*. 2021. URL: https://epics-controls.org/ (visited on 01/10/2022) (cited on page 65).

[Ins05] N. Instruments. *Getting Started with the LabVIEW Embedded Development*. 2005. URL: http://download.ni.com/support/manuals/371853a.pdf (visited on 01/10/2022) (cited on page 63).

[Ins22a] N. Instruments. *cRIO-9024*. 2022. URL: https://www.ni.com/ro-ro/support/model.crio-9024.html (visited on 01/10/2022) (cited on page 63).

[Ins22b] N. Instruments. *Learn NI LabVIEW Basics*. 2022. URL: https://www.ni.com/getting-started/labview-basics (visited on 01/10/2022) (cited on page 63).

[Ins22c] N. Instruments. *NI-9217*. 2022. URL: https://www.ni.com/en-us/support/model.ni-9217.html (visited on 01/10/2022) (cited on page 65).

[Ins22d] N. Instruments. *NI-9476*. 2022. URL: https://www.ni.com/en-us/support/model.ni-9217.html (visited on 01/10/2022) (cited on page 65).

[Ins22e] N. Instruments. *Transferring Data over a Network Using UDP*. 2022. URL: https://www.ni.com/documentation/en/labview-comms/5.0/data/transferring-data-over-network-udp/ (visited on 01/10/2022) (cited on page 63).

[Söd+19] P.-A. Söderström *et al.* "High-Resolution Gamma-ray Spectroscopy with ELIADE at the Extreme Light Infrastructure". In: *Acta Physica Polonica B* 50 (2019), page 329. URL: https://www.actaphys.uj.edu.pl/R/50/3/329/pdf (cited on page 63).

[UML22] UML. *Unified Modeling Language*. 2022. URL: https://www.uml.org (visited on 01/10/2022) (cited on page 64).

[Ur+16] C. Ur *et al.* "Nuclear Resonance Fluorescence Experiments at ELI-NP". In: *Romanian Reports in Physics* 68 (2016), S483. URL: http://www.rrp.infim.ro/2016_68_S/S483.pdf (cited on page 63).

2.3 Annealing Data Acquisition and Monitoring System

Ramirez F.[1,*]

[1] Extreme Light Infrastructure (ELI-NP) & Horia Hulubei National Institute for R & D in Physics and Nuclear Engineering (IFIN-HH), Str. Reactorului No. 30, 077125 Bucharest– Măgurele, Romania

[*] **frangil.ramirez@eli-np.ro**

Abstract

The Annealing Data Acquisition and Monitoring System is a LabView application used for monitoring the process of annealing HPGe (High Purity Germanium) detectors using an Annealing Station while at the same time sharing process data with other systems using a custom communication protocol working on top of the network UDP/IP. The annealing process is a high-temperature process carried out to improve HPGe detectors' resolution. The annealing system collects temperature data from a detector and a pressure reading from a pressure controller to monitor the annealing process. In the next sections, a detailed description of the integrated system is presented, and the benefits from using it are also mentioned.

2.3.1 Introduction

The annealing system is a LabView [Ins22c] application that collects temperature and pressure data from a National Instrument (NI) DAQ [Ins22f] system and a Pfeiffer [Pfe22] gauge controller. Its main function is to allow the monitoring of these process variables and, at the same time, make the data available to other systems.

The integration between a transducer, a data acquisition system, and a pressure controller is the system's heart. These devices connect to the host computer where the LabView executable application runs. First, the transducer has the task of conditioning the temperature signal for the data acquisition system to read it. Then this DAQ is connected via USB cable to the host computer. The pressure controller can be connected via ETHERNET or USB, and the LabView program is capable of establishing communication in any of those ways.

The features of the Annealing system are:

- Collects temperature and pressure data from external devices.
- Plots temperature and pressure values in the time domain.
- Allows the user to save collected data in a text file. The user can choose the folder and file name to log the data, the sample rate at which this data will be recorded, and the start/stop of the recording.
- The system, by default, tries to automatically connect to a NI-USB-DAQ-60016 though the user can also chose to connect to a NI-USB-6163 or a cRio. There is a connection status LED for each device.
- The system automatically connects to any TPG-36X7 controller connected to a USB COM port connected with the Pfeiffer controller.
- The system provides an interface to share the collected data to any other application using a straightforward custom communication protocol (for this, an Annealing "API like" is used with custom communication protocol on top of UDP/IP).

2.3.2 The system integration

2.3.2.1 Hardware integration

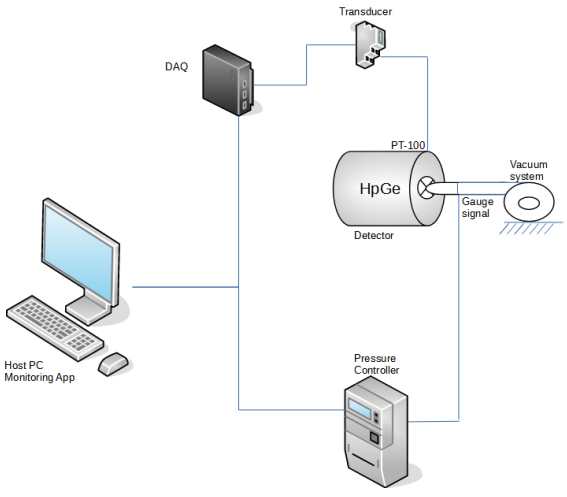

Figure 2.3.1: *General Annealing Integrated System*

The signals involve are the detector inner temperature coming from a PT-100 sensor and the pressure value coming from a gauge sensor as shown in Figure 2.3.1 . From the hardware point of view, the annealing system is an integration of different devices: a signal transducer, a DAQ, a pressure controller, and a host computer.
The NI DAQ uses a USB-DAQ-6001 but could be a USB-DAQ-6163 or even a cRio controller. The pressure controller must be one of the families of Pfeiffer gauge pressure controllers TPG-36X. The LabView application was built to communicate with different protocols according to the hardware available a the time of carrying out the annealing process.
The NI-USB-6001 and a TPG-361 are our system's most commonly used devices. The temperature signal is taken from a 2-wire PT100 sensor (from inside a detector), and in the case of using a NI USB-DAQ as a read-out device, an additional transducer must be used to transform the PT100 resistance signal into a 2-10 volts signal which then can then be wired to the NI-USB device. The NI-USB cannot read PT100 signals directly. However, a cRio with a C-Module NI-9217[Ins22d] (resistance temperature detector (RTD) input module) can be used directly to obtain the temperature readings.
Connections to the host computer are made through USB ports in both cases (for temperature and pressure readings), and there is an additional option to connect the pressure controller via Ethernet, for which additional software provided by the manufacturer is needed.

2.3.2.2 Software integration

From the software point of view three different communication protocols are used:

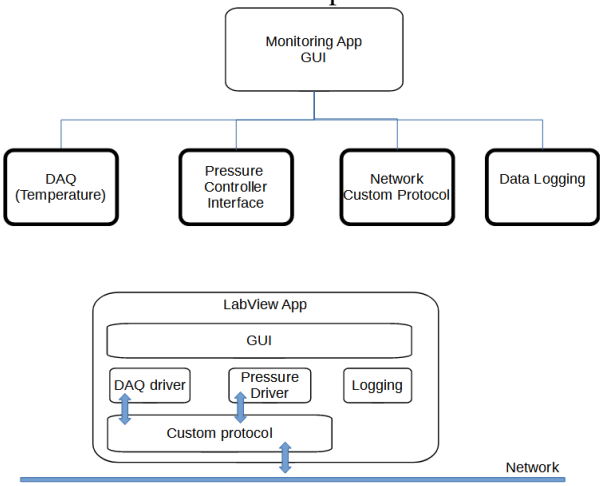

Figure 2.3.2: *Software model of the Annealing application*

communication to the NI-USB-DAQ (which is ready to use in LabView), communication to the pressure controller that requires the implementation of the protocol to be able to interact with the device) and a custom protocol created to make the data available through the network to other systems. It is important to mention that other integrations using protocols like EPICS are not available since the LabView application is a Windows executable, and a license (not available) is needed to use this and other communication protocols.
The general architecture of the LabView application can be seen below:
Figure 2.3.2 shows the core processes of the system. Due to the model's simplicity, the implementation was made with only three modules: the GUI module, the communications module, which has two threads to interface with the DAQ and the pressure controller, and the network integration module. The common programming pattern used was the 'Producer-Consumer-pattern' [Ins22e]".
As an example of the producer-consumer pattern in LabView see Figure 2.3.3. Here there is a combination of the pattern with 'user-events' to respond to data requests from a client using the custom communication protocol on to of UDP/IP protocol.

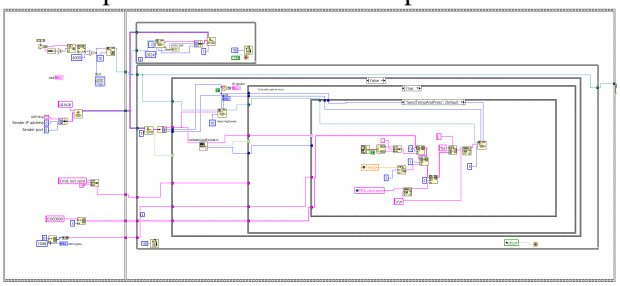

Figure 2.3.3: *Producer-Consumer-pattern in the Annealing LabView app*

The entire communication protocol was implemented for the interaction with the pressure controller. This is, settings on the pressure controller can be made from the LabView application user interface. The next section shows the final application running.

2.3.3 LabView Application

Finally, the LabView application was compiled, and a LabView executable[Ins22a] application was generated. Figure 2.3.4 (see below) shows this graphical user interface. Note the sections to choose the device to connect to for the temperature case on the middle right and the option to interact in more detail with the pressure controller on the bottom right. The

data collected from the input devices is also plotted in real-time. Therefore, it facilitates the monitoring task for the user.
The Annealing system is always ready to share data with other systems that may require it by following the custom protocol. This data sharing is actually used by a Python script that uses a C-library that implements the protocol. This script also logs the data in a persistent database making it available to other monitoring applications like Grafana [Lab22].

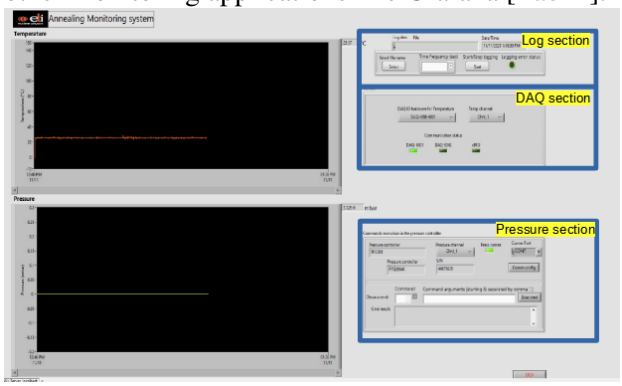

Figure 2.3.4: *Annealing graphical user interface*

The executable application runs continuously during the annealing process on a Windows 10 operating system host PC. No licenses are required since no commercial protocols are used. Only the LabView runtime engine [Ins22b] together with the USB drivers related to communicating with the NI-USB-DAQ need to be installed on the host computer. If the communication with the pressure control is made via Ethernet the correspondent software from the manufacturer must also be installed.

2.3.4 Results

The software architecture has been shown to be appropriate for this simple application.
The programming pattern provides a reliable, stable performance of the application.
The Windows application has been shown to be reliable during the whole annealing procedure, allowing users to monitor it remotely.
The interface channel integration with other systems works smoothly, allowing other systems to work with the data collected and shared correctly.

2.3.5 Conclusion

The LabView Annealing Data Acquisition and Monitoring System is an important tool for acquiring and monitoring data from an Annealing Station and distributing it using a simple interface protocol. Data is displayed user-friendly to allow online surveying of the annealing process. In addition, LabView can connect to external devices with different communication protocols, such as, *i.e.*, Pfeiffer controllers.

References

[Ins22a] N. Instruments. *Introduction to the LabVIEW Application Builder – NI*. 2022. URL: https://www.ni.com/en-us/support/documentation/supplemental/19/introduction-to-the-labview-application-builder.html (visited on 01/10/2022) (cited on page 68).

[Ins22b] N. Instruments. *LabVIEW Runtime Download – NI*. 2022. URL: https://www.ni.com/en-us/support/downloads/software-products/download.labview-runtime.html#411217 (visited on 01/10/2022) (cited on page 69).

[Ins22c] N. Instruments. *Learn NI LabVIEW Basics*. 2022. URL: https://www.ni.com/getting-started/labview-basics (visited on 01/10/2022) (cited on page 67).

[Ins22d] N. Instruments. *NI-9217*. 2022. URL: https://www.ni.com/en-us/support/model.ni-9217.html (visited on 01/10/2022) (cited on page 68).

[Ins22e] N. Instruments. *Producer/Consumer Architecture in LabVIEW – NI*. 2022. URL: https://www.ni.com/en-us/support/documentation/supplemental/21/producer-consumer-architecture-in-labview0.html (visited on 01/10/2022) (cited on page 68).

[Ins22f] N. Instruments. *USB-6001-NI*. 2022. URL: https://www.ni.com/en-us/support/model.usb-6001.html (visited on 01/10/2022) (cited on page 67).

[Lab22] G. Labs. *Grafana: The open observability platform*. 2022. URL: https://grafana.com (visited on 01/10/2022) (cited on page 69).

[Pfe22] Pfeiffer. *pfeiffer-vacuum*. 2022. URL: https://www.pfeiffer-vacuum.com/en/products/measurement-analysis/measurement/centerline/centerline-controllers/16617/centerone-controller-for-1-gauge (visited on 01/10/2022) (cited on page 67).

2.4 The archiving database for the gamma diagnostics stations

Chen G.[1,*] , Matei C.[1] , and Ramirez F.[1]

[1] Extreme Light Infrastructure (ELI-NP) & Horia Hulubei National Institute for R & D in Physics and Nuclear Engineering (IFIN-HH), Str. Reactorului No. 30, 077125 Bucharest– Măgurele, Romania

[*] **guangling.chen@eli-np.ro**

Abstract

The Variable Energy Gamma (VEGA) System of Extreme Light Infrastructure - Nuclear Physics (ELI-NP) is based on the Inverse Compton Scattering of laser light on relativistic electron bunches provided by a warm radio-frequency accelerator. The system will deliver quasi-monochromatic gamma-ray beams with a high spectral density and a high degree of linear polarization. In addition, the Gamma Beam Diagnostics Stations of ELI-NP are implemented to monitor the characteristics of the beams during the performance of the experiments.
An EPICS Archiving Database has been implemented for the Gamma Diagnostics Stations at ELI-NP. This paper describes the design of the system architecture, the configuration of the back-end database structures, as well as the implementation of the web server and web-based GUI.

2.4.1 Introduction

The Variable Energy Gamma (VEGA) System of Extreme Light Infrastructure - Nuclear Physics (ELI-NP) will produce intense gamma-ray beams with a spectral density higher than 0.5×10^4 photons $\mathrm{eV}^{-1}\,\mathrm{s}^{-1}$, a relative energy bandwidth better than 0.5%, high degree of linear polarization at more than 95%, and energy continuously variable from 1 MeV up to 19.5 MeV based on the laser Compton backscattering of laser photons off a relativistic electron beam.
The Gamma Diagnostics Stations are designed and under implementation to measure and monitor the gamma beam diagnostics features [Wel+16]. To optimize the operation of the ELI-NP VEGA system, it is necessary to have the proper means to accurately predict the spatial, spectral, and temporal characteristics of the gamma beam. The ELI-NP Gamma Diagnostics Stations deal with the equipment and techniques meant to optimize the gamma beam in order to make it available for user experiments within required parameters.
The control systems for the diagnostics stations are under implementation based on EPICS [EPI21]. Therefore, to handle the storing and retrieving of the online and offline data, an EPICS-based archiving system is required for the operation of the diagnostics stations and experiment stations.

2.4.2 System design of the archiving database

As a part of the standard EPICS-based control system architecture, the archiving service needs to be run continuously irrespective of user activities for archiving and monitoring process variables' values. The system design of the archiving system interfaced with the EPICS-based control system has shown in Figure 2.4.1.

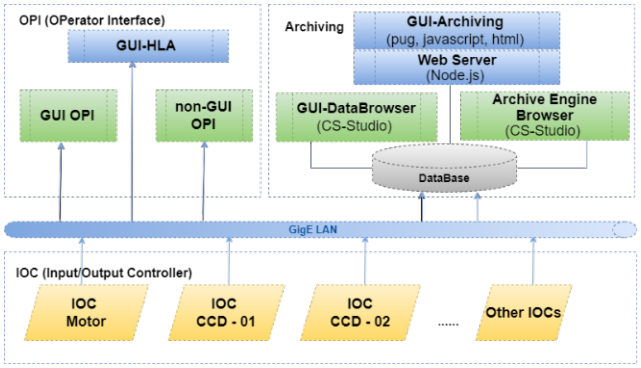

Figure 2.4.1: *The software architecture of the EPICS-based Archiving System.*

The Archiving system, the Operator Interfaces (OPIs), and the Input/Output Controllers (IOCs) are connected to the gigabit Ethernet (GigE) Local Area Network (LAN) which allows the communication between the tiers *via* the Channel Access (CA) protocol.

2.4.3 Design and configuration of the archiving system

The architecture of the archiving system (as shown in Figure 2.4.2) consists of an archive engine, the MySQL RDB (Relational Database), a web server, and the web-based Graphical User Interface (GUI). The Archive Engine samples Process Variable (PV) data, timestamp *etc.*, from EPICS IOCs *via* Channel Access (CA), and places them in a Relational Database. Users can then access the historical data from the database as well as the live data from the PV channels.

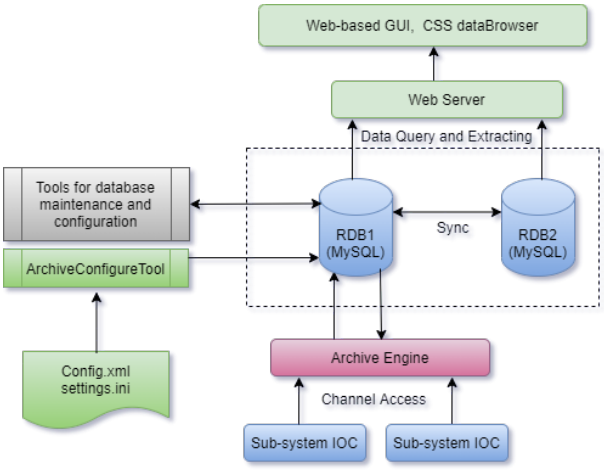

Figure 2.4.2: *The structure and data flow of the archiving system.*

The EPICS Archive Engine Service in CS-Studio has been chosen as the software tool for archiving system development. To configure the archive engine, Phoebus [CSS21], the latest version of CS-Studio, has been chosen as the archive engine configuration tool to read samples from PVs and write them to the RDB. The data browser has also been chosen to browse the historical or monitoring data from the RDB.
Config.xml and settings.ini are the two main configuration files needed to configure the database using the provided ArchiveConfigureTool. Moreover, PhpMyAdmin has been chosen as the tool for database maintenance and configuration.
Databrowser is a built-in tool in CS-Studio. It aggregates live and archived data to plot values over a user-defined time range (e.g., within one hour or among two weeks).

2.4.4 Design and configuration of the database

The diagram below (Figure 2.4.3) shows the basic table structure that the Archive Engine needs to store data in MySQL.

The Archive Engine is configured in these tables. Configurations can be manually inserted into the tables or imported by the configuration files (*.xml) into the RDB using the ArchiveConfigTool.

- chan_grp This table stores the configuration of the group organization.
- channel This table stores the configuration of the channels (PVs).
- smpl_mode This table stores the metadata about sample modes.
- retent This table stores the metadata about retention.

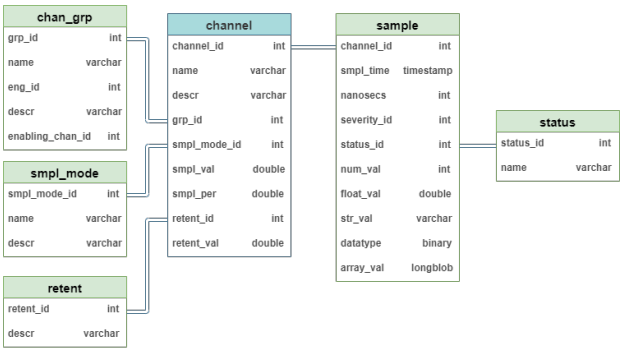

Figure 2.4.3: *The table structure of the archive database*

As a test, we created the group profile to organize all the channels from Beam Profile Station. This table can be extended for other stations such as Beam Energy Station and Beam Polarization Station in future use.
The Archive Engine is configured in these tables. Configurations can be manually inserted into the tables or imported by the configuration files (*.xml) of the old engines into the RDB using the ArchiveConfigTool. We use PhpMyAdmin as the database management tool.
Besides, we stored all the images acquired from the Beam Profile System, the image data, and the image-related parameter files in the file system on the database server.

2.4.5 Design and implementation of the Web Server and Web-based GUI

The main objective of this system is to allow fast, reliable, and safely retrieve PVs, images, and images parameters related data, make them available *via* a network (ELI-NP intranet) in a fast and friendly way. Therefore, the system should allow:

- Connect to the archive RDB.
- Fetch data from the archive RDB tables: PV names, PV data.
- Access static image files and their related parameters.

- List all PVs available in the database.
- Allow users to choose a PV from PVs-list and retrieve and plot its data.
- Allow user to specified date ranges and sampling for data retrieval for a chosen PV.
- List all images available as static files.
- Allow users to choose an image from Images-list and retrieve and display it with the parameters associated with that image.
- Import data option in different formats.

Additionally, some other important features would be added to the system to make it a completely functional website. This functionality is related to:

- User login-logout functionality.
- Role(s) related to users (guest, user, admin).
- Desktop browser support, responsive and build with a known programming pattern.

The web server and the web-based GUI for the archiving system have been implemented based on Node.js, Express, MySQL, Sequelize, Javascript, Pug, HTML, and VS code.
Node.js was chosen for the webserver configuration since it is widely-increasingly used, with frameworks plugins to speed up development, supporting programming patterns and front-end capabilities.
The web-based GUI is implemented using the MVC (model-view-controller) pattern, in order to serve requests in two ways: by using the embedded views and also *via* FigureAPI's fetching and sending raw data.

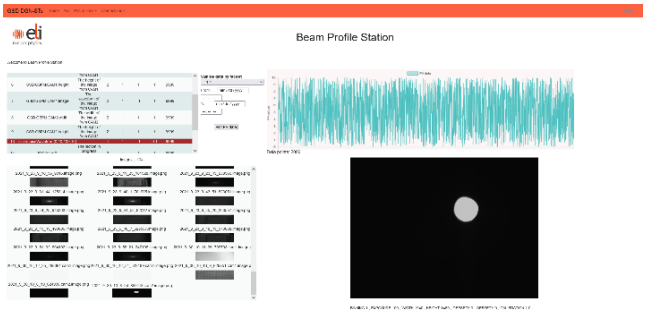

Figure 2.4.4: *EPICS-based archive application GUI*

Figure 2.4.4 shows the results of HTTP requests using the embedded view (GUI). By using the web-based GUI, users can connect to the archive RDB, which stores the data fetched by the archive engine. Users can also browse the data by choosing a PV from the PVs-list and then plot the data immediately. Moreover, the GUI allows users to choose an image from the images list and display it immediately with the parameters associated with the image.

2.4.6 Conclusion

The EPICS based archiving database has been implemented for the Beam Diagnostics Stations. The archive engine has been configured using CSS Phoebus. The web server and the web-based GUI have been implemented using the MVC pattern. The database has been tested with the PV connections to the control of the Beam Profile Station.
This implementation of the archiving database for Beam Diagnostics Stations has been proved as a professional programming structure that helps in the maintenance and readability of the whole system. Moreover, it is reliable enough for being scaled up in the future implementation at ELI-NP.

References

[CSS21] CSS-Phoebus. *CSS-Phoebus*. 2021. URL: https://controlssoftware.sns.ornl.gov/css_phoebus/ (visited on 01/10/2022) (cited on page 72).

[EPI21] EPICS. *The Experimental Physics and Industrial Control*. 2021. URL: https://epics-controls.org/ (visited on 01/10/2022) (cited on page 71).

[Wel+16] H. Weller *et al.* "Gamma Beam Delivery and Diagnostics". In: *Romanian Reports in Physics* 68 (2016), S447–S481 (cited on page 71).

2.5 High frequency low distortion sinewave signal generator

Tracz P.[1,*]

[1] Extreme Light Infrastructure (ELI-NP) & Horia Hulubei National Institute for R & D in Physics and Nuclear Engineering (IFIN-HH), Str. Reactorului No. 30, 077125 Bucharest–Măgurele, Romania

[*] **piotr.tracz@eli-np.ro**

Abstract

The presented HF sinewave signal generator is based on a variable frequency oscillator VFO where an outputting squarewave signal is filtered for harmonics' attenuation and converted into a sinewave signal. The circuit was assembled and tested at the ELI-NP electronic laboratory with the use of equipment and test instruments available at the Gamma System Department. The tests were made with a vector network analyzer, LCR meter, spectrum analyzer, and oscilloscope. This paper presents the theory, results of high-frequency tests, analysis, and conclusions. The HF sinewave signal generator is used for general purposes in the electronic laboratory.

2.5.1 HF Low Distortion Sinewave Signal Generator – Introduction

The circuit diagrams of the VFO, a synthesizer module, and the LPF is presented in Figure 2.5.1. The VFO is designed on the ATmega328 AVR microcontroller pre-programmed with firmware to control the Si5351A synthesizer module, LCD, rotary-encoder for output frequency tuning, and optional GPS receiver to maintain precise frequency output. The three outputs from the Si5351A are labeled Clk0, Clk1, and Clk2. They have a 50-ohm impedance and provide up to a 3.3 V peak-to-peak squarewave. The rotary encoder tunes the main Clk0 output. The Clk1 output is set to a fixed frequency by the configuration parameters. The Clk2 output is reserved for the GPS receiver. The Clk0 and Clk1 outputs have a range of approximately 3.5 kHz to 300 MHz. They are filtered to give a sinewave, but that happens over a relatively narrow frequency range. A low pass filter connected at the output of the Si5351A will attenuate the harmonics, converting the squarewave into a high-quality sinewave signal. The processor can control six relays in the 6-band relay-switched LPFs. This feature is used to automatically select a low pass filter for a specific operating frequency. With a suitable selection of LPF, a clean sinewave can be generated across a wide bandwidth. This way, we get a sinewave signal generator covering at least 3 MHz to 30 MHz.

2.5.1.1 Square- vs. Sine-Wave

According to the Fourier theorem, any signal that is periodic in the time domain can be derived from the sum of sine and cosine signals of different frequencies and amplitudes. Such a sum is referred to as a Fourier series. Because the Fourier transforms of sine and cosine signals are identical in magnitude, the two signals exhibit an identical magnitude spectrum at the same frequency. The ideal square wave with an amplitude of 1 can be represented as an infinite sum of sinusoidal waves and contains only components of odd-integer harmonic frequencies [Rau08]:

$$x(t) \approx \left(sin\left(\omega t\right) + \tfrac{1}{3}sin\left(3\omega t\right) + \tfrac{1}{5}sin\left(5\omega t\right)\right),$$

where $\omega = 2\pi f$.

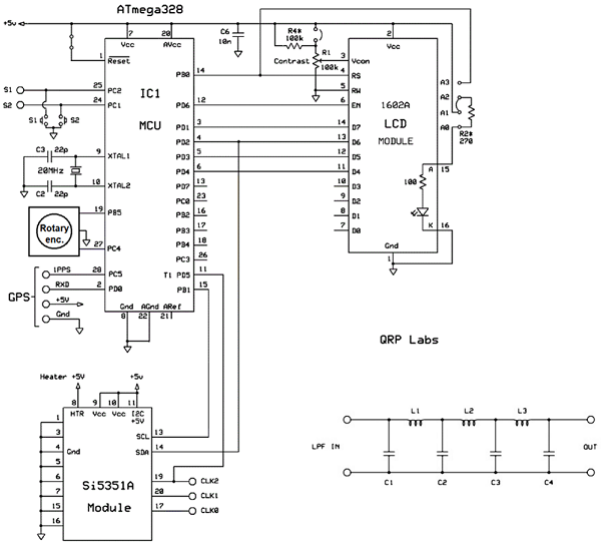

Figure 2.5.1: *HF low distortion sinewave signal generator circuit diagram.*

2.5.2 Low Pass Filters

A low pass filter is a form of filter that allows passing through only signals of lower frequencies. Typically, it is nominally flat until the cut-off point, and then it declines for higher frequencies. The signals with frequencies above the cut-off point are attenuated.

A half-power point for the filters commonly defines the cut-off point. The half-power point is the point at which the output power has dropped to half of the nominal pass-band value, that is, at the level of approximately -3 dB (Figure 2.5.2) [LB00][Ele22].

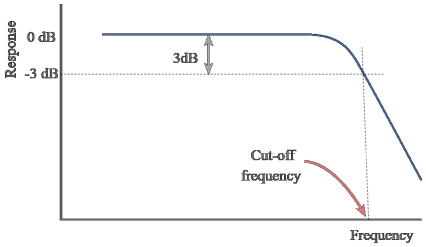

Figure 2.5.2: *The half-power point.*

The low pass filters for the HF sinewave signal generator are built on 7-elements – four capacitors and three inductors wound on toroid type T37-6 or T37-2, and have 50-ohm input and output impedances (Figure 2.5.1). There are six LPFs for six bands (Table 2.5.1).

Table 2.5.1: LPFs and bands.

band	Measure
10-meter band	28.0÷29.7 MHz
15-meter band	21.0÷21.45 MHz
20-meter band	14.0÷14.35 MHz
30-meter band	10.1÷10.15 MHz
40-meter band	7÷7.3 MHz
60-meter band	$\sim$ 5 MHz

The capacitors and inductors were tested with the LCR meter GW-Instek LCR-8110G. The capacitors are low-loss Class-1 ceramic dielectric RF types (also known as CC4) with low-temperature coefficients (NP0 or C0G). The test method standard MIL-STD-202 was used for the test of capacitance. There is a good consistency between specified (in brackets) and measured capacitance (Table 2.5.2).

The accurate measurement of an inductor has always been more difficult than the measurement of other passive components. The coil parasitic distributed capacitance and core/copper resistive losses vary dramatically with frequency. The measured frequency and driving amplitude have to be chosen properly to get usable measuring results. The designated work frequency of the inductor can be used as a rule [Coi03]. The available test instrument allows for tests up to 10 MHz. The results for 30- and 60-meter bands are presented in Figure 2.5.3.

When dealing with high-frequency applications, a key concept is that the electromagnetic wave nature begins to dominate Kirchhoff's current and voltage laws. Basic circuit analysis no longer applies when the wavelength is comparable in size with the discrete electronic components. The parasitic parameters must be taken into account. The consequence is that electric equivalent circuit representation of high-frequency passive elements is more complicated (Figure 2.5.4) [LB00].

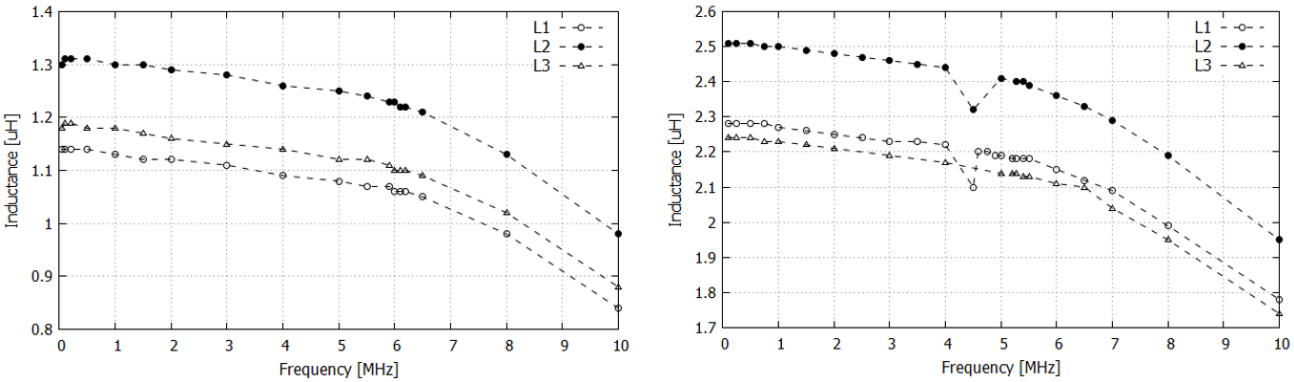

Figure 2.5.3: *Example of bands investigated, 30-meter (left) and 60-meter (right). Specified parts: L1=1.09 µH,L2=1.26 µH,L3=1.09 µH; (T37-6) and L1=2.12 µH,L2=2.30 µH,L3=2.12 µH; (T37-2) .*

An important property of an inductor is its self-inductance. The inductor also has parasitic properties, which the most important are the internal series resistance and the parallel capacitance. The ohmic resistance of the windings mainly determines the series resistance. The parallel capacitance is formed by the individual isolated windings laying next to each other due to electric potentials between turns of the wire, and also terminals of inductor equate to plates. The capacitance of the inductor becomes more significant at higher frequencies. The capacitive reactance of a real inductor rises with frequency, and at a certain frequency, the inductor will behave as a resonant circuit. Above the self-resonant fre-

Table 2.5.2: Capacitance as measured and specified (in brakets)

10-meter	C1 and C4=58 pF and 57 pF (56 pF), C2 and C3=152 pF(150 pF)
15-meter	81 pF and 82 pF (82 pF), 219 pF and 220 pF (220 pF)
20-meter	179 pF and 177 pF (180 pF), 395 pF and 392 pF (390 pF)
30-meter	271 pF and 277 pF (270 pF),566 pF and 572 pF (560 pF)
40-meter	283 pF and 257 pF (270 pF),690 pF and 696 pF (680 pF)
60-meter	688 pF and 681 pF (680 pF), 1210 pF and 1205 pF (1200 pF)

quency, the capacitive reactance is the dominant part of the inductor's impedance. After the pass the resonant frequency, the inductor behaves like a capacitor [Mee18].
The real capacitor is represented by a model consisting of an ideal capacitor with several additional components.

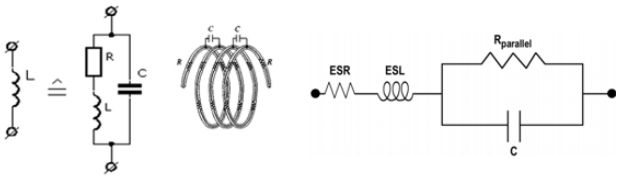

Figure 2.5.4: *Common inductor (left) and capacitor (right) models with parasitic components.*

The equivalent series resistance, ESR, describes losses associated with moving charge through a capacitor. The resistance of the conductive parts like the electrodes and lead material are contributing factors. Also, losses occur within the dielectric material itself. The electrodes and lead wires or terminations of a capacitor are formed from metal conductors. All metal conductors have some inductance associated with them. The inductance tends to resist the changes in the AC current through the capacitor. Equivalent series inductance, ESL, arises from the self-inductance of the device leads, coils formed due to the geometry of the device leads within the circuit, etc. The influence of inductance in capacitors generally can be seen at high frequencies. As the frequency of an applied AC voltage increases, the inductive of the ESL increases to a point at which it is equal to the capacitive reactance of the device. At self-resonance frequency, capacitance behaves as a resistor because the capacitive and inductive reactance, which have opposite signs, cancels each other out, and the impedance seen by the circuit is due only to the purely resistive parts of the capacitor. At frequencies above this point, the capacitor is effectively an inductor. In the model, the ideal capacitance is in parallel with another resistance. This resistance is equal to the insulation resistance of the dielectric and has a relatively large value Ω]) [KEM13].

2.5.2.1 Tests with VNA

The LPFs were tested as standalone devices with Keysight E5071C ENA network analyzer, the scattering parameters, S11, and S21, were measured. The Table 2.5.3 summarizes the measured cut-off frequency for each band.
By exciting the device under test with a well-defined input in terms of frequency and amplitude and recording the network's response for each frequency, a complex number is determined (reflection and/or transmission). In RF engineering, the properties of a DUT are usually described as S-parameters. We can distinguish between incident (a) and reflected waves (b). The incident wave travels from a source to the DUT, the reflected one in the opposite direction. The interface of the DUT to the outside world is one or more pole pairs, which are commonly referred to as ports. A device with one pair of poles is described as a one-port, where one incident (a_1) and one reflected (b_1) wave can propagate simultaneously.

Table 2.5.3: LPFs and bands.

Band name	-3dB cut-off freq. (measure)
10-meter	36.5 MHz
15-meter	25.0 MHz
20-meter	15.7 MHz
30-meter	11.2 MHz
40-meter	8.5 MHz
60-meter	5.7 MHz

The reflection coefficient Γ represents the ratio of the incident to reflected waves on a specific port. It is defined as: $\Gamma = \frac{b_1}{a_1}$. At two-port networks, besides the reflection coefficient on either port, the

Table 2.5.4: Numerical values of the signal generator test.

Freq (MHz)	Freq (meas.) (MHz)	Power (dBm)	Power (mW)	2^{nd} h (dBc)	3^{rd} h (dBc)	4^{th} h (dBc)	5^{th} h (dBc)	7^{th} h (dBc)	8^{th} h (dBc)	9^{th} h (dBc)
5	4.97	11.5	14	-66.8	-60.4	-62.8	-61.6	-67.1	-63.9	-55.6
7	7.0	11.5	14	-67.3	-59.0		-57.0	-44.5	-66.0	-39.6
14	14.1	11.5	14	-70.5	-56.4	-58.5	-28.7	-54.5		
28	28.0	10.9	12	-51.2	-21.0	-54.2	-37.2			

transmission in forward and reverse directions can also be characterized. Below a definition of the S-parameters for two ports is shown.

$$S_{11} = \frac{b_1}{a_1}\,|_{a_2=0} \equiv \frac{reflected\ power\ wave\ at\ port\ 1}{incident\ power\ wave\ at\ port\ 1};$$
$$S_{21} = \frac{b_2}{a_1}\,|_{a_2=0} \equiv \frac{transmitted\ power\ wave\ at\ port\ 2}{incident\ power\ wave\ at\ port\ 1};$$
$$S_{22} = \frac{b_2}{a_2}\,|_{a_1=0} \equiv \frac{reflected\ power\ wave\ at\ port\ 2}{incident\ power\ wave\ at\ port\ 2};$$
$$S_{12} = \frac{b_1}{a_2}\,|_{a_1=0} \equiv \frac{transmitted\ power\ wave\ at\ port\ 1}{incident\ power\ wave\ at\ port\ 2};$$

The S_{11} and S_{22} are equal to the reflection coefficients Γ on the respective ports $\Gamma_{in} = S_{11}$ and $\Gamma_{out} = S_{22}$. The S_{21} and S_{12} are the forward and reverse transmission coefficients, respectively. Most passive components are reciprocal, S_{ij}=S_{ji} for all i and j [CK14][CER10].

Selected screenshots taken with the Tektronix MDO3054 oscilloscope are presented in Figure 2.5.5. Measurements were made in time (left) and frequency (right) domains for chosen frequencies. Table 2.5.4 lists the harmonic order (h) and the power.

2.5.3 Tests on HF Low Distortion Sinewave Signal Generator

The spectrum of the output generated by the HF sinewave signal generator was tested with the spectrum analyzer (Tektronix SA2500, and MDO3054). Electrical signals may be examined in the time domain with the aid of an oscilloscope and in the frequency domain with the aid of a spectrum analyzer. For determining the harmonic content one examines the signal in the frequency domain. The definitive square wave should only contain components of odd-integer harmonic frequencies, nevertheless, the real-world signals may contain all integer harmonics [Rau08].

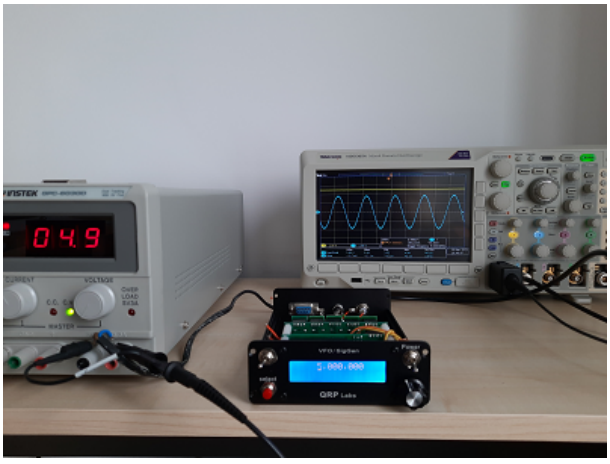

Figure 2.5.5: *Common inductor (left) and capacitor (right) models with parasitic components.*

2.5.4 Conclusion

The amplitude of the 5 MHz spectrum is 11.5 dBm. The higher-order harmonics have an amplitude about −50 dBm (−60 dBc). This is a very good result. The 6^{th} harmonic does not appear, it happens, might be cancelled in digital processing and forming the signal in the circuit. The 9^{th} harmonic is higher than the previous ones. The output sinusoidal signal is the product from filtration of the input square signal where the higher-order harmonics were attenuated. Higher amplitude of the higher-order harmonics may suggest that these harmonic products find a way to the output by bypassing the filter. It may happen by capacitive coupling in the circuit. Noise from capacitive coupling is introduced when the signal traces are routed close to each other. Whenever the trace is routed close to another, noise is capacitively

coupled due to stray capacitances between the two traces. The extra external filtering components or rerouting the signal traces is the option to reduce this effect. The capacitive couplings in the circuit cause that attenuation of the filter is decreasing with increase of frequency.
In the 7 MHz spectrum we can see also inharmonic distortions. These might be products of the synthesis, and intermodulation. Nevertheless, the maximal amplitude about −40 dBm (−50 dBc) is a decent result. The amplitudes of the odd harmonics increase with the increase of the harmonics' order. It may come from the synthesis of the frequencies in digital circuit, and also from the intermodulation distortion. There are three outputs from the module of the synthesizer but only Clk0 outputting signal is filtered, and Clk1 and Clk2 not. This reason, the generator output signal does not give clean sinusoid but might be a product of synthesis of different signals waveform. The digital signal processing generates different distortions, which mix with our signal and its harmonics, and give the noises at the output.
Important role in forming of signals also plays a linearity level of amplifying stages after the generator. The contamination of the harmonic and inharmonic distortions is in agreement to the measurement in time domain – sinusoid is not really clean.
The final conclusion is: even though the output contains the harmonic and inharmonic distortions, the results are very satisfying for this inexpensive equipment.

References

[CK14] F. Caspers and P. Kowina. *RF Measurement Concepts*. 2014 (cited on page 78).

[CER10] CERN. *RF for Accelerators*. 2010 (cited on page 78).

[Coi03] Coilcraft. *Testing Inductors at Application Frequency*. 2003 (cited on page 76).

[Ele22] ElectronicsNotes. *ElectronicsNotes*. 2022. URL: https://www.electronics-notes.com (visited on 01/10/2022) (cited on page 76).

[KEM13] KEMET. *Introduction to Capacitor Technologies*. 2013. (Visited on 01/10/2022) (cited on page 77).

[LB00] R. Ludwig and P. Bretchko. *RF Circuit Design – Theory and Application*. 2000. (Visited on 01/10/2022) (cited on page 76).

[Mee18] Meettechniek. *Measuring self-inductance & ESR*. 2018. URL: https://meettechniek.info/passive/inductance.html (visited on 01/10/2022) (cited on page 77).

[Rau08] C. Rauscher. *Fundamentals of Spectrum Analysis*. 2008. (Visited on 01/10/2022) (cited on pages 75, 78).

2.6 Peer-reviewed publications, talks, PhD/MSc, & Grants for GSD in 2020-2021

Peer-reviewed publications by GSD staff: 01.01.2020 to 31.12.2021

[Băr+21] S. Băruță (Ilie) *et al.* "Characterization of the segmented high-purity germanium clover detector from the ELIADE array at ELI-NP". In: *U.P.B. Sci. Bull.* 83 (2 2021).

Invited talks delivered by GSD staff: 01.01.2020 to 31.12.2021

[Che21] G. Chen. "The Control and Archiving System for the Gamma Beam Profile Station at ELI-NP". In: *International Conference on Accelerator and Large Experimental Physics Control Systems (18th), Shanghai, China, 14-22 October 2021*. 2021. URL: https://accelconf.web.cern.ch/icalepcs2021/doi/JACoW-ICALEPCS2021-TUPV028.html.

3. Laser-Driven Experiments Department (LDED)

The Laser-driven Experiments Department is at the core of ELI-NP's mission to research phenomena in nuclear physics with an all-optical accelerator in the quest to drive scientific progress. Inaugural experiments have already been undertaken and partly analyzed. The main focus is to quantify the high-power laser interaction with matter and develop new applications based on this research.

The high-power laser system at ELI-NP will produce high-energy charged particles, gamma-rays, and neutrons, with peak fluxes orders peak of magnitude higher than hitherto achievable with conventional accelerators. In the E1 experimental area of ELI-NP, this short-duration, high fluxes of nuclear particles will be used to study new kinds of nuclear physics and strong-field QED phenomena, such as:

- Exotic, heavy neutron-rich nuclei produced using new methods involving sequential reactions in plasma
- The stopping power of charged particles bunches in dense plasmas
- Nuclear reactions in hot and dense plasmas to study astrophysical phenomena
- Nuclear excitations and de-excitations in plasmas leading to changes in nuclear
- The study of quantum radiation reaction on beam and plasma electrons accelerated abruptly by the laser field
- The production of abundant electron-positron pairs and energetic gamma-rays in laser interactions with electrons
- High energy gamma-catalyzed production of electron-positron pairs from the vacuum in the laser focus

To achieve these goals, LDED is to implement the experimental setups in three large-scale dedicated areas at ELI-NP: E1, E5, and E6. Each area houses a custom-built large interaction chamber that is connected to the laser system through a specific laser beam transport line. Each chamber is equipped with dedicated, custom-build diagnostic tools.

The flagship E1 target station is dedicated to experiments that utilize two laser beams with 10 PW each. The core scientific mission of early day research at E1 will be to study ion acceleration mechanism and γ-flash generation, which will open up the avenue for a new class of laser-driven nuclear physics experiments.

The experimental area E6 is designated to host strong-field QED experiments with the two 10 PW arms using ultra-relativistic electrons accelerated in gas jet targets. Besides QED-related experiments, the Laser-Wakefield acceleration mechanism will be studied at E6 as well.

Finally, the 1 PW E5 station, which is currently commissioned, will be dedicated to material and biological sciences. Commissioning experiments successfully demonstrated proton acceleration with endpoint energies of around 60 MeV only recently.

The LDED group dedicates parts of its efforts to novel instrumentation and diagnostic methods for the proposed experiments to support the above research. New diagnostic methods, ranging from the optical

to the nuclear field, are necessary because of the unprecedented laser intensities at ELI-NP. Furthermore, a well-equipped laboratory will produce on-site sophisticated laser targets, including nano-structured targets. International collaborations underpin our efforts, and Expert Users have participated in successful commissioning campaigns. Eventually, the work efforts undertaken by LDED staff will support a gamut of laser-driven nuclear physics endeavors by external users once the transition to becoming a User Facility is undertaken.

The reports as depicted in this chapter demonstrate the breadth of LDED expertise. Members of LDED have successfully accrued six external funding grants from ELI-Ro and PED, besides managing the platform grants such as *e.g.*, 'Program Nucleu'. We have published widely in internationally acknowledged journals between 2020 and 2021, and group members have delivered a series of invited talks. Furthermore, two Ph.D. projects were successfully finalized in 2020/21.

As of early 2022, LDED is looking forward with great optimism to continuing their unique endeavor with dedicated work, which will pinnacle in the commissioning of the 10 PW system in 2022.

Experiments at LDED

3.1 First experiment with a laser-focused beam at ELI-NP: laser-driven electron acceleration with the 100 TW laser system

Doria D.[1,*], Ghenuche P. V.[1], Cernăianu M. O.[1], Tomassini P.[1] , Berceanu A.[1] , Ong J. F.[1], Safca N.[1,2], Măgureanu A.[1,2], Talposi M.[1,3], Matei M., Tudor L.[1], Bălăşcuţă S.[1], Gugiu M. M.[1], Cuciuc M.[1], Dancus I.[1] , Diaconescu C. B.[1], Mitu I. O.[1], Nastasa V. V.[1], Negoita F.[1] Rodrigues V. R. M.[1], Rosu M. M.[1], Stutman D.[1,4], Tanaka, K. A.[1], Ur C. A.[1], Ursescu D.[1,3] , Zamfir, N. V.[1], and Ticoş C. M.[1]

[1] Extreme Light Infrastructure (ELI-NP) & Horia Hulubei National Institute for R & D in Physics and Nuclear Engineering (IFIN-HH), Str. Reactorului No. 30, 077125 Bucharest–Măgurele, Romania
[2] Engineering and Applications of Lasers and Accelerators Doctoral School (SDIALA), University Politehnica of Bucharest, Bucharest–Măgurele, Romania
[3] Physics Doctoral School, Bucharest University, Magurele, Ilfov, 077125, Romania
[4] Johns Hopkins University, Baltimore, Maryland 21218, USA

[*] **domenico.doria@eli-np.ro**

Abstract

During the second half of 2020, the first experimental campaign with a focused laser beam was performed at ELI-NP. The campaign was carried out at the E4 experimental area using one of the two 100 TW laser beams of the ELI-NP high-power laser system (HPLS). The experiment consisted in assessing the performance of the HPLS by the acceleration of electrons from a gas target. The laser wake-field acceleration (LWFA) mechanism was investigated by employing a 2 mm long gas-jet with either pure Helium gas or a mixture of Helium plus 2% Nitrogen. The laser system can deliver a beam with maximum energy of 2.5 J, and a pulse duration and central wavelength of 25 fs and 810 nm, respectively. The beam was usually focused down to a normalized vector potential $a_0 = 2.6 \pm 0.3$ by using a parabolic mirror of the focal length of 1500 mm. To investigate the performance of the HPLS, several parameters were checked in real-time by employing many diagnostics which delivered data on a shot-to-shot base. Simulations were performed with a PIC code in support of the experimental data.

3.1.1 Introduction

The commission of the high-power laser system (HPLS) and the laser beam transport system (LBTS) of ELI-NP was successfully finalized a few years ago. In particular, the capability of delivering 10 PW laser shots was demonstrated on the 17th of November 2020 during the 'Inaugural 10 PW Laser and Users Symposium' in front of an international audience of experts. During the same period, the first experiment with a focused laser beam was carried out in the E4 experimental area using one of the two 100 TW laser beams of the HPLS. The experimental campaign was centered on the laser-driven acceleration of electrons, and the aim was to test the performance of the 100 TW laser system and the readiness of the experimental area for such type of experiment. The laser wake-field acceleration (LWFA) of electrons in the bubble regime [PM02] was chosen as it is a well-established acceleration mechanism that has been investigated for about two decades now, and therefore, owing to a vast existing literature. It can provide a good benchmark for the characterization of our laser system. Moreover, in addition to the self-injection mechanism due to the injection of plasma electrons in the (partially broken) plasma wave, we explored the so-called ionization-injection scheme [Che+06], in which electrons extracted by field ionization from the K-shell of a dopant (Nitrogen in our case) got more favorable conditions to be trapped in the plasma wave. To properly investigate the performance of the HPLS, several parameters were checked in real-time by employing many diagnostics which delivered data on a shot-to-shot base and then at full power shot. Also, simulations performed with the quasi-3D PIC code FB-PIC [Leh+16] showed agreement with the acceleration regime observed in the experiment.

3.1.2 Experimental setup

The campaign was carried out at the E4 experimental area of ELI-NP employing a 100 TW laser. The experimental setup consisted of a gas target, a long focal parabolic mirror, and several diagnostics. The gas target was a 2 mm long gas jet with either pure Helium gas or a mixture of Helium plus 2% Nitro-

gen. The laser system can deliver a beam with maximum energy of 2.5 J, and a pulse duration and central wavelength of 25 fs and 810 nm, respectively. The beam was focused by a gold-coated parabolic mirror of the focal length of 1500 mm to a peak intensity of the order of $I_0 \sim 1 \times 10^{19}\,\mathrm{Wcm}^{-2}$. The setup is illustrated in the picture of Figure 3.1.1. The main diagnostic was an electron spectrometer made of a magnetic dipole 16 cm long, with 3 cm gap between the two magnets, and a LANEX screen which image was acquired through an optical system and an ICCD ANDOR camera. The field strength of the dipole was about 0.73 T at the peak, in the middle of the dipole. A few diagnostics for the characterization of the laser beam at full power were set up to grab far-field (FF), near-field (NF), spectrum, and pulse duration. Also, other diagnostics to gain insight onto the laser-plasma interaction were implemented. In particular, the laser energy transmitted through the gas target and backscattered; the shadowgraphy, the interferometry and the self-emission of the interaction; and the Raman forward scattering.

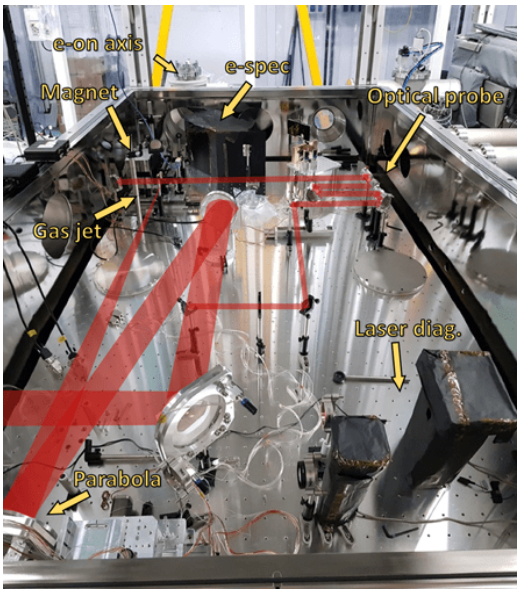

Figure 3.1.1: *Experimental setup at E4. The laser beam path is shown in red, and the most relevant diagnostics and apparatuses used are indicated in yellow.*

3.1.3 Results

The experiment was performed with an electron density of the order of $1 \times 10^{18}\,\mathrm{cm}^{-3}$, either with pure Helium or an admixture of Helium and 2% Nitrogen. The laser energy typically delivered on target was of 1.9 J, with an encircled energy in the focal spot of about 75%, which corresponds to an effective energy in the focus of 1.7 J. The minimum laser waist was (17.5 ± 2.0) µm, that for a best compressed laser pulse gives a laser peak intensity $I_0 = (1.45 \pm 0.30) \times 10^{19}\,\mathrm{Wcm}^{-2}$, that is, a normalized vector potential of $a_0 = 2.6 \pm 0.3$. For each type of gas target, the gas density and the laser focus position were scanned to find favorable conditions for the interaction. The images of the laser channel in the gas through optical probing and the profile of the electron beam onto an on-axis LANEX screen were used to seek the optimum conditions. An example is reported in Figure 3.1.2.

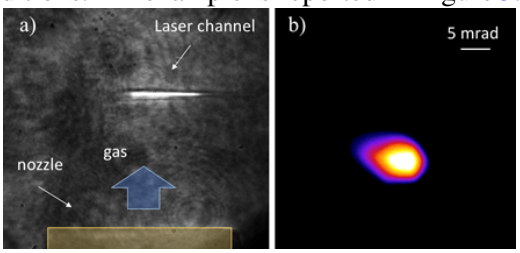

Figure 3.1.2: *a) Shadowgraphy signal (side view diagnostic) of the channel created by the laser at about* 10 ps *from the beginning of the interaction. b) example of a good electron beam profile, as obtained from the process of optimization of the LWFA. The optimized electron beam divergence was about* 5 mrad *FWHM, with pointing fluctuation of about* ±5 mrad.

The maximum electron energy attained with the Helium gas was about 220 MeV with an energy spectrum having a certain degree of monochromaticity. Instead, the maximum energy reached using the admixture was about 320 MeV with a continuum energy spectrum, as typically expected from the employment of a not truncated ionization injection process. The RAW images from the LANEX screen of the electron traces for both gas specimens are shown in Figure 3.1.3.

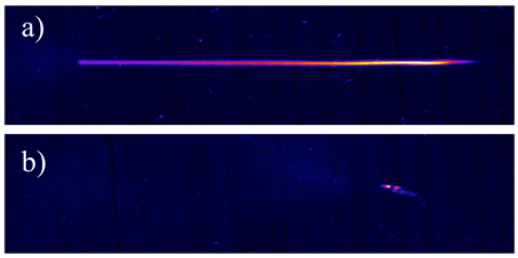

Figure 3.1.3: *a) Electron trace on* LANEX *for the case of gas admixture, and b) for the case of pure Helium gas.*

3.1.4 PIC simulation results

A simulation campaign was performed with the aim of the quasi-3D FB-PIC Particle in cell code [fb-pic].

FB-PIC employs an azimuthal modes decomposition within a Fourier-Bessel framework, owing to the field's fast and accurate description. Moreover, the code is optimized for the usage of a limited number of GPU's with MPI communication, like the ones available in the Laser Gamma Experiments Department (16×V100, 32 GB of memory each). Here, we show results from a simulation in which the laser pulse was described in the far-field as derived by a 6^{th} order Super-Gaussian profile in a near field so as to mimic the deviations from the simplest TEM00 shape partially. The laser pulse with amplitude, duration and minimum waist of $a_0 = 2.4$ $\tau = 25\,\mathrm{fs}$ FWHM, and $w_0 = 19\,\mu\mathrm{m}$ respectively, impinged onto a preformed plasma with a longitudinal profile modeled so as to fit the experimental shape delivered by the gas-jet producer. The maximum plasma density in the simulation was $7.9 \times 10^{18}\,\mathrm{Wcm}^{-3}$.

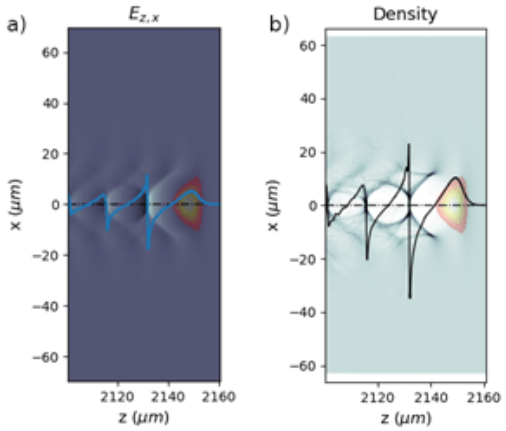

Figure 3.1.4: *Snapshots of the longitudinal electric field (a) and plasma density (b) in the vicinity of the gas-jet axis.*

The simulation box of length and radius of 60 µm and 70 µm, respectively, was resolved with three rotational modes, 48 ppc, and grid size of 33 nm and 330 nm in the longitudinal and radial directions. In Figure 3.1.4 the snapshots of the longitudinal electric field (panel a) and of the plasma density (panel b) are shown. The envelope of the laser pulse amplitude (orange region) and the on-axis accelerating gradient line-out are also shown there. A well-identified sequence of increasingly smaller and less cavitated bubbles is present, with a characteristic spike-like structure of the accelerating field, showing that a deep bubble regime was reached at that time.

3.1.5 Conclusion

The campaign has successfully shown good performances of the 100 TW beam of the HPLS and the capability of the target area E4 for laser-plasma experiments, and in particular for the acceleration of electrons.

3.1.6 Acknowledgment

The work reported was supported by the Project Extreme Light Infrastructure Nuclear Physics (ELI-NP) Phases I (475/12.12.2012) and II (1/07.07.2016), a project co-financed by the Romanian Government and European Union through the European Regional Development Fund. The authors also acknowledge the support of the Romanian Ministry of Education and Research through the PN 19060105 project. The authors also thank the laser team of ELI-NP, Thales team, and other members of LDED and LGED for their technical support.

References

[Che+06] M. Chen *et al.* "Electron injection and trapping in a laser wakefield by field ionization to high-charge states of gases". In: *Journal of Applied Physics* 99.5 (Mar. 2006), page 056109. DOI: 10.1063/1.2179194. URL: https://doi.org/10.1063/1.2179194 (cited on page 87).

[Leh+16] R. Lehe *et al.* "A spectral, quasi-cylindrical and dispersion-free Particle-In-Cell algorithm". In: *Computer Physics Communications* 203 (2016), pages 66–82. ISSN: 0010-4655. DOI: https://doi.org/10.1016/j.cpc.2016.02.007. URL: https://www.sciencedirect.com/science/article/pii/S0010465516300224 (cited on page 87).

[PM02] A. Pukhov and J. Meyer-ter-Vehn. "Laser wake field acceleration: the highly non-linear broken-wave regime". In: *Applied Physics B: Lasers and Optics* 74.4-5 (Apr. 2002), pages 355–361. DOI: 10.1007/s003400200795. URL: https://doi.org/10.1007/s003400200795 (cited on page 87).

3.2 Commissioning of the 1 PW experimental area with an experiment on TNSA ion acceleration

Cernăianu M. O.[1,*], Ghenuche P. V.[1], Rotaru, F.[1], Asavei T.[1], Bălăşcuţă S.[1], Chalus O.[2] Dancus I.[1], Diaconescu C. B.[1], Dinca, L.[1], Dreghici, D. B.[1,3], Ghiţă D. G.[1], Gugiu. M. M.[1], Jalba, C.[1], Lupu, A. M.[1], Măgureanu A.[1,3], Matei D.G.[1], Nastasa V. V.[1], Negoita, F.[1], Popescu, D.[1], Söderström P.-A.[1], Tataru, M.[1], Tanaka, K. A.[1] Ticoş C. M.[1], Tomassini P.[1] , Tudor, L.[1] , Ur, C. A[1], and Doria, D.[1]

[1] Extreme Light Infrastructure (ELI-NP) & Horia Hulubei National Institute for R & D in Physics and Nuclear Engineering (IFIN-HH), Str. Reactorului No. 30, 077125 Bucharest– Măgurele, Romania
[2] Thales Optronique S.A.S., Laser Solutions Unit, Elancourt Cedex, France
[3] Engineering and Applications of Lasers and Accelerators Doctoral School (SDIALA), University Politehnica of Bucharest, Bucharest, Romania

[*] **m.cernaianu@eli-np.ro**

Abstract

During the second half of 2021, the first experimental campaign for the commissioning of the 1 PW experimental area, E5, was performed at ELI-NP. The campaign was carried out using one of the two 1 PW laser beams of the ELI-NP high-power laser system (HPLS). The campaign aimed to test and improve the performance of the HPLS by benchmarking it with proton acceleration *via* the Target Normal Sheath Acceleration (TNSA) mechanism. The experimental campaign was performed employing different types of targets, with or without a plasma mirror (PM), and with laser intensity on the target up to several 1×10^{21} Wcm^{-2}. The lasers' angle of incidence on the target was 45 ° or 26 ° with respect to the target normal, without, or with PM, respectively. The laser generally showed high performance, and a sufficient number of shots was achieved to reliably characterize the performance of the laser against the literature. The maximum proton energy of about 60 MeV was attained with µ*m*-thick foils by employing the PM. The overall campaign was successful and proved that the system was ready for users' access.

3.2.1 Introduction

The high-power laser system (HPLS) and the laser beam transport system (LBTS) of ELI-NP were successfully and fully commissioned about two years ago. In the second half of 2021, the commissioning of the 1 PW area, E5, started [Dor+20; Tan+20]. The campaign was centered on the characterization of one of the two arms of the HPLS. The experiment focused on the laser-driven acceleration of ions to test the performance of the 1 PW laser system and the readiness of the experimental area for such type of experiment with solid targets (see Figure 3.2.1).

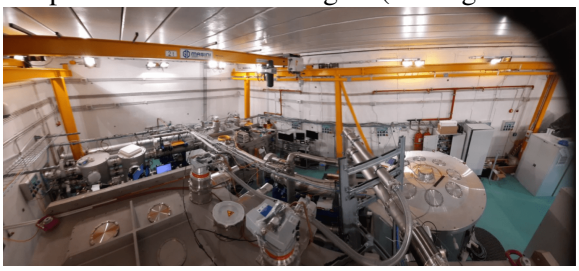

Figure 3.2.1: *Overview of the E5 experimental area.*

The characteristics and performance of the HPLS were investigated directly, using laser diagnostics at low and full power, and indirectly by observing the features of the by-products of the interaction. In particular, the investigation focused on the acceleration of protons via the Target Normal Sheath Acceleration (TNSA) mechanism [RS16]. The proton acceleration via TNSA was chosen as an indirect method for assessing the HPLS features. It is a well-established and robust acceleration mechanism that provides reliable results under specific interaction conditions and owing to a vast existing literature. It can give a good benchmark for the characterization of our laser system. Key parameters of the interaction have been measured, such as the energy spectra of the ion beam and the laser beam characteristics, to infer the qualities of the interaction.

The campaign was carried out at the E5 experimental area of ELI-NP employing a 1 PW laser. The experimental setup consisted of a solid target, a short focal parabolic mirror, and several diagnostics. The laser system can deliver a beam with maximum energy of 24 J, and a pulse duration and central wavelength of 24 fs and 810 nm, respectively. The beam

was focused by a parabolic mirror (OAP) of the focal length of 707 mm to a peak intensity of the order of 1×10^{21} Wcm^{-2}. Various materials were used as targets: aluminium, plastic, and Diamond-like carbon (DLC). The targets were in the form of thin or thick foils, with the thickness ranging from a few hundreds of nanometers to a few tens of micrometers. A target thickness and the laser intensity scan allowed for an adequate characterization of the interaction, then providing information about the quality of the interaction. The ion diagnostics were a Thomson parabola spectrometer (TPS) and a stack of detectors (SD). The TPS was made of a magnetic dipole 50 mm long, an electrostatic deflector 120 mm long, and an Image plate (IP) as detector. The field strength of the dipole was about 0.45 T at the peak, in the middle of the dipole. The SD consisted of a stack of radiochromic films (RCF), CR-39, and plastic filters arranged to detect up to about 60 MeV of proton energy. The SD was designed using the Monte Carlo simulation code SRIM. A few diagnostics for the characterization of the laser beam at full power were set up to grab far-field (FF), near-field (NF), spectrum, and pulse duration. Also, other diagnostics were implemented to gain insight onto the laser-plasma interaction. In particular, the laser energy reflected and backscattered by the target, and an optical probe, with the wavelength as the fundamental, reveals the pre-plasma eventually created by the features of the laser temporal contrast. Also, some of the shots were done using a Plasma Mirror (PM) to improve the laser temporal contrast. In Figure 3.2.2, a picture of the setup (without PM) is shown.

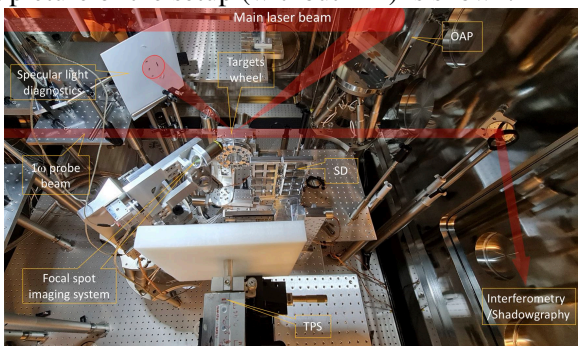

Figure 3.2.2: *Experimental setup used when shooting without the PM. The laser beam paths are shown in red (main beam and probe), and some of the diagnostics and apparatuses used for laser and particle characterization are indicated with labels.*

3.2.2 Results

The experiment was performed with different types of flat targets, with or without PM, and within a range of laser intensities spanning a few orders of magnitude, from 1×10^{19} Wcm^{-2} to 1×10^{22} Wcm^{-2}. The laser had an incident angle on target of about 45 ° or 26 ° with respect to target normal, without, or with PM, respectively. The repeatability of laser energy at full power shot was of $\sim \pm 2\%$, and the pointing stability below 2 µrad at the target position. The laser was focused to a best focal spot of about 3.5 µm at FWHM, with an encircled energy of about 70%. Initially, the laser shots were performed without employing a PM to investigate the laser temporal contrast. The laser intensity was ramped up gradually to study the pre-pulse effect and avoid undesirable side effects due to laser light backscattered into the HPLS. This approach, along with the optical probe system that was probing the interaction at a different time with respect to the main laser pulse arrival time, allowed identifying and removing the sources of a few pre-pulses originally present in the laser beam. After the pre-pulses were removed, a number of shots were done at high laser power up to 1 PW, with or without PM. The ion energy spectra were detected by the TPS and the proton energy spectrum with the SD. High laser power shots on a few micrometers thick aluminium targets, corresponding to a laser intensity of the order of 1×10^{21} Wcm^{-2}, gave the highest proton energy of up to 60 MeV. The highest proton energies were detected with the CR-39, while the RCF showed sensitivity only up to the proton flux corresponding to about 30 MeV to 40 MeV (similarly to the TPS). Figure 3.2.3 shows a number of consecutive RCF as part of an SD that shows the signal impressed by the proton beam obtained by shooting onto an aluminum foil 4.5 µm thick with laser intensity on target of $I_0 = 4.5 \times 10^{21}$ Wcm^{-2}, after reflecting off the PM.

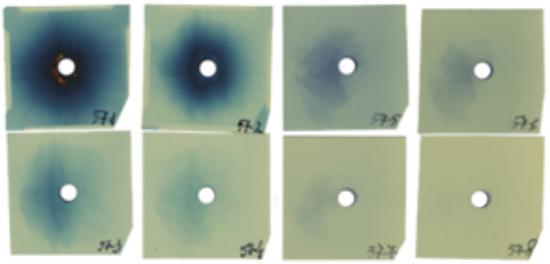

Figure 3.2.3: *Eight consecutive RCF images showing the proton beam. The last layer in the picture (bottom-right) corresponds to a proton energy of about* 30 MeV *(signal not visible in the pic).*

Also, thin foils of DLC with a few hundreds of nanometers thickness were shot at full laser beam energy by employing the PM. The ELI-NP team manufactured the DLC flat targets. Proton and carbon ions were accelerated up to about 38 MeV and 13 MeV

per nucleon, respectively. Figure 3.2.4 depicts the raw image of the signal obtained via TPS on an IP detector.

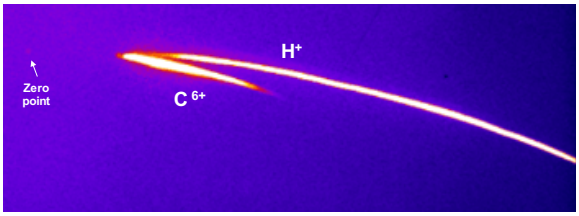

Figure 3.2.4: *Raw image of a TPS signal on an IP detector showing proton and carbon ion signals generated via laser interaction with a* 380 nm *DLC target.*

Data analysis is still ongoing, but these preliminary results clearly show the high performance of the HPLS and the target area, making the system ready for hosting experimental campaigns by external users.

3.2.3 Conclusion

The campaign has successfully achieved the pre-established objectives, that is, making the target area ready for experiments, improving the laser performed, and attaining results consistent with those obtained from comparable HPLS installations as published in the literature. The first part of the commissioning was dedicated to improving the laser performance with particular attention to the laser temporal contrast. The laser energy and pointing stability have been proved to be very good, similar to the pulse duration and focusability. The pre-pulse initially present has been totally removed, improving the temporal contrast dramatically. The second part of the commissioning was devoted to laser-ion acceleration via TNSA to benchmark the HPLS and the target area against the vast data present in the literature. The results are well consistent with the literature and clearly show a very high laser performance.

3.2.4 Acknolwegdement

The work reported was supported by the Project Extreme Light Infrastructure Nuclear Physics (ELI-NP) Phases I (475/12.12.2012) and II (1/07.07.2016), a project co-financed by the Romanian Government and European Union through the European Regional Development Fund. The authors also acknowledge the support of the Romanian Ministry of Education and Research through the PN 19060105 project. The authors also thank the laser team of ELI-NP, the Thales team, and other members of LDED for the technical support.

References

[Dor+20] D. Doria *et al.* “Overview of ELI-NP status and laser commissioning experiments with 1 PW and 10 PW class-lasers”. In: *Journal of Instrumentation* 15.09 (2020), pages C09053–C09053 (cited on page 91).

[RS16] M. Roth and M. Schollmeier. “Ion Acceleration—Target Normal Sheath Acceleration”. In: *Proceedings of the CAS–CERN Accelerator School: Plasma Wake Acceleration, Geneva,Switzerland, 23–29 November 2014*. 2016, pages 231–270. DOI: http://dx.doi.org/10.5170/CERN-2016-001 (cited on page 91).

[Tan+20] K. A. Tanaka *et al.* “Current status and highlights of the ELI-NP research program”. In: *Matter and Radiation at Extremes* 5.2 (Mar. 2020), page 024402. DOI: 10.1063/1.5093535. URL: https://doi.org/10.1063/1.5093535 (cited on page 91).

3.3 Laser-driven population and release of the 2.4 MeV isomer in ^{93}Mo, towards a 'Nuclear Battery'; Resumé of initial steps

Spohr K. M.[1] , Doria D.[1] , Tanaka K. A.[1] , Cernăianu M. O.[1], O'Donnell D.[2] , Nastasa V. V.[1] , Ghenuche P. V.[1] , Söderström P.-A.[1], Bruhaug G.[3] , Forrest C.[3] , and Rinderknecht H.[3]

[1] Extreme Light Infrastructure (ELI-NP) & Horia Hulubei National Institute for R & D in Physics and Nuclear Engineering (IFIN-HH), Str. Reactorului No. 30, 077125 Bucharest–Măgurele, Romania
[2] School of Computing, Engineering and Physical Sciences, University of the West of Scotland, High Street, Paisley, PA1 2BE, Scotland, UK
[,3] University of Rochester Laboratory for Laser Energetics (LLE), Rochester, NY 14623, USA

* **klaus.spohr@eli-np.ro**

Abstract

Multi-PW laser systems can simultaneously provide intense beams of accelerated protons with laser-plasma. This allows study of the production and triggered release of the long-lived ($t_{1/2}$ = 6.85 hr) nuclear isomer ^{93m}Mo with 2.425 MeV. An intermediate short-lived ($t_{1/2}$ = 3.52 ns) state situated only 4.85 keV above can act as a gateway to trigger the immediate release of of the full energy. A laser-driven control of this process will henceforth enable the harvesting of energy densities in the nuclear regime ('Nuclear Battery'). The observation of the release of ^{93m}Mo *via* the intermediate state has already been claimed by Chiara *et al.* [Chi+18], who assigned it to the Nuclear Excitation by Electron Capture NEEC process. However, observation and NEEC interpretation are challenged by the world-renowned experimentalists and theoreticians [WKP19a] in the leading 'Nature' journal. To inform the debate, we plan to use laser-induced MeV protons to produce the isotope *via* ^{93}Nb(p, n)^{93m}Mo and coincidently study its behavior in hot laser-induced plasma. In preparation for a campaign at the 1 PW system at ELI-NP, we were awarded a crucial initial experiment at the 200 TW system at the VEGA system CLPU Salamanca to be performed. Besides, the project became a core issue for the MP3 Rochester campaign, given evidence of the potential impact of the research results on the future of energy storage.

3.3.1 Introduction

Nuclear physics research will benefit from multi-PW lasers' ability to simultaneously provide intense accelerated proton beams with hard X-rays. Facilitating this unique feature allows a study of the production and triggered release of the long-lived ($t_{1/2}$ = 6.85 hr) nuclear isomer ^{93m}Mo. The isomer resides at the high energy of 2.425 MeV, and an intermediate short-lived ($t_{1/2}$ = 3.52 ns) state situated only 4.85 keV above can act as a gateway to trigger the immediate release of its energy, resulting in a 500-fold energy amplification. A laser-driven control of this process will henceforth enable the harvesting of energy densities in the nuclear regime ('Nuclear Battery'). The principle of unsolicited ^{93m}Mo release *via* the intermediate state has already been observed by Chiara *et al.* [Chi+18], who assigned it to the Nuclear Excitation by Electron Capture NEEC process. However, this NEEC interpretation is challenged by the world-renowned theory group of the MPIK[1] [WKP19a]. To achieve complete control of the decay of ^{93m}Mo and solve the theoretical conundrum, we plan to use laser-induced MeV protons to produce the isotope *via* ^{93}Nb(p, n)^{93m}Mo. After production, ^{93m}Mo will be exposed to hr-long high fluxes of MeV X-rays and electrons or directly to the multi-PW laser light to study a possible triggered release. The research will support the theory of nuclear processes in plasma and instigate further research into a 'Nuclear Battery' concept.

The controlled production and triggered release of a nuclear isomer will allow harvesting the highest human-made energy density ratio in the region of 1 GJ/kg, comparable only to nuclear fission ('Nuclear Battery'). Our project will test High Power Laser Plasma Systems (HPLS) 's ability to provide the high level of mastery needed to manipulate isomers accordingly. The isomeric state ^{93m}Mo is the prime candidate for this endeavour as it lies at a staggering 2.425 MeV above the ground-state and has a rather long half-life of $t_{1/2}$ = 6.85 hr. The triggered freeing of the isomer's energy can pro-

[1] Max-Planck Institut für Kernphysik in Heidelberg

ceed *via* an intermediate, short-lived ($t_{1/2}$ = 3.52 ns) state situated only 4.85 keV directly above ^{93m}Mo at 2.430 MeV, see Figure 3.3.1. Therefore, a steered depopulation of the isomer will result in a 500-fold energy amplification. In 2018 Chiara *et al.* confirmed this pathway for triggered depopulation of ^{93m}Mo using a conventional accelerator system, albeit coinciding with the production reaction, hence unsolicited. They claimed the hitherto unobserved Nuclear Excitation by Electron Capture (NEEC) caused by the stopping process of ^{93m}Mo in the production target as triggering mechanism and derived a very high excitation probability of $P_{\mathrm{NEEC}} = 0.010(4)$.

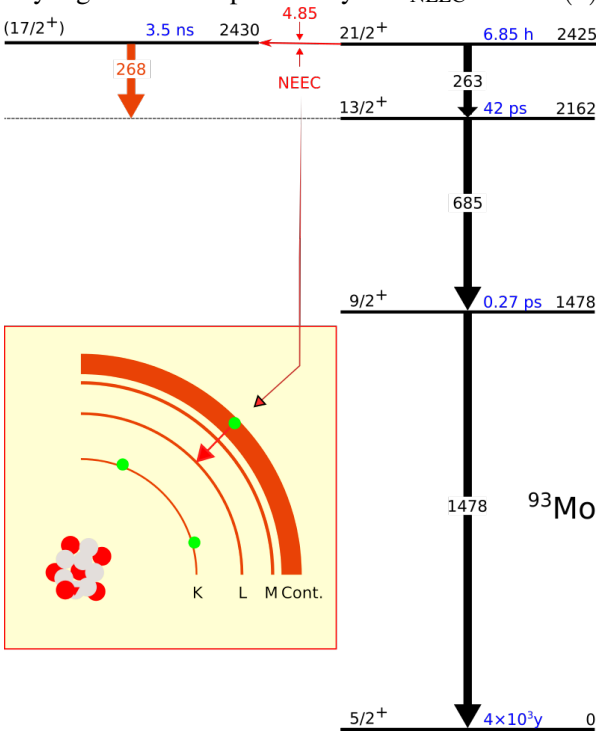

Figure 3.3.1: *NEEC schematics (yellow inset) and partial* ^{93}Mo *level scheme from [DB95]*

NEEC is the reverse of internal conversion. The process sets in when the absorbed electron's kinetic energy plus its atomic binding energy matches the energy difference between two nuclear states [Mor05]. However, the very high value of P_{NEEC} is not supported by the world-renowned theoreticians at the MPIK, who have published widely on that process [Gun+14; Gun+18; PEK07; Pál+08; WKP19b] and derived a value for P_{NEEC} that is a staggering nine orders of magnitude lower [WKP19a] than cited in [Chi+18]. They strongly suggest that another novel and hitherto unobserved process triggers this remarkable effect. Since the experimental evidence is not in question, (only) an investigation at a multi-PW system can clarify the current conundrum between observation and theoretical explanation. At an HPLS one can produce the isomer in question with MeV protons *via* ^{93}Nb(p, n)^{93m}Mo, (Figure 3.3.2, Part a)). A substantial yield can be guaranteed as the irradiation time can be in the order of several hours as $t_{1/2}(^{93m}\mathrm{Mo}) = 6.85\,\mathrm{hr}$. If a depopulation of ^{93m}Mo is achieved with high fluxes of X-rays (Figure 3.3.2, Part b)), it is more likely that photoabsorption is responsible for the results in [Chi+18]. If, however, a keV electron plasma (Figure 3.3.2, Part c)) will lead to depopulation of ^{93m}Mo, independent verification of NEEC is confirmed. Theory suggests that such a keV-plasma is already achieved for $I \gtrsim 1 \times 10^{17}\,\mathrm{Wcm}^{-2}$ in a ^{93}Nb target, which will allow a large surface to be irradiated by a multi-PW laser system [Pál20]. The intensities will be derived from the experimental yields $Y(^{93m}\mathrm{Mo})$ as retrieved in offline activity measurements with a High Purity Ge-detector (HPGe). In any case, our experiment will shed light on the underlying nature of the interaction between the isomer ^{93m}Mo in a flux of keV X-rays and laser-plasma. It would also be exciting to test the isomer's response in Warm Dense Matter (WDM) if the reaction protons can be bundled with specifically designed targets to induce this peculiar state of matter. The proof of controlled production and decay, resulting in a 500-fold energy amplification, will significantly impact further research into the 'Nuclear Battery' concept.

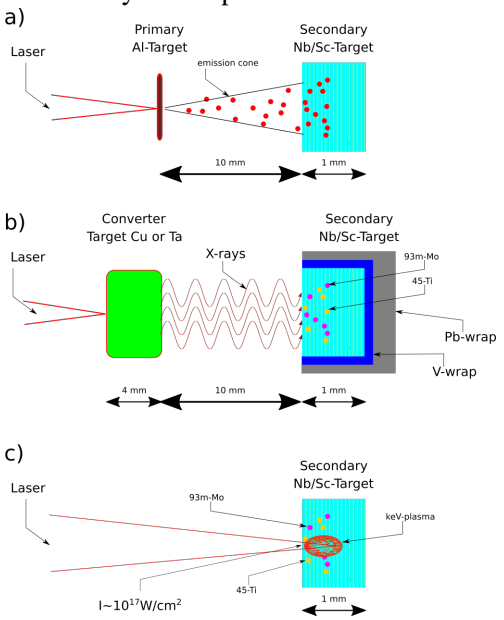

Figure 3.3.2: *Part a) Setup for proton production shots, with the secondary* ^{93}Nb *target. Part b) Setup for the depopulation by X-rays from a Ta-converter target. The wrapping in V- and Pb-sheets is to maximize the X-ray flux. Part c) Direct laser irradiation.*

3.3.2 Approved experimental campaign

The multi-petawatt laser pulses need to provide a focal intensity of I_0 to reach a maximum yield for MeV protons from the primary target. The secondary sandwiched ^{93}Nb reaction target should be in cm-close vicinity for the production experiments (Figure 3.3.2, Part a)). To expose the isotope to keV X-ray radiation the laser pulse should be directed to a 4 mm Ta-converter to provide the highest possible X-ray flux (Figure 3.3.2, Part b)). For direct laser irradiation to induce keV laser-plasma in the secondary target (Figure 3.3.2, Part c)), the ^{93}Nb sandwich target should be shifted towards the laser propagation direction out of the laser's focal spot, to obtain maximum area coverage of $I \gtrsim 1 \times 10^{17}\,\mathrm{Wcm}^{-2}$. Selection and diagnostics of $3\,\mathrm{MeV} \lesssim Ep \lesssim 15\,\mathrm{MeV}$ protons is essential, as well as diagnostic tools to evaluate the laser-plasma in the target (X-ray backlighter). After the hr-long production and induced decay shots, the activity should be measured by an HPGe detector offline.

3.3.3 Conclusion & Scientific impact

The experiment will be essential to study the production and decay of ^{93m}Mo in laser-induced plasma and will follow and enhance inaugural work performed at ELI-NP. Results may settle the prominent dispute between the NEEC interpretation in [Chi+18] (Nature) and [WKP19a] (PRL) that is currently unresolved. Any progress concerning the controlled production and triggered decay of a nuclear isomer has to be seen as a potential landmark experiment, as it will spearhead further technological applications for nuclear isomers, esp. in respect of developing a form of 'Nuclear Battery'.
The controlled release of a MeV isomer by a keV radiation will enable a gamut of potential applications. First on foremost, one can think of medical applications in which a big burst of radiation could be triggered by a relatively modest exposure to X-ray radiation. Moreover, the high probability, as reported in [Chi+18], is very intriguing as it may indicate that there are further hitherto non-observed nor theoretically considered processes at the interface of laser-plasma, atomic, and nuclear physics. A multi-PW system is ideally placed to investigate such interactions that demand an overarching holistic strategy in experimental design.

3.3.4 Acknowledgment

The work draws support from the ELI-RO grant ELI-12 contract (16.10.2020). In addition, the authors are indebted to colleagues at the University of Salamanca, Spain, namely Sophia Malko and Luca Volpe, as well as to theorists from the Max-Planck Institute of Nuclear Physics (MPIK) in Heidelberg, namely Adriana Pálffy-Buß, Yuanbin Wu, and Christoph H. Keitel.

References

[Chi+18] C. J. Chiara *et al.* "Isomer depletion as experimental evidence of nuclear excitation by electron capture". In: *Nature* 554.7691 (Feb. 2018), pages 216–218. DOI: 10.1038/nature25483. URL: https://doi.org/10.1038/nature25483 (cited on pages 95–97).

[DB95] C. Dunford and T. Burrows. "Online Nuclear Data Service". English. In: *Report IAEA-NDS-150 (NNDC Informal Report NNDC/ONL-95/10), International Atomic Energy Agency, Vienna, Austria* 9.1 (1995) (cited on page 96).

[Gun+14] J. Gunst *et al.* "Dominant Secondary Nuclear Photoexcitation with the X-Ray Free-Electron Laser". In: *Physical Review Letters* 112.8 (Feb. 2014). DOI: 10.1103/physrevlett.112.082501. URL: https://doi.org/10.1103/physrevlett.112.082501 (cited on page 96).

[Gun+18] J. Gunst *et al.* "Nuclear excitation by electron capture in optical-laser-generated plasmas". In: *Physical Review E* 97.6 (June 2018). DOI: 10.1103/physreve.97.063205. URL: https://doi.org/10.1103/physreve.97.063205 (cited on page 96).

[Mor05] P. Morel. "Nuclear Excitation by Electronic Processes: NEEC and NEET Effects". In: *AIP Conference Proceedings*. AIP, 2005. DOI: 10.1063/1.1945195. URL: https://doi.org/10.1063/1.1945195 (cited on page 96).

[Pál20] A. Pálffy. Private Communication. 2020 (cited on page 96).

[PEK07] A. Pálffy, J. Evers, and C. H. Keitel. "Isomer Triggering via Nuclear Excitation by Electron Capture". In: *Physical Review Letters* 99.17 (Oct. 2007). DOI: 10.1103/physrevlett.99.172502. URL: https://doi.org/10.1103/physrevlett.99.172502 (cited on page 96).

[Pál+08] A. Pálffy *et al.* "Nuclear excitation by electron capture followed by fast x-ray emission". In: *Physics Letters B* 661.4 (2008), pages 330–334. ISSN: 0370-2693. DOI: https://doi.org/10.1016/j.physletb.2008.02.027. URL: https://www.sciencedirect.com/science/article/pii/S0370269308001858 (cited on page 96).

[WKP19a] Y. Wu, C. H. Keitel, and A. Pálffy. "^{93m}Mo Isomer Depletion via Beam-Based Nuclear Excitation by Electron Capture". In: *Physical Review Letters* 122.21 (May 2019). DOI: 10.1103/physrevlett.122.212501. URL: https://doi.org/10.1103/physrevlett.122.212501 (cited on pages 95–97).

[WKP19b] Y. Wu, C. H. Keitel, and A. Pálffy. "X-ray-assisted nuclear excitation by electron capture in optical laser-generated plasmas". In: *Phys. Rev. A* 100 (6 Dec. 2019), page 063420. DOI: 10.1103/PhysRevA.100.063420. URL: https://link.aps.org/doi/10.1103/PhysRevA.100.063420 (cited on page 96).

3.4 Plasma imaging diagnostics for high-power lasers experiments

Măgureanu A.[1], Bălăşcuţă S.[1], Ghenuche P. V.[1] , Cernăianu M. O.[1], Diaconescu C. B.[1], Ticoş C. M.[1], and Doria D.[1]

[1] Extreme Light Infrastructure (ELI-NP) & Horia Hulubei National Institute for R & D in Physics and Nuclear Engineering (IFIN-HH), Str. Reactorului No. 30, 077125 Bucharest–Măgurele, Romania
[2] Engineering and Applications of Lasers and Accelerators Doctoral School (SDIALA), University Politehnica of Bucharest, Bucharest, Romania

[*] **alexandru.magureanu@eli-np.ro**

Abstract

Plasma imaging diagnostics is a powerful tool for offering precious information, in real-time, about the laser-driven plasma during high-power laser experiments. In this report, we present the design and implementation of a Shadowgraphy system and wavefront sensor measurements in the commissioning experiments of the ELI-NP facility. The Shadowgraphy system was used for imaging the plasma generated by 1 PW laser pulses focused on both a solid target and a gas cell target. To derive the plasma density, the wavefront sensor measured the phase change of the probe beam wavefront going through the plasma channel generated by the focused pulse in the gas cell.

3.4.1 Introduction

The imaging of the plasma generated by ultrashort laser pulses with high peak power focused on gas or solid targets is routinely performed in high-power laser experiments. The Shadowgraphy technique is a powerful and relatively simple technique that usually employs the probe beam as a pick-off from the main beam to illuminate the plasma generated by the focused, intense laser pulse. The side illumination of the plasma creates the shadow image of the interaction, which can be visualized on a CCD camera. In solid targets experiments, the probe beam is imaging the shadow of the expanding plasma created by the focused laser, which rapidly ionizes the solid target [Säv+15][Sch+13]. The technique can be complementary and enhanced by imaging the interaction on a wavefront sensor camera which measures the phase gradient for the measurement of gas or plasma density [Pla+10].

3.4.2 Experimental setup

A significant role in the imaging process is the alignment of the pulsed probe beam, which should be very precisely synchronized with the main pulse. The probe pulse is reflected on a one-inch dielectric pick-up mirror located on the edge of the main pulse. In our setup the main pulse generated by a Ti:Sapphire laser [Lur+20] had a diameter of 200 mm, a peak power up to 1 PW, a pulse duration around of 25 fs, and a near 800 nm central central wavelength. The energy of the probe pulse with 25 mm diameter can be approximately computed from the following formula, considering a flat-top Gaussian laser beam profile:

$$E_{probe} = E_{\text{main}} \cdot \left(\frac{\Phi_{\text{probe}}}{\Phi_{\text{main}}} \right)^2 \approx 0.016 \cdot E_{\text{main}}\,, \quad (3.4.1)$$

where Φ_{main} and Φ_{probe} are the diameters of the main and probe beam, respectively. The probe beam, which has the same pulse duration as the main one, is delayed through a delay line provided with a motorized stage (working steps of 2 µm (6.6 fs) and a 20 cm travel range) that allows the user to change the length of the optical path of the probe beam and to image the interaction at different time scales, a few picoseconds before the interaction of the main pulse with the gas target or after the interaction when the plasma starts to evolve. The imaging system used is presented in Figure 3.4.3.

As can be observed in Figure 3.4.1 the imaging system also presents the SID4 camera, which is a wavefront sensor camera that performs 'Quadri-Wave Lateral Shearing Interferometry' for obtaining the phase map. The technique of lateral shearing interferometry can be used to measure the phase gradient in one direction based on the interference of two identical but tilted wavefronts replicated from the same incident wavefront. This principle was extended in the multiwave interferometry [PS95] that measures more than one gradient in order to recover the full 2D phase-field.

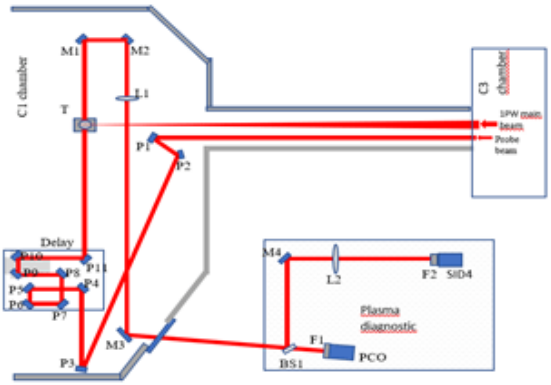

Figure 3.4.1: *Schematic representation of the imaging system*

In Quadri-Wave Lateral Shearing Interferometry, four replicas of the wavefront are created by a specific 2D diffraction grating placed in front of the camera sensor. The field intensity and phase are derived from the integration of the two-phase gradients measured along with two perpendicular directions [Vel+06]. The phase shift measured in the interference image is proportional to the electron density of the plasma and is related to the difference between the index of refraction of plasma and that of vacuum. For a laser pulse propagating a distance „d" in plasma, along the z-axis, the pulse wavefront phase variation is:

$$\Theta = \int_0^d k_p \cdot dz = \int_0^d \frac{N(z)\omega}{c} \cdot dz \qquad (3.4.2)$$

$N(z)$ is the local index of refraction of plasma, ω the laser frequency in plasma, and c is the speed of light. An initial reference phase image is recorded without the gas target by sending the laser pulse through the vacuum. A second laser pulse is then sent through the gas target. The difference in the phase of the two laser pulses is given by Equation 3.4.3, where $N_0 = 1$ is the vacuum refraction index:

$$\Delta\Theta = \int_0^d (N(z) - N_0) \cdot \frac{\omega}{c} \cdot dz \qquad (3.4.3)$$

In the above equation we consider n_e the plasma (electron) density, and $n_{cr} = \frac{\varepsilon_0 \cdot m_e \cdot \omega^2}{e^2}$ the cut-off plasma density at the frequency of the probe beam. The squared plasma frequency is given by $\omega_p^2 = \frac{n_e \cdot e^2}{\varepsilon_0 \cdot m_e}$. The index of refraction $N(z)$ is related to the plasma density: $N^2 = 1 - \frac{n_e}{n_{cr}}$. For plasma densities much smaller than the cut-off density,$N \cong 1 - \frac{n_e}{2n_{cr}}$, such that the phase shift is given by the approximation:

$$\Delta\Theta \cong \int_0^d \frac{n_e(z)}{(2n_{cr})} \cdot \frac{\omega}{c} \cdot dz = \frac{\omega \cdot d}{2 \cdot c} \cdot \frac{\bar{n_e}}{n_{cr}} = \frac{\pi \cdot d}{\lambda} \cdot \frac{\bar{n_e}}{n_{cr}}, \qquad (3.4.4)$$

where $\bar{n_e} = \frac{\int_0^d n_e(z)dz}{d}$ is the average plasma density. From Equation 3.4.4 one can compute an approximate value of the average density along directions parallel to the axis of the probe pulse. SID4 consists of a regular camera and a two-dimensional diffraction grating that generates an interferogram on the camera sensor. The intensity and the wavefront profile $W(x,y)$ of a light beam are derived from the interferogram. The SID4 measures a map of phase changes $\Delta\Theta(x,y)$ on the image plane. In order to extract the index of refraction and the plasma (or gas) density, an algorithm based on the inverse Abel transform is used [Baf21].

3.4.3 Results

Figure 3.4.2 shows the images of a flat foil (placed in the focus of the 1 PW laser pulse) before the interaction of the 1PW pulse with the target (at -20 ps) and after the interaction (at 200 ps), during the proton acceleration experiments at the C3 chamber, in the E5 area. The solid target was a 20 µm thick aluminium foil mounted on a multi-target holder. The expansion of the plasma generated by the main pulse, after 200 ps, can be noticed.

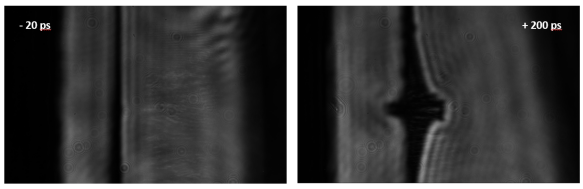

Figure 3.4.2: *Shadowgraphy (side view) image of a solid target at different time scales, before (left) and after (right) the interaction with the main beam*

Also, for the gas experiment, Shadowgraphy images were recorded with a PCO EDGE 5.5 MP scientific camera before and after the interaction of the main pulse with the gas in a 10 mm long 3D printed gas cell. They are presented in Figure 3.4.3. The plasma diagnostic was performed during the electron acceleration experiments at the C1 chamber (also in the 1 PW-E5 area). The window for plasma density calculations performed by the software package provided by Phasics with the SID4 wavefront sensor and a 2D map of the plasma density versus the longitudinal and transversal direction to the plasma channel are presented in Figure 3.4.3.

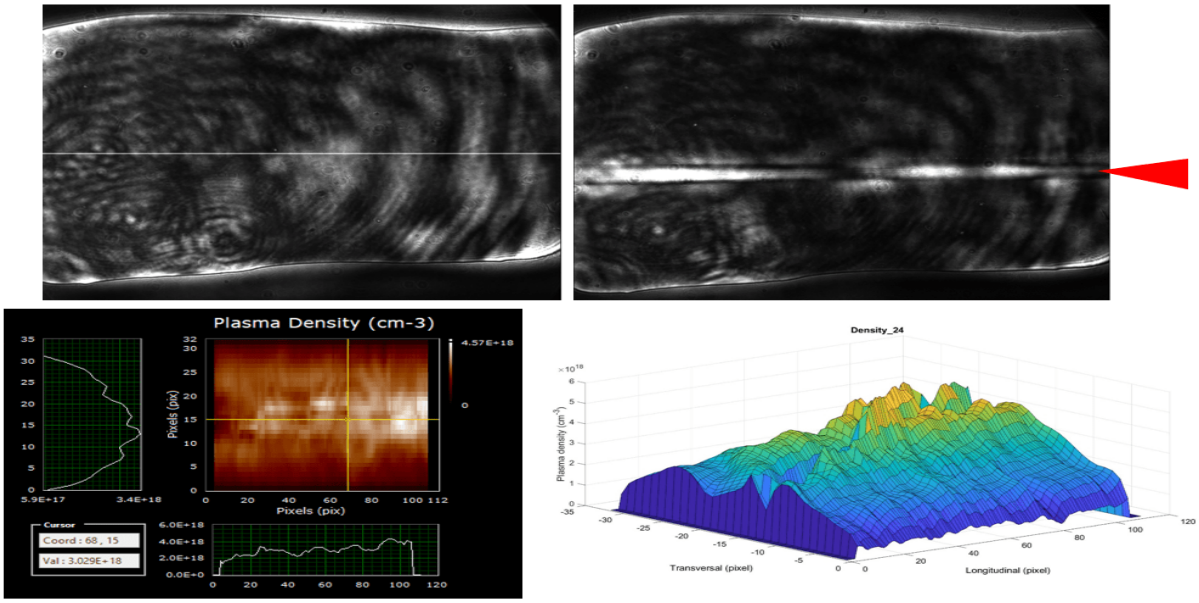

Figure 3.4.3: *Shadowgraphy image of Plasma channel induced by the laser in the 3D printed gas cell (top images) and SID4 wavefront measurements of the density profile along the plasma channel* $\sim 2 \times 10^{18}\,\mathrm{cm}^{-3}$ *to* $4 \times 10^{18}\,\mathrm{cm}^{-3}$ *(bottom images), together with a 2D representations map of the plasma density versus the longitudinal and transversal direction*

3.4.4 Conclusion

The techniques of Shadowgraphy and Quadri-Wavefront Lateral Shearing Interferometry were implemented in the first experiments with solid and gas targets at the E5 area of the 1 PW HPLS. Both techniques were used to retrieve information about the laser-target interaction to be used for the optimization of the 1 PW main laser beam during the commissioning experiments for proton acceleration with a solid target (at the C3 chamber) and electron acceleration with gas targets (at the C1 chamber). The two techniques offer complementary information for the imaging and diagnostics of the laser-driven plasma on ultra-short time scales.

References

[Baf21] G. Baffou. “Quantitative phase microscopy using quadriwave lateral shearing interferometry (QLSI): principle, terminology, algorithm and grating shadow description”. In: *Journal of Physics D: Applied Physics* 54.29 (July 2021). arXiv: 2102.05106, page 294002. ISSN: 0022-3727, 1361-6463. DOI: 10.1088/1361-6463/abfbf9. URL: http://arxiv.org/abs/2102.05106 (visited on 04/01/2022) (cited on page 100).

[Lur+20] F. Lureau *et al.* “High-energy hybrid femtosecond laser system demonstrating 2 × 10 PW capability”. en. In: *High Power Laser Science and Engineering* 8 (2020). Publisher: Cambridge University Press. ISSN: 2095-4719, 2052-3289. DOI: 10.1017/hpl.2020.41. URL: https://www.cambridge.org/core/journals/high-power-laser-science-and-engineering/article/highenergy-hybrid-femtosecond-laser-system-demonstrating-2-10-pw-capability/C10005F3B8BA78E4FA3EF9EAF06C3BFB (visited on 03/30/2022) (cited on page 99).

[Pla+10] G. R. Plateau *et al.* “Wavefront-sensor-based electron density measurements for laser-plasma accelerators”. In: *Review of Scientific Instruments* 81.3 (Mar. 2010). Publisher: American Institute of Physics, page 033108. ISSN: 0034-6748. DOI: 10.1063/1.3360889. URL: https://aip.scitation.org/doi/full/10.1063/1.3360889 (visited on 04/01/2022) (cited on page 99).

[PS95] J. Primot and L. Sogno. “Achromatic three-wave (or more) lateral shearing interferometer”. EN. In: *JOSA A* 12.12 (Dec. 1995). Publisher: Optica Publishing Group, pages 2679–2685. ISSN: 1520-8532. DOI: 10.1364/JOSAA.12.002679. URL: https://opg.optica.org/josaa/abstract.cfm?uri=josaa-12-12-2679 (visited on 04/01/2022) (cited on page 99).

[Säv+15] A. Sävert *et al.* "Direct Observation of the Injection Dynamics of a Laser Wakefield Accelerator Using Few-Femtosecond Shadowgraphy". In: *Physical Review Letters* 115.5 (July 2015). Publisher: American Physical Society, page 055002. DOI: 10.1103/PhysRevLett.115.055002. URL: https://link.aps.org/doi/10.1103/PhysRevLett.115.055002 (visited on 04/01/2022) (cited on page 99).

[Sch+13] M. B. Schwab *et al.* "Few-cycle optical probe-pulse for investigation of relativistic laser-plasma interactions". In: *Applied Physics Letters* 103.19 (Nov. 2013). Publisher: American Institute of Physics, page 191118. ISSN: 0003-6951. DOI: 10.1063/1.4829489. URL: https://aip.scitation.org/doi/10.1063/1.4829489 (visited on 04/01/2022) (cited on page 99).

[Vel+06] S. Velghe *et al.* "Advanced wave-front sensing by quadri-wave lateral shearing interferometry". In: *Interferometry XIII: Techniques and Analysis*. Volume 6292. SPIE, Aug. 2006, pages 117–129. DOI: 10.1117/12.681533. URL: https://www.spiedigitallibrary.org/conference-proceedings-of-spie/6292/62920E/Advanced-wave-front-sensing-by-quadri-wave-lateral-shearing-interferometry/10.1117/12.681533.full (visited on 04/01/2022) (cited on page 100).

3.5 Nomarski Interferometry for plasma density measurements at the C3 interaction chamber

Bălăşcuţă S.[1], Măgureanu A.[1], Cernăianu M. O.[1], and Anghel E.[1]

[1] Extreme Light Infrastructure (ELI-NP) & Horia Hulubei National Institute for R & D in Physics and Nuclear Engineering (IFIN-HH), Str. Reactorului No. 30, 077125 Bucharest–Măgurele, Romania
[2] Politehnica University of Bucharest, Splaiul Independentei nr.313, 060042 Bucharest, Romania

* **septimiu.balascuta@eli-np.ro**

Abstract

We report the implementation of an optical setup for on-shot plasma diagnostic based on Nomarski Interferometry and Shadowgraphy, at the C3 interaction chamber at ELI-NP, where the plasma was generated by laser pulses of: 25 fs, 6 J to 22 J, and central wavelength around 810 which were focused on solid targets. We measured the pre-pulse's arrival time based on the Shadowgraphy images recorded by a CCD camera synchronized with the high-power laser pulses incident on a solid target. We estimated the plasma's expansion rate upon the interaction of the laser pulse with the target. In addition, the optical setup for Nomarski Interferometry was built on the same optical bench, outside the C3 interaction chamber, for on-shot plasma density measurements. The analyzed data refers to the commissioning experiments dedicated to laser-driven protons and carbon ions acceleration.

3.5.1 Introduction

The on-shot measurements of the density of the plasma generated by high-power ultrashort laser pulses focused on solid targets were essential for optimizing the laser-driven protons and ions acceleration. Nomarski Interferometry was used before to measure the high-density warm plasmas [Cao+08], [Giz+94], [Kal+10]. The images of expanding plasma generated in the focus of ultrashort laser pulses were captured on a video camera at each laser pulse, using ultrashort probe laser pulses synchronized with the high-power (main) laser pulse [PBC16]. At the C3 interaction chamber, at the E5 experimental area, the protons and carbon ions were accelerated using 650TW to 860 TW laser pulses focused on solid targets made of aluminum, gold, alumina, and plastic for the commissioning experiments performed in 2021. We will present the optical setups based on Shadowgraphy, and Nomarski Interferometry implemented at the C3 chamber to optimize the laser pulse parameters and the target position for the Target Normal Sheath Acceleration (TNSA) of protons and ions.

The main advantage of the Nomarski interferometer, compared with other interferometry techniques, is the absence of the reference beam because only the probe beam passes through the target. The image is formed by the overlap of the ordinary and extraordinary beams (with orthogonal polarization) generated in the Wollaston prism and after passing through the Glan-Laser polarizer. After passing through the polarizer, the ordinary and extraordinary beams obtain the same polarization and can interfere with the video camera's sensor. Because the active interference image is formed at the intersection of the two polarized beams, the Nomarski Interferometry has a negligible dependence on the interference image resolution on the amplitude of vibrations produced by the vacuum pumps.

3.5.2 The parameters of the probe pulse for plasma diagnostics

The plasma generated in the high-intensity laser pulses focused on solid targets in the high-vacuum ($<10^{-6}$ mbar) of the C3 interaction chamber was imaged at different time intervals from the moment of plasma formation, with a probe beam reflected on a pick-up mirror, at 90 degrees. The pick-up dielectric mirror with high reflectivity in the 750 nm to 1100 nm range was mounted on the edge of the high power (0.65 PW - 0.88 PW) laser pulse with 200 mm diameter at the C3 interaction chamber. The experiments were done with laser pulse energies between 6 J and 22 J. The center of the pick-up mirror was at 9.5 cm radial distance from the axis of the laser beam that had a top-hat intensity profile. The probe pulse had an approximately constant energy density profile along the radial direction. The energy of the probe pulse with 10 mm diameter and flat intensity profile,

reflected by the pick-up mirror, can be computed from equation 3.5.1.

$$E_{\text{probe}} = E_{\text{main}} \left(\frac{\Phi_{\text{probe}}}{\Phi_{\text{main}}} \right)^2 = 55\,\text{mJ} \pm 5\,\text{mJ} \quad (3.5.1)$$

The polarization of the high-power and probe laser pulses was parallel with the optical table (P polarized laser pulses). After it was reflected on the PK mirror, the probe pulse was split by passing through an 8:92 uncoated pellicle beamsplitter (BS1). The 92% transmitted pulse was used for the diagnostic of the laser pulse, while the 8% reflected pulse passed through the delay line, then was sent to the target, and extracted outside the chamber for plasma diagnostic. According to transmission curves provided by Thorlabs, the reflectance of the pellicle beamsplitter in the range 800 nm – 830 nm, for P-polarized laser pulses is 0.03% (for 830 nm) and 2.1% (at 800 nm). The probe pulse's computed energy reflected on the pellicle beamsplitter was 0.02 mJ at 830 nm and 1.26 mJ at 800 nm. We computed this estimated probe pulse energy in section to inform future experiments.

3.5.3 The calculation of the probe pulse intensity for second harmonic generation

The BBO crystal for the generation of the second harmonic probe pulse (with 410 ($\pm$5 nm) center wavelength) for plasma diagnostic will be mounted between the mirrors (M5, M6), on breadboard 1 (Figure 3.5.1) in a rotating mount attached to the optical post with post holder on a motorized stage fixed with screws. The two mirrors, M5 and M6 will be replaced with two off-axis parabolic mirrors (OAP1, OAP2) in a confocal configuration. The user will be able to adjust the position of the BBO crystal along the direction of the probe beam relative to the focal point remotely by changing the position of the motorized stage. Taking in account the reflectivity data of the beamsplitters and mirrors, the energy density of the PD probe pulse at the BBO crystal was estimated to be between $0.02\,\text{mJ}\,\text{cm}^{-2} \pm 0.01\,\text{mJ}\,\text{cm}^{-2}$ (at 830 nm) and $1.4\,\text{mJ}\,\text{cm}^{-2} \pm 0.2\,\text{mJ}\,\text{cm}^{-2}$ (at 800 nm). For a laser pulse with Gaussian temporal profile, the peak pulse power is $P = 0.94(E_p/\tau_p)$ (where E_p is the pulse energy and τ_p is the full width at half maximum (FWHM) pulse duration), the pulse intensity $I = P/(\pi w^2)$ can be between $0.7\,\text{GW}\,\text{cm}^{-2} \pm 0.1\,\text{GW}\,\text{cm}^{-2}$ at 830 nm and $63\,\text{GW}\,\text{cm}^{-2} \pm 6\,\text{GW}\,\text{cm}^{-2}$ at 800 nm, where $w = 5\,\text{cm}$ is the beam radius. According to Jing-yuan Zhang texitet al. ([Zha+98]), in order to generate the second harmonic (SH) with maximum efficiency using ultrashort ($< 100\,\text{fs}$) laser pulses, the thickness of the BBO crystal must be between 0.3 mm and 0.4 mm, and the laser pulse intensity must be between $25\,\text{GW}\,\text{cm}^{-2}$ and $40\,\text{GW}\,\text{cm}^{-2}$. The temporal distribution of the SH pulse spectrum was distorted when the laser pump intensity exceeded $45\,\text{GW}\,\text{cm}^{-2}$. The efficiency of second harmonic generation (SHG) increases with the intensity of the laser pulse up to a maximum and then decreases. The damage threshold of BBO crystals for TEM00 mode laser pulses with 800 nm, 100 fs duration, and 50 Hz repetition frequency is bigger than $45\,\text{GW}\,\text{cm}^{-2}$ [Tur+22]. Therefore the damage threshold of the 0.3 mm thick BBO crystal will not exceed for the PD probe pulses with a central wavelength of around 810 nm and the pulse duration of circa 25 fs, and an intensity between $0.7\,\text{GW}\,\text{cm}^{-2}$ to and $70\,\text{GW}\,\text{cm}^{-2}$.

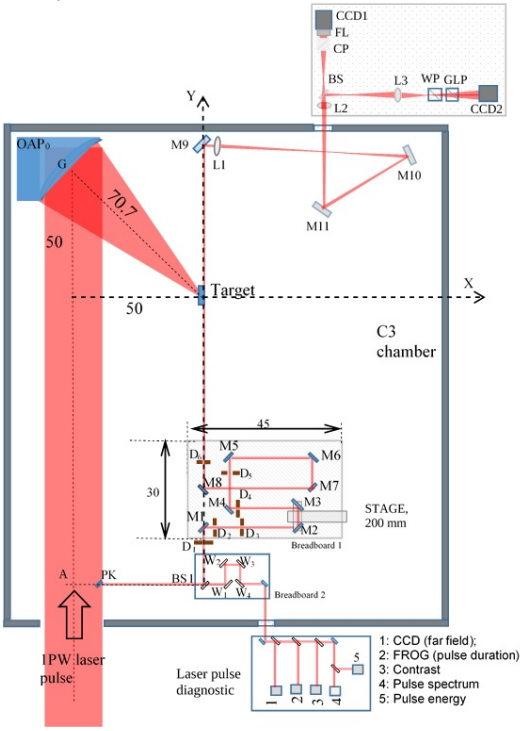

Figure 3.5.1: *Top view of the optical setup at the C3 interaction chamber.*

3.5.4 The optical setup for plasma diagnostic at C3 chamber

During the commissioning experiments at the C3 chamber in 2021, the BBO crystal was not used. Instead, the fundamental PD probe pulse was reflected on the Silver coated mirrors of the delay line setup and passed tangent to the surface of the thin foil (solid target) located in the focus of the high-power (main) laser beam. The delay between the arrival time of the main and probe pulses on target was ad-

justed up to 1.33 ns by controlling the position of a vacuum-compatible linear motorized stage with 200 mm travel. The Shadowgraphy and Nomarski Interferometry optical system for plasma diagnostic with an ultrafast probe pulse are presented in Figure 3.5.1 (left and right figures, respectively). A wire of 20 μm diameter was placed in the location of the target in order to locate the CCD1 and CCD2 cameras at the position of the image. The positions of the two cameras and of the L2 and L3 lenses were adjusted until a clear picture of the wire was seen. The Shadowgraphy image recorded on the CCD1 camera was ten times bigger than the object. During the experiments with high-power laser pulses, the background due to the scattered light from the target was reduced by placing a polarizing beamsplitter cube in front of the CCD1 camera. The optical setup is presented in Figure 3.5.2.

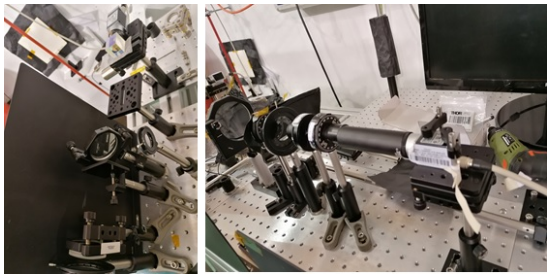

Figure 3.5.2: *The optical setup for the Shadowgraphy and Nomarski Interferometry at the C3 chamber. Pictures were taken from different angles during the commissioning experiments.*

The lenses L1 and L2 were achromatic lenses with focal lengths F1 = 50 cm and F2 = 10 cm, respectively. The first lens (L1) was at 68 cm ± 1 cm distance from the target. The calculations of the distance between lenses L1 and L2 were done with the constraining of a 10 times magnification of the image on CCD1 and CCD2 cameras. The positions of the two images were also computed both analytically and numerically using the model of the two achromatic lenses built-in Optic Studio. Lense L1 was the Achromatic doublet with 76.2 mm (=3 inches), 500 mm effective focal length, and anti-reflective coating for 400 − 700 nm. The calculations were done for two orientations of the achromatic L2 (named as configurations A and B in Figure 3.5.3) while lens L1 was always in configuration A.

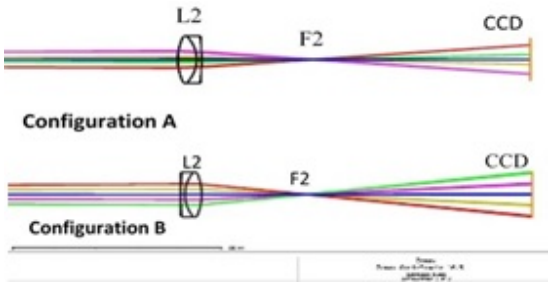

Figure 3.5.3: *The two orientations of the achromatic lens L2 rendered from Optic Studio.*

The distance between lenses L1 and L2 was computed versus the target distance from lens L1 ($X_{1,o}$), for a 10 times magnification of the image (Figure 3.5.4), for the two positions of lens L2. The distances of the Shadowgraphy image relative to lens L2 ($X_{2,i}$) were presented on the right axis.

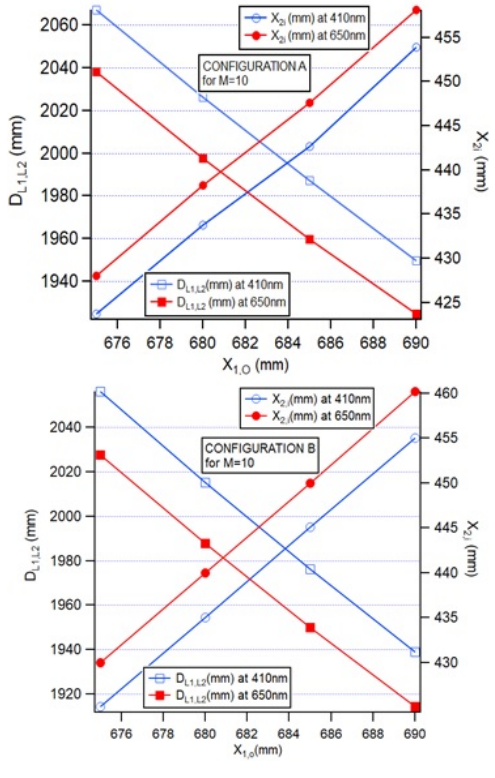

Figure 3.5.4: *The distance between lenses L1 and L2 and the position of the image computed versus the object distance, for a 10 times magnification*

The lens L2 was placed outside the chamber at 202 cm ± 1 cm distance from lens L1. The third lens (L3), with focal length F3=200 mm, used for Nomarski Interferometry, was placed before the Wollaston prism. The magnification given by lens L3 was between 1 and 1.5. We present in Figure 3.5.5 the Shadowgraphy profile image of a 6 μm thick aluminum foil, at −80 ps, −50 ps (before) and at 200 ps (after) the arrival time of the high-power laser pulse on target. It is seen that the pre-pulse arriv-

ing at −50 ps before the main pulse generated a local pre-plasma on the surface of the aluminum foil.

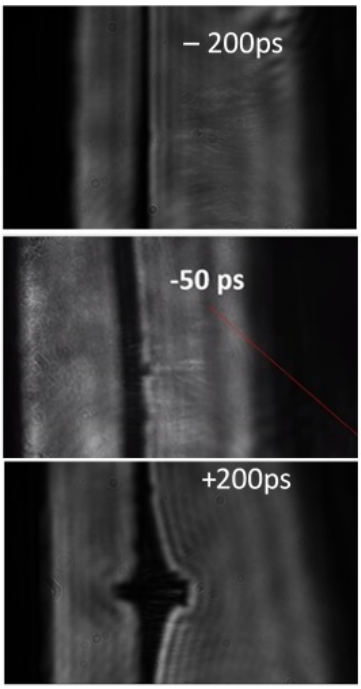

Figure 3.5.5: *Shadowgraphy image of the* 20 µm *Al-foil, taken at* −200 ps, −50 ps, *and* −80 ps, −200 ps *from the arrival time of the high-power laser pulse on target.*

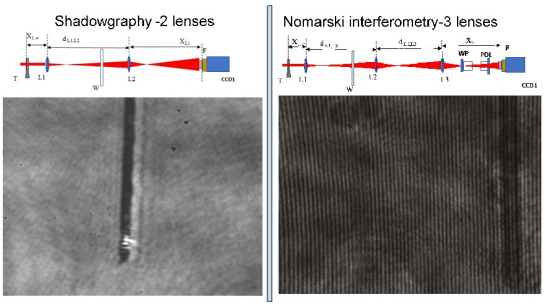

Figure 3.5.6: *The Shadowgraphy image (left side) and the Nomarski interference image (right side) of a* 20 µm *copper wire.*

3.5.5 Nomarski Inteferometry

The CCD2 camera (BASLER model ACA 1600-20 gm) was mounted on a kinematic prism mount and fixed with one clamp. The camera was connected to the power injector with the Power over Ethernet GigE cable. Neutral density filters were mounted in front of the CCD2 camera to attenuate the beam. The Glan - Laser polarizer (GLP) and the Wollaston Prism (WP) were mounted in Rotation Mounts with 1" bore diameter and SM1 threads in order to rotate the polarizer and the Wollaston prism about the laser beam axis 360 degrees. The relative intensities of the ordinary and extraordinary beam spots changed when the Glan polarizer was rotated. The intensities of the two beams after passing through the polarizer (POL) were equal when the angle θ between the axis of the polarizer and the vertical direction was 45 degrees. The amplitudes of the ordinary and extraordinary beams that passed the Glan polarizer were adjusted by simply rotating the polarizer until the interference image was seen clearly. The Wollaston Prism (WP) was mounted in a prism tube (30 mm long) fixed onto the continuous rotation mount (15.5 mm long). The Shadowgraphy and interference images of a 20 µm Cu-wire are presented in Figure 3.5.6.

3.5.6 Conclusion

The distance between lenses L1 and L2 and the distance between lens L1 and the target T was computed in Optic Studio to obtain a real image, ten times bigger than the object, on the CCD1 camera. From the Shadowgraphy images recorded at different time intervals from the moment of plasma generation, the arrival time of the pre-pulse on target was inferred. The same images were used to compute the expansion velocity of the plasma front wave. Nomarski Interferometry was not used during the commissioning experiments, but it will be used for plasma density measurements with solid targets in future experiments.

References

[Cao+08] L. Cao *et al.* "Space-time characterization of laser plasma interactions in the warm dense matter regime". In: *Laser and Particle Beams* 2 (Apr. 2008), pages 239–244. DOI: 10.1017/S0263034607000067 (cited on page 103).

[Giz+94] L. Gizzi *et al.* "Characterization of laser plasmas for interaction studies". In: *Physical Review E* 49 (6 June 1994), pages 5628–5643. DOI: 10.1103/PhysRevE.49.5628. URL: https://link.aps.org/doi/10.1103/PhysRevE.49.5628 (cited on page 103).

[Kal+10] M. Kalal *et al.* "Compact design of a Nomarski interferometer and its application in diagnostics of Coulomb explosions of deuterium clusters". In: *Journal of the Korean Physical Society* 56 (1

Jan. 2010), pages 287–294. DOI: 10.3938/jkps.56.287. URL: https://doi.org/10.3938/jkps.56.287 (cited on page 103).

[PBC16] J. Park, H. Baldis, and H. Chen. "The implementation and data analysis of an inteferometer for instens eshort pulse laser experiments". In: *High Power Laser Science and Engineering* 4 (2016), e26. DOI: 10.1017/hpl.2016.21 (cited on page 103).

[Tur+22] H. Turcicova *et al.* "Laser induced damage threshold (LIDT) of beta-barium borate (BBO) and cesium lithium borate (CLBO) – Overview". In: *Optics and Laser Technology* 149 (2022), page 107876. ISSN: 0030-3992. DOI: https://doi.org/10.1016/j.optlastec.2022.107876. URL: https://www.sciencedirect.com/science/article/pii/S0030399222000330 (cited on page 104).

[Zha+98] J. Zhang *et al.* "Second–harmonic generation from regenerative amplified femtosecond laser pulses in BBO and LBO crystals". In: *Journal of Optical Society of America, B* 15.1 (Jan. 1998), pages 200–209. DOI: 10.1364/JOSAB.15.000200. URL: http://opg.optica.org/josab/abstract.cfm?URI=josab-15-1-200 (cited on page 104).

3.6 The measurement of refraction index and thickness of a glass plate by Mach-Zehnder Interferometry

Bălăşcuţă S.[1], Anghel[1] E. , and Safca [1] N.

[1] Extreme Light Infrastructure (ELI-NP) & Horia Hulubei National Institute for R & D in Physics and Nuclear Engineering (IFIN-HH), Str. Reactorului No. 30, 077125 Bucharest–Măgurele, Romania

[*] **septimiu.balascuta@eli-np.ro**

Abstract

The index of refraction and thickness of a glass plate was measured with a Mach-Zehnder interferometer with two beams (probe and reference) from a helium-neon laser. The sample was a 50 mm × 50 mm glass plate mounted on a manual rotating stage platform with a filter holder, optical post, and post holder. The high of the glass plate was adjusted such that only the bottom half of the probe beam passed through the plate. The interference image of the probe and reference beams were recorded with a CCD camera for angles of rotation of the glass plate between −50° and 50°, with a 2° increment. The index of refraction was extracted from the fit of the relative difference of the inter-fringe distances measured in the top and the bottom halves of the interference image. The thickness of the glass plate was extracted from the fit of the change in the bottom fringe position for 2° rotation of the glass plate. From the plot of the position of fringes in the bottom half of the interference image, the value of the small angle between the directions of the probe and reference beams incident on the CCD camera was inferred.

3.6.1 Introduction

The technique of Mach Zehnder (MZ) interferometry with two arms (named probe and reference beams) was often used for the diagnostic of plasma [Cha+18] in the experiments with high-intensity laser pulses focused in pulsed gas jets [KCK06]. MZ allows to measure the refraction index of glass plates and to extract the ordinary and extraordinary refractive indexes of the birefringent crystal, from the measurements of the phase shift as a function of the rotation of the sample, with Fast-Fourier-transform based fringe analysis for phase retrieval [Nic+02] or with low coherence, con-focal interference microscope [TF96]. We present a novel measurement procedure of the thickness and the index of refraction of a glass plate with an MZ interferometer with a manual rotating stage. The interference images were recorded with a CCD camera for 52 angles of rotations of the glass plate, between 0° and 50° and between 310° and 360°, with a step of 2°. From the relative change in the distance between fringes and in the position of the fringes, we extracted the index of refraction, the thickness of the glass plates, and the small angular deviation from the ideal 45° angle of incidence position of the last beamsplitter plate. The optical setup also included a delay stage with a motorized vacuum stage and a reflective beam expander with two confocal off-axis parabolic mirrors. The delay stage was later used in the commissioning experiments at the E5 area at ELI-NP, for 1 PW laser-driven plasma wakefield acceleration of electrons in a gas target and for the acceleration of protons and Carbon ions in a solid target. The vacuum-compatible motorized stage was used to adjust the time window between the arrival times of the plasma-driving high-power laser pulse and the probe pulse on target remotely.

3.6.2 The optical setup and the measurement procedure

The 50 mm × 50 mm and 1 mm thick UVFS glass plate was mounted on a manual rotating stage with a filter holder. The high of the glass plate was adjusted such that only the bottom half of the probe beam passed through the plate. The interference images were recorded with a BASLER CCD camera (model acA1600-20 gm with CS mount and GigE interface), with 1626 × 1236 pixels and a 4.4 µm size. The CCD camera had a 1/1.8" sensor with 7.2 mm × 5.4 mm size. The angle of incidence on the glass plate was changed by manually rotating the stage with 2° increments from −50° to 50° and then in reverse from 50° to −50°. The interference images were recorded at each rotation angle. In addition, the fringe direction and the inter-fringe distance could be adjusted by slightly rotating the adjustment knobs of the kinematic mount of the beamsplitter located before the CCD camera. The geometry of the Mach-Zehnder interferometer is presented in Figure 3.6.1.

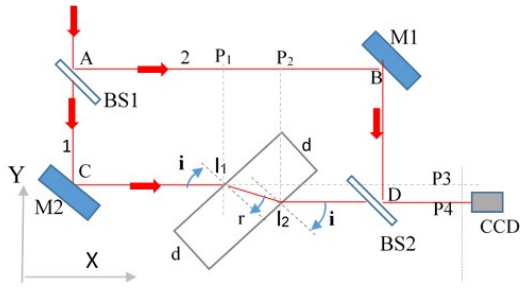

Figure 3.6.1: The Mach-Zehnder setup with two beamsplitters (BS1, BS2), two mirrors (M1, M2) and the UVFS glass plate mounted on the platform of the rotating stage.

In Figure 3.6.1 the angle of incidence i of the probe beam on the glass plate (also named the angle of rotation) is measured in the positive (counterclockwise) direction. For a laser beam propagating along the z-axis in the glass plate with thickness d, the phase change of its wave-front is $\Phi = \int_0^d k_p \cdot dz = \int_0^d N(z)\omega/c \cdot dz$ where $N(z)$ is the local index of refraction, ω is the laser frequency in plasma, and c is the speed of light. The difference in the phases of the two beams of the Mach-Zehnder interferometer is $\Delta\Phi = \int_0^d (N(z) - N_0) \cdot (\omega/c) \cdot dz$, where N_0 is the refraction index of the air. The shift in the fringe position ΔX is proportional with the phase shift $\Delta\Phi$ through the relation $\Delta X/W = \Delta\Phi/(2\pi)$, where W is the fringe width.

For each interference image recorded for rotation angle between $-50°$ to $50°$ with $2°$ step, we measured the inter-fringe distances in the bottom -half and the top half of the image. The position of the fringes is related to the difference between the optical paths of the reference beam and the top- or bottom- half of the probe beam. An IMAGEJ macro was written to read each of the 52 images, compute the position of the minima (dark lines), and then compute the linear fit of the fringe number versus the fringe position in the top and bottom halves of the image. Two rectangular regions were defined with the same left and right boundaries in the top and bottom halves of the image. The slope and the intercept were computed from the linear fit of the fringe numbers and fringe positions for up to 24 fringes in the image's top half and bottom half. The slope is the average distance between two fringes. Consider W_1 and W_0 as the average inter-fringe distances in the image's bottom and top half. As expected, W_0 did not change with the rotation angle in the limits of the errors, but W_1 changed almost linearly. We computed the relative change $(W_1 - W_0)/W_0$ and its error for each rotation angle. The dependence was fit with the model function $f_1(i) = K_0 + K_1 \cdot \sin i \cdot (1 - \sqrt{1 - \sin i^2}/\sqrt{N^2 - \sin i^2}$. The fitting parameters K_0, K_1 and N were computed from the fit: $K_0 = -0.00497 \pm 0.00014$, $K_1 = -0.01939 \pm 0.00397$ and $N = 1.42 \pm 0.16$. The distance between fringes was about 0.28 mm in both the top and bottom halves of the image. The absolute difference $W_1 - W_0$ was between -5 μm and 5 μm.

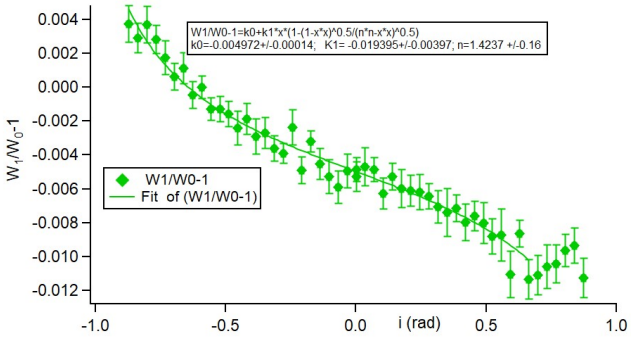

Figure 3.6.2: The relative change in the distance between bottom fringes and top fringes in the interference images recorded for rotation angles from $-50°$ to $50°$

The fitting model $f_1(i)$ was derived from the geometry of Figure 3.6.1 considering an angle of incidence on beamsplitter BS2 equal with $45° + \delta$ where δ is a small misalignment angle from the 45^o angle of incidence. If all angles of incidence were equal with 45°, and the two arms were parallel, the phase change of the probe beam, due to rotation with an angle i of the glass plate, would be $\Delta\Phi = \Phi(i) - \Phi(0) = k \cdot d \cdot (\sqrt{N^2 - (\sin i)^2} - \cos i - N + 1)$, where $k = 2\pi/\lambda$ is the wave-number. The change in the position of the bottom-half fringes would be $X_B(i) - X_B(0) = \frac{W}{\lambda} \cdot d \cdot (\sqrt{N^2 - (\sin i)^2} - \cos i - N + 1)$. As expected the fringes in the top-half of the interference image did not change with the rotation of the glass plate. The small angle of rotation δ contributes to the asymmetry of the plot of $(X_B(i) - X_B(0))/W$ versus the rotation angle, relative to the direction of normal incidence ($i = 0$), like in Figure 3.6.3. The asymmetry is due to an additional contribution to the path difference of the two beams, a term related to the translation of the probe beam axis after passing through the rotated glass plate. The additional term is multiplied by the factor $u = 2\tan\delta/(1 + \tan\delta)$, in the fitting model: $f_2(i) = K_0 + K_1(\sqrt{N^2 - (\sin i)^2} - \cos i - N + 1 + u \cdot \sin i \cdot (1 - \cos i/\sqrt{N^2 - (\sin i)^2}))$ The four fitting parameters are K_0 (the offset constant) $K_1 = d/\lambda\Delta i$, N and u. $\Delta i = \pi/90$rad corresponds to the $2°$ step.

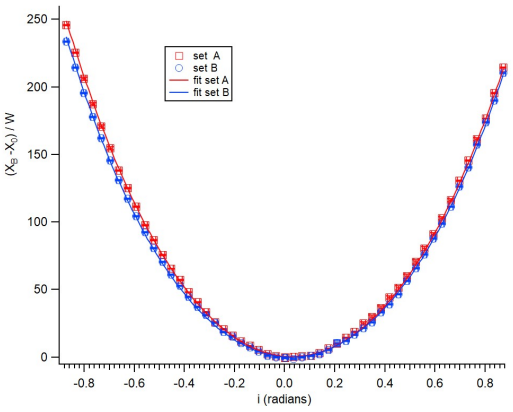

Figure 3.6.3: The change in the positions of the bottom fringes divided with the fringe width was extracted from interference images recorded for increasing and decreasing rotation angle with 2^o step

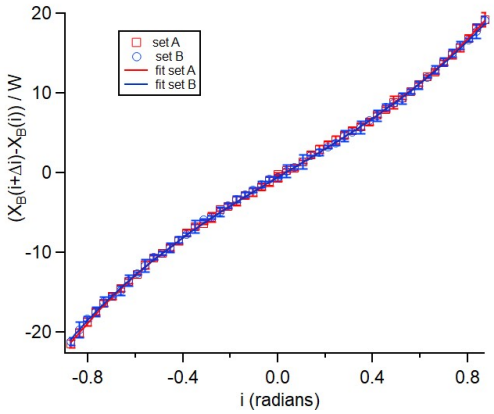

Figure 3.6.4: The increase in the positions of the bottom fringes, due to a 2° increase in the rotation angle of the glass plate, divided by the fringe width, was computed from the two sets of measurements.

The fit had 52 points and 4 fitting parameters such that the number of degrees of liberty was ν=48. The reduced chi2 value, χ^2/ν was between 3 (for set B) and 16 (for set A). Because we used a manual stage, the absolute position of each bottom fringe could not be recorded for small enough increments of the rotation angles or to record both the rotation angle and the intensity of the light in a small region of the interference image [Nic+02]. In order to extract the thickness of the glass plate, we used the value of the index of refraction derived from the fit of the relative differences $(W_1 - W_0)/W_0$ computed at the 52 rotation angles. The average change in the position of the bottom fringes for 2° increments, was computed for each rotation angle: $\Delta X_B(i) = X_B(i+\Delta i) - X_B(i)$ and then divided it with the bottom-fringe width W_1. To decrease the errors, for the rotation angles between $-48°$ and 48°, $\Delta X_B(i)$ was the average of $X_B(i+\Delta i) - X_B(i)$ and $X_B(i) - X_B(i-\Delta i)$. The relative change $\Delta X_B(i)/W_1$ is plotted versus the rotation angle in Figure 3.6.4. The proper fitting model for these data is derivative $\delta f_2(i)/\delta i$ multiplied with Δi: $f_3(i) = K_1 \cdot \sin i \cdot (1 - \cos i/\sqrt{N^2 - (\sin i)^2}) - K_2 \cdot (\cos i \cdot (1 - \cos i/\sqrt{N^2 - (\sin i)^2}) + (\sin i)^2 \cdot (N^2 - 1)/(N^2 - (\sin i)^2)^{1.5})$ The fitting parameters are $K_1 = d/\lambda \cdot \Delta i$, $K_2 = d/\lambda \cdot \Delta i \cdot u$, where $\Delta i = \pi/90$rad. Figure 3.6.4 presents the two sets of data and their fit with the fitting function $f_3(i)$. The two sets of data were computed from interference images recorded for increasing and then decreasing rotation angles (set A and B) with a 2° increment.

Considering N=1.46 a fixed parameter, the two fitting parameter were: K_1 between 55.03 ± 0.10 and 55.3 ± 0.02, K_2 between 1.78 ± 0.04 and 1.79 ± 0.08. The thickness of the glass plate, computed from K_1, was between (0.998 ± 0.025) mm and (1.003 ± 0.043) mm that agrees very well with the thickness of the plate of 1 mm specified by the producer. The small parameter u computed from the ratio K_2/K_1 was between 0.032 ± 0.001 and 0.033 ± 0.001. From the equation $u = 2\tan\delta/(1 + \tan\delta)$, we inferred a misalignment angle δ between 16.3 mrad and 16.8 mrad.

3.6.3 Conclusion

We presented a procedure for measuring the index of refraction and the thickness of a glass plate by recording the interference images in a Mach-Zehnder interferometer and a manual rotating stage. We have shown that a small misalignment angle between the directions of the probe and reference beams (transmitted and respectively reflected on the last beam-splitter) has to be taken into account to model better the dependence in the position of the fringes with the rotation angle and to extract more precise values of the index of refraction or of the thickness of the plate. Furthermore, we show that both parameters can be measured separately from two physical quantities: one from the fit of the relative change of the inter-fringe distance and the other from the fit of the change in the position of the fringes for 2° change in the rotation angle.

References

[Cha+18] Y.-A. Chan *et al.* "Development, setup and implementing of a Mach-Zehnder interferometry for plasma diagnostics". In: 2 (May 2018), pages 1–10 (cited on page 109).

[KCK06] M. Krämer, B. Clarenbach, and W. Kaiser. "A 1 mm interferometer for time and space resolved electron density measurements on pulsed plasmas". In: *Plasma Sources Science and Technology* 15.3 (Apr. 2006), pages 332–337. DOI: 10.1088/0963-0252/15/3/006. URL: https://doi.org/10.1088/0963-0252/15/3/006 (cited on page 109).

[Nic+02] S. de Nicola *et al.* "A Mach–Zehnder interferometric system for measuring the refractive indices of uniaxial crystals". In: *Optics Communications* 202.1 (2002), pages 9–15. DOI: 10.1016/S0030-4018(01)01719-9 (cited on pages 109, 111).

[T F96] I. Y. T. Fukano. "Simultaneous measurement of thicknesses and refractive indices of multiple layers by a low coherence confocal interference microscope". In: *Optics Letters* 21 (1996), pages 1942–1944 (cited on page 109).

3.7 Plasma density determination in the LWFA commissioning experiment at the 100 TW station at ELI-NP

Doria D.[1], Ghenuche P. V.[1], Asavei T.[1], Bălăşcuţă S.[1], Cernăianu M. O.[1], Diaconescu C. B.[1], Ghiţă D. G.[1], Gugiu. M. M.[1], Măgureanu A.[1], Matei D.[1], Nastasa V. V.[1], Neagu L.[1] Tesileanu O.[1] , and Ticoş C. M.[1]

Extreme Light Infrastructure (ELI-NP) & Horia Hulubei National Institute for R & D in Physics and Nuclear Engineering (IFIN-HH), Str. Reactorului No. 30, 077125 Bucharest–Măgurele, Romania

* **catalin.ticos@eli-np.ro**

Abstract

During the Summer and Fall of 2020, the first commissioning experiments employing lasers were carried out at ELI-NP. They consisted of laser-wake field acceleration (LWFA) of electrons in a supersonic gas jet utilizing a 100 TW laser in the E4 experimental area. An off-axis parabola focused the laser with $f/21$ on a spot with diameter $\sim 22\,\mu$m in supersonic jets of pure He and a mixture of He^+ 1.5% N_2, produced by a fast pulsed valve. In addition, a scattered light diagnostic was implemented to monitor the interaction of the laser beam with the gas jet and assess the density of the plasma channel produced by the laser.

3.7.1 Introduction

In the commissioning experiment in E4, the main goal was to accelerate electrons using the LWFA mechanism and benchmark the laser and the experimental setup. A supersonic gas jet obtained from a high-speed Parker valve was used as the target. Several diagnostics were implemented to characterize the laser interaction with the gas jet, including shadowgraphy and spectroscopy of the scattered light. In LWFA the intense laser pulse ionizes the gas and creates a plasma wake that co-propagates with a phase velocity close the group velocity of the laser pulse. Electrons are trapped into this wake and get accelerated by its strong longitudinal electric fields to high energies, in the few to several hundred MeV's and GeV [ESL09].

3.7.2 Raman scattering

The plasma density can be deduced from the scattered light considering the following mechanism: the laser wave excites a Langmuir wave (also called plasma wave) and a scattered wave. The frequency and momentum of all three waves are matched such that the energy and momentum during the process are conserved [Kru03].
Considering the Stokes region of the full scattered light, one can write [Hur+08; Mat+10]:

$$n_e^{Stokes} = \frac{\varepsilon_0 \gamma m_e}{e^2} \frac{\pi^2 c^2}{\lambda_0^2} \left[1 - \left(\frac{\lambda_0}{\lambda_s} \right)^2 \right]^2 \quad (3.7.1)$$

where n_e is the plasma density, γ is the relativistic factor of the electrons, m_e is the electron mass, λ_0 is the central wavelength of the incident laser beam, and λ_s is the wavelength of the scattered light. Here $\gamma = \sqrt{1 + a_0^2/2}$, where a_0 is the normalized vector potential of the laser pulse. For the anti-Stokes region of the spectrum a similar equation can be written, only that the scattered waves have a slightly higher frequency than that of the incident beam:

$$n_e^{AStokes} = \frac{\varepsilon_0 \gamma m_e}{e^2} \frac{\pi^2 c^2}{\lambda_0^2} \left[\left(\frac{\lambda_0}{\lambda_s} \right)^2 - 1 \right]^2 . \quad (3.7.2)$$

3.7.3 Experimental results

The full spectra of the forward scattered light have been measured for each shot with a spectrometer (AVAspec) in the VIS-IR spectrum. Raman scattering is responsible for the shift in wavelength observed in the scattered laser light on the plasma waves formed in the gaseous target. The laser spectrum when no scattering on target takes place is shown in Figure 3.7.1.

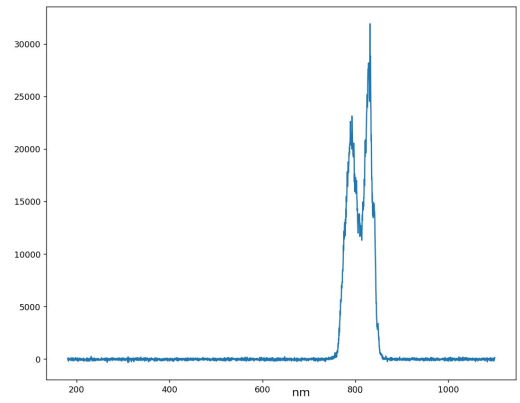

Figure 3.7.1: *Spectrum of the incident laser beam centered at* $\lambda_0 \approx 800\,\text{nm}$

One can see a broad spectrum with a full width $\Delta\lambda \approx 90\,\text{nm}$, centered at 800 nm. The measured spectrum scattered off the plasma is shown in Figure 3.7.2.

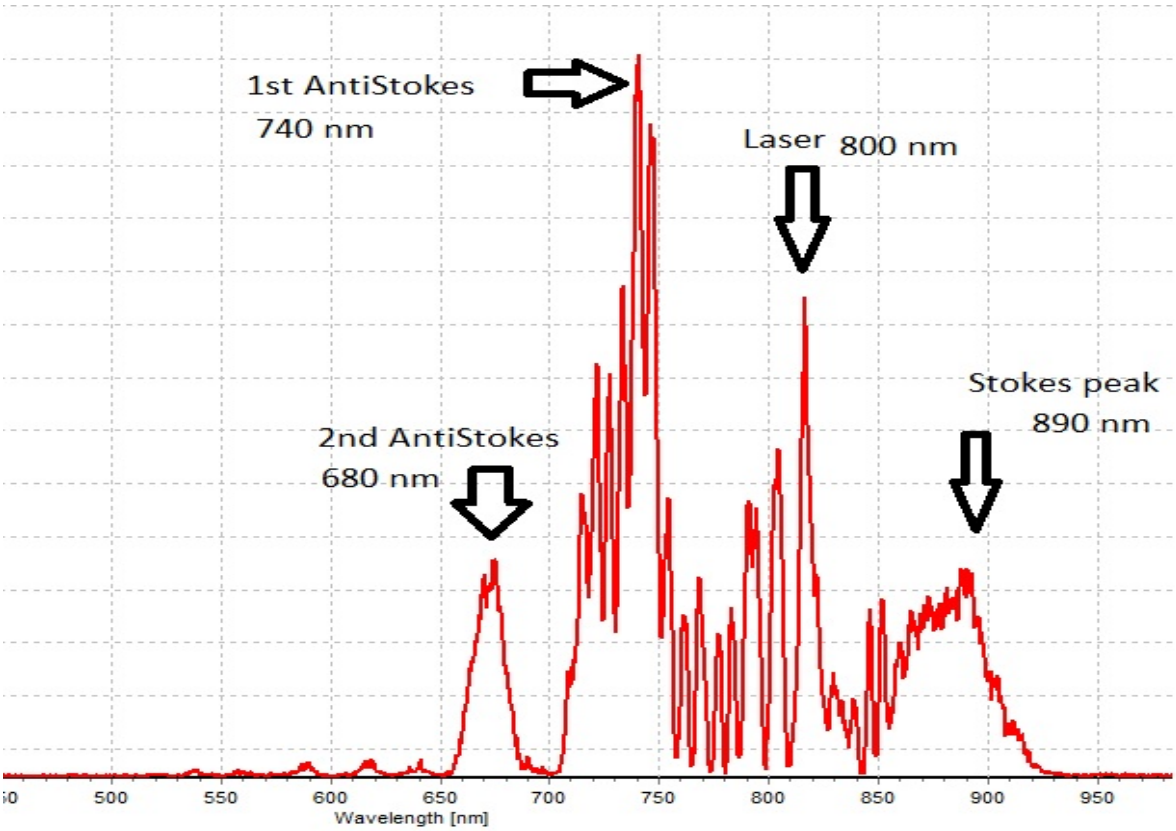

Figure 3.7.2: *Spectrum of scattered light (datafile #69, 01/10/2020).*

In the experiment $a_0 \approx 2.0$ and $\gamma \approx 1.9$. The inferred plasma density from the Stokes and anti-Stokes peaks is

$$n_e^{Stokes} = 2.8 \times 10^{19}\ \text{cm}^{-3} \text{ from Eq. (3.7.1)} \quad (3.7.3)$$

and

$$n_e^{AStokes} = 2.1 \times 10^{19}\ \text{cm}^{-3} \text{ from Eq. (3.7.2)}. \quad (3.7.4)$$

The density presented here is inferred for a particular shot during the commissioning campaign. The experiments were carried out for a wider range of plasma densities $1 \times 10^{18}\,\text{cm}^{-3}$ to $1 \times 10^{19}\,\text{cm}^{-3}$ obtained by varying the backing pressure in the valve up to 10 bar and by focusing the laser at different distances from the nozzle, inside the gas plume.

3.7.4 Conclusion

This is an essential diagnostic result, in line with data reported elsewhere obtained in similar conditions. Furthermore it is well knwon that the acceleration of electrons in the LWFA regime depends on several

parameters, one of them being the plasma density. taining of higher electron energies. Therefore, lower plasma densities can allow the ob-

References

[ESL09] E. Esarey, C. B. Schroeder, and W. P. Leemans. "Physics of laser-driven plasma-based electron accelerators". In: *Review of Modern Physics* 81.37 (2009), page 1229. DOI: 10.1103/RevModPhys.81.1229 (cited on page 113).

[Hur+08] M. S. Hur *et al.* "A method to measure the electron temperature and density of a laser-produced plasma by Raman scattering". In: *Applied Physics Letters* 93.7 (2008), page 07156. DOI: 10.1063/1.2973395 (cited on page 113).

[Kru03] W. L. Kruer. *The Physics of Laser Plasma Interactions*. Boulder: Westview Press, 2003 (cited on page 113).

[Mat+10] T. Matsuoka *et al.* "Stimulated Raman side scattering in laser wakefield acceleration". In: *Physical Review Letters* 105.3 (2010), page 034801. DOI: 10.1103/PhysRevLett.105.034801 (cited on page 113).

Theory at LDED

3.8 Sub femtosecond high-brigthness electron bunches with the Resonant Multi Pulse Ionisation injection

Tomassini P.[1] , Gizzi L. A.[2] , and Doria D.[1]

[1] Extreme Light Infrastructure (ELI-NP) & Horia Hulubei National Institute for R & D in Physics and Nuclear Engineering (IFIN-HH), Str. Reactorului No. 30, 077125 Bucharest–Măgurele, Romania
[2] CNR-INO, via G. Moruzzi 1, 56100 Pisa, Italy

* **paolo.tomassini@eli-np.ro**

Abstract

High-brightness electron beams with sub-femtosecond *rms* duration can be employed either as direct probes or as sources of attosecond hard X-ray photons. Particle In Cell simulations and theory show that the Resonant Multi Pulse Ionisation injection (ReMPI) can be a valid candidate to generate high-quality bunches with tunable length in the range $\approx$ 200 as-2000 as, with normalized emittance not exceeding 100 nm rad and peak current above 1 kA.

3.8.1 Introduction

Laser Wake Field Acceleration of high-quality electron bunches is still an open issue in high-gradient acceleration studies. However, recent encouraging experimental results showed the production of electron bunches having quality (low energy spread, low normalized emittance, high current) large enough to drive a Free Electron Laser [Wan+21]. Among the schemes proposed so far that allow the production of ultra-low emittance ($\varepsilon_n < 100 nmrad$) electron bunches, the Resonant Multi Pulse Ionisation injection (ReMPI) [Tom+19; Tom+17] is the most promising to be experimentally demonstrated with the 100TW and 1PW Ti:Sa laser systems at ELI-NP.

In the ReMPI scheme, a train of pulses excites a large amplitude wakefield through the Multi-Pulse LWFA mechanism, keeping each pulsed electric field under the ionization threshold for the selected dopant, whose electrons (typically on the K-shell) will constitute a source of new free particles. Subsequently, a tightly focused, low amplitude pulse in second/third/fourth harmonics in the tail of the train ionizes the dopant (*e.g.* nitrogen, argon, or krypton), thus injecting the electrons into the wakefield with an ultra-low transverse momentum. As a result, the ionizing pulse extracts the electrons close to the axis. They quiver with a very low transverse momentum and are trapped in the focusing region of the same bucket, thus constituting an ultra-low emittance bunch.

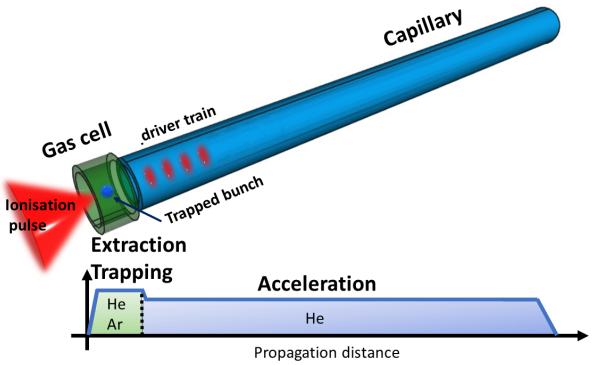

Figure 3.8.1: *Sketch of target sections and pulses in ReMPI. In this example, four pulses of the driver train are propagating inside the He-filled capillary. Behind them and still, in the Ar+He-filled gas cell, the ionizing pulse is extracting electrons from the Ar K-shell. Those electrons will be subsequently trapped in the gas cell and further accelerated in the capillary.*

To produce such a configuration, a single Ti:Sa pulse can be time shaped to constitute the driver train of pulses (*e.g. via* a multiplexing technique [Sid+98]). In contrast, a small portion of the same pulse can be frequency up-converted and delivered with a tight focus for the ionization process. The intensity of the pulses in the driving train must be chosen so that the plasma wave amplitude is large enough to trap the newborn electrons and low enough to be below the threshold for the ionization of the dopant. Theory and simulation already showed that the ReMPI scheme is capable of generating 5 GeV electron bunches with FEL compliant quality [Tom+19]. Moreover, as the delay between the driving train and the ionizing pulse can be tuned in an interval close to one-fourth of the

plasma period, the additional degree of freedom can be employed to disentangle the beam length from the other main parameters (*i.e.* charge, energy, energy spread). We will show, employing Particle In Cell (PIC) simulations, that by setting the amplitude of the plasma wave to reach the nonlinear regime and by tuning the ionization pulse delay with respect to the driver so as the newborn electrons are extracted in regions close to the node of the accelerating field, very short (sub-femtosecond) and high-quality electron bunches can be obtained. The generated low-emittance, ultrashort, and quasi-monochromatic electron bunches with energy ranging from tens of MeV to some GeV can have applications either as direct probes or as drivers of Thomson backscattered X radiation, which will roughly have the same sub-femtosecond duration of the beam.

3.8.2 The ReMPI scheme

In our simulated setup (see Figure 3.8.1), a 0.5 PW Ti:Sa, 25 fs FWHM long laser pulse is employed. The configuration reported here is compliant with the 1 PW laser system installed at ELI-NP. A small fraction of the pulse, converted in second harmonics, is tightly focused on extracting electrons from the K-shell of a high-Z dopant (argon), thus constituting a linearly polarised "ionizing pulse". Those newborn electrons are subsequently trapped and accelerated by the plasma wave created by a train of circularly polarised four sub-pulses (the "driver train") of amplitude $a_0 = 0.65$, obtained by a time shaping of the main portion of the 0.5 PW pulse. As the driving train enters the density plateau of the injector section (the 2 mm long gas cell filled with a mixture of He and Ar (50% + 50%)), a nonlinear wakefield is resonantly excited by the reinforced action of the longitudinal ponderomotive forces of the train sub-pulses. At the end of the train, where the ionizing pulse extracts electrons, a longitudinal electric field with the peak value of $E_{z,max} \simeq 0.7E_0$ is found. Here $E_0 \equiv mc^2 k_p/e \simeq 98\sqrt{n_e[cm^{-3}]}$ is the nonrelativistic wave-breaking limit and $k_p = 2\pi/\lambda_p$ is the Langmuir's wave number. Since the longitudinal electric field is close to the "strong trapping conditions" [Tom+17], newborn electrons from the ionized dopants are suddenly trapped in the peak of the accelerating gradient and are subsequently accelerated. In ReMPI, extracted electrons have a very small transverse momentum and size after the ionizing pulse passage, due to the pulse low amplitude ($a_{0,ion} = 0.42$) and size ($w_{0,ion} = 3.5\,\mu$m). The trapped beam having a charge of 10 pC, therefore, possesses a very high transverse quality, being the normalized emittances in the ionizing pulse and in the driver train polarization planes of $\varepsilon_{n,x} = 0.90$ nm mrad and $\varepsilon_{n,y} = 50$ nm rad, respectively. That result is compatible with a recent analytical theory about the beam emittance in multi-pulse ionization injection schemes (see Equations 48 and 49 in [Tom+21]), which predicts a normalized emittance of about 85 nm rad in the pulse polarization axis.

As the ionizing pulse is diffracted away at the capillary entrance (its Rayleigh length is $Z_{R,ion} = \pi w_{0,ion}^2/\lambda_{ion} \simeq 100\,\mu$m), the driving train and the obtained trapped bunch enter into the boosting section, whose inner diameter is matched so as to guide a pulse with waist of $w_{matched} = 45\,\mu$m. Inside the energy-boosting section, each sub-pulse (but the first one) propagates into a plasma wave excited by the previous pulses of the train; therefore, the time evolution of each pulse is unique in the train and different from a standard evolution of a non-relativistic pulse inside a 1.5 cm long capillary. At the end of the capillary density down ramp, a 0.63 GeV high-brightness electron beam with a peak current of 2.2 kA and slice energy spread at the peak current of 5×10^{-3} has been obtained (see Figure 3.8.2). We stress that the final e-beam energy can be easily tuned in the interval 100'MeV - some GeV, depending on the envisaged usage of the beam. Final energies exceeding ≈ 500 MeV require a pulse guiding technique as in the present setup of Figure 3.8.1, but lower energy beams can be obtained with simpler energy booster targets as a gas cell or a long gas-jet with flat density profile at the plateau.

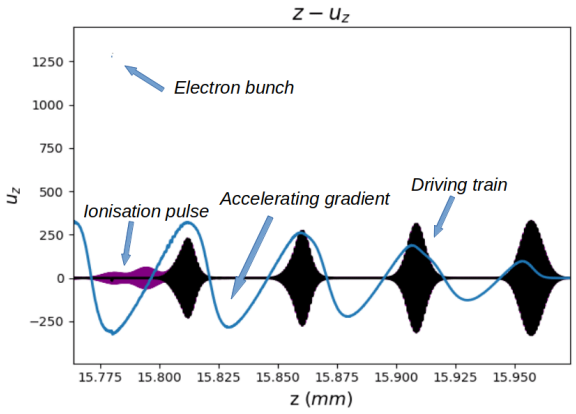

Figure 3.8.2: *Snapshot of the simulation at the end of the plasma plateau. Longitudinal phase-space $(z, u_z = p_z/mc)$ of the accelerated beam, on-axis accelerating gradient (blue line), driving train (black line) and ionising pulse (purple line).*

Simulations have been performed with the PIC code FB-PIC [Leh+16] in a quasi-3D geometry, by

using the $(0,1)$ rotational modes, 24 ppc and resolution $\lambda/24$, $\lambda/8$ in the longitudinal and radial directions, respectively.

3.8.3 Beam length fine-tuning

The longitudinal size of the accelerated beam can be controlled by a fine-tuning of the delay between the ionizing pulse and the driving train. As the newborn electrons are mostly emitted in the vicinity of the ionizing pulse peak, their initial (longitudinal) spatial distribution is centered with the pulse itself. Those electrons lie in a potential field which decreases as they slip back up the trapping point. Therefore, the spatial distributions at the trapping and at the emission points are linked by the rate of change of the potential in the two ending points. A full theory of the transformation function between the two distributions will be published elsewhere [Tom]. Here, we will show the PIC simulation results obtained by scanning the bunch length as a function of the delay between the ionizing pulse and the driving train. We can refer to as "zero delay," the one in which the peak of the ionizing pulse is placed exactly on the node of the accelerating gradient. Therefore, the newborn electrons' center of mass lies in the region of space with the highest electric potential ϕ_e, where the subscript "e" stands for the extraction point. As the longitudinal size l_e of the electron cloud emitted in a time interval lasting a fraction of pulse cycle is of micrometers size (a small fraction of the ionising pulse length), each newborn electrons emitted in a phase $\xi_e = k_p(z-\beta_g ct)$ will initially lie in a potential $\phi_e = 1/2\partial^2\phi/d\xi^2 \times \xi_e^2$, with a very small *rms* variation of $\sigma(\phi_e) = 1/2\partial^2\phi/d\xi^2 \times l_e^2$. Here, $\beta_g c$ is the pulse group velocity. As the electrons slip back towards the trapping point with phase ξ_t, they reach a potential ϕ_t which strongly depends on the trapping position ξ_t. The most favorable configuration is that in which the electric field at the trapping point is at its maximum $E_{\max}$ (see the strong trapping condition in [Tom+17]). At the trapping point, the *rms* beam potential can be evaluated as $\sigma(\phi_t) = |E_{\max}| \times l_t$, where l_t is the beam length at the trapping point. The link between the potential at the trapping and the emission points is easily obtained by using the conservation of the particle Hamiltonian in the case of a quasistatic limit. In turn, the leading term determining the bunch length at the trapping point is

$$l_t \approx \frac{1}{2} l_e^2 \frac{(\partial^2\phi/d\xi^2)|_e}{|E_{\max}|} \ll l_e. \tag{3.8.1}$$

As the phase of the ionizing pulse in the wakefield is acquiring an offset value from the zero point, an additional term in the numerator of Eq. 3.8.1 will increase the final bunch length. This model was explored and confirmed using a series of PIC simulations with different delays of the ionizing pulse.

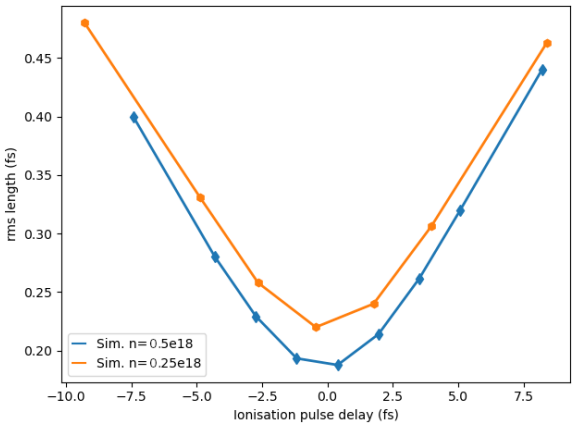

Figure 3.8.3: *Scan of the rms bunch length (duration in attoseconds as a function of the delay of the ionizing pulse with respect to the accelerating field node. The blue line refers to the simulation shown in the current report, while the orange line refers to a similar simulation with low background plasma density.*

In Figure 3.8.3 results from the PIC simulation series with the scan on the ionization pulse delay are reported. There, the *rms* duration of the bunch in femtoseconds is plotted against the delay of the ionization pulse. Two lines are shown, the blue one concerning the set of simulations as the one shown in the report (but the ionization pulse delay) and the orange one concerning similar simulations but with a lower plasma density. As it is apparent, the sequence of simulations shows that the final bunch length depends (almost quadratically) on the ionization pulse delay concerning the node of the accelerating gradient. With the physical parameters reported above, our simulations show that electron bunches as short as ≈ 200 as can be generated at ELI-NP. However, the time delay jitter between the driving train and the ionizing pulse can be detrimental to the generation of (stable) sub-femtosecond pulses. With a fine tuning of the ionizing pulse so as it is (on an average of several shots) synchronized with the node of the accelerating gradient (zero delay in Figure 3.8.3), we can infer that a jitter of ± 4 fs (maximum) will lead to an increase of the beam length from ≈ 200 as to ≈ 250 as. A jitter of ± 10 fs (maximum) is, however, associated with more than 100% increase in the beam length. Therefore, it is recommended that the ionization pulse is obtained via a pickup of the main pulse before its time shaping as a train of pulses. This

would help maintain the jitter between the two in a micrometer size path mismatch induced by mechanical vibrations.

3.8.4 Conclusion

Here we reported a novel method to generate sub-femtosecond, high-quality electron bunches through the Resonant Multi Pulse Ionisation injection and a fine-tuning of both the induced wakefield amplitude and ionization pulse delay with respect to the driving train. Theory and simulations showed that the 1PW laser system at ELI-NP can be employed to investigate such a scheme experimentally. The final energy of the electron bunches can be largely tuned in the interval 100's of MeV - some GeV, depending on the envisaged application of the e-beam, whose length can be as short as 200 as. One possible usage of the electron beam is as a driver for a Thomson backscattering process, constituting a sub-femtosecond, tunable, X, and hard-X tunable rays source. The experimental demonstration at ELI-NP of the proposed method involves the time shaping of the main pulse as a train of four/eight pulses. This can be obtained through multiplexing techniques, but the complexity of the needed setup requires a dedicated study. Finally, the time jitter between the ionizing pulse and the driving train must be carefully monitored and maintained down a few femtoseconds scale.

References

[Leh+16] R. Lehe *et al.* "A spectral, quasi-cylindrical and dispersion-free Particle-In-Cell algorithm". In: *Computer Physics Communications* 203 (2016), pages 66–82. ISSN: 0010-4655. DOI: https://doi.org/10.1016/j.cpc.2016.02.007. URL: https://www.sciencedirect.com/science/article/pii/S0010465516300224 (cited on page 120).

[Sid+98] C. W. Siders *et al.* "Efficient High-Energy Pulse-Train Generation Using a 2 n-Pulse Michelson Interferometer." In: *Applied optics* 37 22 (1998), pages 5302–5 (cited on page 119).

[Tom+19] P. Tomassini *et al.* "High-quality 5 GeV electron bunches with resonant multi-pulse ionization injection". In: *Plasma Physics and Controlled Fusion* 62.1 (2019), page 014010 (cited on page 119).

[Tom] P. Tomassini. "Sub-femtosecond high-brighness electron beams with multi pulse ionisation injection schemes". In: *In Preparation* () (cited on page 121).

[Tom+17] P. Tomassini *et al.* "The resonant multi-pulse ionization injection". In: *Physics of Plasmas* 24.10 (2017), page 103120. DOI: 10.1063/1.5000696. eprint: https://doi.org/10.1063/1.5000696. URL: https://doi.org/10.1063/1.5000696 (cited on pages 119–121).

[Tom+21] P. Tomassini *et al.* "Accurate electron beam phase-space theory for ionisation injection schemes driven by laser pulses". In: *High Power Laser Science and Engineering* (2021), pages 1–17. DOI: 10.1017/hpl.2021.56 (cited on page 120).

[Wan+21] M. Wang *et al.* "The Ame2020 atomic mass evaluation". In: *Chin. Phys. C* 45 (2021), page 030003 (cited on page 119).

3.9 RelNTS: a Relativistic Nonlinear Thomson Scattering simulation tool

Tomassini P.[1]

[1] Extreme Light Infrastructure (ELI-NP) & Horia Hulubei National Institute for R & D in Physics and Nuclear Engineering (IFIN-HH), Str. Reactorului No. 30, 077125 Bucharest–Măgurele, Romania

[*] **paolo.tomassini@eli-np.ro**

Abstract

The accurate simulation of the nonlinear Thomson scattering process by ultrarelativistic electron beams and relativistically intense laser pulses is of great importance for preparing experiments at ELI-NP. Bright and quasi-monochromatic hard X-ray sources, with a tunable energy range of 100's keV-10's MeV can *e.g.* be employed in the study of nuclear physics processes. In contrast, high-flux 10's keV X-ray sources can be used in high-quality contrast phase imaging. Furthermore, structured laser pulses as Laguerre-Gaussian modes containing Orbital Angular Momentum can open new physical scenarios on nuclear matter probing. The RelNTS code has been developed at ELI-NP to simulate in an accurate way the Thomson scattered radiation emitted by relativistic electron beams with arbitrary phase-space shape and laser pulses with arbitrary Laguerre-Gaussian modes $\mathscr{L}_p^l$, which include the standard Gaussian mode as $p = l = 0$. We describe the physical aspects governing the Nonlinear Thomson scattering process and how the code deals with them. Finally, we show results about an all-optical source generating sub-femtosecond long tunable hard-X bursts.

3.9.1 Introduction

Thomson Scattering (TS) is the electromagnetic process in which charged particles (usually electrons as they are the lightest charged particles) absorb one (linear TS) or more (nonlinear TS) photons typically from a laser pulse, emitting one scattered photon without a sizable recoil (*i.e.*, the so-called Thomson limit of the Compton process). If the electrons are ultrarelativistic, the scattered radiation looks frequency-upshifted and is mostly emitted forward with respect to the average velocity of the particles in a a small cone of aperture roughly given by the inverse of their Lorentz gamma factor (see [CEL01] for the first application of TS on LWFA generated electrons). The physics of TS is quite complex in the nonlinear regime, *i.e.*, when the laser pulse strength $a_0 = 8.5 \times 10^{-10}\sqrt{I\lambda^2}$ approaches or exceeds unity. Here, I is the pulse intensity in Wcm$^-$2 and λ is its wavelength in μm. At intensities above the so-called relativistic intensity $I\lambda^2 = 1 \times 10^{18}$ μm$^2\times$Wcm$^{-2}10^{18}$, the extremely intense electric field makes the electrons quivering speed approaching the speed of light, making the magnetic field relevant for the dynamics and thus generating a complex particle motion. For each particle in the beam, the computation in the far-field of the scattered photons distribution can be performed in the classical regime provided that the energy of the electrons is far below tens of GeV, as is the case considered here. A classical result derived by the evaluation of the retarded potentials in the far-field [Jac99], shows that the angular and spectral distribution of the emitted photons can be evaluated through the relation in Equation 3.9.1,

$$\frac{dN}{d\Omega d\omega} = \frac{\alpha\omega}{4\pi^2}\left|\int dt\, \vec{n}\times(\vec{n}\times\vec{\beta})e^{i\omega(t-\vec{n}\cdot\vec{r}/c)}\right|^2 \tag{3.9.1}$$

where α is the fine structure constant, N is the number of emitted photons, Ω, ω, and $\vec{n}$ are the solid angle, the pulsation, and the emission direction of the photon, respectively. The time integral over the whole interaction interval involves the particle speed $c\vec{\beta}(t)$ and position $\vec{r}(t)$. To sum up the contributions of the particles in the bunch, an incoherent summation should be done unless small-scale structures (as small as the emitted radiation wavelength) are present. The evaluation of the particles' trajectories can be performed analytically in the case of plane-wave EM radiation. There, solutions of the equation of motion can further be combined with Equation 3.9.1 so as to give an exact expression of $dN/(d\Omega d\omega)$ for a whole electron bunch counter-interacting with a flat-top pulse [Tom+05]. Semi-analytical codes such as the Thomson Scattering Simulation Tool (TSST), developed by the author starting from 2005, can combine the usage of the analytical results in [Tom+05] with a longitudinal slicing of the pulse to face with long, temporally varying pulses in a limited simulation time.

3.9.2 The RelNTS code

As either ponderomotive forces or structured laser pulses should be faced, the lacking of analytical solutions of the equation of motion forces the usage of numerical schemes to simulate particles quivering and their subsequent X/hard-X-rays emission. The Relativistic Nonlinear Thomson Scattering (RelNTS) code was developed by the author starting in 2021, and its current version 2.2 was released in February 2022 [Tom22]. The code is fully numerical and parallelized for higher computing performance. It can deal with linearly or circularly polarised Laguerre-Gaussian $\mathscr{L}_p^l$ modes, which include the standard TEM00 (Gaussian) mode when $p = l = 0$. The laser pulse is described in terms of the potentials in the radiation gauge $\vec{\nabla}\cdot\vec{a} = 0$, $\phi = 0$ (here $\vec{a} = e\vec{A}/(mc^2)$). Within the paraxial approximation, the vector potential of Laguerre-Gaussian modes with linear polarisation along x and propagating along z can be described in the cylindrical coordinates (r,ϕ,z) as

$$a_x = a_0 \frac{w_0}{w(z)} \mathscr{L}_p^l(u) f(z,t) \exp(i\Psi) \quad (3.9.2)$$

$$a_z = \frac{i}{k_0} \partial_x \phi(x,y) \times a_x \quad (3.9.3)$$

where the well known relations for the Gaussian optics $z_r = \pi w_0^2/\lambda$, $w(z) = w_0\sqrt{1+z^2/z_r^2}$ have been used and

$$\Psi = k_0 \left(z - ct + \frac{1}{2}\frac{r^2 z}{z^2+z_r^2} \right) + \quad (3.9.4)$$

$$+ l\phi(x,y) - (2p+|l|+1)\tan^{-1}(z/z_r) \quad (3.9.5)$$

is the local phase, which differs from the usual TEM00 one by the $l\phi(x,y)$ contribution and by a prefactor $(2p+|l|+1)$ in front of the Guoy's term. The local field phase, therefore, also depends on the transverse position through the azimuthal phase $\phi(x,y)$, thus achieving a corkscrew shape for $l \neq 0$. In Equation 3.9.2 the longitudinal shape $f(z,t)$ can be a standard Gaussian function of $(z-ct)$ or any temporal shape for the fields defined by the user. Finally, the transverse shape of the Laguerre-Gaussian modes can be written in its variable $u = 2r^2/w(z)^2$ as

$$\mathscr{L}_p^l(u) = \sqrt{\frac{p!}{(|l|+p)!}} e^{-u/2} u^{l/2} \times \quad (3.9.6)$$

$$\times \sum_{m=0}^{p} \frac{(-1)^m (|l|+p)!}{(p-m)!(|l|+m)!m!} u^m \quad (3.9.7)$$

whose normalisation has been selected so as to have $\mathscr{L}_0^0(u=0) = 1$ (*i.e.* the mode $p = l = 0$ is described as the usual Gaussian one.

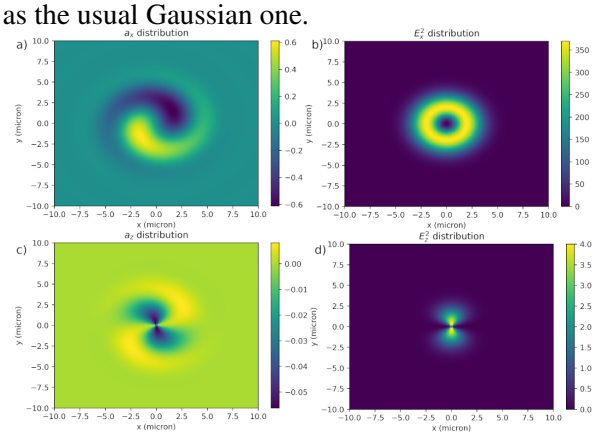

Figure 3.9.1: *Fields and intensity distributions for the linearly polarised $p = 0, l = 1$ mode. The Ti:Sa pulse was focused with $w_0 = 3.0\,\mu$m a) Transverse field a_x, showing the corkscrew structure. b) The transverse distribution of E_x^2 [a.u.]. c) Longitudinal field a_z. d) Transverse distribution of E_z^2 [a.u.], showing that the mode $p = 0, l = 1$ possesses a peak of a_z on the axis of the pulse (the line $x = y = 0$ is singular as the azimuthal phase is not defined there.*

The electron beam is described as the phase space $(\vec{x},\vec{u},w)$, with $\vec{u} = \vec{p}/(mc)$ and w as the weight of the macroparticle. This opens the possibility to directly link the output of PIC simulations (usually from LWFA) to RelNTS. As a first stage, the code numerically solves the equation of motion of a classical charged particle in an EM field. The time derivative of the canonical momentum $\vec{\pi} = \vec{u} - \vec{a}$ is evaluated as [Mel20]

$$\frac{1}{c}\frac{d}{dt}\vec{\pi} = -\frac{1}{\gamma} u_i \vec{\nabla} a_i \,. \quad (3.9.8)$$

The advantage of the usage of Equation 3.9.8 instead of the usual Lorentz force expression is twofold. Firstly, the expression quickly unveils the main quivering contribution of the limiting plane wave configuration ($d_t\vec{\pi} = 0$) from the ponderomotive part. Secondly, its (centered) second-order numerical solution is fast and doesn't involve the prior evaluation of the electric and magnetic fields. Once the tracked trajectories have been evaluated, each particle's contribution to the spectral and angular distribution is numerically evaluated through Eq. 3.9.1. The 4-tensor $\mathscr{F}(\omega,\theta,\phi,m) = \int dt\, \vec{n}\times(\vec{n}\times\vec{\beta}) e^{i\omega(t-\vec{n}\cdot\vec{r}/c)}$ is firstly evaluated for each particle m and for any sampled pulsation ω, with $\vec{n}$ pointing the direction depicted by the spherical angles (θ,ϕ) having reference axis collinear with the average e-beam momentum. At this stage, the evaluation of $\mathscr{F}$ is fully parallelized. The final distribution of the emitted photons is obtained by incoherently summing up the individual

contributions as

$$\frac{dN}{d\Omega d\omega}|_{bunch} = \frac{\alpha\omega}{4\pi^2}\sum_{m=0}^{N-1} w(m)\,|\mathscr{F}(\omega,\theta,\phi,m)|^2\,, \tag{3.9.9}$$

where N is the number of sampled macro particles of the bunch. As an example of RelNTS output relevant for ELI-NP, we consider the head-on collision between a Ti:Sa pulse and a high-quality electron bunch that can be generated by employing one arm of the 1PW laser system. The bunch is obtained using the Resonant Multi Pulse Ionisation injection (ReMPI) scheme, which is able to generate ultra-low emittance beams with Ti:Sa based laser systems [Tom+19; Tom+17]. The PIC simulation that generated the bunch had been described in another paper in the present Report 3.8. The electron beam quality was excellent for a laser-plasma generated bunch, being the transverse emittance below 100 nm rad, the projected energy spread $sigma(E_e)/E_e$ of 1.5% and the slice energy spread of 0.5% at the peak current above 1 kA. The main drawback of the usage of the beam for Thomson scattering sources is due to the low charge ($\simeq$ 10 pC), which limits the source fluence. However, as the beam is also ultrashort and its duration can be tuned down to $\approx$ 200 as, the final duration of the hard-X-ray burst will be similar, thus constituting an attosecond quasi-monochromatic, tunable source. In the current example, we considered a standard TEM00 mode for the counter-propagating pulse delivering 0.1 J in 250 fs. The interaction point was on the pulse focal position, with a minimum waist $w_0 = 15\,\mu$m where the peak pulse amplitude was $a_0 = 0.23$. The tiny nonlinear effects did not generate a sizable broadening of the photon spectrum, and higher harmonics had negligible amplitude. The optimization of the hard-X ray source is out of the scope of the present report. We just sketch here how the number of collected photons N_x and their energy spread $\sigma(E_X)$ depend on the selected acceptance angle θ_c to set its optimal value depending on the needed (quasi) monochromaticity. In Figure 3.9.2 a scan of the *rms* energy spread (orange line) and of the number of collected photons (blue line) as a function of the acceptance angle is shown.

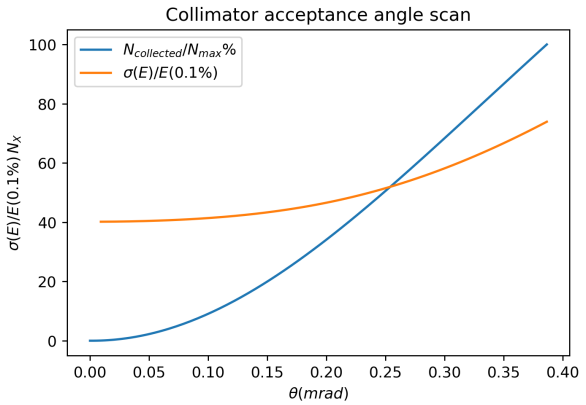

Figure 3.9.2: *Backscattering of an $p = l = 0$ mode pulse onto an high quality electron beam with average energy of* 0.65 GeV. *The blue line shows the fraction of collected photons as the angle of the collimator is reduced from its highest value down to zero. The orange line represents the rms energy spread of the photon source as a function of the collimation angle.*

The minimum energy spread obtainable by the relativistic Thomson backscattering process depends on the e-beam quality through the relation [Tom+05]

$$\frac{\sigma(E_X)}{E} \simeq 2\frac{\sigma(E_e)}{E_e} + \sigma(u_\perp)^2 \simeq 4\%\,, \tag{3.9.10}$$

where $\sigma(u_\perp)$ is the *rms* transverse normalised momentum of the beam. An additional contribution to the hard-X beam energy spread arises from nonlinear effects and a reduction to the Lorentz boost due to large off-axis photons emission, which can be approximated as $(\gamma\theta_c)^2$ for $\gamma\theta_c \ll 1$ (for an accurate prediction of the energy also spread when $\gamma\theta_c \geq 1$ see [Tom+05]). This is fully consistent with the result shown in Figure 3.9.2, where a minimum energy spread of about 4% is obtained with very small acceptance angles. Therefore, as the number of collected photons scales quadratically with θ_c when $\gamma\theta_c \ll 1$, an optimal collimator angle in which the energy spread is close to the minimum achievable one and a relatively large number of photons are collected can be found. In our case, assuming an acceptable energy spread of 5%, an acceptance of 250 mrad is found, which leads to a total number of $N_x = 1.5 \times 1 \times 10^6$ shot^{-1} (1.5×10^7 phs^{-1} at 10 Hz repetition rate). In Figure 3.9.3 the spectrum of the collected photons in a cone of an aperture of 250 µrad is also shown.

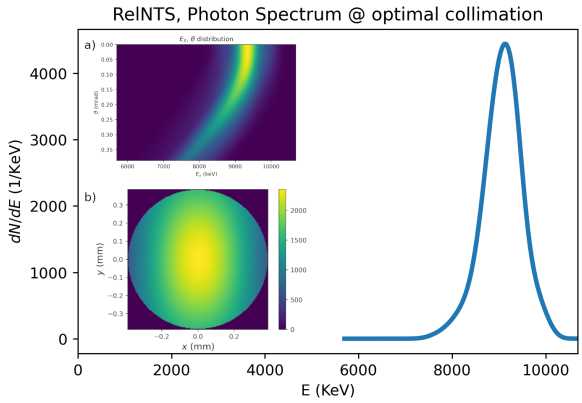

Figure 3.9.3: *Energy spectrum from the head-on collision between a Ti:Sa pulse and an high-quality electron bunch obtained with the ReMPI scheme. Inset a) Energy-deviation angle distribution (integrated along the azimuthal angle). b) Photon yield on a screen.*

There, a quasi-monochromatic energy distribution with a peak energy of 9.3 MeV and energy spread of 5% *rms* is obtained. The energy-angular distributions (with the average on the azimuthal angle) are shown in inset a), while the spatial distribution on a screen placed 1m apart is reported in inset b).

3.9.3 Conclusion

In this report, we have depicted the physical mechanisms behind the Thomson backscattering from a Laguerre-Gaussian pulse (that includes the standard Gaussian mode in the case $p = l = 0$) and a relativistic electron beam. The RelNTS code, developed by the author starting from Sept. 2021, tracks the trajectories of each macro-particle in the electron beam by using a second-order scheme in which the laser pulse is described in terms of the vector potential in the radiation gauge. As the Thomson process is the classical limit of the Compton one, the electromagnetic field of the scattered radiation is evaluated in the far-field by using the Lienard-Wiechert potentials. An example of RelNTS output reported here considered the case of a high-quality electron beam hitting onto a TEM00 pulse, thus generating a quasi-monochromatic hard-X photon beam of energy spread of %, average energy of about 9 MeV and duration of approximately 200 as. The usage of Laguerre-Gaussian modes with $l \neq 0$ would generate a tunable source of beams containing Orbital Angular Momentum.

References

[CEL01] P. Catravas, E. Esarey, and W. Leemans. "Femtosecond x-rays from Thomson scattering using laser wakefield accelerators". In: *Measurement Science and Technology* 12.11 (2001), page 1828 (cited on page 123).

[Jac99] J. D. Jackson. "Classical Electrodynamics". In: *John Wiley and Sons* 3rd Edition (1999) (cited on page 123).

[Mel20] F. Melia. *Electrodynamics*. University of Chicago Press, ISBN 0-226-51958-9, 2020 (cited on page 124).

[Tom22] P. Tomassini. "RelNTS python code". In: *Available upon request on GitHub, https://github.com/TomPaolo/RelNTS/blob/main/RelNTS2.2.py* (2022) (cited on page 124).

[Tom+05] P. Tomassini *et al.* "Thomson backscattering X-rays from ultra-relativistic electron bunches and temporally shaped laser pulses". In: *Applied Physics B* 80.4 (2005), pages 419–436 (cited on pages 123, 125).

[Tom+19] P. Tomassini *et al.* "High-quality 5 GeV electron bunches with resonant multi-pulse ionization injection". In: *Plasma Physics and Controlled Fusion* 62.1 (2019), page 014010 (cited on page 125).

[Tom+17] P. Tomassini *et al.* "The resonant multi-pulse ionization injection". In: *Physics of Plasmas* 24.10 (2017), page 103120. DOI: 10.1063/1.5000696. eprint: https://doi.org/10.1063/1.5000696. URL: https://doi.org/10.1063/1.5000696 (cited on page 125).

3.10 Future studies of cosmogenic ^{26}Al at high-power laser systems

Spohr K. M.[1'*] , Doria D.[1] , and Meyer B. S.[2]

[1] Extreme Light Infrastructure (ELI-NP) & Horia Hulubei National Institute for R & D in Physics and Nuclear Engineering (IFIN-HH), Str. Reactorului No. 30, 077125 Bucharest– Măgurele, Romania
[2] Department of Physics and Astronomy, Clemson University, Clemson, SC 29634-0978, USA

[*] **klaus.spohr@eli-np.ro**

Abstract

The development of the 10 PW laser system at the ELI-NP may lead to an earthbound astrophysical laboratory. High-power laser pulses trigger 10's of MeV ions and radiation, which can create plasma and induce nuclear reactions therein. Due to the high fluxes of reaction-driving beam pulses, high yields of radioactive target nuclei in their ground and excited states can be provided *in situ* in short time scales. Cosmogenic ^{26}Al is a prime candidate for evaluating these new experimental possibilities. For a short duration of $\Delta t \sim 200$ ps, laser-driven protons with energies above $E_p \sim 5$ MeV can induce the compound nucleus reaction ^{26}Mg(p, n)^{26}Al leading to high and comparable yields of the three lowest-lying states in ^{26}Al *including* the short-lived, $t_{1/2} = 1.20$ ns state at 417 keV. This unique possibility offered by laser-driven acceleration invites future studies within the framework of Day-2 experiments at ELI-NP. Moreover, the experimental proposal was included inclusion into the Big Science Question compilation of the MP3 initiative at Rochester in 2022, which foresees the installation of a 30 PW system in the USA [Zue21].

3.10.1 Introduction

The work presented herein will give an answer to the long-standing questions: *"What is a unique feature of all-optical PW accelerators which cannot be achieved with traditional RF-based accelerator technology and how can the CPA technology invented by Strickland and Mourou be best applied to enrich fundamental nuclear physics research?"*.
Laboratory measurements of nuclear reaction rates are made on target nuclei in their ground states. However, in stellar plasma conditions which govern the evolution of abundances in the Universe, the reacting nuclei are distributed among their excited states. Without providing these conditions, a proper experimental accounting of stellar models remains elusive. Nonetheless, direct experiments on the interplay of ground and excited states relevant for nuclear astrophysics have so far escaped scientific investigation since such studies are extremely difficult to realize in Earthbound laboratories driven by existing RF-based accelerator systems. This is mainly due to the short-lived, femtosecond nature of the relevant excited nuclear states in conjunction with the overall rather low instantaneous beam intensities deliverable by RF-based accelerator systems during those short timescales, which result in low spontaneous yields for the promptly decaying excited states. As of today, reaction rate evaluations on excited states have not been measured, and theory relies, therefore, on Hauser-Feshbach calculations [HF52] in which an assumption of a thermal population of excited states is undertaken. This approach is undoubtedly incorrect for a handful of isotopes with longer-lived isomers and for which internal thermalization does not occur. For such nuclei, the equilibration of the longer-lived isomer and the ground state (g.s.) occurs only indirectly via upper-lying levels at high temperatures in the MK to GK regime. The cosmogenic ^{26}Al, the subject of this investigation, is perhaps the most prominent case in nuclear astrophysics for this kind of nuclei due to its importance as an astrophysical clock and our understanding of the astrophysical abundances in our Galaxy [Ili+11] where its presence was discovered by Mahoney *et al.* [Mah+84]. Theoretically, the isotope derives from explosive helium, carbon, oxygen, and silicon burning cycles, as well as novae or supernovae explosions, Wolf-Rayet Stars, red giants, and supermassive stars [Arn69; Die+06]. Moreover, the correlated excesses of its daughter product ^{26}Mg in comparison with stable ^{27}Al provide important constraints on the formation time of primitive meteorites and components therein [Kit+13; LPW76; VCL09].

3.10.2 Spontaneous yields

Core to the depicted concept is the high spontaneous flux of ion-driven reactions as provided by a single short pulse from a HPLS which leads to high temporal yields $Y_i^d(t)$ of excited states by direct population (d) in a nucleus. Assuming that all nuclear levels are numbered subsequently according to their energy E_i, one finds for the direct population of the i-th state;

$$Y_{\mathrm{i}}^{\mathrm{d}}(t) = N \cdot \sigma_{\mathrm{i}} \cdot \phi \cdot (1/\lambda_{\mathrm{i}}) \cdot \begin{cases} (1-\exp\{(-\lambda_{\mathrm{i}} \cdot t)\}), & \text{for } t < t_{\mathrm{irrad}}, \\ [1-\exp\{(-\lambda_{\mathrm{i}} \cdot t_{\mathrm{irrad}})\}] \cdot \exp\{(-\lambda_{\mathrm{i}} \cdot (t-t_{\mathrm{irrad}}))\}, & \text{for } t \geq t_{\mathrm{irrad}}; \end{cases} \quad (3.10.1)$$

wherein N is the number of atoms exposed to the beam in the irradiated sample, σ_{i} the energy dependent cross-section for the direct population of the i-th state in barns, ϕ the beam flux and λ_{i} the total decay rate of the i-th level in s^{-1}. The parameter t_{irrad} represents the irradiation time during which the beam of incoming particles triggers the reaction. The factor $(t - t_{\mathrm{irrad}})$ is the time elapsed after the production of a specific state has stopped. If an indirect population (feeding) of a state *via* higher-lying energetic states occurs in addition, the total yield $Y_{\mathrm{i}}(t)$ for the i-th state, assuming that $1 \leq \mathrm{i} < \mathrm{k} \leq N_{\mathrm{tot}}$, can be calculated as,

$$Y_{\mathrm{i}}(t) = Y_{\mathrm{i}}^{\mathrm{d}}(t) + \sum_{\mathrm{k>i}}^{N_{\mathrm{tot}}} f_{\mathrm{ki}} \cdot \int_0^t |A_{\mathrm{k}}(t')|\,\mathrm{d}t' \quad (3.10.2)$$

in which

$$A_{\mathrm{k}}(t') = -\frac{\mathrm{d}Y_{\mathrm{k}}(t')}{\mathrm{d}t'} \quad (3.10.3)$$

is the instantaneous activity of the feeding state k with half-life λ_{k} and f_{ki} the partial branching ratio of the k-th state to the i-th state. The variable N_{tot} describes the total number of states in the nucleus which feed into the level at E_{i}. To include the possibility that the feeding state at E_{k} is also directly populated by the flux of particles with a specific cross-section of σ_{k}, $A_{\mathrm{k}}(t')$ from Equation (3.10.3) was referred to in Equation (3.10.2).

Equation (3.10.1) shows Y_{i} scales linear with ϕ. Experiments show that $\sim 10^{8-9}$ times higher values for the spontaneous beam fluxes ϕ are achievable with HPLS if compared to typical values associated RF-based technology. Though these extremely high fluxes can only be delivered for ultrashort irradiation time spans t_{irrad} which are in the order of the lifetime of short-lived states, the resulting enhancement in the presented case, $t_{1/2} = 1.20\,\mathrm{ns}$ level at 417 keV in ^{26}Al, will still be in the order of 10^{7-8} larger when compared to a DC or RC beam from a conventional accelerator system.

3.10.3 Yield distributions of excited states and temperature equivalents

The yield ratios between the ground and exited states can be mapped to a corresponding Maxwell-Boltzmann distribution describing a thermal equilibrium represented by a single temperature T via,

$$\frac{Y_2(t)}{Y_1(t)} = \frac{(2 \cdot J_2 + 1)}{(2 \cdot J_1 + 1)} \cdot \exp\left\{-\left(\frac{E_2 - E_1}{\mathrm{k_B} T}\right)\right\}, \quad (3.10.4)$$

in which Y_1 and Y_2 describe the state populations at a given time, J_1 and J_2 are the spin values of the nuclear states at the energies E_1 and E_2. Equation (3.10.4) has been used for the matching of state populations to temperature values of evaporation fragments emitted from a compound nucleus after a fusion reaction. The formation stage for the compound nucleus takes $\sim 1 \times 10^{-21}$ s and the thermal equilibration spans for 1×10^{-15} s before the compound disintegrates. The compound's temperature is given by $k_{\mathrm{B}}T$ [Mor+86] which will only prevail for the fleeting time spans associated with the shortest lifetimes of the decaying excited states exhibiting GK temperatures. The cosmogenic ^{26}Al, was chosen for this evaluation due to its importance for astrophysics and some already existing or soon to be published experimental work [SDM18].

3.10.4 The decay of ^{26}Al

In cold environments, ^{26}Al decays via two prominent β^+ decay routes from its ground and first excited state, which are characterized by very different values of their degree of forbiddenness. This special scenario complicates the evaluation of the effective ^{26}Al decay rate λ_{eff} in a stellar plasma as one cannot assume the first two states existed in an equilibrated thermal distribution. Specifically, the decay from its $J = 5^+$ ground state is a second-order forbidden β^+ decay with a corresponding long half-life of $t_{1/2} = 0.717\,\mathrm{My}$ leading to a branching of 97.24% to the first excited state in ^{26}Mg at 1809 keV. The β^+ decay is followed by a quasi-prompt emission ($t_{1/2} = 476\,\mathrm{fs}$) of the corresponding γ-ray in

^{26}Mg. On the other hand, the first excited state of ^{26}Al at 228 keV (^{26m}Al) decays via a rather fast ($t_{1/2}(^{26m}\mathrm{Al}) = 6.35\,\mathrm{s}$) super-allowed $0^+ \longrightarrow 0^+$ β^+ decay directly into the stable ground state ^{26}Mg$_{\mathrm{g.s.}}$. Due to the high spin difference, a direct electromagnetic transition from the 228 keV level to the ground state $0^+ \longrightarrow 5^+$ in ^{26}Al has an extremely low transition probability and, as such, one is forced to treat the decay of ^{26}Al$_{\mathrm{g.s.}}$ and ^{26m}Al as different species in theoretical evaluations. To shed light on the overall destruction of ^{26}Al one needs to estimate the interplay between these two states in hot environments to be able to calculate the effective decay rate λ_{eff} in stellar plasma. Here, theory predicts that a thermal equilibrium between the long-lived 5^+ ground state and the first isomeric 0^+ state at 228 keV will occur at high temperatures (1×10^6 K to 1×10^9 K) via a manifold of interlinking high-energy transitions which induce a population of short-lived (fs–ns) high-lying energy levels [CPN99; WF80]. The work by Gupta and Meyer, which is referred to in this report, represents the most current and holistic approach [GM01].

3.10.5 Cross-Section of ^{26}Al and its production in laser-plasma experiments

The *in situ* production of ^{26}Al can be done using laser accelerated protons *via* ^{26}Mg(p,n)^{26}Al leading to excited states in ^{26}Al as well as directly populating the ground state ^{26}Al$_{\mathrm{g.s.}}$. Precise measurements of the individual cross sections for ^{26}Al$_{\mathrm{g.s.}}$, ^{26m}Al and the 3^+ level at 417 keV, ^{26}Al$_{417}$, have been carried out over three decades ago by Skelton et al. [SKS87] which is used om this work to evaluate the integral cross sections as shown in Table 1

For more details on the related inaugural experiment see [SDM18].

3.10.5.1 Simulations of population yields for ^{26}Al

Based on Equations (3.10.1) and (3.10.2) and the values of the integrated cross sections σ^{int} from Table 3.10.1, the achievable population yields of the lowest three states in ^{26}Al were theoretically estimated. A short proton irradiation period, $t_{\mathrm{irrad}} = 200\,\mathrm{ps}$ was assumed in line with expected laser parameters and target arrangements.

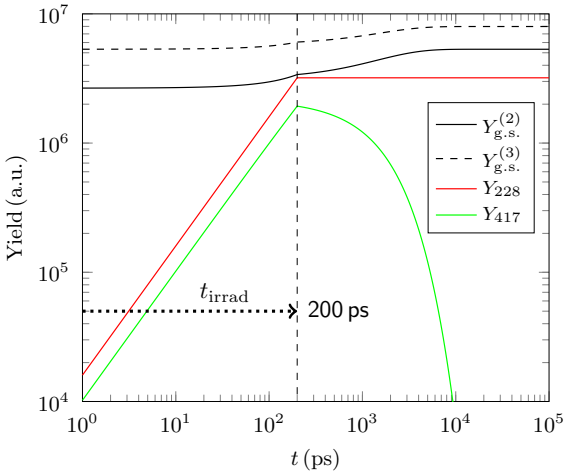

Figure 3.10.1: *Calculated yields Y_{228} (red) and Y_{417} (green) as function of time t per proton pulse with $t_{\mathrm{irrad}} = 200\,\mathrm{ps}$ (vertical dashed line) and $4.988\,\mathrm{MeV} \leq E_{\mathrm{p}} \leq 5.820\,\mathrm{MeV}$. The accumulated yields $Y_{\mathrm{g.s.}}$ for the ground state are superimposed for the 2$^{\mathrm{nd}}$ (solid black) and 3$^{\mathrm{rd}}$ (dashed black) consecutive proton pulses. We assume those pulses to impact on the same target volume in the secondary production target. Note the influence of the direct feeding from the 417 keV level to the ground state from the non-linear enhancement of $Y_{\mathrm{g.s.}}$ during t_{irrad}. A time interval of 100 s between the 2$^{\mathrm{nd}}$ and 3$^{\mathrm{rd}}$ pulse was assumed.*

Figure 3.10.1 shows the calculated distributions of $Y_{\mathrm{g.s.}}$, Y_{228} and Y_{417} deduced from Equations (3.10.1) and (3.10.2) assuming $t_{\mathrm{irrad}} = 200\,\mathrm{ps}$. The extracted values for the associated integral cross sections σ^{int} in the region between $E_{\mathrm{p}} = 4.988\,\mathrm{MeV}$ and $E_{\mathrm{p}} = 5.820\,\mathrm{MeV}$ were taken from Table 3.10.1. The time zero $t_0 = 0$ which is truncated in the logarithmic display, refers to the time of the first reaction induced by the fastest protons arriving in the secondary production target. Although the yield depicted on the $y-$abscissa is in arbitrary units, a.u., the value is aligned with obtainable levels of concentration in units of $1\,\mathrm{cm}^{-3}$ deduced from the inaugural measurements of ^{26m}Al at the RAL. The values can be seen as a minimum estimate for achievable yield concentrations with a PW laser system. We assume all consecutive pulses to impact on the same volume within the secondary production target, hence the yield for ^{26}Al$_{\mathrm{g.s.}}$, $Y_{\mathrm{g.s.}}$, builds up continuously after each pulse due to the very long lifetime of the ground state, $t_{1/2} = 0.717\,\mathrm{My}$. In addition, the ground state is populated by direct feeding from the 417 keV level (Equation (3.10.2)) which decays via an E2 transition. As ^{26}Al is cosmogenic we can assume its original concentration in Mg or MgO, in

Table 3.10.1: Calculated integral cross sections σ^{int} and methods used to measure $\sigma(E)$ for the lowest three states in ^{26}Al.

State	σ^{int}/MeVmb	Method Used in [SKS87]
$\sigma^{\text{int}}_{\text{g.s.}}$	4.9(9)	Total neutron yield from the $^{26}\text{Mg}(\text{p},\text{n}_{\text{tot}})^{26}\text{Al}$ reaction measured. Note, due to the very long half-life of $^{26}\text{Al}_{\text{g.s.}}$, no delayed 511 keV annihilation radiation yield will be measurable emerging from the associated ground state decay.
$\sigma^{\text{int}}_{228}$	30.2(3)	Delayed 511 keV annihilation radiation yield from the $^{26}\text{Mg}(\text{p},\text{n}_{228})^{26\text{m}}\text{Al}$ reaction measured by two NaI(Tl) detectors in coincidence. An irradiation-count cycle with $t_{\text{irrad}} = 6\,\text{s}$ and $t_{\text{count}} = 30\,\text{s}$ was applied.
$\sigma^{\text{int}}_{417}$	19.3(9)	Prompt 417 keV γ-ray yield from the $^{26}\text{Mg}(\text{p},\text{n}_{417})^{26}\text{Al}$ using an ultra-thin target with a thickness of $8.5\,\mu\text{gcm}^{-2}$. The prompt radiation was measured by a $60\,\text{cm}^3$ Ge(Li) detector.

the secondary target probe to be $Y^0_{\text{g.s.}} \sim 0$. Moreover, we consider that two sequential proton pulses are separated by an interval of $t = 100\,\text{s}$ for simplicity which reflects roughly the time interval between two consecutive pulses from the 10 PW system at ELI-NP. The production of the ground state is governed by $\sigma^{\text{int}}_{\text{g.s.}}$ which is significantly lower than for the excited states but builds up continuously in the active secondary target. Crucially for the understanding of temporal yield evolution is the fact that the irradiation time $t < 200\,\text{ps}$ is still lower than the lifetime of the 417 keV state, which allows this state to accrue *comparable* yields with regard to the first excited state at 228 keV per single pulse. For the first couple of pulses, this is even true for comparison with $Y_{\text{g.s.}}$ as can be derived from Figure 3.10.1. The two yields Y_{228} and Y_{417} remain unchanged for the two consecutive pulses shown in Figure 3.10.1 and for any additional subsequent pulse. This is a very special condition only achievable with the ultrashort pulses provided by an all-optical accelerator system.

3.10.6 Temperature equivalents

Using the Maxwell-Boltzmann distribution as depicted in Equation (3.10.4), the ratios of the two yield distributions; $Y_{228}/Y_{\text{g.s.}}$ and $Y_{417}/Y_{\text{g.s.}}$ were mapped into temperature equivalents to emphasize the unique ability of laser-driven experiments to facilitate the short, reaction-driving, ion pulses to mimic temperature-equivalent scenarios as present in hot interstellar conditions. In the absence of a real hot plasma, this interpretation exploits the fact that the hot state of the ^{26}Al compound residue is conserved for fleeting lifetimes after the reaction-driving pulse has impacted. The results for the consecutive pulses numbered, 1, 2, 3, 5, 10, 25, 50 and 100 are displayed in Figure 3.10.2. The theory states that to infer a temperature between the ground state and the first excited state in the case of ^{26}Al is not a straightforward concept, as those states are only connected via higher-lying excited states in low to middle-temperature plasma. Nevertheless, the temperature equivalents between these two states, based on their yield population, remain in the GK temperature regime due to the short time of the populating laser proton pulse. At such high temperatures, thermalization can be assumed in stellar environments [GM01]. Most crucially, for any successive pulse, there exists a defined time t_{equi}, where the T equivalents of the first two excited states are equal, mimicking the conditions of a thermal equilibrium distribution in the absence of real hot temperature conditions in the production target. For the calculated cases, this regime stretches from 3.10 ns in which the temperature equivalent is 1.3 GK for the first pulse to 9.95 ns with $T = 0.4\,\text{GK}$ for the 100$^{\text{th}}$ pulse. Any probing X-ray flash or secondary ion beam would be best timed around t_{equi} to exploit that artificially stellar-like astrophysical scenario mimicking an equilibrium in hot plasma. It is worth noting that for consecutive runs, this particular time increases to almost 10 ns while the temperature-equivalent value decreases. Using RF-based technology, the realization of such conditions characterized by yield distributions resembling high temperatures at short time intervals after reaction-triggering pulses is not possible.

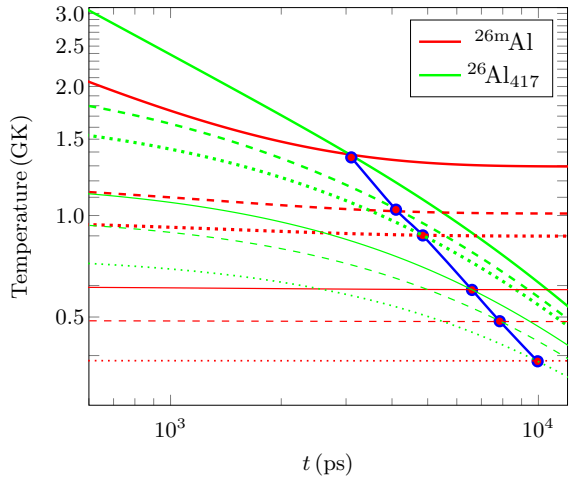

Figure 3.10.2: *Calculated T equivalents for $Y_{228}/Y_{\mathrm{g.s.}}$ (red lines) and $Y_{417}/Y_{\mathrm{g.s.}}$ (green) for consecutive pulse numbers 1 (solid thick), 2 (dashed thick), 3 (dotted thick), 5 (solid thin), 25 (dashed thin) and 100 (dotted thin). The times t_{equi} for each pulse at which the two yield ratios converge to resemble one temperature value T are indicated by the blue & red circles which are connected to a blue line to guide the eye.*

It is the shortness of the fastest transition that demands a short triggering high beam flux ϕ to achieve such scenarios. Moreover, the assumed high yields achievable with an HPLS system are multiple orders of magnitude higher than those of current RF-technology, which summarizes the essence of the contribution these systems can provide for future astrophysical studies. Again, one must emphasize that we are not referring to real hot plasma temperatures. It can be envisaged that once mono-energetic laser proton pulses are achieved, the depicted calculation can be extended to include any of the 64 states below the proton separation energy $S_{\mathrm{p}} = 6.306\,\mathrm{MeV}$ threshold of ^{26}Al. Such a calculation will help in the understanding of the complex interplay between the short-lived states belonging to the e_1 and e_2 ensembles and the longer-lived low lying states as a function of the temperature T, thus allowing us to study the evolution of the effective lifetime τ_{eff} for ^{26}Al.

3.10.7 Conclusion

A pathway for high-power laser physics at the interface of nuclear astrophysics is presented. The example of ^{26}Al showed that laser systems could provide short-lived states in high yields, comparable with those states that exhibit much longer lifetimes. This feature is unique to HPLS due to the ability of all-optical accelerator systems to deliver high temporal fluxes ϕ of reaction-driving protons for the fleeting time spans in the order of the lifetimes of the shortest-lived excited states. Exploiting the fact that the high temperatures within the residual ^{26}Al nuclei prevail for some ultrashort duration after its creation by a compound reaction, high entropy conditions in cold plasma environments can be achieved and potentially be tested with a second radiation or particle beam. In the case of ^{26}Al the yield ratios, $Y_{228}/Y_{\mathrm{g.s.}}$ and $Y_{417}/Y_{\mathrm{g.s.}}$, interpreted in the framework of the Maxwell-Boltzmann statistics, were found to mimic thermal equilibrium at defined times t_{equi} in the range of 300 ps to 10 ns resembling thermalization in a fictitious GK plasma environment.

References

[Arn69] W. D. Arnett. “Explosive nucleosynthesis in stars”. In: *Astrophysical Journal* 157 (1969), page 1369. DOI: 10.1086/150157 (cited on page 127).

[CPN99] A. Coc, M.-G. Porquet, and F. Nowacki. “Lifetimes of ^{26}Al and ^{34}Cl in an astrophysical plasma”. In: *Phys. Rev. C* 61 (1999), page 015801. DOI: 10.1103/PhysRevC.61.015801 (cited on page 129).

[Die+06] R. Diehl *et al.* “Radioactive ^{26}Al from massive stars in the Galaxy”. In: *Nature* 439.7072 (2006), 45–47. ISSN: 0028-0836. DOI: {10.1038/nature04364} (cited on page 127).

[GM01] S. S. Gupta and B. S. Meyer. “Internal equilibration of a nucleus with metastable states: ^{26}Al as an example”. In: *Phys. Rev. C* 64 (2001), page 025805. DOI: 10.1103/PhysRevC.64.025805 (cited on pages 129, 130).

[HF52] W. Hauser and H. Feshbach. “The Inelastic Scattering of Neutrons”. In: *Phys. Rev.* 87 (1952), page 366 (cited on page 127).

[Ili+11] C. Iliadis *et al.* “The effects of thermonuclear reaction rate variations on ^{26}Al production in massive stars: a sensitivity study”. In: *Astrophysical Journal Suppl. Series* 193.1 (2011), page 16. ISSN: 0067-0049. DOI: {10.1088/0067-0049/193/1/16} (cited on page 127).

[Kit+13] N. T. Kita *et al.* "^{26}Al – ^{26}Mg isotope systematics of the first solids in the early solar system". In: *Meteoritics & Planetary Science* 48.8 (2013), pages 1383–1400. DOI: 10.1111/maps.12141 (cited on page 127).

[LPW76] T. Lee, D. Papanastassiou, and G. Wasserburg. "Demonstration of ^{26}Mg excess in Allende and evidence for ^{26}Al". In: *Geophysical Research Letters* 3.1 (1976), 41–44. ISSN: 0094-8276. DOI: {10.1029/GL003i001p00041} (cited on page 127).

[Mah+84] W. A. Mahoney *et al.* "HEAO 3 discovery of ^{26}Al in the interstellar medium". In: *Astrophysical Journal* 286 (1984), pages 578–585. DOI: 10.1086/162632 (cited on page 127).

[Mor+86] D. J. Morrissey *et al.* "Thermal population of nuclear excited states". In: *Phys. Rev. C* 34 (1986), pages 761–763. DOI: 10.1103/PhysRevC.34.761 (cited on page 128).

[SKS87] R. Skelton, R. Kavanagh, and D. Sargood. "^{26}Mg$(p,n)^{26}$Al and ^{23}Na$(\alpha,n)^{26}$Al Reactions". In: *Physical Review C* 35.1 (1987), 45–54. ISSN: 0556-2813. DOI: {10.1103/PhysRevC.35.45} (cited on pages 129, 130).

[SDM18] K. M. Spohr, D. Doria, and B. S. Meyer. "Theoretical discourse on producing high temporal yields of nuclear excitations in cosmogenic ^{26}Al with a PW laser system: The pathway to an astrophysical earthbound laboratory". In: *Galaxies* 7.1 (2018). ISSN: 2075-4434. DOI: 10.3390/galaxies7010004 (cited on pages 128, 129).

[VCL09] J. Villeneuve, M. Chaussidon, and G. Libourel. "Homogeneous distribution of ^{26}Al in the solar system from the Mg isotopic composition of chondrules". In: *Science* 325.5943 (2009), pages 985–988. DOI: 10.1126/science.1173907 (cited on page 127).

[WF80] R. A. Ward and W. A. Fowler. "Thermalization of long-lived nuclear isomeric states under stellar conditions". In: *Astrophysical Journal* 238 (1980), pages 266–286. DOI: 10.1086/157983 (cited on page 129).

[Zue21] J. Zuegel. *For more information on the MP3 project and whitepapers follow:* https://www.lle.rochester.edu/index.php/2021/03/12/call-for-white-papers-multi-petawatt-physics-prioritization-mp3-workshop/. 2021. URL: https://www.lle.rochester.edu/index.php/2021/03/12/call-for-white-papers-multi-petawatt-physics-prioritization-mp3-workshop/ (cited on page 127).

Applied & Technical Work at LDED

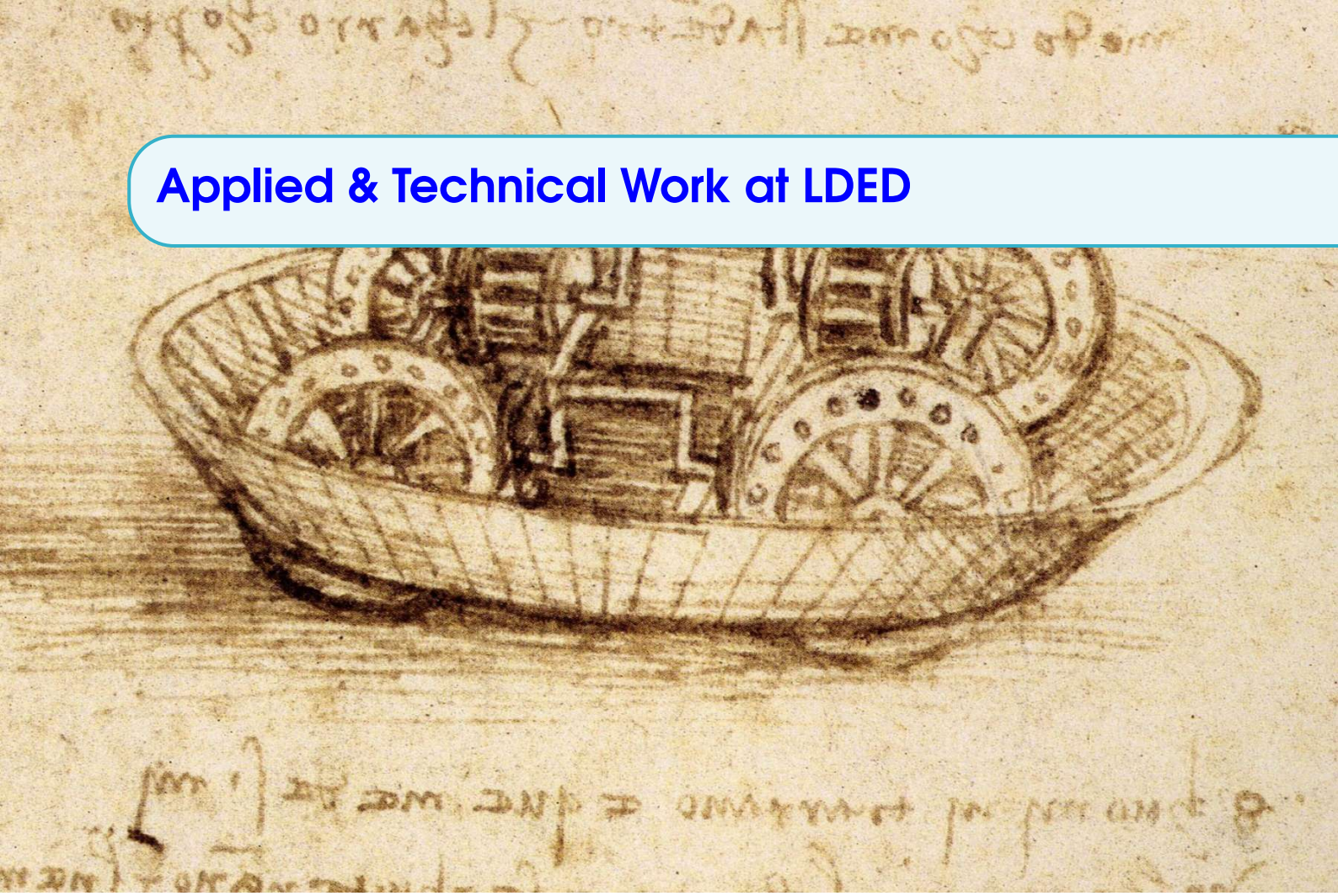

3.11 Preclinical studies of immuno-oncology in combination with intense particle beams at the ELI-NP facility to enhance boron neutron capture therapy (BNCT)

Spohr K. M.[1] , Doria D.[1] , Nastasa V. V.[1] , and Măgureanu A.[1]

[1] Extreme Light Infrastructure (ELI-NP) & Horia Hulubei National Institute for R & D in Physics and Nuclear Engineering (IFIN-HH), Str. Reactorului No. 30, 077125 Bucharest–Măgurele, Romania

[*] **klaus.spohr@eli-np.ro**

Abstract

Inaugural work on a scientific program that merges modern ground-breaking concepts of biomedical immuno-oncology with boron neutron capture therapy (BNCT) is presented. Soon to be patented, the PED-funded project aims to selectively deliver boron nanoparticles exclusively into cancer cells by facilitating the ultra-precise target identification ability of genetically modified $\gamma\delta$ CAR-T cells, which only attack malignant cells. Once delivered inside a malignant cell, the boron nanoparticles can be exposed to bursts of slow neutrons, *e.g.*, provided by the 1 PW-class laser system at ELI-NP to harvest the dose-rate effect of laser-induced intense particle fluxes for therapy. A first theoretical approach to find the optimal delivery conditions for the sonoporation of the boron nanoparticle into the delivering $\gamma\delta$ CAR-T cells by an ultrasound transducer based on the Rayleigh-Plesset formula is depicted. It was found that a sinusoidal driving signal in the MHz-regime extending to an exposure time of 3.2 µs with a pressure amplitude of 400 kPa will be ideal for the boron transfer into the sensitive allogeneic $\gamma\delta$ CAR-T cells.

3.11.1 Introduction

BNCT facilitates the fission reaction that occurs when non-radioactive ^{10}B is irradiated with thermal or epithermal neutrons, n_{th}; $^{10}B + n_{th} \rightarrow {}^{4}He + {}^{7}Li + 2.8\,MeV$; Every reaction produces an energetic α-particle and a ^{7}Li ion, both of which lose their kinetic energy determined by the $Q-$value of the reaction *via* the linear energy transfer (LET) while transgressing through the cell [Loc36]. A maximum range of $\sim 4\,\mu m$ for ^{7}Li and $\sim 9\,\mu m$ for the lighter ^{4}He is found. Since these lengths coincide with the diameter of a human cell, the lethality of the capture reaction is limited *only* to cells in the vicinity of the boron particles [Mos14]. The success of BNCT henceforth depends upon the selective delivery of sufficiently high amounts of ^{10}B to the tumor itself, with only small amounts localized in the surrounding healthy tissue. So far, chemically-based delivery agents used in BNCT are curtailed dramatically in their ability for precision delivery. At best, a three- to the four-fold enhancement of the boron-load into a malignant cell can be achieved if compared to healthy surrounding cells [Mor+07]. That is particularly disconsolate since normal tissue tolerates the flux of slow neutrons due to the rather low nuclear capture reactions that naturally occur on hydrogen and nitrogen. Hence, the related unwanted radiation dose levels experienced by healthy tissue are minimal if a precision delivery mechanism for BNCT can be found.

The utmost precision standard of targeted radiology would constitute the boron nanoparticles exclusively placed right inside the cancerous cell to be targeted. The efficacy of this method is furthermore emphasized as only a single reaction on ^{10}B as described above will deliver enough dose rate to destroy the malignant cell for good. The PED-funded (540/PED/2020) project tries to achieve the related adoptive immunotherapy in the future for the first time in therapeutics by using the unique cancer-detecting abilities of genetically modified $\gamma\delta$ CAR-T cells [Fis+14; Kab+20; WFL20]. This is enhancing previous work on that matter as, *e.g.*, depicted in [Mor+07]. The intelligent Immuno-BNCT precision-delivery method developed at ELI-NP can be regarded as a biologically and physically targeted radiation therapy, representing almost a "magic bullet" approach in the efficient treatment of tumors. This will be primarily of use for patients with hitherto unmet therapeutical needs. The effectiveness of the synergetic method is further supported by the availability of the ^{10}B isotope, which represents 20% of moderately priced ^{nat}B [DB95].

Patented biotechnology has also been able to produce allogeneic[2] $\gamma\delta$ CAR-T cells in culture sizes up to a

[2] allogeneic: healthy cells from a donor to support the diseased

staggering 10^9 specimen, enabling the treatment of an individual patient at a rather low cost, probably soon down to $< 1000\,\$$. This further supports the quest to establish a disruptive interdisciplinary technology at the interface of the newest cell research and established BNCT technology.

3.11.2 First steps of the implementation of the Immuno-BNCT method

The project is implemented with core equipment being purchased. The first task will be to find an efficient way to upload the boron nanoparticles with a sufficiently high yield of $\sim 0.13\,\mathrm{pg}$ per cell $\gamma\delta$ CAR-T cells [Mor+06]. Figure 3.11.2 shows the boron-loading apparatus currently being assembled at ELI-NP.

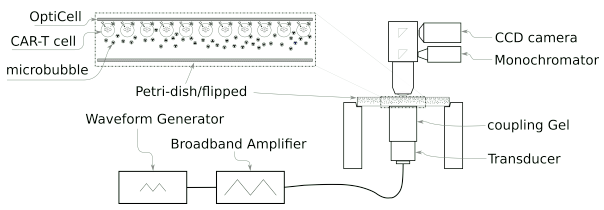

Figure 3.11.1: *Boron Loading Apparatus Assembly (BLAA)*

We firstly have to address the loading of T cells with boron nanoparticles. Sonoporation using a 200 W broadband ultrasound transducer was identified as the best technological approach, following work by [Wan+18a]. The boron loading apparatus assembly (BLAA) is shown in Figure 3.11.2. A core component in the loading procedure will be the use of microbubbles ($\sim 1\,\mu\mathrm{m}$) to which the boron nanoparticles are attached. In order to establish the transfer process, those microbubbles need to approach the $\gamma\delta$ CAR-T cells being driven by a periodical ultrasound signal. An optimal distance of approach was found to be in the order of a few µm. Enforcing a strong pressure of $P(t)$ will lead to the bubbles' explosion at which they express the nanoparticles into the $\gamma\delta$ CAR-T cells. The explosion-induced shock wave burst will rip a temporal whole into the $\gamma\delta$ CAR-T cell membrane if the magnitude of the force exerted via the $P(t)$ is sufficient enough. Care has to be taken not to make the amplitude of $P(t)$ too high to avoid permanent damage to the T cell membrane or destruction of its crucial surface entities, such as the Chimeric Antigen Receptor (CAR) of the T Cell Receptor (TCR), see Figure 3.11.2

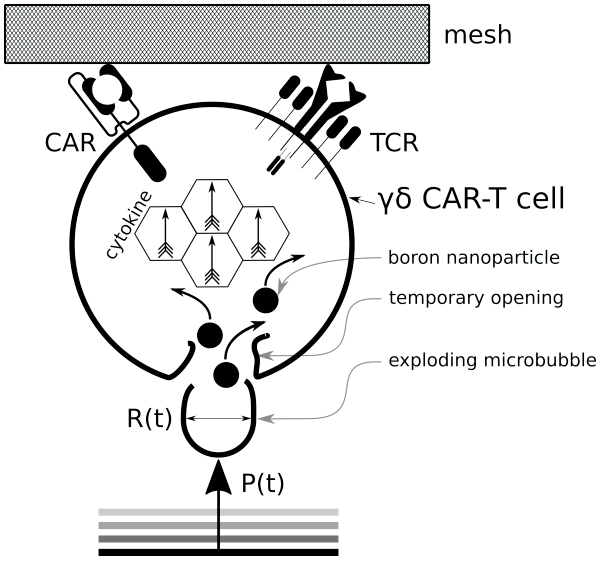

Figure 3.11.2: *Boron loading procedure at the moment of the microbubble's explosion. The temporary cell opening will close once the pressure has seized. The cell's cytokines are depicted as arrows and the implanted boron nanoparticles as black circles. The figure is not to scale.*

Cellular responses such as cell membrane permeability and cytoskeleton disassembly have been researched regarding their dependence on the acoustic driving pressure $P(t)$ and distances between the delivering microbubble, of a diameter of $\sim 1\,\mu\mathrm{m}$ and the cell with dimensions of a few $\sim$ µm. The applicance of a two-dimensional boundary element model was the first step of our research project in which the Rayleigh-Plesset formula describes the temporal change in the buble's radius $R(t)$

$$R(t)\frac{d^2R(t)}{dt^2} + \frac{3}{2}\left(\frac{dR(t)}{dt}\right)^2 + \frac{4\nu_\mathrm{L}}{R(t)}\frac{dR(t)}{dt} + \ldots + \frac{2\gamma}{\rho_\mathrm{L}R(t)} + \frac{\Delta P(t)}{\rho_\mathrm{L}} = 0 \tag{3.11.1}$$

and thus allows for a determination of the pressure amplitude and explosion time at the optimum microbubble's approaching distance. In Equation 3.11.1 ρ_L is the density of the surrounding liquid, ν_L is the kinematic viscosity of the surrounding liquid, γ is the surface tension of the bubble-liquid interface, $\Delta P(t) = P_\infty(t) - P_B(t)$ is the pressure difference between the uniform pressure in the bubble $P_B(t)$ and $P_\infty(t)$ the external pressure 'infinitely' far away from the bubble. Equation 3.11.1 allowed the optimization of the transducer's driving signal with respect to the timing of the disintegration of the microbubble, injecting the theranostic particles into the T cells. We

used the work of Wang *et al.* [Wan+18b] to create a model of the boron-loading process with parameters associated with standard industry microbubble and known mechanic features of $\gamma\delta$ CAR-T cells. The results for $P(t)$ are depicted in Figure 3.11.2.

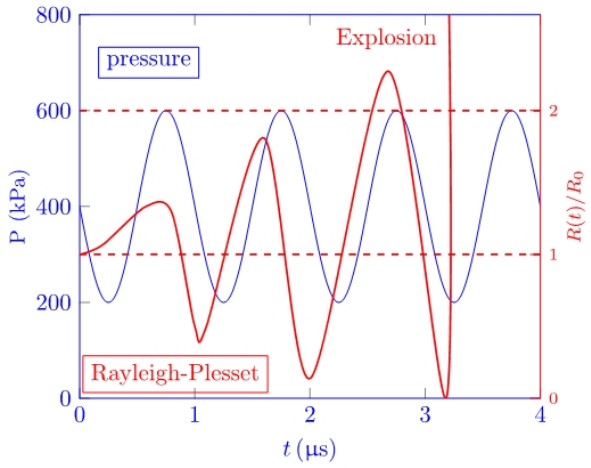

Figure 3.11.3: *P(t) (blue) and R(t) (red) as function of time due to sinusoidal-driving of a standard* 1 µm *microbubble in the BLAA. The explosion is expected after* 3.2 µs.

This allowed us to proceed in designing and implementing our Loading Apparatus Assembly (LAA), which is shown in Figure 3.3.1. The core aim of the simulations and design is to prevent the sensitive manufactured $\gamma\delta$ CAR-T cells from unnecessary stress, thus avoiding compromising efficiency. We need to point out that those cells are not yet available on the free market but will be supplied courtesy of a leading biotech company that indicated an interest in the patent development. Core to this apparatus will be the transducer purchased. The latter is driven by a Wavefront Generator and amplified by a Broadband Amplifier to assure 'Class A' linear power output over the entire frequency range from 10 kHz to 12 MHz for levels of up to 200 W and arbitrary waveforms. At first instance, a sinusoidal pressure activation with an average value of $\overline{P(t)} = 400\,\text{kPa}$ (peak value $P_{\max}(t) = 600\,\text{kPa}$) with a high frequency of 1 MHz to support sonoporation was assumed. The focal spot is maximized to 18 mm by choice of the transducer to allow for the most efficient boron loading. Figure 3.11.2 shows the result of a typical simulation in which the explosion of the delivering microbubble will occur after 3.2 µs. The choice of a waveform with steeper gradients will shorten that loading process up to a factor of two, but also would induce higher force gradients that could become detrimental for the sensitive $\gamma\delta$ CAR-T cells. Hence steeper gradients for $P(t)$ were dismissed for the investigations.

3.11.3 Sketch of Modus Operandi of boron transmission to cancerous cells to be studied

The *modus operandi* of the uploading of the boron nanoparticles follows the natural given cytokine attack (kiss-of-death) of the innate $\gamma\delta$ CAR-T cells during which they express their cytokines into the previously identified malignant cell [AAV16; Seb+19]. This recognition relies on the chemotaxis of $\gamma\delta$ CAR-T cells to recognize the presence of Isopentenyl Pyrophosphate (IPP), a metabolite solely produced in myeloma cells [Li+19].

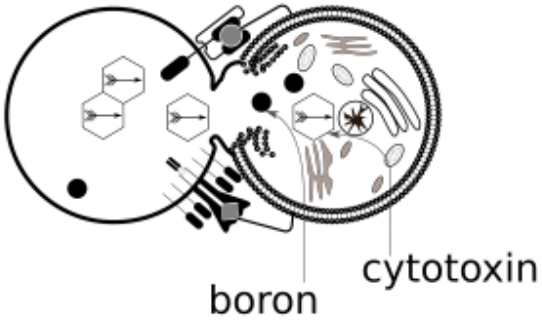

Figure 3.11.4: Kiss-of-Death by $\gamma\delta$ CAR-T with the expression of boron nanoparticles.

The actual transfer of the boron particles processes *via* a pressure gradient during the temporal fusion of the $\gamma\delta$ CAR-T with the compromised cell, see Figure 3.11.3. As the nanoparticles are of approximate weight as cytokine molecules, the same osmotic pressure gradient can deliver them in the wake of the chemical attack of the compromised cancer cell. This part of the pre-clinical investigation is foreseen to start in 2023. Currently, supply chains of allogeneic $\gamma\delta$ CAR-T cells, produced mainly in the UK, are hampered by the pandemic, causing a delay in the biological investigations.

3.11.4 Progress of neutron production at ELI-NP

The project is aligned, in the long-term, to be included in the medical program at the 1 PW station at ELI-NP. It employs thermal and epithermal neutrons produced from nuclear reactions and moderated accordingly. In that respect, it is very different from other campaigns focussing on the use of laser-induced ion beams. Most importantly, as only neutrons are used, it presents an alternative way of pre-

clinical studies at ELI-NP. The use of laser-driven ions-based radiology comes with challenges mainly due to the compromised beam characteristics inherently given by the hitherto exploitable acceleration regimes. Nevertheless, a disruptive entity in oncological studies could be the high temporal dose yield achievable with higher power laser systems. This dose rate effect can also become a key entity of the project. Though at least two years ahead, the preclinical trials of Immuno-BNCT could be envisaged centering around enhancing cancer lethality with the laser-induced beam. At implementation, already high neutron dose rates could be identified, underpinning our research.

3.11.5 Acknowledgment

All of the authors draw support from the PED grant, PN-III-P2.1-PED-2019-2325 (540/PED/2020).

References

[AAV16] H. Almåsbak, T. Aarvak, and M. C. Vemuri. "CAR T Cell Therapy: A Game Changer in Cancer Treatment". In: *Journal of Immunology Research* 2016 (2016), pages 1–10. DOI: 10.1155/2016/5474602. URL: https://doi.org/10.1155/2016/5474602 (cited on page 137).

[DB95] C. Dunford and T. Burrows. "Online Nuclear Data Service". English. In: *Report IAEA-NDS-150 (NNDC Informal Report NNDC/ONL-95/10), International Atomic Energy Agency, Vienna, Austria* 9.1 (1995) (cited on page 135).

[Fis+14] J. P. Fisher *et al.* "$\gamma\delta$ T cells for cancer immunotherapy". In: *OncoImmunology* 3.1 (2014). PMID: 24734216, e27572. DOI: 10.4161/onci.27572. eprint: https://doi.org/10.4161/onci.27572. URL: https://doi.org/10.4161/onci.27572 (cited on page 135).

[Kab+20] D. Kabelitz *et al.* "Cancer immunotherapy with $\gamma\delta$ T cells: many paths ahead of us". In: *Cellular & Molecular Immunology* 17.9 (July 2020), pages 925–939. DOI: 10.1038/s41423-020-0504-x. URL: https://doi.org/10.1038/s41423-020-0504-x (cited on page 135).

[Li+19] Z. Li *et al.* "The JNK signaling pathway plays a key role in methuosis (non-apoptotic cell death) induced by MOMIPP in glioblastoma". In: *BMC Cancer* 19.1 (Jan. 2019). DOI: 10.1186/s12885-019-5288-y. URL: https://doi.org/10.1186/s12885-019-5288-y (cited on page 137).

[Loc36] G. L. Locher. "Biological effects and therapeutic possibilities of neutron". In: *American Journal of Roentgenology* 36 (1936), page 1 (cited on page 135).

[Mor+06] M. W. Mortensen *et al.* "Functionalization and Cellular Uptake of Boron Carbide Nanoparticles. The First Step toward T Cell-Guided Boron Neutron Capture Therapy". In: *Bioconjugate Chemistry* 17.2 (Feb. 2006), pages 284–290. DOI: 10.1021/bc050206v. URL: https://doi.org/10.1021/bc050206v (cited on page 136).

[Mor+07] M. W. Mortensen *et al.* "Next Generation Adoptive Immunotherapy—Human T Cells as Carriers of Therapeutic Nanoparticles". In: *Journal of Nanoscience and Nanotechnology* 7.12 (Dec. 2007), pages 4575–4580. DOI: 10.1166/jnn.2007.18108. URL: https://doi.org/10.1166/jnn.2007.18108 (cited on page 135).

[Mos14] R. L. Moss. "Critical review, with an optimistic outlook, on Boron Neutron Capture Therapy (BNCT)". In: *Applied Radiation and Isotopes* 88 (June 2014), pages 2–11. DOI: 10.1016/j.apradiso.2013.11.109. URL: https://doi.org/10.1016/j.apradiso.2013.11.109 (cited on page 135).

[Seb+19] Z. Sebestyen *et al.* "Translating $\gamma\delta$ T cells and their receptors into cancer cell therapies". In: *Nature Reviews Drug Discovery* 19.3 (Sept. 2019), pages 169–184. DOI: 10.1038/s41573-019-0038-z. URL: https://doi.org/10.1038/s41573-019-0038-z (cited on page 137).

[WFL20] A. D. Waldman, J. M. Fritz, and M. J. Lenardo. "A guide to cancer immunotherapy: from T cell basic science to clinical practice". In: *Nature Reviews Immunology* 20.11 (May 2020), pages 651–668. DOI: 10.1038/s41577-020-0306-5. URL: https://doi.org/10.1038/s41577-020-0306-5 (cited on page 135).

[Wan+18a] M. Wang *et al.* "Sonoporation-induced cell membrane permeabilization and cytoskeleton disassembly at varied acoustic and microbubble-cell parameters". In: *Scientific Reports* 8.1 (Mar. 2018). DOI: 10.1038/s41598-018-22056-8. URL: https://doi.org/10.1038/s41598-018-22056-8 (cited on page 136).

[Wan+18b] S. P. Wang *et al.* “Acoustic bubble dynamics in a microvessel surrounded by elastic material”. In: *Physics of Fluids* 30.1 (Jan. 2018), page 012104. DOI: 10.1063/1.5005534. URL: https://doi.org/10.1063/1.5005534 (cited on page 137).

3.12 Monitoring system for electromagnetic pulses at ELI-NP

Gugiu M. M.[1,*] , Bălăşcuţă S.[1], Cernăianu M. O.[1], Chen S. N.[1] , Doria D.[1], Fuchs J. S.[1] , Ghenuche P. V.[1], Iovanescu R.[1] , Petcu C.[1] , Savu B.[2] , Ticoş C. M.[1], and Tudor L.[1]

[1] Extreme Light Infrastructure (ELI-NP) & Horia Hulubei National Institute for R & D in Physics and Nuclear Engineering (IFIN-HH), Str. Reactorului No. 30, 077125 Bucharest–Măgurele, Romania
[2] Department of Nuclear Physics (DFN) & Horia Hulubei National Institute for R & D in Physics and Nuclear Engineering (IFIN-HH), Str. Reactorului No. 30, 077125 Bucharest–Măgurele, Romania

[*] **marius.gugiu@eli-np.ro**

Abstract

A strong EMP – Electromagnetic Pulse of tens or hundreds of kV/m, ringing transient in the MHz - THz frequency domain, can be generated within the 10 PW vacuum chamber containing the targets as a result of interactions of high-power laser with the matter. This raises significant engineering challenges for the team involved in implementing experimental setups to ensure that the physical phenomena studied at ELI-NP are not hampered by EMP pick-up. Likewise, protecting human beings and electronics from the damaging effects induced by EMP in the facility is mandatory. Thus, the development of a tool to allow monitoring, measurement, and study of the EMP generation mechanisms, establish the source terms of EMP and design a proper EMP shielding for susceptible diagnostics at EMP represent a high priority for ELI-NP.

3.12.1 Introduction

The highly intense ultrashort pulse lasers, with power at the level of 1 PW and above, are in rapid development all over the world and are beginning to be used more and more often in plasma and nuclear physics studies. These areas of research promise, very soon, a multitude of discoveries and practical applications. Taking advantage of the unique characteristics of the new ELI-NP research infrastructure, with its two ultra-high power of 10 PW, reaching intensities up to 1×10^{22} Wcm^{-2} to23 Wcm^{-2}, several fundamental nuclear physics studies in new electron and ion acceleration regimes will become accessible [Neg+16]. Due to the very harsh environment of non-ionizing and ionizing radiation specific to the PW class laser experiments, so far, passive diagnostics, without susceptible semiconductor electronics, were chosen to be used. They give useful results but are not viable solutions for the high repetition rate experiments, which impose the development and implementation of active diagnostics. This issue constitutes a serious engineering challenge and represents a high priority for nuclear laser-driven experiments at ELI-NP. An impressively strong EMP – electromagnetic pulse of tens or hundreds of kVm^{-1}, ringing transient in the MHz to THz frequency range, can be generated within the vacuum chamber containing the targets as a result of interactions of high-power laser with matter [Mea+04]. The EMP is emitted from the vacuum chamber through ports and wiring into the surrounding area, where it is modified by reflection and absorption from equipment and the walls of the experimental area. The EMP is also propagated down the beam tube to the laser components. In this context, protecting human beings and electronics from the damaging effects induced by EMP is mandatory. Besides that, the unique physical phenomena to be studied should not be hampered by EMP pick-up [Ede+09]. In the meantime, electromagnetic interference induced by EMP should be avoided. Otherwise, any experiment running in parallel in the building, such as the envisaged experiments with gamma-ray beams, should not be disturbed by EMP produced by lasers. Thus, developing a tool to allow measurement and study of the EMP generation mechanisms is essential for the operation of the experimental installations at ELI-NP. The optimal operation of the Monitoring System for Electro-Magnetic Pulse (MSEMP) is the key to establishing the source terms of EMP, the strict control of unwanted conducted and radiated EMP emission, developing of models, and developing of efficient EMP shielding system.

3.12.2 Hardware design and implementation progress

As it is built now, MSEMP is a complete system that can capture up to twelve EMP field waveforms for monitoring and offline analysis. The field sensors are both B-Dot and D-Dot sensors, covering the fre-

quency range from 50 MHz up to 10 GHz. MSEMP has the possibility of simultaneously measuring the electric and magnetic fields. Therefore, it can fully characterize the EMP produced within one target chamber, in a vacuum chamber located in its vicinity, in the experimental area, and outside the experimental area. The system can be controlled either locally from the electronics rack located in the technical corridor or remotely, for instance, by an authenticated user in the ELI-NP control room. At the time of the report, the system is built and installed in the E5 experimental area and is used in the commissioning experiment designed for electron acceleration by using the 1 PW laser beam. The block diagram of the MSEMP is given in Figure 3.12.1.

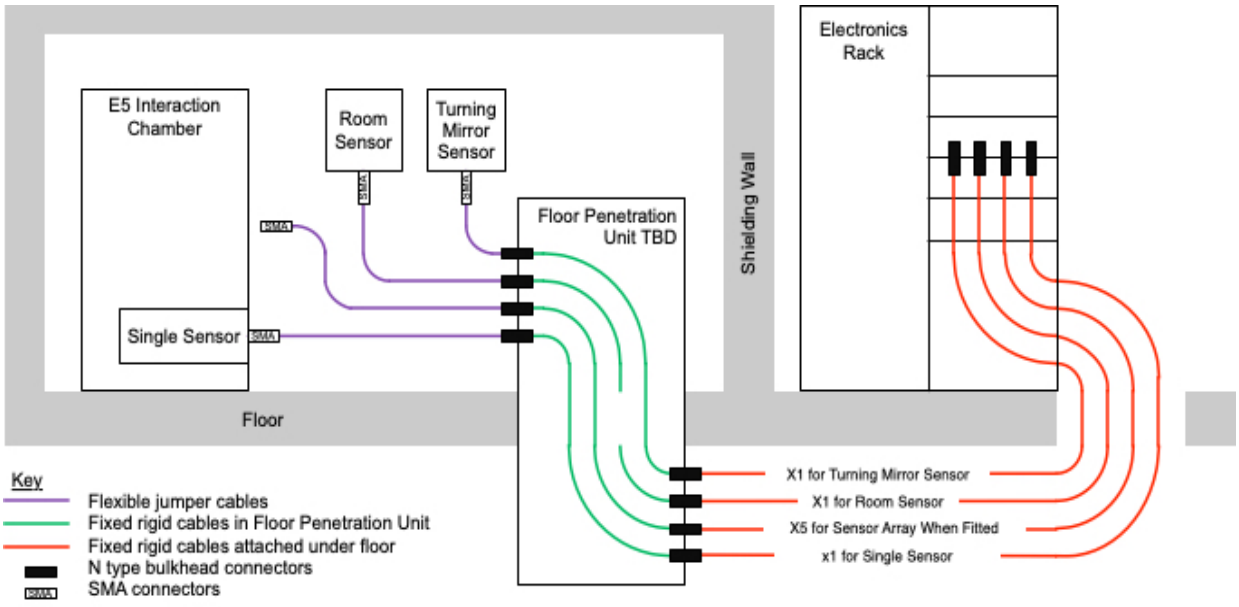

Figure 3.12.1: *The Block diagram of the cabling from the electronic rack to the E5 experimental area.*

3.12.3 Software design and implementation progress

The software design architecture for online analysis and its implementation is completed, including the man-machine interface screens and graphical data display in the time domain. The laser and the other devices used in the experiments are triggered by the clock in the laser oscillator with pulses at 10 Hz. Hence, the timing pulses at 10 Hz (for 100 TW laser), 1 Hz (1 PW) and 1/60 Hz (10 PW) needed to trigger the oscilloscopes before the arrival of the EMP, are available to be used with the time delay generator of the MSEMP system. A LabView application software is now under development, and so far, it enables the MSEMP to operate as an automatic system. The software has the following elements implemented: the man-machine interface, the system configuration, waveform capture process, and waveform archiving (to hold all necessary waveforms and data for offline analysis in files), and will include the offline analysis and the control system interface soon, too. The man-machine interface enables, now, the MSEMP to be controlled by a person using the keyboard and GUI-s (Graphical User Interface), to change from local to remote control and vice versa, to access and view, edit and store the system configuration, to select slow or fast mode capture (the fast mode is not implemented yet), to request start or stop of waveform recording. The system configuration includes all values (sensor data and equipment data) needed to produce calibrated waveforms and frequency spectra from the raw data uploaded from the oscilloscopes. Likewise, the following functions will be implemented soon: access to waveform archive to view graphically and download selected data, access to a history file to view peak EMP histories graphically and run offline analysis. The software running the waveforms capture is considered in the waveform capture cycle and is able, for the moment, to capture up to twelve waveforms when it is triggered at 1 Hz. The slow waveform capture process uses a permanent storage medium for the archive. The file and his name contain all data and required history information needed for offline processing, including the calculation of frequency spectra. The software, as produced, is

tested in the E5 experiment, and the results show that it is working correctly.

3.12.4 Preliminary results for EMP measurements

In the following, we report preliminary results for EMP measurements achieved on only one channel of MSEMP selected from the available 7 channels in the commissioning experiment for ion acceleration, conducted in the E5 experimental area with pulsed (fs) high power (0.9 PW) laser beams. This corresponds to a single probe of the Sensor Array and is a magnetic flux B-dot probe produced by Montena Technology [T22], model SFM2G, with a 3 dB transition frequency at 2 GHz, and 160 ps rise time. The probe was fitted in the E5-C3 vacuum chamber to measure transverse (East-West) magnetic fields and was located under a diagnostic table at the point 0.65 m above the floor, 0.35 m from the sidewall and 0.45 m from the end wall, as shown in Figure 3.12.2.

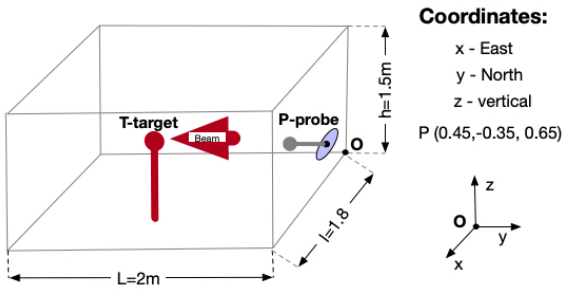

Figure 3.12.2: *EMP measurement configuration in the C3-E5 vacuum chamber.*

Differential signal balancing and common-mode rejection was performed by a BL3-5G balun (balanced to the unbalanced converter) from Montena, having a bandwidth of 500 Hz to 3.5 GHz. The absolute time was taken from the synchronization system of the laser and a photodiode, placed on the light path of the laser far-field diagnostics. The signal from the probe was transported via semirigid cable with subminiature version A connectors to maintain isolation up to 18 GHz. The attenuation of the signals at 1 GHz was 61.48 dB (1185.77 voltage ratio loss). Typical waves taken with a Tektronix oscilloscope, model MSO56, having 1 GHz analog bandwidth and set to sample at 12.5 GHz are shown in Figure 3.12.3. The signal is corrected for attenuation and compensates for cable losses in the frequency domain. The results are typical of those obtained for aluminium targets, with the laser beam energy varying from 21 J to 23 J. The EMP rings transient about 720 ns.

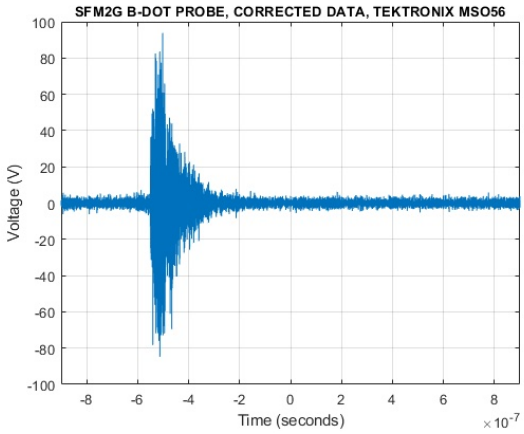

Figure 3.12.3: *Voltage versus time data.*

The waveforms were integrated to give a voltage proportional to the magnetic field and Fourier - transformed to find the frequency spectrum of the magnetic field at the probe head. According to Figure 3.12.4 where the magnetic field strength versus frequency at the probe head is shown, the signal presents harmonics and high-frequency noise, reduced by the integration procedure applied. Our main expectation is that the C3-E5 vacuum chamber acts as a resonator that 'rings' at specific frequencies related to the chamber geometry when excited by an EMP impulse.

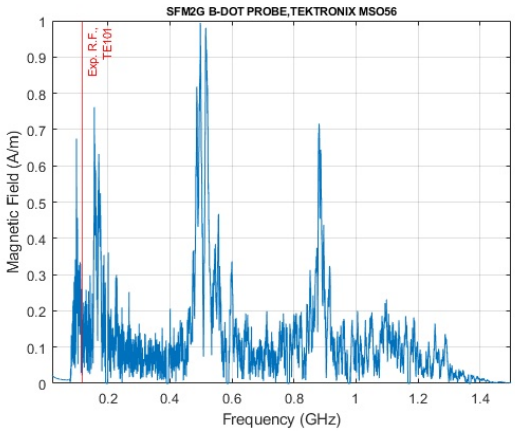

Figure 3.12.4: *The frequency spectrum of the magnetic field probe inside the C3-E5 target chamber. A simulated resonant frequency of the C3-E5 chamber (*116.2 MHz*) is shown in red.*

To estimate the resonance frequency of interest, a simple simulation model for rectangular cavity structure has been performed using the commercial software Comsol Multphyiscs [M22]. The expected field pattern in the interior C3-E5 vacuum chamber corresponds to dominant resonant mode TE_{101} (116.2 MHz) and is shown in Figure 3.12.5.

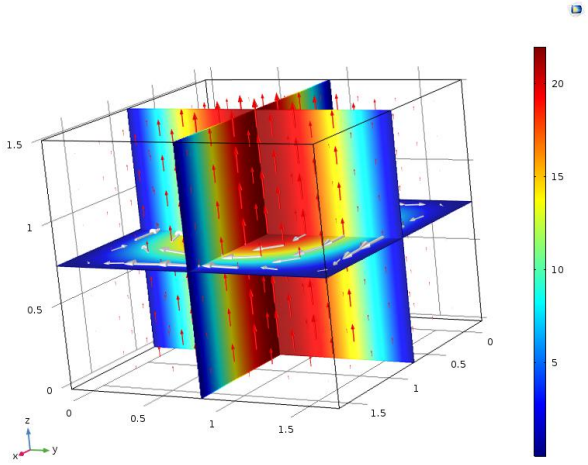

Figure 3.12.5: *Numerical simulation of C3-E5 vacuum chamber as a rectangular cavity. Electric and magnetic fields with TE_{101} (116.2 MHz) mode. Red arrows represent the electric field, and white arrows, the magnetic field.*

Here, the coordinate system is chosen according to the axis indicated in Figure 3.12.2. Figures 3.12.4 and 3.12.5 illustrate the proximity between this simulated resonant frequency TE_{101} and the peaks of the fields excited within the C3-E5 vacuum chamber. The results are satisfactory for the time being, considering that the equipment that populates the C3-E5 vacuum chamber was not included in the simulated model and knowing that their presence is considerably modified by absorptions and reflections of the various traveling modes of oscillation in the chamber resonator.

3.12.5 Conclusion

MSEMP was successfully used in the solid target-laser interaction experiment, performed in August-September in the E5 experimental area, and continues to operate properly in ongoing experiments. Our ultimate goal is to design an optimized version for performing EMP measurements in experiments with the 10 PW laser beams, scheduled soon at ELI-NP. The design of MSEMP will incorporate new ideas obtained during experiments conducted in the E5 area, will consider adding all missing elements and changing the cable routing through the building, and will take into account all the needs to complete the software design. Preliminary results achieved with MSEMP prove that it is a powerful tool for studying the EMP events caused by high-power fs-class lasers with a high repetition rate.

References

[Ede+09] D. C. Eder *et al.* “Mitigation of Electromagnetic Pulse (EMP) Effects from Short-Pulse Lasers and Fusion Neutrons”. In: (2009). DOI: https://doi.org/10.2172/950076 (cited on page 141).

[M22] C. M. “Comsol Multiphysics”. In: (2022). URL: https://www.comsol.com (cited on page 143).

[Mea+04] M. J. Mead *et al.* “Electromagnetic pulse generation within a petawatt laser target chamber”. In: *Review of Scientific Instruments* 75.9 (2004), page 4225. DOI: https://doi.org/10.1063/1.1787606 (cited on page 141).

[Neg+16] F. Negoita *et al.* “Laser driven nuclear physics at ELI-NP”. In: *Romanian Reports in Physics* 68 (2016), S37–S144. URL: http://www.rrp.infim.ro/2016_68_S/S37.pdf (cited on page 141).

[T22] M. T. “Montena Technology”. In: (2022). URL: https://www.montena.com (cited on page 143).

3.13 Peer-reviewed publications, talks, PhD/MSc, & Grants for LDED in 2020-2021

Peer-reviewed publications by LDED staff: 01.01.2020 to 31.12.2021

,

[Abd+20] M. H. M. Abdelrehman *et al.* "Effect of background atmosphere and substrate temperature on SrO:Bi3+(0.2 mol%) thin films produced using pulsed laser deposition with different lasers". In: *Physica B-Condensed Matter* 581 (Mar. 2020). DOI: 10.1016/j.physb.2019.411757.

[Ass+20] R. W. Assmann *et al.* "EuPRAXIA Conceptual Design Report". In: *European Physical Journal-Special Topics* 229.24, SI (Dec. 2020), pages 3675–4284. ISSN: 1951-6355. DOI: 10.1140/epjst/e2020-000127-8.

[Ass+21] R. W. Assmann *et al.* "EuPRAXIA Conceptual Design Report (vol 229, pg 3675, 2020)". In: *European Physical Journal-Special Topics* 229.1, S (Feb. 2021), pages 4285–4287. ISSN: 1951-6355. DOI: 10.1140/epjst/e2021-100018-5.

[Ben+20] J. Benito *et al.* "Detailed spectroscopy of doubly magic Sn-132". In: *Physical Review C* 102.1 (July 2020). ISSN: 2469-9985. DOI: 10.1103/PhysRevC.102.014328.

[Ber+20] T. A. Berry *et al.* "Octupole states in Tl-207 studied through beta decay". In: *Physical Review C* 101.5 (May 2020). ISSN: 2469-9985. DOI: 10.1103/PhysRevC.101.054311.

[BT20] O. Budriga and C. M. Ticos. "Modeling the electron acceleration in relativistic channels for space irradiation applications". In: *Plasma Physics and Controlled Fusion* 62.12 (Dec. 2020). DOI: 10.1088/1361-6587/abb74c.

[Cal+21] S. Calinescu *et al.* "Coulomb and nuclear excitations of Zn-70 and Ni-68 at intermediate energy". In: *Physical Review C* 104.3 (Sept. 2021). ISSN: 2469-9985. DOI: 10.1103/PhysRevC.104.034318.

[Car+20] R. J. Carroll *et al.* "Competition between Allowed and First-Forbidden beta Decay: The Case of Hg-208 -> Tl-2(0)8". In: *Physical Review Letters* 125.19 (Nov. 2020). ISSN: 0031-9007. DOI: 10.1103/PhysRevLett.125.192501.

[Con+20] G. Constantin *et al.* "Cutting Behavior of Al0.6CoCrFeNi High Entropy Alloy". In: *Materials* 13.18 (Sept. 2020). DOI: 10.3390/ma13184181.

[Cra+19] D. Craciun *et al.* "Microstructural investigations of 800 keV Ar ions irradiated nanocrystalline ZrN thin films". In: *Surface Engineering* 36.3 (Sept. 2019), pages 326–333. DOI: 10.1080/02670844.2019.1668677. URL: https://doi.org/10.1080/02670844.2019.1668677.

[Din+20] A. Dinache *et al.* "Spectroscopic Characterization of Emulsions Generated with a New Laser-Assisted Device". In: *Molecules* 25.7 (Apr. 2020). DOI: 10.3390/molecules25071729.

[Dor+20] D. Doria *et al.* "Overview of ELI-NP status and laser commissioning experiments with 1 PW and 10 PW class-lasers". In: *Journal of Instrumentation* 15.9 (Sept. 2020). DOI: 10.1088/1748-0221/15/09/C09053.

[Ghe+21] C. C. Gheorghiu *et al.* "Structuring Free-Standing Foils for Laser-Driven Particle Acceleration Experiments". In: *Frontiers in Physics* 9 (Sept. 2021). DOI: 10.3389/fphy.2021.727498.

[Gir+21] V. Girard-Alcindor *et al.* "Probing nuclear forces beyond the nuclear drip line: the cases of F-16 and F-15". In: *European Physical Journal A* 57.3 (Mar. 2021). ISSN: 1434-6001. DOI: 10.1140/epja/s10050-021-00410-1.

[Giz+20] L. A. Gizzi *et al.* "Intense proton acceleration in ultrarelativistic interaction with nanochannels". In: *Physics Review Research* 2.3 (Sept. 2020). DOI: 10.1103/PhysRevResearch.2.033451.

[Giz+21] L. A. Gizzi *et al.* "Enhanced laser-driven proton acceleration via improved fast electron heating in a controlled pre-plasma". In: *Scientific Reports* 11.1 (July 2021). ISSN: 2045-2322. DOI: 10.1038/s41598-021-93011-3.

[Gro+20] A. Groza *et al.* "Assessment of Angular Spectral Distributions of Laser Accelerated Particles for Simulation of Radiation Dose Map in Target Normal Sheath Acceleration Regime of High Power Laser-Thin Solid Target Interaction-Comparison with Experiments". In: *Applied Sciences-Basel* 10.12 (June 2020). DOI: 10.3390/app10124390.

[Hsu+21] S.-M. Hsu *et al.* "Qualitative Analysis of Remineralization Capabilities of Bioactive Glass (NovaMin) and Fluoride on Hydroxyapatite (HA) Discs: An In Vitro Study". In: *Materials* 14.14 (July 2021), page 3813. DOI: 10.3390/ma14143813. URL: https://doi.org/10.3390/ma14143813.

[Iri+20] S. A. Irimiciuc *et al.* "Multiple structure formation and molecule dynamics in transient plasmas generated by laser ablation of graphite". In: *Spectrochimica Acta Part B-Atomic Spectroscopy* 165 (Mar. 2020). DOI: 10.1016/j.sab.2020.105774.

[Iri+21a] S. A. Irimiciuc *et al.* "In situ optical and electrical analysis of transient plasmas generated by ns-laser ablation for Ag nanostructured film production". In: *Vacuum* 193 (Nov. 2021). DOI: 10.1016/j.vacuum.2021.110528.

[Iri+21b] S. A. Irimiciuc *et al.* "Langmuir Probe Technique for Plasma Characterization during Pulsed Laser Deposition Process". In: *Coatings* 11.7 (July 2021). DOI: 10.3390/coatings11070762.

[Iri+21c] S. A. Irimiciuc *et al.* "On the Dynamics of Transient Plasmas Generated by Nanosecond Laser Ablation of Several Metals". In: *Materials* 14.23 (Nov. 2021), page 7336. DOI: 10.3390/ma14237336. URL: https://doi.org/10.3390/ma14237336.

[Iri+21d] S. A. Irimiciuc *et al.* "Understanding pulsed laser deposition process of copper halides via plasma diagnostics techniques". In: *Journal of Applied Physics* 130.24 (2021), page 243302. DOI: 10.1063/5.0077082.

[Jon+20] S. Jongile *et al.* "Structure of Si-33 and the magicity of the N=20 gap at Z=14". In: *Physical Review C* 102.2 (Aug. 2020). ISSN: 2469-9985. DOI: 10.1103/PhysRevC.102.024321.

[Lab+20] L. Labate *et al.* "Toward an effective use of laser-driven very high energy electrons for radiotherapy: Feasibility assessment of multi-field and intensity modulation irradiation schemes". In: *Scientific Reports* 10.1 (Oct. 2020). ISSN: 2045-2322. DOI: 10.1038/s41598-020-74256-w.

[Lel+21] V. Lelasseux *et al.* "Design and commissioning of a neutron counter adapted to high-intensity laser matter interactions". In: *Review of Scientific Instruments* 92.11 (Nov. 2021). ISSN: 0034-6748. DOI: 10.1063/5.0057828.

[Lop+20] M. Lopez Rios *et al.* "Effects of nickel content on the microstructure, microhardness and corrosion behavior of high-entropy AlCoCrFeNix alloys". In: *Scientific Reports* 10.1 (Dec. 2020). DOI: 10.1038/s41598-020-78108-5.

[Lur+20] F. Lureau *et al.* "High-energy hybrid femtosecond laser system demonstrating 2 x 10 PW capability". In: *High Power Laser Science and Engineering* 8 (Dec. 2020). DOI: 10.1017/hpl.2020.41.

[Mal+21] V. Malinovschi *et al.* "Influence of sodium aluminate concentration and process duration on microstructure, mechanical and electrochemical behavior of PEO coatings formed on CP-Ti". In: *Surface and Coatings Technology* 418 (2021), page 127240. ISSN: 0257-8972. DOI: https://doi.org/10.1016/j.surfcoat.2021.127240. URL: https://www.sciencedirect.com/science/article/pii/S025789722100414X.

[MST20] E. Molnar, D. Stutman, and C. Ticos. "Optimizing direct laser-driven electron acceleration and energy gain at ELI-NP". In: *European Physical Journal D* 74.12 (Dec. 2020). ISSN: 1434-6060. DOI: 10.1140/epjd/e2020-10423-x.

[Ngh+20] P. A. P. Nghiem *et al.* "Toward a plasma-based accelerator at high beam energy with high beam charge and high beam quality". In: *Physical Review Accelerators and Beams* 23.3 (Mar. 2020). ISSN: 2469-9888. DOI: 10.1103/PhysRevAccelBeams.23.031301.

[Ou+20] N. C. Ou *et al.* "Synthesis and Evaluation of Molybdenum Imido-Thiolato Complexes for the Aerosol-Assisted Chemical Vapor Deposition of Nitrogen-Doped Molybdenum Disulfide". In: *Organometallics* 39.7 (Feb. 2020), pages 956–966. DOI: 10.1021/acs.organomet.9b00705. URL: https://doi.org/10.1021/acs.organomet.9b00705.

[Pav+20] E.-M. Pavelescu *et al.* "Influence of electron irradiation and rapid thermal annealing on photoluminescence from GaAsNBi alloys". In: *Applied Physics Letters* 117.14 (Oct. 2020). ISSN: 0003-6951. DOI: 10.1063/5.0027400.

[Per+20] X. Pereira-Lopez *et al.* "Low-lying single-particle structure of C-17 and the N=14 sub-shell closure". In: *Physics Letters B* 811 (Dec. 2020). ISSN: 0370-2693. DOI: 10.1016/j.physletb.2020.135939.

[Pie+21] M. Piersa-Silkowska *et al.* "First beta-decay spectroscopy of In-135 and new beta-decay branches of In-134". In: *Physical Review C* 104.4 (Oct. 2021).

[Pre+21] G. Predoi *et al.* "Preparation and Characterization of Dextran Coated Iron Oxide Nanoparticles Thin Layers". In: *Polymers* 13.14 (July 2021). DOI: 10.3390/polym13142351.

[PGC21] P. Prepelita, F. Garoi, and V. Craciun. "Structural and optical characteristics determined by the sputtering deposition conditions of oxide thin films". In: *Beilstein Journal of Nanotechnology* 12 (Apr. 2021), pages 354–365. DOI: 10.3762/bjnano.12.29.

[Sad+20] A. Sadet *et al.* "Applications of Singlet Order to the Study of Biomolecules and Molecular Interactions". In: *Long-Lived Nuclear Spin Order: Theory and Applications*. Edited by G. Pileio. Volume 22. New Developments in NMR. 2020, pages 248–265.

[Saf+21] N. Safca *et al.* "Perpective on using Talbot-Lau X-ray Phase Contrast Imaging for Atherosclerosis Diagnosis". In: *University Politecnica of Bucharest Scientific Bulletin-Series A-Applied Mathematics and Physics* 83.3 (2021), pages 257–266.

[San+20] D. Sangwan *et al.* "A broad energy range (100 MeV-10 GeV) electron spectrometer for high power laser wakefield acceleration experiments". In: *AIP Advances* 10.5 (May 2020). DOI: 10.1063/5.0001980.

[SPG21] A. N. State, H. Petrascu, and D. G. Ghita. "Experimental set-up for high precision nuclear physics measurements at the IFIN-HH 9MV tandem accelerator". In: *Nuclear Instruments & Methods in Physics Research Section B-Beam Interactions with Materials and Atoms* 499 (July 2021), pages 53–60. DOI: 10.1016/j.nimb.2021.05.002.

[Str+20] M. Stryjczyk *et al.* "Decay studies of the long-lived states in Tl-186". In: *Physical Review C* 102.2 (Aug. 2020). ISSN: 2469-9985. DOI: 10.1103/PhysRevC.102.024322.

[Tan+20] K. A. Tanaka *et al.* "Current status and highlights of the ELI-NP research program". In: *Matter and Radiation at Extremes* 5.2 (Mar. 2020). DOI: 10.1063/1.5093535.

[Tic+21] D. Ticos *et al.* "Rotation of a strongly coupled dust cluster in plasma by the torque of an electron beam". In: *Physicsl Review E* 103.2 (Feb. 2021). ISSN: 2470-0045. DOI: 10.1103/PhysRevE.103.023210.

[Tis+21] B. Tiss *et al.* "The effect of vacuum and air annealing in the physical characteristics and photocatalytic efficiency of In2S3:Ag thin films produced by spray pyrolysis". In: *Materials Chemistry and Physics* 270 (Sept. 2021), page 124838. DOI: 10.1016/j.matchemphys.2021.124838. URL: https://doi.org/10.1016/j.matchemphys.2021.124838.

[Toz+20] T. Tozar *et al.* "Anti-staphylococcal activity and mode of action of thioridazine photoproducts". In: *Scientific Reports* 10.1 (Oct. 2020). DOI: 10.1038/s41598-020-74752-z.

[TST20] S. Tzenov I, K. M. Spohr, and K. A. Tanaka. "Dispersion properties, nonlinear waves and birefringence in classical nonlinear electrodynamics". In: *Journal of Physics Communications* 4.2 (Feb. 2020). DOI: 10.1088/2399-6528/ab72c7.

[VI21] C. V. Vraciu and R. Iovanescu. "Convective Flow of Nanofluid Round Plumes in the Presence of Magnetic Field". In: *Romanian Journal of Physics* 66.5-6 (2021).

[Yao+21] W. Yao *et al.* "Laboratory evidence for proton energization by collisionless shock surfing". In: *Nature Physics* 17.10 (Oct. 2021), pages 1177+. DOI: 10.1038/s41567-021-01325-w.

[Zha+20] N. T. Zhang *et al.* "Constraining the C-12+C-12 astrophysical S-factors with the C-12+C-13 measurements at very low energies". In: *Physics Letters B* 801 (Feb. 2020). DOI: 10.1016/j.physletb.2019.135170.

Invited talks delivered by LDED staff: 01.01.2020 to 31.12.2021

[Dor21a] D. Doria. "Commissioning experiments with the 100 TW and 1 PW lasers at ELI-NP". In: *5th Asia-Pacific Conference on Plasma Physics (AAPPS-DPP2021), 26th of September - 1st of October 2021*. 2021.

[Dor21b] D. Doria. "Laser-driven experiments relevant to the PW areas commissioning". In: *Carpathian Summer School of Physics 2020 - CSSP 2020, Sinaia, Romania, 18th - 27th of August 2021*. 2021.

[Dor21c] D. Doria. "Recent progress on ELI-NP facility implementation". In: *8th ELI-ALPS User Workshop, Szeged, Hungary, 8th - 9th of November 2021*. 2021.

[Dor21d] D. Doria. "Recent progress on ELI-NP facility implementation". In: *47th Conference on Plasma Physics - Satellite Meeting, Online, 28th - 29th of June 2021*. 2021.

[Măg21] A. Măgureanu. "Targets used in laser-driven proton acceleration based on TNSA mechanism". In: *Carpathian Summer School of Physics 2020 - CSSP 2020, Sinaia, Romania, 18th - 27th of August 2021*. 2021.

[Spo21a] K. M. Spohr. "Laser-plasma triggered production and release of the 2.4 MeV isomer in ^{93m}Mo, towards a Nuclear Battery". In: *3rd International Conference on Nuclear Photonics 2020, Kurashiki, Japan, 7th-11th of June 2021*. 2021.

[Spo21b] K. M. Spohr. "Nuclear Physics with High Power Lasers". In: *ELI Summer School 2021 (ELISS 2021) - ELI Beamlines, Prague, Czech Republic, Online, 24th to 27th of August 2021*. 2021.

[Spo21c] K. M. Spohr. "Nuclear Physics with the High Power Laser Systems at ELI-NP". In: *Workshop on Nuclear Photonics and Research Opportunities at ELI-NP, Bucharest–Măgurele, Romania, Online, 9th of September 2021*. 2021.

[Tom21] P. Tomassini. "High-quality axially symmetric electron beams generation with multi-pulse ionization injection schemes". In: *47th EPS conference on Plasma Physics*. 2021.

Successful PhD projects within the LDED group: 01.01.2020 to 31.12.2021

[Pop20] D. Popescu. "Contributions on the operational optimization of complex research infrastructures". PhD thesis. The University Politehnica of Bucharest, 2020.

[Tud20] L. Tudor. "Methods for Characterization of Particle Pulses Generated by High Power Laser Interaction with Matter". PhD thesis. The University Politehnica of Bucharest, 2020.

External Grant generation by members of the LDED group as PI: 01.01.2020 to 31.21.2021

[Cra20] V. Craicun. "ELI_04: In-situ real-time Langmuir probe and target current investigations of fs-laser irradiated optical components and targets, (1,000,000 Lei)". In: *ELI-RO* (Oct. 2020).

[Dor20] D. Doria. "ELI_10: Investigation of laser-driven gamma burst (1,000,000 Lei)". In: *ELI-RO* (Oct. 2020).

[FB20] J. Fuchs and S. Balascuta. "ELI_11: Coherent Transition Radiation imaging of the High Intensity Focused Laser Pulse (991275 Lei)". In: *ELI-RO* (Oct. 2020).

[Gug20] M. Gugiu. "ELI_02: Development of a measurement and monitoring system for EMP at ELI-NP, (1,087,500 Lei)". In: *ELI-RO* (Oct. 2020).

[Spo20a] K. M. Spohr. "ELI_12: Laser-plasma triggered release of the 2.4 MeV isomer in ^{93m}Mo using the 1 PW system at ELI-NP (1,000,000 Lei)". In: *ELI-RO* (Oct. 2020).

[Spo20b] K. M. Spohr. "PN-III-P2-2.1-PED-2019-2325: Preclinical studies of immuno-oncology in combination with intense particle beams at the ELI-NP facility to enhance boron neutron capture therapy (BNCT) (600,000 Lei)". In: *PED* (Nov. 2020).

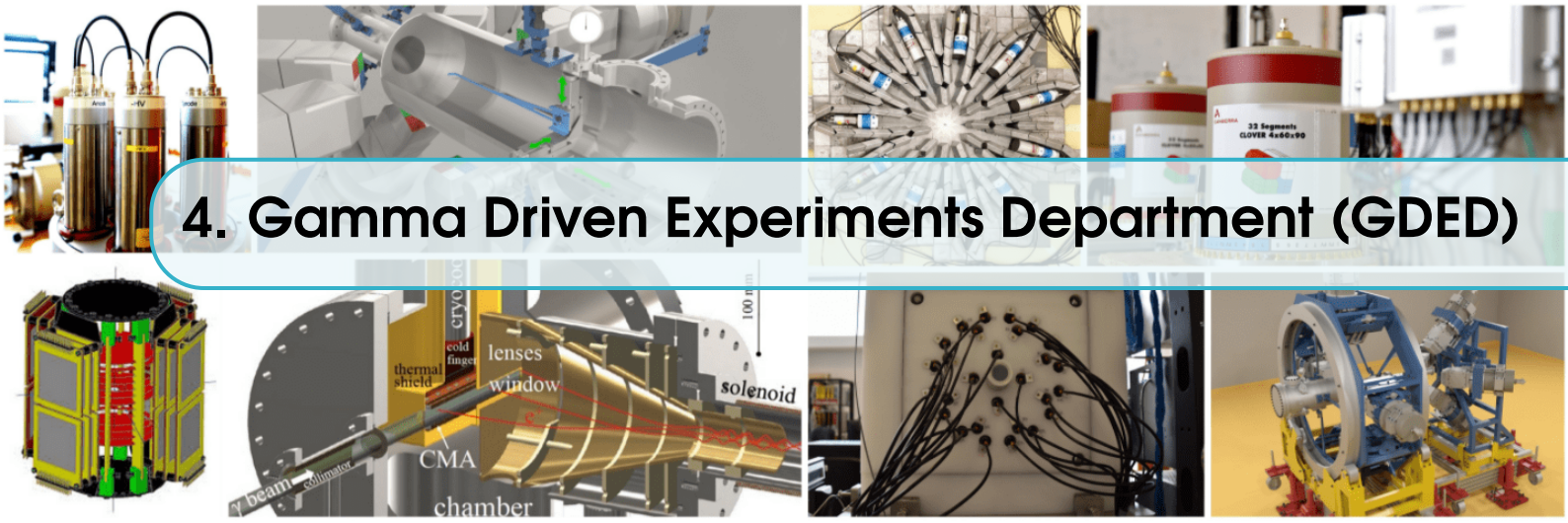

4. Gamma Driven Experiments Department (GDED)

THE GAMMA DRIVEN EXPERIMENTS DEPARTMENT at ELI-NP faced the implementation of several main tasks in 2020/21. These tasks were related to the implementation of the experimental setups for the γ-beam at ELI-NP, which included the assembling and testing of the performance of the individual detectors and of the detector arrays. Parallel to this, the team was involved, together with the international nuclear photonics community, in defining the commissioning and day-one experiments at the VEGA facility, as well as we were preparing the ambitious in-house research program. The team members continued collaborating and established new collaborations with different research groups from all over the globe. We continued to be an active part of the international research community by participating remotely in studies in different laboratories, analyzing data, participating in conferences and other scientific events, and publishing the experimental results. The members of the GDED team published about 80 papers in peer-refereed international journals and in conference proceedings and gave 35 invited and contributed talks. The main achievements of the GDED team related to the preparation of the experimental setups at ELI-NP in the reported period are the source characterization and commissioning of the ELIGANT-GN array (see [Söd+22] and the reports of P.-A. Söderström *et al.* and A. Gutoiu *et al.*), the advance towards full implementation of the ELIADE array (see [Cap+21] and the reports of D. Testov *et al.*, F. Zhu *et al.* and A. Dhal *et al.*), the construction of the positron beamline (see the report of N. Djourelov *et al.*), the simulation of the VEGA γ beam (see the report of P. Constantin) and the implementation of the DELILA data acquisition system (see the report of S. Aogaki *et al.*).

In addition, the GDED team has prepared, in collaboration with colleagues from the IFIN-HH DNP department, an experimental campaign with the ELI-NP large-volume $CeBr_3$ and $LaBr_3$(Ce) detectors coupled to the ROSPHERE at the IFIN-HH 9 MV tandem accelerator, the ELIFANT array (see the report of P.-A. Söderström *et al.*). The experiments within this campaign will be carried out in the period January-June 2022. The DELILA DAQ will be used for data processing.

In preparation for in-house experiments at ELI-NP, the GDED team has achieved a number of key physics results in the reported period. It is worth mentioning the determination of the electromagnetic character of the $\gamma\gamma/\gamma$ decay in ^{137}Ba from an in-house measurement, which was published in Nature Communications [Söd+20], the measurement of the ^{7}Li$(\gamma,t)^{4}$He ground-state cross-section between $E_\gamma = 4.4$ MeV and 10 MeV obtained in an experiment carried at the HIγS FEL facility at Duke University [Mun+20], the effective atomic number evaluation using quasi-monoenergetic γ rays and neural networks [Tur+20], the development of NRF algorithms for cargo inspection [Lan+21; TIU21], the optimization of the positron moderation in a magnetic bottle [DS21], the simulation of first experimental setups for in-cell studies of multinucleon transfer reactions [Spa+20], to list only a few. Members of the GDED team performed theoretical studies related to, *e.g.*, microscopic structure of the pigmy dipole resonance (see [Spi+20; Wei+21] and the reports of N. Tsoneva *et al.*, systematic studies of E1 strength function [XGK21].

In conclusion, the GDED team successfully met the challenge of the medical crisis in the last two years and moved towards the finalization of the implementation of the foreseen experimental setups at ELI-NP. The parameters of the γ beam were simulated, and the team worked towards the preparation of commissioning and the first experiments at the VEGA *gamma*−beam system. In addition, the team prepared the ELIFANT array for experiments at the IFIN-HH 9 MV tandem and is active in obtaining key physics results at different laboratories around the world.

References

[Cap+21] L. Capponi *et al.* "First in-beam experiment with the ELIADE detectors: a spectroscopic study of ^{130}La". In: *J. Instrum.* 16 (2021), T12001. DOI: https://doi.org/10.1088/1748-0221/16/12/T12001 (cited on page 151).

[DS21] N. Djourelov and A. Serban. "Optimization of a device for positron moderation based on a magnetic bottle". In: *Nuclear Instruments and Methods in Physics Research Section A: Accelerators, Spectrometers, Detectors and Associated Equipment* 1014 (2021), page 165699. ISSN: 0168-9002. DOI: https://doi.org/10.1016/j.nima.2021.165699. URL: https://www.sciencedirect.com/science/article/pii/S0168900221006847 (cited on page 151).

[Lan+21] H. Lan *et al.* "Nuclear resonance fluorescence drug inspection". In: *Scientific Reports* 11.1 (2021), page 1306. DOI: 10.1038/s41598-020-80079-6. URL: https://doi.org/10.1038/s41598-020-80079-6 (cited on page 151).

[Mun+20] M. Munch *et al.* "Measurement of the ^{7}Li$(\gamma,t)^{4}$He ground-state cross section between $E_\gamma = 4.4$ and 10 MeV". In: *Phys. Rev. C* 101 (5 May 2020), page 055801. DOI: 10.1103/PhysRevC.101.055801. URL: https://link.aps.org/doi/10.1103/PhysRevC.101.055801 (cited on page 151).

[Söd+20] P.-A. Söderström *et al.* "Electromagnetic character of the competitive $\gamma\gamma/\gamma$-decay from ^{137m}Ba". In: *Nature Communications* 11.1 (2020), page 3242. DOI: 10.1038/s41467-020-16787-4. URL: https://doi.org/10.1038/s41467-020-16787-4 (cited on page 151).

[Söd+22] P.-A. Söderström *et al. ELIGANT-GN – ELI Gamma Above Neutron Threshold: The Gamma-Neutron setup*. Nucl. Instrum. Methods Phys. Res. A, in print. 2022 (cited on page 151).

[Spa+20] A. Spataru *et al.* "Production of Exotic Nuclei via MNT Reactions Using Gas Cells". In: *Acta Phys. Pol.* 51 (2020), page 807. DOI: https://doi.org/10.5506/APhysPolB.51.817 (cited on page 151).

[Spi+20] M. Spieker *et al.* "Accessing the single-particle structure of the Pygmy Dipole Resonance in ^{208}Pb". In: *Phys. Rev. Lett.* 125 (2020), page 102503 (cited on page 151).

[Tur+20] G. V. Turturica *et al.* "Effective Z evaluation using monoenergetic gamma rays and neural networks". In: *Eur. Phys. J. Plus* 135 (2020), page 140 (cited on page 151).

[TIU21] G. Turturica, V. Iancu, and C. Ur. "A neural-network based approach to cargo inspections using photon spectroscopy". In: *Nuclear Instruments and Methods in Physics Research Section A: Accelerators, Spectrometers, Detectors and Associated Equipment* 1010 (2021), page 165553. ISSN: 0168-9002. DOI: https://doi.org/10.1016/j.nima.2021.165553. URL: https://www.sciencedirect.com/science/article/pii/S0168900221005386 (cited on page 151).

[Wei+21] M. Weinert *et al.* "Microscopic Structure of the Low-Energy Electric Dipole Response of ^{120}Sn". In: *Phys. Rev. Lett.* 127 (2021), page 242501 (cited on page 151).

[XGK21] Y. Xu, S. Goriely, and E. Khan. "Systematical studies of the $E1$ photon strength functions combining the Skyrme-Hartree-Fock-Bogoliubov plus quasiparticle random-phase approximation model and experimental giant dipole resonance properties". In: *Phys. Rev. C* 104 (4 Oct. 2021), page 044301. DOI: 10.1103/PhysRevC.104.044301. URL: https://link.aps.org/doi/10.1103/PhysRevC.104.044301 (cited on page 151).


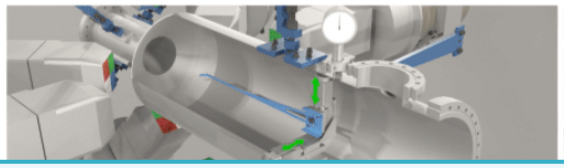

Experiments at GDED

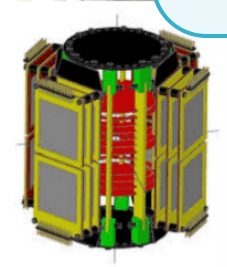
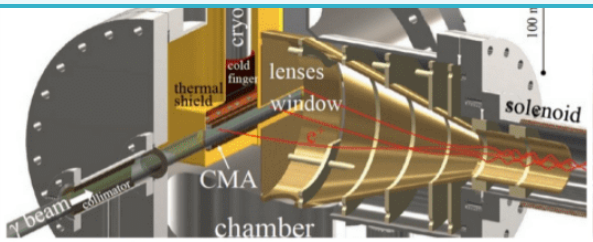

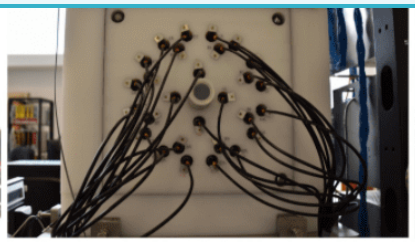
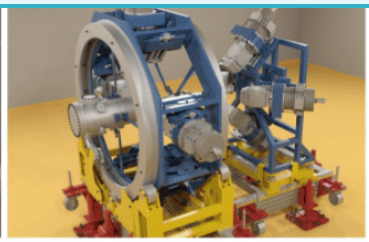

4.1 Neutron correlations following spontaneous fission of ^{252}Cf during the ELIGANT-GN source commissioning

Söderström P.A.[1*] Cuciuc M.[1], Balabanski D. L.[1], and Xu Y.[1]

[1] Extreme Light Infrastructure (ELI-NP) & Horia Hulubei National Institute for R&D in Physics and Nuclear Engineering (IFIN-HH), Str. Reactorului No. 30, 077125 Bucharest–Măgurele, Romania

[*] **par.anders@eli-np.ro**

Abstract

In this report, we will present the first physics results and the current status of the analysis of the data collected during the first source commissioning of ELIGANT-GN using a ^{252}Cf source. We show some basic as well as more complex neutron correlations, as well as γ-ray spectra. These results are compared with the theoretical results from the FREYA and TALYS codes.

4.1.1 Introduction

Correlations between observables are one of the fundaments on which the entire scientific body of knowledge in nuclear physics is built. A significant fraction of our understanding of nuclear structure physics originates from measurements of correlations between observables like energy, time, or angle between combinations of γ-rays, particles, and ions. One recent example of the importance of correlations in nuclear fission is the observation of correlations between the populations of how excited nuclear states of different angular momentum and how this information can be used to gain insights into the primary mechanism behind the generation of nuclear angular momentum in the fission process [Wil+21]. The importance and impact on this type of information are clear from the debate regarding the implication of these measurements that was sparked following the publication of the previously cited data [Kaw+21; Mar+21; RV21; Ste+21].

During the source commissioning of the ELIGANT-GN [Cam+16; Krz+19; Söd+22] setup at ELI-NP, a setup specifically designed for correlation measurements in photonuclear reactions, a large set of data was collected using a ^{252}Cf source. Due to many detectors of different types and the resulting high efficiency and sizeable angular coverage, this data set allows us a unique possibility to explore more subtle properties of nuclear fission through the correlation of observables.

4.1.2 FREYA

The results obtained here will be discussed within the context of the FREYA fission model [VRV18], developed at Lawrence Livermore National Laboratory for fast generation of complete fission events. Given an isotope of a fissionable nucleus, complete kinematic information of both fission fragments and neutrons and γ rays emitted in the process is generated from either spontaneous fission or neutron-induced fission.

The basic outline of the procedure within the FREYA model is as follows: For each event in FREYA, the fission fragments are determined from the sampling of the known yields, the fission Q-value for the event is calculated, and the energy is transferred into kinetic energy and excitation energy of the fission fragments. The most recent results on fission yields of ^{252}Cf used by FREYA is from Reference [GHV14]. Once the masses, angles, and energies of the fission fragments have been obtained, the de-excitation of the fission fragments is assumed to proceed linearly according to the sequence neutron evaporation, statistical γ-ray emission, and γ-ray emission from discreet states, as shown in Figure 4.1.1.

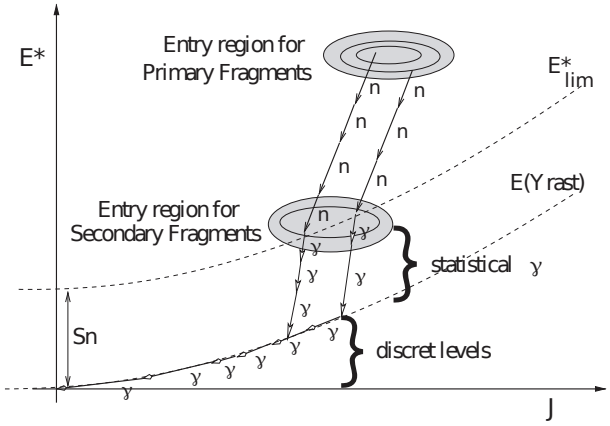

Figure 4.1.1: *Principle of the de-excitation of fission fragments in FREYA depending on fragment spin, J, and excitation energy, E^*. S_n denotes the neutron separation energy. From Reference [LS10].*

For the results reported here, $3 \cdot 10^7$ fission events were generated, corresponding to approximately 5 minutes of ^{252}Cf decay with an activity of 3.7 MBq. Assuming an average singles efficiency of 1% for neutron and γ-ray detectors, the same statistics, as reported here, translates to 7 hours for detected multiplicity one events. The expected statistics in all the higher multiplicity events should be scaled accordingly.

4.1.3 Measurements

One of the two main components of ELIGANT-GN is the array of $LaBr_3$:Ce and $CeBr_3$ detectors intended to, with the future γ-ray beam, detect γ-ray de-excitation of high-energy states, for example, the giant dipole resonance. For this report, however, we are mainly interested in continuous γ-ray spectra, partially for generating fission triggers, but partially to look at the γ-decay properties of the fission fragments via prompt fission γ-ray spectra and how these correlate with a selection of neutron observables. For a more detailed overview of the photon distribution in FREYA, see Reference [VR17].

With the absence of a dedicated fission-fragment detector, the first role of the γ-ray detectors in this commissioning experiment is to distinguish the fission events from other types of decay and ambient room background. As ^{252}Cf only has a fission branching ratio of 3.09%, other γ rays associated with α decay of ^{252}Cf and its daughters can be emitted. However, this type of event will typically have a very low γ-ray multiplicity and low excitation energy. On the other hand, fission events will be of the opposite type, with high multiplicity and high energy released. Thus, using ELIGANT-GN as a γ-ray calorimeter, distributions based on total energy and total multiplicity can be produced for a clean selection of fission events [Söd+22].

The sources used in this commissioning were the standard low-energy γ-ray sources ^{60}Co, ^{137}Cs, and ^{152}Eu, for low-energy γ-ray calibrations. For high-energy γ-ray calibrations and neutron cross-talk characterization, a PuBe source [Söd+21] was used. The fission data was collected using a ^{252}Cf source with an activity of 3.2 MBq at the time of measurement. The calculated activity composition of the Cf source at the time of measurements, based on the mass composition from the production, was 0.2% of ^{249}Cf, 6.7% ^{250}Cf, 0.04% ^{251}Cf, and 93% ^{252}Cf. In total, the ^{252}Cf data consists of 11 days of active data taking, periodically interrupted for regular recalibrations and alignments.

4.1.4 Preliminary results

One of the first quantities of interest to examine in these measurements is the prompt fission γ-ray spectrum in the $LaBr_3$:Ce and $CeBr_3$ detectors. Besides the physics interest of this spectrum, its properties will provide information on the quality of both the fission trigger, the energy calibrations, and the GEANT4 simulations. An example of such a spectrum, without any selection on neutron multiplicity or similar, is shown in Figure 4.1.2 compared both to FREYA calculations, the TALYS [KHD08; KR12] statistical code, and previously published data [Obe+15]. The spectrum has already been calibrated and unfolded, where the procedure used for simulation and unfolding is identical to the one outlined in reference [Söd+19].

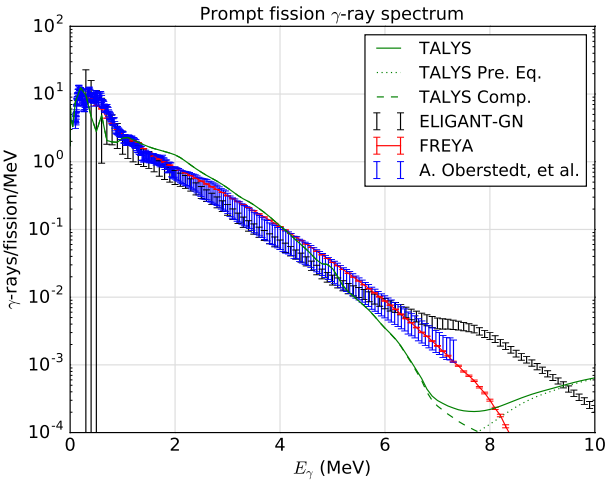

Figure 4.1.2: *Prompt fission γ-ray spectrum from ELIGANT-GN, compared to FREYA spontaneous fission calculations, TALYS photo-fission calculations separated into pre-equilibrium and compound components, and the results by Oberstedt, et al. [Obe+15].*

Interestingly, the general absolute distribution and the slope of the distribution agree well with both calculations and previously published data, providing confidence that the quality of the data collecting and sorting procedures is reasonable. Another interesting aspect to note is the appearance of a structure just out of reach from the previous measurement that the theory code FREYA does not reproduce. While the origin of this structure can not be determined, it can be investigated more in detail from the influence of, for example, neutron multiplicity and neutron- and γ-ray angular correlations.

Another essential aspect to verify is the quality of the neutron angular-correlation reconstruction. The impact of bad cross-talk rejection, time alignment, and efficiency estimation that can significantly

influence other correlation measurements would be evident in this case. Such an angular correlation function, $W(\theta)$, between two neutrons with relative angle $\theta_{1,2}$ is shown in Figure 4.1.3, compared with FREYA calculations and previous data from [Sch+19]. In our work and the FREYA calculations, an additional condition was applied to the data, that the neutron energies should be equal for both neutrons, $E_1 = E_2$. The reason for this condition is that the neutron energies are reconstructed using time-of-flight, and by requiring a time-difference of less than 11 ns between two neutrons, all detector cross-talk could be eliminated. However, for the separate neutrons to arrive at the detector within the time interval, however, requires both neutrons to have the same energy.

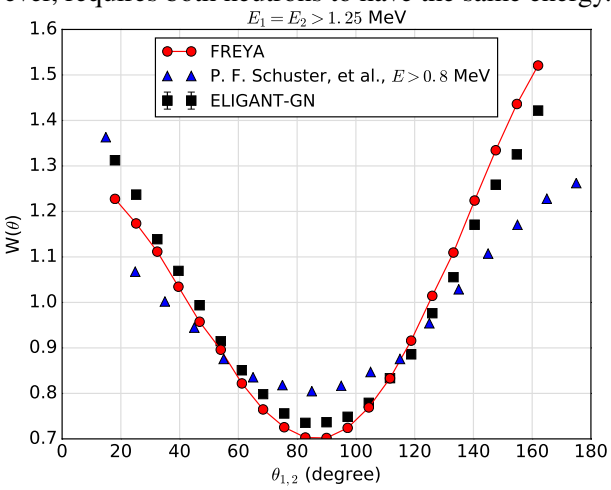

Figure 4.1.3: *Neutron angular correlations from ELIGANT-GN, FREYA calculations, and the results by Schuster, et al. [Sch+19].*

The results from our measurements show excellent agreement with the FREYA calculations. There was a minor discrepancy between our data and the data from [Sch+19], which could be explained by the relatively large energy threshold implemented in this work. It was shown in [Sch+19] that the angular correlations become flatter at lower minimum energies while the slope increases with energy.

With the previously known data reproduced, we can also examine previously not measured correlations. As ELIGANT-GN consists of both liquid scintillators for high-energy neutron detection and lithium-glass scintillators for low-energy neutron detection, it can be interesting to look at the angular correlations between high-energy and low-energy neutrons. While the uncertainties are more significant due to the lower yield and the lower efficiency in the low-energy neutron region, a trend is clear, significantly more asymmetric than the high-energy neutron correlations, and FREYA well reproduces it. Such a distribution is shown in Figure 4.1.4.

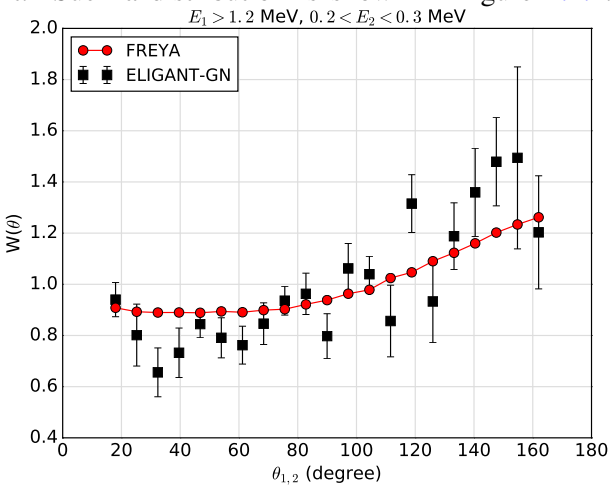

Figure 4.1.4: *Neutron angular correlations between high-energy and low-energy neutrons from ELIGANT-GN and FREYA calculations.*

With the high statistics from the large efficiency of the ELIGANT-GN array together with the large granularity, one can take the correlation spectra one step further and look at the three-neutron angular correlations. This can be a useful way to probe the distribution of the neutron emission between the different fission fragments. Given that the neutrons emitted isotropically in the center-of-mass system are given a kinetic energy boost in the direction of the fission fragment, we expect three neutrons from the same fragment to all have small angles, $\theta_{1,2}$, $\theta_{1,3}$, and $\theta_{2,3}$, relative to each other.

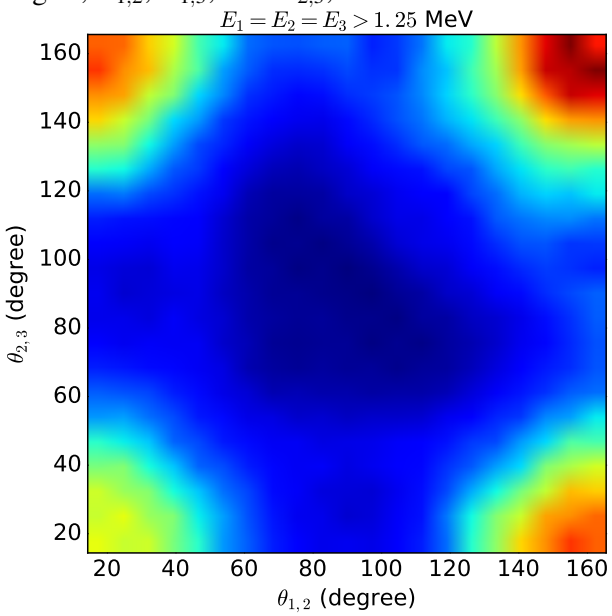

Figure 4.1.5: *Three-neutron angular correlations in from ELIGANT-GN.*

If one of the neutrons originates from the other fragment, with a momentum direction back-to-back rela-

tive to the partner fragment, we expect these neutrons to be boosted in the opposite direction with the consequence that two of the angles $\theta_{1,2}$, $\theta_{1,3}$, and $\theta_{2,3}$ being large with only one of these angles remaining small. Thus, by assigning the neutrons in a three-neutron event randomly to an index and comparing two of these three angles to each other, we expect to get an indication of how large a fraction of the higher multiplicity neutron-emission events is dominated by emission from a single fragment, and how large fraction correspond to evenly distributed neutron emission. Such a distribution is shown in Figure 4.1.5. Also, this distribution is well reproduced by FREYA, both qualitatively and quantitatively, and can be used for further evaluation of the decay process of the primary fission fragments.

Another interesting aspect of the three-neutron correlation data is the neutron anisotropy related to the angular momentum vector. This topic has been discussed, for example, in Reference [Chi+18], from which also Figure 4.1.6 is adapted.

Under this assumption, we can look at the three-neutron correlated events. By randomly selecting two neutrons in directions, $\vec{\Theta}_1 = (\theta_1, \phi_1)$ and $\vec{\Theta}_2 = (\theta_2, \phi_2)$, at approximately 90° emission relative to each other, $\theta_{1,2}$, we can define the neutron emission plane where the fission axis should lie and the spin vector, $\vec{J} = \vec{\Theta}_1 \times \vec{\Theta}_2$, to be perpendicular to this plane. In this way, we can test the assumption by taking the angle between the third neutron, $\vec{\Theta}_n = (\theta_n, \phi_n)$, and the assumed spin vector, $\theta_{n,J}$. In the case of extreme correlation, the third neutron should be emitted precisely at 90° relative to the assumed spin vector. The third neutron should be isotropic relative to the assumed spin vector in the other limit of no correlation.

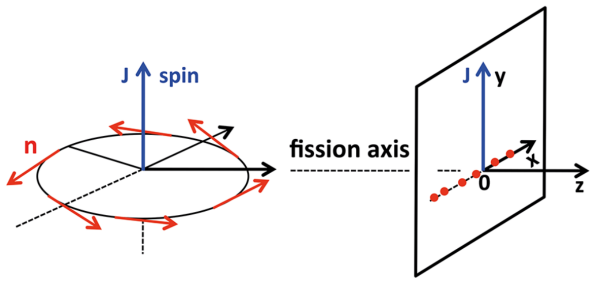

Figure 4.1.6: *Assumed extreme anisotropy in the center-of-mass of the fission fragment. Figure adapted from Reference [Chi+18].*

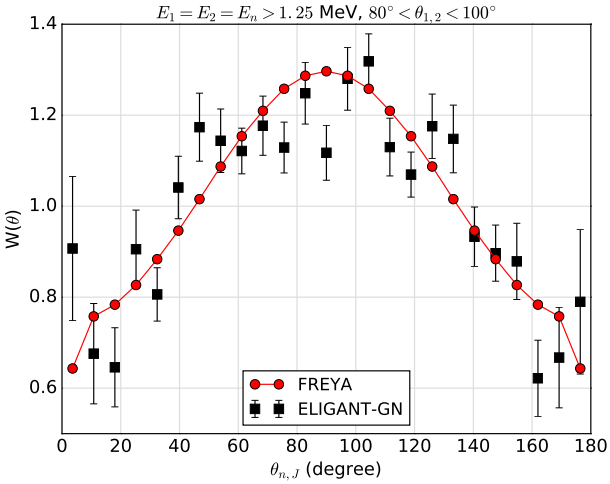

Figure 4.1.7: *Angular correlations in the three-neutron emission events between the third neutron and the assumed spin vector $\vec{J}$, where two neutrons approximately emitted at 90° relative to each other have been used to define the spin vectur under the assumption of extreme anisotropy.*

Such a distribution of the third neutron relative to the assumed spin vector is shown in Figure 4.1.7, together with the corresponding FREYA calculations. Indeed, even these rather complex neutron correlations are well reproduced by the FREYA code. These results are promising for further investigations of neutron and γ-ray correlations using the ELIGANT-GN data collected during the first source commissioning.

4.1.5 Outlook

Based on these preliminary results, the quality of the collected data looks promising for a deeper investigation of a large number of possible correlation observables. In addition to the angular correlations discussed here, one can also investigate the correlation in the energy spectra. From the successful reconstruction of the angular momentum vector, it would be exciting to investigate the prompt-fission γ-rays relative to this observable, as it could offer the opportunity to extract multipolarity distributions, particularly in the region of the unexpected high-energy structure presented here.

References

[Cam+16] F. Camera *et al.* "Gamma above the neutron threshold experiments at ELI-NP". In: *Rom. Rep. Phys.* 68 (2016), S539 (cited on page 155).

[Chi+18] A. Chietera *et al.* "Angular correlations in the prompt neutron emission of spontaneous fission of ^{252}Cf". In: *Eur. Phys. J. A* 54 (2018), page 98 (cited on page 158).

[GHV14] A. Göök, F.-J. Hambsch, and M. Vidali. "Prompt neutron multiplicity in correlation with fragments from spontaneous fission of ^{252}Cf". In: *Phys. Rev. C* 90 (2014), page 064611 (cited on page 155).

[Kaw+21] T. Kawano *et al.* "Influence of nonstatistical properties in nuclear structure on emission of prompt fission neutrons". In: *Phys. Rev. C* 104 (2021), page 014611 (cited on page 155).

[KHD08] A. J. Koning, S. Hilaire, and M. C. Duijvestijn. "TALYS-1.0". In: *Proceedings of the International Conference on Nuclear Data for Science and Technology*. Edited by O. Bersillon *et al.* Volume 211. EDP Sciences, 2008, page 058 (cited on page 156).

[KR12] A. J. Koning and D. Rochman. "Modern Nuclear Data Evaluation with the TALYS Code System". In: *Nucl. Data Sheets* 113 (2012), page 2841 (cited on page 156).

[Krz+19] M. Krzysiek *et al.* "Simulation of the ELIGANT-GN array performances at ELI-NP for gamma beam energies larger than neutron threshold". In: *Nucl. Instrum. Methods Phys. Res. A* 916 (2019), page 257 (cited on page 155).

[LS10] O. Litaize and O. Serot. "Investigation of phenomenological models for the Monte Carlo simulation of the prompt fission neutron and γ emission". In: *Phys. Rev. C* 82 (2010), page 054616 (cited on page 155).

[Mar+21] P. Marević *et al.* "Angular momentum of fission fragments from microscopic theory". In: *Phys. Rev. C* 104 (2021), page L021601 (cited on page 155).

[Obe+15] A. Oberstedt *et al.* "Impact of low-energy photons on the characteristics of prompt fission γ-ray spectra". In: *Phys. Rev. C* 92 (2015), page 014618 (cited on page 156).

[RV21] J. Randrup and R. Vogt. "Generation of Fragment Angular Momentum in Fission". In: *Phys. Rev. Lett.* 127 (2021), page 062502 (cited on page 155).

[Sch+19] P. F. Schuster *et al.* "High resolution measurement of tagged two-neutron energy and angle correlations in ^{252}Cf(sf)". In: *Phys. Rev. C* 100 (2019), page 014605 (cited on page 157).

[Söd+19] P.-A. Söderström *et al.* "High-Resolution Gamma-ray Spectroscopy with ELIADE at the Extreme Light Infrastructure". In: *Acta Physica Polonica B* 50 (2019), page 329. URL: https://www.actaphys.uj.edu.pl/R/50/3/329/pdf (cited on page 156).

[Söd+21] P.-A. Söderström *et al.* "Characterization of a plutonium–beryllium neutron source". In: *Applied Radiation and Isotopes* 167 (2021), page 109441. ISSN: 0969-8043. DOI: https://doi.org/10.1016/j.apradiso.2020.109441. URL: https://www.sciencedirect.com/science/article/pii/S0969804320305832 (cited on page 156).

[Söd+22] P.-A. Söderström *et al. ELIGANT-GN – ELI Gamma Above Neutron Threshold: The Gamma-Neutron setup*. Nucl. Instrum. Methods Phys. Res. A, in print. 2022 (cited on pages 155, 156).

[Ste+21] I. Stetcu *et al.* "Angular Momentum Removal by Neutron and γ-Ray Emissions during Fission Fragment Decays". In: *Phys. Rev. Lett.* 127 (2021), page 222502 (cited on page 155).

[VRV18] J. M. Verbeke, J. Randrup, and R. Vogt. "Fission Reaction Event Yield Algorithm FREYA 2.0.2". In: *Comput. Phys. Commun.* 222 (2018), page 263 (cited on page 155).

[VR17] R. Vogt and J. Randrup. "Improved modeling of photon observables with the event-by-event fission model FREYA". In: *Phys. Rev. C* 96 (2017), page 064620 (cited on page 156).

[Wil+21] J. N. Wilson *et al.* “Angular momentum generation in nuclear fission”. In: *Nature* 590 (2021), page 566 (cited on page 155).

4.2 Preparation of a joint experimental campaign using ELI-NP detectors at ROSPHERE at IFIN-HH

Aogaki S.[1], Balabanski D. L.[1], Borcea R.[2], Ciocan G.[1], Constantin P.[1], Costache C.[2], Cuciuc M.[1], Filipescu D. M.[2], Kuşoğlu A.[3], Mărginean N.[2], Mihai C.[2], Nichita D.[1], Roman T.[1], Rotaru A.[1], Serban A. B.[1], Spataru A.[1], Stan L.[2], State A.[1], Söderström P.A.[1,*] Testov D.[1], Turturică A.[2], Turturică G.[1], Ujeniuc S.[2], Ur C. A.[1], and Vasilca V.[1]

[1] Extreme Light Infrastructure (ELI-NP) & Horia Hulubei National Institute for R&D in Physics and Nuclear Engineering (IFIN-HH), Str. Reactorului No. 30, 077125 Bucharest–Măgurele, Romania
[2] Horia Hulubei National Institute for R&D in Physics and Nuclear Engineering (IFIN-HH), Str. Reactorului No. 30, 077125 Bucharest–Măgurele, Romania
[3] Department of Physics, Faculty of Science, Istanbul University, Vezneciler/Fatih, 34134, Istanbul, Turkey

[*] **par.anders@eli-np.ro**

Abstract

In this report we present the installation and the first tests of the ELI-NP large volume $LaBr_3$:Ce and $CeBr_3$ detectors from ELIGANT, ELIADE, and Beam Diagnostics in the ROSPHERE setup at the 9 MV Tandem facility in IFIN-HH.

4.2.1 Introduction

For the autumn 2021 Program Advisory Committee of the nuclear physics department at IFIN-HH, experimental proposals aiming at merging the existing large-volume $LaBr_3$:Ce and $CeBr_3$ detectors from ELI-NP with the 9 MV Tandem accelerator complex and the ROSPHERE mechanical structure and anti-Compton shields were discussed. The main idea is to place the detectors from ELIGANT-GN [Cam+16; Krz+19; Söd+22], ELIADE [Ur+16], and Beam Diagnostics [Wel+16] in the ROSPHERE [Buc+16] mechanical structure, including the anti-Compton shields, for an array with high efficiency and low background in the high-energy γ-ray region. The plans were well received, and several groups from Romania and abroad got beam-time assigned for various physics cases. These experiments are now scheduled for a long campaign in spring 2022. In particular, the following experimental topics are approved and expected to run:

- A. Y. Deo, *et al. Alpha Clustering in* ^{213}At
- *A. Oberstedt, A. Dragic et al. The* $^{72}Ge(p,p'\gamma)$ *reaction – cross-section and* $\gamma\gamma$ *decay measurements*
- *B. Million, F. Camera, et al. Position-Sensitivity in large volume* $LaBr_3$*:Ce:Sr and performances of the ELIGANT-GN detectors using 15.1 MeV gamma-rays*
- *C. Borcea, et al. GDR excitations of fission fragments*
- *D. Nichita, P.-A. Söderström, et al. Study of dipole strength below particle separation energy in* ^{56}Fe
- *F. Camera, F. Crespi, et al. Study of the isospin symmetry in* ^{72}Kr *at low temperature*
- *O. Wieland, E. Gamba, et al. Search for pygmy dipole strength in* $^{58,60}Ni$ *at finite temperature*
- *P. Constantin, P.-A. Söderström, et al. Spectroscopy of the first excited* 2^+ *state of* ^{10}B *with inelastic proton scattering*
- *S. Pascu, et al. Detailed investigation of low-lying states of* ^{144}Sm
- *T. Kawabata, et al. Measurement of the Radiative-Decay Probability of the Hoyle State*

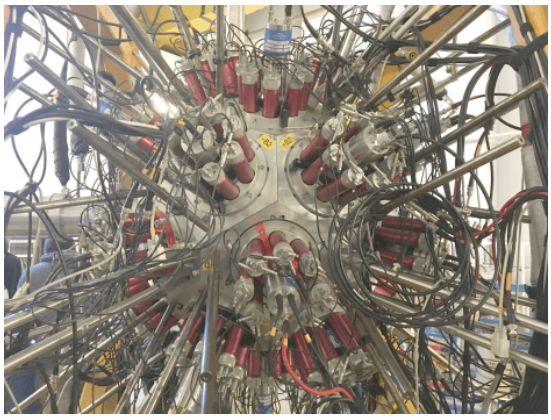

Figure 4.2.1: *Photograph of the large volume* $LaBr_3$*:Ce and* $CeBr_3$ *detectors from ELI-NP mounted in ROSPHERE.*

In this report we will present the status of this

joint installation, shown in Figure 4.2.1, together with some basic characteristics of the setup.

4.2.2 Detectors and mechanics

Within this campaign the work-horse will be the ELI-NP large-volume scintillators, particularly 15 $LaBr_3$:Ce detectors and 10 $CeBr_3$ detectors. All detectors are cylindrical, with a diameter of 76 mm and a height of 76 mm. Each detector is coupled with a Hamamatsu R11973 PMT, with 23.3% quantum efficiency [Söd+22]. The BGO shields of ROSPHERE are of two types, referred to as the Canberra or Ortec type depending on which kind of HPGe detector they are intended for. They consist of 8 optically separated trapezoidal BGO crystals, read-out by either eight R6094 (Ortec) or eight R3998 (Canberra) Hamamatsu PMTs. The thickness of the crystals is between 22 mm and 29 mm, and the lengths are 178.6 mm (Ortec) and 146.6 mm (Canberra) [Buc+16].

To mount the $LaBr_3$:Ce and $CeBr_3$ detectors, dedicated holders were designed, and 3D printed.These holders are designed individually for each combination and are mounted in the back of the anti-Compton shields in the existing screw holes.

In addition to the $LaBr_3$:Ce and $CeBr_3$ detectors, several of the proposed instruments require specific additional detector systems to be integrated both mechanically and in the data acquisition software and hardware. These include, for example, HPGe detectors from the ROSPHERE [Buc+16], the SORCERER [Bec+20] solar-cell based charged particle tagger, the CORSET [Koz+08] dual micro-channel plate setup for tagging of fission fragments, and a dedicated silicon-strip detector setup with digital read-out and pulse-shape discrimination capabilities to be used for the Hoyle-state experiment.

4.2.3 GEANT4

The properties of the detector system have been simulated to understand some key performance parameters like efficiency and anti-Compton rejection capabilities. The simulations have been performed both at the Nuclear Physics Department using GEANT4 [Ago+03] and at ELI-NP with the dedicated GROOT [Lat+17] framework. Both approaches show good agreement with source tests performed in E8 at ELI-NP. A typical rendering of the geometry from GROOT is shown in Figure 4.2.2. Note that the anti-Compton shields can include target-facing collimators made of tungsten that can improve the peak-to-total ratio of the detection system, with the cost of reducing efficiency by approximately 50% due to shadowing of the $LaBr_3$:Ce and $CeBr_3$ crystals.

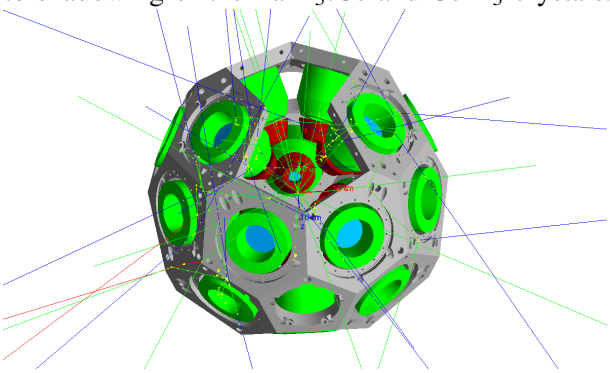

Figure 4.2.2: GEANT4 *rendering of the detector setup, including optional collimators (in red).*

Typical efficiency curves of the setup are shown in Figure 4.2.3, where the different curves correspond to the setup with and without the frontal collimators. Note that the simulations with collimators only contain 22 out of the 25 detectors for the possibility of mounting some of the previously mentioned ancillary detectors.

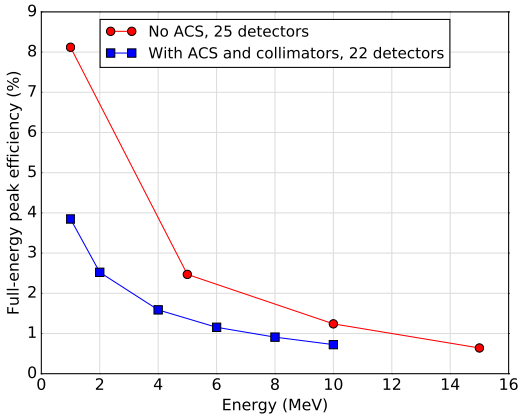

Figure 4.2.3: *Simulated detector efficiency without anti-Compton shields and 25 detectors, compared to the case with anti-Compton shields and mounted collimators with 22 detectors in the structure.*

In Figure 4.2.4, we show GEANT4-generated spectra from a source moving with a velocity of $\beta = 0.14$ in the beam direction, emitting 15 MeV γ-rays, after Doppler correction. Here, 10^6 events have been generated. A large fraction of the original events have been rejected, significantly decreasing the overall efficiency for observing such high-energy γ-rays. However, the anti-Compton rejected spectrum show an obvious peak at the correct energy. In contrast, the non-rejected spectrum has a broad structure where the full-energy peak is barely visible.

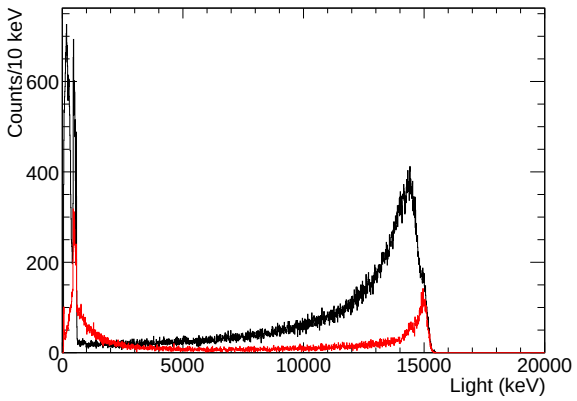

Figure 4.2.4: *Simulated Doppler corrected energy spectra from a* 15 MeV *γ-ray source moving with a velocity of* $\beta = 0.14$ *without (black) and with (red) anti-Compton shields. The setup consisted of 22 detectors in these simulations.*

4.2.4 Data acquisition

The data from the detectors is transmitted to the electronics room at the 9 MV Tandem area, where two options of data taking are available. One option is to use the existing data acquisition framework from ROSPHERE, described in detail in Reference [Buc+16]. The other option is to use the CAEN based digital data acquisition from ELIGANT-GN.

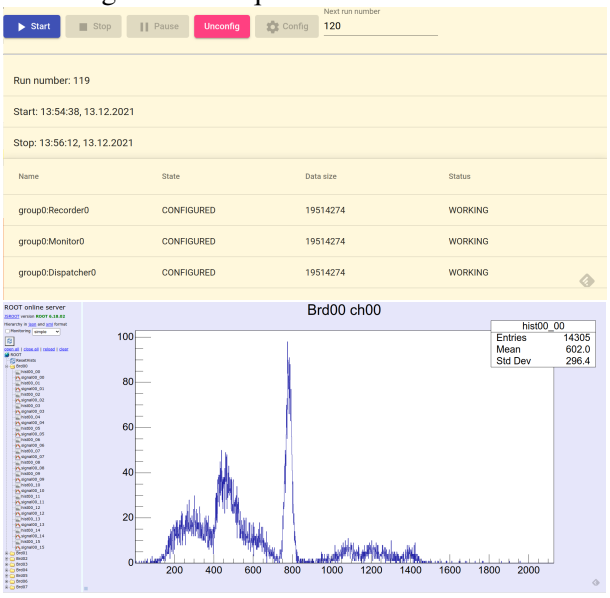

Figure 4.2.5: *Browser interface of the DELILA data acquisition for control (top) and monitoring (bottom) of the data read-out.*

Two options are currently available on the computer controlling the digitizers to read out the digital data acquisition system. One option is CoMPASS, the software developed by CAEN specifically for this type of electronics. The other option is the DELILA software developed in-house at ELI-NP dedicated for the γ-ray beam experiments. DELILA is based on a DAQ-Middleware developed by the KEK organization in Japan. It can control CAEN digitizers with both DPP-PHA and DPP-PSD firmware, as well as saving waveforms. It does an internal time-sorting of the data so that the events are written out in the temporal order that they arrive in the digitizers, and the output data is stored in ROOT trees. It can be controlled and monitored from any computer within the network using a browser-based GUI, shown in Figure 4.2.5.

4.2.5 Source measurements

Following the installation of the detectors and the data acquisition at the Tandem facilities, the experimental setup was characterised using radioactive sources. The low-energy calibration data were collected using standard sources of ^{60}Co and ^{56}Co, giving clean calibration points at 511 keV, 1173 keV, 1238 keV, 1772 keV, and 3254 keV.

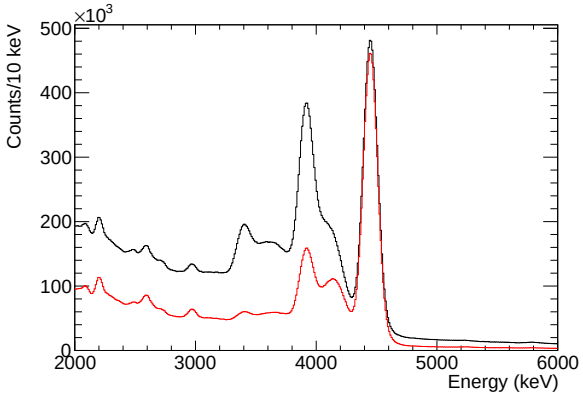

Figure 4.2.6: *Energy spectrum without (black) and with (red) anti-Compton suppression in the region of the 4 MeV γ-rays with a PuBe source.*

For higher-energy calibration points, the composite plutonium-beryllium (PuBe) source [Söd+21] was used for populating the first 2^+ state of ^{12}C at 4.44 MeV, and a combination of the PuBe source in the center of a specifically designed sphere containing a homogeneous mixture of paraffin and nickel was used to obtain a calibration point at 9 MeV. The 4 MeV region of this data is shown in Figure 4.2.6, where the impact of the anti-Compton suppression both of the spectrum as a whole and especially of the first and second escape peaks can be seen clearly.

An even larger impact can be seen in the 9 MeV region, shown in Figure 4.2.7, where the reduction of the background in the spectrum is almost a factor of three. In both cases, dig-

ital electronics were used to collect data together with the DELILA data acquisition software.

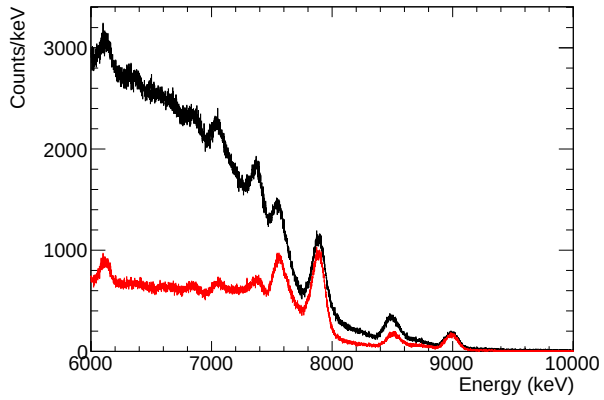

Figure 4.2.7: *Energy spectrum without (black) and with (red) anti-Compton suppression in the region of the 9 MeV γ-rays a PuBe source in the center of a nickel-paraffin sphere.*

As discussed earlier, in addition to the primary γ-ray detectors, several of the experiments will require the integration of ancillary detectors in the data acquisition chain. One of the first scheduled experiments intended to use the SORCERER [Bec+20] setup for charged-particle tagging.

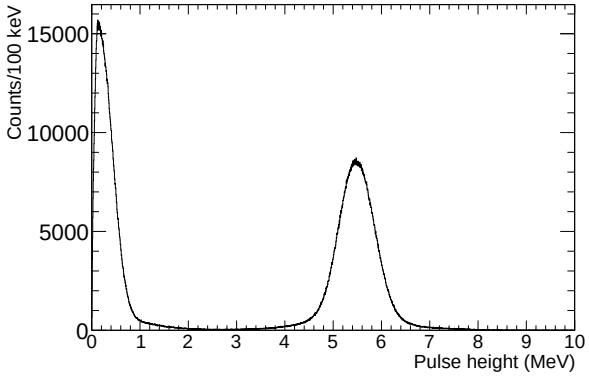

Figure 4.2.8: *Summed pulse-height spectrum of six SORCERER detectors obtained with digital data acquisition from an α source with energies of around* 5.5 MeV.

Therefore, another test performed was the integration of SORCERER in the DELILA software. For this purpose, a V1725S digitizer with DPP-PHA firmware from the ELIGANT-TN setup [Cam+16] was included in the data flow, with six SORCERER detectors connected to one channel each. The SORCERER setup was used without any voltage biasing of the solar cells, giving approximately 5 mV pulse height from an α source with energies of approximately 5.5 MeV to the digitizers. Trapezoidal filtering of the signal was applied in the digitizer firmware, and the resulting pulse-height spectrum is shown in Figure 4.2.8.

4.2.6 First in-beam tests

In addition to the source measurement characterizations, a short beam time was carried out to verify the detector performances in-beam. Several different target combinations were tried, and these are currently under analysis. Here, we will show some preliminary results from one of these runs. In this particular run, a proton beam with an energy of 7.2 MeV was used on a ^{11}B target.

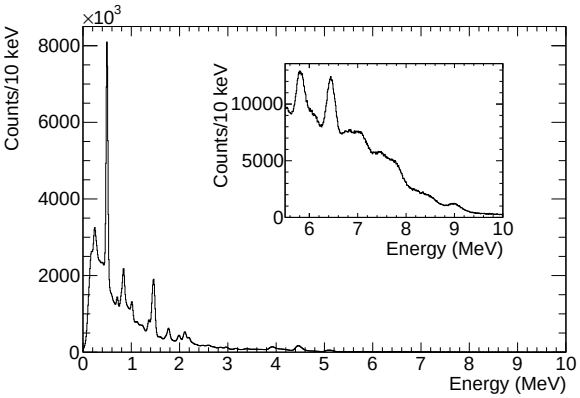

Figure 4.2.9: *Energy spectrum from the in-beam run with a proton beam on a ^{11}B target. The inset is showing the high-energy region above* 5.5 MeV*5.*

The data corresponding to run number 13, with slightly less than 3 hours of data taking, is shown in Figure 4.2.9.

4.2.7 Summary

The ELI-NP $LaBr_3$:Ce and $CeBr_3$ detectors have been installed in the ROSPHERE setup at the 9 MV Tandem facility. The first source, as well as in-beam characterizations, have begun. Data from these tests are currently under analysis, and more information about the setup's performance will be collected during the first two weeks of 2022 in dedicated beam time. In the middle of January 2022, the first experiments of the experimental campaign are expected to start.

References

[Ago+03] S. Agostinelli *et al.* "GEANT4–a simulation toolkit". In: *Nucl. Instrum. Methods Phys. Res. A* 506 (2003), page 250 (cited on page 162).

[Bec+20] T. Beck *et al.* "SORCERER: A novel particle-detection system for transfer-reaction experiments at ROSPHERE". In: *Nucl. Instrum. Methods Phys. Res. A* 951 (2020), page 163090 (cited on pages 162, 164).

[Buc+16] D. Bucurescu *et al.* "The ROSPHERE γ-ray spectroscopy array". In: *Nucl. Instrum. Methods Phys. Res. A* 837 (2016), page 1 (cited on pages 161–163).

[Cam+16] F. Camera *et al.* "Gamma above the neutron threshold experiments at ELI-NP". In: *Rom. Rep. Phys.* 68 (2016), S539 (cited on pages 161, 164).

[Koz+08] E. M. Kozulin *et al.* "The CORSET time-of-flight spectrometer for measuring binary products of nuclear reactions". In: *Instrum. Exp. Tech.* 51 (2008), page 44 (cited on page 162).

[Krz+19] M. Krzysiek *et al.* "Simulation of the ELIGANT-GN array performances at ELI-NP for gamma beam energies larger than neutron threshold". In: *Nucl. Instrum. Methods Phys. Res. A* 916 (2019), page 257 (cited on page 161).

[Lat+17] D. Lattuada *et al.* "A fast and complete GEANT4 and ROOT Object-Oriented Toolkit: GROOT". In: *EPJ Web Conf.* 165 (2017), page 01034 (cited on page 162).

[Söd+21] P.-A. Söderström *et al.* "Characterization of a plutonium–beryllium neutron source". In: *Applied Radiation and Isotopes* 167 (2021), page 109441. ISSN: 0969-8043. DOI: https://doi.org/10.1016/j.apradiso.2020.109441. URL: https://www.sciencedirect.com/science/article/pii/S0969804320305832 (cited on page 163).

[Söd+22] P.-A. Söderström *et al. ELIGANT-GN – ELI Gamma Above Neutron Threshold: The Gamma-Neutron setup*. Nucl. Instrum. Methods Phys. Res. A, in print. 2022 (cited on pages 161, 162).

[Ur+16] C. Ur *et al.* "Nuclear Resonance Fluorescence Experiments at ELI-NP". In: *Romanian Reports in Physics* 68 (2016), S483. URL: http://www.rrp.infim.ro/2016_68_S/S483.pdf (cited on page 161).

[Wel+16] H. Weller *et al.* "Gamma Beam Delivery and Diagnostics". In: *Romanian Reports in Physics* 68 (2016), S447–S481 (cited on page 161).

4.3 Status of the ELIADE γ-ray spectrometer

Testov D.[1], Suliman G.[1,2], Dhal A.[1], Balabanski D. L.[1], Aogaki S.[1], Brezeanu M.[1,3], Ban S.-R.[1,2], Niţescu G.[1,2], Petcu C.[1], Ramirez F.[1], Vasile A.[1,2], and Zhu F.[1,4]

[1] Extreme Light Infrastructure (ELI-NP) & Horia Hulubei National Institute for R&D in Physics and Nuclear Engineering (IFIN-HH), Str. Reactorului No. 30, 077125 Bucharest–Măgurele, Romania
[2] Politehnica University of Bucharest, 313 Splaiul Independentei, Sector 6, 060042 Bucharest, Romania
[3] Faculty of Physics, University of Bucharest, Strada Atomiștilor 405, 077125, Măgurele, Romania
[4] University of Liverpool, L693BX, Liverpool, United Kingdom

* **dmitry.testov@eli-np.ro**

Abstract

ELIADE ((ELI)-NP (A)rray of (DE)tectors is the γ-ray spectrometer installed at the Extreme Light Infrastructure Nuclear Physics (ELI-NP) implemented by the National Institute of Physics and Nuclear Engineering Horia Hulubei (IFIN-HH). Almost fully polarized γ-beams, provided by the Variable Energy Gamma (VEGA) system at low energy bandwidth, will trigger studies in the field of nuclear structure and applied science using Nuclear Resonance Fluorescence methods performed at ELIADE. The implementation and the present status of ELIADE are discussed.

4.3.1 Introduction

At ELI-NP, the γ-ray beam will be delivered at a continous variable energy up to the maximum of ∼19.5 MeV and total flux of 10^{11}/s produced by the VEGA system [VEG21]. The linear polarization of 95% and the average relative bandwidth of 0.5% will enhance the experimental horizon for experiments below and above the particle emission threshold in (stable) nuclei. The response of a nucleus to the injected electromagnetic radiation, below the particle separation threshold, will be studied at the ELIADE γ-ray spectrometer. It consists of eight Clover 32-folded High Purity Germanium (HPGe) detectors [Ur+16] arranged at a minimum 15 cm distance from the target into two rings at 90° and 135° to the beam direction. Each ring comprises four Clover detectors. In order to enhance sensitivity to the high-energy γ-rays, four large volume ancillary (3 in × 3 in) $CeBr_3$ detectors are installed in the 90° ring in a way that the polar angle between the Clover and $CeBr_3$ detectors in the ring is 45° with respect to the target position Figure 4.3.1. It is foreseen to use the segmented Compton suppression to veto the events escaping the germanium crystals. The effect on the quality of γ-ray spectra recorded by ELIADE is discussed by simulations in Ref. [Zhu21].
Clover detectors are of the TIGRESS type [Scr+05] containing four crystals each. The crystals are divided longitudinally and laterally into eight segments providing thus the better count rate and angular resolution characteristics. The segmentation also allows the so-called „add-back" procedure, which improves the quality of the recorded spectra on the basis of the hit pattern of crystals and segments. The 40 output signals from each clover are fed to inputs of CAEN v1725 digitizers (14 bit resolution at 250 MS/s) [CAE21c]. The data acquisition system, the (D)igital (E)xtreme (L)ight (I)nfrastructure (L)istmode (A)cquisition (DELILA), is home designed [Aog21]. It is based on the Middleware-DAQ [Yas+10] which is in use in different research laboratories and shows good real time operation and reliability. DELILA has web-based interface and allows online visualisation of the data using a root server. The development of DELILA is discussed in Ref. [Aog21].

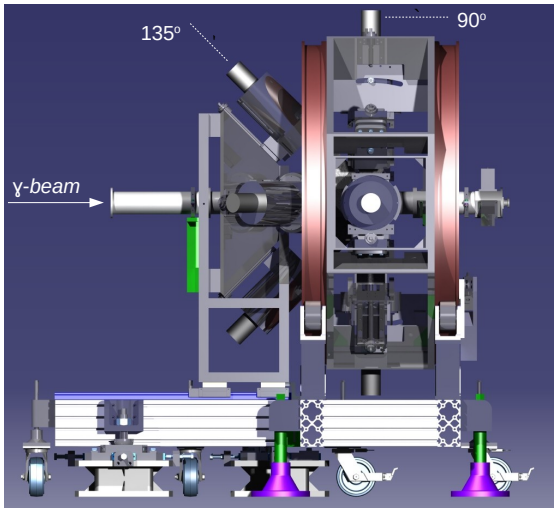

Figure 4.3.1: 3D view of the ELIADE γ-ray spectrometer

The performance of one of the Clover detectors installed in the testing position, see Figure 4.3.2 was characterized using DELILA. A spectrum recorded using a standard ^{152}Eu source placed at 35.5 cm from the surface of the detector is shown in Figure 4.3.3. It shows the calibrated spectra for all 32 segments and four core signals from the detector.

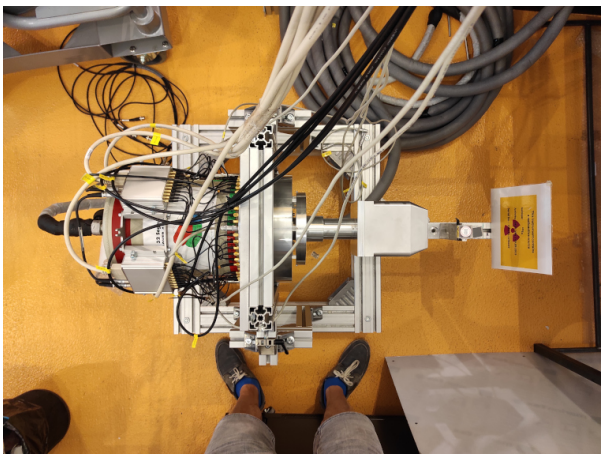

Figure 4.3.2: *Experimental setup for the characterization of Clover detectors.*

Most of the mechanical works on the ELIADE structure were completed. Thus, the crane to load the Clovers to the backward part of the spectrometer was installed. The overhead cable support tray was designed and constructed around ELIADE to connect the detectors to the corresponding electronic modules installed at the nominal position in the E8 experimental area. It allowed starting mounting of detectors inside the structure. The current view of ELIADE is shown in Figure 4.3.4.

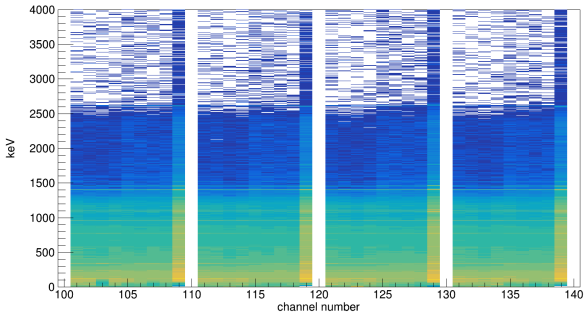

Figure 4.3.3: *Recorded spectra of a ^{152}Eu source for one detector.*

Before characterization and loading the detectors inside the ELIADE structure, they are subject to the annealing procedure. This is a standard procedure that allows to remove the possible contaminants from germanium crystals and to recover the vacuum in the cap where the crystals are located. The process is very delicate and requires a special setup developed and installed in the spectroscopy laboratory LP51. Details about the setup and the annealing procedure are described in Ref. [Dha21b].

Figure 4.3.4: The present view of the ELIADE γ-ray spectrometer installed at the E8 experimental area.

The Clover HPGe detectors are constantly kept under the temperature of about -195°C, the boiling point of the liquid nitrogen. In addition, a dedicated automatic cooling system to deliver the liquid nitrogen to the detectors was designed and constructed as reported in Ref. [Dha21a].

4.3.2 Monitoring, Alarm and Control System

In order to control constantly the parameters of the ELIADE array, timely report the personnel on its extraordinary events, and interact with the automatic cooling system, the Alarm, and Control for ELIADE (MACE) was introduced. The monitoring parameters are the room temperature, valve temperature, crystal temperature, high voltage applied to the detectors, and the corresponding leakage current. EPICS (Experimental Physics and Industrial Control System) [CAEa] is used to communicate with the cRIO controller of the Cooling System and the High voltage unit (CAEN SY4527 [CAEb]).

The MACE consists of the passive and active sub-routing. The MACE passive routing provides simple communication with the cRIO and SY4572 by *HVMonitor* and *LN2Monitor* actors correspondingly. The actors are scripts developed in the Python Programming language using the PyEpics interface [PyE21]. The actors store the values for all the monitoring parameters in real time in databases which can be visualized by an open-source monitoring platform [Gra21]. An example of the timing diagram for the valve and crystal temperatures is shown in Figure 4.3.5. The monitoring system allows instant messages/calls noti-

fication of the personal as the parameters are outside the predefined ranges. However, the system cannot notify in case of a local network failure.

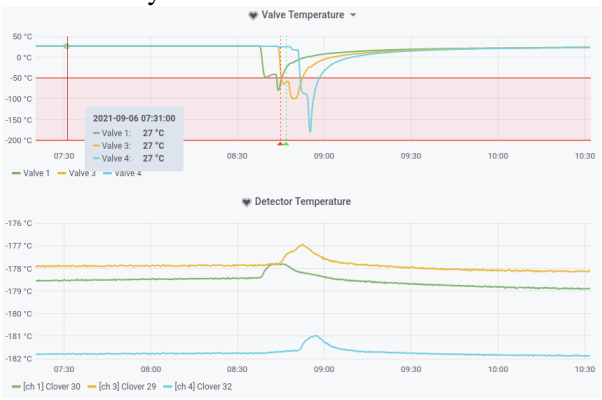

Figure 4.3.5: The temperature diagrams corresponding to three channels (three Clover HPGe detectors) of the Cooling System. Top: valve temperature, bottom: crystal temperature. One filling cycle that happened before 9 a.m. is visible.

The MACE active sub-routine is featured to issue calls to the personnel via the cellular network when the local network is disturbed. Moreover, it has direct feedback on both the Cooling and High Voltage systems and can act independently if the personnel cannot resolve the situation timely.

The MACE active sub-routine is distributed into the *Monitor*, *Control*, *Alarm* and *Graphical User Interface* (GUI) actors, developed in the Python Programming language, running in parallel as threads. The *Monitor* communicates with the CRIO microcontroller and stores the actual values of the crystal temperature in the Redis database. The *Control* interrogates the Redis database to call the *Alarm* if the temperature is outside the predefined range. Based on the temperature the specific alarm level is triggered (see Figure 4.3.6). The level 0 corresponds to the normal state when no alarms are triggered. When the temperature reaches level 1 a cellular call to the personnel is issued. Further increase up to level 2 in the temperature triggers a filling of all the detectors. Finally, if the situation is not resolved and the temperature exceeds level 3, the bias of the corresponding detector is ramped down to 0 V. The Graphical User Interface allows setting the alarm levels and displaying the current status of MACE.

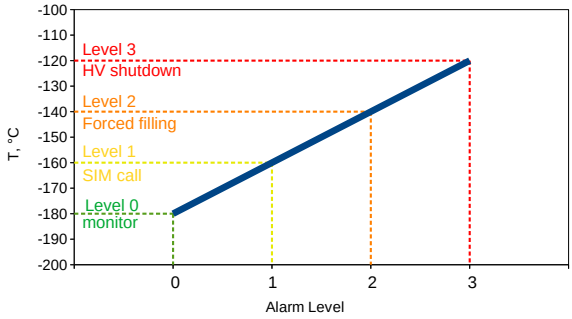

Figure 4.3.6: the Alarm levels of MACE

4.3.3 Test and characterization of the detectors $CeBr_3$ detectors

For the ELIADE array, 3 in x 3 in $CeBr_3$ detectors were provided by SCIONIX and had R1924A Hamamatsu photomultiplier tubes [ham21]. The performance of the detectors was tested using a set of standard γ-ray calibration sources. The negative -900 V bias was applied by the CAEN AG7236DN [CAE21a] high voltage board operated in the CAEN SY4527 [CAEb] crate. The output signal from the photomultiplier was fed to a v1730 CAEN digitizer (14 bit resolution at 500 MS s^{-1}) [CAE21d]. The data acquisition was made using CoMPASS Multiparametric DAQ Software [CAE21b]. A typical waveform from a detector is shown in Figure 4.3.7.

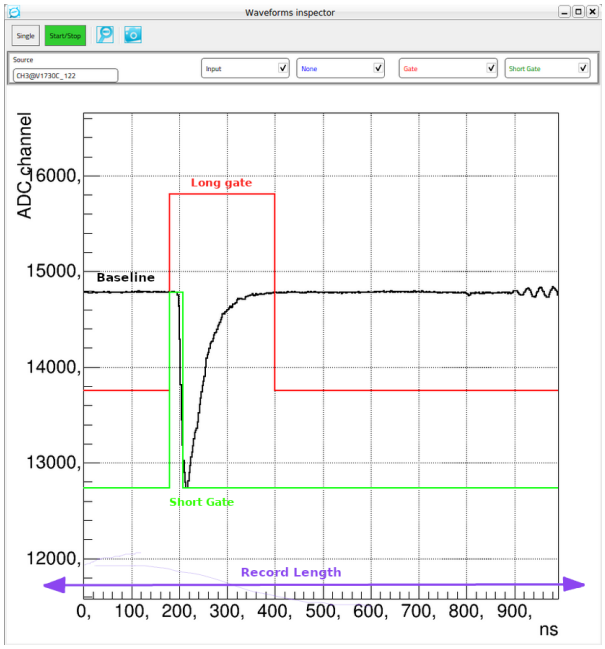

Figure 4.3.7: *A typical waveform from a $CeBr_3$ detector. A screen shot from CoMPASS DAQ. The major parameters for the Pulse Shape Analysis are illustrated in table 4.3.1*

The experimental setup for characterisation of

the detectors is shown in Figure 4.3.8. The resolution and the efficiency of all four detectors measured for the 662 keV γ-ray from a ^{137}Cs placed at 20 cm from the surface of the detector are reported in Table 4.3.2. A spectrum recorded individually for each detector is shown in Figure 4.3.9.

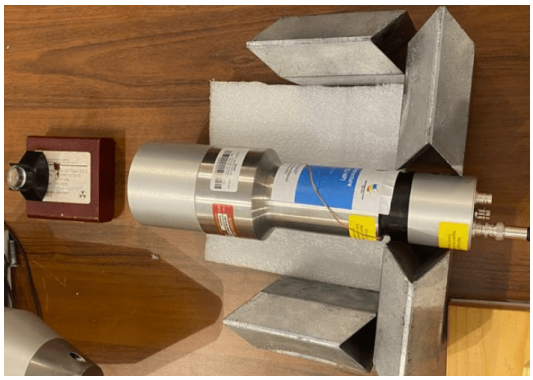

Figure 4.3.8: *Experimental setup for the characterization of $CeBr_3$ detectors.*

Table 4.3.1: Parameters of the v1730 digitizer used for characterization of $CeBr_3$ and CsI detectors.

Parameter	$CeBr_3$	CsI
HV, V	-900	+900
Record length, ns	10000	1024
Pre-trigger, ns	200	120
Input Dynamic, Vpp	0.5	0.5
DC Offset, %	10	10
Threshold, LsB	100	80
Trigger holdoff, ns	1024	1024
Energy Coarse Gain, fC/(LSB x Vpp)	10	10
Long Gate, ns	220	180
Short gate, ns	30	250
Discriminator Mode	Leading Edge	Leading Edge

Table 4.3.2: Resolution and efficiency measured for $CeBr_3$ detectors for the 662 keV γ-ray line of ^{137}Cs source.

No.	Resolution(%)	Efficiency (%)
E01	4.55 ±0.54	0.36 ± 0.07
E02	4.48 ±0.48	0.35 ± 0.07
E03	4.83 ±0.44	0.36 ± 0.07
E04	4.47 ±0.40	0.35 ± 0.07

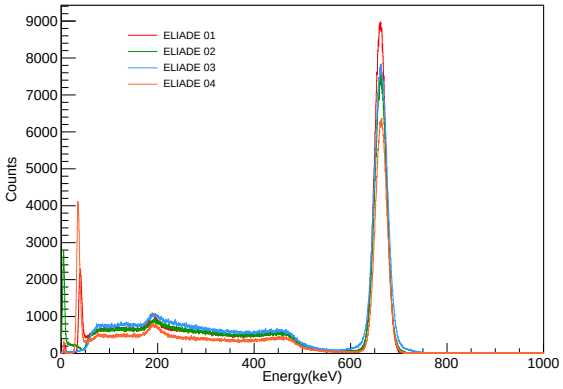

Figure 4.3.9: *Typical spectra recorded for a $CeBr_3$ detector using a ^{137}Cs source.*

Additionally, the efficiency as a function of distance was measured using ^{137}Cs, ^{22}Na and ^{60}Co sources in the range from 5 cm to 50 cm from the surface of the detector, see Figure 4.3.10. This curve is important to validate the simulation of ELIADE.

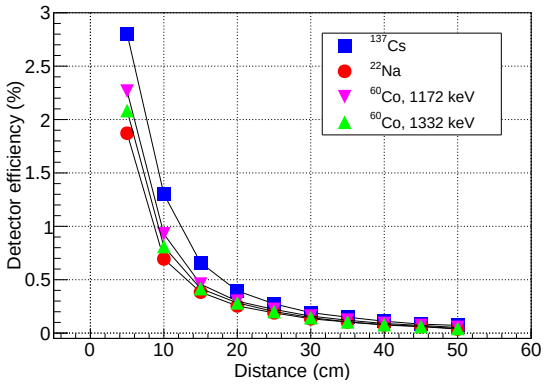

Figure 4.3.10: *Efficiency as a function of distance measured for one of $CeBr_3$) for different sources as indicated in the legend. Uncertainty values do not extend over the dot size.*

The characteristics of $CeBr_3$ were measured, and the detectors were transferred to the IFIN-HH Tandem to support the experimental campaign [S A+21].

4.3.4 Test and characterization of CsI (back-catchers) active anti-Compton shield)

In order to improve the quality of the recorded γ-ray spectra by the Clover HPGe detectors, the Compton background will be rejected by the active Compton shield (ACS). The active shield will consist of three modules (namely, front, side and back) of scintillator detectors. The simulations and the impact of this shield on the measurements are discussed in Ref. [Zhu21]. This chapter reports the characterization of the back modules – the back catch-

ers – using standard calibration sources. As is seen from Figure 4.3.11 each detector consists of two parts (A and B). Each part has four CsI crystals coupled to R1924A Hamamatsu photo-multiplier tubes (PMT) [ham21]. The +950 V high voltage was applied to each detector via the eight-channel distribution box equipped with potentiometers to modify the gain for crystals individually. The ^{137}Cs calibration source was placed at 5 cm as is shown in Figure 4.3.11. Signals from PMTs were directly fed to the v1730 digitizer controlled by the DELILA data acquisition system [Aog21]. The parameters for the acquisition are listed in Table 4.3.1.

Figure 4.3.11: *Experimental setup for the characterization of CsI detectors.*

The resulted γ-ray spectra recorded for individual crystals are presented in Figure 4.3.12 a) and b). The back-catchers installed at ELIADE Clover detectors under the real experimental conditions may have only two (or one) data acquisition channels for every back-catcher. Therefore, firstly, the performance of the back-catchers were characterized by organizing OR scheme from signals of 4 crystals of each part. The resulting spectra for parts A and B are illustrated in Figure 4.3.12 c). The measured resolution and efficiency for the 662 keV γ-ray for part A were 11.7(5)% and 2.5(2)%, correspondingly; and 11.5(5)% and 2.4(2)% for the part B. The resolution of 12.2(4)% and the efficiency of 4.92(2)% were measured by organizing scheme OR from signals of all 8 crystals, see the spectrum in Figure 4.3.12 d). The same procedure was repeated for eight detectors confirming the parameters provided by the producer, see Figure 4.3.13. The next step is to construct time correlations between Clover and CsI detectors to use anti-coincidence mode for the anti-Compton rejection.

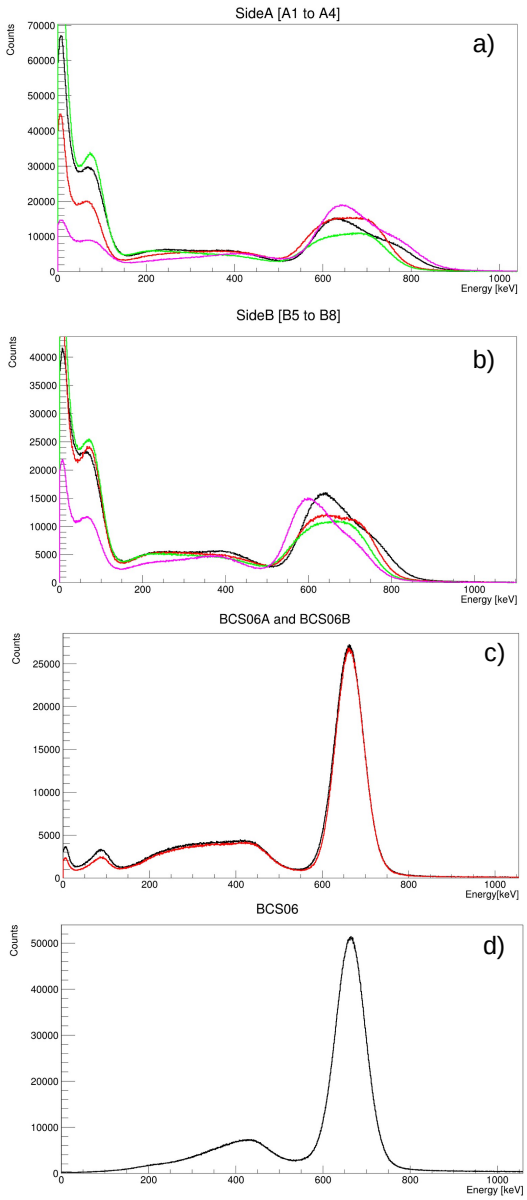

Figure 4.3.12: *Typical $\gamma-$ray spectra for a ^{137}Cs source recorded a) and b) by individual crystals; c) by part A and part B; d) by all crystals of the whole detector, see text for details*

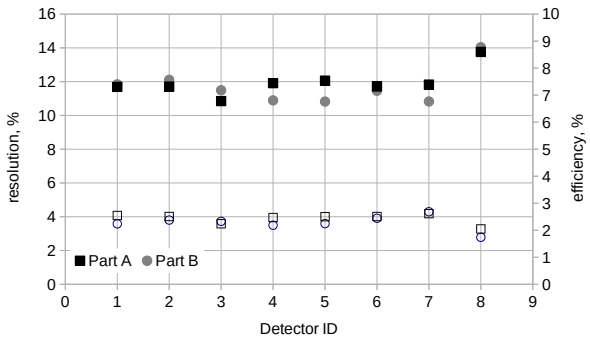

Figure 4.3.13: *Resolution (full dots) and efficiency (open dots) for part A (rectangles) and part B (circles) for eight back-catcher detectors.*

4.3.5 Conclusion

The ELIADE $\gamma-$ray spectrometer was well advanced within 2021. Mechanical construction work in the E8 experimental needed for installation of the Clover HPGe detectors inside the frame was completed. The new cooling system was installed. The monitoring, alarm, and control system (MACE) to allow the safe long-term operation of the setup was introduced. The DELILA data acquisition was developed. The characterization of $LaBr_3$(Ce) and CsI detectors was completed. The characterization of Clover detectors, including the development of the AddBack procedure, is in progress.

References

[Aog21] S. Aogaki. "DELILA (Digital Extreme Light Infrastructure List-mode Acquisition) project status report". In: (2021) (cited on pages 167, 171).

[CAE21a] CAEN. *AG7236*. 2021. URL: https://www.caen.it/products/ag7236/ (cited on page 169).

[CAE21b] CAEN. *compass*. 2021. URL: https://www.caen.it/products/compass/ (cited on page 169).

[CAE21c] CAEN. *v1725*. 2021. URL: https://www.caen.it/products/v1730/ (cited on page 167).

[CAE21d] CAEN. *v1730*. 2021. URL: https://www.caen.it/products/v1730/ (cited on page 169).

[CAEa] CAEN. *EPICS*. URL: https://www.caen.it/subfamilies/epics/ (cited on page 168).

[CAEb] CAEN. *SY4527*. URL: https://www.caen.it/products/sy4527/ (cited on pages 168, 169).

[Dha21a] A. Dhal. "Liquid nitrogen cooling set-up and automated filling control system for ELIADE clover detectors". In: (2021) (cited on page 168).

[Dha21b] A. Dhal. "Setting up an annealing station, annealing and testing of ELIADE clover detectors". In: (2021) (cited on page 168).

[Gra21] Grafana. *Grafana*. 2021. URL: https://grafana.com// (cited on page 168).

[ham21] hamamatsu. *R1924A*. 2021. URL: https://www.hamamatsu.com/us/en/product/type/R1924A/index.html (cited on pages 169, 171).

[PyE21] PyEPICS. *PyEPICS*. 2021. URL: https://cars9.uchicago.edu/software/python/pyepics3/ (cited on page 168).

[S A+21] S. Aogaki *et al.* "Preparation of a joint experimental campaign with ELI-NP detectors in ROSPHERE". In: (2021) (cited on page 170).

[Scr+05] H. Scraggs *et al.* "TIGRESS highly-segmented high-purity germanium clover detector". In: *Nucl. Instrum. Methods Phys. Res. A* 543.2 (2005), pages 431–440. ISSN: 0168-9002. DOI: https://doi.org/10.1016/j.nima.2004.12.012. URL: https://www.sciencedirect.com/science/article/pii/S0168900205000185 (cited on page 167).

[Ur+16] C. Ur *et al.* "Nuclear Resonance Fluorescence Experiments at ELI-NP". In: *Romanian Reports in Physics* 68 (2016), S483. URL: http://www.rrp.infim.ro/2016_68_S/S483.pdf (cited on page 167).

[VEG21] VEGA. *Variable Energy Gamma System at ELI-NP*. 2021. URL: https://www.eli-np.ro/rd2_second.php/ (cited on page 167).

[Yas+10] Y. Yasu *et al.* "Functionality of DAQ-Middleware". In: *IEEE Transactions on Nuclear Science* 57 (2010), pages 487–490 (cited on page 167).

[Zhu21] F. Zhu. "GEANT4 model for the anti-compton shield for ELIADE". In: (2021) (cited on pages 167, 170).

4.4 GEANT4 simulations of the ELIADE setup

Zhu F.[1,2,*] Testov D.[1,3], Turturică G.[1], and Vasile A.[1,4]

[1] Extreme Light Infrastructure (ELI-NP) & Horia Hulubei National Institute for R&D in Physics and Nuclear Engineering (IFIN-HH), Str. Reactorului No. 30, 077125 Bucharest–Măgurele, Romania
[2] University of Liverpool, L69 3BX, Liverpool, United Kingdom
[3] Joint Insitute for Nuclear Research, Dubna, Russia
[4] Politehnica University of Bucharest, 313 Splaiul Independentei, Sector 6, 060042 Bucharest, Romania

[*] **fan.zhu@eli-np.ro**

Abstract

The initial versions of the simulation on which this work is based were originally developed as tools to aid in the design of the Compton-suppression shield. The design drawings for the ELIADE clover detectors were used to create an accurate simulation of its geometry, and proposed forms of the Compton-suppression shield can be tested. Following this, the simulation is used to establish the optimal position of the lateral segmentation line for the ELIADE HPGe clovers, and for preliminary research for the development of first-interaction position determination algorithms.
For all of these purposes, the simulation proved to be of benefit. However, the accuracy of the simulation was not, and could not be, tested against a sufficiently similar physical reference, until the prototype detectors had been designed and constructed.

4.4.1 Introduction

The ELIADE setup at ELI-NP is one of the key setups at GDED. In particular for experiments with the Gamma Beam System (GBS), this setup was proposed to perform nuclear resonance fluorescence (NRF) measurements taking advantage of unique features of the GBS. ELIADE detector array, consist of eight segmented HPGe clover detectors where each crystal is divided into eight segments in a similar manner to the TIGRESS [Scr+05] array at TRIUMF in Canada.

Due to the very high photon beam intensity, a very large number of 511 keV photons from positron annihilation will reach the detectors together with the high energy photons from the NRF reaction of interest. This number can be decreased by the use of passive shields, designed in a modular fashion that allows them to become one of the user-defined experimental conditions. In ELIADE configuration, active Compton suppression shields are also used. These shields are of modular type being composed of three different types of shields: a rear side shield made of BGO, a side shield made of BGO and a back catcher made of CsI. The detector's cryostats are fitted with holders for the modular anti-Compton shields[Ur+16].

With the lack of purchase for the Compton-suppression shield and holders, the opportunity to compare the simulation to a suitable reference is limited now. However with the purchase of the ELIADE detectors and one prototype set of Compton-suppression shield, after the detector annealing work, some separate source measurements can be done. By simulating the exact experimental conditions under which data were collected with the prototype detector and suppression shield pieces, the accuracy of the simulation could be tested.

4.4.2 GEANT4 code

The geometry of the clover detectors was implemented in a GEANT4 simulation. The full ELIADE array and Compton suppression shields were also implemented in the simulation package. The geometry chosen for the simulations is the one with four segmented clover detectors at 98°and four segmented clover detectors at 135°. The geometry of the ELIADE array and anti-Compton shielding is shown in Figure 4.4.1. The ELIADE simulation is performed with GEANT4 version 10.06 (with patch 03).
In this figure, HPGe clover detectors (in grey) are shielded by front BGO (in magenta), side BGO (in dark blue) and back catcher CsI (in yellow), in the simulation lead shielding cover and DURAL holder were also implanted (not shown in Figure 4.4.1). All shielding and detectors in simulation are defined as sensitive crystals.

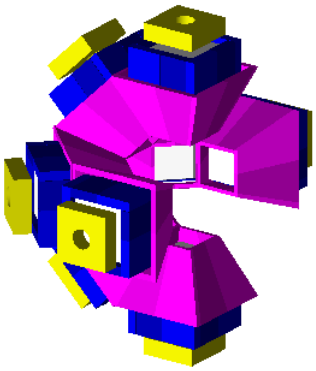

Figure 4.4.1: *The ELIADE array and anti-Compton shield simulated in GEANT4*

4.4.3 Validation

This GEANT4 simulation of detector efficiency is validated against experimental results, both for clover detector and anti-Compton shields. The efficiency was calculated as the ratio between the number of detected photon within any sensitive cube and the number of emitted photons. The total gamma detection efficiency as a function of photon energy for the total array, as well as with the passive and active shielding, are shown in Figures 4.4.2 and 4.4.3.

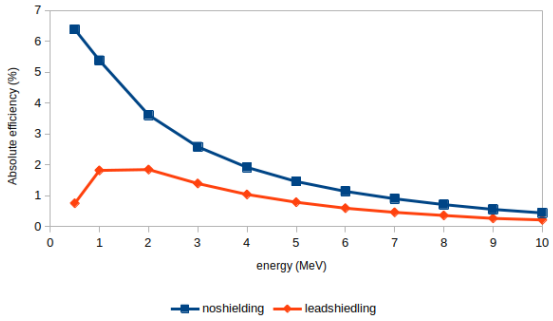

Figure 4.4.2: *Simulated detection efficiency with and without lead shielding*

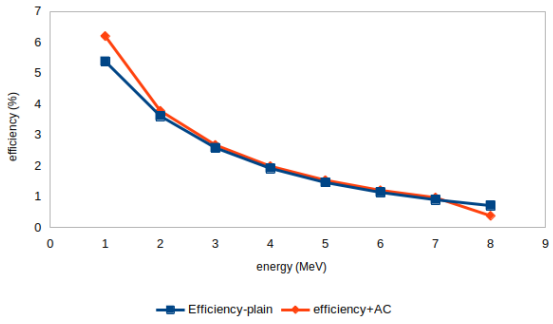

Figure 4.4.3: *Simulated detection efficiency with and without Anti-Compton shield*

In Figure 4.4.2, a 2 cm thick absorber was placed in front of the detector with no other shieldings around. A lead/copper absorber reduces the low-energy background radiation, below 500 keV. The influence of using a thick lead shield in front of the detectors was studied in GEANT4 by calculating the clover detector response to photons with energies between 500 keV and 10 MeV emitted from the center of the array. The importance of these absorbers is well-know from other NRF setups.

Besides the detection efficiency, the validation of anti-Compton materials are also finished. The source used in the anti-Compton validation measurements is ^{137}Cs, placed at a distance of 5 cm from the BGO detector and 10 cm from CsI back catcher. Data retrieval run for 5 minutes. Table 4.4.1 shows the validation results, all the measurements were done with the help by the ELIADE group members, Dmitry Testov, Andrei Vasile, Gabriel Turturica and others.

Table 4.4.1: Anti-Compton shielding validation results

detector	measured efficiency	simulated efficiency	measured resolution
BGO front shield	5.1% (0.00226)	5.3%	25.9%
BGO side shield	5.2% (0.00228)	4.9%	26.4%
CsI back catcher	1.9% (0.00138)	1.2%	17.0%

In Table 4.4.1, the efficiency was calculated as the ratio between the number of the detected photons within any sensitive cube and the number of emitted photons. The energy resolution in the simulation was defined based on the parameters from the measured data. Due to the fitting function for simulated spectra, the calculated resolution can be slightly different than it was set in the simulation. From these figures and the table, it is clear that the agreement is good for the clover detector and anti-Compton shielding implemented in GEANT4 simulation. The anti-rejection analysis is also finished, and add-back schemes are still ongoing.

4.4.4 Conclusion

We have implemented a GEANT4 simulation code for the ELIADE array. The detector response in the simulations is well understood and can accurately reproduce several cases of gamma emission, both source-related and experiment at ELI-NP. In order to optimize the quality of the spectrum, the focus should be on the add-back technique from now.

References

[Scr+05] H. Scraggs *et al.* "TIGRESS highly-segmented high-purity germanium clover detector". In: *Nuclear Instruments and Methods in Physics Research A* 543 (2005), page 431. DOI: https://doi.org/10.1016/j.nima.2004.12.012 (cited on page 173).

[Ur+16] C. Ur *et al.* "Nuclear Resonance Fluorescence Experiments at ELI-NP". In: *Romanian Reports in Physics* 68 (2016), S483. URL: http://www.rrp.infim.ro/2016_68_S/S483.pdf (cited on page 173).

4.5 Simulation of the VEGA gamma beam

Constantin, P.[1,*]

[1] Extreme Light Infrastructure (ELI-NP) & Horia Hulubei National Institute for R&D in Physics and Nuclear Engineering (IFIN-HH), Str. Reactorului No. 30, 077125 Bucharest–Măgurele, Romania

[*] **paul.constantin@eli-np.ro**

Abstract

The VEGA facility will become operational in 2023, delivering a gamma beam with the highest spectral density and lowest bandwidth available worldwide. A suite of several experimental setups will be commissioned for a wide range of research programs in fundamental and applied nuclear science. This report presents the simulation module implemented within the GEANT4 framework that has been developed to study the gamma beam generation, collimation, and interaction with experimental setups.

4.5.1 Introduction

The Variable Energy Gamma-ray (VEGA) facility will provide in the second half of next year the future top gamma beam available as a user facility to the research community in Europe and worldwide. It will complement the already operational high-power lasers [Dor+20] of the Extreme Light Infrastructure - Nuclear Physics (ELI-NP) center near Bucharest, Romania.

Its beamline consists of a warm linac which accelerates electrons up to an energy $T_e = 740$ MeV and injects them in a storage ring where they collide inside an optical cavity with laser photons at a frequency of 71.4 MHz. The back-scattered photons are boosted in energy by a factor of $4\gamma^2 = 8.4 \cdot 10^6$, where $\gamma = T_e/m_e$ is the relativistic electron factor, and transformed into a gamma beam with the maximum energy of 20 MeV. The inherently high forward focusing of this gamma beam, with an angular divergence of the order $\sigma_\theta \approx 1/\gamma < 1$ mrad, is increased by selecting only the low-angle, high-energy component with the collimation system described downstream.

The VEGA gamma beam compares favorably with the leading gamma beams obtained via Laser Compton Back-scattering (LCB) and is currently in operation, namely LEPS (Japan) [Mur+14] and HIGS (USA) [Wel+09]. A comparison of the main parameters of these facilities is presented in Table 4.5.1. In addition, the top intensity and spectral density are quoted for both LEPS and HIGS facilities.

Through its Gamma Driven Experiments Department (GDED) and its international collaborators, the ELI-NP center has developed several experimental setups to be used with the VEGA beam. They implement the research programs approved by the International Science Advisory Board (ISAB) of ELI-NP and published in a special issue of the Romanian Reports in Physics journal [Bal+16; Bob+16; Cam+16; Djo+16; Sul+16; Tes+16; Ur+16; Wel+16]. Fundamental nuclear physics is very well represented with dedicated programs for nuclear resonance fluorescence with the ELIADE array, photo-nuclear reactions above the neutron threshold with the ELIGANT array, nuclear astrophysics studies with the ELISSA and ELITPC arrays, and photo-fission with the ELIBIC and ELITHGEM arrays. ELI-NP also has a diverse applied research program comprising medical and industrial studies setups. The secondary positron beamline ELIPS is developed for material science applications.

Table 4.5.1: Comparison between the main gamma beam parameters at LEPS, HIGS and VEGA: energy E, bandwidth $\Delta E/E$, intensity I and spectral density SD.

Facility	LEPS	HIGS	VEGA
Location	Japan	USA	Romania
E [MeV]	1500−2400	1−100	0.2−20
$\Delta E/E$ [%]	1.2	0.8	0.5
I [γ/s]	10^7	$3{\cdot}10^9$	10^{11}
SD [γ/s/eV]	–	30	$5{\cdot}10^3$

It is very important to provide the entire ELI-NP community of setup designers, experiment developers, and data analyzers with a software tool for the VEGA beam generation. The best framework for this program is the GEANT4 C++ library [Ago+03] because this is the usual choice in nuclear physics simulations. Furthermore, this tool should accommodate the specificity of all research programs since they require sampling of different regions in the gamma

beam phase space when simulating the response of the detectors.

The work presented here briefly describes the simulation software for the simulation of the VEGA gamma beam from the electron-laser Compton interaction to its collimation system.

4.5.2 Simulation software

The main module, called *GammaGenerator*, takes as input the parameters of the electron and laser beams. For the electron beam, these are the energy E, the energy spread σ_E, the normalized emittance ε, the Twiss parameters α, and β, the bunch length σ_z, and the bunch charge Q. The laser beam parameters are the wavelength λ, the Rayleigh range β_0, the pulse power P, polarizarion degree ρ_d, and angle ρ_a. The beam−beam collision parameters are the crossing angle δ and the bunch−pulse collision frequency f.

The module starts by computing the expected event rate according to the following equation:

$$\frac{N_\gamma}{t} = \sigma_T L_{sc} \frac{QP\lambda}{\hbar c e}, \; L_{sc} = \frac{1}{2\pi\beta\varepsilon + \lambda\beta_0/2} \quad (4.5.1)$$

where $\sigma_T \approx 0.667$ b is the Thomson cross section and L_{sc} is the single collision luminosity [Sun+09].

The numerical value from Equation 4.5.1, corresponding to the electron and laser beam parameters specified by the user, is printed at the standard output (stdout) and should be used for scaling any output parameter proportional to the gamma beam intensity.

The module uses the CLHEP C++ library [CER] of space and Lorentz vectors and transformations to define all particle states and their modifications. In particular, the 4-momenta of the initial electron P_e^μ, the initial photon P_p^μ and the final gamma P_g^μ are initialized as *G4LorentzVector*. Also, 3-vectors for the electron position $\vec{r}_e$, photon polarization $\vec{\rho}_p$, gamma Stokes vector $\vec{\xi}_g$ and boost vector $\vec{b}$ from electron laboratory frame to its rest frame are initialized as *G4ThreeVector*.

In the next step, the electron $\vec{r}_e$ and P_e^μ vectors are generated using the input electron beam parameters E, σ_E, ε, α, β, and σ_z. Then, a photon is assumed to exist at $\vec{r}_e$, and its P_p^μ and $\vec{\rho}_p$ vectors are generated using the input laser beam parameters λ, β_0, ρ_d and ρ_a. The photon vectors are rotated with respect to the z axis, along which the electron beam propagates, by the crossing angle δ.

Once the initial states of the incoming electron and photon are generated, the Compton scattering can proceed. First, all initial vectors are transformed to the electron rest frame, with a boost $\vec{b}$, and the photon is aligned on $+z$. Working in this reference frame simplifies all equations significantly. For example, the exact energy−angle equation becomes:

$$\frac{1}{E_g} = \frac{1}{E_p} + \frac{1 - cos(\theta_g)}{mc^2} \quad (4.5.2)$$

where E_g and θ_g are the gamma energy and emission angle, and E_p is the photon energy. Then, E_g is generated from the energy differential cross-section $d\sigma/dE_g$ applied in the interval resulting from Equation 4.5.2 with $|cos(\theta_g)| \leq 1$. Once E_g is known, θ_g is directly computed from Equation 4.5.2. The azimuthal angle ϕ_g is generated from the angular differential cross-section $d\sigma/d\phi_g$ applied in the interval $[0, 2\pi]$. Finally, the mean linear component of the gamma Stokes vector $< \xi_{g3} >$ is calculated and the resulting gamma 4-momentum P_g^μ is boosted back to the laboratory frame.

The equations and algorithms used in writing the above module were compiled from several sources. The main ones were the articles by C. Sun and collaborators describing the code used for the gamma source at HIGS facility [SW11; Sun+09], the internal note by G. Suliman describing an older version of the gamma source code at ELI-NP facility [Sul14], and the CAIN software manual [Toy].

As it stands now, this module makes two main assumptions. The first is that the electron and laser beams have the space-time structure described by the parameters at the beginning of this section, and no distortions, like satellite peaks and tails, are present. The second is that the two beams are perfectly synchronized hence electron bunches and laser pulses overlap at their centers when they collide.

4.5.3 Beam properties after interaction

The *GammaGenerator* module was tested by comparing the simulation results with the general features of an LCB gamma source and with the expected beam properties from its constructor, Lyncean Technologies Inc. Only a brief description of these test results is given here, an in-depth analysis remaining to be detailed in an upcoming publication.

The first reproduced quantity from Table 4.5.1 is the total intensity I of $10^{11}\,\gamma$/s. Note that including an electron recoil correction in the total cross-section from Equation 4.5.1 results in a correction of about 3%.

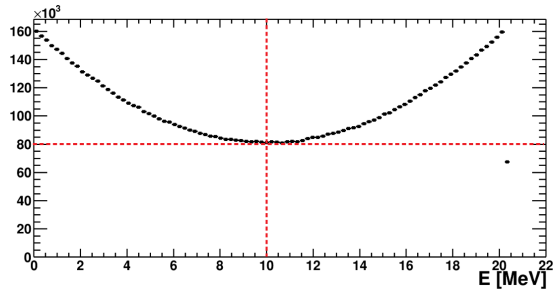

Figure 4.5.1: *The gamma beam energy spectrum for the highest energy reachable at VEGA facility. The dashed red lines show the location of the saddle point with minimum intensity.*

The energy spectrum has the typical U shape with the maximum intensity I_{max} at $E_{max,1}(\theta = \pi) = 0\,\text{MeV}$ and at $E_{max,2}(\theta = 0) = 4\gamma^2 E_L = 20\,\text{MeV}$. The saddle point with minimum intensity should be at $E_{min} \approx E_{max,2}/2$ and have the intensity $I_{min} \approx I_{max}/2$ [SW11]. These general features can indeed be observed in the spectra, as shown in Figure 4.5.1 for the highest gamma energy.

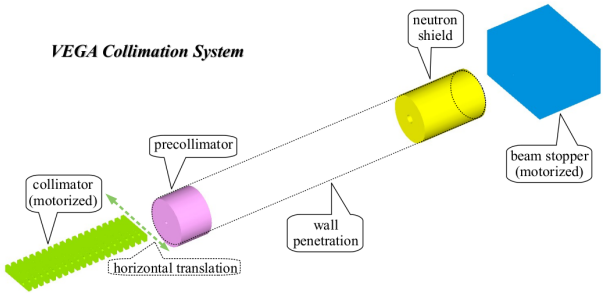

Figure 4.5.2: *The components of the VEGA collimation system: the beam stopper in blue, the neutron shield in yellow, the pre-collimator in pink, and the primary beam collimator in green. The interaction point is on the right side.*

4.5.4 Beam properties after collimation

The second module of the VEGA beam simulation tool is the *CollimationSystem* method of the standard GEANT4 class *DetectorConstruction*. It is a software implementation of the beam collimation system, which is comprised of several components, as shown in Figure 4.5.2. In their order from the interaction point, which is located at 7.68 m to the right of the beam stopper, these components are:

- a rectangular motorized beam stopper, shown in blue, made of 20 cm thick tungsten with a 5 mm hole;
- a cylindrical neutron shield, shown in yellow, made of 20 cm thick borated polyethylene with a 25 mm hole;
- a cylindrical pre-collimator, shown in pink, made of 10 cm thick lead with a 10 mm hole;
- a shielding wall made of concrete, not shown in Figure 4.5.2, with a penetration in which the neutron shield and the pre-collimator are encapsulated;
- the primary beam collimator, shown in green, a stack of 20 tungsten plates with 1 cm thickness and 1 cm gaps.

A vacuum beam pipe with kapton windows covers the distance between the exit window of the optical cavity around the interaction point and the beam stopper. The spaces between all of the above components of the collimation systems are filled with air.

The primary beam collimator is motorized and can translate horizontally in order to align one of its 7 holes with the gamma beam. The diameters of these holes are 0.5 mm, 0.7 mm, 0.9 mm, 1.1 mm, 1.4 mm, 3 mm, and 10 mm.

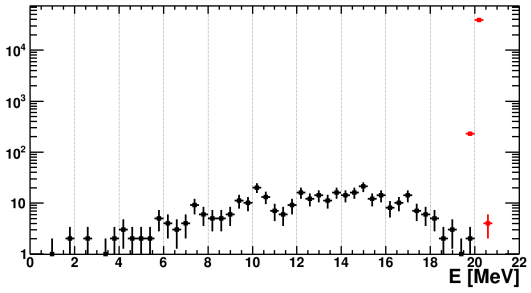

Figure 4.5.3: *The gamma beam energy spectrum for the highest energy after collimation with the* 0.7 mm *aperture. The primary gamma component is shown in red and the non-primary component in black.*

For given gamma beam properties at the interaction point, the choice of the primary collimator aperture is the main control method for the beam divergence, bandwidth, and flux on targets.

As an example, if one passes the highest energy beam with the energy spectrum shown in Figure 4.5.1 through the collimation system with the aperture of 0.7 mm, the resulting energy spectrum obtained is that shown in Figure 4.5.3. Two components can be observed in this spectrum. The high intensity, narrow bandwidth component shown in red contains collimated primary gammas and has $E = 20.2\,\text{MeV}$ with $\Delta E/E = 0.49\%$. The low intensity, broad component shown in black contains the non-primary particles (photons, electrons, and positrons) generated by interactions in the collimator system. The particular geometry chosen for the primary collimator, which alternates 20 plates with 20 air gaps, reduces the scattering of the gamma beam on the internal wall of the

apertures. The background level is expected to be more than three orders of magnitude lower than that of the primary gammas.

4.5.5 Summary and outlook

A simulation tool for the VEGA gamma beamline was implemented within the GEANT4 framework. It will evaluate the detector response and estimate the background levels for the various experimental setups developed by the GDED department at ELI-NP and its international partners.

Work on evaluating the beam properties at the interaction point and after the collimation system has been started, and some results were shown here. A more comprehensive publication with detailed results of this study is in preparation.

4.5.6 Acknowledgment

The author would like to thank G. Suliman for the discussions on software implementation of the Compton scattering process and C. Matei and B. Hornberger for the clarification of the VEGA beam parameters.

References

[Ago+03] S. Agostinelli *et al.* "GEANT4–a simulation toolkit". In: *Nucl. Instrum. Methods Phys. Res. A* 506 (2003), page 250 (cited on page 177).

[Bal+16] D. Balabanski *et al.* "Photofission experiments at ELI-NP". In: *Rom. Rep. Phys.* 68 (2016), S621 (cited on page 177).

[Bob+16] M. Bobeica *et al.* "Radioisotope production for medical applications at ELI-NP". In: *Rom. Rep. Phys.* 68 (2016), S885 (cited on page 177).

[Cam+16] F. Camera *et al.* "Gamma above the neutron threshold experiments at ELI-NP". In: *Rom. Rep. Phys.* 68 (2016), S539 (cited on page 177).

[CER] CERN. *CHLEP Project at CERN*. URL: https://proj-clhep.web.cern.ch (cited on page 178).

[Djo+16] N. Djourelov *et al.* "Positron production by gamma beam at ELI–NP". In: *Rom. Rep. Phys.* 68 (2016), S735 (cited on page 177).

[Dor+20] D. Doria *et al.* "Overview of ELI-NP status and laser commissioning experiments with 1 PW and 10 PW class-lasers". In: *Journal of Instrumentation* 15.09 (2020), pages C09053–C09053 (cited on page 177).

[Mur+14] N. Muramatsu *et al.* "Development of high intensity laser-electron photon beams up to 2.9GeV at the SPring-8 LEPS beamline". In: 737 (2014), pages 184–194. ISSN: 0168-9002. DOI: https://doi.org/10.1016/j.nima.2013.11.039 (cited on page 177).

[Sul+16] G. Suliman *et al.* "Gamma-beam industrial applications at ELI-NP". In: *Rom. Rep. Phys.* 68 (2016), S799 (cited on page 177).

[Sul14] G. Suliman. *ELI-NP internal note "Simulations for the Gamma Source at ELI-NP*. Technical report. ELI-NP, 2014 (cited on page 178).

[SW11] C. Sun and Y. K. Wu. "Theoretical and simulation studies of characteristics of a Compton light source". In: *Phys. Rev. ST Accel. Beams* 14 (4 Apr. 2011), page 044701. DOI: 10.1103/PhysRevSTAB.14.044701 (cited on pages 178, 179).

[Sun+09] C. Sun *et al.* "Energy and energy spread measurements of an electron beam by Compton scattering method". In: *Phys. Rev. ST Accel. Beams* 12 (6 June 2009), page 062801. DOI: 10.1103/PhysRevSTAB.12.062801 (cited on page 178).

[Tes+16] O. Tesileanu *et al.* "Charged Particle Detection at ELI–NP". In: *Rom. Rep. Phys.* 68 (2016), S699 (cited on page 177).

[Toy] K. Toyota. *CAIN user manual v2.35, 2011, KEK Tsukuba, Japan* (cited on page 178).

[Ur+16] C. Ur *et al.* "Nuclear Resonance Fluorescence Experiments at ELI-NP". In: *Romanian Reports in Physics* 68 (2016), S483. URL: http://www.rrp.infim.ro/2016_68_S/S483.pdf (cited on page 177).

[Wel+16] H. Weller *et al.* "Gamma Beam Delivery and Diagnostics". In: *Romanian Reports in Physics* 68 (2016), S447–S481 (cited on page 177).

[Wel+09] H. R. Weller *et al.* "Research opportunities at the upgraded HIγS facility". In: *Progress in Particle and Nuclear Physics* 1 (2009), pages 257–303. ISSN: 0146-6410. DOI: https://doi.org/10.1016/j.ppnp.2008.07.001 (cited on page 177).

4.6 Study of exotic nuclei produced in multinucleon transfer reactions at the IGISOL facility

Spataru A.[1,2,*], Balabanski D. L.[1], Constantin P.[1], Karpov A. V.[3], and Saiko V. V.[3]

[1] Extreme Light Infrastructure Nuclear Physics (ELI-NP), Horia Hulubei National Institute for R&D in Physics and Nuclear Engineering (IFIN-HH), Reactorului street No. 30, 077125, Bucharest-Măgurele, Romania
[2] Doctoral School in Engineering and Applications of Lasers and Accelerators, University Politechnica of Bucharest, 060042, Bucharest, Romania
[3] Flerov Laboratory of Nuclear Reactions, Joint Institute for Nuclear Research, Dubna, Moscow Oblast, 141980 Russia

[*] **anamaria.spataru@eli-np.ro**

Abstract

An experimental program is developed for studies of heavy neutron-rich isotopes produced via the gas cell at the IGISOL facility via multinucleon transfer (MNT) reactions. Such experimental programs are an excellent opportunity for studying the behaviour of exotic nuclei in gas cells that can be used in the future in studies of exotic nuclei using the ELISOL experimental setup at ELI-NP. The work presented here involves calculations of energy-angle distributions, which have been carried out in GEANT4 using reaction cross-sections from a Langevin-type model. The results involve using two thicknesses of a target placed in front of the gas cell. The objective of the analysis was to calculate the energy and angles of the ions of interest before entering the gas cell.

4.6.1 Introduction

In extreme stellar environments, the rapid neutron capture process (r-process) synthesizes heavy neutron-rich elements with short half-lives and small cross-sections. Their production is challenging and is the central focus of the nuclear facilities around the world because their study is of great interest as they can improve our knowledge of the structure of nuclei far away from stability, *e.g.*, in the vicinity of the $N = 126$ closed neutron shell. In recent years, it has been proven that large cross-sections can be generated in this region with the multinucleon transfer (MNT) process [Wat+15]. This type of reaction involves the exchange of nucleons between two colliding nuclei at near Coulomb barrier energies. The present paper aims to investigate the kinematics of an MNT reaction using the gas-cell technique at the Ion Guide Isotope Separator On-Line (IGISOL) facility at JYFL Accelerator Laboratory.

4.6.2 Theoretical models

The standard approach used to describe the MNT process belongs to the deep inelastic grazing collisions studies of A. Winther [Aag94] which is used in the simulation code GRAZING. The model uses a semi-classical approach to describe the incoming particles, which does not include the nuclear deformations and the fission process of the generated MNT products. Recent studies using the Langevin equation have resulted in a new model [KS17; SK19]. It considers an increased number of degrees of freedom and a complete description of the reaction products after evaporation, allowing the Langevin-type model to accurately describe the MNT reactions.

4.6.3 IGISOL facility

The IGISOL facility at JYFL uses the gas-cell technique to study exotic nuclei from nuclear reactions. A first study using the current MNT setup configuration has been performed using the α-decaying isotopes of the ^{136}Xe + ^{209}Bi reaction [Dic+20]. The experimental setup, shown schematically in Figure 4.6.1 consists of a helium-filled stopping cell for thermalization of the ions of interest, a SextuPole Ion Guide (SPIG) for extraction, and a mass separator dipole magnet that guides the ions to the detection setups. A beam dump is placed between the target and the gas cell for the MNT reaction to stop the primary beam from entering the helium gas. The reaction products mainly go around the beam dump due to the large emission angles, which are typical for the MNT reaction, and enter the gas cell through a havar window that separates the vacuum in the reaction chamber from the helium gas in the stopping cell. The target is mounted on the Heavy-ion

IGISOL (HIGISOL) platform [Vil+19], which allows for changes in the target-to-cell distance and the movement of the target with respect to the beam axis.

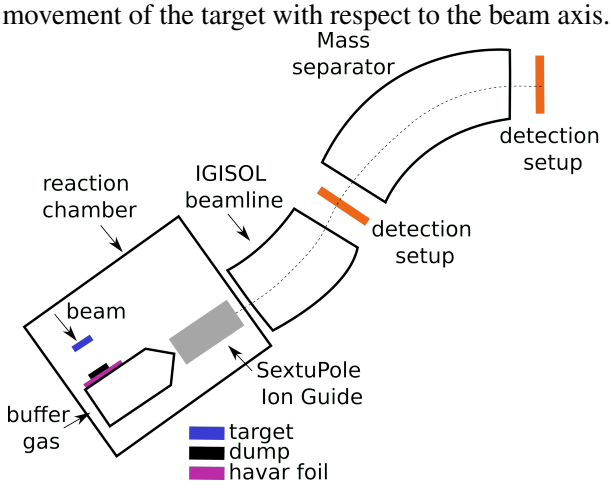

Figure 4.6.1: *Schematic drawing of the MNT setup configuration at the IGISOL facility at JYFL*

4.6.4 GEANT4 simulations

The MNT reaction studies at the IGISOL involve the use of a ^{136}Xe beam at an energy of 885 MeV and a ^{198}Pt target of 3 µm and 6 µm thickness. Simulations of the generation and release of the reaction products from the target have been performed with the GEANT4 [Ago+03] simulation toolkit. The purpose of the simulations was to study the energy (E) - angle (θ) distributions of the ions of interest that are released from the target, hit the beam dump, or enter the havar foil. For this, three modules regarding the primary beam generation, the Langevin-type model reaction cross-sections, and the experimental setup's geometry were added to the framework.

4.6.5 Results

The analysis focused on the target-like-fragments (TLFs), defined as the ions with a mass number, A, bigger than 198. They are emitted predominantly at high angles from the beam axis, which facilitates the beam dump and their separation from the projectile-like fragments (PLFs), ions with up to 5 extra or fewer nucleons than the projectile ions.

In Figure 4.6.2 the (E - θ) distributions of the TLFs that are released from the two targets are shown together with those for the ions that hit the beam dump or enter the havar foil. At both thicknesses, the TLFs are shown to be released at large angles ($\theta > 30°$) and low energies. All ions with $\theta > 40°$ are stopped in the beam dump. These results allow having, in both cases, a high number of TLFs that hit the havar foil. However, in the case of the 6 µm target, the TLFs are released at lower E/A than for the 3 µm target because of the increased number of scatterings in the target.

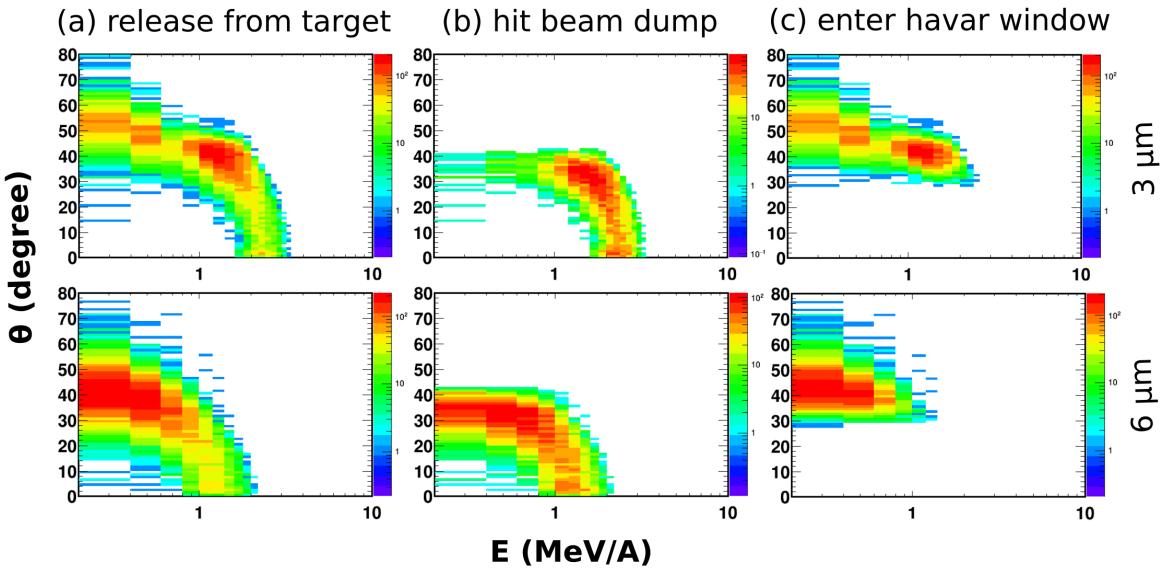

Figure 4.6.2: *Simulated (E - θ) distributions of the TLFs that: (a) are released from the target, (b) hit beam dump, (c) enter havar window, considering a* 3 µm *and* 6 µm *thick target.*

4.6.6 Conclusion

In this study, we discussed the GEANT4 simulations of the ^{136}Xe + ^{198}Pt reaction at IGISOL. The work focused on the TLFs that are released from the target and hit the havar window. The results show that a big part of TLFs are produced at high angles and low energies, facilitating their stopping in the gas cell.

In the future, a detailed study that includes the thermalization of the TLFs in the helium gas of the stopping cell will be performed.

4.6.7 Acknowledgment

The authors would like to thank Anu Kankainen, Olga Beliuskina, and Timo Dickel for the fruitful discussions. The authors from ELI-NP acknowledge the support of the Romanian Ministry of Research and Innovation under research contract PN 19 06 01 05.

References

[Aag94] Aage Winther. "Grazing reactions in collisions between heavy nuclei". In: *Nucl. Phys. A* 572 (1994), pages 191–235 (cited on page 181).

[Ago+03] S. Agostinelli *et al.* "GEANT4–a simulation toolkit". In: *Nucl. Instrum. Methods Phys. Res. A* 506 (2003), page 250 (cited on page 182).

[Dic+20] T. Dickel *et al.* "Multi-nucleon transfer reactions at ion catcher facilities - a new way to produce and study heavy neutron-rich nuclei". In: *J. Phys.: Conf. Ser.* 1668 (2020), page 012012. DOI: 10.1088/1742-6596/1668/1/012012 (cited on page 181).

[KS17] A. Karpov and V. Saiko. "Modeling near-barrier collisions of heavy ions based on a Langevin-type approach". In: *Phys. Rev. C* 96 (2017), page 024618 (cited on page 181).

[SK19] V. Saiko and A. Karpov. "Analysis of multinucleon transfer reactions with spherical and statically deformed nuclei using a Langevin-type approach". In: *Phys. Rev. C* 99 (2019), page 014613 (cited on page 181).

[Vil+19] M. Vilén *et al.* "High-precision mass measurements and production of neutron-deficient isotopes using heavy-ion beams at IGISOL". In: *Phys. Rev. C* 100 (2019), page 054333. DOI: 10.1103/PhysRevC.100.054333 (cited on page 182).

[Wat+15] Y. X. Watanabe *et al.* "Pathway for the Production of Neutron-Rich Isotopes around the N=126 Shell Closure". In: *Phys. Rev. Lett.* 115 (2015), page 172503. DOI: 10.1103/PhysRevLett.115.172503 (cited on page 181).

4.7 Ion catchers with gamma beam-driven production

Nichita D.[1,2,*], Balabanski D. L.[1,2], and Constantin P.[1]

[1] Extreme Light Infrastructure (ELI-NP) Horia Hulubei National Institute for R&D in Physics and Nuclear Engineering (IFIN-HH), Reactorului 30, 077125 Bucharest–Măgurele, Romania
[2] Doctoral School in Engineering and Applications of Lasers and Accelerators, University Politechnica of Bucharest, Splaiul Independenței 313, 060042 Bucharest, Romania

[*] **dragos.nichita@eli-np.ro**

Abstract

This report presents estimations of the production yields, extraction efficiency, and transport survival of exotic neutron-rich nuclei generated via photo-fission of actinides. A case study is done by simulating photo-fission in a stack of $^{238}UO_2$ thin targets placed in a High Areal Density Orthogonal extraction Cryogenic Stopping Cell irradiated by a γ beam delivered by the proposed Gamma Factory (GF) at CERN.

4.7.1 Introduction

Radioactive Ion Beam (RIB) production has been at the forefront of nuclear physics developments for the last decades mainly because the study of exotic nuclei far away from the valley of stability help in understanding the nuclear structure and constrain the theoretical nuclear models. Having reliable information about the nuclear matter, especially for exotic conditions, significantly impacts several domains ranging from astrophysics and understanding the birth and development of our Universe. The same can be said for applications in medical physics and industry. However, even with the many RIB facilities around the world in existence, there are still many neutron-rich nuclei that have not been measured yet due to small production cross-sections and short lifetimes, as shown in Figure 4.7.1.
The gray area in the Segrè diagram shows the nuclei that have not been measured in the Laboratory. The contour indicates the neutron drip-line [Bas04]. This work sketches a possible solution for promoting RIB-based research to the most exotic neutron-rich nuclei.

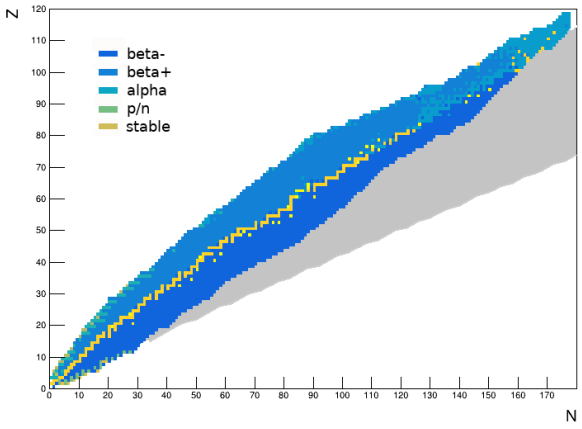

Figure 4.7.1: *Isotope chart function of proton number (Z) and neutron number (N) showing the decay modes and unmeasured nuclei region (gray).*

4.7.2 Experimental setup

The experimental setup consists of a High Areal Density Orthogonal extraction Cryogenic Stopping Cell (HADO-CSC) [Dic+16] filled with He gas enclosing a special design target system summing 50 3 µm thin $^{238}UO_2$ targets inclined at an angle of 10° with respect to the incident beam. Those parameters have been found to be optimal in a previous study [Nic+20]. The sketch of this setup is shown in Figure 4.7.2.

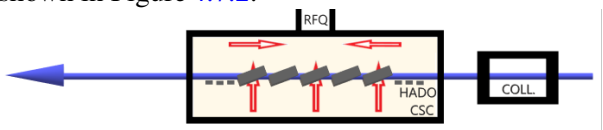

Figure 4.7.2: *HADO-CSC setup sketch with its target system (dark grey) enclosed in He gas (yellow) and the electric drift fields (red arrows). The γ beam (purple) is collimated (COLL) to the target area to minimize background. The RIB is formed with the help of a Radio-Frequency Quadrupole (RFQ).*

The gamma beam specifications used in this case study are taken from the Gamma Factory (GF) project [Kra15] that is proposed for development at CERN. The Gamma Factory project shows that the partially stripped ions traveling close to the speed of light inside the accelerating system can be used to

create a high-intensity gamma beam. By absorbing laser photons, the resonant X-ray decay of the relativistic ions is turned into more energetic photons due to the Lorentz boost. Furthermore, the thin target design [Con+17] facilitates a fast and efficient release of the fission fragments produced via the photo-fission reaction. The ions are extracted using drift electric fields, and the transport on the walls is done with radio-frequency carpets [Rot+19].

4.7.3 Production yield estimations

GEANT4 simulations have been performed for the case where the target system is 100 m away from the gamma beam interaction point, and the beam is collimated to irradiate within the target system dimensions. The full intensity of the gamma beam of about $1 \times 10^{17} n_\gamma s^{-1}$, is reduced to about $1 \times 10^{15} n_\gamma s^{-1}$ that hits the target system at the simulated distance and after the collimation. The integrated yield of the fission fragments that are being released into the CSC gas is about $1 \times 10^{12}\, n_{ion}\, s^{-1}$ [Nic+21]. The paths of the ions in the gas of the HADO-CSC are shown in Figure 4.7.3.

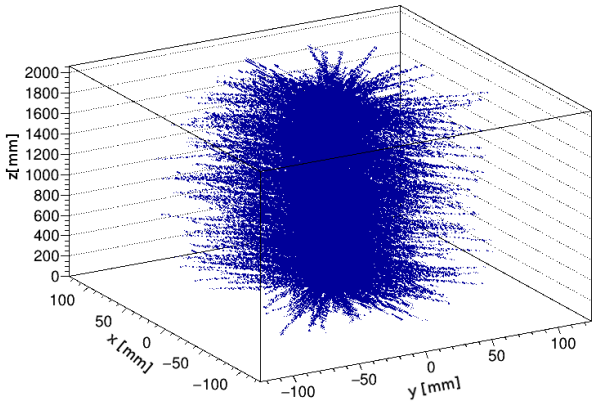

Figure 4.7.3: *3D plot of the CSC, where ions are being released from the target and stopped in the gas of the cell.*

According to the simulation, the mean energy of each released ion is close to 40 MeV, so this sums up to about 4×10^{13} MeV deposited into the gas each second. This energy deposition creates ionization in the He and thus a charged gas cloud mainly localized in the vicinity of the target system. This dense charged area generates an additional electric field that could disrupt the main drift electric field and perturb the ion extraction, so this impact was further investigated.

4.7.4 Extraction and transport

The position of each main charge carrier, fission fragments, and He^+ ions has been transferred into SIMION where a full Particle In Cell (PIC) analysis was done in order to analyze the generated electric fields due to the space charge effect and the extraction efficiency accordingly. The study computed each ion movement after recalculating at each step the combined electric field generated by all charges in the cell. An optimum setup was achieved with a systematic study of variation in the drift electric field from as low as $10\,V\,cm^{-1}$ to a maximum of $10\,V\,cm^{-1}$ and in the charge created inside the cell from 0.4 µC to 1.4 µC. The charge variation was done by changing the beam regime from continuous to different pulsed time structures. The highest extraction efficiency, thus highest ions yield available for study, is around 7×10^{10} [Nic+21] which is much higher than what can be currently achieved for the refractory elements at other facilities.

4.7.5 Results and conclusions

These results indicate an opportunity to measure exotic neutron-rich isotopes closer to the neutron drip line than ever before, offering a possibility of the direct study of nuclei in the r-process path region. In Figure 4.7.4 we show an example of extracted yields for the Indium isotopic chain. The r-process region, which is enclosed within the black lines, is entirely populated. In short, the realization of the GF project at CERN will open the avenue for studies of exotic nuclei further away towards the neutron drip-line.

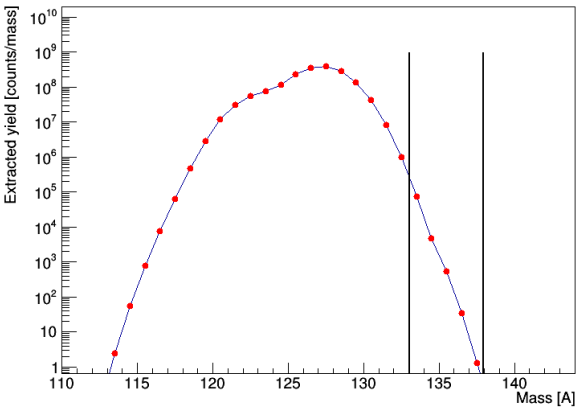

Figure 4.7.4: *Indium isotope chain yield (red) and r-process path window (black) [SB06]*

References

[Bas04] D. Basu. "Neutron and proton drip lines using the modified Bethe–Weizsacker mass formula". In: *Int. J. Mod. Phys. E* 13, No.4 (2004), pages 747–758. DOI: https://doi.org/10.1142/S0218301304002491 (cited on page 185).

[Con+17] P. Constantin *et al.* "Design of the gas cell for the IGISOL facility at ELI-NP". In: *Nucl. Instrum. Methods Phys. Res. B* 397 (2017), pages 1–10. DOI: https://doi.org/10.1016/j.nimb.2017.02.032 (cited on page 186).

[Dic+16] T. Dickel *et al.* "Conceptual design of a novel next-generation cryogenic stopping cell for the Low-Energy Branch of the Super-FRS". In: *Nucl. Instrum. Methods Phys. Res. B* 376 (2016), page 216. DOI: https://doi.org/10.1016/j.nimb.2016.01.015 (cited on page 185).

[Kra15] M. W. Krasny. The Gamma Factory proposal for CERN. arXiv:1511.07794 [hep-ex]. 2015. arXiv: 1511.07794 [hep-ex] (cited on page 185).

[Nic+20] D. Nichita *et al.* "Optimization of photo-fission fragment production in the ELISOL setup at ELI-NP". In: *U.P.B. Sci. Bull. A* 82 (2020), page 297 (cited on page 185).

[Nic+21] D. Nichita *et al.* "Radioactive ion beams production at the Gamma Factory". In: *Ann. Phys. (Berl.)* In press (2021). DOI: https://doi.org/10.1002/andp.202100207 (cited on page 186).

[Rot+19] A. Rotaru *et al.* "Simulation of circular radio-frequency carpets for ion extraction from cryogenic stopping cells". In: *U.P.B. Sci. Bull. A* 81 (2019), page 197 (cited on page 186).

[SB06] H. Schatz and K. Blaum. "Nuclear masses and the origin of the elements". In: *Europhys. News* 37 (2006), pages 16–21. DOI: https://doi.org/10.1051/epn:2006502 (cited on page 186).

4.8 Study of the $LaBr_3$ detectors response function change due to temperature oscillations

Gutoiu R. A.[1,2,*], Nichita D.[1,3], Söderström P.A.[1], and Roman T.[1]

[1] Extreme Light Infrastructure (ELI-NP) & Horia Hulubei National Institute for R&D in Physics and Nuclear Engineering (IFIN-HH), Str. Reactorului No. 30, 077125 Bucharest–Măgurele, Romania
[2] University of Bucharest, Faculty of Physics, P.O.Box MG-11, RO-077125, Bucharest–Măgurele, Romania
[3] Doctoral School in Engineering and Applications of Lasers and Accelerators, University Politechnica of Bucharest, 060042 Bucharest, Romania

[*] **alexandru.gutoiu@eli-np.ro**

Abstract

This work reports a systematic analysis of the $LaBr_3$ detectors response function change due to temperature oscillation. A ^{60}Co source is used to take experimental data, and the position drift of the 1173 keV gamma is calculated individually for 10 minutes parts of a 24 hours run. The results show a strong correlation of the detector response with the change in temperature so correcting methods are briefly suggested in the conclusion.

4.8.1 Introduction

In order to push the limits of science forward, more and more efficient and precise equipment is needed. One of the most used devices for measuring ionizing radiation in experimental nuclear physics is the scintillation detector. Although the scintillation process is one of the oldest techniques on the record, it remains probably the most used for this purpose. The ionizing radiation passes through certain materials and produces scintillation light. In a typical detector unit, the scintillation light produced interacts with a semitransparent photo-cathode, and through the photoelectric effect, photo-electrons are produced. Because the number of generated electrons is too small to be properly measured, an electron multiplier is typically used (Photo-Multiplier Tube or PMT). The amplified electric signal is analyzed, and ideally, the integral of each signal amplitude and the energy of the detected radiation should be linear proportional.

Due to its reasonably good energy resolution and its fast decay time, $LaBr_3$ detectors are used in applications involving high counting rates and fast timing. The energy resolution can approach the Poisson statistical limit of scintillators [Ilt+06]. An improvement in the timing performance can further be obtained by doping the crystal with cerium. [Sha+03].

In this work, we will analyse the impact of the temperature variation on the detector response function for the "ELI Gamma Above Neutron Threshold: The Gamma-Neutron" (ELIGANT) $LaBr_3$:Ce detectors.

4.8.2 Experimental setup

For the experimental study reported here, 15 $LaBr_3$:Ce scintillator detectors were used. The experiment was performed using the "ELIGANT" setup [Cam+16; Krz+19; Söd+22] developed at ELI-NP. Data from a ^{60}Co source was collected for 24 hours using the above-mentioned detectors and saved using CoMPASS software.

Alongside the scintillators' response, the temperature and humidity data were taken. The response data has been acquired by the "ELIGANT" digital Data Acquisition (DAQ). The data was divided into time windows for the analysis, each having about 10 minutes. Each window was then analysed separately to compare the data stability over time. The temperature was also collected at 10 minutes intervals using a thermal sensor mounted in the experimental room.

4.8.3 Analysis

Figure 4.8.1 shows the decay scheme of ^{60}Co with the two energies corresponding to the specific transitions.

By analysing the full-energy peaks positions of the gamma spectrum of ^{60}Co, one can observe that those positions are not constant in time. The shift is attributed to the temperature change in the experimental room. Figure 4.8.2 shows the spectrum of ^{60}Co taken using one of the $LaBr_3$:Ce detectors, at two different windows in time, corresponding to two different temperatures of the environment (25.6 °C - black spectrum and 23.2 °C - red spectrum). A

third full-energy peak appears due to intrinsic radioactivity from ^{138}La with transition corresponding to a 1435 keV gamma emission. One can also observe 789 keV γ-rays from ^{138}Ce together with the associated β-decay continuum.

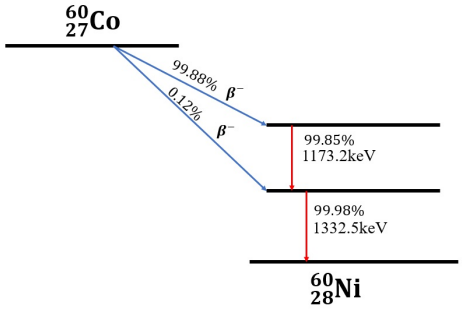

Figure 4.8.1: *Decay scheme for ^{60}Co*

The first full-energy peak corresponding to an energy of 1173 keV was taken as a reference, and for each time window, we have fitted the peak with a Gaussian function extracting the mean value.

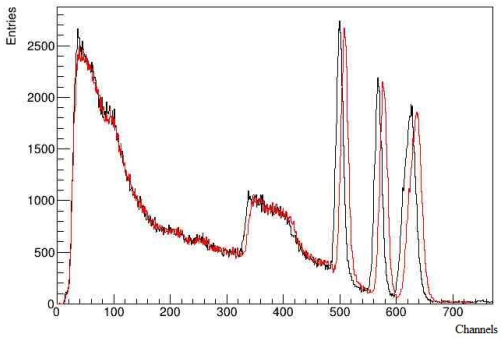

Figure 4.8.2: *Raw ^{60}Co spectrum for 25.6°C (black) and 23.2°C (red)*

4.8.4 $LaBr_3$ response versus temperature - results

In Figure 4.8.3 we show the relative drift from the average for all $LaBr_3$:Ce gamma detectors and the temperature deviations from the mean value as a function of time. A strong correlation is noted.

The relative drift of the channel for each detector was calculated using the formula:

$$\varepsilon_i = \frac{P_i - \bar{P}}{\bar{P}} \cdot 100$$

where ε_i, P_i, $\bar{P}$ are the relative drift for the i-th 10min data file, the position of the 1173 keV peak obtained by fitting the i-th data file and the peak position at the reference temperature of 25°C.

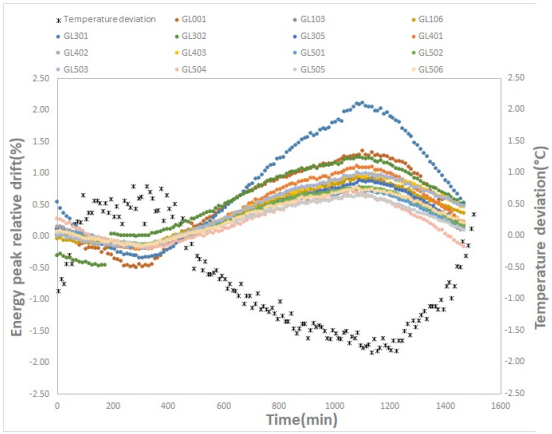

Figure 4.8.3: *Relative drift [%] of the 1173 keV peak position for each detector and temperature fluctuation from average [°C] in time [min]*

For the temperature absolute deviation, we computed:

$$\Delta\tau_i = \tau_i - \bar{\tau}$$

where $\Delta\tau_i$, τ_i and $\bar{\tau}$ represent the temperature absolute deviation, the temperature for the i-th time interval and the average temperature in the experimental room, $\bar{\tau}$=25°C. From these data, we could observe an inverse proportionality relation between ε_i and $\Delta\tau_i$. Figure 4.8.4 shows the plot of the average channel drift from all 15 $LaBr_3$:Ce detectors function of temperature. For this the value $\bar{\tau}$=25°C was used as reference temperature and $\bar{P}$ is the peak mean position for the corresponding temperature.

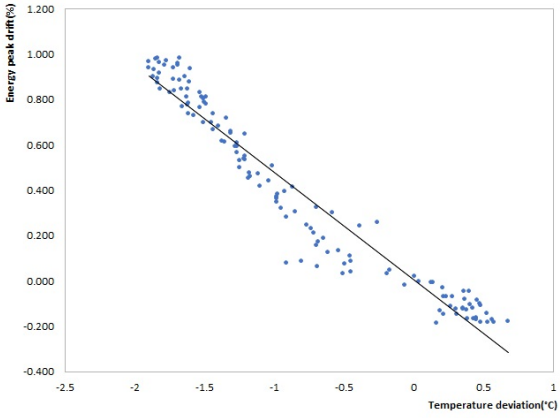

Figure 4.8.4: *Average relative drift of the position of the 1173 keV ^{60}Co photopeak with temperature variation*

By using the slope of the fitting line (see Figure 4.8.4), one can determine the average drift with temperature as $-0.475\%/°C$. These results are in agreement with others found in literature [Mos+06].

4.8.5 Conclusion

An important impact can be observed collectively on all the detectors and some individual contributions. The latter is far less important. Due to the temperature not always being stable, difficulties can appear in data collection and analysis. One way to monitor these is by putting a thermal sensor in the experimental room. An energy calibration should be made using data taken at the same temperature to assure coherent results. The data acquisitions should be divided into shorter duration runs so each could be correlated with the temperature at that time or synchronized with the correct calibration. Knowing the dependence between the drift of the channels and temperature fluctuation, one could even adapt the calibration for every data acquisition window obtained by applying a correcting factor determined as a function of temperature. Regardless of the method used, one should always consider the possibility of the detector response function drift, verify and account for it, especially in the case of the scintillators, which we were shown to be quite sensitive to temperature change.

References

[Cam+16] F. Camera *et al.* "Gamma above the neutron threshold experiments at ELI-NP". In: *Rom. Rep. Phys.* 68 (2016), S539 (cited on page 189).

[Ilt+06] A. Iltis *et al.* "Lanthanum halide scintillators: Properties and applications". In: *Nuclear Instruments and Methods in Physics Research Section A: Accelerators, Spectrometers, Detectors and Associated Equipment* 563.2 (2006), pages 359–363. DOI: https://doi.org/10.1016/j.nima.2006.02.192 (cited on page 189).

[Krz+19] M. Krzysiek *et al.* "Simulation of the ELIGANT-GN array performances at ELI-NP for gamma beam energies larger than neutron threshold". In: *Nucl. Instrum. Methods Phys. Res. A* 916 (2019), page 257 (cited on page 189).

[Mos+06] M. Moszyński *et al.* "Temperature dependences of LaBr3(Ce), LaCl3(Ce) and NaI(Tl) scintillators". In: *Nuclear Instruments and Methods in Physics Research Section A: Accelerators, Spectrometers, Detectors and Associated Equipment* 568.2 (2006), pages 739–751. ISSN: 0168-9002. DOI: https://doi.org/10.1016/j.nima.2006.06.039 (cited on page 190).

[Sha+03] K. Shah *et al.* "LaBr3:Ce scintillators for gamma-ray spectroscopy". In: *IEEE Transactions on Nuclear Science* 50.6 (2003), pages 2410–2413. DOI: 10.1109/TNS.2003.820614 (cited on page 189).

[Söd+22] P.-A. Söderström *et al. ELIGANT-GN – ELI Gamma Above Neutron Threshold: The Gamma-Neutron setup*. Nucl. Instrum. Methods Phys. Res. A, in print. 2022 (cited on page 189).

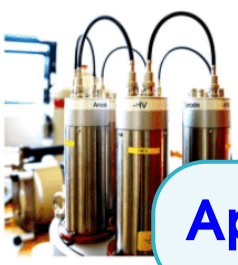
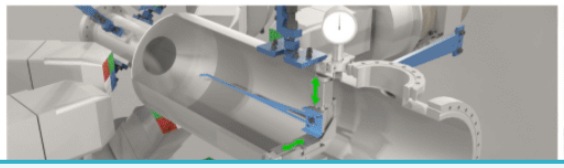

Applied and Technical Work at GDED

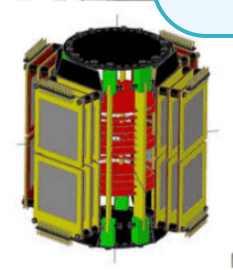
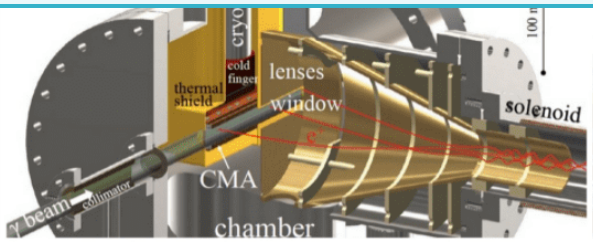

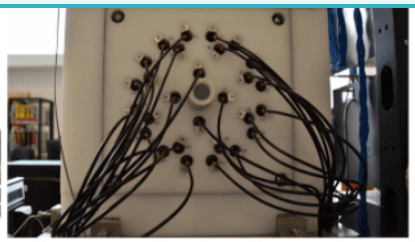


4.9 Annealing and post-annealing testing of ELIADE clover HPGe detectors

Dhal A.[1,*], Testov D.[1,2], Ramirez F.[1], Aogaki S.[1], Turturică G.[1], Suliman G.[1,3], Niţescu G.[1,3], Petcu C.[1], Tatulea B.[1], Ur C. A.[1], and Balabanski D. L.[1],

[1] Extreme Light Infrastructure (ELI-NP) & Horia Hulubei National Institute for R & D in Physics and Nuclear Engineering (IFIN-HH), Str. Reactorului No. 30, 077125 Bucharest–Măgurele, Romania
[2] Joint Institute for Nuclear Research, 6 Joliot-Curie St., 141980 Dubna, Russia
[3] Physics Department, University POLITEHNICA of Bucharest, Splaiul Independenţei No. 313, 060042 Bucharest - Sector 6, Romania

[*] **anukul.dhal@eli-np.ro**

Abstract

Within the ELI-NP project the main detection system used for Nuclear Resonance Fluorescence (NRF) studies is represented by ELIADE (ELI-NP Array of DEtectors) - a multi detector array encompassing eight high-purity germanium (HPGe) segmented clover detectors and four cerium bromide ($CeBr_3$) detectors. The resolution and efficiency of HPGe detectors deteriorates over time, and in order to restore these operational characteristics, their germanium crystals need to be periodically annealed. In this report, we present the setup of a dedicated annealing station, the procedure for annealing HPGe clover detectors, as well as the post-annealing testing of a number of such detectors using standard radioactive sources.

4.9.1 Introduction

Radiation damage (mainly of the neutron-induced kind) is responsible for the deterioration of the energy resolution and, consequently, the efficiency of high-purity germanium (HPGe) segmented clover detectors. This damage triggers the appearance of defects within the germanium crystals, leading to an improper charge collection process which continues to deteriorate over time [Gor08; Kno10]. Additionally, the prolonged storage of HPGe detectors at room temperature induces significant de-gassing from several internal components and sealing substances located inside the vacuum chamber of the detector, thereby essentially contributing to a similar reduction in the operational parameters described above. Therefore, in order to restore the resolution of an HPGe detector, its germanium crystal needs to be annealed through a controlled heating process for a specific period, all the while maintaining vacuum inside the detector throughout the respective heating and cooling cycles. For this purpose, we have set up an annealing station at ELI-NP [Gal+18; Tan+20] for restoring the capabilities of the HPGe clover detectors (4×60×90 Seg32 type) [Scr+05] used in the ELIADE array [Söd+19; Ur+16].

4.9.2 Annealing setup

A schematic representation of the annealing setup is shown in Figure 4.9.1. The germanium crystals of the HPGe detectors are enclosed within a vacuum-sealed chamber and, therefore, a high degree of vacuum needs to be preserved for the entire duration of the annealing process. To begin with, this vacuum-tight chamber needs to be connected to an external turbo vacuum pump using a special pumping sleeve (*i.e.* VOP11) designed by the manufacturer (*i.e.* Canberra) to be compatible with the segmented clover detectors.

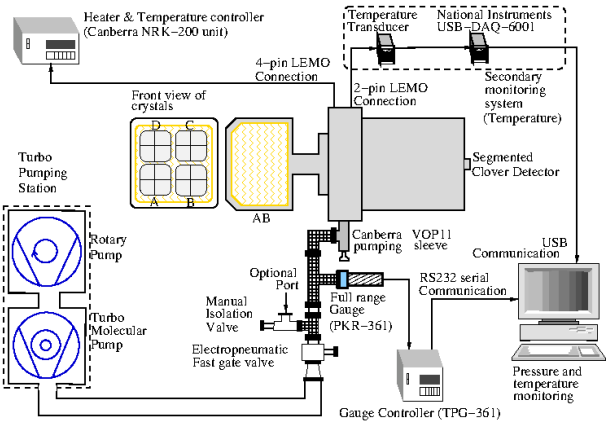

Figure 4.9.1: *A schematic representation of the annealing setup for HPGe clover detectors.*

A vacuum of $\leq 1 \times 10^{-6}$ mbar needs to be maintained during the annealing process. In the present work, the vacuum level was monitored by a pressure gauge (PKR-361, Pfeiffer) connected to the pumping line in the vicinity of the detector. In order to be annealed, the germanium crystal needs to undergo a thermal cycle involving heating and cooling. The heating is performed at 75 °C for $\sim$ 60 hours, followed by

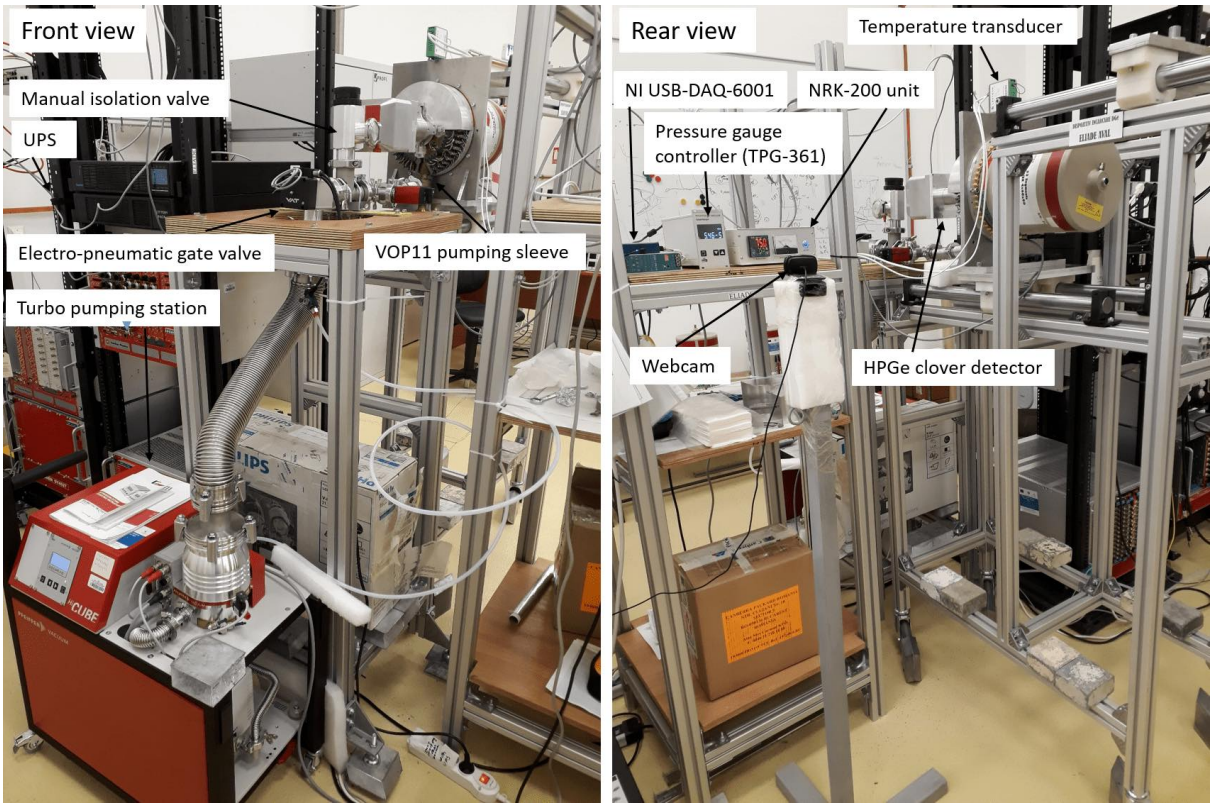

Figure 4.9.2: *Complete annealing setup with all of its different components under operation during the annealing process of one of the ELIADE HPGe segmented clover detectors.*

a total cooling time back to room temperature of $\sim$ 40 hours. A "neutron damage repair kit" (NRK-200 unit) was used to control the heating during the annealing process described here. The variation of the HPGe detectors' internal temperature and pressure was carefully monitored to ensure a smooth operation of the heating and cooling phases. Minor pressure fluctuations can indicate residual outgassing from the detector or could be caused by the pumping station itself. Nevertheless, any large fluctuations observed in either pressure or temperature need to be thoroughly investigated to root out their possible cause and then implement safety measures to prevent future reappearance. For this reason, the pressure and temperature parameters were monitored continuously throughout the annealing process described here, both online and in-person. To protect the system in the event of a power failure, a fast gate valve was also installed as part of the pumping circuit so as to close immediately ($\leq$ 1 s) should such an event occur, thereby safeguarding both the crystals as well as the vacuum inside the detector during the annealing cycle. Furthermore, all of the annealing station's components are powered through an Uninterrupted Power supply (UPS) unit for extra safety. Apart from the turbo pump, all of the vacuum components of the setup are mounted on a custom-designed annealing table featuring a circular cut out at the top which allows the bellow tube coming from the pump to pass through this hole and connect to the vacuum components mounted on top of the table. The detector support table has also been specifically designed to feature a movable metal platform upon which the HPGe clover detector can be fixed in a horizontal position during the annealing process.

4.9.3 Annealing procedure

Prior to the start of the annealing process, the preamplifier cover is removed from the HPGe detector, a supportive rectangular metal plate is affixed to its body, and the VOP11 sleeve is screwed onto its exposed pumping port. The detector is then placed horizontally on the support table, with the A & B crystal sides facing downward. The attached rectangular plate is then fixed to the metal platform on the support table, thereby allowing the detector to slide in an axial direction so as to facilitate the coupling and de-coupling of its vacuum port to the external pumping line. Since the detector is mounted in a horizontal position with the A & B sides facing downward, the affixed VOP11 sleeve will also be oriented perpendicular to the floor. The bellow of the

external pumping line is then connected to the open port on the VOP11 sleeve. The complete annealing station setup, with all of its different operating components pictured during the annealing of one of the ELIADE HPGe clover detectors, is shown here in the Figure 4.9.2.

After the detector has been connected to the pumping line, the pump is turned on with the vacuum port of the detector still closed until the vacuum reaches $\sim 7\times10^{-6}$ mbar or better. Once that level has been reached, the hex screw protecting the vacuum port of the detector is carefully unscrewed through a steady anti-clockwise rotation of the VOP11 piston, all the while monitoring any fluctuations in pressure. The vacuum port will normally be opened fully after $\sim$ 10 to 15 anti-clockwise rotations, after which the piston of the VOP11 sleeve should be pulled down slowly and smoothly until it reaches the end of travel. By doing so, the hex screw blocking the vacuum port becomes attached to the head of the piston and is slowly pulled down along with it. This particular step typically triggers a pressure spike as the detector is opened to the rest of the vacuum system, after which the pressure slowly goes down to the previous or a slightly higher vacuum level over the next $\sim$ 4 hours. Once that new baseline of stability is reached, the heating procedure can begin by connecting the NRK-200 unit to the 4-pin Lemo connector on the detector and switching it on. The temperature value is thus set to 75 °C, which takes $\sim$ 8 hours to reach starting from room temperature. As the temperature inside the detector slowly increases, the system's pressure also rises since the initial heating of the germanium crystals creates outgassing. However, once a steady internal temperature has been reached, the vacuum level will start improving toward its initial value or even better. Once the heating cycle is completed after $\sim$ 60 hours, the heating temperature is dialed back to 25 °C to allow the detector to cool down slowly. It usually takes $\sim$ 40 hours for the germanium crystal to drop back to room temperature. The NRK-200 unit is switched off and disconnected from the detector at the end of the cooling process. Following that, the detector's vacuum port is closed tightly using the VOP11 piston before the pump is stopped, the pumping line is disconnected from the VOP11 sleeve, and the detector is dismounted from the table. Finally, the VOP11 sleeve is itself carefully disconnected, after which the detector is removed from the rectangular metal plate, and the pre-amplifier cover is reattached to its body.

4.9.3.1 The monitoring process

The continuous monitoring of the vacuum level, crystal temperature, and electric power supply is essential during the entire annealing procedure to protect the detector from overheating and vacuum loss. For example, should the vacuum deteriorate due to issues related to the pump or the appearance of a leak within the system, then the heating needs to be stopped, and the detector's vacuum port must be closed using the VOP11 piston. Similarly, if the internal temperature rises too far beyond the set point of 75 °C, then the heater needs to be switched off. Last but not least, in the event of a power failure, all of the components powered via the UPS need to be shut down before their battery runs out. To this end, monitoring the UPS's charge associated with the annealing setup becomes equally important.

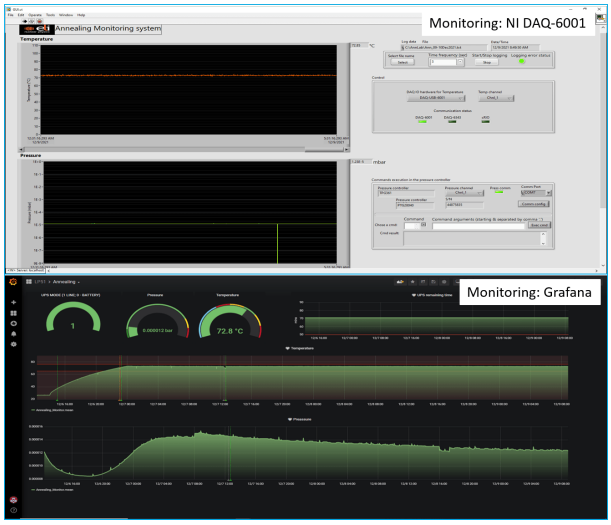

Figure 4.9.3: *Screen captures of online monitoring displays for NI DAQ-6001 (upper panel) and Grafana (lower panel).*

The pressure gauge controller communicates with the annealing computer through USB, allowing the online monitoring of this parameter. The germanium crystal's temperature is also monitored online using a DAQ-6001 module from National Instruments (NI). The DAQ-6001 module receives this information from the 2-pin Lemo connector of the detector via a temperature transducer. These critical parameters feed into the monitoring software based on a LabVIEW script. The Grafana web application interfaces with the NI database and the UPS to provide real-time pressure, temperature, and UPS status updates. In the case of an adverse event, Grafana automatically sends alarm messages to registered email addresses and alert texts to SIM cards. Screen captures of the online monitoring displays of both the NI DAQ-6001 module and Grafana are shown here

in Figure 4.9.3. As an added precaution, the vacuum level and crystal temperature values displayed on their respective controller units are also monitored online through a webcam installed next to the annealing setup.

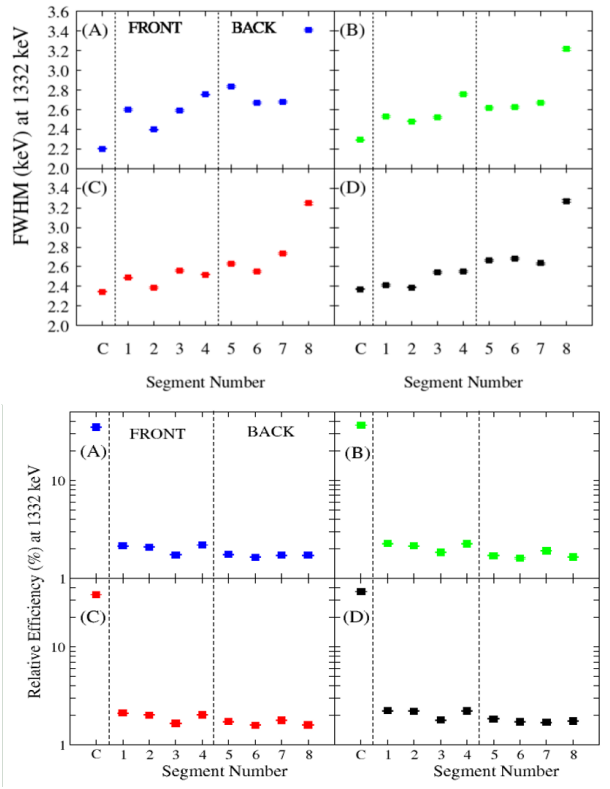

Figure 4.9.4: *Measured resolutions (upper panel) and relative efficiencies (lower panel) for the* 1332 keV *γ-ray peak of* ^{60}*Co. The numbers 1 - 8 and 'C' on the x-axis represent the segment numbers and core signals of the respective detector.*

4.9.4 The post-annealing testing

After a minimum of 24 hours have passed from the end of the annealing process, the detector is cooled down with liquid nitrogen (LN2). Thorough observations are made to ensure the detector is vacuum-tight, and the detector's response to the initial cooling is normal. The pre-amplifier power supply ($\pm$12 V) is then applied to the detector after another $\sim$ 24 hours have passed following the start of the LN2 cooling. A minimum of 6 hours after that, the high-voltage power supply (+3500 V) is applied while constantly monitoring the crystal's response to the applied voltage. Finally, by that point the HPGe detector is ready for measurements.

During the testing process of the first three annealed detectors (S/N - 29, 30 & 32), an analog data acquisition (DAQ) system was used. Standard ^{60}Co and ^{152}Eu radioactive sources were positioned axially 25 cm away from the front face of the detector, and measurements were taken separately for each source. Using the analog DAQ, we took the pre-amplifier signal outputs from the detector to shaping amplifiers, followed by a six-channel Multiport II MCA (Multi-Channel Analyzer). Data collection was performed via the Gamma Analysis software GENIE [Tec]. The resolutions and relative efficiencies of the individual segments and cores were measured for all three detectors. These were then compared to the datasheet from the manufacturer and our earlier analog results obtained in 2016. Our present measurement results were comparable both to those measured in 2016 and those specified in the datasheet. The resolution and relative efficiency of the individual segments and cores of one of the segmented clover detectors (*i.e.* S/N-32), obtained at the 1332 keV γ-peak using a ^{60}Co radioactive source, are shown here in Figure 4.9.4. The details of these test measurement results were also recently reported in [Cap+21].

4.9.5 Summary

The newly-built annealing setup and its associated monitoring systems are all working optimally. By the time of writing, five HPGe clover detectors had been annealed successfully. The tests performed using standard radioactive sources confirmed the restoration of their original operational characteristics. In the near future, the annealing setup will be upgraded with the addition of a residual gas analyzer (RGA).

4.9.6 Acknowledgments

The authors would like to thank all of the members of the Technical Division of ELI-NP for their help with installing the annealing station. The authors would also like to thank all of the junior technicians, PhD students, postdocs, engineers, and researchers of the Gamma Driven Experiments Department (GDED) and the Gamma System Department (GSD) of ELI-NP for their help and support in the annealing process.

References

[Cap+21] L. Capponi *et al.* "First in-beam experiment with the ELIADE detectors: a spectroscopic study of ^{130}La". In: *J. Instrum.* 16 (2021), T12001. DOI: https://doi.org/10.1088/1748-0221/16/12/T12001 (cited on page 198).

[Gal+18] S. Gales *et al.* "The extreme light infrastructure—nuclear physics (ELI-NP) facility: new horizons in physics with 10 PW ultra-intense lasers and 20 MeV brilliant gamma beams". In: *Reports on Progress in Physics* 81.9 (2018), page 094301. DOI: 10.1088/1361-6633/aacfe8 (cited on page 195).

[Gor08] G. Gordon R. John Wiley & Sons, Ltd., 2008, page 54 (cited on page 195).

[Kno10] G. F. Knoll. John Wiley & Sons, Inc., 2010, page 460 (cited on page 195).

[Scr+05] H. Scraggs *et al.* "TIGRESS highly-segmented high-purity germanium clover detector". In: *Nuclear Instruments and Methods in Physics Research A* 543 (2005), page 431. DOI: https://doi.org/10.1016/j.nima.2004.12.012 (cited on page 195).

[Söd+19] P.-A. Söderström *et al.* "High-Resolution Gamma-ray Spectroscopy with ELIADE at the Extreme Light Infrastructure". In: *Acta Physica Polonica B* 50 (2019), page 329. URL: https://www.actaphys.uj.edu.pl/R/50/3/329/pdf (cited on page 195).

[Tan+20] K. A. Tanaka *et al.* "Current status and highlights of the ELI-NP research program". In: *Matter and Radiation at Extremes* 5.2 (Mar. 2020), page 024402. DOI: 10.1063/1.5093535. URL: https://doi.org/10.1063/1.5093535 (cited on page 195).

[Tec] M. Technologies. *Gamma Analysis Software*. URL: https://www.mirion.com/products/genie-2000-gamma-analysis-software (cited on page 198).

[Ur+16] C. Ur *et al.* "Nuclear Resonance Fluorescence Experiments at ELI-NP". In: *Romanian Reports in Physics* 68 (2016), S483. URL: http://www.rrp.infim.ro/2016_68_S/S483.pdf (cited on page 195).

4.10 Liquid nitrogen cooling setup and automated filling control system for the ELIADE clover detectors

Dhal A.[1,*], Ramirez F.[1], Suliman G.[1,2], Roman T.[1], Ciocan G.[1], Testov D.[1,3], Petcu C.[1], Tatulea B.[1], Ur C. A.[1], and Balabanski D. L.[1],

[1] Extreme Light Infrastructure (ELI-NP) & Horia Hulubei National Institute for R & D in Physics and Nuclear Engineering (IFIN-HH), Str. Reactorului No. 30, 077125 Bucharest–Măgurele, Romania
[2] Physics Department, University POLITEHNICA of Bucharest, Splaiul Independenţei No. 313, 060042 Bucharest - Sector 6, Romania
[3] Joint Institute for Nuclear Research, 6 Joliot-Curie St., 141980 Dubna, Russia

[*] **anukul.dhal@eli-np.ro**

Abstract

In this report, we present a liquid nitrogen (LN2) cooling station built in-house for the segmented clover detectors of the ELI-NP Array of DEtectors (ELIADE) of ELI-NP. The LN2 filling process is fully automated and controlled using a compactRIO (cRIO) system from National Instruments. The associated LabVIEW software monitors the germanium crystal temperatures as well as the temperatures of external Pt100 sensors, which used for detection of overflow of LN2 from detectors during a filling process. The Graphic User Interface (GUI), Command Line Interface (CLI), and Text User Interface (TUI) are used for both controlling and monitoring the cooling process. Alert and warning message modes are activated via the cRIO system as a precaution should adverse events occur.

4.10.1 Introduction

High-purity germanium detectors (HPGe) are well known for their excellent energy resolution and efficiency, paired with a minimum associated noise level. However, such detectors cannot operate at room temperature due to the large leakage current produced by the thermally induced electrons across the small semiconductor bandgap (*i.e.* 0.7 eV). In order to minimize the leakage current, one needs to cool down the detector to the temperature of liquid nitrogen (LN2) of 77 K. For this reason, nearly all modern-day germanium detectors are fitted with an LN2 storage dewar which is thermally insulated toward the outside. A thermal contact (*i.e.* cold finger) extends to the crystal to keep it cool [Gor08; Kno10].

At ELI-NP [Gal+18; Tan+20], we designed and set up a custom LN2 cooling station for the HPGe $4 \times 60 \times 90$ SEG32-type [Scr+05] detectors of ELIADE [Söd+19; Ur+16]. In order to keep our detectors cool and under safe operational parameters they are being filled with LN2 every 12 hours. E-mail alert and warning messaging options were introduced as part of the automated cooling control system software.

4.10.2 The cooling station setup

The mechanical support structure and the LN2 distribution panels (shown in Figure 4.10.1) were designed and assembled in-house at ELI-NP. The design features a compact configuration so that all of the detector filling valves and the external Pt100 sensors with their Teflon holders corresponding to the LN2 overflow lines are all in proximity to one another. The solenoid valves (1327 series, Jefferson Valves) used in the distribution panel are of the 'normally open' and 'normally closed' type. Rectangular Teflon blocks ($50 \times 50 \times 40$ mm^3) are used for the Pt100 sensor holders, with an option for the passage of overflow LN2 from the detectors through the Teflon blocks when the Pt100 sensors are being held in the path of the LN2 flow. All of the distribution lines are connected with Teflon tubes, while the couplings were fashioned from brass. Specially-designed bayonet tubes were used for the inlet and overflow of LN2 at each detector filling port.

4.10.3 The working principle

Transfer of LN2 from a 200 L storage dewar to the HPGe clover detectors is done through a distribution panel as shown in Figure 4.10.2. The LN2 flow is controlled via electromechanical solenoid valves. Each solenoid valve is associated with a corresponding Pt100 sensor located downstream from the detector. The 'inlet valve' (V1) controls the flow of LN2 from the external 200 L dewar, while the 'purge valve' (V2) at the end of the distribution line acts

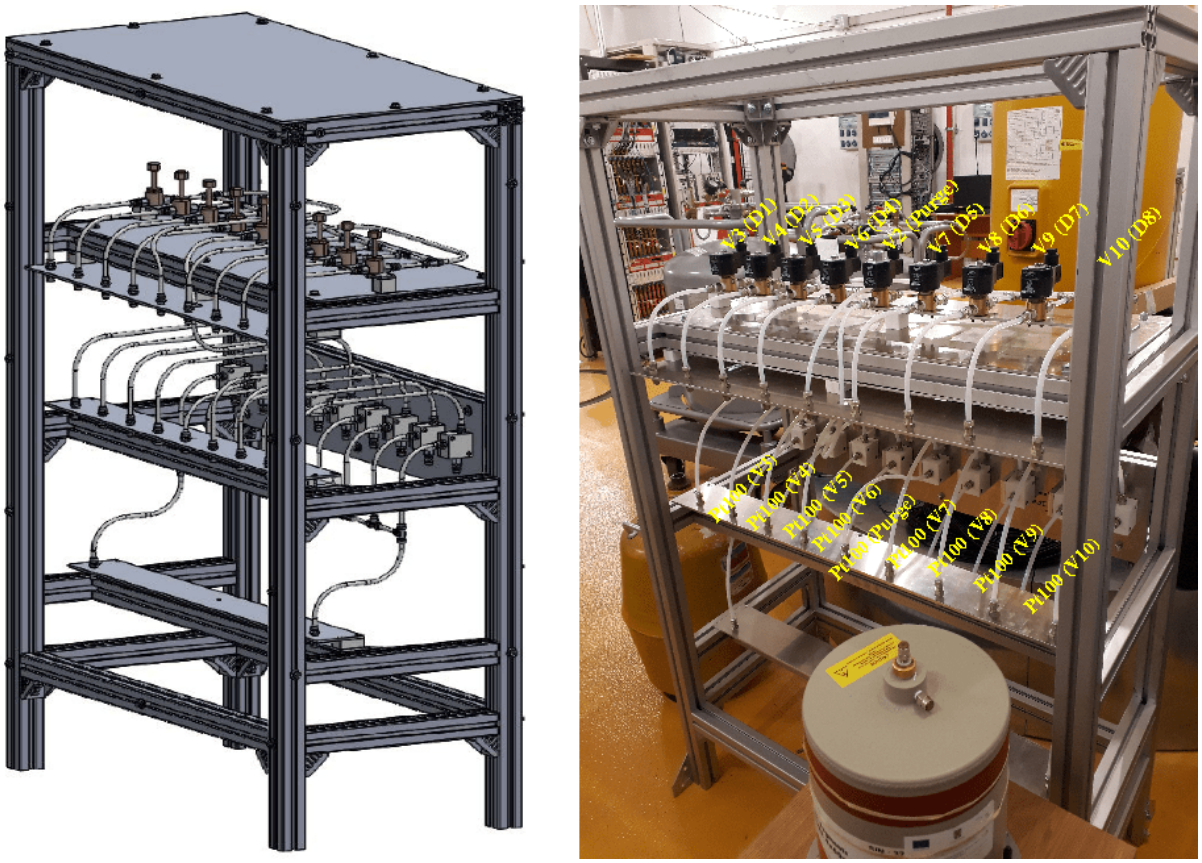

Figure 4.10.1: *Design of the liquid nitrogen distribution panel (left panel) and the real assembly (right panel) of the system for cooling eight HPGe clover detectors, before the installation of the external thermal insulation wrapping.*

as a dump for the LN2 vapours produced during the 'boiling' process of the elements in the distribution line during a filling cycle. Each detector has its associated valve in its respective filling line. All valves from the distribution line are of the 'normally closed' type, apart from the 'purge valve', which is 'normally open'. When an automated filling process starts, the 'inlet valve' of the distribution lines opens, and LN2 starts flowing through before being dumped through the already open 'purge valve'. Once the cooling liquid starts to flow through the 'purge valve', the Pt100 sensor detects the LN2 temperature (*i.e.* 77 K), and the autofill program closes the 'purge valve'. Immediately after the 'purge valve' has been closed, one of the detector filling valves (*i.e.* V3 - V10) opens, and LN2 starts filling the detector dewar. The overflow port of the detector is connected to the dump line via the Pt100 sensor. Therefore, once a detector's dewar has been completely filled and LN2 begins to overflow and dumped, the Pt100 sensor detects the LN2 temperature again. The autofill program then immediately sends a signal to close the corresponding filling valve of the filled detector and opens the next detector's filling valve in line. This way, all detectors get filled with LN2 one by one.

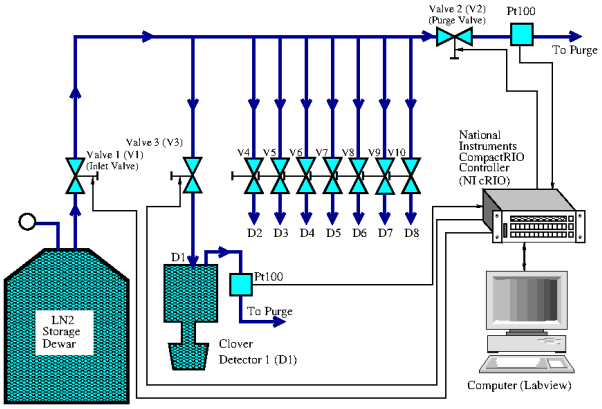

Figure 4.10.2: *Schematic representation of the LN2 distribution panel and the control system for cooling eight HPGe clover detectors. D1 - D8 corresponds to Detector 1 - Detector 8.*

The program can also control the filling of two or three HPGe detectors simultaneously. When the filling process of all of the detectors connected to the distribution line has been completed, the program closes the 'inlet valve' from the 200 L dewar while the 'purge valve' is continued to be kept in closed condition for 6 minutes. After 6 minutes, once the

Pt100 sensor corresponding to the 'purge valve' detects positive temperatures, then it gets opened (normal mode) to release the trapped LN2 inside the distribution panel. On the other hand, if the 'purge valve' sensor's detected temperature is still negative after 6 minutes have passed since the 'inlet valve' closure, then the 'purge valve' gets closed again and waits for another 6 minutes to get opened.

4.10.4 The filling control system

The cRIO system [Cor] from National Instruments, along with the LabVIEW software, is used for the automated LN2 filling control and real-time monitoring of the detector temperature, as well as of the external Pt100 sensors. The automated filling process is carried out at a specific preset time as per the description outlined in the previous section. A partial view of the control system, featuring the cRIO chassis with its associated modules, its power supply unit, and the front panel of the voltage distribution chassis is shown here in Figure 4.10.3. All of the resistance read-outs from the Pt100 sensors (both external and internal) and the resistance read-outs from the chassis are fed to the cRIO control system.

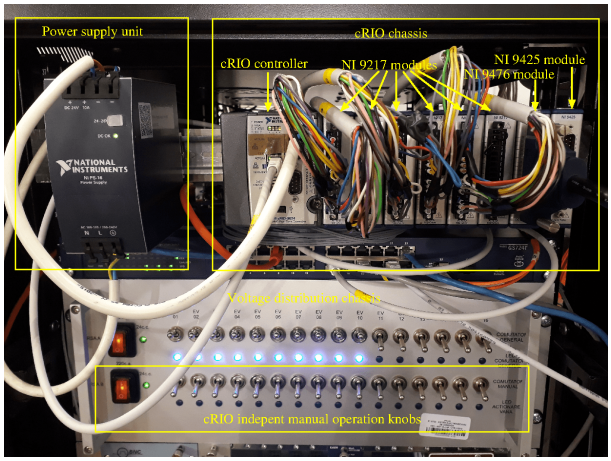

Figure 4.10.3: *The cRIO control system and its power supply unit along with the front panel of the voltage distribution chassis.*

The cRIO control system can work both in standalone mode and be remotely operated from other devices connected to the same network. The Graphic User Interface (GUI) of the LN2 filling control system is shown here in Figure 4.10.4. The system offers the possibility of operating in three modes - automatic, manual, or semi-manual. By default, the system runs in automatic mode and performs the filling process on its own, whereas user intervention is required for both the manual and semi-manual modes. Once all of the required parameters have been set, the control system performs the automated filling operation after a set interval of time (*e.g.* 12 hours). Unless one needs to change some parameters or perform any debugging in the control algorithm, the system runs on its own in automatic mode. Once the cooling process has been finished, the system automatically schedules the next filling 12 hours later and starts a reverse time counter in the GUI. To switch to other modes, the corresponding GUI buttons (indicated here in Figure 4.10.4) need to be activated by clicking on the 'Change State' button. In all three operation modes, the user can stop the filling process, if necessary, by clicking on the 'Stop' button in the GUI.

The detectors can also be filled in the manual mode, but this, of course, requires the physical presence of a user. This mode becomes especially important should the cRIO control system stop responding, either due to software issues or any communication problem. In this scenario, one has to fill the detectors by physically opening and closing the corresponding valves using the ON/OFF knobs located on the front panel of the voltage distribution chassis (indicated here in Figure 4.10.4 with blue ON LEDs).

4.10.5 The monitoring process

In the GUI of the control system, as shown in Figure 4.10.4, the crystal temperature of each detector is displayed in blue text. The values of these temperatures are updated every second. Similarly, the external Pt100 sensor temperatures corresponding to each detector are displayed next to each valve sign. A portion of the GUI shows the real-time variation of the detector temperatures and the valves in a graphical representation. Using the cursor on the graph, it is possible to see the temperature variation throughout the past hours. The state of each detector can also be seen in the top-right corner of the GUI (as indicated in Figure 4.10.4). The yellow colour signifies that a detector is enabled in the cRIO algorithm and is due to be filled, whereas the dark green colour refers to a disabled detector that will not be filled. Similarly, the yellow rectangle next to a valve sign means that that particular valve is open, while the dark green colour corresponds to a closed state. One should note that this color always remains yellow for the 'purge valve', other than during a filling process since this is a 'normally open' type valve. The autofill control program has different set points for temperatures for both the external and internal Pt100 sensor readings. There are also set points for the time duration for filling a detector. Should any issue

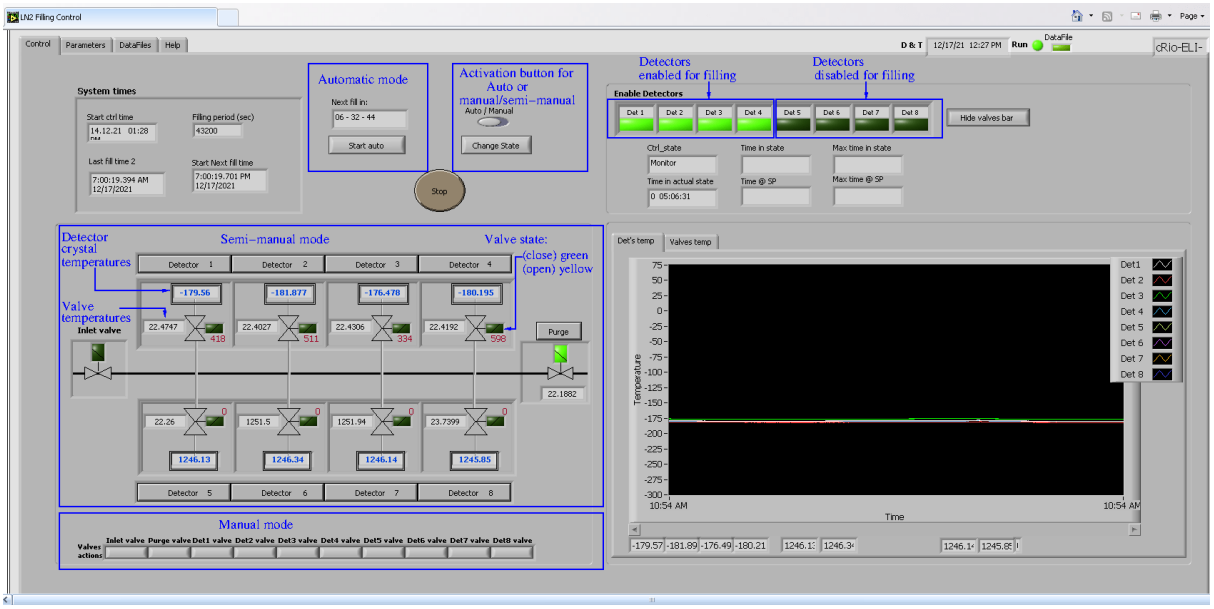

Figure 4.10.4: *GUI of the LN2 filling control and monitoring system.*

arise, the cRIO controller sends alarm messages to the e-mail addresses that have been registered in the system. Otherwise, it sends general e-mail notifications about the status of the filling process. The cRIO controller also sends e-mail alerts if the valves suffer any abnormal open/close operations at times other than the scheduled filling ones.

The Command Line Interface (CLI) and the Python script Text-based User Interface (TUI) are two interface modes for control and monitoring purposes. The CLI communicates directly from the cRIO controller through a TCP/UDP link to any computer connected to the same network as the cRIO controller. Once the interface has been established between the computer and cRIO, one can control the different operations of the autofill program via multiple user-defined command lines. Furthermore, it is also possible to monitor different parameters when needed. Controlling and monitoring its operation through the Python script TUI is easier than CLI, since no commands for controlling are given, except for some numerics defined as part of the TUI script. The TUI script uses an Application Programming Interface (API) and EPICS (Experimental Physics and Industrial Control System) to communicate with the CLI and the cRIO controller.

The interface between cRIO and the Grafana web application provides an online overview of the cooling process. Additionally, Grafana sends out alarm messages through e-mails, texts through the Telegram instant messaging service, and SIM calls to the registered mobile number(s) in case of emergency. A webcam is also installed to visually inspect the filling process if needed.

4.10.6 Summary

At the time of writing, the newly-built setup for the LN2 filling of eight HPGe clover detectors operates without issue. The cooling station can be relocated to different points of the experimental area depending on whether detectors are mounted on the ELIADE array or deposited in the storage area. The automated LN2 filling of the detectors is carried out smoothly by the cRIO control system over the user-specified intervals of time, without requiring any manual intervention apart from refilling the 200 L storage dewar. Soon, the system will be upgraded to fit alongside the ELIADE support frame and use 400 L storage dewars instead.

4.10.7 Acknowledgments

The authors would like to thank all of the Technical Division of ELI-NP members for their help and support in setting up LN2, the cooling station. In addition, the authors would like to thank all junior technicians, Ph.D. students, post-docs, and engineers of the Gamma Driven Experiments Department (GDED) and the Gamma System Department (GSD) of ELI-NP for their help and support. Finally, the staff members responsible for the LN2 plant of ELI-NP are highly acknowledged for their efforts in supplying us with LN2 smoothly and timely.

References

[Cor] N. I. Corp. *CompactRIO Systems*. URL: https://www.ni.com/pdf/manuals/375233f.pdf (cited on page 203).

[Gal+18] S. Gales *et al.* "The extreme light infrastructure—nuclear physics (ELI-NP) facility: new horizons in physics with 10 PW ultra-intense lasers and 20 MeV brilliant gamma beams". In: *Reports on Progress in Physics* 81.9 (2018), page 094301. DOI: 10.1088/1361-6633/aacfe8 (cited on page 201).

[Gor08] G. Gordon R. John Wiley & Sons, Ltd., 2008, page 40 (cited on page 201).

[Kno10] G. F. Knoll. John Wiley & Sons, Inc., 2010, page 424 (cited on page 201).

[Scr+05] H. Scraggs *et al.* "TIGRESS highly-segmented high-purity germanium clover detector". In: *Nuclear Instruments and Methods in Physics Research A* 543 (2005), page 431. DOI: https://doi.org/10.1016/j.nima.2004.12.012 (cited on page 201).

[Söd+19] P.-A. Söderström *et al.* "High-Resolution Gamma-ray Spectroscopy with ELIADE at the Extreme Light Infrastructure". In: *Acta Physica Polonica B* 50 (2019), page 329. URL: https://www.actaphys.uj.edu.pl/R/50/3/329/pdf (cited on page 201).

[Tan+20] K. A. Tanaka *et al.* "Current status and highlights of the ELI-NP research program". In: *Matter and Radiation at Extremes* 5.2 (Mar. 2020), page 024402. DOI: 10.1063/1.5093535. URL: https://doi.org/10.1063/1.5093535 (cited on page 201).

[Ur+16] C. Ur *et al.* "Nuclear Resonance Fluorescence Experiments at ELI-NP". In: *Romanian Reports in Physics* 68 (2016), S483. URL: http://www.rrp.infim.ro/2016_68_S/S483.pdf (cited on page 201).

4.11 Status of the implementation of the positron beamline at ELI-NP

Djourelov N.[1,*], Serban A. B.[1,2], Ciocan G.[1], Udup E.[1], Covali A.[1], and Nedelcu C. V.[1]

[1] Extreme Light Infrastructure (ELI-NP) & Horia Hulubei National Institute for R&D in Physics and Nuclear Engineering (IFIN-HH), Str. Reactorului No. 30, 077125 Bucharest–Măgurele, Romania
[2] Politehnica University of Bucharest, 313 Splaiul Independentei, Sector 6, 060042 Bucharest, Romania

[*] **nikolay.djourelov@eli-np.ro**

Abstract

The implementation state of the laboratory for slow e^+ beams at ELI-NP is summarized. The necessary changes made in the design of the ELIPS laboratory due to the new VEGA system as a source of γ-beam are described. The generation of slow positrons will be turned on when the maximal energy of the γ-beam is set to less than 9 MeV. The generation of the positron beam can run in parasitic mode simultaneously with other experiments with the γ -beam. The simulation showed that by using a converter/moderator assembly made of platinum foils, the intensity of the primary e^+-beam can reach 1×10^7 s^{-1}. Facilitating a frozen layer of neon atoms, this value can be boosted tenfold to 1×10^8 s^{-1}.

4.11.1 Introduction

Worldwide, slow e^+ beamlines of high intensity of 1×10^7 s^{-1} are based on the (γ, e^+e^-) reaction with γ-rays in the MeV regime [GV12]. One possibility is the use of bremsstrahlung radiation generated by deceleration of relativistic electrons in a target [Aka+90; Hyo+11; Kra+06; Wan+04]. Another possibility is the use of γ radiation present in nuclear reactors. They may originate either from the fission process [Sch+01] or from a radioactive decay after thermal neutron capture reaction (n, γ) [Hat+07; Hug+13; Mas+15; Xu+14]. The most important technical constraints of using the bremsstrahlung γ-rays are the dissipation of heat generated by the γ-absorption and the radioactivity created by activation [ORo+11]. These restraints can be avoided with the use of energy-tunable beam of γ-rays [DOL16; Hug+12].

A high-brilliance and high-intensity gamma beamline, created by the inverse Compton scattering process in which the laser light pulses are scattered off relativistic electron bunches, will be one of the main research tools at ELI-NP. It will also be available for the creation of beams of secondary particles. The construction of the Variable Energy Gamma (VEGA) System was awarded to Lyncean Technologies Inc.. Its delivery, installation, and acceptance are scheduled to be completed in 2023. The VEGA system comprises an electron accelerator with a storage ring and a high-finesse Fabry-Perot cavity. This new VEGA system necessitated a revision in the design of the beamline of ELI's Positron Source (ELIPS) [Djo+17]. The revision tries to maximize the use of previously purchased vacuum hardware parts, electronics, *etc.* to be cost effective.

4.11.2 New location of the ELIPS laboratory

The storage ring and the high-quality Fabry-Perot cavity, where the photon-e^- interaction point of the VEGA system is located, will be built in the GSR hall of the ELI-NP experimental building. Hall ERA2 has been designated as a new room for the ELIPS laboratory (see Figure 4.11.1).

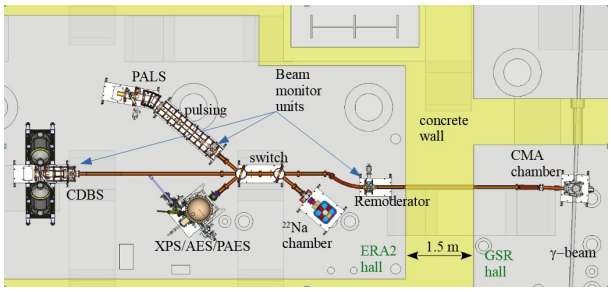

Figure 4.11.1: *The layout of the ELIPS with instrumentation.*

A Coincidence Doppler Broadening Spectrometer (CDBS) and its simpler version Doppler Broadening Spectrometer (DBS) are under assembling. For CDBS, two couples of two HPGe detectors, facing each other, are used to detect annihilation γ-rays in time and energy condition coincidence [Aso+96]. Electron momentum distributions extracted from CDBS spectra carry information on the chemical surrounding of the e^+ annihilation sites that is extremely valuable for identifying the type of defects in metals and semiconductors [Ciz18; TM13]. For the DBS,

the HPGe detectors operate independently but will be exposed to a significantly higher background. Due to the quickness of the data acquisition, the DBS is advantageous for depth profile measurements with integral information of the electron momentum at the annihilation site.

A Positron Annihilation Lifetime Spectroscopy (PALS) system is under construction. Simulations of the pulsing, based on the chopping and bunching method [DD17b], showed that the width of positron pulses at the target would be shortened to ~ 100 ps (FWHM). The start signal for PALS will be provided from the pulsing section electronics. A fast detector in a μ-metal shield behind the sample will provide the stop signal. An energy filter, a bent longitudinal magnetic field [DD17a], will minimize the distortions in the spectra due to e^+ backscattering. PALS is a powerful technique for the determination of the size (type) of open volume defects and their relative concentrations. Also, if a positronium is formed within the studied material, PALS is used as a porosimetry tool sensitive to both open and closed nano- and micro-pores [Zal15]. Both CDBS and PALS are equipped with sample load lock systems to avoid venting the main beamlines and chambers, and they are capable of storing ten samples for measurements with no vacuum break in the load lock. The sample end-station design allows the HPGe detectors to be moved to the PALS beamline, and each of them to be set to work in timing coincidence with a fast BaF_2 detector aligned in anti-colinear direction. Such a setup will allow us to apply the Age MOmenton Correlation (AMOC) technique. AMOC combines PALS with DBS and records time-correlated energy spectra. It is useful for studies of chemical reactions which involve positrons [Sto+91].

The third instrument already in operation is an X-ray Photo-electron Spectroscopy (XPS) /Auger Electron Spectroscopy (AES) multi-functional system for surface analysis. The XPS/AES instrument will be coupled to the e^+-beamline by a termination of the guiding magnetic field and applying an electrostatic focusing of the positrons on the target. Thus, the sample can be irradiated by X-rays and electrons and by positrons. PAES is a complementary technique to AES mainly used to examine the topmost atomic layer of a surface [Faz+10; LH07; OJF09]. Some of the positrons from a low-energy (few tens eV) and high-intensity e^+-beam are trapped in a potential well at the target surface and annihilate the inner atomic shell electrons, creating core-hole excitation, resulting in Auger e^- emission [OJF09].

4.11.3 Slow positron production using the VEGA γ-beam

Some aspects of the geometry optimization of the CMA made of platinum foils [DOL16; Djo+17] were redone because of the new characteristics of the γ-beam that the VEGA system will generate. The important characteristics which affect the efficiency of the CMA are the energy, intensity, and the spot size at the $\gamma-$CMA interaction point. The γ-ray maximum energy will be tunable up to 20 MeV. The slow positron generation will be turned off at energies $gt9$ MeV to avoid activation issues of Pt material. It will be realized by a vertical off-axis displacement of the CMA inside the CMA vacuum chamber with the help of a linear shift translator. The shortest distance from the photon-e^- interaction point where the CMA can be placed is 7.5 m. The GEANT4 simulations (we used a gamma generation code written by our colleague Dr. Paul Constantin) showed that the spot is asymmetrical, vertically flattened (see Figure 4.11.2), and its size decreases with the energy.

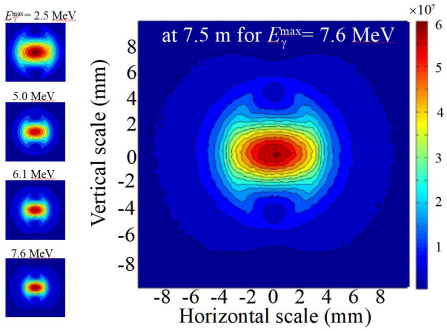

Figure 4.11.2: *The simulated γ-beam spot at a distance of* 7.5 m *from the photon-e^- interaction point for different maximum energies of the γ-rays.*

The optimization of the CMA sizes for a beam of γ-rays with maximal energy $E_\gamma^{max} = 3.5$ MeV [DOL16] by GEANT4 simulation showed a very broad peak of the CMA efficiency as a function of the foil thickness. Simulations also confirmed this finding at different E_γ^{max} for the VEGA γ-beam. The thickness of 127 μm of the already purchased platinum foil gives conversion and moderation efficiencies very close to the efficiencies obtained for the optimal thicknesses across the full range of energies for slow e^+ production by the VEGA γ-beam. The time-averaged intensity of the γ-beam is guaranteed to be higher than 1.1×10^{11} s^{-1}. At this intensity and $E_\gamma^{max} = 7.6$ MeV, the simulated interactions with a 150 mm long CMA consisting of 72 Pt-foils of sizes $16 \times 6 \times 0.127$ mm^3 and 2 mm gaps between them showed that the intensity of the slow e^+ beam will be $1.25(3) \times 10^7$s^{-1}. Moderation by a layer of frozen neon gas directly

on the surface of the CMA foils, due to the better neon moderation efficiency, could lead to intensity of the primary e^+-beam exceeding $1.3 \times 10^7 s^{-1}$. We also plan to implement a 'remoderation' station (see Figure 4.11.1), working in transmission geometry, to be used for an improvement of the beam quality by reducing the transversal momentum of the slow positrons. The primary slow positrons extracted from the CMA and accelerated to 5 keV energy will be magnetically focused on a 150 nm thick single-crystal Ni foil and remoderated. Thus, the spot of the primary slow e^+-beam of $\approx$ 12 mm (FWHM) could be decreased a few times but at the expense of reduced intensity (to 10%-50% of the one of the primary beam).

It is important to note that when the CMA is used for e^+ production, other experiments can be performed simultaneously with the γ-beam of reduced intensity because the optimized CMA will not interact with $>60\%$ of the γ-rays. Another possibility is to use CMA with central holes ($\varnothing = 2.5$ mm) in the foils. This will let γ-rays with the highest energy and $\sim$ 2% narrow bandwidth pass through the CMA without any loss [DOL17]. In this case, the slow e^+ beam intensity will be reduced only by 10% for $E_\gamma^{max} = 2.5$ MeV and 21% for $E_\gamma^{max} = 7.6$ MeV. This loss can be considered a very reasonable sacrifice compared to the gain of γ-beam time for e^+ production in parasitic mode. It has to be mentioned that due to the γ-beam spot asymmetry, the orientation of the CMA for extraction of the slow positrons in the vertical direction would reach a slightly higher e^+-beam intensity (by $\sim$7% for $E_\gamma^{max} = 7.6$ MeV) as found out by simulations. Due to the complexity of the technical realization, this possibility will be explored only if the asymmetry is confirmed by the characterization of the operational γ-beam.

In contrast to the former design [Djo+17], there is no need for an e^+-pulse stretcher. The γ-beam timing structure is determined by the re-circulation of the relativistic electrons in the VEGA storage ring with a frequency of 40 MHz. Thus, each e^+-pulse, with a length at the sample end-stations of a few hundred ns, will contain about 10 e^+ and no pile-up effects are expected neither for HPGe, nor BaF_2 ones.

4.11.4 CDBS chamber upgrade

An upgrade of the CDBS chamber is under construction (Figure 4.11.3). It includes a PALS system by secondary e^- tagging [Mar+13]. The slow e^+-beam, vertically offset to avoid interaction with an MCP detector placed on the chamber axis, is aligned back with the axis by an E×B filter. Positrons accelerated to a few keV upon hitting a sample, leading to generation of secondary electrons. The E×B filter decouples the e^- and e^+ trajectories, and the MCP detector registers secondary electrons. The MCP signal is used to provide a start signal for the PALS spectrometer. The signal from a fast BaF_2 detector discriminated for detecting 511 keV gamma radiation is used to provide a stop signal.

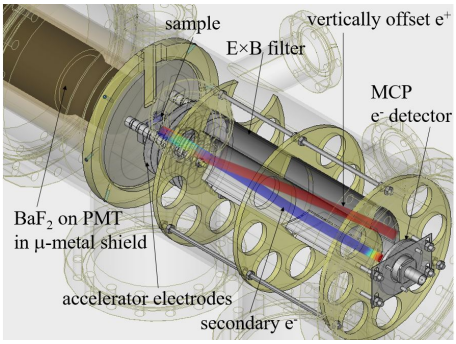

Figure 4.11.3: *The design of secondary electron tagging system in the CDBS chamber with simulated trajectories of positrons and secondary electrons.*

Our simulations showed that for incident energy of positrons >0.5 keV, the ToF jitter of the secondary electrons at the MCP detector is <0.1 ns (FWHM). Therefore, the PALS by secondary electron tagging will have a time resolution <0.5 ns (FWHM). The close placement of the accelerator to the sample does not allow suppression of the spectrum deterioration due to backscattered e^+ [Mar+13]. For this reason, the system will be used for the measurement of long positron lifetimes (>1 ns).

4.11.5 Summary

The construction of the γ-beam system VEGA at ELI-NP required a redesigning of the e^+-spectroscopy instruments and e^+-beamline configuration of ELIPS. The intensity of the primary e^+-beam at the use of a CMA made of platinum foils was estimated to reach 1×10^7 s^{-1}. If neon moderation is applied, the intensity could exceed 1×10^8 s^{-1}. The CMA will be produced with a central hole ($\varnothing = 2.5$ mm) in the foils. This will allow a simultaneous run of slow e^+ production with other γ-beam experiments. Most of the components (vacuum hardware and pumps, mechanical support, power supplies, electronics, detectors, *etc.*) of the ELIPS laboratory have been purchased, and the beamlines and sample end-stations are assembled.

4.11.6 Acknowledgement

The mechanical workshop team's technical and engineering support and skillful manufacturing of many components are gratefully acknowledged.

References

[Aka+90] T. Akahane *et al.* "Stretching of slow positron pulses generated with an electron linac". In: *Applied Physics A* 51.2 (1990), pages 146–150. ISSN: 1432-0630. DOI: 10.1007/BF00324279. URL: https://doi.org/10.1007/BF00324279 (cited on page 207).

[Aso+96] P. Asoka-Kumar *et al.* "Increased Elemental Specificity of Positron Annihilation Spectra". In: *Phys. Rev. Lett.* 77 (10 1996), pages 2097–2100. DOI: 10.1103/PhysRevLett.77.2097. URL: https://link.aps.org/doi/10.1103/PhysRevLett.77.2097 (cited on page 207).

[Ciz18] J. Cizek. "Characterization of lattice defects in metallic materials by positron annihilation spectroscopy: A review". In: *J. Mater. Sci. Technol.* 34.4, 577 (2018), page 577. DOI: 10.1016/j.jmst.2017.11.050. URL: http://www.jmst.org/EN/abstract/article_26620.shtml (cited on page 207).

[DD17a] D. Dinescu and N. Djourelov. "Using a Bent Tube as an Energy Filter for a Positron Beam. Simulations on Determining the Optimum Angle of the Bend". In: *Acta Phys. Pol. A* 132.5 (2017), pages 1624–1627 (cited on page 208).

[DD17b] N. Djourelov and D. Dinescu. "Design and simulation of a pulsed positron beam at ELI-NP". In: *J. Phys.: Conf. Ser.* 791.1 (2017), page 012010. DOI: 10.1088/1742-6596/791/1/012010. URL: http://stacks.iop.org/1742-6596/791/i=1/a=012010 (cited on page 208).

[DOL16] N. Djourelov, A. Oprisa, and V. Leca. "Source of slow polarized positrons using the brilliant gamma beam at ELI-NP. Converter design and simulations". In: *Nucl. Instrum. Methods Phys. Res. A* 806 (2016), pages 146–153. ISSN: 0168-9002. DOI: http://dx.doi.org/10.1016/j.nima.2015.10.009 (cited on pages 207, 208).

[DOL17] N. Djourelov, A. Oprisa, and V. Leca. "Project for a Source of Polarized Slow Positrons at ELI-NP". In: *Defect and Diffusion Forum* 373 (2017), pages 57–60. DOI: 10.4028/www.scientific.net/DDF.373.57 (cited on page 209).

[Djo+17] N. Djourelov *et al.* "Status of the project for a positron laboratory at ELI-NP". In: *Journal of Physics: Conference Series* 791 (2017), page 012011. DOI: 10.1088/1742-6596/791/1/012011. URL: https://doi.org/10.1088%2F1742-6596%2F791%2F1%2F012011 (cited on pages 207–209).

[Faz+10] N. Fazleev *et al.* "Oxidation and thermal reduction of the Cu(100) surface as studied using positron annihilation induced Auger electron spectroscopy (PAES)". In: *Surface Science* 604.1 (2010), pages 32–37. ISSN: 0039-6028. DOI: https://doi.org/10.1016/j.susc.2009.10.016. URL: http://www.sciencedirect.com/science/article/pii/S0039602809006669 (cited on page 208).

[GV12] S. Golge and B. Vlahovic. "Review of Low-Energy Positron Beam Facilities". In: *Proceedings of IPAC2012, New Orleans, Louisiana, USA*. 2012, pages 1464–1466 (cited on page 207).

[Hat+07] A. Hathaway *et al.* "Implementation of a prototype slow positron beam at the NC State University PULSTAR reactor". In: *Nucl. Instrum. Methods Phys. Res. A* 579.1 (2007). Proceedings of the 11th Symposium on Radiation Measurements and Applications, pages 538–541. ISSN: 0168-9002. DOI: https://doi.org/10.1016/j.nima.2007.03.036. URL: http://www.sciencedirect.com/science/article/pii/S0168900207005578 (cited on page 207).

[Hug+12] C. Hugenschmidt *et al.* "High-intensity and high-brightness source of moderated positrons using a brilliant γ beam". English. In: *Appl. Phys. B* 106 (2012), pages 241–249. ISSN: 0946-2171. DOI: 10.1007/s00340-011-4594-0 (cited on page 207).

[Hug+13] C. Hugenschmidt *et al.* "The Upgrade of the Neutron Induced Positron Source NEPOMUC". In: *Journal of Physics: Conference Series* 443 (2013), page 012079. DOI: 10.1088/1742-6596/443/1/012079. URL: https://doi.org/10.1088%2F1742-6596%2F443%2F1%2F012079 (cited on page 207).

[Hyo+11] T. Hyodo *et al.* "KEK-IMSS Slow Positron Facility". In: *Journal of Physics: Conference Series* 262 (2011), page 012026. DOI: 10.1088/1742-6596/262/1/012026. URL: https://doi.org/10.1088%2F1742-6596%2F262%2F1%2F012026 (cited on page 207).

[Kra+06] R. Krause-Rehberg *et al.* "EPOS—An intense positron beam project at the ELBE radiation source in Rossendorf". In: *Applied Surface Science* 252.9 (2006). Proceedings of the Tenth International Workshop on Slow Positron Beam Techniques for Solids and Surfaces, pages 3106–3110. ISSN: 0169-4332. DOI: https://doi.org/10.1016/j.apsusc.2005.08.109. URL: http://www.sciencedirect.com/science/article/pii/S0169433205012134 (cited on page 207).

[LH07] S. Legl and C. Hugenschmidt. "A novel time-of-flight spectrometer for PAES". In: *physica status solidi c* 4.10 (2007), pages 3981–3984. DOI: 10.1002/pssc.200675802. eprint: https://onlinelibrary.wiley.com/doi/pdf/10.1002/pssc.200675802. URL: https://onlinelibrary.wiley.com/doi/abs/10.1002/pssc.200675802 (cited on page 208).

[Mar+13] H. Marinov *et al.* "Design, simulation and performance of a slow positron beam with secondary electron tagging for positron annihilation lifetime spectroscopy". In: *Nucl. Instrum. Methods Phys. Res. A* 729 (2013), pages 569–575. ISSN: 0168-9002. DOI: https://doi.org/10.1016/j.nima.2013.08.045. URL: https://www.sciencedirect.com/science/article/pii/S0168900213011716 (cited on page 209).

[Mas+15] P. Mascher *et al.* "The Mcmaster Intense Positron Beam Facility - an Update". In: *17th International Conference on Positron Annihilation Book of Abstracts*. 2015 (cited on page 207).

[ORo+11] B. E. O'Rourke *et al.* "Simulations of slow positron production using a low-energy electron accelerator". In: *Rev. Sci. Instrum.* 82 (2011), page 063302. DOI: doi:http://dx.doi.org/10.1063/1.3599156 (cited on page 207).

[OJF09] T. Oka, S. Jinno, and M. Fujinami. "Analytical methods using a positron microprobe". In: *Analytical Sciences* 25 (2009), pages 837–844. DOI: 10.1002/pssc.200675802. URL: https://www.jstage.jst.go.jp/article/analsci/25/7/25_7_837/_pdf (cited on page 208).

[Sch+01] H. Schut *et al.* "Performance of an Intense Nuclear-Reactor Based Positron Beam". In: *Materials Science Forum* 363 (2001), pages 430–432. DOI: 10.4028/www.scientific.net/MSF.363-365.430 (cited on page 207).

[Sto+91] H. Stoll *et al.* "Positron age-momentum correlation studies of defects and positronium by an MeV positron beam". In: *Nucl. Instrum. Methods Phys. Res. B* 56-57 (1991), pages 582–585. ISSN: 0168-583X. DOI: https://doi.org/10.1016/0168-583X(91)96101-P. URL: http://www.sciencedirect.com/science/article/pii/0168583X9196101P (cited on page 208).

[TM13] F. Tuomisto and I. Makkonen. "Defect identification in semiconductors with positron annihilation: Experiment and theory". In: *Rev. Mod. Phys.* 85 (2013), pages 1583–1631 (cited on page 207).

[Wan+04] B. Y. Wang *et al.* "The Slow Positron Beam Based on Beijing Electron-Positron Collider". In: *Materials Science Forum* 445 (2004), pages 513–515. DOI: 10.4028/www.scientific.net/MSF.445-446.513 (cited on page 207).

[Xu+14] Q. Xu *et al.* “Positron beam facility at Kyoto University Research Reactor”. In: *Journal of Physics: Conference Series* 505 (2014), page 012030. DOI: 10.1088/1742-6596/505/1/012030. URL: https://doi.org/10.1088%2F1742-6596%2F505%2F1%2F012030 (cited on page 207).

[Zal15] R. Zaleski. “Principles of positron porosimetry”. In: *Nukleonika* 60.4 (2015), pages 795–800. DOI: 10.1515/nuka-2015-0143 (cited on page 208).

4.12 DELILA: Digital Extreme Light Infrastructure List-mode Acquisition - project status report

Aogaki, S.[1,*]

[1] Extreme Light Infrastructure - Nuclear Physics (ELI-NP) & Horia Hulubei National Institute for R&D in Physics and Nuclear Engineering (IFIN-HH), Str. Reactorului No. 30, 077125 Bucharest–Măgurele, Romania

[*] **sohichiroh.aogaki@eli-np.ro**

Abstract

DELILA (Digital Extreme Light Infrastructure List-mode Acquisition) is a data acquisition (DAQ) program used at ELI-NP (and somewhere). The main features are network transparency, web monitoring and controller, and handling electronics data. The main framework is DAQ-Middleware based on a robotics middleware [Yas+10]. The backend was mainly written in C++, and the front-end was written in TypeScript and HTML and using a dashboard tool [Gra18]. The interface between the frontend and backend is MongoDB and InfluxDB [Inf; Mon].

4.12.1 Introduction

The development of DAQ software is one of the key tasks in experimental physics today. In the past, researchers have used a variety of tools to record the scientific data (*e.g.*, pen and paper). In the 19th century, scientists used oscillographs to record scientific data mechanically. In the early 19th century, physicists progressed by *e.g.* using silver halide film (old-style photograph) to record the tracks of particles. With the availability of computers, researchers used software and hardware to record scientific data. In the early 1970s, the Computer-Aided Measurement And Control (CAMAC) emerged as electronic data recording standards [82]. The CAMAC system provides Analog to Digital Converter (ADC), and Time to Digital Converter (TDC) with some modules to be read out by computers. At almost the same time, the Nuclear Instrumentation Module (NIM) standard was defined and used especially in the fields of particle, and nuclear physics [Cos+90]. The NIM standard modules are used widely, such as *e.g.*, logic gates, power supplies, *etc.* . From the 1980s onwards, VERSA Module Eurocard (VME) bus modules were introduced to record the scientific data [Can+79].

Since the 1990s, Field-Programmable Gate Array (FPGA) has been facilitated in a wide variety of scientific and engineering fields. One FPGA package provides ADC, TDC, and logic gates and reduces the spaces and wires. Many experimental groups, especially groups supporting large-scale experiments, have replaced the CAMAC, NIM, VME-based DAQ system (analog DAQ) with FPGA packages (digital DAQ). Today we can see some variations of digital DAQ hardware available on the market. The price of FPGA was decreased, and its performance has increased year by year. The portrayed DELILA system aims to use CAEN digitizers. The central part of DELILA is the CAEN digitizer handling tools. The taken data is transported by DAQ-Middleware and plotted and stored by using ROOT libraries[BR96]. DAQ-Middleware provides the software framework including the data transfer path and the state machine. DELILA uses some components controlled by DAQ-Middleware and constructs the specific DAQ system. The developer writes the components inheriting the DAQ-Middleware base class. Each component runs independently and receives the current state from the DAQ-Middleware operator component every 10 ms. The states are config, unconfig (unconfigure), start (running), stop, and pause. The developer within the work displayed herein added additional states as sub-states of the running state.

4.12.2 The design of DELILA

Figure 4.12.1 shows the schematic diagram of DELILA. The yellow rectangle and small picture at the most left show the CAEN digitizers. The green rounded corners and rectangles show the components of DELILA based on DAQ-Middleware template. All components are written in C++. The data-readout component communicates with CAEN digitizers to program FPGA and fetches the experimental data. The readout component calculates the trigger timing using threshold crossing information from the digitizers. The readout component makes one packet, including fetched data and some information, and

sends it to the monitor and recorder components. The recorder component sorts the data by timestamp and stores the data. The file format of the fetched data is a ROOT file format. The data recorded are module number, channel number, timestamp, calculated trigger time, ADC (charge) information, and signal (optional). The monitor component also receives the packet and plots the data by using the JavaScript version of ROOT, JSROOT.

The database used is MongoDB and InfluxDB. The run information is recorded into MongoDB (start time, stop time, comments for the run). InfluxDB records the real-time event information. The web servers used are Apache as providing the communication with the DAQ controller and a web API server using Oat++ [FK97][Str]. Oat++ is written in C++ and easy to implement ROOT data analysis libraries. Merging all web servers' functions into the Oat++ server has been developed.

Figure 4.12.2 shows the user interfaces (UI) of DELILA. The left shows the controller web page of DELILA. The controller page is written in JavaScript and TypeScript. The middle shows the monitor by using ROOT libraries. The right shows the event rate monitor by using Grafana. Now those and small parts are the completely separated web pages. All web page applications will be merged into a single-page application.

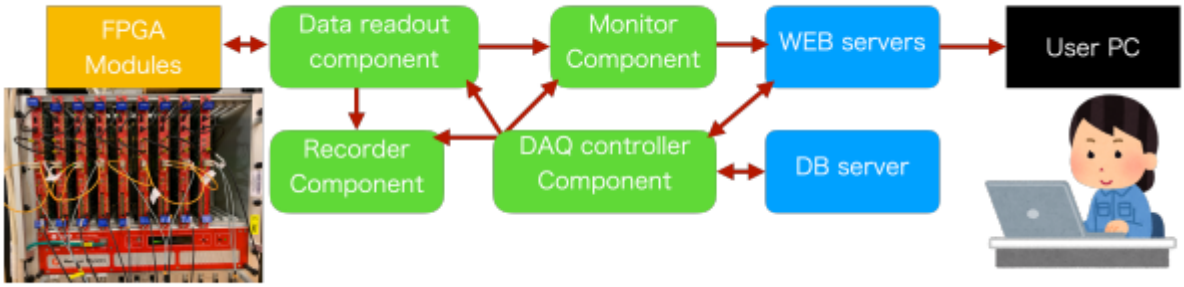

Figure 4.12.1: *At the most left, there are CAEN digitizers inserted into the VME crate. Green rounded corners rectangles show components of data taking, monitor and record. Blue rounded corners rectangles are the database servers. The arrows show the data transfer stream.*

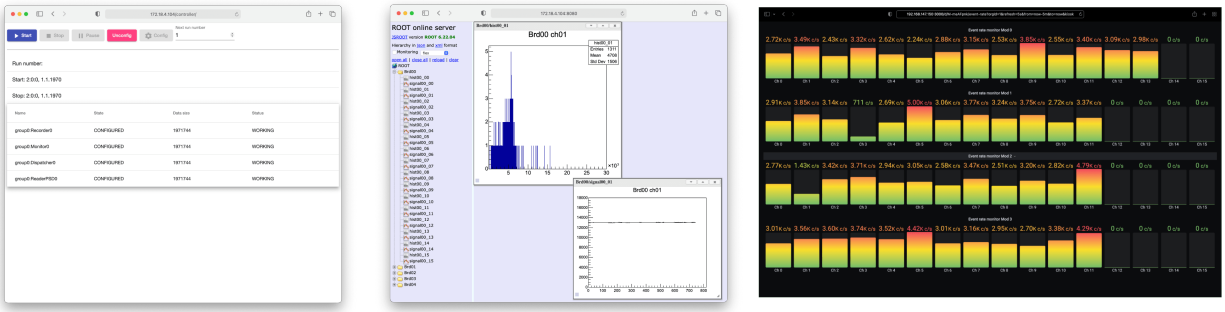

Figure 4.12.2: *User interfaces of DELILA. On the left: Controller of DELILA. Middle: Monitor by using ROOT. Right: Event rate monitor by Grafana.*

4.12.3 Requirements and solutions

The reason for constructing the in-house DAQ system is to keep flexibility for the future. DELILA has to fit the experiments at ELI-NP. Under this context, we need the following requirements.

4.12.3.1 Open source

Almost all codes, libraries, and OS are open-source software. The CAEN libraries are not open-source. The Linux device drivers of CAEN devices are open-source. We can make our open-source libraries based on the registered information of manuals. However,

it risks illegal back-engineering and takes a long time to implement. So the developer decided to use not open source libraries.

4.12.3.2 Tested on reliable environments

DELILA is used at ELI-NP experimental hall and detector laboratory. Moreover, DELILA was tested at the IFIN-HH Tandem accelerator. The event rate monitor in Figure 4.12.2 shows the obtained test results from that campaign. It is worth noting that the DAQ-Middleware is also used at KEK, J-Parc in Japan.

4.12.3.3 Implementing the new hardware in an easy way

The backend of DELILA is written in C++. Usually, the developer can call any device driver functions of Linux from DELILA and implement new hardware. If the hardware does not provide any manuals and driver sources, the implementation is difficult or impossible. In any case, one needs to check the device driver of any new hardware.

4.12.3.4 Multiple computer systems

DAQ-Middleware provides the function of network transparency using TCP/IP and xinetd of Linux. In the case of computers being connected to the same LAN, DELILA can handle many computers. The UIs are constructed as web pages and allow the user to control using any computers in the same network.

4.12.3.5 Robustness for high event rates

The event rate monitor in Figure 4.12.2 shows over 2k cps event rate with 50 channels. The data size of it is still under the limit of handling. The data writing speed is a kind of bottleneck. For ordinarily HDD, the system was frozen by waiting for the data writing. The recorder component has two main functions sorting data and writing data. The developer made the writing function as a child process and allowed mDELILA not to wait to finish the data writing. In the future, ELI-NP will use a network storage system. The developer plans to make a separate data handling application to handle a large amount of data, considering the potential of a slow network environment.

4.12.4 Conclusion

DELILA has the essential functions of the DAQ system for the experiments and was tested in several environments. In 2022, DELILA will be used for experiments at the IFIN-HH 9 M tandem beam. By then, the UI environment will be improved and new hardware integrated.

References

[BR96] R. Brun and F. Rademakers. “ROOT - An Object Oriented Data Analysis Framework”. In: *AIHENP’96 Workshop, Lausane*. Volume 389. 1996, pages 81–86 (cited on page 213).

[Can+79] M. D. Canon *et al.* “A Virtual Machine Emulator for Performance Evaluation (Summary)”. In: *Proceedings of the 7th ACM Symposium on Operating Systems Principles (SOSP)*. 1979 (cited on page 213).

[Cos+90] L. Costrell *et al.* “Standard NIM Instrumentation System”. In: (May 1990). DOI: 10.2172/7120327. URL: https://www.osti.gov/biblio/7120327 (cited on page 213).

[FK97] R. T. Fielding and G. E. Kaiser. “The Apache HTTP Server Project.” In: *IEEE Internet Comput.* 1.4 (1997), pages 88–90. URL: http://dblp.uni-trier.de/db/journals/internet/internet1.html#FieldingK97 (cited on page 214).

[Gra18] Grafana Labs. *Grafana Documentation*. 2018. URL: https://grafana.com/docs/ (visited on 07/25/2019) (cited on page 213).

[82] *IEEE Standard Modular Instrumentation and Digital Interface System (CAMAC) (Computer Automated Measurement and Control)*. 1982 (cited on page 213).

[Inf] InfluxDB. *Influx databse*. URL: https://www.influxdata.com/ (cited on page 213).

[Mon] MongoDB. *Mongo databse*. URL: https://www.mongodb.com/ (cited on page 213).

[Str] L. Stryzhevskyi. *Oat++*. URL: https://oatpp.io/ (cited on page 214).

[Yas+10] Y. Yasu *et al.* “Functionality of DAQ-Middleware”. In: *IEEE Transactions on Nuclear Science* 57 (2010), pages 487–490 (cited on page 213).


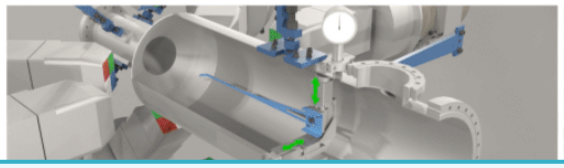

Theory Work at GDED

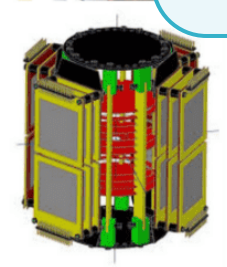
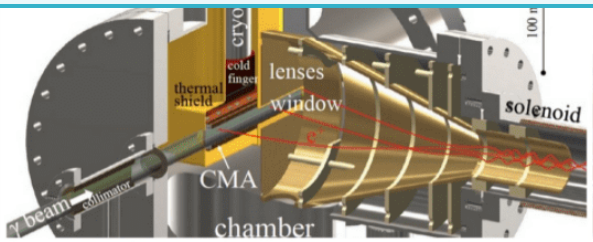

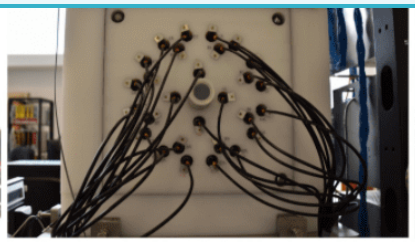
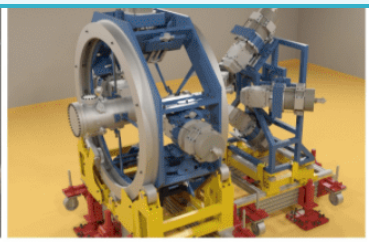

4.13 Microscopic structure of the Pygmy Dipole Resonance in ^{208}Pb

Tsoneva, N.[1,*]

[1] Extreme Light Infrastructure (ELI-NP) Horia Hulubei National Institute for R&D in Physics and Nuclear Engineering (IFIN-HH), Reactorului 30, 077125 Bucharest–Măgurele, Romania

[*] **nadia.tsoneva@eli-np.ro**

Abstract

The first comprehensive study of the single-particle structure of the pygmy dipole resonance (PDR) in neutron-excess double-magic ^{208}Pb is presented. Theoretical calculations performed with a microscopic approach based on the energy-density functional plus quasiparticle-phonon model (EDF + QPM) theory are compared with a novel ^{207}Pb(d,p)^{208}Pb experiment, the Large Scale Shell Model (LSSM) and other available experimental data. Furthermore, different properties of the dipole strength distributions are discussed in order to elucidate the microscopic structure of the PDR in detail. The studies will support ELI Gamma Above Neutron Threshold (ELIGANT) day-one experiments at ELI-NP.

4.13.1 Introduction

Theoretical investigations of spectral distributions of low-energy dipole excited states and their relation to the pygmy dipole resonance (PDR) [BCL15; SAZ13] were performed in the double-magic ^{208}Pb nucleus. The PDR is a low-energy electric dipole mode known to be compatible with neutron skin vibrations against the isospin symmetric nuclear "core" [TL08; TL11; TL16; TLS04]. Our studies of nuclear reactions of astrophysical interest show that the reaction cross-sections strongly depend on the low-energy part of the electromagnetic dipole strength function, which is connected to the photoabsorption cross-section [Rau+13; Ton+17; Tso+15]. It is known that lead isotopes play an important role in the s-process of nucleosynthesis. In particular, for the semi-magic ^{206}Pb we found that the presence of PDR mode in this nucleus affects strongly the ^{205}Pb radiative neutron capture cross-section, a reaction related to the destruction of ^{205}Pb during the s-process [Ton+17]. However, the mechanism of the neutron capture process by the nucleus is not yet fully understood. Theoretical microscopic models explain the PDR as a sequence of exciting one-particle-one-hole excitations ($1p-1h$), which act coherently and therefore cause an increased transition strength [TL08; TL16]. However, the degree of the collectivity of PDR is still questionable, and no experimental access to it has been found. With this work, we want to find an answer to some of these questions.

4.13.2 Theoretical Model

Successful description of the low-energy γ-strength functions and branching ratios connecting ground and excited states of the PDR can be achieved in our microscopic theoretical approach, which incorporates self-consistent EDF theory and the three-phonon QPM [TL08; TL16; TLS04]. An essential advantage of the EDF+QPM approach is the description of the nuclear excitations in terms of QRPA phonons as building blocks of the three-phonon QPM model space [GS94; V G76] which provides a microscopic way to multi-configuration mixing. For spherical even-even nuclei, the model Hamiltonian is diagonalized on an orthonormal set of wave functions constructed from one-, two- and three-phonon configurations:

$$\Psi_\nu(JM) = \Big\{ \sum_i R_i(J\nu) Q^+_{JMi} + \sum_{\substack{\lambda_1 i_1 \\ \lambda_2 i_2}} P^{\lambda_1 i_1}_{\lambda_2 i_2}(J\nu) \Big[Q^+_{\lambda_1\mu_1 i_1} \times Q^+_{\lambda_2\mu_2 i_2} \Big]_{JM} + \sum_{\substack{\lambda_1 i_1 \lambda_2 i_2 \\ \lambda_3 i_3 I}} T^{\lambda_1 i_1 \lambda_2 i_2 I}_{\lambda_3 i_3}(J\nu) \Big[\Big[Q^+_{\lambda_1\mu_1 i_1} \otimes Q^+_{\lambda_2\mu_2 i_2} \Big]_{IK} \otimes Q^+_{\lambda_3\mu_3 i_3} \Big]_{JM} \Big\} \Psi_0 \quad (4.13.1)$$

where R, P, and T are unknown amplitudes, and ν labels the number of the excited states.

The electromagnetic transition matrix elements are calculated for transition operators, including the interaction of quasiparticles and phonons [Pon+98] where exact commutation relations are implemented, which is a necessary condition in order to satisfy the Pauli principle.

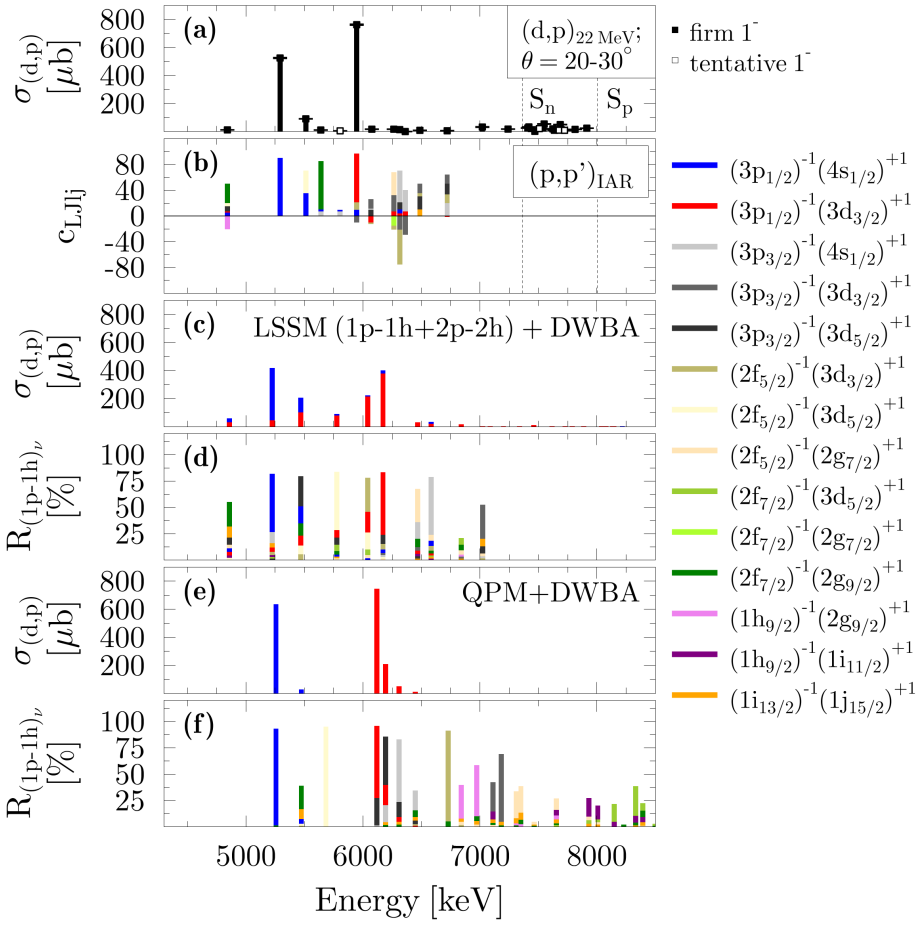

Figure 4.13.1: *(Color online) (a) Angle-integrated (d,p) cross-sections σ(d,p). (b) C_{LJlj} amplitudes from $(p,p')_{\mathrm{IAR}}$. (c) σ(d,p) predicted by combining LSSM spectroscopic factors with DWBA calculations. (d) Decomposition of the LSSM wave functions into neutron $1p-1h$ components relative to the total wave function Ψ_{total}.(e), (f) same as (c), (d) but for EDF+QPM [Spi+20]*

4.13.3 Discussion

The first detailed investigation of the one-particle character of the PDR in ^{208}Pb based on new experimental data and its theoretical explanation is discussed in Ref.[Spi+20]. Theoretical predictions from EDF+QPM and Large-Scale-Shell-Model (LSSM) are compared with novel data from (d,p) and resonant proton scattering experiments performed at the Q3D spectrograph of Maier-Leibnitz-Laboratory in Garching, Germany. Two different transfer configurations through which 1^- states of ^{208}Pb can be populated from the J^π=1/2$^-$ ground state of ^{207}Pb have been distinguished; namely $(3p_{1/2})^{-1}(4s_{1/2})^{+1}$ $(l=0)$, and $(3p_{1/2})^{-1}(3d_{3/2})^{+1}$ $(l=2)$. The measured angular distributions are found in excellent agreement with Distorted-Wave-Born-Approximation (DWBA) model calculations [Spi+20]. In addition, the detailed, high-resolution (d,p) experimental study of the PDR in ^{208}Pb is supplemented with available experimental data to discuss the microscopic structure of the PDR by comparing it to the state-the-art theoretical models: EDF+QPM and LSSM [Spi+20]. The neutron $1p-1h$ configurations that contribute to the formation of the PDR are accessed from (d,p) data up to the proton separation energy S_p and for a limited number of states from the results of resonant proton scattering via isobaric analog resonances $(p,p')_{\mathrm{IAR}}$, which probes components that could not be populated in the selective one-neutron transfer reaction [Spi+20]. The model-

independent, angle-integrated (d,p) cross-sections and C_{Ljj} amplitudes from (p,p')$_{\mathrm{IAR}}$ are shown in Figure 4.13.1 in comparison to a selection of other experimental data on the PDR in ^{208}Pb [Spi+20]. The (d,p) strength pattern [Figure 4.13.1 (a)] is dominated by the two strongly populated 1^- states at 5292 and 5947 keV, corresponding to the major fragments of the $(3p_{1/2})^{-1}(4s_{1/2})^{+1}$ [S=0.77(4)] and $(3p_{1/2})^{-1}(3d_{3/2})^{+1}$ [S=0.66(4)] neutron $1p-1h$ strength, respectively. Figures,4.13.1 (c,d,e,f) present the results of EDF+QPM and LSSM calculations [Spi+20]. The differential cross-sections $d\sigma/d\Omega$, predicted theoretical spectroscopic factors, *i.e.*, the overlap of the ^{207}Pb ground state with excited 1^- states in ^{208}Pb when adding a neutron, were combined with the DWBA calculations. Unprecedented access to the theoretical wave functions demonstrating the $1p-1h$ neutron origin of the PDR in ^{208}Pb has been achieved. In particular, EDF+QPM predicts a dominant $(3p_{1/2})^{-1}(4s_{1/2})^{+1}$ [$S_{5.32\,\mathrm{MeV}}$=0.92] fragment and in agreement with experiment, the $(3p_{1/2})^{-1}(3d_{3/2})^{+1}$ strength to be mainly concentrated in one state [$S_{6.12\,\mathrm{MeV}}$=0.68]. The total (d,p) cross-section value, obtained from the EDF+QPM theory is $\Sigma\sigma_{(d,p)(\mathrm{QPM})} = 1676\,\mu$b. It is found in very good agreement with the total experimental (d,p) cross-section value which can be taken as a sum of $\sum_{\leq S_n}\sigma_{(d,p)(\mathrm{exp.})} = 1524(17)\,\mu$b below and $\sum_{\geq S_n}\sigma_{(d,p)(\mathrm{exp.})} = 254(9)\,\mu$b above the neutron threshold S_n, respectively. However, also the QPM does not fragment the $l=0$ and $l=2$ strength sufficiently to describe the strength above S_n. Due to the doubly-magic nature of ^{208}Pb, the $1p-1h$ structure of the QRPA phonons dominates the configuration mixing and polarization contributions (compare [Ton+17]). In order to improve the comparison with experiment, dynamic effects beyond the static mean field would need to be implemented.

4.13.4 Conclusion

The presented EDF+QPM studies have proved the neutron single-particle origin of PDR in the double-magic ^{208}Pb nucleus, which was confirmed by comparison with novel experimental data and LSSM calculations. Furthermore, the obtained results established (d,p) reactions as additional, valuable experimental probes to study the microscopic structure of PDR and its collectivity. This is achieved through unprecedented access to theoretical wave functions. Knowledge of the microscopic structure PDR is important for the accurate determination of neutron capture reaction rates for astrophysics.

4.13.5 Acknowledgment

N. Tsoneva was supported by the EU Development Fund and Competitiveness Operational Program for the Extreme Light Infrastructure -Nuclear Physics (ELI-NP) Project Phase II (1/07.07.2016, COP, ID1334) and the contract PN 19 06 01 05 sponsored by the Romanian Ministry of Research and Innovation.

References

[BCL15] A. Bracco, F. C. L. Crespi, and E. G. Lanza. "Gamma decay of pygmy states from inelastic scattering of ions". In: *The European Physical Journal A* 51 (2015), page 99 (cited on page 219).

[GS94] M. Grinberg and C. Stoyanov. "Distribution of two-phonon strength in even N = 82 nuclei". In: *Nucl. Phys. A* 573 (1994), page 231 (cited on page 219).

[Pon+98] V. Y. Ponomarev *et al.* "Boson forbidden low-energy E1-transitions in spherical nuclei". In: *Nucl. Phys. A* 635 (1998), page 470 (cited on page 220).

[Rau+13] R. Raut *et al.* "Cross-Section Measurements of the ^{86}Kr(γ,n) Reaction to Probe the s-Process Branching at ^{85}Kr". In: *Phys. Rev. Lett.* 111 (2013), page 112501 (cited on page 219).

[SAZ13] D. Savran, T. Aumann, and A. Zilges. "Experimental studies of the Pygmy Dipole Resonance". In: *Prog. Part. Nucl. Phys.* 70 (2013), page 210 (cited on page 219).

[Spi+20] M. Spieker *et al.* "Accessing the single-particle structure of the Pygmy Dipole Resonance in ^{208}Pb". In: *Phys. Rev. Lett.* 125 (2020), page 102503 (cited on pages 220, 221).

[Ton+17] A. Tonchev *et al.* "Pygmy and core polarization dipole modes in ^{206}Pb: Connecting nuclear structure to stellar nucleosynthesis". In: *Phys. Lett. B* 773 (2017), page 20 (cited on pages 219, 221).

[TL08] N. Tsoneva and H. Lenske. "Pygmy dipole resonances in the tin region". In: *Phys. Rev. C* 77 (2008), page 024321 (cited on page 219).

[TL11] N. Tsoneva and H. Lenske. "Pygmy Quadrupole Resonance in Skin Nuclei". In: *Phys. Lett. B* 695 (2011), page 174 (cited on page 219).

[TL16] N. Tsoneva and H. Lenske. "Energy-Density Functional Plus Quasiparticle-Phonon Model Theory as a Powerful Tool for Nuclear Structure and Astrophysics". In: *Physics of Atomic Nuclei* 79 (2016), pages 885–903 (cited on page 219).

[TLS04] N. Tsoneva, H. Lenske, and C. Stoyanov. "Probing the nuclear neutron skin by low-energy dipole modes". In: *Phys. Lett. B* 586 (2004), page 213 (cited on page 219).

[Tso+15] N. Tsoneva *et al.* "Pygmy resonances and radiative nucleon captures for stellar nucleosynthesis". In: *Phys. Rev. C* 91 (2015), page 044328 (cited on page 219).

[V G76] V. G. Soloviev. *Theory of complex nuclei*. Oxford: Pergamon Press, 1976 (cited on page 219).

4.14 Microscopic structure of the Pygmy Dipole Resonance in ^{120}Sn

Tsoneva N.[1,*]

[1] Extreme Light Infrastructure (ELI-NP) Horia Hulubei National Institute for R&D in Physics and Nuclear Engineering (IFIN-HH), Reactorului 30, 077125 Bucharest–Măgurele, Romania

[*] **nadia.tsoneva@eli-np.ro**

Abstract

New studies on the single-particle structure of the pygmy dipole resonance (PDR) in neutron-excess semi-magic ^{120}Sn are presented. Theoretical calculations performed with a microscopic approach based on the energy-density functional plus quasiparticle-phonon model (EDF + QPM) and reaction theory are compared to a novel ^{119}Sn(d,pγ)^{120}Sn experiment and other available experimental data. Furthermore, different properties of the dipole strength distributions are discussed in order to elucidate the microscopic structure of the PDR in detail. The studies will support ELI Gamma Above Neutron Threshold (ELIGANT) day-one experiments at ELI-NP.

4.14.1 Introduction

In the semi-magic ^{120}Sn nucleus, theoretical investigations of the spectral distributions of low-energy excited dipole states and their relation to the pygmy dipole resonance (PDR) [Wei+21] were carried out. The PDR is a low-energy electric dipole mode known to be compatible with neutron skin oscillations against the isospin symmetric nuclear "core" [BCL15; SAZ13; TL08; TL11; TL16; TLS04]. Recent studies of nuclear reactions of astrophysical interest show that the reaction cross-sections depend strongly on the low-energy part of the electromagnetic dipole strength function and the PDR, which is related to the photoabsorption cross-section [Rau+13; Ton+17; Tso+15]. It is known that tin isotopes play an important role in the s- and r-process of nucleosynthesis. From our investigations of neutron-excess nuclei from different regions of atomic mass, we found that the presence of the PDR mode in these nuclei strongly affects the neutron capture radiation cross-section associated with the synthesis of heavy elements in the Universe [Ton+17; Tso+15]. However, the mechanism of neutron capture by the nucleus is not yet fully understood. Theoretical microscopic models explain the PDR as a sequence of excited one-particle-one-hole ($1p-1h$) excitations, which act coherently and therefore cause an increased transition strength [TL08; TL16]. However, the degree of the collectivity of PDR is still questionable, and no experimental observations for it have been found in the case of semi-magic nuclei, where a large nuclear level density is expected when approaching the neutron threshold. With this work we want to find answers to some of these questions.

4.14.2 Theoretical Model

Theoretically, a novel approach was developed that combines the EDF + QPM theory [TL16; V G76] with the nuclear reaction model (EDF + QPM + reaction) [Wei+21] to consistently derive (d,p) cross-sections, γ-decay branchings, (d,pγ) yields, and energy-integrated (γ,γ') cross-sections.
Since ground-state correlations are small, we describe the ^{119}Sn target as a pure $s_{1/2}$ hole in the ^{120}Sn 'core'. Within this approximation, the (d,p) reaction populates one-phonon 1^- states that contain $3p_{1/2}$ and $3p_{3/2}$ one-quasiparticle states, and the corresponding angular differential cross-section populating a 1^- state ν can be written as [Wei+21]:

$$\frac{d\sigma_\nu}{d\Omega}(\theta) = \frac{\mu_i\mu_f}{(2\pi\hbar^2)^2}\frac{k_f}{k_i}\Big|u_{3p_{1/2}}R_{3p_{1/2}}(\nu)\,\psi^{3p_{1/2}}_{\frac{1}{2}\frac{1}{2}}\,T_{p_{1/2}}(\theta) + u_{3p_{3/2}}R_{3p_{3/2}}(\nu)\,\psi^{3p_{3/2}}_{\frac{1}{2}\frac{3}{2}}\,T_{p_{3/2}}(\theta)\Big|^2 \tag{4.14.1}$$

where R are the one-phonon amplitudes defined in [V G76], $T_{p_{1/2}}$ and $T_{p_{3/2}}$ are the DWBA (d,p) T-matrices (see, e.g. [Wei+21]) populating the corresponding $p_{1/2}$ and $p_{3/2}$ states, respectively, θ is the deflection angle, μ_i,μ_f are the reduced masses in the incident and outgoing channels, k_i,k_f are the respective momenta, $u_{3p_{3/2}}$ and $u_{3p_{1/2}}$ are the one-quasiparticle occupation numbers obtained by solving BCS equations [V G76].

4.14.3 Discussion

The first detailed investigation of the one-particle character of the PDR in semi-magic ^{120}Sn based

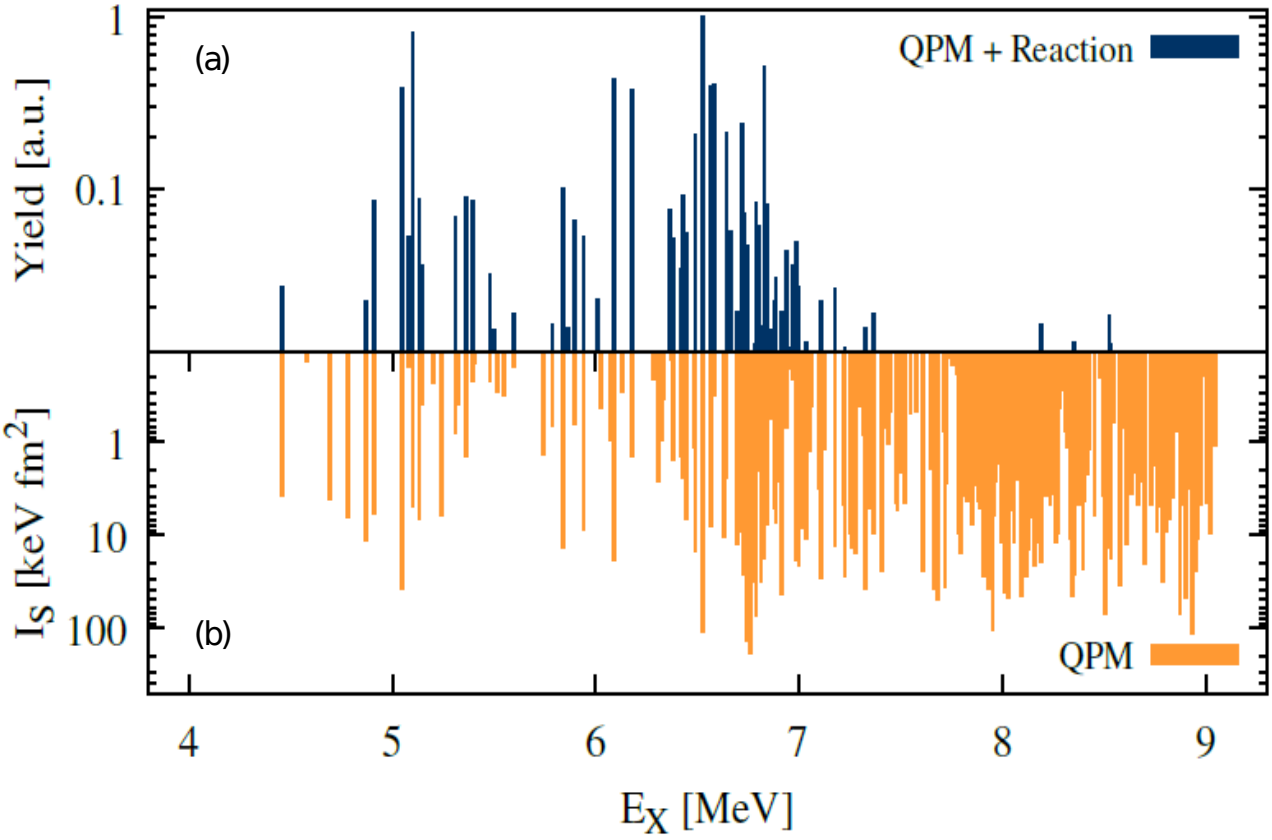

Figure 4.14.1: Rrelative ^{119}Sn(d,pγ)^{120}Sn yields from the EDF+QPM+Reaction formalism and (b) predicted energy-integrated cross-sections I_S, both taking into account γ-decay branching predicted by the EDF+QPM. Theoretical (d,pγ) cross-sections were calculated at scattering angles identical to the experiment [Wei+21].

on a novel theoretical approach and experimental data is discussed in Ref.[Wei+21]. In contrast to the case of the double-magic ^{208}Pb nucleus [Spi+20], the PDR in an open-shell nucleus ^{120}Sn is characterized by a much higher level density. In comparison, the ^{119}Sn(d,pγ)^{120}Sn reaction is studied in a novel experiment performed at the University of Cologne with the combined SONIC@HORUS setup for coincident particle-spectroscopy [Wei+21]. In order to describe the observed fragmentation pattern of the PDR mode in semi-magic nucleus ^{120}Sn, one must go beyond QRPA and take into account the interaction between quasiparticles and phonons. That is achieved by the three-phonon QPM approach, introduced in Section II. The theoretical results of (d,pγ) yields, and energy-integrated (γ, γ') cross-sections in ^{120}Sn obtained from the three-phonon QPM calculations are shown in Figure 4.14.1. Below 7 MeV, one-phonon configurations dominate the spectral distributions while above 7 MeV, two-phonon and three-phonon configurations begin to contribute significantly. The theoretical observations are found in very good agreement with the novel (d,pγ) experiment from Ref. [Wei+21]. The theoretical (d,pγ) strength is fragmented at lower energies, and it reproduces the experimental centroid energy of 6.49 MeV as well as summed (γ,γ') cross-sections for states excited with both probes: $\sum I_S^{\mathrm{QPM}} = 243\,\mathrm{keV\,fm^2}$ and $\sum I_S^{\mathrm{QPM}} = 360\,\mathrm{keV\,fm^2}$ for states with a theoretical relative (d,pγ) yield larger than 1% and 0.5%, respectively. Experimentally, a summed energy-integrated cross-section of $\sum I_S^{\mathrm{NRF}} = 337\,\mathrm{keV\,fm^2}$ is determined from the NRF data [Wei+21].

4.14.4 Conclusion

The presented EDF+QPM and reaction theory studies have proved the neutron single-particle origin of PDR in the semi-magic ^{120}Sn nucleus, which was confirmed by comparison with novel experimental data. Furthermore, the obtained results established (d,p) and (d,pγ) reactions as additional, valuable ex-

perimental probes to study the microscopic structure of PDR and its collectivity. This is achieved through unprecedented access to theoretical wave functions. Knowledge of the microscopic structure PDR is important for the accurate determination of neutron capture reaction rates for astrophysics.

4.14.5 Acknowledgment

N. Tsoneva was supported by the EU Development Fund and Competitiveness Operational Program for the Extreme Light Infrastructure -Nuclear Physics (ELI-NP) Project Phase II (1/07.07.2016, COP, ID1334) and the contract PN 19 06 01 05 sponsored by the Romanian Ministry of Research and Innovation.

References

[BCL15] A. Bracco, F. C. L. Crespi, and E. G. Lanza. "Gamma decay of pygmy states from inelastic scattering of ions". In: *The European Physical Journal A* 51 (2015), page 99 (cited on page 223).

[Rau+13] R. Raut *et al.* "Cross-Section Measurements of the ^{86}Kr(γ,n) Reaction to Probe the s-Process Branching at ^{85}Kr". In: *Phys. Rev. Lett.* 111 (2013), page 112501 (cited on page 223).

[SAZ13] D. Savran, T. Aumann, and A. Zilges. "Experimental studies of the Pygmy Dipole Resonance". In: *Prog. Part. Nucl. Phys.* 70 (2013), page 210 (cited on page 223).

[Spi+20] M. Spieker *et al.* "Accessing the single-particle structure of the Pygmy Dipole Resonance in ^{208}Pb". In: *Phys. Rev. Lett.* 125 (2020), page 102503 (cited on page 224).

[Ton+17] A. Tonchev *et al.* "Pygmy and core polarization dipole modes in ^{206}Pb: Connecting nuclear structure to stellar nucleosynthesis". In: *Phys. Lett. B* 773 (2017), page 20 (cited on page 223).

[TL08] N. Tsoneva and H. Lenske. "Pygmy dipole resonances in the tin region". In: *Phys. Rev. C* 77 (2008), page 024321 (cited on page 223).

[TL11] N. Tsoneva and H. Lenske. "Pygmy Quadrupole Resonance in Skin Nuclei". In: *Phys. Lett. B* 695 (2011), page 174 (cited on page 223).

[TL16] N. Tsoneva and H. Lenske. "Energy-Density Functional Plus Quasiparticle-Phonon Model Theory as a Powerful Tool for Nuclear Structure and Astrophysics". In: *Physics of Atomic Nuclei* 79 (2016), pages 885–903 (cited on page 223).

[TLS04] N. Tsoneva, H. Lenske, and C. Stoyanov. "Probing the nuclear neutron skin by low-energy dipole modes". In: *Phys. Lett. B* 586 (2004), page 213 (cited on page 223).

[Tso+15] N. Tsoneva *et al.* "Pygmy resonances and radiative nucleon captures for stellar nucleosynthesis". In: *Phys. Rev. C* 91 (2015), page 044328 (cited on page 223).

[V G76] V. G. Soloviev. *Theory of complex nuclei*. Oxford: Pergamon Press, 1976 (cited on page 223).

[Wei+21] M. Weinert *et al.* "Microscopic Structure of the Low-Energy Electric Dipole Response of ^{120}Sn". In: *Phys. Rev. Lett.* 127 (2021), page 242501 (cited on pages 223, 224).

4.15 Peer-reviewed publications, talks, PhD/MSc, & Grants for GDED in 2020-2021

Peer-reviewed publications by GDED staff: 01.01.2020 to 31.12.2021

[Ali+20] K. Ali *et al.* "Selective Isotope CT Imaging Based on Nuclear Resonance Fluorescence Transmission Method". In: *IEEE Transactions on Nuclear Science* 67.8 (2020), pages 1976–1984. DOI: 10.1109/TNS.2020.3004565.

[Aye+20] S. Ayet San Andrés *et al.* "Mass and half-life measurements of neutron-deficient iodine isotopes". In: *European Physical Journal A* 56.5, 143 (2020), page 143. DOI: 10.1140/epja/s10050-020-00153-5.

[Bar+21] S. Baruta (Ilie) *et al.* "Characterization of the segmented high-purity germanium clover detector from the ELIADE array at ELI-NP". In: *University politehnica of Bucharest scientific bulletin-series A-applied mathematics and physics* 83.2 (2021), pages 253–266. ISSN: 1223-7027.

[BXN21] A. Berceanu, Y. Xu, and Y. F. Niu. "Temperature effects on neutron-capture cross sections and rates through electric dipole transitions in hot nuclei". In: *Phys. Rev. C* 104 (4 Oct. 2021), page 044332. DOI: 10.1103/PhysRevC.104.044332. URL: https://link.aps.org/doi/10.1103/PhysRevC.104.044332.

[Bou+20] F. Boulay *et al.* "g Factor of the ^{99}Zr $(7/2^+)$ Isomer: Monopole Evolution in the Shape-Coexisting Region". In: *Phys. Rev. Lett.* 124 (11 Mar. 2020), page 112501. DOI: 10.1103/PhysRevLett.124.112501. URL: https://link.aps.org/doi/10.1103/PhysRevLett.124.112501.

[Bur+21] K. Burdonov *et al.* "Characterization and performance of the Apollon short-focal-area facility following its commissioning at 1 PW level". In: *Matter and Radiation at Extremes* 6.6 (2021), page 064402. DOI: 10.1063/5.0065138. eprint: https://doi.org/10.1063/5.0065138. URL: https://doi.org/10.1063/5.0065138.

[Can+20] R. L. Canavan *et al.* "Half-life measurements in ^{164,166}Dy using $\gamma-\gamma$ fast-timing spectroscopy with the ν-Ball spectrometer". In: *Phys. Rev. C* 101 (2 Feb. 2020), page 024313. DOI: 10.1103/PhysRevC.101.024313. URL: https://link.aps.org/doi/10.1103/PhysRevC.101.024313.

[Cap+21] L. Capponi *et al.* "First in-beam experiment with the ELIADE detectors: a spectroscopic study of ^{130}La". In: *Journal of Instrumentation* 16.12 (Dec. 2021), T12001. DOI: 10.1088/1748-0221/16/12/t12001. URL: https://doi.org/10.1088/1748-0221/16/12/t12001.

[Dau+21] J. M. Daugas *et al.* "Magnetic moment of the $11/2^-$ isomeric state in ^{99}Mo and neutron spin g factor quenching in $A \approx 100$ nuclei". In: *Phys. Rev. C* 104 (2 Aug. 2021), page 024321. DOI: 10.1103/PhysRevC.104.024321. URL: https://link.aps.org/doi/10.1103/PhysRevC.104.024321.

[Dic+20] T. Dickel *et al.* "Multi-nucleon transfer reactions at ion catcher facilities - a new way to produce and study heavy neutron-rich nuclei". In: *J. Phys.: Conf. Ser.* 1668 (2020), page 012012. DOI: 10.1088/1742-6596/1668/1/012012.

[DS21] N. Djourelov and A. Serban. "Optimization of a device for positron moderation based on a magnetic bottle". In: *Nuclear Instruments and Methods in Physics Research Section A: Accelerators, Spectrometers, Detectors and Associated Equipment* 1014 (2021), page 165699. ISSN: 0168-9002. DOI: https://doi.org/10.1016/j.nima.2021.165699. URL: https://www.sciencedirect.com/science/article/pii/S0168900221006847.

[Ene+20] V. L. Ene *et al.* "Defect Structure Determination of GaN Films in GaN/AlN/Si Heterostructures by HR-TEM, XRD, and Slow Positrons Experiments". In: *Nanomaterials* 10.2 (2020). ISSN: 2079-4991. DOI: 10.3390/nano10020197. URL: https://www.mdpi.com/2079-4991/10/2/197.

[Esc+21] S. Escrig *et al.* "Persistence of the $Z = 28$ shell gap in $A = 75$ isobars: Identification of a possible $(1/2^-)$ μs isomer in ^{75}Co and β decay to ^{75}Ni". In: *Phys. Rev. C* 103 (6 June 2021), page 064328. DOI: 10.1103/PhysRevC.103.064328.

[Fro+20] A. Frotscher *et al.* "Sequential Nature of $(p,3p)$ Two-Proton Knockout from Neutron-Rich Nuclei". In: *Phys. Rev. Lett.* 125 (1 June 2020), page 012501. DOI: 10.1103/PhysRevLett.125.012501. URL: https://link.aps.org/doi/10.1103/PhysRevLett.125.012501.

[Gje+21a] D. Gjestvang *et al.* "Excitation energy dependence of prompt fission γ-ray emission from ^{241}Pu*". In: *Phys. Rev. C* 103 (3 Mar. 2021), page 034609. DOI: 10.1103/PhysRevC.103.034609. URL: https://link.aps.org/doi/10.1103/PhysRevC.103.034609.

[Gje+21b] D. Gjestvang *et al.* "The study of prompt fission γ rays at the Oslo Cyclotron Laboratory". In: European Physical Journal Web of Conferences 256 (2021), page 00005. DOI: 10.1051/epjconf/202125600005.

[Gug+21] L. A. D. Gugoasa *et al.* "Graphene-Gold Nanoparticles Nanozyme-Based Electrochemical Sensor with Enhanced Laccase-Like Activity for Determination of Phenolic Substrates". In: *Journal of The Electrochemical Society* (2021).

[Häf+21a] G. Häfner *et al.* "First lifetime investigations of $N > 82$ iodine isotopes: The quest for collectivity". In: *Phys. Rev. C* 104 (1 July 2021), page 014316. DOI: 10.1103/PhysRevC.104.014316. URL: https://link.aps.org/doi/10.1103/PhysRevC.104.014316.

[Häf+21b] G. Häfner *et al.* "Spectroscopy and lifetime measurements in ^{134,136,138}Te isotopes and implications for the nuclear structure beyond $N = 82$". In: *Phys. Rev. C* 103 (3 Mar. 2021), page 034317. DOI: 10.1103/PhysRevC.103.034317. URL: https://link.aps.org/doi/10.1103/PhysRevC.103.034317.

[Hay+21] S. Hayakawa *et al.* "Constraining the Primordial Lithium Abundance: New Cross Section Measurement of the ^{7}Be + n Reactions Updates the Total ^{7}Be Destruction Rate". In: *The astrophysical Journal Letters* 915.1, L13 (2021), page L13. DOI: 10.3847/2041-8213/ac061f.

[Hu+21] J. Hu *et al.* "Advancement of Photospheric Radius Expansion and Clocked Type-I X-Ray Burst Models with the New ^{22}Mg$(\alpha,p)^{25}$Al Reaction Rate Determined at the Gamow Energy". In: *Phys. Rev. Lett.* 127 (17 Oct. 2021), page 172701. DOI: 10.1103/PhysRevLett.127.172701. URL: https://link.aps.org/doi/10.1103/PhysRevLett.127.172701.

[Juh+21] M. M. Juhász *et al.* "First spectroscopic study of ^{63}V at the $N = 40$ island of inversion". In: *Phys. Rev. C* 103 (6 June 2021), page 064308. DOI: 10.1103/PhysRevC.103.064308. URL: https://link.aps.org/doi/10.1103/PhysRevC.103.064308.

[KJW21] D. Kahl, J. Jose, and P. J. Woods. "Uncertainties in the ^{18}F(p,α)^{15}O reaction rate in classical novae". In: *Astronomy and Astrophysics* 653 (2021), A64. DOI: https://doi.org/10.1051/0004-6361/202140339.

[Ker+20] R. Kern *et al.* "Restoring the valence-shell stabilization in ^{140}Nd". In: *Phys. Rev. C* 102 (4 Oct. 2020), page 041304. DOI: 10.1103/PhysRevC.102.041304. URL: https://link.aps.org/doi/10.1103/PhysRevC.102.041304.

[Lan+21] H. Lan *et al.* "Nuclear resonance fluorescence drug inspection". In: *Scientific Reports* 11.1 (2021), page 1306. DOI: 10.1038/s41598-020-80079-6. URL: https://doi.org/10.1038/s41598-020-80079-6.

[Led+21] C. Lederer-Woods *et al.* "Destruction of the cosmic γ-ray emitter ^{26}Al in massive stars: Study of the key ^{26}Al(n,α) reaction". In: *Phys. Rev. C* 104 (3 Sept. 2021), page L032803. DOI: 10.1103/PhysRevC.104.L032803. URL: https://link.aps.org/doi/10.1103/PhysRevC.104.L032803.

[Lel+21] V. Lelasseux *et al.* "Design and commissioning of a neutron counter adapted to high-intensity laser matter interactions". In: *Review of Scientific Instruments* 92.11 (2021), page 113303. DOI: 10.1063/5.0057828. eprint: https://doi.org/10.1063/5.0057828. URL: https://doi.org/10.1063/5.0057828.

[Liz+20] C. Lizarazo *et al.* "Metastable States of ^{92,94}Se: Identification of an Oblate K Isomer of ^{94}Se and the Ground-State Shape Transition between $N = 58$ and 60". In: *Phys. Rev. Lett.* 124 (22 June 2020), page 222501. DOI: 10.1103/PhysRevLett.124.222501. URL: https://link.aps.org/doi/10.1103/PhysRevLett.124.222501.

[Mar+21] I. Mardor *et al.* "Mass measurements of As, Se, and Br nuclei, and their implication on the proton-neutron interaction strength toward the $N = Z$ line". In: *Phys. Rev. C* 103 (3 Mar. 2021), page 034319. DOI: 10.1103/PhysRevC.103.034319. URL: https://link.aps.org/doi/10.1103/PhysRevC.103.034319.

[Mar+20] Mardor, Israel *et al.* "Determining spontaneous fission properties by direct mass measurements with the FRS Ion Catcher". In: *EPJ Web Conf.* 239 (2020), page 02004. DOI: 10.1051/epjconf/202023902004. URL: https://doi.org/10.1051/epjconf/202023902004.

[Mis+21] I. Miskun *et al.* "Separation of atomic and molecular ions by ion mobility with an RF carpet". In: *International Journal of Mass Spectrometry* 459 (2021), page 116450. ISSN: 1387-3806. DOI: https://doi.org/10.1016/j.ijms.2020.116450. URL: https://www.sciencedirect.com/science/article/pii/S1387380620303730.

[Moo+21] B. Moon *et al.* "Nuclear structure of Te isotopes beyond neutron magic number $N = 82$". In: *Phys. Rev. C* 103 (3 Mar. 2021), page 034320. DOI: 10.1103/PhysRevC.103.034320. URL: https://link.aps.org/doi/10.1103/PhysRevC.103.034320.

[Mun+20] M. Munch *et al.* "Measurement of the ^{7}Li$(\gamma,t)^{4}$He ground-state cross section between $E_\gamma = 4.4$ and 10 MeV". In: *Phys. Rev. C* 101 (5 May 2020), page 055801. DOI: 10.1103/PhysRevC.101.055801. URL: https://link.aps.org/doi/10.1103/PhysRevC.101.055801.

[Nic+20a] D. Nichita *et al.* "Optimization of photo-fission fragment production in the ELISOL setup at ELI-NP". In: *U.P.B. Sci. Bull. A* 82 (2020), page 297. URL: https://www.scientificbulletin.upb.ro/rev_docs_arhiva/rez8b1_923628.pdf.

[Nic+20b] D. Nichita *et al.* "Test bench for silicon strip detectors: front-end electronics and DAQ". In: *U.P.B. Sci. Bull. A* 82 (2020), page 245. URL: https://www.scientificbulletin.upb.ro/rev_docs_arhiva/fulld47_346483.pdf.

[Nic+21] D. Nichita *et al.* "Radioactive ion beams production at the Gamma Factory". In: *Ann. Phys. (Berl.)* In press (2021). DOI: https://doi.org/10.1002/andp.202100207.

[Nya+21] B. M. Nyakó *et al.* "Medium-spin states of the neutron-rich nucleus ^{87}Br". In: *Phys. Rev. C* 103 (3 Mar. 2021), page 034304. DOI: 10.1103/PhysRevC.103.034304. URL: https://link.aps.org/doi/10.1103/PhysRevC.103.034304.

[OO21] A. Oberstedt and S. Oberstedt. "Exploring the fission barrier of ^{235}U". In: *Phys. Rev. C* 104 (2 Aug. 2021), page 024611. DOI: 10.1103/PhysRevC.104.024611. URL: https://link.aps.org/doi/10.1103/PhysRevC.104.024611.

[Obe+20a] A. Oberstedt *et al.* "Prompt γ-ray characteristics from ^{235}U(n, f) at $\overline{E_n}$= 1.7 MeV". In: *The European Physical Journal A* 56.9 (2020), page 236. DOI: 10.1140/epja/s10050-020-00246-1. URL: https://doi.org/10.1140/epja/s10050-020-00246-1.

[Obe+20b] A. Oberstedt *et al.* "Time response and its impact on prompt fission γ-ray spectra characteristics". In: *The European Physical Journal A* 56.7 (2020), page 196. DOI: 10.1140/epja/s10050-020-00209-6. URL: https://doi.org/10.1140/epja/s10050-020-00209-6.

[Obe+21] A. Oberstedt *et al.* "Systematic study of the de-excitation of neutron-rich nuclei produced in different fission reactions". In: European Physical Journal Web of Conferences 256, 00012 (Sept. 2021), page 00012. DOI: 10.1051/epjconf/202125600012.

[Qi+20] L. Qi *et al.* "Potential of prompt γ-ray emission studies in fast-neutron induced fission: a first step". In: *The European Physical Journal A* 56.3 (2020), page 98. DOI: 10.1140/epja/s10050-020-00108-w. URL: https://doi.org/10.1140/epja/s10050-020-00108-w.

[Rod+20] L. V. Rodríguez *et al.* "Doubly-magic character of ^{132}Sn studied via electromagnetic moments of ^{133}Sn". In: *Phys. Rev. C* 102 (5 Nov. 2020), page 051301. DOI: 10.1103/PhysRevC.102.051301. URL: https://link.aps.org/doi/10.1103/PhysRevC.102.051301.

[San+20] S. San Andres *et al.* "Mass and half-life measurements of neutron-deficient iodine isotopes". In: *The European Physical Journal A* 56 (May 2020). DOI: 10.1140/epja/s10050-020-00153-5.

[Sav+21] M. Savin *et al.* "A New Hybrid Sensitive PANI/SWCNT/Ferrocene-Based Layer for a Wearable CO Sensor". In: *Sensors* 21.5 (2021). ISSN: 1424-8220. DOI: 10.3390/s21051801. URL: https://www.mdpi.com/1424-8220/21/5/1801.

[Ser+21] A. B. Serban *et al.* "Studies of Defect Structure in Epitaxial AlN/GaN Films Grown on (111) 3C-SiC". In: *Nanomaterials* 11.5 (2021). ISSN: 2079-4991. DOI: 10.3390/nano11051299. URL: https://www.mdpi.com/2079-4991/11/5/1299.

[Sim+20] O.-G. Simionescu *et al.* "Properties of Nitrogen-Doped Nano-Crystalline Graphite Thin Films and Their Application as Electrochemical Sensors". In: *Journal of The Electrochemical Society* 167.12 (Jan. 2020), page 126510. DOI: 10.1149/1945-7111/abb1d4. URL: https://doi.org/10.1149/1945-7111/abb1d4.

[Söd+20] P.-A. Söderström *et al.* "Electromagnetic character of the competitive $\gamma\gamma/\gamma$-decay from ^{137m}Ba". In: *Nature Communications* 11.1 (2020), page 3242. DOI: 10.1038/s41467-020-16787-4. URL: https://doi.org/10.1038/s41467-020-16787-4.

[Söd+21] P.-A. Söderström *et al.* "Characterization of a plutonium–beryllium neutron source". In: *Applied Radiation and Isotopes* 167 (2021), page 109441. ISSN: 0969-8043. DOI: https://doi.org/10.1016/j.apradiso.2020.109441. URL: https://www.sciencedirect.com/science/article/pii/S0969804320305832.

[Spa+20a] A. Spataru *et al.* "Multi-nucleon transfer reactions in ^{238}U+^{64}Ni using GRAZING model". In: *U.P.B. Sci. Bull. A* 82 (2020), page 285. URL: https://www.scientificbulletin.upb.ro/rev_docs_arhiva/rez923_256342.pdf.

[Spa+20b] A. Spataru *et al.* "Production of Exotic Nuclei via MNT Reactions Using Gas Cells". In: *Acta Phys. Pol.* 51 (2020), page 807. DOI: https://doi.org/10.5506/APhysPolB.51.817.

[Spi+20] M. Spieker *et al.* "Accessing the single-particle structure of the Pygmy Dipole Resonance in ^{208}Pb". In: *Phys. Rev. Lett.* 125 (2020), page 102503. DOI: 10.1103/PhysRevLett.125.102503.

[Sta+20] A. State *et al.* "Ion extraction from gas cells with supersonic jets formed in Laval nozzles". In: *U.P.B. Sci. Bull. A* 82.2 (2020), page 197. ISSN: 1223-7027. URL: https://www.scientificbulletin.upb.ro/rev_docs_arhiva/fullb75_790381.pdf.

[Tan+20] K. Tanaka *et al.* "Current status and highlights of the ELI-NP research program". In: *Matter and Radiation at Extremes* 5 (2020), page 024402. DOI: https://doi.org/10.1063/1.5093535.

[Tra+21] M. Travar *et al.* "Experimental information on mass- and TKE-dependence of the prompt fission γ-ray multiplicity". In: *Physics Letters B* 817 (2021), page 136293. ISSN: 0370-2693. DOI: https://doi.org/10.1016/j.physletb.2021.136293. URL: https://www.sciencedirect.com/science/article/pii/S0370269321002331.

[Tso21c] N. Tsoneva. "Probing the Single-Particle Neutron Origin of the Pygmy Dipole Resonance". In: *Bulg. J. Phys.* 48 (2021), pages 587–596. DOI: https://doi.org/10.55318/bgjp.2021.48.5-6.587.

[Tur+20] G. V. Turturica *et al.* "Effective Z evaluation using monoenergetic gamma rays and neural networks". In: *Eur. Phys. J. Plus* 135 (2020), page 140. DOI: 10.1140/epjp/s13360-020-00122-3.

[TIU21] G. Turturica, V. Iancu, and C. Ur. "A neural-network based approach to cargo inspections using photon spectroscopy". In: *Nuclear Instruments and Methods in Physics Research Section A: Accelerators, Spectrometers, Detectors and Associated Equipment* 1010 (2021), page 165553. ISSN: 0168-9002. DOI: https://doi.org/10.1016/j.nima.2021.165553. URL: https://www.sciencedirect.com/science/article/pii/S0168900221005386.

[Var+21] P. Varasteanu *et al.* "Exploring the impact of MoS_2 on the performance of the planar solid micro-supercapacitor". In: *Materials Chemistry and Physics* 265 (2021), page 124490. ISSN: 0254-0584. DOI: https://doi.org/10.1016/j.matchemphys.2021.124490. URL: https://www.sciencedirect.com/science/article/pii/S025405842100273X.

[Wei+21] M. Weinert *et al.* "Microscopic Structure of the Low-Energy Electric Dipole Response of ^{120}Sn". In: *Phys. Rev. Lett.* 127 (24 Dec. 2021), page 242501. DOI: 10.1103/PhysRevLett.127.242501. URL: https://link.aps.org/doi/10.1103/PhysRevLett.127.242501.

[Wil+21] J. N. Wilson *et al.* "Angular momentum generation in nuclear fission". In: *Nature* 590 (2021), page 566. DOI: 10.1038/s41586-021-03304-w.

[XGK21] Y. Xu, S. Goriely, and E. Khan. "Systematical studies of the $E1$ photon strength functions combining the Skyrme-Hartree-Fock-Bogoliubov plus quasiparticle random-phase approximation model and experimental giant dipole resonance properties". In: *Phys. Rev. C* 104 (4 Oct. 2021), page 044301. DOI: 10.1103/PhysRevC.104.044301. URL: https://link.aps.org/doi/10.1103/PhysRevC.104.044301.

[Yaj+21] R. Yajzey *et al.* "Spectroscopy of the T=2 mirror nuclei ^{48}Fe/^{48}Ti using mirrored knockout reactions". In: *Physics Letters B* 823 (2021), page 136757. ISSN: 0370-2693. DOI: https://doi.org/10.1016/j.physletb.2021.136757. URL: https://www.sciencedirect.com/science/article/pii/S0370269321006973.

[Zam+21] G. Zamfirova *et al.* "PALS and nanoindentation as complementary methods for investigating cellulose derivatives (esters and carbamates)". In: *Materials Today: Proceedings* 34 (2021). 12th International Conference on Composite Science and Technology, pages 304–310. ISSN: 2214-7853. DOI: https://doi.org/10.1016/j.matpr.2020.04.089. URL: https://www.sciencedirect.com/science/article/pii/S2214785320327048.

[Zha+21] L. Y. Zhang *et al.* "Direct Measurement of the Astrophysical $^{19}F(p,\alpha\gamma)^{16}O$ Reaction in the Deepest Operational Underground Laboratory". In: *Phys. Rev. Lett.* 127 (15 Oct. 2021), page 152702. DOI: 10.1103/PhysRevLett.127.152702. URL: https://link.aps.org/doi/10.1103/PhysRevLett.127.152702.

[Zha+20] N. Zhang *et al.* "Constraining the $^{12}C+^{12}C$ astrophysical S-factors with the $^{12}C+^{13}C$ measurements at very low energies". In: *Physics Letters B* 801 (2020), page 135170. ISSN: 0370-2693. DOI: https://doi.org/10.1016/j.physletb.2019.135170. URL: https://www.sciencedirect.com/science/article/pii/S0370269319308925.

Contributed and invited talks delivered by GDED staff: 01.01.2020 to 31.12.2021

[Bal20a] D. Balabanski. "Extreme Light: A New Tool in Nuclear Physics - Research on Medical Applications at ELI-NP". In: *International summer school: Innovative technologies of nuclear medicine and radiotherapy*. 2020.

[Bal20b] D. Balabanski. "Research on medical radioisotopes at ELI-NP". In: *ELI-NP Autumn School (ELIAS 2020), Magurele (Romania)*. 2020.

[Bal20c] D. Balabanski. "Status of ELI-NP". In: *Low-Energy Community Meeting, Los Alamos (USA)*. 2020.

[Bal21a] D. Balabanski. "Experimental programme with high-brilliance gamma beams at ELI-NP". In: *3rd International Conference on Nuclear Photonics (NP2020)*. 2021.

[Bal21b] D. Balabanski. "Present day research opportunities with quasimonochromatic gamma beams". In: *International Workshop "Shapes and Dynamics of Atomic Nuclei: Contemporary Aspects" (SDANCA-21), Sofia (Bulgaria)*. 2021.

[Bal21c] D. Balabanski. "Short overview of the ELI-NP experimental setups". In: *Workshop "New Trends in Nuclear Physics Detectors" (NTNPD-2021), 25 – 27 October 2021, Heavy Ion Laboratory, the University of Warsaw (Poland)*. 2021.

[Con20] P. Constantin. "ELI-IGISOL facility implementation". In: *HADO-CSC Workshop SOREQ, Yavne (Israel)*. 2020.

[Con21a] P. Constantin. "RIB production at the Gamma Factory". In: *ISOLDE collaboration meeting CERN, Geneve (Switzerland)*. 2021.

[Con21b] P. Constantin. "S523: In-cell multi-nucleon transfer reactions at the FRS Ion Catcher". In: *Super-FRS experiment collaboration meeting GSI, Darmstadt (Germany)*. 2021.

[Dha21] A. Dhal. "ELIADE: A state-of-the-art facility for probing nuclear structure by NRF process". In: *Third International Conference on Nuclear Photonics (NP2020)*. 2021.

[Kah21a] D. Kahl. "Me, Al Cameron, and the Heat Death of the Universe". In: *Carpathian School of Physics, Sinaia (Romania)*. 2021.

[Kah21b] D. Kahl. "Radioactive nuclides in outerspace". In: *Invited seminar at JYFL, Jyväskylä (Finland)*. 2021.

[Kah21c] D. Kahl. "Time Projection Chambers". In: *New Trends in Nuclear Physics Detectors, Warsaw, Poland*. 2021.

[Kah21d] D. Kahl. "Uncertainties in the $^{18}F(p,\alpha)^{15}O$ reaction rate in classical novae". In: *National Astronomy Meeting 2021, Bath (UK)*. 2021.

[Kah21e] D. Kahl. "Uncertainties in the $^{18}F(p,\alpha)^{15}O$ reaction rate in classical novae". In: *Nuclear Burning in Massive Stars, Kyoto (Japan) & Melbourne (Australia)*. 2021.

[Kah21f] D. Kahl. “Uncertainties in the ^{18}F(p,α)^{15}O reaction rate in classical novae”. In: *Nuclei in the Cosmos (NIC XVI), Chengdu (China)*. 2021.

[Nic20a] D. Nichita. “Radioactive Ion Beams production possibility at the Gamma Factory”. In: *ISOLDE users meeting workshop*. 2020.

[Nic20b] D. Nichita. “RIB production at the Gamma Factory”. In: *Physics with the Gamma Factory*. 2020.

[Obe20a] A. Oberstedt. “Comparing Apples and Oranges …”. In: *Uppsala, Sweden: Applied Nuclear Physics Breakfast Meeting*. 2020.

[Obe20b] A. Oberstedt. “Our fission research – the past, the present, and the future”. In: *Uppsala, Sweden: Seminar Applied Nuclear Physics*. 2020.

[Obe21a] A. Oberstedt. “Photo-fission at ELI-NP – our main experimental setups”. In: *IIT Ropar, India & ELI-NP, Romania: Workshop on Nuclear Photonics and Research Opportunities at ELI-NP*. 2021.

[Obe21b] A. Oberstedt. “The shape isomer in ^{235}U and fission fragment properties – access to barrier parameters?” In: *GSI Darmstadt, Germany: S530 Meeting*. 2021.

[Pet20] T. Petruse. “Cryogenic stopping cells”. In: *ELI Autumn School*. 2020.

[Söd20] P.-A. Söderström. “Neutron detection techniques and possible applications for diagnostics in high-power laser environments”. In: *BLIN4: Beam Line and INstrumentation: Fourth Workshop, Online, June 29, 2020*. 2020.

[Söd21a] P.-A. Söderström. “Electric dipole response of low-mass nuclei for the mass evolution of extra-galactic ultra-high energy cosmic rays”. In: *Carpathian Summer School of Physics 2020. Exotic Nuclei and Nuclear/Particle Astrophysics (VIII)*. 2021.

[Söd21b] P.-A. Söderström. “ELIGANTs at ELI-NP”. In: *Workshop on Nuclear Photonics and Research Opportunities at ELI-NP*. 2021.

[Söd21c] P.-A. Söderström. “Neutron detectors for spectroscopy and cross-section measurements at ELI-NP”. In: *New Trends in Nuclear Physics Detectors (NTNPD-2021), Heavy Ion Laboratory, University of Warsaw, Warsaw, Poland, 25-27 October 2021*. 2021.

[Tes21] D. Testov. “Neutron production in (α,n) reactions”. In: *LXXI International conference ”NUCLEUS – 2021. Nuclear physics and elementary particle physics. Nuclear physics technologies*. 2021.

[Tso21a] N. Tsoneva. “Probing the 1p-1h neutron origin of the Pygmy Dipole Resonance”. In: *International Workshop "Shapes and Dynamics of Atomic Nuclei: Contemporary Aspects"*. 2021.

[Tso21b] N. Tsoneva. “Probing the Microscopic Structure of New Modes of Nuclear Excitations at ELI-NP”. In: *Third International Conference on Nuclear Photonics (NP2020)*. 2021.

[Tso21d] N. Tsoneva. “Pygmy and Core Polarization Modes: Connecting Nuclear Structure to Stellar Nucleosynthesis”. In: *Nuclear Seminar at Florida State University, USA*. 2021.

[Tso21e] N. Tsoneva. “Studying the nature of the low-energy dipole response with a microscopic theory involving multi-phonon coupling”. In: *Second PANDORA Workshop*. 2021.

[Vas21] V. Vasilca. “The Production of Medically Relevant Radioisotopes at ELI-NP”. In: *Carpathian Summer School of Physics, Sinaia, Romania*. 2021.

[Xu20a] Y. Xu. “TALYS calculation based on the γ-beam properties at ELI-NP: Two-particle emission from g+17O”. In: *PANDORA Workshop 2020*. 2020.

Successful Ph.D projects within the GDED group: 01.01.2020 to 31.12.2021

[Din20] D. Dinescu. “Simulation and design of the ELI-NP positron source and the slow positron beam pulsing system”. PhD thesis. The University Politehnica of Bucharest, 2020.

[Rot21] A. Rotaru. “Development of techniques for ion-beam analysis and ion manipulation”. PhD thesis. The University Politehnica of Bucharest, 2021.

External Grant generation by members of the GDED group as PI: 01.01.2020 to 31.12.2021

[Djo20] N. Djourelov. “ELI_05: Slow positrons from magnetic bottle/POSBOT (999 442 Lei)”. In: *ELI-RO* (Oct. 2020).

[Xu20b] Y. Xu. “ELI_15: Systematic Study of Astrophysical Radiative Capture Reactions with Complete Reaction Mechanism and Up-to-date Nuclear Ingredients (SSARCR) (750 000 Lei)”. In: *ELI-RO* (Oct. 2020).

5. Laser Gamma Experiments Department (LGED)

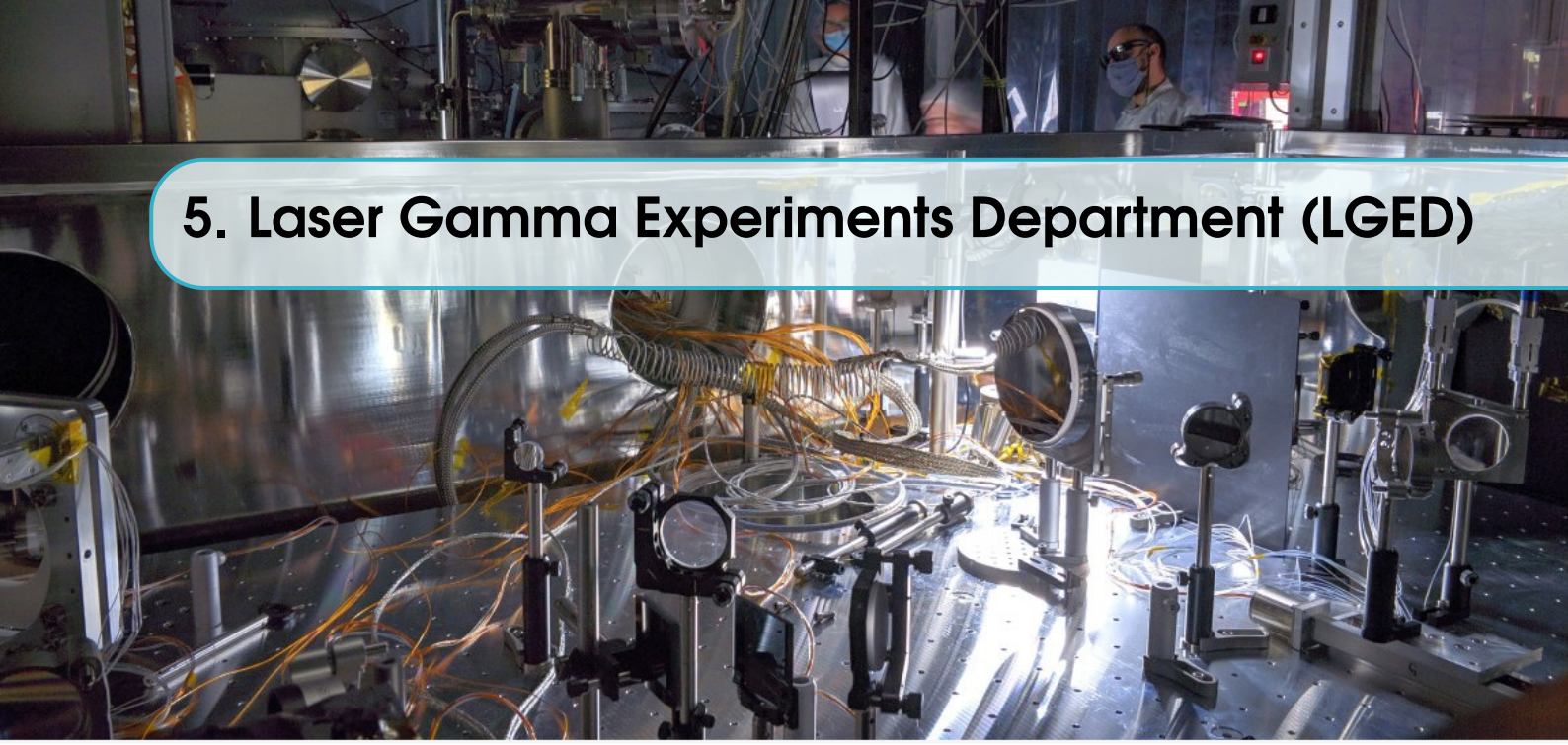

The Laser Gamma Experiments Department at ELI-NP proposes an ambitious research program encompassing fundamental physics and applied science. The department prepares for the related experiments and operates the E7 and E4 experimental areas. Besides, the Biophysics and Biomedical Applications Group, portrayed in detail in the next chapter, is a sub-group of the Laser Gamma Experiments Department (LGED) with a focus on biomedical research.

The E4 area, featuring two 100 TW laser beams with a high pulse repetition rate (10 Hz) was the first one to operational at ELI-NP in 2020, hosting an experiment for the spectral broadening of the laser pulses (for subsequent temporal compression) and a laser-Wakefield acceleration experiment, in which electron energies above 200 MeV were obtained.

In 2021 the commissioning experiment endorsed by the ELI-NP International Scientific Advisory Board had started in E4, focusing on detecting light axion-like dark matter through photon-photon interactions. The experimental campaign requires reaching extremely high sensitivity. Therefore several beamtime sessions are foreseen for gradual improvement in the setup and detection. Three beamtime sessions took place in 2021, and two more are foreseen in the first half of 2022 will complete the commissioning phase of E4. This experimental area will enter the user facility operation afterward, with experiment proposals received from the users and evaluated by an international scientific panel of experts.

The E7 area aims to combine plasma and nuclear physics, recreating conditions in which astrophysical phenomena occur with the help of additional beam types (such as laser and gamma beams), which can be used simultaneously in experiments. Therefore, the preparatory activities for the definition of the setup in E7 for the commissioning experiment (creation of nuclear isomer states) have continued, together with the construction of the setup – with procurement procedures starting and ongoing for the vacuum system and other equipment and components. Also, the experimental physics and numerical simulation teams have restarted the activities of refining the feasibility study for the commissioning experiment in E7, allowing a fine-tuning of the final optimizations in the implementation applied to the setup.

LGED features a powerful theory and numerical Simulations group, which during 2021, has ramped up several collaborations with external institutions (in Italy, Greece, and Germany) and, internally, with other research departments of ELI-NP (LDED, GDED). The LGED Biophysics and Biomedical Applications group has continued the research and collaboration with several Romanian and international research institutions, companies, and hospitals, publishing high-level research in prestigious journals. In addition, they are proposing, with a remarkable success rate, ambitious projects for funding in the open calls in Romania and at the European level.

LGED has continued hiring new personnel and expanding the areas of competencies, aiming to increase the research groups' competitiveness and foreseeing the facility's steady operation mode, including user access and our very own research programs.

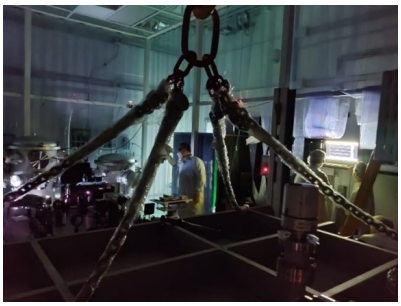

Figure 5.0.1: Ongoing experiment in the E4 experimental area.

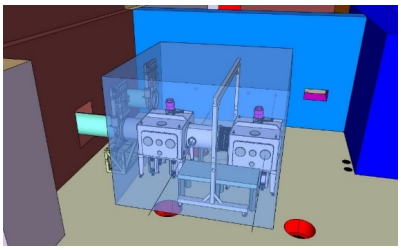

Figure 5.0.2: CAD drawing of the E7 area with the vacuum chamber system.

Figure 5.0.3: Biophysics laboratory

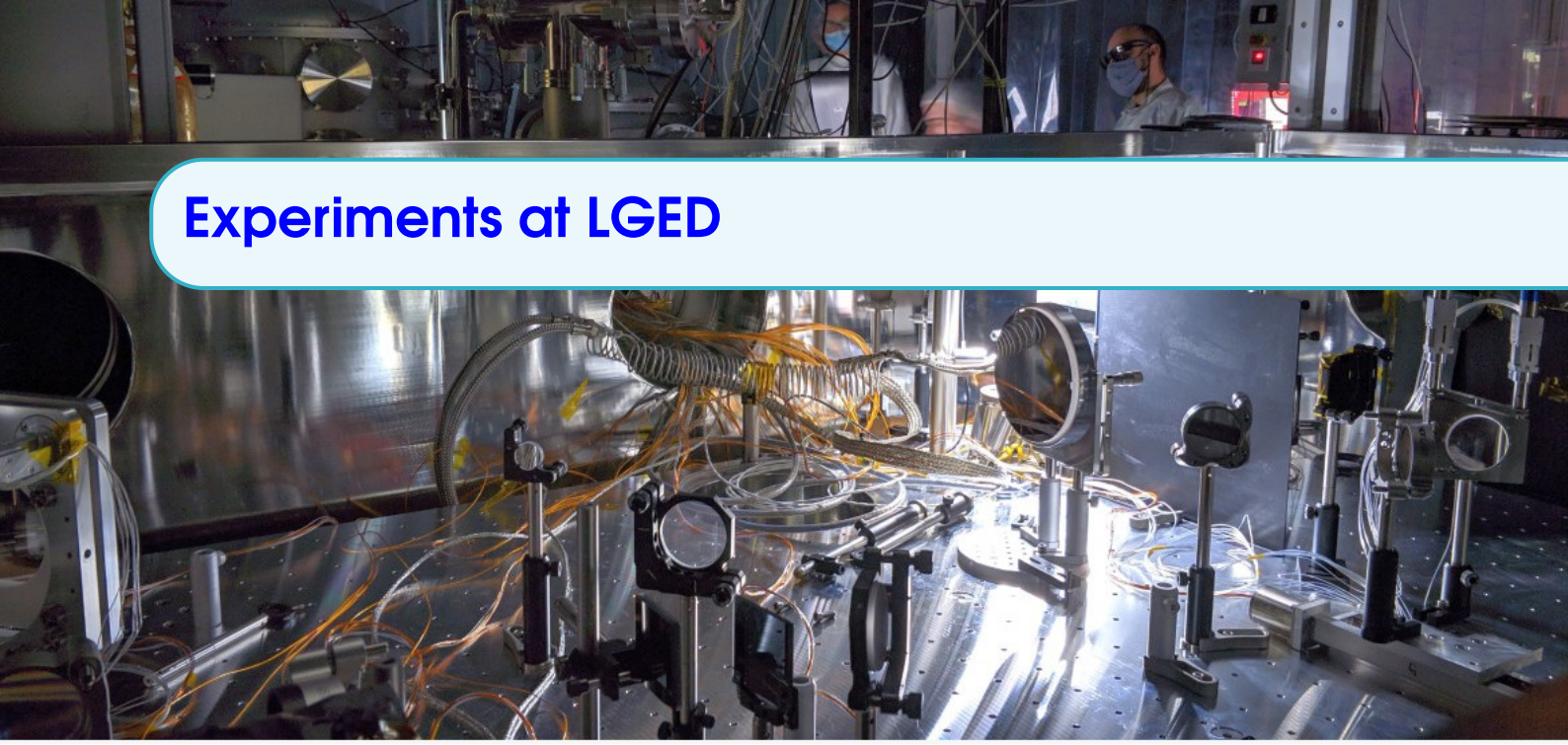

Experiments at LGED

5.1 Start-up of the commissioning experiments in the E4 area

Nakamiya Y.[1,2,*] , Tesileanu O.[1] , Rosu M. M.[1] , Rodrigues V. R. M.[1] , Neagu L.[1] , Chiochiu C.[1] , Tamlyn J.[1] , Cuciuc M.[1] , Ishibashi F.[2] , Kirita Y.[2] , Homma K.[2] , and Sakabe S.[3]

[1] Extreme Light Infrastructure (ELI-NP) & Horia Hulubei National Institute for R & D in Physics and Nuclear Engineering (IFIN-HH), Str. Reactorului No. 30, 077125 Bucharest–Măgurele, Romania
[2] Graduate School of Advanced Science and Engineering, Hiroshima University, Kagamiyama, Higashi-Hiroshima 739-8526, Japan
[3] Advanced Research Center for Beam Science, Institute for Chemical Research, Kyoto University, Gokasho, Uji, Kyoto 611-0011, Japan

[*] **yoshihide.nakamiya@eli-np.ro**

Abstract

The Technical Design Reports of the Extreme Light Infrastructure - Nuclear Physics (ELI-NP) included the one devoted to the Laser Gamma Experiments Department (LGED) [Hom+16], describing the proposed experiments to be performed during the commissioning phase of the facility in the E4 and E7 experimental areas. The E4 experimental area of ELI-NP has access to two 100 TW short-pulse laser beams, with a high repetition rate of 10 Hz. The integrated vacuum chamber system in E4 was installed and commissioned in 2019, and in 2020 ramp-up, "early-experiments" took place. In January 2021, the setup installation for the commissioning experiments had started. The high-sensitivity experiment proposed for the commissioning phase of E4 aims for searching dark-matter candidate particles in the low-mass, below-eV region. This paper describes the current implementation and commissioning of the experimental setups and subsystems built in the E4 area and the first results obtained in this endeavour.

5.1.1 Introduction

The search for axion-like particles, possibly constituents of the dark matter in the Universe, is now technically feasible at the high power laser facilities due to the high concentration of photons overcoming the seemingly extremely low probability of the photon-photon interactions.

As described in [Hom+21; HHT12; HKI21], the search for axion-like particles can be performed by overlapping two intense laser beams ("creating" and "inducing") with different wavelengths to probe nonlinearities of the photon-photon interaction in a vacuum. The focus geometry defines the energy range of the search. This type of search is encouraged by the fact that we have two examples, at 100 MeV (neutral pion) and 100 GeV (Higgs) energy scales, at which coupling to two photons is possible so that the scenario could also be encountered in other energy ranges [Hom14].

The experiment has been proposed in the ELI-NP Whitebook for the 100 TW and 1 PW laser pulse power levels, starting at the 100 TW beam due to the higher repetition rate and smaller optical elements for the tuning of the detection system.

Indeed, the main aims of the commissioning experiments of this new research facility are two-fold: to ramp up the equipment and operation of the high-power laser system and generate scientifically sound results to demonstrate the facility's capacity to deliver high-impact science. Knowing this, it comes then as natural the fact that for the lowest power output of the ELI-NP laser system (100 TW), for which the fastest (and easiest) ramp-up was expected. Therefore, we chose a complex, potentially high-impact experiment for the commissioning phase.

The experimental team of LGED began installing the setup in January 2021 and, throughout the year, focused on preparing and performing three beam-time sessions and analyzing the resulting data. In the following sections, we will present the experimental activities and some preliminary results and lessons learned from the performance of the commissioning experiment.

5.1.2 Installation and Commissioning of The Experimental Setup

The missions of commissioning experiments are not only to carry out the proposed scientific program of axion-like particle search but also to construct the fundamental infrastructure and the subsystems of the experiment with its functionality, linking with ramping up the High-Power Laser System (HPLS).

In this section, the installation works' achievements and the experimental setups' commissioning

results are shown step-by-step.

5.1.2.1 Preparation of the Experimental Area

All experimental areas of ELI-NP, including the E4 experimental area under discussion here, are designed to cope with experiments in which high dose rate radiations are produced, hence the requirement that they are at a pressure below the pressure of the external environment (in order to collect to a controlled exhaust the potentially activated air). Therefore, the experimental areas are not cleanrooms themselves, but there are locally installed soft- or hard-wall cleanrooms where the optics requests high cleanliness conditions. In E4 there is a soft-wall cleanroom, covering most of the vacuum chamber system and the three optical tables used in the commissioning experiment.

Measurements have been performed with a particle detector prior to and during the beamtime sessions, to evaluate the cleanliness of the area. The average results place the cleanroom environment in E4 between ISO 6 and ISO 7 classes, according to ISO 14644-1, which was considered adequate for the experiments.

Before installing the optical setup in the vacuum interaction chamber, the mass spectrum of the residual gas under vacuum conditions was also measured. The results in Figure 5.1.1 show one dominant peak corresponding to water molecules (which is mitigated by venting with dry nitrogen and longer pump-down sessions) and components of the atmosphere (CO_2, N_2) and alcohol (traces from the cleaning process of the chamber). As a result, the chamber was found to be relatively free of contaminants, and the optical setup installation could proceed.

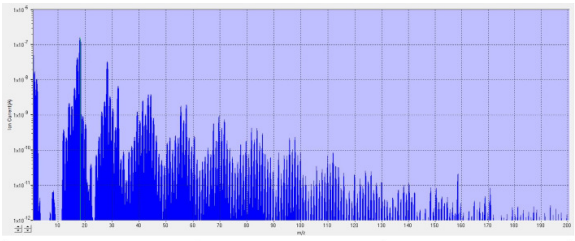

Dominant Peaks (AMU) above 1E-9 A	Intensity (Amps)	Fragment / Possible origin
2	8.13E-9	H2+ / H2, He++ / He
18.15	1.63E-7	H2O+ / H2O
28.2	3.28E-8	N2+ / N2, CO+ / CO2, C2H5 / CxHy
32	6.53E-9	O2+ / O2
44	3.84E-9	CO2+ / CO2 N2O+ / N2O C2H4OH+ / C2H5OH – alcohol C3H8+ / C3H8 - propane

Figure 5.1.1: *Results of the RGA measurement of the residual gas in the VE1 vacuum chamber. The vertical axis in the top figure is ion current (A) and the horizontal axis shows the mass-to-charge ratio m/z.*

In order to avoid contamination, after completing the installation and tuning work in VE1, before closing the lid of the chamber, the optical table inside, the internal walls, and the lid sealing were carefully cleaned with alcohol.

5.1.2.2 Installation of the Optical Setup

The commissioning experiment requires two pulsed laser beams with different wavelengths overlapping in space and time at a focus. Therefore one needs a signal light with different wavelengths from the lasers. Such a process is regarded as the four-wave mixing (FWM) phenomena [But65] on the vacuum target. The High Power Laser System (HPLS) of ELI-NP is based on Ti:Sapphire lasers, with the central wavelength of 810 nm and the pulse duration of 22 fs at optimal compression. In addition to HLPS laser, Nd:YAG laser with the central wavelength of 1064 nm and the pulse duration of the order of 10 ns was prepared for this experiment as "inducing" light for FWM process. Therefore, the optical setups in the interaction chamber should be dedicated to combining the two lasers and separating the FWM signal light from the others, as shown in Figure 5.1.2.

The Nd:YAG laser and He:Ne Continuous-Wave (CW) one were installed in upstream of the optical system. Both lasers are placed on the big optical table beside the interaction chamber, as shown in Figure 5.1.3. The Nd:TAG laser enables to delivery up to 500 mJ of pulse energy. The He:Ne CW laser is used for the alignment of optics in the interaction chamber, in particular for coarse alignment of Off-Axis Parabolic mirror (OAP) to minimize the astigmatism OAP itself potentially produces.

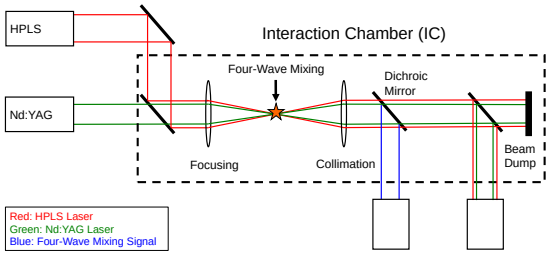

Figure 5.1.2: *Conceptual drawings of the experimental setup.*

The optical setup for four-wave mixing and focusing of the lasers was built in the interaction chamber VE1, which is seen behind the big optical table in the photograph. The optical components for Laser Diagnostics (LD) are shown in the left side of the interaction chamber VE1 in Figure 5.1.3. In addition, shot-by-shot far-field monitoring devices were

built on this table. The optics for signal detection were placed over the other big vacuum chamber VE2, which takes on a gray-coloured jacket for the vacuum bakeout.

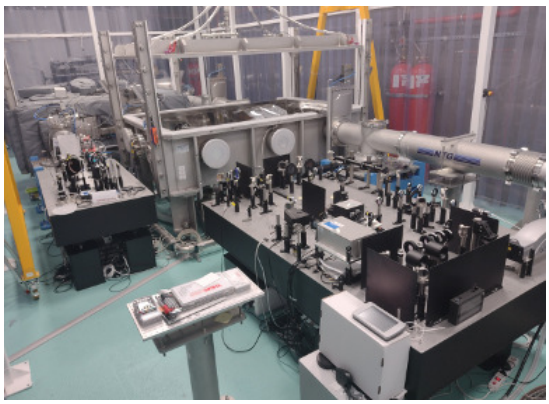

Figure 5.1.3: *The optical setups in the E4 experimental area.*

5.1.2.3 Implementation of Motor Control System

The commissioning experiment requires systematic measurement of the four-wave mixing generation in a wide range of parameter regimes such as vacuum pressure, laser energy, etc. These requirements increase the demands of automation to adjust the mirror orientation with remote control and switch the optical path to pick up the laser for calibration without breaking the vacuum inside the interaction chamber.

Figure 5.1.4 shows a typical configuration in the air side (left) and vacuum side (right) for motor control. 34 motorized linear and rotational motion stages obtained from Standa Ltd were prepared and configured for remote operation using four Ethernet-based 12-axes motor controllers and two DN250 CF-F electrical feedthroughs. Eight-core stranded copper wire cables were used for the air-side connections, and special Kapton-insulated wiring was completed for use in the interaction chamber VE1. Each air-side eight-core cable was prepared with the insulation stripped back 8 cm, shielding stripped, stranded core wires insulation stripped back 3 mm, IPA cleaned, exposed strands twisted, one end tinned, and the other end crimped. The cable connection was completed with one end soldered onto an HDB15M connector with appropriate shrink tubing and the crimp side into a bayonet-style DIN-19 connector of MIL-C-26482 series. Each Kapton-insulated wire was stripped back 3 mm, IPA cleaned and crimped into a vacuum side DIN-19 connector. Any loose wiring was wrapped in Teflon tape at steady separations to avoid accidents in the chamber during alignment.

A pin reassignment based on the technical configurations of the stepper or DC motors of the linear translation stages and mirror mounts respectively was completed to support up to two motors on one DIN-19 connector wherever possible. In addition, a standard pin assignment was prepared, merging the operating parameters so that the air-side cables could be easily used interchangeably between stages. Each stage was monitored for precision, accuracy, temperature fluctuations in addition to its general operating parameters before and after rewiring it from its company-provided test connectors. In addition, the new connectors, wires, and stages were IPA cleaned to minimize contamination from debris and oils from exposure during the preparation and mounting process. This ensured optimal operation of the chamber at designed vacuum levels. Once all the stages and mounts were inserted in VE1 and connected through the electrical feedthrough, the absolute positions, speeds, and translation limits were configured as per experimental needs.

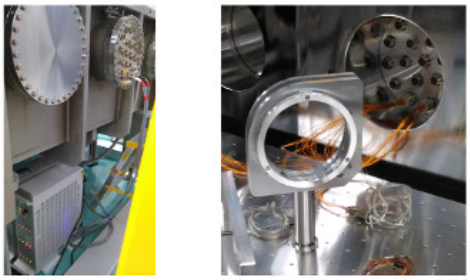

Figure 5.1.4: *(Left) Configuration in the airside. A cable connection was made from the motor controller placed under the interaction chamber to the feedthroughs attached to the chamber. (Right) Configuration in the vacuum side. Vacuum compatible Kapton-insulated wires are connected to the motorized actuator on the mirror mount.*

5.1.2.4 Implementation of Data Acquisition System

The commissioning experiment requires timing synchronization between HPLS laser and Nd:YAG laser with good timing jitter below 1 ns. Therefore, the timing and trigger control system was configured to fulfill these requirements. Figure 5.1.5 shows the block diagram of the trigger system configured in the E4 area. The trigger signal is delivered at 10 Hz *via* optical fiber cable not to distort the pulse shape of the trigger signal with keeping the original good timing jitter even after transmitting the signal at the distance of 100 m from HPLS to the E4 area. The trigger signal is converted into TTL signal via FO-to-TTL converter at the E4 area. The TTL signal is input in the DG645 digital delay generator obtained

from Stanford Research System. It has a rubidium Timebase to keep timing jitter below 1 ns in the wide range of timing delay change on demands of the experimental setup. A Trigger Orchestrator makes further provision of TTL signal (TO) built in-house. A TO was installed to provide an excellent variety of trigger patterns, particularly for periodically taking the noise that emerged in the 10 Hz signal of the data acquisition. The outputs from the TO are branched into two lines. One is used to operate the Nd:YAG laser. Relative timing delay between flash-lamp timing (Lamp) and Q-Switch timing is optimized via the 2nd DG645 timing module (DG645 No.2) to maximize the output energy of a laser pulse. The other one is used as the trigger signal in taking the data for any TTL-based detection devices. In addition to the aforementioned functions, single-shot or low-repetition shots of HPLS laser can also be selected if of need. The delay generator just after FO-to-TTL converter can operate mechanical shutter upstream of HPLS as well as connect to the 1st DG645 (DG645 No.1).

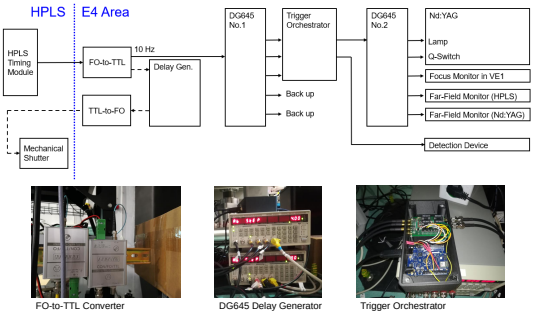

Figure 5.1.5: *The block diagram for timing control and trigger signal provision with the photographs for key modules.*

The local data network in the experimental area is connected to the institute's 10 Gbps network via a gateway workstation for secure access from the Users Room. When the energy of the laser pulses is above 25 mJ, or when material targets are used in the experiments (hence ionizing radiation could be produced), the personnel has to operate the equipment remotely (from the Users Room) when pulses are delivered.

The local network in E4 is split into two blocks connected via optical fiber at 10 Gbps: a block served by a high speed, 10 Gbps, PoE-capable Ethernet switch, dedicated to equipment such as the CMOS cameras running at the laser repetition rate (10 Hz) and the related data acquisition workstations, and a block connected to a 1 Gbps switch for the equipment that does not have large data throughput (such as motor controllers, oscilloscopes *etc.*). However, these two blocks are a single logical network, ensuring easy data transfer between the DAQ computers in the area. In addition, some equipment (such as the surveillance cameras) in the area can also be connected directly to the institute's network (outside the local protected network) via a dedicated switch.

The data acquired during the day on the DAQ computers in the experimental area is automatically copied overnight to network-attached storage (NAS) in a RAID configuration for data protection located outside E4.

5.1.3 Results of the First Beamtime Sessions

Three beamtime sessions took place in 2021 in the E4 experimental area. The aims of these sessions were to install, properly align and ramp up the experimental setup and advance the understanding of the background signals. After understanding and controlling the background signals and sources at a certain energy level of the laser pulses, one can proceed to the next step in energy. During the sessions in 2021, we have increased the energy of the laser pulses up to ∼20 mJ for each of the HPLS and Nd:YAG pulses.

The characterization and understanding of the background sources is closely related to the appropriate knowledge of the laser pulse characteristics. Therefore, we have devoted special attention to these aspects (some results are described in 5.1.3.1). Also, the vacuum control, described in subsection 5.1.3.2, is essential to understand the background signal generated from the atomic processes in the residual gas. The measurement of the four-wave mixing signals in the air (i.e., at atmospheric pressure) allowed us to verify the adequate timing synchronization of the geometrically overlapped laser pulses in space.

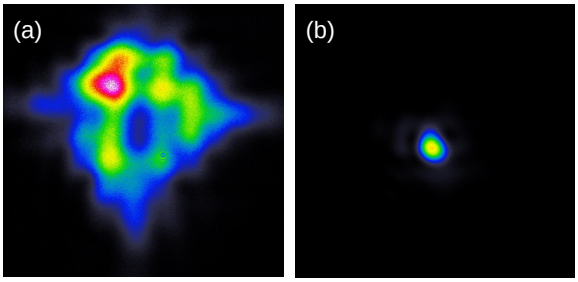

Figure 5.1.6: *(a) The laser beam profile at focus before optimizing deformable mirror configuration. (b) The laser beam profile at focus before optimizing deformable mirror configuration.*

5.1.3.1 Laser Pulse Characteristics

The optimization of the focusing of HPLS laser is one of the challenging issues to control data quality. The first adjustment was performed to minimize the aberration of the off-axis parabolic mirror (OAP). The adjustment of OAP orientation to get good focusing was carried out by 5 axes motorized actuators and stages, that is, yaw, pitch, x, y, and z-translation. He:Ne CW laser was used for the first adjustment. He:Ne laser has the beam diameter of ~ 27 mm at e^{-2} after two-step beam expansion from the laser head. The description of the first adjustment with He:Ne laser is given in Section 5. After installing OAP inside the vacuum chamber, the fine-tuning was also carried out using the same He:Ne laser. At this stage, the aberration of OAP was minimized as long as the angle of incidence of the laser into the OAP was correctly set.

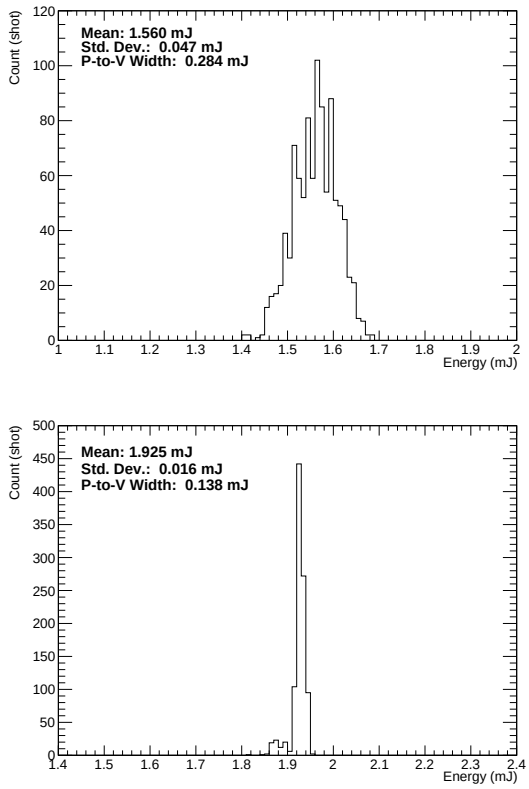

Figure 5.1.7: *(Top) Histogram of the laser pulse energy with 1000 laser shots statistics for HPLS laser. (Bottom) Histogram of the laser pulse energy with 1000 laser shots statistics for Nd:YAG laser.*

The second adjustment of the beam profile at the focus was carried out using a deformable mirror built in the HPLS area. The focusing properties of HPLS laser with initial settings were not perfect for focusing the laser beam on the target in the experimental area since long propagation distance from HPLS to the E4 area has difficulties of relaying the similar image on the deformable mirror to the target point. So we fine-tuned the deformable mirror configuration to be safe enough not to damage the pulse compressor and to get the best-effort focusing quality on the target. As a result, astigmatism shown in (a) of Figure 5.1.6 was minimized, and a well-focused beam profile was seen after its adjustment as shown in (b) of Figure 5.1.6.

Laser energies were measured just before the OAP for focusing. Figure 5.1.7 shows the histogram of the laser pulse energy with 1000 laser shots statistics. Energy stability of HPLS and Nd:YAG laser were 3.2% and 0.8% as standard deviation, respectively.

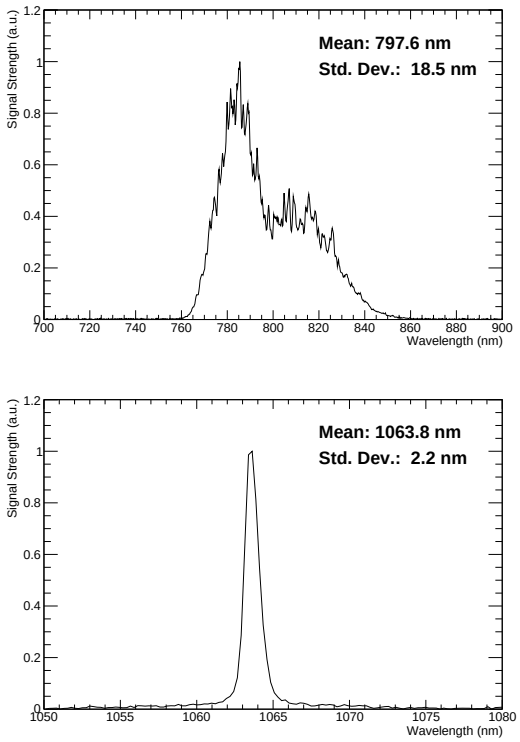

Figure 5.1.8: *(Top) Spectrum of HPLS laser averaged over 100 laser shots. (Bottom) Spectrum of Nd:YAG laser averaged over 100 laser shots.*

Spectra of the lasers were also measured inside the interaction chamber VE1. The results are shown in Figure 5.1.8. The bandwidth of HPLS and Nd:YAG laser were $797.6\,\text{nm} \pm 18.5\,\text{nm}$ and $1063.8\,\text{nm} \pm 2.2\,\text{nm}$, respectively.

5.1.3.2 Vacuum Control

Controlling and monitoring vacuum is critical to characterize the background four-wave mixing generation from the residual gas in the interaction chamber. In particular, tracking the change of vacuum pressure is important to evaluate background level precisely and suppress systematic uncertainties of the background

yield in the measurements for a long time.

The vacuum controlling and monitoring system is based on a Programmable Logic Controller (PLC) system. PLC system logs the system parameters such as vacuum pressures, valve position, pump parameters *etc.* with a frequency of up to 1 Hz. The PLC sinks itself every 15 min with a Stratum2 Network Time Protocol (NTP) server to ensure better than 20 msec timestamp accuracy. All the mission-critical data generated by the system is stored locally on an industrial Single Level Cell (SLC) Flash and is backed up daily on three other remote locations (solid-state media and RAID6 array). The actions on the system are documented on an ELOG Electronic Logbook server.

The vacuum pressure level control was carried out using a manually actuated needle valve placed on the lid of the interaction chamber VE1. Figure 5.1.9 shows the stability of vacuum pressure as a consequence of vacuum control via needle valves. The plateau region of vacuum pressure indicates that accurate and stable vacuum pressure was produced over the vacuum pressure range from 3×10^{-7} mbar and 5×10^{-3} mbar3×10^{-7} mbar.

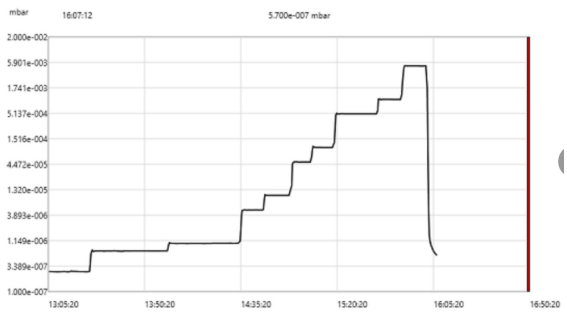

Figure 5.1.9: *Vacuum pressure as a function of time. The flat region of vacuum pressure is made at the wide range of vacuum pressures between* 3×10^{-7} mbar *and* 5×10^{-3} mbar.

The measurements were done up to the maximum pressure allowed in VE1 before the interlock on the pressure gauges on the beam transport system would automatically close the gate valves to the pulse compressor, stopping the beam. This maximum pressure attained was 5×10^{-3} mbar. The interlocks on the beam transport system are set by the Laser Systems Department team in such a way as to ensure low enough pressure in the pulse compressor, to avoid exposing the optics inside too long to air and contaminants, and to minimize the probability of occurrence of damage.

5.1.3.3 Four-wave Mixing in the Air

After optimizing the HPLS laser's focusing, the alignment of Nd:YAG laser was also optimized to overlap spatially with the HPLS laser not only at the focus but also before the OAP. Timing synchronization was carried out by a timing control device which is explained in Section 5.1.2.4.

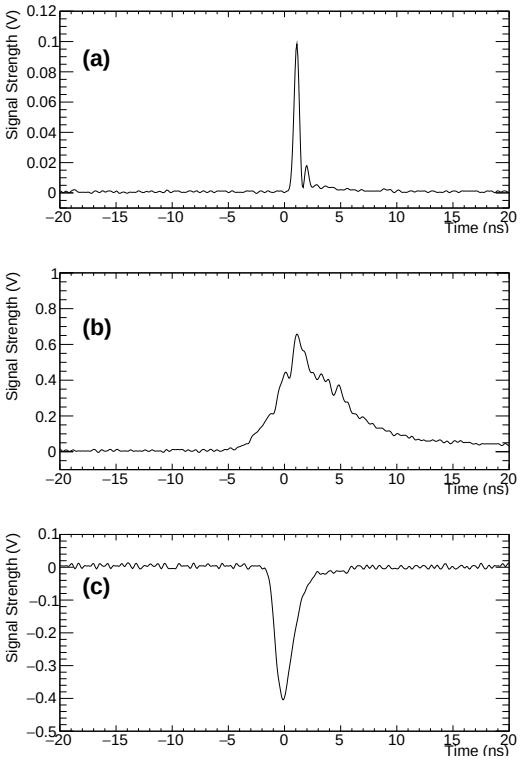

Figure 5.1.10: *(a) Raw signal of HPLS laser measured by Si photodiode in the Laser Diagnostics. (b) Raw Signal of Nd:YAG laser measured by InGaAs photodiode in the Laser Diagnostic. (c) Four-wave mixing signal measured by photomultiplier tubes in Signal Detection. The four-wave mixing signal was observed at atmospheric pressure with spatio-temporal overlaps of two lasers.*

Figure 5.1.10 (a) and (b) show the raw waveform signals measured by photodiodes, which were placed in Laser Diagnostics. The timing of both lasers was synchronized with 1 ns accuracy. Figure 5.1.10 (c) shows the four-wave mixing signal coming from the interaction points. The stacks of dichroic mirrors and short pass filters reject the residual laser lights, and the signal lights below 700 nm are selected. In addition, the signal detection device was covered by the black curtain to avoid any of off-axis scattering background lights. Figure 5.1.10 strongly indicates that the performance of our experimental system, with its optimized control process for good spatio-temporal overlap, fits well into its design.

5.1.4 Conclusion

Installation and commissioning of the experimental infrastructure and subsystems in E4 were started through the commissioning experiment in 2021. The experimental setups and functions were optimized for the experiment of axion-like particle search, in particular, dedicated to achieving and monitoring spatio-temporal overlap efficiently and systematically.

In order to calibrate the experimental systems and characterize the initial condition of the interaction, the basic characteristics of HPLS laser pulses were measured. A step-by-step tuning process finely adjusted the profile at the focus for OAP and HPLS laser beams. The performance of the stability of vacuum control was also demonstrated in the vacuum pressure range from 3×10^{-7} mbar to 5×10^{-3} mbar. As a consequence of the completion of installation and calibration, four-wave mixing signal generation was obtained at atmospheric pressure in the interaction between the lasers and the atoms inside the interaction chamber when we achieved spatio-temporal overlap between HPLS laser and Nd:YAG laser at focus and separate the four-wave mixing light from the residual lasers. The result shows that all the subsystems in the experimental setup were functional and controlled.

The experiments for the search for axion-like particles via photon-photon interactions will continue at ELI-NP in the E4 area in the first part of 2022, with two more commissioning beamtime sessions. Then the SAPPHIRES collaboration intends to apply for beamtime to continue the experiments in the user-facility mode of operation of ELI-NP.

The path foreseen now for the increase of sensitivity and signal to noise ratio includes several future steps to be implemented, among which one could mention: upgrades of the optical setup to mitigate the four-wave mixing background generated by the optical elements; Nd:YAG laser with improved performance (higher energy/pulse and Single Longitudinal Mode); moving the focusing setup to the UHV interaction chamber VE2 and increasing the vacuum level locally around the focus with differential pumping; switching to an ultrashort pulse laser instead of the Nd:YAG for the inducing beam.

5.1.5 Acknowledgment

We wish to acknowledge the support of the Laser Systems Department personnel, who ensured a smooth operation of the High Power Laser System, accommodating all the requests from LGED. They always helped in the experimental area with beam diagnostics and alignment issues.

References

[But65] P. Butcher. *Nonlinear optical phenomena*. Athens, Ohio: Ohio University Press, 1965 (cited on page 240).

[Hom14] K. Homma. In: *Eur. Phys. J. Spec. Top* 223 (2014), page 1131. DOI: 10.1140/epjst/e2014-02164-4. URL: https://doi.org/10.1140/epjst/e2014-02164-4 (cited on page 239).

[Hom+16] K. Homma *et al.* In: *Rom. Rep. Phys.* 68 (2016), S233 (cited on page 239).

[Hom+21] K. Homma *et al.* In: *J. High Energ. Phys.* 12 (2021), page 108. DOI: 10.1007/JHEP12(2021)108. URL: https://doi.org/10.1007/JHEP12(2021)108 (cited on page 239).

[HHT12] K. Homma, D. Habs, and T. Tajima. In: *Appl. Phys. B* 106 (2012), page 229. DOI: 10.1007/s00340-011-4567-3. URL: https://doi.org/10.1007/s00340-011-4567-3 (cited on page 239).

[HKI21] K. Homma, Y. Kirita, and F. Ishibashi. In: *Universe* 7 (2021), page 479. DOI: 10.3390/universe7120479. URL: https://doi.org/10.3390/universe7120479 (cited on page 239).

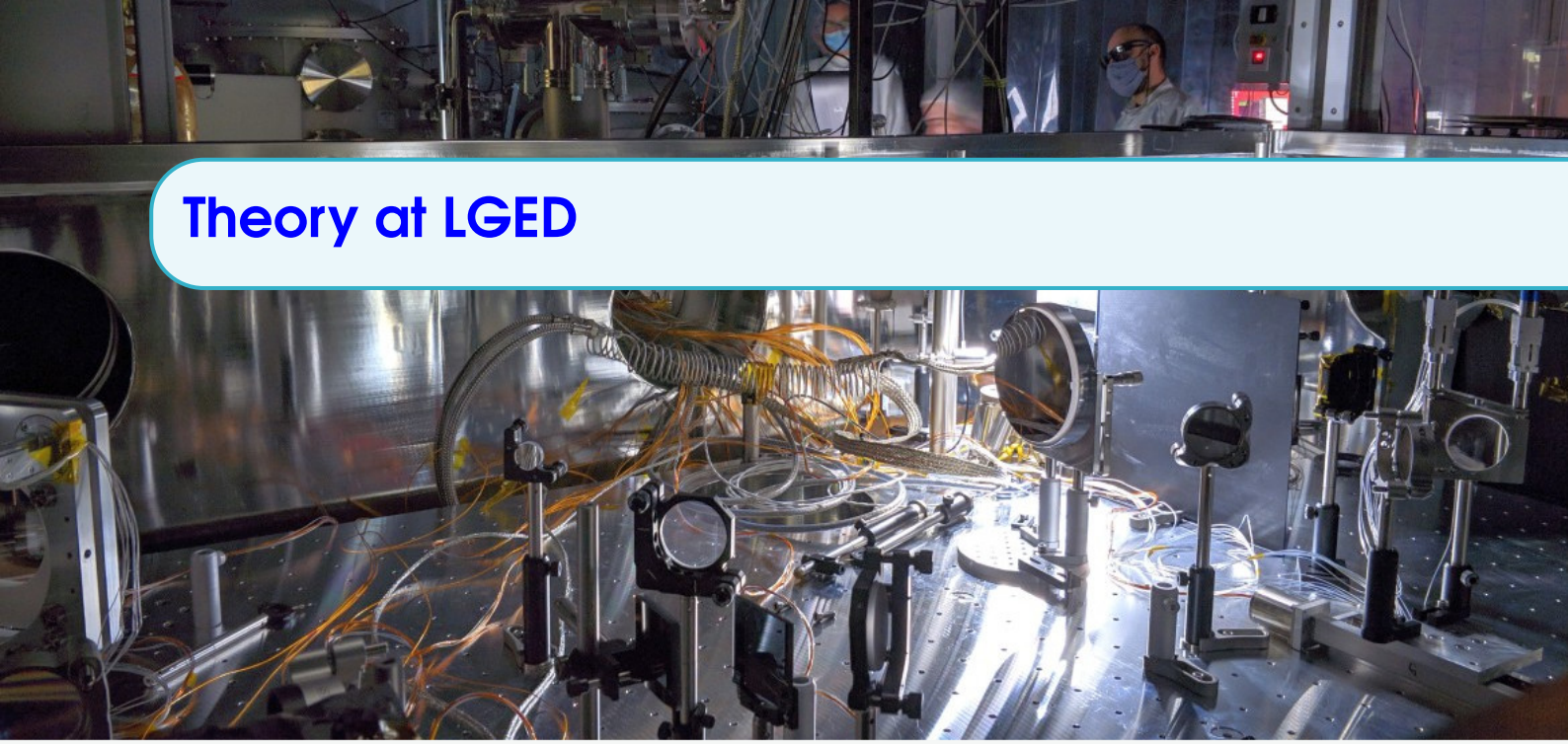

Theory at LGED

5.2 Stokes Phenomenon, pair production and Hawking radiation

Cesim D. K. [1,*]

[1] Extreme Light Infrastructure (ELI-NP) & Horia Hulubei National Institute for R & D in Physics and Nuclear Engineering (IFIN-HH), Str. Reactorului No. 30, 077125 Bucharest–Măgurele, Romania

[*] **cesim.dumlu@eli-np.ro**

Abstract

The following report gives a summary of the past and ongoing research. In [Dum20], we have looked into the Hawking radiation and its relation to the Stokes phenomenon that plays a central role in analogous phenomena such as the Schwinger mechanism. We have analyzed the semiclassical damping factor, otherwise known as the grey body factor, within the phase integral approach and found that the damping factor is controlled by the global parameters of the gravitational potential. In other words, the conformal cross-ratios. We also briefly mention the proposal submitted for the MP3 project on observing nonlinear Breit-Wheeler pair production. We conclude by outlining the ongoing research, mainly related to photon scattering and pulse shaping, which we believe will be relevant for the upcoming experiments.

5.2.1 Introduction

Briefly stated, Stokes phenomena encode the changes in the asymptotic form of a given function when analytically continued to a different region of the complex plane. A canonical example is the Airy function which reads:

$$\begin{aligned} \mathrm{Ai}(r) &\sim \frac{1}{2}\pi^{-\frac{1}{2}} r^{-\frac{1}{4}} e^{-\frac{2}{3}r^{3/2}}, \quad \mathrm{Arg}(r) = 0 \\ \mathrm{Ai}(r) &\sim \frac{1}{2}\pi^{-\frac{1}{2}} r^{-\frac{1}{4}} (e^{-\frac{2}{3}r^{3/2}} + i e^{\frac{2}{3}r^{3/2}}), \\ & \frac{2\pi}{3} \leq \mathrm{Arg}(r) \leq \frac{4\pi}{3} \end{aligned} \tag{5.2.1}$$

As seen above, the Airy function displays damping behavior as $r \to \infty$, whereas it becomes completely oscillatory for negative values of r, with two components having phases of opposite signs. Asymptotic expansions of such functions and integrals play a central role in QED processes that take place in the field of a plane-wave [NR64; NR67], in the Schwinger effect[DD10; Sch51] and in quantum mechanical scattering problems in general. In [Dum20] we have studied the Hawking radiation, a closely related to the phenomenon of the Schwinger effect, in which a black hole emits particles, and these particles are seen as the radiation by an observer situated far away from a black hole. The motivation behind this study is twofold. In the prominent work, [DR76], the analytic continuation of the modes was performed without using the collapsed geometry of Hawking in order to explain the tunneling effect. But in doing so, negative norm states were employed. In our approach, we performed the analytic continuation without invoking negative norm states, but more importantly, we have also shown why Stoke's phenomenon is relevant. The second motivation pertains to the greybody factors, responsible for the damping of the emission reaching out to the asymptotic observers. In another prominent analysis, [MS97], the greybody factors were calculated using an asymptotic matching procedure. In this procedure, one locally expands the gravitational potential in the regions near and far to the event horizon and searches for *local* solutions. The greybody factor can be found once the asymptotic expansions of near and far region solutions are matched in an appropriately chosen matching region. This approach is *local* in the sense that it approximates the form of gravitational potential depending on the distance with respect to the horizon. In our approach, no local expansion on the scattering potential is made, it is treated exactly, but because WKB solutions are used, the greybody factors' accuracy is somewhat limited compared to the asymptotic matching method. The upside of our approach is that because gravitational potential is treated exactly, the greybody factor given by the semiclassical action reveals an interesting analytic structure that depends on what might be called the *global* features of the scattering potential, such as the cross-ratios. We have found out that the greybody factor is controlled by three independent cross-ratios formed by the zeroes and poles of the gravitational potential.

5.2.1.1 MP3 project and proposals

Along with a few members from the LGED group, the author has joined working groups formed under the MP3 project. One of this project's main goals is to establish collaborative, multi-disciplinary

workgroups to address the "science questions" related to the development of a multi-petawatt facility at Rochester University and the areas of theoretical/experimental interest. In this respect, the author has prepared and submitted an experimental proposal on the observation of nonlinear Breit-Wheeler pair production. The primary incentive behind this proposal is to study the pair production phenomenon in a regime which have not been probed before. In this regime, the theoretical predictions point to a different scaling behavior of the pair production probability than the regime which was probed in the famous SLAC-E144 experiment performed almost three decades ago [Bur+97]. To elaborate, for the SLAC parameters, the pair production probability roughly scales as:

$$W \sim \eta^{2n_0} \tag{5.2.2}$$

Where $\eta = eE_0/m\omega_0 c$ is, the dimensionless intensity parameter, and n_0 denotes the number of absorbed low energy photons. Remarkably, this scaling behavior was indeed confirmed by the measurements performed at different intensities. The advent of ultra-intense lasers opened up the possibility to explore pair production in a new regime where the number of absorbed photons gets large *i.e.* $\eta \gg 1$. In this regime, the laser pulse, up to a good approximation, can be treated as a constantly crossed field[Elk+11]. The corresponding pair production rate is approximate:

$$W \approx \frac{3}{16}\sqrt{\frac{3}{2}}\frac{\alpha m^2 c^4}{\hbar^2 \omega_\gamma}\rho_\gamma \chi\, e^{-\frac{8}{3\chi}}, \quad \chi = \frac{2\hbar\omega_\gamma}{mc^2}\frac{E_0}{E_s}, \chi \ll 1 \tag{5.2.3}$$

Here, ρ_γ and ω_γ are respectively the density and energy of gamma photons, α is the fine-structure constant, and E_s is the critical field strength, otherwise known as the Schwinger field. The above formula shows that χ plays the role of scaling parameter in the intense field regime, and it shows exponential sensitivity to both gamma photon energy and the peak field strength.

The envisaged setup involves a two-step process. In the first step, gamma rays are generated via nonlinear Compton scattering in which GeV scale electron beam has collided against a secondary petawatt class laser. Subsequently, these gamma rays travel through the focal spot of the primary, multi-petawatt laser, which would provide seed photons to overcome the pair production threshold energy. Overall, there are vast technical challenges involved in this project; the intensity measurement, the beam diagnostics, producing higher density electron beams, to name a few, will push the field further into the innovation zone. Tailoring optical pulses at such intensities and producing high brilliance gamma beams will be tremendous technical achievements in their own right. Furthermore, a successful collision between the two beams requires extremely accurate and precise synchronization. Overcoming such an obstacle is a formidable task, but once it is accomplished, a similar collision setup can be used for measuring the birefringent property of QED vacuum, which still remains to be verified in the laboratory. For more details on the proposed experiments and the project, we refer the reader to [Zue21].

5.2.2 Ongoing Research

The author has been working in close collaboration with several LGED members on the issue of realistic pulse shaping. The state-of-the-art calculations for intense field QED processes generically use beam profiles which are plane wave or Gaussian and, in some cases, the higher mode extensions of Gaussian beam *i.e.* Hermite-Gauss or Laguerre-Gauss beams. Compared to a pure plane wave, a Gaussian beam is considered realistic, but this notion becomes questionable when the inner workings of a high-power laser system (HPLS) are considered. This especially becomes relevant when strong focusing effects come into effect, rendering paraxial approximation made in the derivation of the Gaussian profile not so valid. In addition to the focusing effects, the Gaussian profile implies the spectral density of the pulse is also roughly Gaussian. But this may be considered as somewhat the idealized case, which may not accurately reflect the experimental conditions, because the mode distribution under ideal conditions can take flat-top or super-Gaussian forms rather than a Gaussian. From the theoretical perspective, the main objective of this ongoing effort is to account for such subtleties in pulse shaping and study its effects on the relevant QED processes.

Another ongoing effort is related to induced/stimulated photon scattering in intense, focused beams. The scattering of photons in a vacuum is purely a quantum effect. Recently, indirect evidence for this phenomenon was reported by ATLAS collaboration[Aad+19], yet on the other hand, direct evidence that would come from a direct collision between a pair of photon beams is still lacking. This is because the scattering cross-section for the process is extremely small. In order to attain a significant

signal level over the background, one in principle needs ultra-brilliant and extremely energetic gamma beams whose production and control appear to be out of reach with the currently available technology. During the mid 1960's and 1970's however, several authors realized the number of scattered photons could be enhanced in a laser background [AA66; Dew74; MP63]. The enhancement factor for the scattering is proportional to the number of scattering centers which roughly scales with the number of quanta in the laser pulse. The observation of such a process, which is sometimes dubbed stimulated/induced photon scattering, could be within reach in the near future as the progress in the development of HPLS continues. Based on induced scattering, the author has initiated a project in which the collision between two Laguerre-Gauss beams is considered. The primary motivation for this study has come from a recent work[Abo+19], in which the authors argue that the orbital angular momentum modes of the light could increase the signal-to-noise ratio in an appropriately chosen collision geometry.

References

[AA66] V. A.A. "Induced Scattering of Light by Light". In: *Sov. Phys. JETP* 23 (1966), page 681. URL: http://www.jetp.ras.ru/cgi-bin/dn/e_023_04_0681.pdf (cited on page 251).

[Aad+19] G. Aad *et al.* "Observation of Light-by-Light Scattering in Ultraperipheral Pb + Pb Collisions with the ATLAS Detector". In: *Phys. Rev. Lett.* 123 (5 July 2019), page 052001. DOI: 10.1103/PhysRevLett.123.052001. URL: https://link.aps.org/doi/10.1103/PhysRevLett.123.052001 (cited on page 250).

[Abo+19] R. Aboushelbaya *et al.* "Orbital Angular Momentum Coupling in Elastic Photon-Photon Scattering". In: *Phys. Rev. Lett.* 123 (11 Sept. 2019), page 113604. DOI: 10.1103/PhysRevLett.123.113604. URL: https://link.aps.org/doi/10.1103/PhysRevLett.123.113604 (cited on page 251).

[Bur+97] D. L. Burke *et al.* "Positron Production in Multiphoton Light-by-Light Scattering". In: *Phys. Rev. Lett.* 79 (9 Sept. 1997), pages 1626–1629. DOI: 10.1103/PhysRevLett.79.1626. URL: https://link.aps.org/doi/10.1103/PhysRevLett.79.1626 (cited on page 250).

[DR76] T. Damour and R. Ruffini. "Black-hole evaporation in the Klein-Sauter-Heisenberg-Euler formalism". In: *Phys. Rev. D* 14 (2 July 1976), pages 332–334. DOI: 10.1103/PhysRevD.14.332. URL: https://link.aps.org/doi/10.1103/PhysRevD.14.332 (cited on page 249).

[Dew74] R. L. Dewar. "Induced scattering of light by light in a vacuum". In: *Phys. Rev. A* 10 (6 Dec. 1974), pages 2107–2111. DOI: 10.1103/PhysRevA.10.2107. URL: https://link.aps.org/doi/10.1103/PhysRevA.10.2107 (cited on page 251).

[Dum20] C. K. Dumlu. "Stokes phenomenon and Hawking radiation". In: *Phys. Rev. D* 102 (12 Dec. 2020), page 125006. DOI: 10.1103/PhysRevD.102.125006. URL: https://link.aps.org/doi/10.1103/PhysRevD.102.125006 (cited on page 249).

[DD10] C. K. Dumlu and G. V. Dunne. "Stokes Phenomenon and Schwinger Vacuum Pair Production in Time-Dependent Laser Pulses". In: *Phys. Rev. Lett.* 104 (25 June 2010), page 250402. DOI: 10.1103/PhysRevLett.104.250402. URL: https://link.aps.org/doi/10.1103/PhysRevLett.104.250402 (cited on page 249).

[Elk+11] N. V. Elkina *et al.* "QED cascades induced by circularly polarized laser fields". In: *Phys. Rev. ST Accel. Beams* 14 (5 May 2011), page 054401. DOI: 10.1103/PhysRevSTAB.14.054401. URL: https://link.aps.org/doi/10.1103/PhysRevSTAB.14.054401 (cited on page 250).

[MS97] J. Maldacena and A. Strominger. "Universal low-energy dynamics for rotating black holes". In: *Phys. Rev. D* 56 (8 Oct. 1997), pages 4975–4983. DOI: 10.1103/PhysRevD.56.4975. URL: https://link.aps.org/doi/10.1103/PhysRevD.56.4975 (cited on page 249).

[MP63] J. Mckenna and P. M. Platzman. “Nonlinear Interaction of Light in a Vacuum”. In: *Phys. Rev.* 129 (5 Mar. 1963), pages 2354–2360. DOI: 10.1103/PhysRev.129.2354. URL: https://link.aps.org/doi/10.1103/PhysRev.129.2354 (cited on page 251).

[NR64] A. I. Nikishov and V. I. Ritus. “QUANTUM PROCESSES IN THE FIELD OF A PLANE ELECTROMAGNETIC WAVE AND IN A CONSTANT FIELD. PART I”. In: *Zh. Eksperim. i Teor. Fiz.* 19 (Feb. 1964), page 529. URL: https://www.osti.gov/biblio/4032026 (cited on page 249).

[NR67] A. I. Nikishov and V. I. Ritus. “Pair Production by a Photon and Photon Emission by an Electron in the Field of an Intense Electromagnetic Wave and in a Constant Field”. In: *Soviet Journal of Experimental and Theoretical Physics* 25 (Dec. 1967), page 1135 (cited on page 249).

[Sch51] J. Schwinger. “On Gauge Invariance and Vacuum Polarization”. In: *Phys. Rev.* 82 (5 June 1951), pages 664–679. DOI: 10.1103/PhysRev.82.664. URL: https://link.aps.org/doi/10.1103/PhysRev.82.664 (cited on page 249).

[Zue21] J. Zuegel. *For more information on the MP3 project and whitepapers follow:* https://www.lle.rochester.edu/index.php/2021/03/12/call-for-white-papers-multi-petawatt-physics-prioritization-mp3-workshop/. 2021. URL: https://www.lle.rochester.edu/index.php/2021/03/12/call-for-white-papers-multi-petawatt-physics-prioritization-mp3-workshop/ (cited on page 250).

5.3 Electron Transport in a nanowire irradiated by an intense laser pulse

Ong J. F.[1,*], Ghenuche P. V.[1] , and Tanaka K. A.[1]

[1] Extreme Light Infrastructure (ELI-NP) & Horia Hulubei National Institute for R & D in Physics and Nuclear Engineering (IFIN-HH), Str. Reactorului No. 30, 077125 Bucharest–Măgurele, Romania

[*] **jianfuh.ong@eli-np.ro**

Abstract

Electron transport in a nanowire exhibits a distinct behavior following intense laser pulse irradiation. We use a three-dimensional particle-in-cell simulation to observe a large-amplitude particle-driven Wakefield excitation followed by electron acceleration in the solid density. Besides, we observed the quiver of the electrons across the nanowire under the action of the surrounding laser electric field and facilitating deeper Wakefield propagation in the nanowire with more than two times energy gain over a flat target. These results open new insights into the laser-energy coupling with nanostructure targets. radiation sources, and motivate the Wakefield acceleration in solid density plasma.

5.3.1 Introduction

The laser-nanowire interaction has driven interest owing to its high laser energy absorption [Bar+17; Cao+10; Hab+16; Kah+08; Pur+13]. The laser energy conversion up to $\sim 71\%$ was recently demonstrated in the relativistic laser intensity regime ($\sim 10^{19}\,\mathrm{Wcm}^{-2}$) [Par+21]. This makes align nanowire array an outstanding X-ray and gamma-ray [Hol+17; Kul+00; MdG18; Mon+11; Nis+01; Ovc+11] source, and the application in nuclear photonic, enhanced ion acceleration [Bin+18], attosecond bunch generation [Ma+06; Nau+04], as well as efficient micro fusion [Bar+17; Cur+18; Kay+16]. Therefore, understanding the electron dynamics and transport in the nanostructure is fundamental for the control of these applications.

When the rising edge of the laser pulse approaches the nanowire, it first ionizes the electrons and strips them off in the direction of laser polarization. This forward current results in the return current on the nanowire surface due to the requirement of local charge neutrality. The return current then induces an azimuthal magnetic field surrounding the nanowire and pinches the nanowire radially inward, delivering $1000\times$ increases in electron density. The laser continues propagating between the wires until the plasma blowout fills the space. The electron dynamics in the nanowire that contributed to the high laser energy absorption have not been addressed in detail and demand further clarification. Therefore, it is critical to understand electron transport using numerical simulation with a high spatial and temporal resolution to identify the absorption dynamics.

In the following, we summarized the results obtained in [OGT21]. The 3D PIC simulations show that a Wakefield is excited by fast electron bunches generated at the tip of the nanowire. This Wakefield has an amplitude of the order of $\mathrm{TV\,m}^{-1}$, oscillating at the plasma frequency and propagating deep into the nanowire. The laser fields then brush up the side surfaces and swing the electron across the nanowire. These electrons assist the Wakefield to propagate deeper into the nanowire resulting in more than $2\times$ energy gain over a flat target.

5.3.2 Methods

The simulations were performed using three-dimensional (3D) PICONGPU [Bur+10]. The simulation box is discretized by $256 \times 4069 \times 256$ cells with the spatial resolution $\Delta x = \Delta z = 7.81$ nm, $\Delta y = 1.97$ nm, and a temporal resolution $\Delta t = 3.16$ as. Each cell consists of 10 macroparticles ion species. Field ionization and mobile ion are implemented, except collisional ionization. The 5^{th} order particle shape function and the current smoothing are used to suppress the numerical heating. The laser pulse is modeled as a linearly polarized plane wave with the central wavelength $\lambda_\mathrm{L} = 0.8$ μm and a peak intensity $I_0 = 10^{22}$ W cm^{-2} ($a_0 = 68$), simulating the conditions available at ELI-NP [Tan+20]. The laser is irradiated onto the nanowire at normal incidence. Here, $a_0 = eE_0/(mc\omega_\mathrm{L})$ is the normalized laser amplitude, where E_0 is the peak laser field strength, $\omega_\mathrm{L} = 2\pi/\lambda_\mathrm{L}$ is laser central frequency, and e and m being the charge and mass of electron. The laser temporal profile is $a(t) = a_0 \exp\left[-(t-t_0)^2/\tau_L^2\right]$ with $\tau_L = 13.2$ fs (22 fs FWHM), and $t_0 = 2\tau_L$. A carbon nanowire with length $L = 5$ μm and diameter

$d = 300$ nm is placed horizontally at the center of the simulation box. The carbon nanowire has a step-like profile with density 0.52 g cm^{-3} ($n_i = 15n_{\rm cr}$).

5.3.3 Results

The rising edge of the laser pulse first ionizes the carbon atoms at the surface of the nanowire. Then, the E_x component of the laser field strips off electrons and accelerates them forward by the B_z component as shown in Figure 5.3.1 (a). A return current is then generated on the surface of the nanowire to maintain the current quasi-neutrality, where the forward current is negative (blue), and the return current is positive (red), as shown in Figure 5.3.1 (d). In addition, the electron displacement from the plane of the nanowire tip ($y \leq 1$ μm) is observed. This is caused by the $\mathbf{J} \times \mathbf{B}$ heating [Kru03] due to the oscillating term of the ponderomotive force of the linearly polarized laser field incident normally on the target. A sinusoidal current inside the nanowire is generated soon after laser irradiation (see Figure 5.3.1 (d)). The electric field component E_y and the density perturbation $\delta n_e/n_0 = n_e/n_0 - 1$ are shown in Figure 5.3.1 (c). The constant $n_0 = 76n_{\rm cr}$ is the average electron density created by field ionization along the nanowire. However, the maximum density at the plane of the nanowire tip is $n_e = 2n_0 = 152n_{\rm cr}$ due to the compression caused by the laser radiation pressure. The nanowire is opaque to the laser field even under self-induced transparency and rules out the penetration of the laser field into the nanowire. In conjunction with the density, E_y has a peak of approximately 8 TV m^{-1}, which corresponds to $eE_y/(mc\omega_{\rm L}) \approx 2$. This nanoscale charge separation field is one order larger in magnitude and a thousand times smaller in scale than the one that a typical laser Wakefield acceleration can achieve in an underdense plasma. Further analysis of the current density spectrum gives a spike at plasma frequency $\omega_{\rm pe} = \omega_{\rm L}\sqrt{n_0/n_{\rm cr}} = 8.7\omega_{\rm L}$ as shown in Figure 5.3.1 (b).

The driving force for the Wakefield excitation is attributed to the electron bunches generated by the $\mathbf{J} \times \mathbf{B}$ heating at the nanowire tip. Typically, electron bunches generated in this way are separated by $0.5\lambda_{\rm L}$ interval or at $2\omega_{\rm L}$ frequency as evident in Figure 5.3.1 (c). They are accelerated into the nanowire with large forward momentum $p_y/(mc) \sim 30$. The longitudinal momentum of the bulk electrons shown in the inset of Figure 5.3.1(c) exhibits a wave-like structure. The peak-to-peak interval is the plasma wavelength $\lambda_{\rm p} = 2\pi v_{\rm p}/\omega_{\rm p} \approx 90$ nm, where $v_{\rm p} = 0.98c$ is the plasma wave phase velocity. Note that the phase space in Figure 5.3.1 (c) is restricted to $0.9\,\mu{\rm m} \leq x \leq 1.1\,\mu{\rm m}$, such that electrons in the transverse skin layer and those outside the nanowire are excluded.

To compare the electron energy gain inside the nanowire over a flat target, the electron energy spectra are taken at $t = 20$ fs are shown in Figure 5.3.1 (f). Beyond this point, the nanoscale Z pinch begins and leads to the collapsing of the Wakefield. The electron energy spectrum is recorded up to this point to minimize the effects of pinching and as well ion response to the Wakefield. For a fair comparison, the energy spectra are restricted to $0.9\,\mu{\rm m} \leq x \leq 1.1\,\mu{\rm m}$ in nanowire and flat target. One would have overestimated the energy gain if all the electrons in the simulation were taken into account. The energy spectra show a similar enhancement to the measurements reported in [Hab+16; Mor+19]. Generally, the nanowire overcomes the flat target more than $3\times$ in electron energy gain, which remains at a reasonable value compared to the 2D simulation presented in [OGT21]. This is because the amplitude of the Wakefield attenuates with distance into the target due to the velocity dispersion of the $2\omega_{\rm L}$ bunches and the interaction with the wake induced within the bunch itself [Esa+96]. However, in the nanowire, the energetic entering electrons act as a drive bunch, continuously exciting the Wakefield during the nanowire crossing and leading to the extended propagation in the nanowire over a flat target. This subsequently results in enhanced energy absorption.

As expected, electron crossing remains unaffected in the 3D geometry despite the presence of a large transverse surface current (see Figs. 5.3.1 (g)). This is evident through the transverse phase space diagram, $p_x/(mc)$ in Figure 5.3.1 (i), which match the beam position of the J_x component in Figure 5.3.1 (h). The electron crosses the nanowire rather than absorbed as discussed in [SD17]. This posts the question of the validity of vacuum heating around the nanowire surface. A small amount of $p_z/(mc)$ component also present inside the nanowire as shown in Figure 5.3.1 (j). This differs from the nanocluster interaction, where electrons are circulating around the surface rather than oscillating through the structure [DG15; LG21]. On the other hand, the energy absorption rate by electrons trapped in the Wakefield at the initial irradiation phase is $\sim 0.1\%$. Despite the small conversion rate, the nanowire's energy enhancement and Wakefield penetration outperform the flat target.

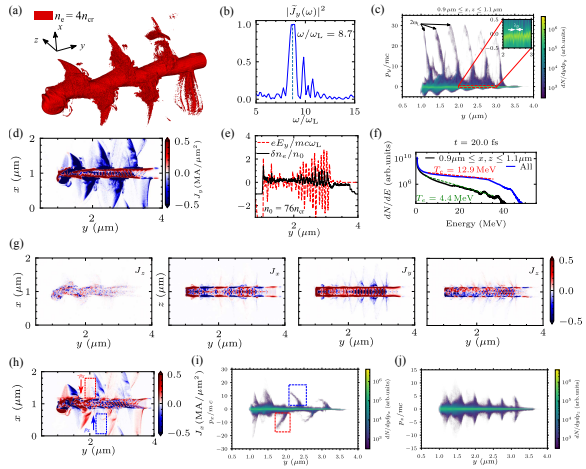

Figure 5.3.1: *3D simulation results with* PICONGPU *code for linearly polarized laser field at* $t = 13$ fs. *(a) The isosurface of electron density at* $n_e = 4n_{cr}$. *(b) The frequency spectrum associated with the longitudinal current density,* J_y. *(c) The longitudinal electron phase space inside the nanowire. (d) The current density components,* J_y *taken at* $z = 1\,\mu$m. *(e) The longitudinal density perturbation (solid line) and Wakefield (dashed line) along the nanowire center. (f) The total electron energy spectra at* $t = 20$ fs *with the one inside the nanowire. (g) The transverse current components. (h) The transverse current density,* J_x *where the dashed boxes indicate the returning electron that will cross the nanowire with the corresponding transverse momentum,* $p_x/(mc)$ *in (i). (j) The transverse momentum component,* $p_z/(mc)$.

5.3.4 Conclusion

In summary, we have reported the Wakefield generation in a solid density nanowire immediately following the interaction with an intense laser pulse. The driving force of the Wakefield is identified to be the $2\omega_L$ electron bunches generated by the $\mathbf{J} \times \mathbf{B}$ heating at the tip of the nanowire. The Wakefield is oscillating at the plasma frequency, and its amplitude can reach several TVm^{-1}. In addition, the laser electric field normal to the nanowire surface swings the electron across the nanowire, challenging the effectiveness of vacuum heating around the nanowire surface. The crossing electrons act as a drive bunch and facilitate a deeper Wakefield propagation into the nanowire, resulting in more than $2\times$ energy gain over a flat target. These interplay open new insights into the laser volumetric heating of nanostructure targets. The enhanced electron energy gain will offer efficient X-ray and $\gamma-$ray sources. The observation of such a large-amplitude Wakefield excitation may motivate the development of plasma Wakefield acceleration in solid density plasma [Zha+16].

References

[Bar+17] C. Bargsten *et al.* "Energy penetration into arrays of aligned nanowires irradiated with relativistic intensities: Scaling to terabar pressures". In: *Science Advances* 3.1 (2017), page 1601558. DOI: 10.1126/sciadv.1601558. URL: https://advances.sciencemag.org/content/3/1/e1601558 (cited on page 253).

[Bin+18] J. H. Bin *et al.* "Enhanced Laser-Driven Ion Acceleration by Superponderomotive Electrons Generated from Near-Critical-Density Plasma". In: *Phys. Rev. Lett.* 120 (7 Feb. 2018), page 074801. DOI: 10.1103/PhysRevLett.120.074801. URL: https://link.aps.org/doi/10.1103/PhysRevLett.120.074801 (cited on page 253).

[Bur+10] H. Burau *et al.* "PIConGPU: A Fully Relativistic Particle-in-Cell Code for a GPU Cluster". In: *IEEE Transactions on Plasma Science* 38.10 (Oct. 2010), pages 2831–2839. ISSN: 1939-9375. DOI: 10.1109/TPS.2010.2064310 (cited on page 253).

[Cao+10] L. Cao *et al.* "Enhanced absorption of intense short-pulse laser light by subwavelength nanolayered target". In: *Physics of Plasmas* 17.4 (2010), page 043103. DOI: 10.1063/1.3360298. URL: https://doi.org/10.1063/1.3360298 (cited on page 253).

[Cur+18] A. Curtis *et al.* "Micro-scale fusion in dense relativistic nanowire array plasmas". In: *Nature Communications* 9.1 (Mar. 2018), page 1077. ISSN: 2041-1723. DOI: 10.1038/s41467-018-03445-z. URL: https://doi.org/10.1038/s41467-018-03445-z (cited on page 253).

[DG15] L. Di Lucchio and P. Gibbon. "Relativistic attosecond electron bunch emission from few-cycle laser irradiated nanoscale droplets". In: *Phys. Rev. ST Accel. Beams* 18 (2 Feb. 2015), page 023402. DOI: 10.1103/PhysRevSTAB.18.023402. URL: https://link.aps.org/doi/10.1103/PhysRevSTAB.18.023402 (cited on page 254).

[Esa+96] E. Esarey *et al.* "Overview of plasma-based accelerator concepts". In: *IEEE Transactions on Plasma Science* 24.2 (1996), pages 252–288 (cited on page 254).

[Hab+16] H. Habara *et al.* "Efficient energy absorption of intense ps-laser pulse into nanowire target". In: *Physics of Plasmas* 23 (June 2016), page 063105. DOI: 10.1063/1.4953092 (cited on pages 253, 254).

[Hol+17] R. Hollinger *et al.* "Efficient picosecond x-ray pulse generation from plasmas in the radiation dominated regime". In: *Optica* 4.11 (Nov. 2017), pages 1344–1349. DOI: 10.1364/OPTICA.4.001344. URL: http://www.osapublishing.org/optica/abstract.cfm?URI=optica-4-11-1344 (cited on page 253).

[Kah+08] S. Kahaly *et al.* "Near-Complete Absorption of Intense, Ultrashort Laser Light by Sub-λ Gratings". In: *Phys. Rev. Lett.* 101 (14 Sept. 2008), page 145001. DOI: 10.1103/PhysRevLett.101.145001. URL: https://link.aps.org/doi/10.1103/PhysRevLett.101.145001 (cited on page 253).

[Kay+16] V. Kaymak *et al.* "Nanoscale Ultradense *Z*-Pinch Formation from Laser-Irradiated Nanowire Arrays". In: *Phys. Rev. Lett.* 117 (3 July 2016), page 035004. DOI: 10.1103/PhysRevLett.117.035004. URL: https://link.aps.org/doi/10.1103/PhysRevLett.117.035004 (cited on page 253).

[Kru03] W. L. Kruer. *The Physics of Laser Plasma Interactions*. Boulder: Westview Press, 2003 (cited on page 254).

[Kul+00] G. Kulcsár *et al.* "Intense Picosecond X-Ray Pulses from Laser Plasmas by Use of Nanostructured "Velvet" Targets". In: *Phys. Rev. Lett.* 84 (22 May 2000), pages 5149–5152. DOI: 10.1103/PhysRevLett.84.5149. URL: https://link.aps.org/doi/10.1103/PhysRevLett.84.5149 (cited on page 253).

[LG21] L. D. Lucchio and P. Gibbon. "Post-acceleration of electron bunches from laser-irradiated nanoclusters". In: *Physica Scripta* 96.5 (Mar. 2021), page 055603. DOI: 10.1088/1402-4896/abe77f. URL: https://doi.org/10.1088/1402-4896/abe77f (cited on page 254).

[Ma+06] Y.-Y. Ma *et al.* "Dense quasi-monoenergetic attosecond electron bunches from laser interaction with wire and slice targets". In: *Physics of Plasmas* 13.11 (2006), page 110702. DOI: 10.1063/1.2388958. URL: https://doi.org/10.1063/1.2388958 (cited on page 253).

[MdG18] B. Martinez, E. d'Humières, and L. Gremillet. "Synchrotron emission from nanowire array targets irradiated by ultraintense laser pulses". In: *Plasma Physics and Controlled Fusion* 60.7 (June 2018), page 074009. DOI: 10.1088/1361-6587/aac5a3. URL: https://doi.org/10.1088%2F1361-6587%2Faac5a3 (cited on page 253).

[Mon+11] S. Mondal *et al.* "Highly enhanced hard x-ray emission from oriented metal nanorod arrays excited by intense femtosecond laser pulses". In: *Phys. Rev. B* 83 (3 Jan. 2011), page 035408. DOI: 10.1103/PhysRevB.83.035408. URL: https://link.aps.org/doi/10.1103/PhysRevB.83.035408 (cited on page 253).

[Mor+19] A. Moreau *et al.* "Enhanced electron acceleration in aligned nanowire arrays irradiated at highly relativistic intensities". In: *Plasma Physics and Controlled Fusion* 62.1 (Nov. 2019), page 014013. DOI: 10.1088/1361-6587/ab4d0c. URL: https://doi.org/10.1088%2F1361-6587%2Fab4d0c (cited on page 254).

[Nau+04] N. Naumova *et al.* "Attosecond Electron Bunches". In: *Phys. Rev. Lett.* 93 (19 Nov. 2004), page 195003. DOI: 10.1103/PhysRevLett.93.195003. URL: https://link.aps.org/doi/10.1103/PhysRevLett.93.195003 (cited on page 253).

[Nis+01] T. Nishikawa *et al.* "Nanocylinder-array structure greatly increases the soft X-ray intensity generated from femtosecond-laser-produced plasma". In: *Applied Physics B* 73 (2001), pages 185–188. DOI: 10.1007/s003400100625. URL: https://doi.org/10.1007/s003400100625 (cited on page 253).

[OGT21] J. F. Ong, P. Ghenuche, and K. A. Tanaka. "Electron transport in a nanowire irradiated by an intense laser pulse". In: *Phys. Rev. Research* 3 (3 Sept. 2021), page 033262. DOI: 10.1103/PhysRevResearch.3.033262. URL: https://link.aps.org/doi/10.1103/PhysRevResearch.3.033262 (cited on pages 253, 254).

[Ovc+11] A. Ovchinnikov *et al.* "Characteristic X-rays generation under the action of femtosecond laser pulses on nano-structured targets". In: *Laser and Particle Beams* 29.2 (2011), pages 249–254. DOI: 10.1017/S026303461100022X (cited on page 253).

[Par+21] J. Park *et al.* "Absolute laser energy absorption measurement of relativistic 0.7 ps laser pulses in nanowire arrays". In: *Physics of Plasmas* 28.2 (2021), page 023302. DOI: 10.1063/5.0035174. eprint: https://doi.org/10.1063/5.0035174. URL: https://doi.org/10.1063/5.0035174 (cited on page 253).

[Pur+13] M. A. Purvis *et al.* "Relativistic plasma nanophotonics for ultrahigh energy density physics". In: *Nature Photonics* 7.10 (Oct. 2013), pages 796–800. ISSN: 1749-4893. DOI: 10.1038/nphoton.2013.217. URL: https://doi.org/10.1038/nphoton.2013.217 (cited on page 253).

[SD17] C. Shukla and A. Das. "Observation of enhanced absorption of laser radiation by nanostructured targets in PIC simulations". In: *Physics of Plasmas* 24.9 (2017), page 093118. DOI: 10.1063/1.4993107. URL: https://doi.org/10.1063/1.4993107 (cited on page 254).

[Tan+20] K. A. Tanaka *et al.* "Current status and highlights of the ELI-NP research program". In: *Matter and Radiation at Extremes* 5.2 (2020), page 024402. DOI: 10.1063/1.5093535. URL: https://doi.org/10.1063/1.5093535 (cited on page 253).

[Zha+16] X. Zhang *et al.* "Particle-in-cell simulation of x-ray wakefield acceleration and betatron radiation in nanotubes". In: *Phys. Rev. Accel. Beams* 19 (10 Oct. 2016), page 101004. DOI: 10.1103/PhysRevAccelBeams.19.101004. URL: https://link.aps.org/doi/10.1103/PhysRevAccelBeams.19.101004 (cited on page 255).

5.4 Temperature effects on neutron-capture cross sections and rates through electric dipole transitions in hot nuclei

Berceanu A.[1,*] , Xu Y.[1] , and Niu Y. F.[1]

[1] Extreme Light Infrastructure (ELI-NP) & Horia Hulubei National Institute for R & D in Physics and Nuclear Engineering (IFIN-HH), Str. Reactorului No. 30, 077125 Bucharest–Măgurele, Romania

[*] **andrei.berceanu@eli-np.ro**

Abstract

The temperature evolution of electric dipole transition strengths of Sn isotopes is studied using self-consistent QRPA and finite-temperature RPA models based on a relativistic density functional. For tin isotopes lighter than ^{132}Sn, temperature only shows its effect at high values of 2 MeV, while for neutron-rich tin isotopes heavier than ^{132}Sn, the low-lying strength distributions get fragmented and spread to the lower-energy region already at temperature of]SI1MeV. Using these electric dipole transition strengths as inputs for the TALYS code, the temperature effects on (n,γ) cross sections are studied. For tin isotopes lighter than ^{132}Sn, temperature causes an enhancement of neutron capture cross-section at high temperatures of 2 MeV, while for neutron-rich tin isotopes heavier than ^{132}Sn, the cross-section is primarily enhanced already at temperature $T = 1.0$ MeV, and the bump of cross-section caused by the pygmy dipole resonance also becomes broader. The change in neutron-capture rate can be as large as 70% for ^{136}Sn, considering the temperature effects on electric dipole transition strength in the final compound nucleus with a temperature of 0.86 MeV (corresponding to $T = 10$ GK in the astrophysical environment). The change is around 20% for tin isotopes lighter than ^{132}Sn and above 40% for those heavier than ^{132}Sn.

5.4.1 Introduction

The origin of heavy elements from iron to uranium has been one of the long-standing open questions in physics [Has02]. It has been known that the rapid neutron capture process (r-process) produces about half of these heavy elements [Qia03]. However, the identification of the sites for r-process is still under investigation. The observation of GW170817 neutron star mergers (NSM) provides evidence that NSM can be one of the possible sites [AHA17; Col17; DPS17; Kas+17; PDB17; Wat+19]. In principle, the different astrophysical sites should produce unique abundance pattern signatures due to distinct environmental conditions like temperature, density, and neutron densities, which helps us identify the main r-process site directly[Mum+16]. For such a purpose, accurate nuclear physics inputs for r-process network calculations are crucial, including nuclear mass, β-decay half-lives, neutron-capture rates, and so on [Mum+16]. For a recent extensive calculation of nuclear mass and β-decay half-lives by microscopic theories, one can refer to [Xia+18] and [Ney+20]. However, the r-process involves a large number of neutron-rich nuclei far from the stability line, which are difficult to produce and measure due to experimental limitations.

With the development of radioactive ion beam facilities, the measurements of nuclear mass and β-decay half-lives are approaching the r-process path [Hua+21; Lor+15; Wan+21; Wu+17; Xu+14], while the measurement of neutron-capture cross-section is still a big challenge. Therefore, the theoretical predictions of neutron-capture cross sections and rates are necessary for studying the r-process. For the study of neutron-capture processes, the statistical Hauser-Feshbach [HF52] model is usually adopted, which requires the electric dipole transition strength function as an important input.

The dipole strength function can be conventionally described by a phenomenological Lorentzian model or its extensions with an energy- and temperature-dependent width[CHO09], where the parameters are mainly fitted to available data from stable nuclei. However, the reliable extrapolation to neutron-rich nuclei requires microscopic models. It is difficult for the large-scale shell model to describe the E1 transitions, since the E1 transition connects different major shells [Sie17], so a practical choice is the quasiparticle random phase approximation (QRPA) model, based on density functional theories. Large-scale QRPA calculations of the E1 strength function have been performed based on the zero-range Skyrme density functional, and the dipole strengths were used to estimate the radiative neutron capture cross-section for all nuclei of relevance in astrophysical applications [GK02; GKS04]. Recently, based on the finite-range Gogny force, the axially

symmetric deformed QRPA approach was applied to the large-scale calculation of E1 γ-ray strength function [Mar+16]. The resulting strength functions improved at low γ-ray energies by using shell model results are employed in the study of radioactive neutron and proton capture cross-sections [Gor+18].

Compared to the non-relativistic density functional, the covariant density functional theory (CDFT) has the advantage of producing the spin-orbit splitting naturally, and has been applied very successfully to the description of a variety of nuclear structure phenomena, [Men+06]. Based on the relativistic density functional, the self-consistent QRPA approach has been developed and applied to the study of the dipole strength function of typical nuclei, including the giant resonance part, as well as the low-lying strength [Paa+03]. In neutron-rich nuclei, the presence of the pygmy dipole resonance (PDR) [Paa+07] results in the failure of the conventional Lorentzian describes the low-lying part of the dipole strength. Based on the relativistic QRPA (RQRPA) approach, the properties of PDR have been investigated in detail [Paa+09b; Vre+12]. Furthermore, the influence of the enhancement of neutron-capture cross sections and rates on low-lying strength has been investigated based on the relativistic quasiparticle time blocking approximation (QTBA), where the correlations beyond QRPA approaches are included, and it was concluded that the neutron-capture rates are sensitive to the fine structure of the low-lying dipole strength [Lit+09].

Neutron capture processes relevant for astrophysics, like the r-process, occur in stellar environments with high temperatures. However, the temperature effects are usually not included in the microscopic calculation of dipole strength functions. Temperature effects are normally included in a phenomenological approach, as a parameter in the Lorentzian function for the calculation of neutron-capture rates [Gor98; GK02; GP19]. In this case, the fine structure changes and/or novel structure induced by temperature effects are missing in the calculation of neutron capture rates, despite its potentially important impact. Experimentally, the giant dipole resonance (GDR) built on a hot nucleus can be measured by fusion-evaporation reactions and inelastic scattering with light ions. For the latter method, the effect of temperature can be decoupled from that of angular momentum [Ram+96]. For a review of experimental studies of hot giant resonances and a compilation of GDR data in hot nuclei, one can find in Refs. [SB06] and [ST07]. However, these studies are limited to stable nuclei and focus on the GDR energy region, where the evolution of GDR width with temperature is paid special attention. The self-consistent finite-temperature relativistic random-phase approximation (FTRRPA) model was developed, and it was shown that low-lying dipole strengths are modified by temperature effects, including the concentration of new low-lying dipole strength for ^{60,62}Ni, and the modification of PDR for ^{68}Ni and ^{132}Sn [Niu+09]. Later, based on the Woods-Saxon mean-field, the thermal continuum QRPA (TCQRPA) model explains the low-energy enhancement of the dipole strength functions with the inclusion of temperature effects [LB13]. More recently, the self-consistent finite temperature QRPA based on Skyrme density functional was developed [Yük+17], and new low energy dipole excitations were discovered [Yük+17; Yük+19], similar to [LB13; Niu+09].

With these discoveries, it is interesting to see what are the consequences of the modifications of low-lying dipole strength with the microscopic inclusion of temperature effects on the neutron capture cross-sections and rates. Previous sensitivity studies have shown that the neutron-capture rates of Sn isotopes are essential for r-process simulation in different astrophysical environments [Mum+16]. Therefore, in this work, taking Sn isotopes as an example, we calculate the electric dipole strength at finite temperature using a self-consistent FTRRPA model. We correspondingly investigate the influence on neutron capture cross sections and rates using the same these dipole strength functions. The dipole strengths at zero temperature are calculated by an RQRPA model, with the inclusion of pairing correlations. Within the mean-field approach, there is a critical temperature above which the pairing correlations vanish [Niu+13], although this sharp phase transition is washed out by including thermal fluctuations beyond mean-field [GLS13]. This tells us that, at relatively high temperatures, the pairing correlations are not so important anymore, so we use the FTRRPA model to calculate dipole strength functions at finite temperature. The neutron capture cross-sections and rates are calculated using the TALYS code [KHD04].

5.4.2 Formalism

The self-consistent RQRPA model used for zero-temperature calculations is formulated based on the canonical basis from a relativistic Hatree-Bogoliubov (RHB) calculation – see details in Ref. [Paa+03]. The density-dependent meson-nucleon couplings are used in the relativistic Lagrangian, and in our calculations, we will use the parameter set DD-ME2

[Lal+05]. The Gogny force of D1S interaction [BGG91] is used as the particle-particle interaction, accounting for pairing correlations.

The FTRRPA model is formulated based on the single-particle states from the relativistic mean-field (RMF) model at finite temperature (FTRMF) in a self-consistent way, which means that the same relativistic density functional is used for the mean-field in FTRMF and for the residual two-body interaction in FTRRPA. The same parameter set DD-ME2 is used for finite-temperature calculations. The FTRRPA equation reads [Niu+09]

$$\begin{pmatrix} A & B \\ -B^* & -A^* \end{pmatrix} \begin{pmatrix} X \\ Y \end{pmatrix} = E_\nu \begin{pmatrix} X \\ Y \end{pmatrix}, \quad (5.4.1)$$

where

$$A = \begin{pmatrix} (\varepsilon_m - \varepsilon_i)\delta_{ii'}\delta_{mm'} & \\ & (\varepsilon_\alpha - \varepsilon_i)\delta_{\alpha\alpha'}\delta_{ii'} \end{pmatrix} + \begin{pmatrix} (n_{i'} - n_{m'})V_{mi'im'} & n_{i'}V_{mi'i\alpha'} \\ (n_{i'} - n_{m'})V_{\alpha i'im'} & n_{i'}V_{\alpha i'i\alpha'} \end{pmatrix}, \quad (5.4.2)$$

and

$$B = \begin{pmatrix} (n_{i'} - n_{m'})V_{mm'ii'} & n_{i'}V_{m\alpha'ii'} \\ (n_{i'} - n_{m'})V_{\alpha m'ii'} & n_{i'}V_{\alpha\alpha'ii'} \end{pmatrix}. \quad (5.4.3)$$

V is the residual two-body interaction, derived from the relativistic Lagrangian with density-dependent meson-nucleon couplings [NVR02]. The thermal occupation factors n_k denote a Fermi-Dirac distribution for states in the Fermi sea with index m, i, and 0 for states in the Dirac sea with index α. Due to temperature effects, the configuration space includes not only particle-hole (ph) pairs, but also particle-particle (pp) and hole-hole (hh) pairs. The transition strength for a multipole operator Q_J is

$$B(J, E_\nu) = \left| \sum_{mi} (X^{\nu,J}_{mi} + (-1)^J Y^{\nu,J}_{mi}) \langle m||Q_J||i\rangle (n_i - n_m) \right|^2 \quad (5.4.4)$$

The discrete spectra are averaged with a Lorentzian distribution of width $\Gamma = 1$ MeV in the present calculations to get the response function as the following,

$$R(E) = \sum_\nu B(J, E_\nu) \frac{\Gamma/2\pi}{(E - E_\nu)^2 + \Gamma^2/4}. \quad (5.4.5)$$

The compound nucleus contribution (CNC) is usually dominant to the capture reaction in the energy range of astrophysics interest, which is well described by the Hauser-Feshbach model [HF52]. In this model the cross section of the CNC for neutron reaction $A + n = B + \gamma$ can be written as

$$\sigma^{CNC}(E) = \sum_{x=0}^{A} \sum_{x=0}^{B} \sigma^{CNC}_{A^x + n -> B^x + \gamma}(E). \quad (5.4.6)$$

The summation $\sum_{x=0}^{A}$ and $\sum_{x=0}^{B}$, where the energy level scheme is represented by the x-th excited states (x=0 refers to the ground state), take over all the possible states (ground and excitation states) of the target A and the residual nucleus B. Each state is characterized by its spin S^x_A, parity π^x_A and excitation energy E^x_A for the target A (and similarly for the residual nucleus B).

The expression of the cross section $\sigma^{CNC}_{A^x+n->B^x+\gamma}(E)$ is given by

$$\begin{aligned} &\sigma^{CNC}_{A^x+n->B^x+\gamma}(E_n) \\ &= \frac{\pi}{k^2} \sum_{J=mod(S_{A^x}+S_n,1)}^{l_{max}+S_{A^x}+S_n} \sum_{\Pi=-1}^{1} \frac{2J+1}{(2S_{A^x}+1)(2S_n+1)} \\ &\times \sum_{J_a=|J-S_{A^x}|}^{J+S_{A^x}} \sum_{l_i=|J_n-S_n|}^{J_n+S_n} \sum_{\lambda=|J-S_{B^x}|}^{J+S_{B^x}} \sum_{l_f=|\lambda-S_\gamma|}^{\lambda+S_\gamma} \delta^\pi_{C_n} \delta^\pi_{C_\gamma} \\ &\times \frac{\langle T^J_{C_n,l_i,J_n}(E_n)\rangle \langle T^J_{C_\gamma,l_f,\lambda}(E_\gamma)\rangle}{\sum_{Clj} \delta^\pi_C \langle T^J_{Clj}(E_C)\rangle} W^J_{C_n l_i J_n C_\gamma l_f \lambda} \end{aligned} \quad (5.4.7)$$

where E_n the incident energy of neutron; k the wave number of the relative motion; l_{max} the maximum value of the relative orbital momentum; J and Π the total angular momentum and the parity of the compound nucleus; S_{A^x} the spin of the target A^x; S_n the spin of neutron; J_n the total angular momentum of neutron; l_i the relative orbital momentum of the target A^x and neutron; S_{B^x} the spin of the residual nucleus B^x; λ the multi-polarity of photon (total angular momentum); S_γ the spin of photon; l_f the relative orbital momentum of the residual nucleus B^x and the photon; E_γ the energy of photon; C_n the channel label of the initial system (A^x+n) designated by C_n=(n, S_n, E_n, E_{A^x}, S_{A^x}, π_{A^x}); C_γ the channel label of the final system (B^x+γ) designated by C_γ=(γ, S_γ, E_γ, E_{B^x}, S_{B^x}, π_{B^x}); $\delta^\pi_{C_n}$=1 if $\pi_{A^x}\pi_n(-1)^{l_i}$=Π and 0 otherwise; $\delta^\pi_{C_\gamma}$=1 if $\pi_{B^x}\pi_\gamma(-1)^{l_f}$=$\Pi$ and 0 otherwise; π_n the parity of the neutron; π_γ the parity of photon; T the transmission coefficient; $\sum_{Clj} \delta^\pi_C \langle T^J_{Clj}(E_C)\rangle$ the sum of the transmission coefficient T for all of the possible decay channels C of the compound nucleus; and W the width fluctuation correction factor. The γ-ray transmission coefficient T_{Xl} with the multipolarity l of type X ($X = E$ or M for electric or magnetic) is given by

$$T_{Xl}(E_\gamma) = 2\pi f_{Xl}(E_\gamma) E_\gamma^{2l+1}, \quad (5.4.8)$$

in which E_γ is the γ-ray energy and $f_{Xl}(E_\gamma)$ is the energy-dependent γ-ray strength function. For the electric dipole (E1) case, $f_{E1}(E_\gamma)$ has the following relation with the response function,

$$f_{E1} = \frac{16\pi}{27(\hbar c)^3} R(E). \tag{5.4.9}$$

In the present study, the neutron capture reaction cross sections and reaction rates are calculated with TALYS code [KHD04], which has been employed in the studies of nuclear astrophysical reactions [Lan+18]. TALYS is a software package for the simulation of nuclear reactions, which provides a a complete description of all reaction channels and observables. Many state-of-the-art nuclear models, including the reaction mechanism of compound nuclei described by the Hauser-Feshbach model are implemented in TALYS. In particular, the transmission coefficient of the photon channel is determined from the electric dipole transition strengths, which is an essential input for the calculations of neutron capture cross sections and reaction rates. Here, the strength functions extracted from the present self-consistent RQRPA and finite-temperature RPA models are imported into the present TALYS calculations to systematically study the (n,γ) cross sections and reaction rates on the isotopes of tin (Sn).

5.4.3 Results and Discussions

In Figure 5.4.1, electric dipole transition strengths of even-even Sn isotopes from $A = 126$ to $A = 146$ at different temperatures $T = 0$ MeV, 1.0 MeV, and 2.0 MeV are shown. At zero temperature, pairing correlations are included self-consistently both in the ground state by Bogoliubov transformation and in the QRPA by residual interaction in the particle-particle channel. At $T = 1.0$ MeV, the pairing correlations already collapse, and the FTRRPA model can be applied. From Figure 5.4.1, the total evolution trend of electric dipole response with neutron number as well as temperature can be clearly seen. The electric dipole response can be divided into the giant resonance region between 10 MeV to 20 MeV and the low-energy region below 10 MeV. At $T = 0$ MeV , the centroid energy of giant resonance, is smoothly down-shifted with increasing mass, showing the giant resonance's collectivity. In the low-energy region, for isotopes lighter than ^{134}Sn, there is mainly one peak, while a new peak appears starting at ^{134}Sn, and its strength increases while its energy becomes lower with increasing mass number.

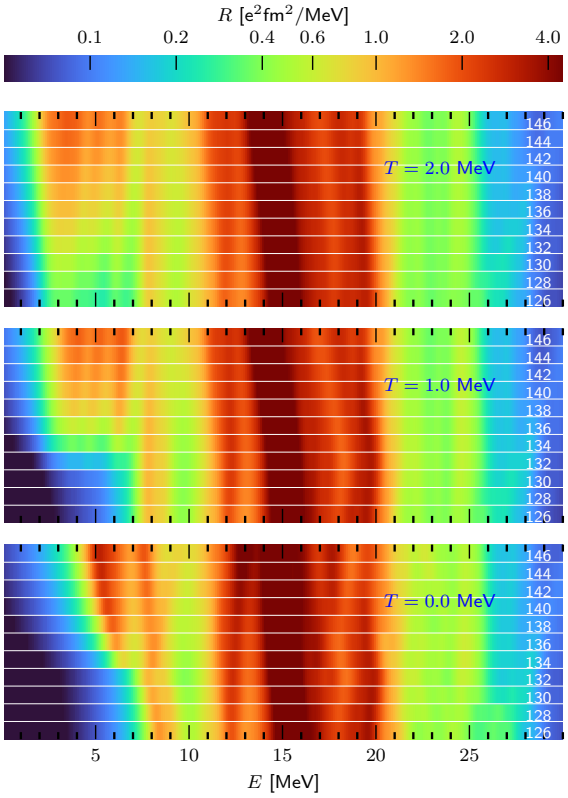

Figure 5.4.1: *Electric dipole transition strength R of even-even Sn isotopes as a function of excitation energy E, for temperatures $T = 0$ MeV calculated by RQRPA model and $T = 1$ MeV and $T = 2$ MeV calculated by FTRRPA model, based on the energy density functional DD-ME2. Each slice represents a different Sn isotope, with the mass number A annotated to the right. Reprinted with permission from Berceanu, A., Y. Xu, and Y. F Niu, Physical Review C 104.4 (2021): 044332. Copyright 2021 by the American Physical Society.*

In order to understand the physics of these low-lying states, we plot the corresponding transition densities for three typical nuclei ^{126}Sn , ^{136}Sn, and ^{146}Sn in Figure 5.4.2. In ^{126}Sn, there is one peak , and in ^{136,146}Sn, there are two typical peaks in the low-energy region smaller than 10 MeV of the dipole transition strength distributions, which can be seen from Figure 5.4.1 and in Table 5.4.1 in details. For all these selected states, there are common features in transition densities. The neutron and protons have the same phase in transition densities in the interior of the nucleus, and there are extra neutron transition densities in the surface of the nucleus. This is the typical feature of a PDR state. So these low-lying states can be considered as PDR states. At higher temperatures, the centroid energy of giant resonance is down-shifted with increasing mass number faster than the zero-temperature case. However, the main

difference from the zero-temperature case remains in the low-energy region. The pygmy dipole resonance becomes fragmented and spans a broader energy region at $T = 1.0$ MeV starting from ^{134}Sn. At $T = 2.0$ MeV, even for ^{126}Sn, new low-lying peaks appear due to temperature effects, and their strength increases with increasing mass number. These changes with neutron number as well as temperature in the low-energy region would affect the (n,γ) cross-section directly, as we shall discuss in detail in Figure 5.4.3.

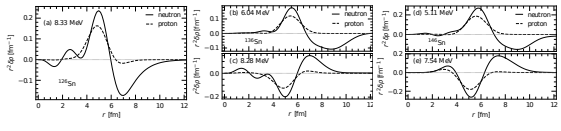

Figure 5.4.2: *Transition densities of neutrons and protons for the low-lying peaks of three Sn isotopes at $T = 0$ MeV, including the peak at $E = 8.33$ MeV in ^{126}Sn [panel(a)], the peaks at $E = 6.04$ MeV [panel(b)] and $E = 8.28$ Mev [panel(c)] in ^{136}Sn, as well as the peaks at $E = 5.11$ MeV [panel(d)] and $E = 7.54$ MeV [panel(e)] in ^{146}Sn, calculated by RQRPA model based on the energy density functional DD-ME2. Reprinted with permission from Berceanu, A., Y. Xu, and Y. F. Niu, Physical Review C 104.4 (2021): 044332. Copyright 2021 by the American Physical Society.*

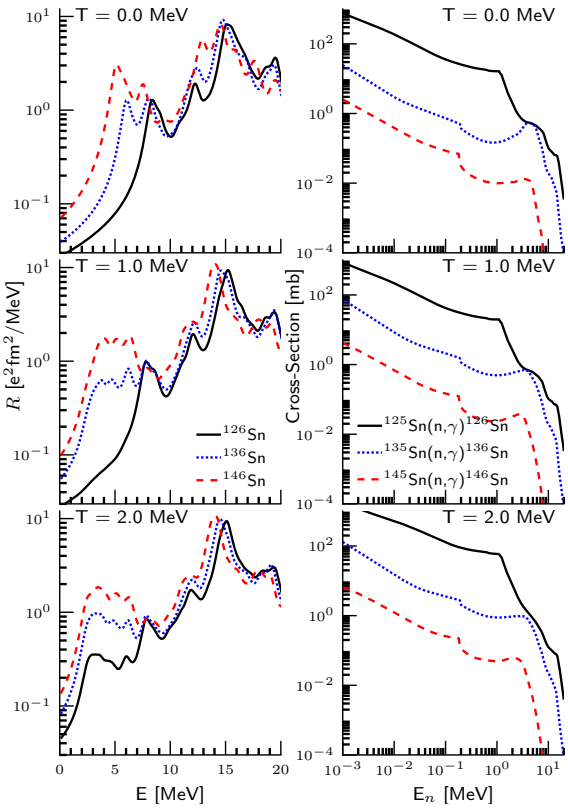

Figure 5.4.3: *Electric dipole transition strength R as a function of excitation energy E (left column) and the corresponding (n,γ) cross-section as a function of neutron energy E_n (right column), for $T = 0$ MeV (top row), $T = 1$ MeV (middle row), and $T = 2$ MeV (bottom row). The three lines in each panel correspond to different nuclei: ^{126}Sn (black solid), ^{136}Sn (blue dotted) and ^{146}Sn (red dashed). Reprinted with permission from Berceanu, A., Y. Xu, and Y. F. Niu, Physical Review C 104.4 (2021): 044332. Copyright 2021 by the American Physical Society.*

In Figure 5.4.3, electric dipole transition strengths for three selected nuclei ^{126}Sn, ^{136}Sn and ^{146}Sn are compared at three different temperatures $T = 0$ MeV, $T = 1$ MeV, and $T = 2$ MeV respectively. Using these transition strengths as γ-ray strength functions for the TALYS calculation, the corresponding (n,γ) cross sections are also shown in Figure 5.4.3. At zero temperature one can note apparent changes in the low-energy region with increasing neutron number. The low-lying peak at $E = 8.33$ MeV for ^{126}Sn is down-shifted to $E = 8.28$ MeV, $E = 7.54$ MeV for ^{136}Sn and ^{146}Sn respectively. In addition, new peaks with $E = 6.04$ MeV and $E = 5.11$ MeV appear for ^{136}Sn and ^{146}Sn, respectively. The main single-particle transition configurations for these low-lying states are listed in Table 5.4.1. For the relatively high peaks around 8 MeV of ^{126}Sn and ^{136}Sn, these states are made of several neutron single-particle transitions across the $N = 82$ shell gap.

The lower-lying peaks of ^{136}Sn and ^{146}Sn appear due to the large neutron excess of these two nuclei, and they are composed of several neutron single-particle transitions above the $N = 82$ shell gap. For the higher peak in ^{146}Sn, the transitions across the $N = 82$ shell gap are mainly blocked, with only $\nu 1h_{11/2} \rightarrow \nu 1i_{13/2}$ left, and hence the main configurations of this state are still neutron transitions above the $N = 82$ shell gap. The neutron-capture cross-section decreases by several orders of magnitude with increasing neutron number. However, for ^{135}Sn (n,γ) ^{136}Sn, around the $E_n = 6$ MeV region, there is a bump in the cross section, and it even reaches the same cross-section as ^{125}Sn (n,γ) ^{126}Sn. This is the reflection of the newly appeared PDR in ^{136}Sn, which strongly enhances the low-lying γ-ray strength function. Similarly, the strong pygmy peak in the electric dipole strength of ^{146}Sn is also clearly seen in the cross-section for the neutron capture on ^{145}Sn, agreeing with [Lit+09].

Table 5.4.1: The main single-particle transition configurations ii' with $X^2_{ii'} - Y^2_{ii'}$ larger than 5% for selected low-lying dipole states with energies E at $T = 0.0, 1.0$, and 2.0 MeV for ^{126}Sn. Reprinted with permission from A. Berceanu, Y. Xu, and Y. F. Niu, Physical Review C 104.4 (2021): 044332. Copyright 2021 by the American Physical Society.

$T = 0$ MeV & $E = 8.33$ MeV		$T = 1.0$ MeV & $E = 7.75$ MeV		$T = 2.0$ MeV & $E = 7.78 MeV$	
config.	$X^2 - Y^2$	config.	$X^2 - Y^2$	config.	$X^2 - Y^2$
$\nu 3s_{1/2} \to \nu 3p_{3/2}$	43.26%	$\nu 3s_{1/2} \to \nu 3p_{3/2}$	43.26%	$\nu 3s_{1/2} \to \nu 3p_{3/2}$	49.65%
$\nu 2d_{3/2} \to \nu 3p_{3/2}$	12.63%	$\nu 2d_{3/2} \to \nu 3p_{3/2}$	23.07%	$\nu 2d_{3/2} \to \nu 3p_{3/2}$	20.39%
$\nu 2d_{3/2} \to \nu 3p_{1/2}$	9.92%	$\nu 2d_{3/2} \to \nu 3p_{1/2}$	11.89%	$\nu 2d_{3/2} \to \nu 3p_{1/2}$	10.67%
$\nu 3s_{1/2} \to \nu 3p_{1/2}$	6.84%				

At $T = 1.0$ MeV, the low-lying peaks are also strongly enhanced with increasing neutron number. However, instead of the clear pygmy structure of those low-energy states at $E = 6.04$ MeV and 5.11 MeV in ^{136}Sn and ^{146}Sn, they become much more fragmented and are dominated by one single-particle transition. This behavior in the low-lying peaks is also reflected in the neutron capture cross sections, similar to the zero-temperature case, but with a broader bump for the capture on ^{135}Sn and ^{145}Sn due to the broader low-lying peaks in ^{136}Sn and ^{146}Sn. At even higher temperatures, although new low-lying peaks also start to appear in ^{126}Sn, they are still less visible than those in ^{136}Sn and ^{146}Sn. The trend with increasing neutron number at $T = 2.0$ MeV is similar to that at $T = 0$ MeV.

Finally, we study the change of the neutron-capture rate if the same temperature of the astrophysical environment is assumed for the final compound nucleus. The assumption is valid because, in the finite-temperature mean-field theory, we treat nuclei as a grand canonical ensemble characterized by a fixed temperature and chemical potential in a thermal statistical equilibrium state [ER93]. Similar applications have been made in this way for electron-capture cross sections and rates in a core-collapse supernova, where Gamow-Teller transition strength distributions in hot nuclei with the temperature of supernova environment are used [Dzh+10; Niu+11; Paa+09a].

5.4.4 Summary

In summary, the electric dipole transition strengths of Sn isotopes at zero and finite temperatures are studied by a self-consistent QRPA and finite-temperature RPA model based on relativistic density functionals. The temperature effects on electric dipole transitions are mainly the modification of low-lying strengths. For tin isotopes lighter than ^{132}Sn, the low-lying excitation states are made of several single-particle transitions across the $N = 82$ shell gap, so the temperature has a small effect, and when the temperature is 2 MeV, new single-particle transitions appear due to thermal unblocking effects. For tin isotopes heavier than ^{132}Sn, where the single-particle transitions above the $N = 82$ shell gap enter into the configurations of low-lying states, the temperature starts to play an important role already from $T = 1.0$ MeV, where the PDR becomes fragmented and spreads to the lower-energy region. Using these electric dipole transition strengths as inputs for the TALYS code, the (n, γ) cross-section is calculated, and the modification of these low-lying strengths are reflected directly in the neutron capture cross-section. Being lighter than ^{132}Sn, only very high temperatures, *e. g.* $T = 2.0$ MeV cause a large enhancement of the cross-section. However, being heavier than ^{132}Sn, the cross-section is largely enhanced already at $T = 1.0$ MeV, and the bump around $E_n = 5$ MeV caused by PDR also becomes broader. The neutron-capture rate can be changed by as much as 70% for ^{136}Sn by considering the temperature effect on electric dipole transition strength of the final compound nucleus with a temperature of 0.86 MeV, the same value as the astrophysical environment, and this change is around 20% for nuclei lighter than ^{132}Sn and above 40% for those heavier than ^{132}Sn.

5.4.5 Acknowledgment

This work is supported by the National Natural Science Foundation of China under Grants No. 12075104, the Fundamental Research Funds for the Central Universities under Grant No. Lzujbky-2019-11, and the Romanian Ministry of Research and Innovation under the contract PN 19 06 01 05. This work is also funded by the Institute of Atomic Physics (Magurele, Romania) under the ELI-RO program contract ELI_15/16.10.2020.

References

[AHA17] I. Arcavi, G. Hosseinzadeh, and D. Andrew Howell. "Optical emission from a kilonova following a gravitational-wave-detected neutron-star merger". In: *Nature* 551 (2017), page 64 (cited on page 259).

[BGG91] J. F. Berger, M. Girod, and D. Gogny. In: *Comput. Phys. Commun.* 63 (1991), page 365 (cited on page 261).

[CHO09] R. Capote, M. Herman, and P. Oblozinsky. "RIPL – Reference Input Parameter Library for Calculation of Nuclear Reactions and Nuclear Data Evaluations". In: *Nucl. Data Sheets* 110 (2009), page 3107 (cited on page 259).

[Col17] L. S. Collaboration. "Multi-messenger Observations of a Binary Neutron Star Merger". In: *ApJL* 848 (2017), page L12 (cited on page 259).

[DPS17] M. R. Drout, A. L. Piro, and B. J. Shappee. "Light curves of the neutron star merger GW170817/SSS17a: Implications for r-process nucleosynthesis". In: *Science* 358 (2017), page 1570 (cited on page 259).

[Dzh+10] A. A. Dzhioev *et al.* "Gamow-Teller strength distributions at finite temperatures and electron capture in stellar environments". In: *Phys. Rev. C* 81 (1 Jan. 2010), page 015804 (cited on page 264).

[ER93] J. L. Egido and P. Ring. In: . *Phys. G: Nucl. Part. Phys.* 19 (1993), page 1 (cited on page 264).

[GLS13] D. Gambacurta, D. Lacroix, and N. Sandulescu. "Pairing and specific heat in hot nuclei". In: *Phys. Rev. C* 88 (3 Sept. 2013), page 034324. DOI: 10.1103/PhysRevC.88.034324 (cited on page 260).

[Gor98] S. Goriely. "Radiative neutron captures by neutron-rich nuclei and the r-process nucleosynthesis". In: *Phys. Lett. B* 436 (1998), page 10 (cited on page 260).

[GK02] S. Goriely and E. Khan. "Large-scale QRPA calculation of E1-strength and its impact on the neutron capture cross section". In: *Nucl. Phys. A* 706 (2002), page 217 (cited on pages 259, 260).

[GKS04] S. Goriely, E. Khan, and M. Samyn. "Microscopic HFB + QRPA predictions of dipole strength for astrophysics applications". In: *Nucl. Phys. A* 739 (2004), page 331 (cited on page 259).

[GP19] S. Goriely and V. Plujko. "Simple empirical E1 and M1 strength functions for practical applications". In: *Phys. Rev. C* 99 (2019), page 014303 (cited on page 260).

[Gor+18] S. Goriely *et al.* "Gogny-HFB+QRPA dipole strength function and its application to radiative nucleon capture cross section". In: *Phys. Rev. C* 98 (2018), page 014327 (cited on page 260).

[Has02] E. Haseltin. In: *Discover* 23 (2002), page 37 (cited on page 259).

[HF52] W. Hauser and H. Feshbach. "The Inelastic Scattering of Neutrons". In: *Phys. Rev.* 87 (1952), page 366 (cited on pages 259, 261).

[Hua+21] W. J. Huang *et al.* "The Ame2020 atomic mass evaluation". In: *Chin. Phys. C* 45 (2021), page 030002 (cited on page 259).

[Kas+17] D. Kasen *et al.* "Origin of the heavy elements in binary neutron-star mergers from a gravitational-wave event". In: *Nature* 551 (2017), page 80 (cited on page 259).

[KHD04] A. J. Koning, S. Hilaire, and M. C. Duijvestijn. In: *NRG-report* (2004), 21297/04.62741/P (cited on pages 260, 262).

[Lal+05] G. A. Lalazissis *et al.* In: *Phys. Rev. C* 71 (2005), page 024312 (cited on page 261).

[Lan+18] H. Y. Lan *et al.* "Determination of the photodisintegration reaction rates involving charged particles: Systematic calculations and proposed measurements based on the facility for Extreme Light Infrastructure–Nuclear Physics". In: *Phys. Rev. C* 98 (5 Nov. 2018), page 054601. DOI: 10.1103/PhysRevC.98.054601 (cited on page 262).

[LB13] E. Litvinova and N. Belov. "Low-energy limit of the radiative dipole strength in nuclei". In: *Phys. Rev. C* 88 (2013), 031302(R) (cited on page 260).

[Lit+09] E. Litvinova *et al.* "Low-lying dipole response in the relativistic quasiparticle time blocking approximation and its influence on neutron capture cross sections". In: *Nucl. Phys. A* 823 (2009), pages 26–37. ISSN: 0375-9474 (cited on pages 260, 263).

[Lor+15] G. Lorusso *et al.* In: *Phys. Rev. Lett.* 114 (19 May 2015), page 192501 (cited on page 259).

[Mar+16] M. Martini *et al.* "Large-scale deformed quasiparticle random-phase approximation calculations of the γ-ray strength function using the Gogny force". In: *Phys. Rev. C* 94 (2016), page 014304 (cited on page 260).

[Men+06] J. Meng *et al.* "Relativistic continuum Hartree Bogoliubov theory for ground-state properties of exotic nuclei". In: *Prog. Part. Nucl. Phys.* 57.2 (2006), page 470. ISSN: 0146-6410. DOI: https://doi.org/10.1016/j.ppnp.2005.06.001 (cited on page 260).

[Mum+16] M. R. Mumpower *et al.* "The impact of individual nuclear properties on r-process nucleosynthesis". In: *Prog. Part. Nucl. Phys.* 86 (2016), page 86 (cited on pages 259, 260).

[Ney+20] E. M. Ney *et al.* "Global description of β^- decay with the axially deformed Skyrme finite-amplitude method: Extension to odd-mass and odd-odd nuclei". In: *Phys. Rev. C* 102 (3 Sept. 2020), page 034326 (cited on page 259).

[NVR02] T. Nikšić, D. Vretenar, and P. Ring. "Relativistic random-phase approximation with density-dependent meson-nucleon couplings". In: *Phys. Rev. C* 66 (Dec. 2002), page 064302. DOI: 10.1103/PhysRevC.66.064302 (cited on page 261).

[Niu+09] Y. F. Niu *et al.* "Low-energy monopole and dipole response in nuclei at finite temperature". In: *Phys. Lett. B* 681 (2009), page 315. DOI: 10.1016/j.physletb.2009.10.046 (cited on pages 260, 261).

[Niu+11] Y. F. Niu *et al.* "Stellar electron-capture rates calculated with the finite-temperature relativistic random-phase approximation". In: *Phys. Rev. C* 83 (4 Apr. 2011), page 045807 (cited on page 264).

[Niu+13] Y. F. Niu *et al.* "Pairing transitions in finite-temperature relativistic Hartree-Bogoliubov theory". In: *Phys. Rev. C* 88 (3 Sept. 2013), page 034308. DOI: 10.1103/PhysRevC.88.034308. URL: https://link.aps.org/doi/10.1103/PhysRevC.88.034308 (cited on page 260).

[Paa+03] N. Paar *et al.* "Quasiparticle random phase approximation based on the Relativistic Hartree-Bogoliubov model". In: *Phys. Rev. C* 67 (Mar. 2003), page 034312. DOI: 10.1103/PhysRevC.67.034312 (cited on page 260).

[Paa+09a] N. Paar *et al.* "Calculation of stellar electron-capture cross sections on nuclei based on microscopic Skyrme functionals". In: *Phys. Rev. C* 80.5 (Nov. 2009), page 055801 (cited on page 264).

[Paa+09b] N. Paar *et al.* "Isoscalar and Isovector Splitting of Pygmy Dipole Structures". In: *Phys. Rev. Lett.* 103 (July 2009), page 032502. DOI: 10.1103/PhysRevLett.103.032502 (cited on page 260).

[Paa+07] N. Paar *et al.* "Exotic modes of excitation in atomic nuclei far from stability". In: *Rep. Prog. Phys.* 70 (2007), page 691 (cited on page 260).

[PDB17] E. Pian, P. D'Avanzo, and S. Benetti. "Spectroscopic identification of r-process nucleosynthesis in a double neutron-star merger". In: *Nature* 551 (2017), page 67 (cited on page 259).

[Qia03] Y.-Z. Qian. "The Origin of the Heavy Elements: Recent Progress in the Understanding of the r-Process". In: *Prog. Part. Nucl. Phys.* 50 (2003), page 153 (cited on page 259).

[Ram+96] E. Ramakrishnan *et al.* "Giant Dipole Resonance Built on Highly Excited States of ^{120}Sn Nuclei Populated by Inelastic α Scattering". In: *Phys. Rev. Lett.* 76 (12 Mar. 1996), pages 2025–2028 (cited on page 260).

[SB06] D. Santonocito and Y. Blumenfeld. "Evolution of the giant dipole resonance properties with excitation energy". In: *The European Physical Journal A - Hadrons and Nuclei* 30.1 (2006), pages 183–202. DOI: 10.1140/epja/i2006-10116-7 (cited on page 260).

[ST07] A. Schiller and M. Thoennessen. "Compilation of giant electric dipole resonances built on excited states". In: *Atom. Data Nucl. Data. Tab.* 93 (2007), page 549 (cited on page 260).

[Sie17] K. Sieja. "Electric and Magnetic Dipole Strength at Low Energy". In: *Phys.Rev. Lett.* 119 (2017), page 052502 (cited on page 259).

[Vre+12] D. Vretenar *et al.* "Low-energy isovector and isoscalar dipole response in neutron-rich nuclei". In: *Phys. Rev. C* 85 (4 Apr. 2012), page 044317. DOI: 10.1103/PhysRevC.85.044317 (cited on page 260).

[Wan+21] M. Wang *et al.* "The Ame2020 atomic mass evaluation". In: *Chin. Phys. C* 45 (2021), page 030003 (cited on page 259).

[Wat+19] D. Watson *et al.* "Identification of strontium in the merger of two neutron stars Identification of strontium in the merger of two neutron stars". In: *Nature* 574 (2019), page 497 (cited on page 259).

[Wu+17] J. Wu *et al.* In: *Phys. Rev. Lett.* 118 (7 Feb. 2017), page 072701 (cited on page 259).

[Xia+18] X. Xia *et al.* "The limits of the nuclear landscape explored by the relativistic continuum Hartree–Bogoliubov theory". In: *Atomic Data and Nuclear Data Tables* 121-122 (2018), pages 1–215. ISSN: 0092-640X (cited on page 259).

[Xu+14] Q. Xu *et al.* "Positron beam facility at Kyoto University Research Reactor". In: *Journal of Physics: Conference Series* 505 (2014), page 012030. DOI: 10.1088/1742-6596/505/1/012030. URL: https://doi.org/10.1088%2F1742-6596%2F505%2F1%2F012030 (cited on page 259).

[Yük+17] E. Yüksel *et al.* "Multipole excitations in hot nuclei within the finite temperature quasiparticle random phase approximation framework". In: *Phys. Rev. C* 96 (2 Aug. 2017), page 024303. DOI: 10.1103/PhysRevC.96.024303 (cited on page 260).

[Yük+19] E. Yüksel *et al.* "Nuclear excitations within microscopic EDF approaches: Pairing and temperature effects on the dipole response". In: *Eur. Phys. J. A* 55 (2 2019), page 230 (cited on page 260).

5.5 Theoretical study for an all-optical vacuum birefringence measurement experiment at ELI-NP

Ataman S.[1,*]

[1] Extreme Light Infrastructure (ELI-NP) & Horia Hulubei National Institute for R & D in Physics and Nuclear Engineering (IFIN-HH), Str. Reactorului No. 30, 077125 Bucharest–Măgurele, Romania

[*] **stefan.ataman@eli-np.ro**

Abstract

An all-optical vacuum birefringence experiment becomes closer to feasibility as multi-petawatt class laser facilities come into existence around the world. Intensities in the order of $I_L \sim 10^{23}$ V/m can be expected in a focused spot size $\sim 3\,\mu$m. We discuss an all-optical interferometric scheme of Mach-Zender type and study its phase sensitivity. The goal is to arrive at the optimum interferometric scheme to maximize the sensitivity so that a vacuum birefringence experiment becomes feasible.

5.5.1 Introduction

Vacuum birefringence (VBir) [BB70; KN64; MP63] is one of the QED predictions yet to be tested in a lab environment. A consequence of the Heisenberg-Euler effective Lagrangian [EK35; HE36; Sch51], to this day the only experimental evidence comes from astrophysical events [Mig+17], with some doubts [Cap+17] still existing.

On the terrestrial experimental side, one must mention the purely magnetic field VBir experimental efforts [Bak+98; Cad+14; Ejl+20; IZ79; Mei+10]. The PVLAS collaboration reported more sensitive measurements gradually [Del+14; Del+16; Zav+12] placing their experimental sensitivity at a factor of 50 above the QED limit, with no vacuum birefringence signal detected.

However, the advent of ultra-short petawatt class lasers completely changed the paradigm [Di +12], leading to the availability of unprecedented electric/magnetic field intensities. While 1 PW laser facilities are almost commonplace, multi-PW lasers have been already reported: GIST [Sun+17] (4.2 PW in 2017), ELI-NP [Gal+18; Lur+20] (10 PW in 2020). Focused intensities of 2×10^{22} W/cm^2 [Yan+08] have been obtained already more than a decade ago while 5.5×10^{22} W/cm^2 was recently reported [Yoo+19]. The upcoming EP-OPAL [Zue+14] facility is expected to go beyond these values for a maximum pulse power of 75 PW.

The prospect of these high intensities and their configuration (perpendicular E and B fields, both perpendicular to the probe beam propagation) makes vacuum birefringence a compelling experimental proposal. Indeed, in this scenario, one has a magneto-electric birefringence in the quantum vacuum, a discussed by Rikken and Rizzo [RR00; RR03].

A Mach-Zehnder-based interferometric proposal was introduced in reference [Ata18] and its experimental feasibility was estimated for classical light probe beams as well as for non-classical (squeezed light) probes. It was shown that such a measurement is actually feasible under reasonably optimistic experimental assumptions.

We review this proposition in the following and also show possible evolutions, including more complicated input states and non-balanced interferometers.

5.5.2 All-optical interferometric setup

In the following we detail a vacuum birefringence experimental proposals based on a Mach-Zehnder interferometer [Ata18] (see also Figure 5.5.1).

We assume a (weak) probe beam propagating through a disturbed vacuum. We assume the vacuum is disturbed by a strong (multi PW-class) counter-propagating laser. Taking into account the magneto-electric effect [RR00], too, the probe beam parallel ($\parallel$) or perpendicular ($\perp$) to the PW laser polarization sees a refraction index [Ata18; LP05; RR03]

$$\left\{ \begin{array}{c} n_{QED,\parallel} \\ n_{QED,\perp} \end{array} \right\} = 1 + 2\xi \times \left\{ \begin{array}{c} 4 \\ 7 \end{array} \right\} \times E_L^2 \quad (5.5.1)$$

where $n_\parallel$ ($n_\perp$) is the vacuum refraction index when the probe beam's polarization is parallel (perpendicular) to the pump beam's polarization and we have the constant [Ata18; LP05]

$$\xi = \frac{\hbar e^4}{180\pi\varepsilon_0 m_e^4 c^7} \approx 9.2039\times10^{-41} \quad \frac{\mathrm{m}^2}{\mathrm{V}^2}. \quad (5.5.2)$$

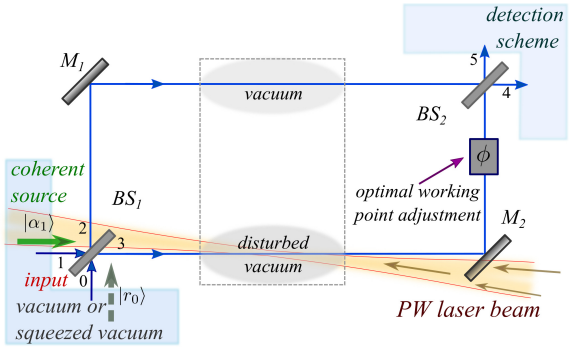

Figure 5.5.1: *Mach-Zender experimental setup of the proposed all-optical vacuum birefringence experiment.*

Consider the probe beam (of wavelength λ_p and frequency $\omega_p = 2\pi c/\lambda_p$) counter-propagating (see Figure 5.5.1) over a length $b = 2z_R$ (depth of focus) with a pump laser that disturbed the vacuum where $z_R = \pi w_0^2/\lambda_L$ is the Rayleigh distance. Here λ_L is the pump laser wavelength and w_0 the Gaussian beam's waist. The phase shift of this beam in respect with the same beam propagated in an unperturbed vacuum is $\Delta\varphi_{QED,\parallel/\perp} = \omega_p b/c\left(n_{QED,\parallel/\perp} - 1\right)$ and plugging in the the values from Eq. (5.5.1) yields

$$\left\{ \begin{array}{c} \Delta\varphi_{QED,\parallel} \\ \Delta\varphi_{QED,\perp} \end{array} \right\} = \frac{8\pi^2 w_0^2 \xi}{\lambda_p \lambda_L} \times \left\{ \begin{array}{c} 4 \\ 7 \end{array} \right\} \times E_L^2 \quad (5.5.3)$$

For obvious reasons, it is interesting from an experimental point of view to have $\lambda_p \neq \lambda_L$. Throughout the depth of focus we assume a constant electrical field (equal to its maximum specified value, E_L). We assume $E_L \sim 10^{15}$ V/m. For a probe wavelength $\lambda_p = 532$ nm, a pump laser wavelength $\lambda_L = 820$ nm and a waist size of $w_0 \approx 3\mu$m, the QED-predicted phase shifts are

$$\left\{ \begin{array}{c} \Delta\varphi_{QED,\parallel} \\ \Delta\varphi_{QED,\perp} \end{array} \right\} \approx \left\{ \begin{array}{c} 6 \\ 10 \end{array} \right\} \times 10^{-7}. \quad (5.5.4)$$

5.5.2.1 Classical light

The phase sensitivity of an interferometer using classical light (lasers in this case) is lower bounded by the standard quantum limit (SQL) [Cav81; DJK15]

$$\Delta\varphi_{SQL} \geq \frac{1}{\sqrt{\langle N\rangle}} \quad (5.5.5)$$

where $\langle N\rangle$ denotes the average number of photons. Considering a pulsed probe laser of pulse length

$$\tau_p \sim \tau_L \sim 25 \text{ fs} \quad (5.5.6)$$

and requiring

$$\Delta\varphi_{SQL} \sim \Delta\varphi_{QED,\parallel} \sim \Delta\varphi_{QED,\perp} \sim 10^{-7} \quad (5.5.7)$$

we find the needed peak power of the pulsed probe laser [Ata18]

$$P_p = \frac{\hbar\omega_p}{(\Delta\varphi_{SQL})^2 \tau_p} \sim 10 \text{ TW} \quad (5.5.8)$$

Such peak powers for femto-second class lasers are nowadays readily available.

The proposed Mach-Zehnder type interferometer is depicted in Figure 5.5.1. Input port 1 is assumed to be fed with the coherent source (probe laser) while input port 0 is kept in the vacuum state (dark port). This implies the SQL translating into the phase sensitivity (5.5.5). The result can also be confirmed by computing the quantum Fisher information and using the quantum Cramér-Rao bound [API18; DJK15].

Considering the high input (pulse) power, the interferometer is likely to be used with a single-mode intensity [API18; Gar+17], or a balanced homodyne [Ata19; Gar+17] detection scheme. The working point (*i. e.* sweet spot) is tuned via the phase shift ϕ (piezo element, optical trombone *etc.*).

5.5.2.2 Non-classical light

However, the SQL phase sensitivity scaling (5.5.5) can be surpassed by using non-classical states of light [Cav81; DJK15]. Indeed, the ultimate phase sensitivity to be expected from quantum metrology is [DJK15; HB93]

$$\Delta\varphi_{HL} \approx \frac{1}{\langle N\rangle} \quad (5.5.9)$$

also called the Heisenberg limit (HL).

The most promising technique to go beyond the SQL is squeezed light [Cav81; Yue76]. Indeed, one can add squeezed vacuum into the unused port 0, therefore the input state vector can be written as

$$|\psi_{in}\rangle = |r_0\alpha_1\rangle = \hat{S}_0(r)\hat{D}_1(\alpha)|0\rangle \quad (5.5.10)$$

where the squeeze operator is defined by [GK05]

$$\hat{S}_0(r) = e^{\frac{r}{2}\left[\hat{a}_0^2 - \left(\hat{a}_0^\dagger\right)^2\right]} \quad (5.5.11)$$

where $r \in \mathbb{R}^+$ is the squeezing factor. The best achievable phase sensitivity measurement with input state (5.5.10) is [LC13; LC14; PS08]

$$\Delta\varphi_{CSV} \geq \frac{1}{\sqrt{|\alpha|^2 e^{2r} + \sinh^2 r}} \quad (5.5.12)$$

The phase sensitivity $\Delta\varphi_{CSV}$ from Eq. (5.5.12) reaches the Heisenberg limit (5.5.9) only if we impose [PS08]

$$|\alpha|^2 \approx \sinh^2 r \approx \frac{\langle N\rangle}{2} \quad (5.5.13)$$

However, this condition is not realistic in the ultra-high intensity regime, where usually one has $|\alpha|^2 \gg \sinh^2 r$. In this case, for the input state (5.5.10), we have the phase sensitivity

$$\Delta\varphi_{CSV} \approx \frac{e^{-r}}{|\alpha|} = \frac{e^{-r}}{\sqrt{\langle N\rangle}} = e^{-r}\Delta\varphi_{SQL}. \quad (5.5.14)$$

Thus, one can expect from squeezing an improvement in the order of e^{-r} wrt the standard quantum limit. This would amount to roughly one order of magnitude for the squeezing factors reported in the literature.

For from being a theoretical proposal only, enhanced sensitivity via squeezed states is an existing and mature technology as proved by the LIGO and VIRGO gravitational-wave interferometers [Abb+20; Tse+19]

5.5.2.3 Non-balanced Mach-Zehnder interferometer

Although non-balanced interferometers were thought to yield lower performance in terms of phase sensitivity, recent studies [Ata20; Ata22; Zho+20] showed that this assertion is not true especially if an external phase reference is available, as is the case for a homodyne detection scheme.

Thus, a squeezed-coherent plus squeezed vacuum input state applied to a non-balanced interferometer applied to a non-balanced MZI is able to beat the phase sensitivity [Ata20].

These conclusions have been strengthened and extended in reference [Ata22], where it has been shown that the quantum Fisher information for a squeezed-coherent plus squeezed-coherent input state maximized in a non-balanced case, too [Ata22]. While this is not proof that a detection scheme exists, it is a strong incentive to provide it.

5.5.2.4 Discussion about the required tools

The tools required for this proposal are as follows. The central tool is, obviously, the multi PW-class laser. It is assumed that the maximum expected laser intensity ($I \sim 10^{23}$ W/cm^2) translates into a focused maximum electric field of the order $E_L \approx 10^{15}$ V/m. It is also assumed that a suitable focusing mirror will be available. The focused spot size where an almost maximum electric field can be assumed is assumed to be in the order of $\sim 3\ \mu$m.

The proposed experimental setup (Figure 5.5.1) is relying on high-sensitivity interferometry. It is also assumed that the whole setup is in a vacuum, including the detection part. It is assumed that the probe laser's polarization is known and controllable ($\parallel$ and $\perp$ wrt the pump laser).

Due to the smallness of the expected phase shift, seismic isolation and environmental vibration-damping have to be considered, including suspended mirrors by double or multiple pendulums [Aso+04] and eventually employing active actuators [NC08].

The phase sensitivity can be taken beyond the shot-noise limit in future evolutions. The theoretical Heisenberg scaling (5.5.9) seems unrealistic for this experimental setup, however as detailed in equation (5.5.14), improvements can be expected by adding squeezed vacuum [Ata18]. However, additional challenges have to be mentioned when discussing squeezed vacuum sources. The "natural bandwidth" of the OPA (optical parametric amplifier) generated squeezed states is in the tens to hundreds of megahertz [Bre+98; Vah+08; Vah+16]. In this bandwidth range, the record in squeezing has been achieved. However, ultra-broadband squeezed light ($B \sim 13.4$ THz in the telecommunication band $\lambda = 1535$) has been reported [Wak+14]. Therefore, not bandwidth seems to be the problem, but the maximum amount of squeezing in the ultra-broadband case.

5.5.3 Expected scientific impact

QED is indeed an accurate and well-tested theory. Here, one must mention the $g-2$ for the electron 12 digit theory-experiment matching, the Lamb shift, Dellbrück scattering, *etc.*. However, one fundamental process (predicted way before the inception of QED as a theory), namely the 4-field interaction [EK35; HE36] with only photons in both the input and the output states, lacks experimental verification. To this day, to the best of our knowledge, there is no direct experimental evidence of this interaction.

This QED interaction (considered only to first-order since laboratory fields obey $E \ll E_S$ and $B \ll B_S$) implies two effects: light by light scattering and vacuum birefringence (VBir). While the first effect is microscopic, VBir is a macroscopic effect that can be seen as a direct manifestation of the quantum vacuum. The only experiment to date supporting light-by-light scattering in a vacuum is the ALTAS/CMB experiment involving $\gamma-\gamma$ pair emission during Pb-Pb peripheral collisions [Aab+17; Sir+19]. However, this experiment was performed in the high energy domain ($\hbar\omega \gg m_e c^2$), and the involved photons were "quasi-real".

Thus, as we stand today, this purely quantum mechanical effect needs a direct laboratory verification in the low energy regime. Its confirmation would close one of the last QED predictions needing experimental validation. However, this low energy limit

comes with additional benefits since many beyond-SM particles are expected to lie in this regime.

5.5.4 Conclusion

Besides being a major milestone in the high field QED community, a precise result in the low energy vacuum birefringence measurement would probe for axion-like particles [Gra+15], milli-charged particles [GJR06], chameleons/Dark Energy [KW04] as well as certain candidates for Dark Matter [HHK14].

Indeed, the deviation for the QED predictions is not ruled out, and any such experimental result will immediately point to new physics.

The proposed interferometric setup is a radical departure from the already proposed purely magnetic or gamma-ray vacuum birefringence detection experiments. Its main advantage lies in its simplicity and offers the supplementary benefit of future evolutions via non-classical input states.

References

[Aab+17] M. Aaboud *et al.* "Evidence for light-by-light scattering in heavy-ion collisions with the ATLAS detector at the LHC". In: *Nature Physics* 13.9 (Sept. 2017), pages 852–858. DOI: 10.1038/nphys4208 (cited on page 271).

[Abb+20] B. P. Abbott *et al.* "Prospects for observing and localizing gravitational-wave transients with Advanced LIGO, Advanced Virgo and KAGRA". In: *Living Reviews in Relativity* 23 (1 2020), page 3. DOI: 10.1007/s41114-020-00026-9. URL: https://doi.org/10.1007/s41114-020-00026-9 (cited on page 271).

[Aso+04] Y. Aso *et al.* "Stabilization of a Fabry–Perot interferometer using a suspension-point interferometer". In: *Physics Letters A* 327.1 (2004), pages 1–8. ISSN: 0375-9601. DOI: 10.1016/j.physleta.2004.04.066. URL: https://www.sciencedirect.com/science/article/pii/S0375960104006231 (cited on page 271).

[Ata18] S. Ataman. "Vacuum birefringence detection in all-optical scenarios". In: *Phys. Rev. A* 97 (6 June 2018), page 063811. DOI: 10.1103/PhysRevA.97.063811. URL: https://link.aps.org/doi/10.1103/PhysRevA.97.063811 (cited on pages 269–271).

[Ata19] S. Ataman. "Optimal Mach-Zehnder phase sensitivity with Gaussian states". In: *Phys. Rev. A* 100 (6 Dec. 2019), page 063821. DOI: 10.1103/PhysRevA.100.063821. URL: https://link.aps.org/doi/10.1103/PhysRevA.100.063821 (cited on page 270).

[Ata20] S. Ataman. "Single- versus two-parameter Fisher information in quantum interferometry". In: *Phys. Rev. A* 102 (1 July 2020), page 013704. DOI: 10.1103/PhysRevA.102.013704. URL: https://link.aps.org/doi/10.1103/PhysRevA.102.013704 (cited on page 271).

[Ata22] S. Ataman. "Quantum Fisher information maximization in an unbalanced interferometer". In: *Phys. Rev. A* 105 (1 Jan. 2022), page 012604. DOI: 10.1103/PhysRevA.105.012604. URL: https://link.aps.org/doi/10.1103/PhysRevA.105.012604 (cited on page 271).

[API18] S. Ataman, A. Preda, and R. Ionicioiu. "Phase sensitivity of a Mach-Zehnder interferometer with single-intensity and difference-intensity detection". In: *Phys. Rev. A* 98 (4 Oct. 2018), page 043856. DOI: 10.1103/PhysRevA.98.043856. URL: https://link.aps.org/doi/10.1103/PhysRevA.98.043856 (cited on page 270).

[Bak+98] D. Bakalov *et al.* "Experimental method to detect the magnetic birefringence of vacuum". In: *Quantum and Semiclassical Optics: Journal of the European Optical Society Part B* 10.1 (1998), page 239. DOI: 10.1088/1355-5111/10/1/027. URL: http://stacks.iop.org/1355-5111/10/i=1/a=027 (cited on page 269).

[BB70] Z. Bialynicka-Birula and I. Bialynicki-Birula. "Nonlinear Effects in Quantum Electrodynamics. Photon Propagation and Photon Splitting in an External Field". In: *Phys. Rev. D* 2 (1970), pages 2341–2345. DOI: 10.1103/PhysRevD.2.2341. URL: https://link.aps.org/doi/10.1103/PhysRevD.2.2341 (cited on page 269).

[Bre+98] G. Breitenbach *et al.* "Broadband detection of squeezed vacuum: A spectrum of quantum states". In: *EPL (Europhysics Letters)* 44.2 (1998), page 192. DOI: 10.1209/epl/i1998-00456-2. URL: http://stacks.iop.org/0295-5075/44/i=2/a=192 (cited on page 271).

[Cad+14] A. Cadène *et al.* "Vacuum magnetic linear birefringence using pulsed fields: status of the BMV experiment". In: *Eur. Phys. J.* D68 (2014), page 16. DOI: 10.1140/epjd/e2013-40725-9. arXiv: 1302.5389 [physics.optics] (cited on page 269).

[Cap+17] L. M. Capparelli *et al.* "A note on polarized light from magnetars". In: *The European Physical Journal C* 77.11 (Nov. 2017), page 754. ISSN: 1434-6052. DOI: 10.1140/epjc/s10052-017-5342-3. URL: https://doi.org/10.1140/epjc/s10052-017-5342-3 (cited on page 269).

[Cav81] C. M. Caves. "Quantum-mechanical noise in an interferometer". In: *Phys. Rev. D* 23 (8 1981), pages 1693–1708. DOI: 10.1103/PhysRevD.23.1693. URL: https://link.aps.org/doi/10.1103/PhysRevD.23.1693 (cited on page 270).

[Del+14] F. Della Valle *et al.* "First results from the new PVLAS apparatus: A new limit on vacuum magnetic birefringence". In: *Phys. Rev. D* 90.9 (2014), page 092003. DOI: 10.1103/PhysRevD.90.092003 (cited on page 269).

[Del+16] F. Della Valle *et al.* "The PVLAS experiment: measuring vacuum magnetic birefringence and dichroism with a birefringent Fabry–Perot cavity". In: *Eur. Phys. J. C* 76.1 (2016), page 24. DOI: 10.1140/epjc/s10052-015-3869-8 (cited on page 269).

[DJK15] R. Demkowicz-Dobrzański, M. Jarzyna, and J. Kołodyński. "Quantum Limits in Optical Interferometry". In: *Progress in Optics* 60.Supplement C (2015), pages 345–435. DOI: 10.1016/bs.po.2015.02.003 (cited on page 270).

[Di +12] A. Di Piazza *et al.* "Extremely high-intensity laser interactions with fundamental quantum systems". In: *Rev. Mod. Phys.* 84 (3 Aug. 2012), pages 1177–1228. DOI: 10.1103/RevModPhys.84.1177. URL: https://link.aps.org/doi/10.1103/RevModPhys.84.1177 (cited on page 269).

[Ejl+20] A. Ejlli *et al.* "The PVLAS experiment: A 25 year effort to measure vacuum magnetic birefringence". In: *Physics Reports* 871 (2020). The PVLAS experiment: A 25 year effort to measure vacuum magnetic birefringence, pages 1–74. ISSN: 0370-1573. DOI: 10.1016/j.physrep.2020.06.001. URL: https://www.sciencedirect.com/science/article/pii/S0370157320302428 (cited on page 269).

[EK35] H. Euler and B. Kockel. "Über die Streuung von Licht an Licht nach der Diracschen Theorie". In: *Naturwissenschaften* 23 (1935), pages 246–247. DOI: 10.1007/BF01493898 (cited on pages 269, 271).

[Gal+18] S. Gales *et al.* "The extreme light infrastructure—nuclear physics (ELI-NP) facility: new horizons in physics with 10 PW ultra-intense lasers and 20 MeV brilliant gamma beams". In: *Reports on Progress in Physics* 81.9 (2018), page 094301. DOI: 10.1088/1361-6633/aacfe8 (cited on page 269).

[Gar+17] B. T. Gard *et al.* "Nearly optimal measurement schemes in a noisy Mach-Zehnder interferometer with coherent and squeezed vacuum". In: *EPJ Quantum Technology* 4.1 (Apr. 2017), page 4. DOI: 10.1140/epjqt/s40507-017-0058-8. URL: https://doi.org/10.1140/epjqt/s40507-017-0058-8 (cited on page 270).

[GK05] C. Gerry and P. Knight. *Introductory Quantum Optics*. Cambridge University Press, 2005. DOI: 10.1017/CBO9780511791239 (cited on page 270).

[GJR06] H. Gies, J. Jaeckel, and A. Ringwald. "Polarized Light Propagating in a Magnetic Field as a Probe for Millicharged Fermions". In: *Phys. Rev. Lett.* 97 (14 Oct. 2006), page 140402. DOI: 10.1103/PhysRevLett.97.140402. URL: https://link.aps.org/doi/10.1103/PhysRevLett.97.140402 (cited on page 272).

[Gra+15] P. W. Graham *et al.* "Experimental Searches for the Axion and Axion-Like Particles". In: *Annual Review of Nuclear and Particle Science* 65.1 (2015), pages 485–514. DOI: 10.1146/annurev-nucl-102014-022120. URL: https://doi.org/10.1146/annurev-nucl-102014-022120 (cited on page 272).

[HE36] W. Heisenberg and H. Euler. "Consequences of Dirac Theory of the Positron". In: *Z. Physik* 98 (1936), pages 714–732. DOI: 10.1007/BF01343663 (cited on pages 269, 271).

[HB93] M. J. Holland and K. Burnett. "Interferometric detection of optical phase shifts at the Heisenberg limit". In: *Phys. Rev. Lett.* 71 (9 Aug. 1993), pages 1355–1358. DOI: 10.1103/PhysRevLett.71.1355. URL: https://link.aps.org/doi/10.1103/PhysRevLett.71.1355 (cited on page 270).

[HHK14] K. Homma, T. Hasebe, and K. Kume. "The first search for sub-eV scalar fields via four-wave mixing at a quasi-parallel laser collider". In: *Progress of Theoretical and Experimental Physics* 2014.8 (Aug. 2014), page 083C01. ISSN: 2050-3911. DOI: 10.1093/ptep/ptu087. URL: https://doi.org/10.1093/ptep/ptu087 (cited on page 272).

[IZ79] E. Iacopini and E. Zavattini. "Experimental Method to Detect the Vacuum Birefringence Induced by a Magnetic Field". In: *Phys. Lett.* 85B (1979), page 151. DOI: 10.1016/0370-2693(79)90797-4 (cited on page 269).

[KW04] J. Khoury and A. Weltman. "Chameleon Fields: Awaiting Surprises for Tests of Gravity in Space". In: *Phys. Rev. Lett.* 93 (17 Oct. 2004), page 171104. DOI: 10.1103/PhysRevLett.93.171104. URL: https://link.aps.org/doi/10.1103/PhysRevLett.93.171104 (cited on page 272).

[KN64] J. J. Klein and B. P. Nigam. "Birefringence of the Vacuum". In: *Phys. Rev.* 135 (1964), B1279–B1280. DOI: 10.1103/PhysRev.135.B1279. URL: https://link.aps.org/doi/10.1103/PhysRev.135.B1279 (cited on page 269).

[LC13] M. D. Lang and C. M. Caves. "Optimal Quantum-Enhanced Interferometry Using a Laser Power Source". In: *Phys. Rev. Lett.* 111 (17 Oct. 2013), page 173601. DOI: 10.1103/PhysRevLett.111.173601. URL: https://link.aps.org/doi/10.1103/PhysRevLett.111.173601 (cited on page 270).

[LC14] M. D. Lang and C. M. Caves. "Optimal quantum-enhanced interferometry". In: *Phys. Rev. A* 90 (2 Aug. 2014), page 025802. DOI: 10.1103/PhysRevA.90.025802. URL: https://link.aps.org/doi/10.1103/PhysRevA.90.025802 (cited on page 270).

[LP05] A. N. Luiten and J. C. Petersen. "Erratum to: "On detection of vacuum birefringence using intense laser pulses" [Phys. Lett. A 330 (2004) 429]". In: *Phys. Lett. A* 346 (2005), page 385. DOI: 10.1016/j.physleta.2005.08.038 (cited on page 269).

[Lur+20] F. Lureau *et al.* "High-energy hybrid femtosecond laser system demonstrating 2 × 10 PW capability". In: *High Power Laser Science and Engineering* 8 (2020), e43. URL: https://doi.org/10.1017/hpl.2020.41 (cited on page 269).

[MP63] J. Mckenna and P. M. Platzman. "Nonlinear Interaction of Light in a Vacuum". In: *Phys. Rev.* 129 (5 Mar. 1963), pages 2354–2360. DOI: 10.1103/PhysRev.129.2354. URL: https://link.aps.org/doi/10.1103/PhysRev.129.2354 (cited on page 269).

[Mei+10] H.-H. Mei *et al.* "Axion Search with Q & A Experiment". In: *Mod. Phys. Lett.* A25 (2010), pages 983–993. DOI: 10.1142/S0217732310000149 (cited on page 269).

[Mig+17] R. P. Mignani *et al.* "Evidence for vacuum birefringence from the first optical-polarimetry measurement of the isolated neutron star RX J1856.5-3754". In: *Monthly Notices of the Royal Astronomical Society* 465.1 (2017), pages 492–500. DOI: 10.1093/mnras/stw2798 (cited on page 269).

[NC08] K. Numata and J. Camp. "Interferometric testbed for nanometer level stabilization of environmental motion over long time scales". In: *Appl. Opt.* 47.36 (2008), pages 6832–6841. DOI: 10.1364/AO.47.006832. URL: http://ao.osa.org/abstract.cfm?URI=ao-47-36-6832 (cited on page 271).

[PS08] L. Pezzé and A. Smerzi. "Mach-Zehnder Interferometry at the Heisenberg Limit with Coherent and Squeezed-Vacuum Light". In: *Phys. Rev. Lett.* 100 (7 Feb. 2008), page 073601. DOI: 10.1103/PhysRevLett.100.073601. URL: https://link.aps.org/doi/10.1103/PhysRevLett.100.073601 (cited on page 270).

[RR00] G. L. J. A. Rikken and C. Rizzo. "Magnetoelectric birefringences of the quantum vacuum". In: *Phys. Rev. A* 63 (2000), page 012107. DOI: 10.1103/PhysRevA.63.012107 (cited on page 269).

[RR03] G. L. J. A. Rikken and C. Rizzo. "Magnetoelectric anisotropy of the quantum vacuum". In: *Phys. Rev. A* 67 (2003), page 015801. DOI: 10.1103/PhysRevA.67.015801 (cited on page 269).

[Sch51] J. Schwinger. "On Gauge Invariance and Vacuun Polarization". In: *Phys. Rev.* 82 (1951), pages 664–679. DOI: 10.1103/PhysRev.82.664 (cited on page 269).

[Sir+19] A. Sirunyan *et al.* "Evidence for light-by-light scattering and searches for axion-like particles in ultraperipheral PbPb collisions at $\sqrt{s_{NN}} = 5.02$ TeV". In: *Physics Letters B* 797 (2019), page 134826. ISSN: 0370-2693. DOI: 10.1016/j.physletb.2019.134826. URL: https://www.sciencedirect.com/science/article/pii/S0370269319305404 (cited on page 271).

[Sun+17] J. H. Sung *et al.* "4.2 PW, 20 fs Ti:sapphire laser at 0.1 Hz". In: *Opt. Lett.* 42.11 (June 2017), pages 2058–2061. DOI: 10.1364/OL.42.002058. URL: http://ol.osa.org/abstract.cfm?URI=ol-42-11-2058 (cited on page 269).

[Tse+19] M. Tse *et al.* "Quantum-Enhanced Advanced LIGO Detectors in the Era of Gravitational-Wave Astronomy". In: *Phys. Rev. Lett.* 123 (23 Dec. 2019), page 231107. DOI: 10.1103/PhysRevLett.123.231107. URL: https://link.aps.org/doi/10.1103/PhysRevLett.123.231107 (cited on page 271).

[Vah+08] H. Vahlbruch *et al.* "Observation of Squeezed Light with 10-dB Quantum-Noise Reduction". In: *Phys. Rev. Lett.* 100 (3 Jan. 2008), page 033602. DOI: 10.1103/PhysRevLett.100.033602. URL: https://link.aps.org/doi/10.1103/PhysRevLett.100.033602 (cited on page 271).

[Vah+16] H. Vahlbruch *et al.* "Detection of 15 dB Squeezed States of Light and their Application for the Absolute Calibration of Photoelectric Quantum Efficiency". In: *Phys. Rev. Lett.* 117 (11 Sept. 2016), page 110801. DOI: 10.1103/PhysRevLett.117.110801. URL: https://link.aps.org/doi/10.1103/PhysRevLett.117.110801 (cited on page 271).

[Wak+14] K. Wakui *et al.* "Ultrabroadband direct detection of nonclassical photon statistics at telecom wavelength". In: *Scientific Reports* 4 (2014), page 4535. DOI: 10.1038/srep04535. URL: http://dx.doi.org/10.1038/srep04535 (cited on page 271).

[Yan+08] V. Yanovsky *et al.* "Ultra-high intensity- 300-TW laser at 0.1 Hz repetition rate". In: *Opt. Express* 16.3 (Feb. 2008), pages 2109–2114. DOI: 10.1364/OE.16.002109. URL: http://www.opticsexpress.org/abstract.cfm?URI=oe-16-3-2109 (cited on page 269).

[Yoo+19] J. W. Yoon *et al.* "Achieving the laser intensity of 5.5×10^{22} W/cm^2 with a wavefront-corrected multi-PW laser". In: *Opt. Express* 27.15 (July 2019), pages 20412–20420. DOI: 10.1364/OE.27.020412. URL: http://www.opticsexpress.org/abstract.cfm?URI=oe-27-15-20412 (cited on page 269).

[Yue76] H. P. Yuen. "Two-photon coherent states of the radiation field". In: *Phys. Rev. A* 13 (6 June 1976), pages 2226–2243. DOI: 10.1103/PhysRevA.13.2226. URL: https://link.aps.org/doi/10.1103/PhysRevA.13.2226 (cited on page 270).

[Zav+12] G. Zavattini *et al.* "MEASURING THE MAGNETIC BIREFRINGENCE OF VACUUM: THE PVLAS EXPERIMENT". In: *Int. J. Mod. Phys. A* 27.1 (2012), page 1260017. DOI: 10.1142/S0217751X12600172 (cited on page 269).

[Zho+20] W. Zhong *et al.* "Quantum-enhanced interferometry with asymmetric beam splitters". In: *Science China Physics, Mechanics & Astronomy* 63 (2020), page 260312. DOI: 10.1007/s11433-019-1503-0. URL: https://doi.org/10.1007/s11433-019-1503-0 (cited on page 271).

[Zue+14] J. D. Zuegel *et al.* "Status of High-Energy OPCPA at LLE and Future Prospects". In: *CLEO: 2014*. Optical Society of America, 2014, JTh4L.4. DOI: 10.1364/CLEO_AT.2014.JTh4L.4. URL: https://doi.org/10.1364/CLEO_AT.2014.JTh4L.4 (cited on page 269).

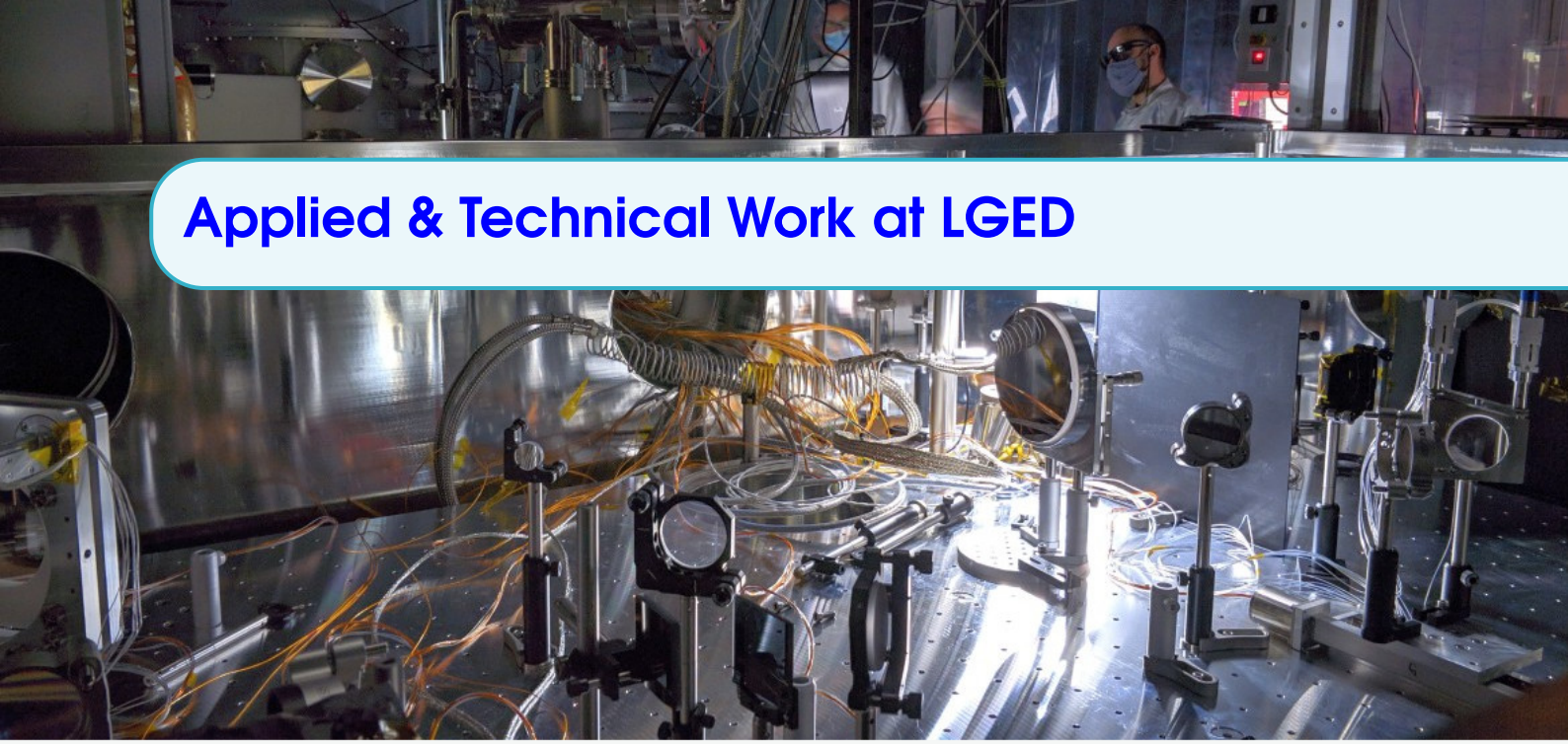

Applied & Technical Work at LGED

5.6 Design and implementation of off-axis parabolic mirror assembly used for 100 TW laser commissioning experiment at ELI-NP

Rodrigues V. R. M.[1,*] , Nakamiya Y.[1,2] , Liviu Neagu[1] , Tamlyn J.[1] , Rosu M. M.[1] , Chiochiu C.[1] , and Tesileanu O.[1]

[1] Extreme Light Infrastructure (ELI-NP) & Horia Hulubei National Institute for R & D in Physics and Nuclear Engineering (IFIN-HH), Str. Reactorului No. 30, 077125 Bucharest–Măgurele, Romania
[2] Institute for Chemical Research, Kyoto University, Uji, Kyoto, 611-0011, Japan

[*] **vanessa.rodrigues@eli-np.ro**

Abstract

Based on experimental requirements, commercially procured motorized stages were adapted into a compact assembly with careful design and tolerances allowing for aberration-free focusing of intense laser beams. Here we also report a robust yet straightforward alignment guide to an off-axis parabolic mirror by precision-tuning along the designed five axes and by following a systematic method to optimize performance. This technique was established for the 100 TW short-pulse laser experiment at ELI-NP designed for an axion-like particle search.

5.6.1 Introduction

In the latter half of 2021, the Laser Gamma Experiments Department at Extreme Light Infrastructure-Nuclear Physics, Măgurele, Romania, carried out a 100 TW laser commissioning experiment of vacuum chamber VE1 in the experimental area E4 – one we fondly call the Dark Matter Search experiment [Ata+17; Tan+20].
Essentially, it required to combine two intense laser beams of different wavelengths. Under the right conditions, the non-linear phenomenon of four-wave mixing will occur to produce a signal and idler beam [Ata+17; Hom+16].
The work depicted herein has focused on the mechanics of this event. The optimum selection of a focusing optical element is critical to this experiment. With options of lenses and curved mirrors available to us, we needed to strategically identify the core specifications of the optical element within the experimental constraints. Keeping in mind that two collinear beams of intense light of different wavelengths and large diameters need to be accurately combined to the same focus, aspheric mirrors and parabolic mirrors in specific were the ideal choices, minimizing non-linear optical effects and aberrations.

Off-axis parabolic mirrors are designed to allow the user to focus an incoming parallel beam of light to an accessible focal point without invading the incident beam path. This presents us with the unique opportunity to tune the focal point using an imaging system placed directly at the focus.

5.6.2 The 5-axes mirror mount assembly

The setup required two off-axis parabolic (OAP) mirrors to be configured in a telescopic arrangement. The internal width of the VE1 chamber was 1600 mm, and while the preferred Y offset for the optical element was calculated to be 500 mm, the designed configuration was set to fit in a 1000 ± 10 mm $\times$ 270 ± 10 mm space. We, therefore, procured a large aperture (6") protected gold mirror with an effective focal length 520 mm and for AOI 7.5° to accommodate the experimental requirements. Furthermore, for the expected incident laser beam height of 225 mm and a diameter of 50 mm to 55 mm, we identified compatible translation stages to complement this parabolic mirror based on its dimension, degrees of freedom, travel range and load capacity from Standa Ltd. to fit this expectation for motion under 1×10^{-6} mbar vacuum.

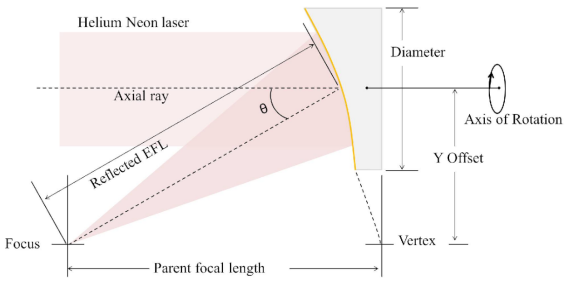

Figure 5.6.1: *Schematic of a parabolic mirror to understand off-axis full angle θ at effective focal length EFL.*

5.6.2.1 Design

With designs in AutoCAD, the appropriate adaptors were machined in-house, and the translation stages were assembled to achieve the standard height of 225 mm with flexibility in tuning. From a mechanical perspective, the assembly simply comprised a base plate, XY stage, XY to vertical stage adaptor plates, vertical stage, a three-piece mirror mount adaptor plate, mirror mount, and another OAP mirror support ring with Teflon supports, as displayed in Figure 5.6.2. The mechanics in green are commercially purchased from Standa, while the mechanics in grey were designed and machined in-house. In addition to these conditions, it was also necessary to consider the fact that the assembly had to be completely automated. In other words, all the stages were to be motorized for remote access control and precision tuning. While the linear translation was managed with stepper motors, the mirror mount control used DC actuators.

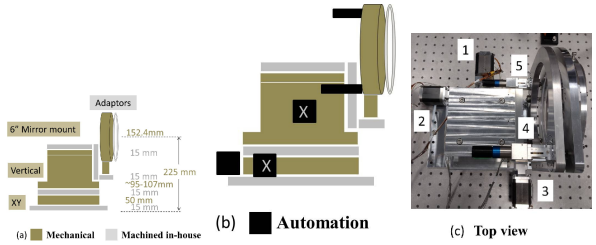

Figure 5.6.2: *(a) Side view of OAP mirror assembly design overview (b) with up to five motorized axes. (c) Top view of the final implemented model with the five (labeled) axes.*

With this design, we successfully drafted and assembled an off-axis parabolic mirror assembly with up to five motorized axes which allowed motion in the horizontal (orthogonal to incident laser beam propagation), longitudinal (in the incident laser beam propagation), vertical, pitch (tip action of the mirror) and yaw (tilt action of the mirror).

The horizontal and vertical translation was for centering, the pitch and yaw were for pointing, while the longitudinal was used for any offset correction.

5.6.2.2 Automation

Each of the stages was supplied with sub-D9 test connectors. Once the initial operation tests for precision and accuracy were completed before use in the assembly, they had to be rewired for use in the vacuum chamber VE1. The need was to connect them through the electrical feedthrough using hermetically sealed bayonet-style connectors of MIL-C-26482 series with crimp contacts. The pins were reassigned based on this 19-way bayonet connector for air-side and in a vacuum. An 8-core stranded cable was used for air-side connection, while the vacuum side cabling was simply rewired with crimp contacts or Kapton insulated wire extensions were made to reach the feedthrough.

The motorized stages were then connected *via* the feedthrough to a multi-axis 8SMC5 motor controller that is Ethernet-based. This allowed monitoring and manipulating the translation stage positions remotely and synchronously using Standa's software XILab. The arrangement is as demonstrated in Figure 5.6.3. In this manner, two assemblies were constructed before commencing full operation tests with loads. Each stage was tested for precision, accuracy, temperature monitoring, establishing translation stage limits, and finally positioning them at the midpoint of the range before the optical tuning study.

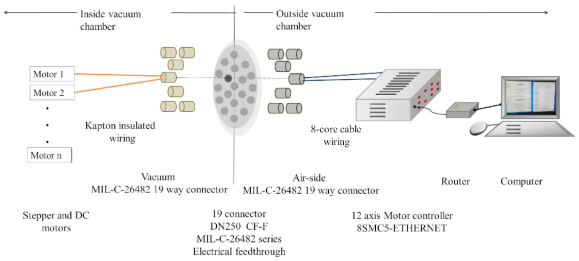

Figure 5.6.3: *Block diagram of the remote access connection of motorized translation stages and mounts for experimental use.*

Due to the shape of the parabola, the thickness of the mirror varies along its diameter. While most mounts are designed to match the standard mirror thickness of 25.4 mm, attempting to fit the parabolic mirror in this design was a challenge. An adaptor ring with Teflon supports was proposed and made to provide a strengthened grip while cushioning vibrations on the mirror during translation.

5.6.2.3 Tuning

Using a helium-neon laser for alignment, the incident beam was expanded to a comparable expected diameter at the height of 225 mm in a two-step beam expansion setup. Once it was confirmed that the incident beam is well collimated, we begin the tuning process to obtain a configuration as shown in Figure 5.6.4

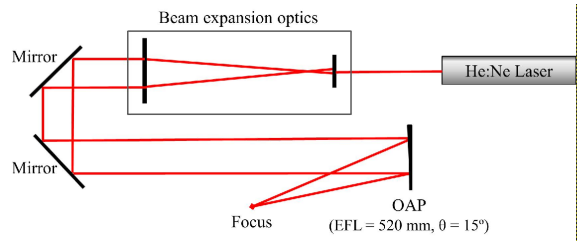

Figure 5.6.4: *Schematic of optical alignment setup with Helium Neon laser.*

In simplest terms, we established a six-step optical alignment approach for the off-axis parabola, the key idea of which is highlighted below.

Firstly, know your reference trajectory. This was achieved using a plane mirror mounted on a rotation stage and a pair of irises inserted such that the laser beam passes clearly through or is incident at its center. Rotate the plane mirror by the expected incident angle of the OAP, thus identifying the expected reflected beam path. The next step is center tuning, where we substituted the plane mirror with the OAP mounted in the assembly, and the laser beam is incident at its center. It can be fine-tuned using the horizontal and vertical translation stages. Then is the need for offset and pointing. Here we observe the new reflected beam being misaligned from the expected trajectory marked earlier since the designed assembly is not at its optimal position. This initial offset can be corrected using the longitudinal translation stage, and any pointing can be adjusted using the yaw and then pitch (if necessary). This next step involves orientation correction. Using the total diameter of the beam, we observed the focus of the OAP using a CMOS camera to spot astigmatism at the focus or at an out-of-focus point, as shown in Figure. 5.6.5 (a). By rotating the OAP clockwise or anticlockwise, astigmatism could be configured to the vertical or horizontal orientation, as shown in Figure 5.6.5 (b). This allowed for more translation range in fine-tuning the focus by fitting into the degrees of freedom of the assembly.

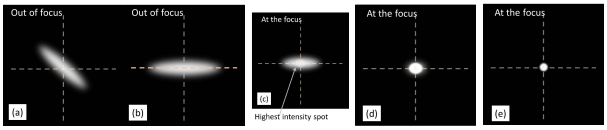

Figure 5.6.5: *Simulated images of expected laser beam spot that can be used as a guidance tool in alignment. An out-of-focus beam spot (a) deviated from desired orientation, and (b) corrected for tuning. A focused laser beam spot (c) with astigmatism, (d) after coarsely adjustment and (e) after fine adjustment to eliminate astigmatism.*

We replaced the CMOS camera with one coupled with an aspheric lens (11 mm) mounted on an XYZ stage to observe the focus. Using an iterative approach, begin the coarse focus adjustment to steadily eliminate astigmatism, as suggested by Figures 5.6.5 (c)-(d), by translating pairs of stages *i. e.*, pitch and vertical, and yaw and horizontal, while maintaining the path line through the irises.

We identified a plane along the laser propagation direction away from the focus and continued fine focus adjustment iteratively to patiently eliminate any remnant astigmatism at this position. Care was also taken to correct any deviation from previous alignment steps. This allowed us to obtain a clean, focused beam, as shown in Figure 5.6.5 (e), without aberrations bearing the smallest spot size and highest intensity spot.

5.6.3 Conclusion

The mechanics and automation of the mirror assembly were designed to meet experimental requirements. First, the off-axis parabolic mirror alignment procedure was established successfully with a helium-neon laser on the optical table, as demonstrated in Figure 5.6.1. Next, the same procedure was repeated for the alignment of the second off-axis parabolic mirror that was to be used in the signal collection path. Following this process, a post-data analysis was conducted on each mirror to measure and optimize the best focusing profiles before the iterative motorized alignment was repeated for the two design wavelengths of the 100 TW laser commissioning experiment.

5.6.4 Acknowledgment

We acknowledge and thank the support of the Technical Division Department personnel who coordinated to meet our requirements for design check and machining parts in-house.

References

[Ata+17] S. Ataman *et al.* "Experiments with combined laser and gamma beams at ELI-NP". In: *AIP Conference Proceedings* 1852.1 (2017), page 070002. DOI: 10.1063/1.4984872. URL: https://aip.scitation.org/doi/abs/10.1063/1.4984872 (cited on page 279).

[Hom+16] K. Homma *et al.* "Combined Laser Gamma Experiments at ELI-NP". In: *Rom. Rep. Phys.* 68 (2016), S233–S274. URL: http://www.rrp.infim.ro/2016_68_S.html (cited on page 279).

[Tan+20] K. A. Tanaka *et al.* "Current status and highlights of the ELI-NP research program". In: *Matter and Radiation at Extremes* 5.2 (Mar. 2020), page 024402. DOI: 10.1063/1.5093535. URL: https://doi.org/10.1063/1.5093535 (cited on page 279).

5.7 Peer-reviewed publications, talks, PhD/MSc, & Grants for LGED in 2020-2021

(Achievements by the Biophysics and Biomedical Applications sub-group of LDED are listed in the next chapter.)

Peer-reviewed publications by LGED staff: 01.01.2020 to 31.12.2021

[Ata21] S. Ataman. "Einstein's time dilation and the relativistic Doppler shift: avoiding the pitfalls". In: *European Journal of Physics* 42.2 (Jan. 2021), page 025601. DOI: 10.1088/1361-6404/abbf3f. URL: https://doi.org/10.1088/1361-6404/abbf3f.

[OGT21] J. F. Ong, P. Ghenuche, and K. A. Tanaka. "Electron transport in a nanowire irradiated by an intense laser pulse". In: *Phys. Rev. Research* 3 (3 Sept. 2021), page 033262. DOI: 10.1103/PhysRevResearch.3.033262. URL: https://link.aps.org/doi/10.1103/PhysRevResearch.3.033262.

[Păl+20] A. M. Pălici *et al.* "OAM tomography with Heisenberg–Weyl observables". In: *Quantum Science and Technology* 5.4 (July 2020), page 045004. DOI: 10.1088/2058-9565/ab9e5b. URL: https://doi.org/10.1088/2058-9565/ab9e5b.

[Set+21] K. Seto *et al.* "Experimental design of radiation reaction by 1 PW laser pulse and linear accelerator electron bunch". In: *High Energy Density Physics* 38 (2021), page 100919. ISSN: 1574-1818. DOI: https://doi.org/10.1016/j.hedp.2020.100919. URL: https://www.sciencedirect.com/science/article/pii/S1574181820301427.

[Taz+20] I. Tazes *et al.* "Target normal sheath acceleration and laser wakefield acceleration particle-in-cell simulations performance on CPU & GPU architectures for high-power laser systems". In: *Plasma Physics and Controlled Fusion* 62.9 (Aug. 2020), page 094005. DOI: 10.1088/1361-6587/aba17a. URL: https://doi.org/10.1088/1361-6587/aba17a.

[ZS21] M. Zeng and K. Seto. "Radiation reaction of betatron oscillation in plasma wakefield accelerators". In: *New Journal of Physics* 23.7 (July 2021), page 075008. DOI: 10.1088/1367-2630/ac12fa. URL: https://doi.org/10.1088/1367-2630/ac12fa.

Invited talks delivered by LGED staff: 01.01.2020 to 31.12.2021

[Jia20a] O. Jian Fuh. "LASER-PLASMA INTERACTION AT RELATIVISTIC INTENSITY AND ITS APPLICATIONS". In: *POPULAR SCIENCE SERIES 30, Universiti Teknologi Malaysia* (2020).

[Jia20b] O. Jian Fuh. "Simulation of high power laser experiments by using high performance computer". In: *EGI Conference 2020* (2020).

[Jia21a] O. Jian Fuh. "Electron transport in the nanowire target irradiated by an intense laser pulse". In: *TARG5 Targetry for High Repetition Rate Laser-Driven Sources Workshop* (2021).

[Jia21b] O. Jian Fuh. "Laser-Plasma Interaction and Its Applications With 10 PW Lasers at ELI-NP". In: *Topical Meeting on Photonics* (2021).

[Jia21c] O. Jian Fuh. "Relativistic High-Power Laser-Matter Interaction and Its Applications". In: *PHYSICS COFFEE TALK, Universiti Sains Malaysia* (2021).

[Set21b] K. Seto. "Theoretical studies on a radiating electron in high-intensity laser pulse". In: *International Conference on High Energy Density Sciences 2021* (2021).

External Grant generation by members of the LGED as PI: 01.01.2020 to 31.12.2021

[Set21a] K. Seto. “Proiectul: PN 19 06 01 05 “Cercetari teoretice si experimentale asupra interactiei campurilor electromagnetice foarte intense cu materia; cercetare-dezvoltare in domeniul tehnologiilor de interes pentru ELI-NP”. Faza: Nr. XXV – „Fenomene stocastice în interacția laser-electron” (Tema 5)”. In: *Nucleu Program* (June 2021).

6. Biophysics and Biomedical Applications (BBA)

THE BIOPHYSICS AND BIOMEDICAL APPLICATIONS (BBA) group is a sub-group of the Laser Gamma Experiments Department (LGED) focused on biomedical applications with a distinct interest in harvesting the unique features to be provided by the high power laser systems for life sciences at ELI-NP, based on the rationale summarized below.

The short timescale of high-power laser pulses opens a new research window for radiobiology research and radiotherapy. Recent studies show that the time window for radiation doses in radiotherapy influences the cellular response. Reactive molecules are generated and persist for different times and in various forms upon radiation. Short bursts of radiation-triggered free radicals have recently been shown to feature low toxicity for healthy tissue in radiobiology studies. Molecular investigations are necessary to fully understand these effects with dose-rate scales ranging from Gy/ms to Gy/ns and generate biomedical applications to exploit them fully. We aim to extend the opportunities that arise from recent progress in pre-clinical and clinical research using high dose rates of radiation, 'FLASH', to laser-accelerated particles and photons. The Biophysics and Biomedical Applications team investigates biomolecular effects of radiation by magnetic resonance and other types of biospectroscopy.

We develop atomic-resolution techniques based on metabolomics and hyperpolarized magnetic resonance to follow reaction kinetics in cells, *in vivo*, and *in vitro* - investigations financed by UEFISCDI projects PCE (PN-III-P4-ID-PCE-2020-2642), and SGS-ERC (SGS-ERC-RO-NO-2019-0010). Molecular transformations triggered by radiation-generated free radicals in cells are followed on different timescales. Both nuclear and electronic magnetic resonance, chromatography techniques, and computational chemistry are employed to discover the molecular basis of radiotherapy to better orient and personalize the treatment. The potential for applications in radiotherapy is developed together with our clinical partners at Amethyst Radiotherapy (collaborators in UEFISCDI project 545 PED 2020 - PN-III-P2-2.1-PED-2019-4212).

Magnetic resonance imaging can similarly follow biological processes *in vitro* and *in vivo*. Our approach affords to translate the findings from bench to bedside, as any results from radiobiology and in-cell NMR investigations can be applied immediately in collaboration with our current partners in clinics to a radiotherapy setting with MRI follow-up. An accurate molecular assessment of the effectiveness and reduction in toxicity afforded by high dose-rate radiation is thus pursued, up to the dose rates afforded by high-power lasers. As radiation delivery on short time scales is improved, new combinations of photon and particle radiation delivery on cells on different time scales will result. Research on radiobiological effects will be extended to explorations using radiation-enhancers or radioprotective drugs. The adjuvant effect of both chemotherapy agents and antioxidants will be tried subsequent to FLASH irradiation on cells. The translation step of research findings to the clinic in the framework of current and future collaborations

will indicate new avenues of research. A detailed description of the team and the laboratory is given in: https://www.eli-np.ro/biophysics_lab.php

6.1 Towards FLASH water radiolysis followed by EPR and NMR spectroscopy

Fidel I.[1,3] , Zăgrean-Tuza C.[1,4] , Popescu R.[2] , Tuță C.[2] , Vasilca S.[1,2,5] , Neguț C. D.[2] , Chiricuță I.-C.[6] , Cucoaneș A.[1] , Vodă M. A.[1,*] , and Vasos P. R.[1,3,*]

[1] Extreme Light Infrastructure (ELI-NP) & "Horia Hulubei" National Institute for R & D in Physics and Nuclear Engineering (IFIN-HH), Str. Reactorului No. 30, 077125 Bucharest– Măgurele, Romania
[2] "Horia Hulubei" National Institute for R & D in Physics and Nuclear Engineering (IFIN-HH), Str. Reactorului No. 30, 077125 Bucharest– Măgurele, Romania
[3] Interdisciplinary School for Doctoral Studies, University of Bucharest, 36-46 Mihail Kogălniceanu Bd, RO-050107, Bucharest, Romania
[4] Department of Chemistry, Faculty of Chemistry and Chemical Engineering, Babes-Bolyai University, 11 Arany Janos Street, RO-400028, Cluj-Napoca, Romania
[5] Department of Analytical Chemistry, Faculty of Chemistry, University of Bucharest, 90-92 Panduri, RO-050663, Bucharest, Romania
[6] Amethyst Radiology Therapy Center, 42 Odăii Street, RO-075100, Otopeni, Romania

[*] **mihai.voda@eli-np.ro, paul.vasos@eli-np.ro**

Abstract

High-dose radiotherapy delivered in very short periods (FLASH) is expected to reduce the toxicity on healthy tissue while maintaining tumor response. In the quest to reveal the mechanistic understanding of FLASH, we embarked on a research strategy that considers both primary and secondary effects of radiation on living cells. The generation and evolution of free radicals in water upon irradiation (primary outcome) were studied by Electron Paramagnetic Resonance (EPR), indicating an increased benefit from using proton beams. As secondary effects, the metabolic profile of tumor cells cultures was investigated by Nuclear Magnetic Resonance (NMR) spectroscopy combined with High-Performance Liquid Chromatography (HPLC). Significant changes were observed in the level of metabolites responsible for cell membrane integrity and one-carbon metabolisms, such as choline and sarcosine.

6.1.1 Introduction

Radiation therapy has recently been introduced as the main strategy in many cancer patients' treatment schemes, especially when it comes to radiation-responsive tumour types such as breast, lung, prostate, colon, head, and neck area cancers. The working principle of such therapy is the production of reactive oxygen species via aerobic water radiolysis. Even though the therapeutic effects of such treatment cannot be observed immediately, low-energy electrons and hydroxyl radicals generated during water radiolysis trigger the disruption of cellular metabolism by attacking the DNA, mainly the nucleotide guanine, which has the lowest ionization potential [Sch+18]. Damaged DNA can no longer convey the correct information for protein synthesis, thus gradually altering the cellular metabolism at all levels. Consequently, the irradiated cell is no longer viable, and apoptosis is triggered, resulting in cancer cell death and patient recovery on the curative side. The main drawback of radiotherapy is that in both its application forms (external and internal) healthy cells are also affected, especially when tumour cells exhibit a higher degree of radioresistance. Therefore, the treatment efficacy has to be balanced against toxicity towards neighbouring healthy tissues without completely eliminating the side effects. A very promising radiation strategy, rooted in experimental tests in the 1980's, is the concept of FLASH irradiation. As the name hints, the basis of FLASH irradiation strategy is the application of high doses of radiation during very short periods of time. While conventional radiation therapy uses dose rates of $0.04\,\mathrm{Gy\,s^{-1}}$ over 8 min of irradiation, FLASH strategy employs dose rates of $50\,\mathrm{Gy\,s^{-1}}$ or even higher over 500 ms of irradiation. Proton beams are well-suited to deliver such high and ultra-high dose rates due to their dose distribution described by the Bragg peak, which ensures a precise radiation deposition at cancer tissue while preserving the surrounding healthy ones [Asa+19; Fav+14; VHL19]. While high-energy photon and electron beams are traditionally used in clinical FLASH radiation therapy, laser-driven proton acceleration by Target Normal Sheath Acceleration (TNSA), Radiation Pressure Acceleration (RPA) and Light Sail Acceleration (LSA)

have emerged as very promising acceleration mechanisms [Cha+21], which may find broad applications in clinical radiation therapy in the future.

While FLASH irradiation with laser-accelerated proton beams is truly an auspicious perspective in cancer therapy, the underlying mechanisms of the FLASH effect are still debated. There are two main mechanisms taken into consideration: the formation and recombination pattern of free radicals produced during irradiation and local oxygen depletion. Free radical generation, which starts with the very radiolysis of water and is propagated by cellular targets, is the primary effect of irradiation on cells which further triggers metabolic disruptions that result in cell death. However, an important aspect to point out is the fact that cancer cells generally have a higher basal expression level of antioxidant enzymes, thus rendering DNA deterioration by free radicals more difficult. When it comes to tumour oxygenation, cancer cells are highly adapted to hypoxia so that they skip the Krebs cycle and rely mostly on glycolysis; as such, oxygen depletion as a cause of FLASH effect efficacy should be considered carefully.
The Biophysics team at ELI-NP is part of the Laser Gamma Experiments Department, which aims at studying the primary and secondary effects of high and ultra-high dose irradiation in vitro, made possible by ELI-NP-designed high-power lasers and gamma rays sources pertaining to the FLASH therapy methodology. The main goal is to understand the mechanism of FLASH irradiation and its long-term effects on cancer cells.

6.1.2 Primary Effects

Primary effects of irradiation include the generation of reactive oxygen species following water radiolysis. Electron Paramagnetic Resonance (EPR) spectroscopy can investigate the production of free radicals, a technique that generates characteristic signals for paramagnetic moieties at fixed microwave frequencies while sweeping the magnetic field. As free radicals generated during aerobic water radiolysis, such as H, OH, and O_{2^-}, are reactive and cannot be assessed directly, we employed the spin trapping technique [Mar+17] to determine the nature and concentration of such species produced after irradiation. The produced free radical is trapped by a nitrone-based molecule (Figure 6.1.1 (A), generating a new paramagnetic center with prolonged half-life and a specific splitting pattern to aid identification; qualitative information can be subtracted by double integrating the EPR signal. The signal area is proportional to spin concentration in the sample.

The spin trap of choice, in this case, is BMPO (5-tert-Butoxycarbonyl-5-methyl-1-pyrroline-N-oxide), used to identify free radicals generated after water radiolysis triggered by different dose-rates of gamma rays and proton beams at the partner institution. So far, we identified hydrogen and hydroxyl radicals following water radiolysis by gamma rays, while the proton beams only yielded hydroxyl radicals (Figure 6.1.1) (B). The methodology of the gamma rays has not shown any clear free radical recombination at higher dose rates. However, proton beams-generated high dose rates, already promising future candidates in clinical settings, exhibited a decrease in free radical production, pointing to a likely recombination step. Future perspectives in primary effects assessment involve shifting the radiation protocols towards proton beams at high and ultra-high dose-rates while combining the EPR spectroscopy with fluorescence spectroscopy. The latter enables free radical identification and quantification at very low concentration limits. Tests with spin traps and fluorescent probes in cancer cell lines are also planned.

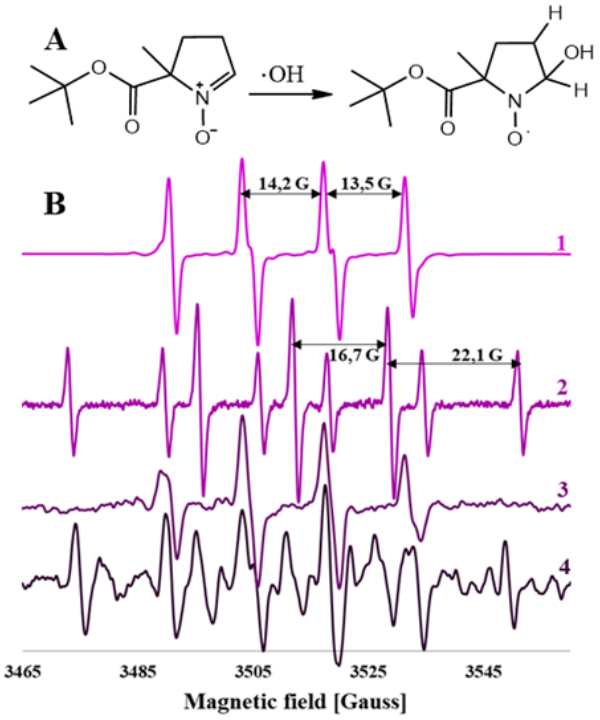

Figure 6.1.1: *A. Structure of the spin trap BMPO (left) and its adduct with hydroxyl radical (right). B. EPR spectra of free radicals in the presence of BMPO (1 is BMPO-OH, 2 is BMPO-H), identified based on splitting pattern and hyperfine coupling constants (in Gauss). Upon irradiation (3- proton beams and 4- gamma rays) various populations of free radicals adducts are obtained.*

6.1.3 Secondary Effects

Secondary effects of radiation are not immediately detected and arise mainly from metabolic disruptions triggered by damaged DNA inability to convey the protein synthesis information correctly. As such, the transient presence of free radicals imprints drastic changes that can be observed in the protein profile of the cells and the (relative) concentration of small metabolites. A possible route to identify new irradiation metabolic markers is Nuclear Magnetic Resonance (NMR) spectroscopy combined with High-Pressure Liquid Chromatography. NMR spectroscopy has gained popularity in metabolomics, as it provides a compositional fingerprint (metabolite fingerprinting) and accurate identification and quantification of metabolites (metabolite profiling). A schematic overview of the NMR workflow for metabolomics research is depicted in Figure 6.1.2. We have employed these techniques to investigate the metabolite profile of cell cultures grown at lab scale and its variation after irradiation. The results were analysed qualitatively and quantitatively, underlining important differences in levels of metabolites related to cellular membrane integrity, such as choline and sarcosine. These NMR metabolomics methods can be employed to map specific metabolic pathways and relate those with radiation protocols, which can be tuned in terms of dose rate and dose magnitude, type of radiation, *etc.* .

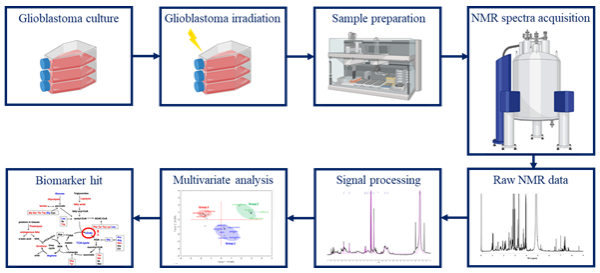

Figure 6.1.2: *NMR-based metabolomics workflow [Gir+14; Sah+20]*

References

[Asa+19] T. Asavei *et al.* "Laser-driven radiation: Biomarkers for molecular imaging of high dose-rate effects". In: *Medical Physics* 46.10 (2019), e726–e734. URL: https://onlinelibrary.wiley.com/doi/abs/10.1002/mp.13741 (cited on page 287).

[Cha+21] P. Chaudhary *et al.* "Radiobiology Experiments With Ultra-high Dose Rate Laser-Driven Protons: Methodology and State-of-the-Art". In: *Frontiers in Physics* 9 (2021), page 75. URL: https://www.frontiersin.org/article/10.3389/fphy.2021.624963 (cited on page 288).

[Fav+14] V. Favaudon *et al.* "Ultrahigh dose-rate FLASH irradiation increases the differential response between normal and tumor tissue in mice". In: *Science Translational Medicine* (2014). URL: https://www.science.org/doi/abs/10.1126/scitranslmed.3008973 (cited on page 287).

[Gir+14] P. Giraudeau *et al.* "Reference and normalization methods: Essential tools for the intercomparison of NMR spectra". In: *Journal of Pharmaceutical and Biomedical Analysis* 93 (2014), pages 3–16. URL: https://www.sciencedirect.com/science/article/pii/S0731708513003269 (cited on page 289).

[Mar+17] V. Marchand *et al.* "Use of a cocktail of spin traps for fingerprinting large range of free radicals in biological systems". In: *PLOS ONE* 12.3 (2017), e0172998. URL: https://journals.plos.org/plosone/article?id=10.1371/journal.pone.0172998 (cited on page 288).

[Sah+20] N. K. Sahoo *et al.* "An overview on NMR spectroscopy based metabolomics". In: *International Journal of Pharmaceutical Sciences and Developmental Research* 6.1 (2020), pages 016–020. URL: https://www.peertechzpublications.com/articles/IJPSDR-6-129.php (cited on page 289).

[Sch+18] R. Schürmann *et al.* "The Physico-Chemical Basis of DNA Radiosensitization: Implications for Cancer Radiation Therapy". In: *Chemistry – A European Journal* 24.41 (2018), pages 10271–10279. URL: https://onlinelibrary.wiley.com/doi/abs/10.1002/chem.201800804 (cited on page 287).

[VHL19] M. Vozenin, J. Hendry, and C. L. Limoli. "Biological Benefits of Ultra-high Dose Rate FLASH Radiotherapy: Sleeping Beauty Awoken". In: *Clinical Oncology* 31.7 (2019), pages 407–415. URL: https://www.sciencedirect.com/science/article/pii/S0936655519301517 (cited on page 287).

6.2 Detection of paramagnetic species by relaxometry in the Earth field and structural characterization of paramagnetic compounds

Topor A.[1,2] , Teleanu F.[1,3] , Cucoaneș A.[1] , Vodă M. A.[1,*] , and Vasos P. R.[1,3,*]

[1] Extreme Light Infrastructure (ELI-NP) & Horia Hulubei National Institute for R & D in Physics and Nuclear Engineering (IFIN-HH), Str. Reactorului No. 30, 077125 Bucharest– Măgurele, Romania
[2] Inorganic Chemistry Laboratory, Faculty of Chemistry, University of Bucharest, 23 Dumbrava Roșie Street, 020464 Bucharest, Romania
[3] Interdisciplinary School for Doctoral Studies, University of Bucharest, 36-46 Mihail Kogălniceanu Bd, RO-050107, Bucharest, Romania

[*] **mihai.voda@eli-np.ro, paul.vasos@eli-np.ro**

Abstract

Nuclear Magnetic Resonance (NMR) can be employed to study the radiolysis of biological samples by means of water signal lifetime dependence on the presence of free radicals with very short lifespans. We investigated the relaxation behaviour of water as a function of the concentration of stable paramagnetic compounds such as TEMPO ($S = 1/2$) and Mn-II ions ($S = 5/2$), using a benchtop Earth-field NMR spectrometer. We have shown that even with low-sensitivity, low-cost portable NMR equipment, we may still accurately monitor the relaxation enhancement at concentrations as low as few μM. To obtain a concentration of 10 μM free radicals, GEANT4-DNA simulations of radiolysis with gamma-rays from ^{60}Co have indicated a necessary dose of approximately 40 Gy. We are also investigating heterobimetallic paramagnetic compounds containing both 3d and 4f metal ions by high-resolution NMR spectroscopy. We aim to develop a strategy to obtain anisotropy data about the electronic spin system and the magnetic easy-axis without direct susceptometry measurements, the goal being to characterize the single-molecule magnet behaviour of such compounds.

6.2.1 Enhanced relaxation of nuclear magnetization in the presence of paramagnetic species

Photon and particle radiations strike the molecular machinery of living organisms mainly via created free radicals, paramagnetic species that can be sensed by spectroscopy at various frequencies. This study aims to identify NMR relaxation agents that are suitable for Earth-Field NMR studies in tandem with a radiolysis experiment on biological samples. The principle at work is the measurement of ^{1}H-NMR relaxation times of water in the presence of paramagnetic compounds [Ber+16] Both longitudinal (T_1) and transverse (T_2) relaxation times can be measured as a function of the concentration of the paramagnetic agent.

The NMR relaxation behaviour of TEMPO and Mn(II) compounds was followed. The first is a $S = 1/2$ species, while the second is a $S = 5/2$ species. The experiments were carried out on a Terranova benchtop NMR (Magritek), using the saturation-recovery and the spin-echo / CPMG pulse sequences for T_1 and T_2 measurements. The results of the NMR relaxation times dependence on the concentration of paramagnetic agent are presented in Figure 6.2.1.

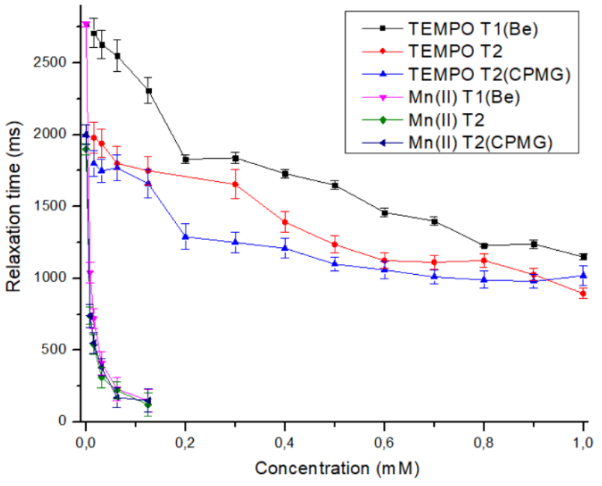

Figure 6.2.1: *^{1}H NMR relaxation time constants of water protons as a function of concentration of paramagnetic agent. Measurements were conducted on a Terranova benchtop Earth-filed NMR spectrometer.*

For characterizing biological samples after radiolysis, it is important to determine the lower concentration

limit at which the paramagnetic agent still exhibits a visible effect on water relaxation. Using TEMPO we can explore regimes down to 15.6 µM at which $T_1 = 2710\,\text{ms}$, and $T_2 = 1980\,\text{ms}$, and with Mn(II) we were able to go down to 7.8 µM with $T_1 = 1040\,\text{ms}$, $T_2 = 740\,\text{ms}$. Preliminary GEANT4-DNA simulations of water radiolysis with gamma-rays from ^{60}Co with suggested that using a dose rate of $1\,\text{Gy}\,\text{y}^{-1}$, we expect $2.47 \times 10^{-7}\,\text{M}\,\text{s}^{-1}$ as a free radical generation rate. To reach the level of 10 µM free radical concentration range, relevant to relaxometry capability Earth-field NMR data, a dose of $\sim 40\,\text{Gy}$ is needed.

6.2.2 Paramagnetic NMR studies of bi-centric paramagnetic compounds

Single-molecule magnets are intensely investigated due to their unique property of slow magnetic relaxation induced by magnetic anisotropy at the molecular scale, which allows for applications in spintronics, information storage, and/or processing. [Cor20] This research starts from compounds previously obtained but which are for the moment challenging to investigate due to their two paramagnetic centers.[Top+21] The goal is to extract anisotropy data about the electronic system from NMR spectroscopy[PPG19] and to attempt to obtain the magnetic easy-axis without direct susceptometry. We have first chosen simpler compounds which are isostructural 3d-4f molecules such as ZnLa and ZnTb published by Towatari *et al.* (Figure 6.2.2 inset) [Tow+13]. Both 1D and 2D NMR spectra have been recorded on ZnLa and ZnTb compounds, only the 1D spectrum of ZnTb is shown in Figure 6.2.2. With only the solvent signal unambiguously assigned, it is impossible to assign any proton signals inside the molecule from a first-hand look due to the strong paramagnetic anisotropy that induces both strong upshifts and downshifts in the ^{1}H signals. 2D spectroscopy for the moment is problematic as only the aromatic region shows correlations. Further experimental tweaking by lowering the delay times may be needed in the future.

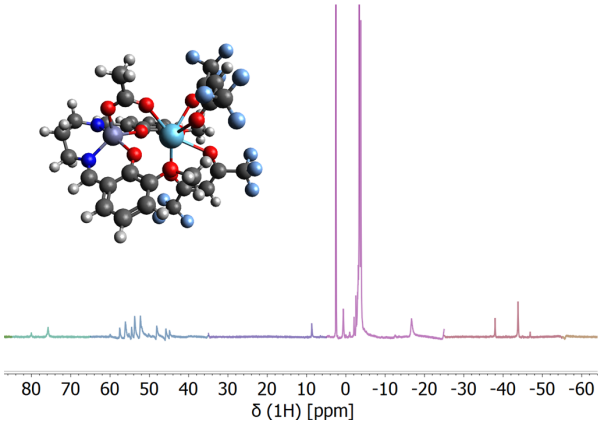

Figure 6.2.2: *1D ^{1}H NMR spectrum of ZnTb compound. Notice the large spectral dispersion of the protons' resonances due to the paramagnetic Tb centre*

References

[Ber+16] I. Bertini *et al. NMR of Paramagnetic Molecules: Applications to Metallobiomolecules and Models*. Elsevier, 2016. 510 pages. ISBN: 978-0-444-63448-1 (cited on page 291).

[Cor20] E. Coronado. "Molecular magnetism: from chemical design to spin control in molecules, materials and devices". In: *Nature Reviews Materials* 5 (2020). URL: https://www.nature.com/articles/s41578-019-0146-8 (cited on page 292).

[PPG19] A. Pell, G. Pintacuda, and C. Grey. "Paramagnetic NMR in solution and the solid state". In: *Progress in Nuclear Magnetic Resonance Spectroscopy* 111 (2019), pages 1–271. URL: https://www.sciencedirect.com/science/article/pii/S0079656517300523 (cited on page 292).

[Top+21] A. Topor *et al.* "Design of FeIII-LnIII binuclear complexes using compartmental ligands: synthesis, crystal structures, magnetic properties, and ab initio analysis". In: *Journal of Materials Chemistry C* 9.33 (2021), pages 10912–10926. URL: https://pubs.rsc.org/en/content/articlelanding/2021/tc/d1tc00894c (cited on page 292).

[Tow+13] M. Towatari *et al.* "Syntheses, Structures, and Magnetic Properties of Acetato- and Diphenolato-Bridged 3d–4f Binuclear Complexes [M(3-MeOsaltn)(MeOH)x(ac)Ln(hfac)2] (M = ZnII, CuII, NiII, CoII; Ln = LaIII, GdIII, TbIII, DyIII; 3-MeOsaltn = N,N'-Bis(3-methoxy-2-oxybenzylidene)-1,3-propanediaminato; ac = Acetato; hfac = Hexafluoroacetylacetonato; x = 0 or 1)". In: *Inorganic Chemistry* 52.10 (2013), pages 6160–6178. URL: https://doi.org/10.1021/ic400594u (cited on page 292).

6.3 Peer-reviewed publications, talks, PhD/MSc, & Grants for BBA in 2020-2021

Peer-reviewed publications by BBA staff: 01.01.2020 to 31.12.2021

[Sad+20] A. Sadet *et al.* "Applications of Singlet Order to the Study of Biomolecules and Molecular Interactions". In: *LONG-LIVED NUCLEAR SPIN ORDER: THEORY AND APPLICATIONS*. Edited by G. Pileio. Volume 22. New Developments in NMR. 2020, pages 248–265. ISBN: 978-1-78801-997-2; 978-1-78801-568-4.

[Tan+20] K. A. Tanaka *et al.* "Current status and highlights of the ELI-NP research program". In: *Matter and Radiation at Extremes* 5 (Mar. 2020). DOI: 10.1063/1.5093535. URL: https://doi.org/10.1063/1.5093535.

[TSV21] F. Teleanu, A. Sadet, and P. R. Vasos. "Symmetry versus entropy: Long-lived states and coherences". In: *Progress in Nuclear Magnetic Resonance Spectroscopy* 122 (Feb. 2021), pages 63–75. DOI: 10.1016/j.pnmrs.2020.12.002. URL: https://doi.org/10.1016/j.pnmrs.2020.12.002.

[TV21] F. Teleanu and P. R. Vasos. "Mechanisms of coherent re-arrangement for long-lived spin order". In: *Magnetic Resonance* 2 (Oct. 2021), pages 741–749. DOI: 10.5194/mr-2-741-2021. URL: https://doi.org/10.5194/mr-2-741-2021.

[Tel+20] F. Teleanu *et al.* "Magnetization Lifetimes Prediction and Measurements Using Long-Lived Spin States in Endogenous Molecules". In: *Molecules* 25 (Nov. 2020). DOI: 10.3390/molecules25235495. URL: https://doi.org/10.3390/molecules25235495.

[Tel+21] F. Teleanu *et al.* "Rotating-Frame Overhauser Transfer via Long-Lived Coherences". In: *SYMMETRY-BASEL* 13.9 (Sept. 2021). DOI: 10.3390/sym13091685.

Invited talks delivered by BBA staff: 01.01.2020 to 31.12.2021

[Vas21a] P. Vasos. "Dynamic Nuclear Polarisation with high resolution detection , Long Lived States and Coherences emerging concepts in Magnetic Resonance considerations on their potential for the community". In: *Processes in Molecules Symposium, ITIM Cluj-Napoca*. 2021.

[Vas21c] P. Vasos. "TBA". In: *Central European Physical Chemistry Conference CEEC-PHYSCHEM„ (Rescheduled)*. 2021.

External Grant generation by members of the BBA as PI: 01.01.2020 to 31.12.2021

[MC20] G. Manda and A. Cucoanes. "PN III/Programul 5/Subprogramul 5.1 - ELI-RO: Metode biologice avansate pentru investigarea raspunsului la stres al celulelor normale si pre-leucemice iradiate la ELI-NP aplicatii in astrobiologie si radioterapie FLASH / CELLI, (250,000 EUR)". In: *ELI-RO* (2020).

[Vas20] P. Vasos. "PN-III-P2-2.1-PED-2019-4212: Apparatus for real-time detection of molecular effects in cells irradiated with different dose-rates: towards online observation of radiobiological effects of laser-driven radiation (640,000 Lei)". In: *PED* (Nov. 2020).

[Vas21b] P. Vasos. "PN-III-P4-ID-PCE-2020-2642: Water hyperpolarization for radiation biomarkers (1,190,530 Lei)". In: *PCE* (Jan. 2021).

[ZV20] B. Zorila and P. Vasos. "Post-Doctoral Project Nr. PD 42 / 2020: Efectele extractelor de propolis asupra membranelor lipidice bio-mimetice - o abordare biofizica avansata, (50,000 EUR)". In: *PD* (2020).

7. Target Laboratory (TL)

THE TARGET LABOARTORY (TL) group is an independent group at ELI-NP and constitutes the most complex laboratory in the division. The Target Laboratory, has a strong research component to develop special materials used as targets in experiments.

The laboratory comprises a gamut of state-of-the-art equipment and a specialized team of material scientists and engineers. First and foremost, it caters to the demands of targets and provides support throughout an experiment's entire implementation process. This spans from the proposal evaluation of the target assembly to the technical feasibility to target delivery. Along with those procedures, R&D activities are continuously developed and upgraded to novel target designs where applicable.

The manufacturing process starts after establishing the procedure in correlation with the research process. The Target Laboratory, currently encompassing 315 m^2 area of cleanroom-environment (ISO 6 and ISO 7), is dedicated to the development, fabrication, characterization, and micro-assembly of targets for experiments with high power lasers and gamma beams. In-house production of targets (within ELI-NP's Target Laboratory) results in a series of benefits. First and foremost, one can directly develop the specified targets in collaboration with the project leads of acknowledged experiments. Other advantages include the avoidance of damage to fragile targets (which usually occurs during transportation), meeting specific target requirements in terms of chemical stability and purity, and ongoing optimization of target key parameters. Besides that manifold of options, one should emphasize the possibilities of the custom-made specimen and last-moment modifications and adjustments of the targets. Additionally, there exist the possibility of in-situ target characterization and bulk production to reduce manufacturing costs due to the in-house development of technologies and methodologies.

7.1 ELI-NP Target Laboratory research infrastructure - update

Gheorghiu C. C.[1] , Ionescu S. C.[1] , Zai I.-M.[1] , Popa D.[1] , and Leca V.[1,*]

[1] Extreme Light Infrastructure (ELI-NP) & Horia Hulubei National Institute for R & D in Physics and Nuclear Engineering (IFIN-HH), Str. Reactorului No. 30, 077125 Bucharest– Măgurele, Romania

[*] **victor.leca@eli-np.ro**

Abstract

Embedded within the ELI-NP's Scientific Division, the Target Laboratory is dedicated to the development, fabrication, characterization and micro-assembly of solid targets used in high-power lasers and gamma beams experiments. Accommodating a wide range of state-of-the-art equipment and methods, the Targets Laboratory is set up to address demands for targets and provide support throughout the entire process, from proposal evaluation to technical feasibility and target delivery. Moreover, R&D activities are continuously performed to develop and upgrade improved novel target designs. Several upgrades of the existing equipment and newly implemented capabilities are presented. In addition to these activities, precise micromechanical structures and custom-made assemblies are frequently manufactured to meet the high technical specifications of the required targets and equipment.

7.1.1 Introduction

The on-site Target Laboratory is currently encompassing 315 m^2 area of ISO 6 and ISO 7 cleanroom-environment. Divided into six rooms specifically dedicated to their embedded techniques and purposes, it includes a wide variety of state-of-the-art equipment dedicated to manufacturing, analysis, and micro-machining processes [Ghe+16]:

- FABRICATION ROOM AND LITHOGRAPHY ROOM contains: *i)* several deposition techniques, such as ultra-high vacuum (UHV) sputter deposition system, for thin and thick film deposition of metals, oxides, and nitrides, equipped with ion milling source, and metal nanoparticle deposition tool (NanoGen); UHV e-beam deposition system, for fabrication of thin and ultrathin metallic films; a spin-coating system, for polymer-based films/coatings; *ii)* various structuring techniques, such as reactive ion etching (RIE) tool for chemical and physical etching of semiconductors and dielectrics materials; an Ar-ion milling unit, part of the UHV sputter system, for precise dry etching; *iii)* setups for photolithography with UV-light, including: a spin coater, a mask aligner, and hot plates, for target structuring by pattern transfer via a mask, with a lateral resolution down to 500 nm; an Electron Beam Lithography (EBL) unit for structuring custom patterns with sub-50 nm resolution.
- CHARACTERIZATION ROOM includes several analysis tools, such as: X-ray diffractometer (XRD) for microstructural characterization, crystal structure determination (phase, orientation, lattice parameters), X-ray reflectivity, SAXS/USAXS, microfocus, of a wide variety of samples, either as films, bulk, nanoparticles, or powders; Scanning Electron Microscope (SEM) for morphological and microstructural characterization (topography, morphology), local composition (elemental analysis with an Energy Dispersive Spectroscopy detector), and microstructural-crystallographic analysis (Electron Backscatter Diffraction detector); Atomic Force Microscope (AFM), for atomic resolution morphology, texture, roughness measurements; and optical profilometry analysis with white-light interferometry, for fast 2D/3D surface profiling, morphology, roughness, thickness determination, and interface characteristics (step height, flatness, depth, waviness, curvature, *etc.*).
- CHEMISTRY ROOM incorporates two ovens (a tubular oven and a calcination oven) used for thermal treatments of the substrates under vacuum, air, or controlled atmosphere gas; chemical fumes, for safe handling of chemicals; pH-meters; ultra-pure water systems; an analytical balance.

- MICRO-MECHANICAL/MICRO-ASSEMBLY ROOM encompasses several optical microscopes and several tools for precision mechanics and micro-machining processing of targets, accompanied by a set of related accessories (orientation fixtures and parts, devices, tool holders, tools).
- STORAGE ROOM is dedicated to and equipped for safe storage of chemical solutions, glassware, accessories, and consumables needed for the laboratory activities.

7.1.2 Updated capabilities and methods

In addition to the wide variety of the existing equipment and methods in the Target Laboratory, new tools and capabilities have been implemented during the last year. This way, new complementary activities were developed related to surface treatments, microprocessing operations, and novel target fabrication research strategies using electrochemical methods. Among them, we can briefly describe a selection of the most important:

- ELECTROCHEMICAL SETUP (Figure 7.1.1) consisting of a water-cooled double-jacketed electrochemical cell with a two-electrode system, a DC power supply (PSU 400–3.8, GW Instek), 2 bench-top multimeters (Peaktech 4075) for current and voltage monitoring connected to a PC interface, a four channels oscilloscope (Siglent SDS2204X PLUS) for AC pulsed electrodeposition, a refrigerated heating circulator bath (Huber CC508) for temperature control, and an Autolab PGSTAT302N potentiostat, used to control the electrochemical potential in the three-electrode cell, during metallic nanowire growth. The setup is currently used for aluminium anodization resulting in porous alumina, which then can be used either as free-standing targets or as templates for the fabrication of metallic nanowires [Ghe+21].

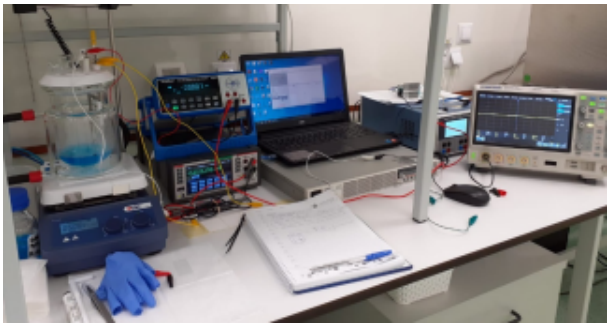

Figure 7.1.1: *Electrochemical setup*

- CUTTING MACHINE (Brilliant 220, QATM), Figure 7.1.2, allows precise wet abrasive cutting operations (precision of 0.001 mm) of wafers or of materials of different geometries.
- LAPPING/POLISHING MACHINE (LamPlan M.M.8400), Figure 7.1.3, allows multiple lapping and polishing applications of wafers or of optical components (lapping, thickness abrasion, grinding, polishing), either for their reconditioning or for improved surface quality (roughness, waviness..). In addition, it includes an automatic dosing unit (M.M.709) for the precise distribution of diamond abrasive suspensions.

Figure 7.1.2: *Cutting machine*

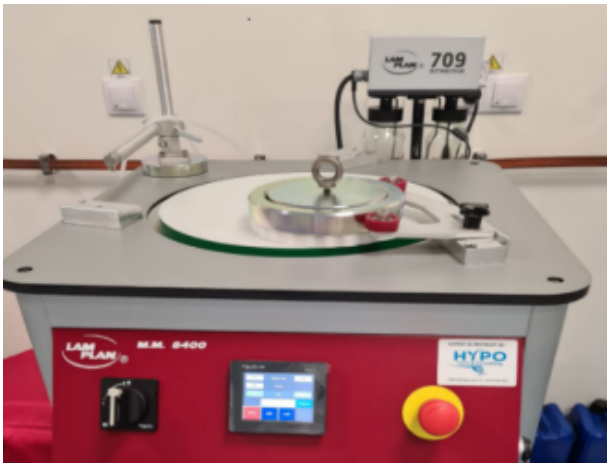

Figure 7.1.3: *Polishing machine*

- BENCHTOP PLASMA TREATMENT SYSTEM (Henniker Plasma HPT-100), Figure 7.1.4, is a tool for mild plasma surface treatment suitable for surface cleaning, etching, surface activation to improve adhesion and surface modification of the different types of materials (polymers, metals, glass, or ceramics), under controlled atmosphere (e.g., air, oxygen, hydrogen, argon, nitrogen). With a 100 mm diameter plasma process chamber, the system is mainly

used to remove the surface contaminants of the wafers before the deposition process.

Figure 7.1.4: *Benchtop plasma treatment system*

- OPTICAL TABLES (ThorLabs) have been purchased in order to provide a thermally stable and rigid (antivibration) base for high-sensitive microscopy analysis (with nanometric resolution), such as atomic force microscopy and optical profilometry. It includes self-leveling active table supports and honeycomb core breadboards.
- BONDING MACHINE (TPT Wire Bonder GmbH) is a thermosonic wedge bonder that will allow the bonding of the wires required to measure the electrical properties of our probes.
- MICROMECHANICAL MACHINES located inside and outside the cleanroom area, includes tools for mechanics operations and micromechanics processing: precision lathe, bench vise, manual press, grinding and drilling machines, metal saw, threading machine, etc. This category includes instrumentation for examination and precision measurements of micromechanical components (optical microscope, micrometers, calipers).

Along with the equipment mentioned above, Target Laboratory has been accommodated with all the necessary raw materials, consumables, accessories, equipment spare parts, laboratory furniture, chemical fumes, as well as safe storage cabinets for the handling of chemicals, making the laboratory fully operational on a wide range of activities related to solid targets production.

7.1.3 MICROMECHANICAL STRUCTURES AND ASSEMBLIES

Micromechanical structures and custom-made assemblies manufactured in the micromechanical room from Target Laboratory are components used for specific targets fabrication or assembly processes for experiments.

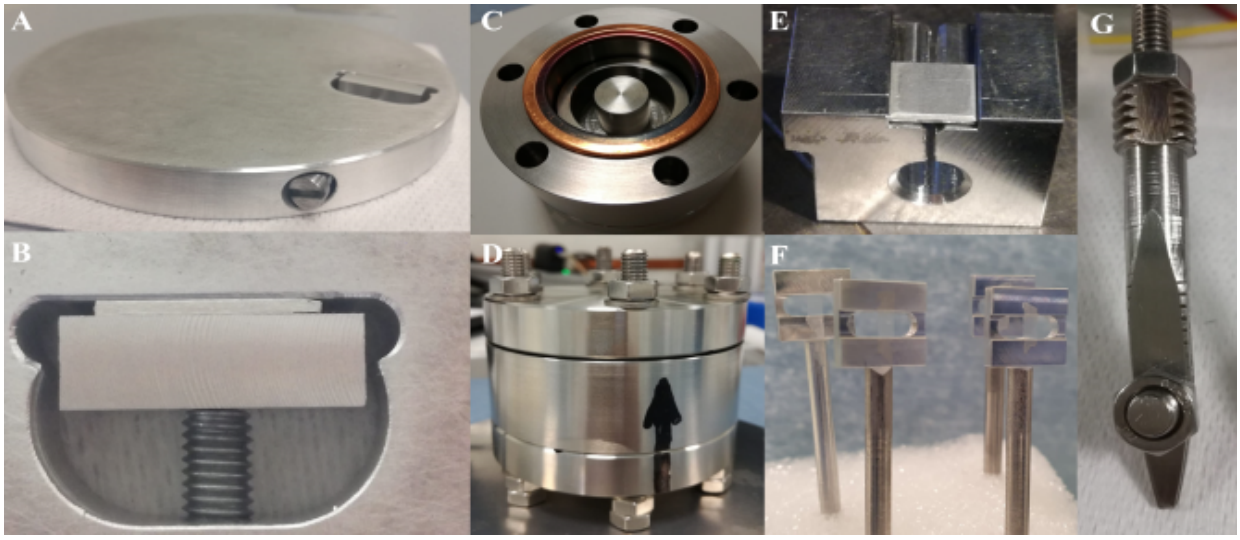

Figure 7.1.5: *(A) and (B) Cross-section polishing tool; (C) and (D) Gas cell; (E) Component for frame manufacturing system; (F) Target frames; (G) Electrode support.*

A selection of these structures is presented in Figure 7.1.5 and are shortly described below:

- CROSS-SECTION POLISHING TOOL This structure allows polishing of the probes after being cut on the cross-section. In addition, it is helpful to reduce the surface roughness below 1 micrometer to be able to observe nanostructures from a lateral view (see Figure 7.1.5 A-B).
- GAS CELL The gas cell is envisaged to be used in the decomposition processes of hydrogen-containing powders under pressure and temperature to obtain hydrogen (see Figure 7.1.5 C-D).

- FRAME MANUFACTURING SYSTEM The frame manufacturing system was developed to be used in the production of target frames for laser experiments (see Figure 7.1.5 E).
- TARGET FRAMES The C-shaped target frames mounted on a stalk are fabricated to support thin targets prepared for laser experiments (see Figure 7.1.5 F).
- ELECTRODE SUPPORT The purpose of the electrode support, made of stainless steel, is to fix the thin aluminium plates used in electrochemical processes in a corrosive electrolyte (see Figure 7.1.5 G).

References

[Ghe+16] C. C. Gheorghiu *et al.* "Overview on the target fabrication facilities at ELI-NP and ongoing strategies". In: *Journal of Instrumentation* 11 (2016). ISSN: 17480221. DOI: 10.1088/1748-0221/11/10/C10011 (cited on page 297).

[Ghe+21] C. C. Gheorghiu *et al.* "Structuring Free-Standing Foils for Laser-Driven Particle Acceleration Experiments". In: *Frontiers in Physics* 9 (2021), page 515. DOI: 10.3389/fphy.2021.727498 (cited on page 298).

7.2 ELI-NP Target Laboratory - research activities

Gheorghiu C. C.[1] , Ionescu S. C.[1] , Zai I.-M.[1] , Popa D.[1] , and Leca V.[1,*]

[1] Extreme Light Infrastructure (ELI-NP) & Horia Hulubei National Institute for R & D in Physics and Nuclear Engineering (IFIN-HH), Str. Reactorului No. 30, 077125 Bucharest– Măgurele, Romania

[*] **victor.leca@eli-np.ro**

Abstract

Several research activities have been performed and are continuously developed within the ELI-NP Target Laboratory, mainly focused on fabrication, simulation, and testing of micro/nanostructured targets. Among them are solid targets for bio-medical and space applications (two elements targets), metallic gratings on thin foils (Au, Cu), nanostructured targets (porous alumina, metallic nanowires), freestanding targets on a large area (single or multiple element targets as (ultra)thin/thick films of metals, nitrides, hydrides, oxides, multilayers, hybrid structures). Material science studies performed within the Target Laboratory comprise several directions, such as developing non-destructive methods (XRD-based) for quantitative analysis of defects concentration in materials – experimental and theoretical studies.

7.2.1 Micro/Nanostructured target strategies

7.2.1.1 Synthesis of freestanding porous alumina and metallic nanowires

Nanowires (NWs) are structures with a high aspect ratio, with diameters of several hundred nanometers or less, with a length of several micrometers to tens of micrometers, which gives them unique magnetic, optic, and electric properties [Liu17] that can be used in new and innovative experiments and applications development. Metallic NWs have many applications in technology, especially electronics [Pat07] but also in biomedicine [SV18], where interaction and influence with different types of cells are studied [Mus+21]. Moreover, with the new development in recent years of the high power laser field, the resulted simulations showed that laser interaction with targets as arrays of aligned NWs could create terabar pressures [Bar+17]. Vertically aligned NWs are nanostructured targets of a high degree of complexity. The technique for their productions falls into two main categories: 'bottom-up', including techniques like Vapor-Liquid-Solid (VLS), Chemical Vapor Deposition, Hydrothermal, Molecular Beam Epitaxy, Electrodeposition; and 'top-down' methods, including Reactive Ion Etching, Metal Assisted Chemical Etching. Particle-in-cell simulations data shows the efficient coupling between high-intensity laser pulses and targets structured with metallic NW "forest". [Val+21] The electrodeposition method was chosen within Target Laboratory to obtain vertically aligned NWs with diameters of tens to hundreds of nanometers and hundreds of nanometers to tens of micrometers in length. The main advantages of the electrodeposition fabrication technique are a) its flexibility, allowing to obtain different characteristics for NWs (metal type, diameter, length, distance between NWs) by modifying the process parameters (anodization voltage and temperature, time, composition of electrodeposition bath) and b) this method does not require costly equipment or extreme conditions. For NWs fabrication, the electrodeposition method uses a template to grow NWs vertically. For this, polycarbonate membranes or anodic aluminum oxide (AAO) can be used as templates, the latter being obtained from aluminum subjected to anodization, during which arrays of nanopores with high aspect ratios are formed [She+13]. The two-step anodization method is used, where the anodizing voltage is maintained constant in both steps, as well as the rest of the parameters (temperature, electrolyte solution, stirring speed), except for the exposure time, which may be changed, accordingly to the desired AAO thickness [Gel+06]. As observed in Figure 7.2.1, after the first anodization step, the alumina layer formed on the aluminum plate is dissolved to produce regular, and aligned templates [Ahm+16]. After the AAO is obtained on the aluminum substrate in a second anodization step, the template is ready to be used as such, with the bottom layer (called "barrier layer") either removed or thinned.

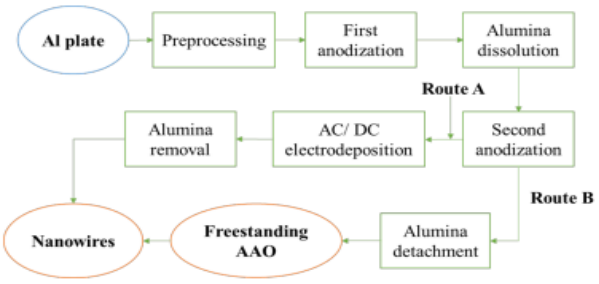

Figure 7.2.1: *Block diagram for NW fabrication process.*

The alumina template can also be detached [Hon+15] from the aluminum substrate (route B) and then used as a target in laser experiments. DC (direct current) or pulsed AC (alternating current) electrodeposition of metallic NWs can be performed for the following step. This process results in an array of metallic NWs of copper, nickel, cobalt, gold, silver, or other metals, or a combination of them, depending on the electrolyte solution. Once the NWs are deposited in the porous template, the alumina can be chemically dissolved, and the ordered array of NWs liberated.

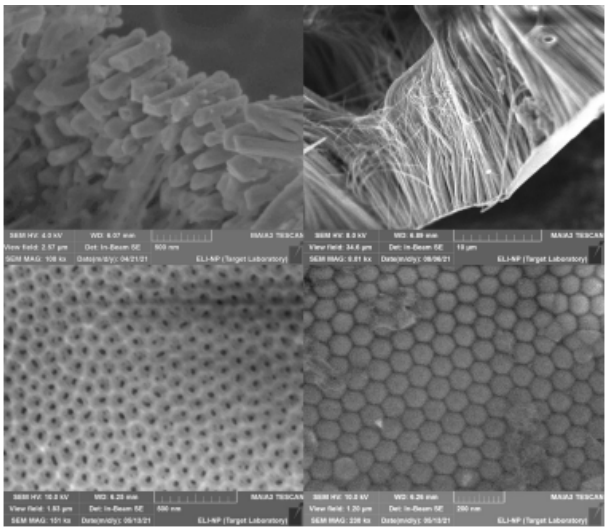

Figure 7.2.2: *Top left: SEM image of short copper NWs (scale 500 nm); Top right: SEM image of 10 µm long copper NWs (scale 10 µm); Bottom left: Front side of AAO (scale 500 nm); Bottom right: back side of AAO (scale 200 nm).*

Cu NWs were deposited in porous alumina template using DC and pulsed AC electrodeposition method, using copper sulfate and boric acid solution, resulting in NWs of 500 nm to 10 µm long and 50 nm to 200 nm in diameter, on an aluminium substrate. For pulsed AC electrodeposition, experiments at different voltages and frequencies have been performed to test the parameters for an optimized deposition process. The freestanding alumina resulted after applying the detachment method of stair-like reverse biases is characterized by a 7 µm to 100 µm thickness range, with a pore diameter of 30 nm to 100 µm and 30 nm to 100 µm of interpore distance. In addition, the parameters for the detachment process (number of stairs and duration of each and final stair, temperature) have been optimized to result in a nearly defect-free, freestanding alumina used in laser experiments. In Figure 7.2.2 SEM images of 500 nm long Cu NWs are shown on the top left, and longer Cu NWs of 10μm on the top right, along with the open pores of the front side of the AAO on the bottom left, and the backside of the barrier layer of the freestanding AAO, on the bottom right. Cu NWs and freestanding alumina templates with or without opened bottom pores are of interest for laser-driven particle acceleration experiments. They will be used at the ELI-NP facility to investigate the improvement of the energy of the accelerated ions at intensities beyond 10^{21} $\frac{W}{cm^2}$ [Ghe+21b].

7.2.1.2 Periodic Gratings on Metallic Foils

Targets with micro-gratings on the irradiated side showed to improve the laser acceleration performances significantly. In the last years, microstructured metallic foils showed a particular interest and are intensively used in high-power laser research (like laser-driven nuclear physics, proton radiography, or initial oncology studies). For this matter, the development and optimization of the manufacturing process within the Target Laboratory [Ghe+21a; Ghe+21b] allowed to successfully obtain one-micron gratings features of two different shapes: rectangle or sinusoidal profile, on self-supporting metallic foils (Au and Cu foils), see Figure 7.2.3.

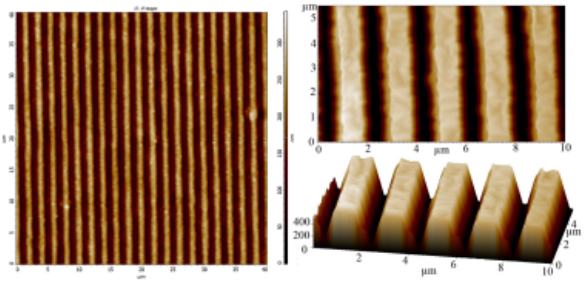

Figure 7.2.3: *AFM images of rectangular profile Au gratings*

Several aspects have been addressed, like foils pre-processing, handling difficulties, and optimization of the engraving procedure, essential for efficient production and improved quality of metallic gratings. The results confirmed that additional preliminary steps, including lamination and dry cleaning

by Ar-ion milling of the foils, lead to a controlled surface structuring and a good topography for the subsequent microstructures. Moreover, experimental and theoretical investigations were undertaken to study the influence of the process's key parameters on the quality of the final patterned foils. This includes a study of the electron-beam lithographic process (employing Monte Carlo simulations), resist development (developer composition, time, and temperature tests), resist removal (different physical and chemical methods), and etching processes (gas flow, etching time, power, cooling time, and sample temperature evaluation) A selection of the fabricated gratings was used in a few experimental studies for investigation of coupling efficiency of the laser energy onto the grating targets and for the acceleration of high energy particle beams (electrons and ions), in collaboration with the Institute of Laser and Plasma Physics at Heinrich-Heine-Universität Düsseldorf. Comparative studies with flat thin foils showed that the electron beams emitted by grating targets could have up to 4 times higher flux, better collimation, and efficiency than compared to flat target foils for emission direction along the target surface. Furthermore, the investigation of protons and carbon ions acceleration showed the influence of flux and cut-off-energy, with enhanced ion beam properties for grating targets. In addition, experimental investigations of the efficiency of the laser energy coupling performed at different laser incidence angles showed that at small incidence angles (up to 30°), the grating targets presented a better laser coupling [Ghe+21a].

7.2.2 Material studies

One of the topics on materials studied of interest within the Target Laboratory relates to studies of structural defects in materials using non-destructive methods, such as X-ray diffraction (XRD) with highly monochromatic, convergent X-ray beam, a tool available within the laboratory. The XRD spectra contains information about the threading dislocations (type, concentration, correlation length), spectra that can be mathematically modeled. A method developed by Kaganer *et al.* [Kag+05], where the tail of the omega scan is fitted using the integral, is the base of the model. The method is currently automatized and implemented within Target Laboratory. Most of the results of these studies are published in several papers (see, *e.g.*, [Ser+21]).

The Target Laboratory also performs theoretical research activities, namely computational calculations using different codes based on density-functional theory (DFT) such as SIESTA, CALYPSO, and ELK. These calculations aim to identify potential new structures in a theoretical manner before studying them experimentally. Additionally, the stabilization studies for crystalline structures at different pressures using the CALYPSO code are then further investigated using the ELK code, using calculation methods that are based on electron-photon interactions.

References

[Ahm+16] N. Ahmad *et al.* "Influence of voltage variation on structure and magnetic properties of Co1x Sn x (X = 0.3–0.7) nanowire alloys in alumina by electrochemical deposition". In: *Applied Physics A* 123 (Dec. 2016). DOI: 10.1007/s00339-016-0682-7 (cited on page 301).

[Bar+17] C. Bargsten *et al.* "Energy penetration into arrays of aligned nanowires irradiated with relativistic intensities: Scaling to terabar pressures". In: *Science Advances* 3.1 (2017), e1601558. DOI: 10.1126/sciadv.1601558 (cited on page 301).

[Gel+06] G. Gelves *et al.* "Multigram Synthesis of Copper Nanowires Using AC Electrodeposition into Porous Aluminum Oxide Templates". In: *J. Mater. Chem.* 16 (July 2006). DOI: 10.1039/B603442J (cited on page 301).

[Ghe+21a] C. C. Gheorghiu *et al.* "Fabrication of micron-sized periodic gratings in free-standing metallic foils for laser-plasma experiments". In: *High Power Laser Science and Engineering* 1-52 (2021). DOI: 10.1017/hpl.2021.57 (cited on pages 302, 303).

[Ghe+21b] C. C. Gheorghiu *et al.* "Structuring Free-Standing Foils for Laser-Driven Particle Acceleration Experiments". In: *Frontiers in Physics* 9 (2021), page 515. DOI: 10.3389/fphy.2021.727498 (cited on page 302).

[Hon+15] Y. K. Hong *et al.* "High-yield and environment-minded fabrication of nanoporous anodic aluminum oxide templates". In: *RSC Adv.* 5 (Mar. 2015). DOI: 10.1039/C5RA00198F (cited on page 302).

[Kag+05] V. M. Kaganer *et al.* "X-ray diffraction peak profiles from threading dislocations in GaN epitaxial films". In: *Phys. Rev. B* 72 (4 2005), page 045423. DOI: 10.1103/PhysRevB.72.045423. URL: https://link.aps.org/doi/10.1103/PhysRevB.72.045423 (cited on page 303).

[Liu17] J. Liu. *Well-Organized Inorganic Nanowire Films: Assemblies and Functionalities*. Springer Theses. Springer Singapore, 2017. ISBN: 9789811039478. URL: https://books.google.ro/books?id=b7c-DgAAQBAJ (cited on page 301).

[Mus+21] V. Mussi *et al.* "Silver-coated silicon nanowire platform discriminates genomic DNA from normal and malignant human epithelial cells using label-free Raman spectroscopy". In: *Materials Science and Engineering: C* 122 (2021), page 111951. ISSN: 0928-4931. DOI: https://doi.org/10.1016/j.msec.2021.111951 (cited on page 301).

[Pat07] F. Patolsky. "Detection, stimulation, and inhibition of neuronal signals with high-density nanowire transistor arrays (vol 313, pg 1100, 2006)". In: *Science* 317 (July 2007), pages 320–320 (cited on page 301).

[Ser+21] A. Serban *et al.* "Studies of Defect Structure in Epitaxial AlN/GaN Films Grown on (111) 3C-SiC". In: *Nanomaterials* 11.5 (2021). ISSN: 2079-4991. DOI: 10.3390/nano11051299. URL: https://www.mdpi.com/2079-4991/11/5/1299 (cited on page 303).

[SV18] A. Serrà and E. Vallés. "Advanced electrochemical synthesis of multicomponent metallic nanorods and nanowires: Fundamentals and applications". In: *Applied Materials Today* 12 (June 2018). DOI: 10.1016/j.apmt.2018.05.006 (cited on page 301).

[She+13] L. Shen *et al.* "Preparation of anodic aluminum oxide (AAO) nano-template on silicon and its application to one-dimensional copper nano-pillar array formation". In: *Korean Journal of Chemical Engineering* 30 (Jan. 2013). DOI: 10.1007/s11814-012-0124-y (cited on page 301).

[Val+21] S. Vallières *et al.* "Enhanced laser-driven proton acceleration using nanowire targets". In: *Scientific Reports* 11 (Jan. 2021). DOI: 10.1038/s41598-020-80392-0 (cited on page 301).

7.3 Peer-reviewed publications, talks, PhD/MSc, & Grants for TL in 2020-2021

Peer-reviewed publications by TL staff: 01.01.2020 to 31.12.2021

[Ene+20] V. L. Ene *et al.* "Defect Structure Determination of GaN Films in GaN/AlN/Si Heterostructures by HR-TEM, XRD, and Slow Positrons Experiments". In: *Nanonmaterials* 10.2 (Feb. 2020). DOI: 10.3390/nano10020197.

[Ghe+21a] C. C. Gheorghiu *et al.* "Fabrication of micrometre-sized periodic gratings in free-standing metallic foils for laser-plasma experiments". In: *High Power Laser Science and Engineering* 10 (Dec. 2021). ISSN: 2095-4719. DOI: 10.1017/hpl.2021.57.

[Ghe+21b] C. C. Gheorghiu *et al.* "Structuring Free-Standing Foils for Laser-Driven Particle Acceleration Experiments". In: *Frontiers in Physics* 9 (Sept. 2021). ISSN: 2296-424X. DOI: 10.3389/fphy.2021.727498.

[LSD20] V. Leca, N. D. Scarisoreanu, and M. Dinescu. "Microstructural and electrical transport properties of RBa2Cu3O7-delta(R = Y, Pr) based thin films and ramp-type Josephson junctions". In: *Romanian Reports in Physics* 72.3 (2020). ISSN: 1221-1451.

[Ser+21] A. B. Serban *et al.* "Studies of Defect Structure in Epitaxial AlN/GaN Films Grown on (111) 3C-SiC". In: *Nanomaterials* 11.5 (May 2021). DOI: 10.3390/nano11051299.

Invited talks delivered by TL staff: 01.01.2020 to 31.12.2021

[Ion21b] S. Ionescu. "Synthesis of freestanding porous alumina and copper nanowires by electrochemical methods". In: *13th International Conference on Physics of Advanced materials (24-30 September 2021), Sant Feliu de Guixols, Spain*. 2021.

[Ion21c] S. Ionescu. "Synthesis of freestanding porous alumina and copper nanowires for high power laser applications". In: *TARG5 Targetry for High Repetition Rate Laser-Driven Sources Workshop (25-27 October 2021), Dresden, Germany*. 2021.

[Lec21] V. Leca. "ELI-NP Targets Laboratory". In: *ELI Summer School (24-27 August 2021) - ELI Beamlines*. 2021.

[Zai21c] I. Zai. "Threading dislocations study of GaN thin films with XRD". In: *Rigaku XRD Forum - Thin films Workshop (10-13 February 2021), Neu-Isenburg Germany*. 2021.

Successful M.Sc. theses within the TL group: 01.01.2020 to 31.12.2021

[Ion21a] S. Ionescu. "Synthesis of porous alumina and copper NWs by electrochemical methods". Master's thesis. The University Politehnica of Bucharest, 2021.

[Zai21b] I. Zai. "X-ray diffraction investigations of GaN and Sr0.85La0.15CuO2 thin films". Master's thesis. The Faculty of Physics of the University of Bucharest, 2021.

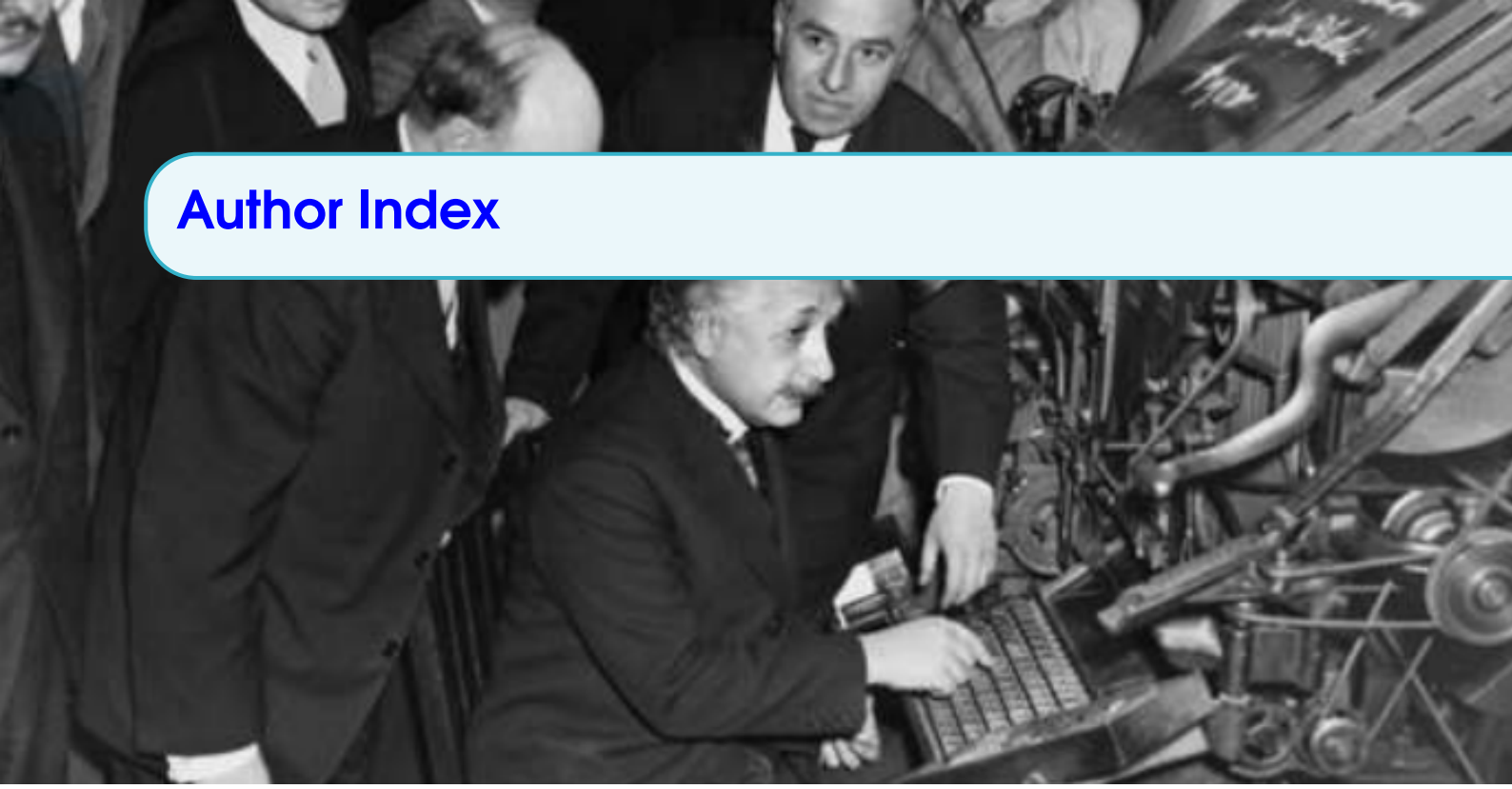

Author Index